UNIVERSIDAD COMPLUTENSE DE MADRID

FACULTAD DE CIENCIAS FÍSICAS

Departamento de Física de la Tierra, Astronomía y Astrofísica II

(Astrofísica y Ciencias de la Atmósfera)

TESIS DOCTORAL

Stellar populations, formation and evolution of quiescent galaxies since intermidiate redshifts fromo multifilter surveys

Poblaciones estelares, formación y evolución de galaxias quiescentes a desplazamientos al rojo intermedios a partir de cartografiados multifiltro

MEMORIA PARA OPTAR AL GRADO DE DOCTOR

PRESENTADA POR

Luis Alberto Díaz García

Director

Andrés Javier Cenarro Lagunas

Madrid, 2017

Stellar populations, formation and evolution of quiescent galaxies since intermediate redshifts from multifilter surveys

Poblaciones estelares, formación y evolución de galaxias quiescentes a desplazamientos al rojo intermedios a partir de cartografiados multifiltro

Ph. D. Thesis
Luis Alberto Díaz García

Supervised by
Dr. Andrés Javier Cenarro Lagunas

UNIVERSIDAD
COMPLUTENSE
MADRID

FACULTAD DE CIENCIAS FÍSICAS
DEPARTAMENTO DE FÍSICA DE LA TIERRA, ASTRONOMÍA Y ASTROFÍSICA II (ASTROFÍSICA Y CIENCIAS DE LA ATMÓSFERA)
UNIVERSIDAD COMPLUTENSE DE MADRID

April 2017

This document was performed by TEXIS v.1.0+.

This document was designed for double-sided printing.

Stellar populations, formation and evolution of quiescent galaxies since intermediate redshifts from multifilter surveys

Poblaciones estelares, formación y evolución de galaxias quiescentes a desplazamientos al rojo intermedios a partir de cartografiados multifiltro

Thesis to obtain the Ph. D. degree in Astrophysics:

Luis Alberto Díaz García

Supervised by

Dr. Andrés Javier Cenarro Lagunas

FACULTAD DE CIENCIAS FÍSICAS
DEPARTAMENTO DE FÍSICA DE LA TIERRA, ASTRONOMÍA Y ASTROFÍSICA II
(ASTROFÍSICA Y CIENCIAS DE LA ATMÓSFERA)
UNIVERSIDAD COMPLUTENSE DE MADRID

April 2017

To my parents, friends and family
who were a constant source of
support and encouragement.

Nothing in life is to be feared, it is only to be understood. Now is the time to understand more, so that we may fear less.

Marie Curie

We are a way for the cosmos to know itself.

Carl Sagan

Acknowledgements

Service to others is the rent you pay for your room here on earth.
Muhammad Ali

There is a large list of people involved in this work who should be mentioned at least in this short part, not only for their direct participation, but for their continuous support which becomes an indispensable source of encouragement, which was essential for the development of this thesis.

To get started, I highlight the support of my parents, brother and sister-in-law who since the beginning encouraged me to start my degree courses on Physics, that constitutes the very preliminary origin of this thesis. Since then, they afforded and supported all the decisions that have triggered the present thesis, which would not exist without them. Specially, I would like to emphasize that without my nephew's affection this work would not have been possible, as her endless source of happiness was essential for continuing fighting against the adversities. Of course, all my friends are rather included, my true friends whose friendship was always present at all times specially during my down moments. Amongst them I would like to emphasize the following ones: Alejandro Benito, Álvaro Macarro, Ana Pérez, Carlos Alberto Martín, Carlos García, Daniel Castellón, Eva Alonso, Francisco Barbero, Javier Benito, Javier Seisdedos, Jesús Gil, Judit Borrallo, Julia Menéndez, Lali Hernández, Laura González, Luis Villar, María Ángeles Curto, María Ángeles León, Marta Encinas, Nayra Calvo, Rubén González, and Sergio Marcos. I greatly appreciate their support, but also when they shared their free time with me taking some drinks out or going out for dinner simply, allowing me taking a breath which constituted the fuel for starting and continuing the hard work that constitutes a research, even though the large distance amongst us.

Obviously, I strongly appreciate the support of my supervisor Javier Cenarro, who trusted on me since the beginning for the development of this thesis. His continuous discussions and revisions of the results throughout the writing of this thesis, and their related papers, were indispensable and essential for the improvement of the great outcomes faced along this research. Although during the first years he could be very hard asking me for a more intensive and sophisticated work, time proved he was right, as without his strict criteria the reliability of our results would not be the same. It is worth mentioning that during the hardest and last stage, i. e. the writing of the present book, he encouraged me all time offering his very limited time for revisions and support. For these aspects and probably much more, I can mention that he was a source of inspiration and I am very grateful for it, because this will be the basis for the development of incoming and more sophisticated researches.

The role of Mariano Moles was essential for the creation of "Centro de Estudios de Física del Cosmos de Aragón" (CEFCA) and the "Observatorio Astrofísico de Javalambre" (OAJ) from the scratch, as without them the composition of this thesis would not have been possible. His continuing struggle during years for

obtaining the support and the necessary funds for its creation are very grateful for me, but also for the whole Astronomical community as his legacy will also shed light on the understanding of the Universe.

In addition, I acknowledge all the support, suggestions, discussions, and advices of my CEFCA colleagues, which were indispensable for the correct operation of many of the analysis techniques and methodologies carried out along the full development of the present thesis. Moreover, I thank for the interest and confidence of many of them, as many of the techniques (specially the code MUFFIT) will be used in future works owing to the reliability deposited, which constitutes an extra support for continuing with many and similar interesting projects. In this sense, it is remarkable the encouragement of Alessandro Ederoclite, Alicia Romero, Álvaro Orsí, Ángel López, Antonio Marín, Axel Yanes, Carlos Hernández, Carlos López, César Iñiguez, David Cristobal, David Muniesa, Fernando Rueda, Gema Julián, Gonzalo Vilella, Inés Muñoz, Héctor Vázquez, Izaskun San Román, Javier Cenarro, Javier Hernández, Jesús Varela, Jonás Chaves, Jose Luis Lamadrid, Juanjo Sánchez, Kerttu Viironen, Luis Guillén, Luisa Valdivielso, Mariano Moles, Miguel Chioare Díaz, Natalio Maicas, Natascha Greisel, Nestor Lasso-Cabrera, Rafael Bello, Rafael Logroño, Ramón Iglesias, Raúl Angulo, Sergio Chueca, Sergio Rueda, Siddhartha Gurung, Silvia Bonoli, Silvia Vaquero, and Tamara Civera . In particular, I emphasize the contribution of Carlos López San-Juan, who carried out a rigorous supervision for the implementation of some methodologies, which were essential for many aspects of the results, as well as the interesting discussions and implications of many of the results. I also appreciate to Gonzalo Vilella, Jonás Chaves and Ramón Iglesias that they allowed me to sleep over in their flat when I was back to Teruel for the final revisions and discussions of this thesis. This largely facilitated the eventual necessity of lodging, and also the friendly company and conversations during dinners were very pleasant and they made feel as at my own home.

I would like to thank Alberto Molino, one of key members of the ALHAMBRA collaboration, for his enthusiasm and tight dedication to this project. His continuous efforts for updating and improving the ALHAMBRA catalogues, as well as many of their products, and his quick responses to many of the questions that appears during the development of this thesis made possible many of the achievements reached in this work. It is also noticeable and grateful the close treatment of many of the collaborators inside the ALHAMBRA project by their constructive advices and feedbacks.

It is also remarkable the support of the Borrás and López-Malla family members. For all the celebrations, meetings, and the love that they made me feel, whom I miss a lot as they treated me as another family member. Thanks to Alberto Borrás and Sao López-Malla who allowed me to enjoy their home for several weekends. I specially acknowledge the company of Gemma Borrás for standing by me, as well as bearing me and sharing her best and worst moments for various years. Her companion and encouragement was essential to bear the hard work involved in the development of this thesis, as well as her support to overcome all the difficulties that appeared during its development.

The commitment and help of Ignacio Ferreras should be also mentioned here. He made possible two stays in the Mullard Space Science Laboratory (MSSL), partially financed by the Royal Astronomical Society (RAS), which were very fruitful for the development of part of this work. All time, I felt very comfortable working in MSSL, specially for the support and supervision of Ignacio, who was always ready for taking a coffee, lunch or just for talking about any interesting topic. Furthermore, these visits opened my mind and allowed me to meet new people from different countries and habits. Along the time expended in UK, I discovered my English limitations and this was a good excuse for diving into abroad languages. This was an experience that I would recommend to everybody and I am very grateful for it.

I would like to thank to "Caja Rural de Teruel" for financially supporting the development of this thesis. It is worth mentioning that despite the economical problems suffered in Spain, indeed globally extended, there are institutions that still invest in social projects such as pre-doctoral grants and scientific researches, rather than the selfish economic enrichment. Although it is necessary to highlight that the main responsible of these grants was Mariano Moles, the first director and founder of CEFCA, who made possible that many of us could access to Astronomy in a professional way.

In addition, travel expenses for meetings and technical support were financially co-supported by the

"Programa Nacional de Astronomía y Astrofísica" of the Spanish Ministry of Economy and Competitiveness under grant AYA2012-30789, as well as by FEDER funds and the Government of Aragón, through the Research Group E103.

In addition, I acknowledge the people involved in the project TEXIS for providing their sets of scripts that strongly facilitated the composition of the present thesis report in LATEX language.

Teruel, April 2017

Contents

Index of figures

Index of tables

Summary of the present Ph. D. thesis

> *Real knowledge is to know the extend of one's ignorance.*
>
> Confucius

This Ph. D. thesis aims at improving our understanding of the evolution of quiescent galaxies since $z \sim 1$, with the ultimate goal of providing a general picture for the formation and evolution of these objects along the history of the Universe. Making use of data from the ALHAMBRA survey and the SED-fitting code MUFFIT, developed as part of this work, this thesis is novel at facing for the first time an extensive, observational study that comprises the time evolution of the number density of quiescent galaxies, as well as their masses, stellar populations (ages, metallicities and extinctions) and sizes, to ultimately build up a phenomenological evolutionary model based on the merger, "frosting" and "progenitor bias" scenarios that tries to reconcile the observed trends in the above parameters.

The stellar population parameters of quiescent galaxies are obtained by the novel and generic code MUFFIT. This code was created and fully developed by us, and it is specifically designed to analyse the stellar content of galaxies with available multi-filter data. MUFFIT performs an error-weighted χ^2-test, for comparing the multi-filter fluxes of galaxies with the synthetic photometry of mixtures of two SSPs, to provide the most likely range of stellar population parameters: ages, metallicities, extinctions, redshifts, and stellar masses, and uncertainties. To improve the diagnostic reliability, MUFFIT identifies and removes from the analysis those bands that are significantly affected by emission lines.

For the construction of a reliable sample of quiescent galaxies, we combine the efficiency of the empiric colour-colour UVJ-diagrams and the extinctions retrieved via MUFFIT, to built a dust-corrected UVJ-diagram of intrinsic colours clean of dusty star-forming galaxies. Moreover, we carry out a one-by-one visual inspection to remove those sources whose photometry can be compromised and spurious detections, as well as a removal of contaminating cool stars. The stellar mass completeness is obtained by a novel methodology based on stellar mass functions, yielding a final sample of 8 547 galaxies at $0.1 \leq z \leq 1.1$ with a photo-z accuracy of $\sigma_{\mathrm{NMAD}} = 0.006$, which constitutes the reference sample of quiescent galaxies for this work.

Through the stellar population parameters of quiescent galaxies retrieved by MUFFIT using ALHAMBRA data, we build, for the first time, the analytic probability distribution functions of mass-weighted age, metallicity, and extinction for accurately studying the evolution of the quiescent galaxy population at different stellar mass bins. These distributions were statistically corrected of uncertainty effects by a maximum likelihood estimator method specifically performed for this aim. Mainly, quiescent galaxies show older ages at larger cosmic times, solar and super-solar metallicities predominantly, and low extinction values ($A_V \sim 0.2$). As expected, there is a tight relation between the stellar mass of quiescent galaxies and their ages and metallicities. The more massive the quiescent galaxy is, the older and more metal-rich it is. We find evidences to support that the evolution of quiescent galaxies differs respect a passive evolution, and that the median mass-weighted metallicity exhibits a decrease of 0.1–0.2 dex since $z \sim 0.6$–1.0. All the qualitative

results were confirmed using two different sets of SSP models (Bruzual & Charlot, 2003; Vazdekis et al., 2016, BC03 and EMILES respectively) and alternative assumptions for the star formation history.

A novel phenomenological model is developed for discerning the impact of mergers, "frosting" (ongoing star formation), and the "progenitor" bias (new quenched galaxies) on the evolution of massive ($\log_{10} M_\star > 11.2$) quiescent galaxies from $z = 1$ to $z = 0.2$. Contributions from mergers are based on observational constraints from photometric and spectroscopic cosmological surveys, whereas the assumption of "frosting" is accounted by a straightforward star formation efficiency (τ_f). The "progenitor" bias is included through various assumptions. Our results point out that "frosting" is an indispensable mechanism for explaining the evolution of quiescent galaxies, that along with mergers and the "progenitor" bias are able to simultaneously affect the number density and the stellar populations of massive quiescent galaxies since $z \sim 1$. For the first time and through the phenomenological model, we greatly reconcile the evolution with redshift of both the observed stellar populations (ages and metallicities) and number densities of massive quiescent galaxies with the predictions expected for a scenario in which mergers, "frosting" (with efficiency $\tau_f = 0.02$–0.08 Gyr^{-1}), and the "progenitor" bias are involved.

We also explore whether there exist correlations between the size of quiescent galaxies and their stellar population parameters. For this aim, we select all the quiescent galaxies from ALHAMBRA with reliable sizes in HST fields. By hundreds of galaxies with stellar population parameters, we discern that there are correlations between the stellar content of quiescent galaxies and their sizes at a fixed stellar mass range. In this sense, the more compact the quiescent galaxy, the older, more rich in metals, and lower SFR/sSFR values exhibits. In addition, there are hints pointing out that there exists a slight correlation with extinction. From these results, some scenarios (e. g. "puffing-up" scenario) for explaining the growth in size of quiescent galaxies are discarded.

Using a compilation of 379 massive (stellar mass $M_\star \gtrsim 10^{11}$ M$_\odot$) spheroid-like galaxies from the NIR Palomar/DEEP2 survey, we found that the probability of finding companions around the host galaxy is independent of its size at a given mass, as the companions are not located preferentially around the more compact or extensive massive spheroid-like galaxies.

In view of these results, mergers, "frosting", and the "progenitor" bias are suitable mechanisms to reproduce the observed evolution of quiescent galaxies since $z \sim 1$. In addition, we find evidences that would support that the formation and evolution of the stellar populations of quiescent galaxies relate to the stellar mass, but also with the stellar mass density of the galaxy.

Resumen de la tesis doctoral

Real knowledge is to know the extend of one's ignorance.

Confucius

En esta tesis doctoral buscamos ampliar nuestro conocimiento en torno a la evolución de las galaxias quiescentees desde $z \sim 1$, con el objetivo final de dar una visión global de la formación y evolución de estos objetos a lo largo de la historia del Universo. Haciendo uso de los datos procedentes del cartografiado ALHAMBRA y del código de ajuste espectral (SED-fitting) MUFFIT, desarrollado como parte de este trabajo, esta tesis lleva a cabo por primera vez un extenso estudio observacional que recoje la evolución temporal y la densidad numérica de las galaxias quiescentes, así como sus masas, poblaciones estelares (edades, metalicidades y extinciones), para finalmente construir un modelo fenomenológico evolutivo basado en fusiones de galaxias, "frosting" (remanentes de formación estelar), y el "progenitor" bias, tratando de reconciliar las tendencias observacionales para estos parámetros.

La obtención de las poblaciones estelares de galaxias quiescentes se lleva a cabo por el código MUFFIT, el cuál se ha desarrollado en este trabajo. Este código nace con el objetivo específico de analizar el contenido estelar de galaxias procedentes de cartografiados multifiltro. MUFFIT lleva a cabo un test de χ^2 pesado con errores para comparar los flujos de las galaxias con la fotometría sintética de mezclas de dos modelos SSP, y así obtener sus parámetros poblacionales: edad, metalicidad, extinción, desplazamiento al rojo, masa estelar y sus incertidumbres. Para mejorar el diagnóstico, MUFFIT identifica y retira del análisis aquellas bandas afectadas significativamente por líneas de emisión.

Para la obtención de la muestra de galaxias quiescentes, se combina la eficiencia de los diagramas color-color tipo UVJ y las extinciones obtenidas por MUFFIT, para construir un diagrama UVJ corregido de extinción libre de galaxias con formación estelar y enrojecidas por polvo. Para aumentar la pureza de la muestra de galaxias quiescentes, se realizó una inspección visual para eliminar las detecciones espúreas o con fotometría errónea, y un análisis para la eliminación de estrellas frías. Para la completitud en masa, se desarrolló un método basado en funciones de masa, dando lugar a una muestra final de 8 547 galaxias quiescentes a $0.1 \leq z \leq 1.1$ con una precisión de desplazamientos al rojo fotométricos en torno a $\sigma_{\rm NMAD} = 0.006$.

Gracias a las poblaciones estelares de las galaxias quiescentes obtenidas por medio de MUFFIT y de los datos de ALHAMBRA, hemos construido por primera vez las funciones de probabilidad de edad y metalicidad pesada en masa y extinción, para estudiar de una forma más precisa la evolución de la población quiescente, así como sus correlaciones con la masa estelar. Estas distribuciones fueron corregidas estadísticamente de incertidumbres mediante un método de maximización de la "likelihood" específicamente diseñado para este caso. Las galaxias quiescentes muestran edades más viejas en épocas más recientes y metalicidades solares y subsolares predominantemente, junto con extinciones bajas ($A_V \sim 0.2$). Como se esperaba, existe una estrecha relación entre las masa estelar y la edad y metalicidad de las galaxias quiescentes: cuanto más masiva es la galaxias, más vieja y metálica es. También, podemos afirmar que encontramos que las galaxias

quiescentes no evolucionan pasivamente desde $z \sim 1$: la evolución de la edad no corresponde a la esperada en un escenario pasivo puro y la mediana de la metalicidad experimenta un descenso de 0.1–0.2 dex desde $z \sim 0.6$–1.0. Estos resultados son confirmados cualitativamente para dos conjuntos de modelos SSP (Bruzual & Charlot, 2003; Vazdekis et al., 2016, BC03 y EMILES respectivamente), y para diferentes historias de formación estelar.

Desarrollamos un modelo fenomenológico para esclarecer cuál es el papel desempeñado por las fusiones de galaxias (mergers), "frosting" (remanentes de formación estelar) y el "progenitor" bias (nuevas incorporaciones en la población quiescente) en la evolución de las galaxias quiescentes masivas ($\log_{10} M_\star > 11.2$) desde $z = 1$ hasta $z = 0.2$. La contribución de los mergers está restringida a medidas observacionales de otros trabajos, mientras que el "frosting" es incorporado por medio de un factor de eficiencia de formación estelar (τ_f). Para el "progenitor" bias se utilizan varias aproximaciones para su inclusión. Como resultado encontramos que el "frosting" es totalmente necesario para reproducir la evolución de las galaxias quiescentes masivas, que junto con mergers y "progenitor" bias son capaces de reproducir la evolución de esta población de galaxias masivas desde $z \sim 1$. Por primera vez y a través de este modelo fenomenológico, somos capaces de reconciliar la evolución observada de las poblaciones estelares y las densidades numéricas de las galaxias quiescentes masivas con las predicciones estimadas para un escenario de evolución en el que las fusiones de galaxias, "frosting" y "progenitor" bias están involucrados.

También se explora la posible existencia de correlaciones entre los tamaños de las galaxias quiescentes y sus poblaciones estelares. Para este objetivo, se seleccionan todas las galaxias quiescentes en nuestra muestra con medidas de tamaños o radios efectivos en campos HST. Por medio de unos cientos de galaxias, obtenemos que existen correlaciones entre el tamaño de la galaxia quiescente y sus poblaciones a una masa fija, en el sentido que: las galaxias quiescentes más compactas a una masa dada son más viejas, más metálicas y presentan SFR/sSFR menores que las más extensas. También existe una ligera correlación con la extinción. Estos resultados descartarían que ciertos mecanismos como el "puffing up" pueden contribuir al crecimiento en tamaño de esta población.

Usando una recopilación de 379 galaxias esferoidales con masa estelar $M_\star \gtrsim 10^{11}\,\mathrm{M}_\odot$ del cartografiado NIR Palomar/DEEP2, encontramos que la probabilidad de hallar galaxias compañero en torno a estas galaxias esferoidales masivas es independiente del tamaño de los esferoides masivos para una masa fija, ya que estos compañeros no se encuentran preferentemente en torno a las galaxias más compactas o más extensas.

A la vista de estos resultados, escenarios que involucran fusiones, "frosting", y el "progenitor bias" son capaces de reproducir la evolución observada para las galaxias quiescentes. Además, encontramos evidencias que apoyarían que la masa estelar desempeña un papel en la evolución y formación de las galaxias, pero que donde la densidad de masa estelar (o tamaño) de la galaxia también puede jugar un papel.

1 Introduction

–Timon?
–Yeah?
–Ever wonder what those sparkling dots are up there?
–Pumbaa, I don't wonder, I know.
–Oh? What are they?
–They're fireflies. Fireflies that got stuck up in that big bluish-black thing.
–Oh, gee. I always thought they were balls of gas burning billions of miles away.
–Pumbaa, with you, everything's gas.

Dialogue from the film "The Lion King" (1994, Walt Disney studios)

Since man started to observe the sky with telescopes, there were a set of sources that differs from typical point stars: the spiral nebulae. These sources triggered a large debate about their nature, that nowadays is known as the "Great Debate". This debate was hold on 6 April 1920 by Harlow Shapley and Heber Curtis for discerning whether spiral nebulae lay on the outskirts of the Milky Way (MW) or they were huge stellar systems further than the limits of our galaxy. At present, the answer is easy, but in the early 1900s most of the astronomers accepted that the MW was a unique and lonely system in the Universe. On 1923 at Mount Wilson Observatory (California), Edwin Hubble broke the discussion estimating the distance to the galaxy M31, one of the spiral nebulae, after finding a Cepheid variable (called V1). This fact altered the course of modern astronomy, and it can be considered the origin of extragalactic astronomy.

1.1 Classification of galaxies

Edwin Hubble himself realised the first attempt for classifying galaxies through morphological features of galaxies: the tuning-fork diagram (Hubble, 1926, 1936, presented as a diagram shaped like the letter Y, see also Fig. 1.1). This diagram classifies galaxies in different nebular types depending on the presence or not of spiral arms. Thus, nebular types without spiral arms were called ellipticals (denoted as E), and they span from globular bodies (E0) to elongated spheroids (E7) depending of the projected ellipticity (from 0 to 7). On the other hand, the sequence of nebulae with spiral arms, denoted as S, is double: one contains normal spiral galaxies (S), whereas the other one is composed of barred spirals (SB). Each of the spiral sequences was subdivided in three types "a", "b", and "c" depending of the shape of the spiral arms. Actually, the tuning-fork diagram was originally proposed as an evolutionary sequence of galaxies, in which galaxies recently formed presented a E0 like shape evolving towards S and SB types. After decades of study, we found out that the evolutionary sequence proposed by Edwin Hubble largely differs from the reality, but this

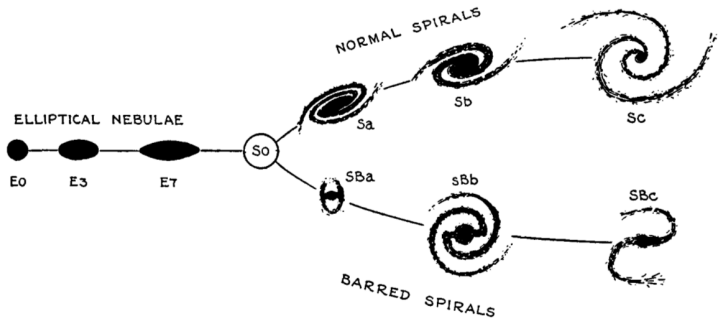

Figure 1.1: The tuning-fork diagram, further details in text. Picture taken from Hubble (1936).

classification is still extensively used today for splitting galaxies in different types owing to the correlation between colour and morphology.

Besides morphological criteria, there are more modern classifications of galaxies that involve galaxy colours or other physical properties, that at the same time, they are tightly related to the intrinsic properties of their stellar content. These diagrams present a common feature: galaxies exhibit an empirical bimodality in their distributions of properties, that is, we can distinguish two main types of galaxies in the Universe. This conciliates with the original idea of Hubble, in which two types of galaxies are enough for describing the kind of galaxies populating the Universe, where the main difference is the presence of efficient star formation processes or not: (i) galaxies with predominant red colours, usually called red sequence, passive, quiescent and even sometimes "dead" galaxies; with typical elliptic morphologies or early-type galaxies; (ii) and the blue ones, also referred as star-forming, blue-cloud, or main sequence galaxies; usually with spiral morphologies or late-type galaxies.

One of the most extended diagrams for disentangling different types of galaxies involves rest-frame colours and absolute magnitudes (Bell et al., 2004; Baldry et al., 2004; Brown et al., 2007). These diagrams, usually referred as colour–magnitude diagrams (CMD), present a bimodal distribution of galaxies. As mentioned above, there is a numerous population of galaxies with $U - V$ blue colours lying on the CMD lower parts (the so-called blue cloud) with typical young stellar populations. Whereas in the red part of the CMD, there is a dominant population of massive galaxies, called red-sequence galaxies, with predominant older and more evolved stellar populations. In between, some authors defend that there is a third sub-population of galaxies, the green valley, with a significant overdensity of active galactic nuclei (AGN, Nandra et al., 2007; Bundy et al., 2008; Georgakakis et al., 2008; Silverman et al., 2008; Hickox et al., 2009; Schawinski et al., 2009), that some authors interpret as a mechanism to produce a transition of galaxies from the blue-cloud to the red-sequence (e. g. Faber et al., 2007; Schawinski et al., 2007). Although, there are evidences to support that galaxies belonging to the green valley are mainly reddened-by-dust star-forming galaxies (Bell et al., 2005; Cowie & Barger, 2008; Brammer et al., 2009; Cardamone et al., 2010). During the last decade, the rest-frame colour–colour diagrams, specially the UVJ diagram, has become one of the most extended methods for separating these two kinds of galaxies (e. g. Daddi et al., 2004; Williams et al., 2009; Arnouts et al., 2013). The advantage of these diagrams is that they use two colours (one in the blue part of the SED, e. g. $U - V$ or $NUV - r$; the other one in the red part, e. g. $V - J$ or $r - K$), that reduce the contamination of dusty star-forming galaxies in the passive or quiescent sample with predominant red colours and low star formation (e. g. Williams et al., 2009; Arnouts et al., 2013; Ilbert et al., 2013; Moresco et al., 2013). The efficiency of these colour–colour diagrams resides in that galaxies empirically present a more separated loci between red and blue populations than typical colour–magnitude diagrams, in which both populations appear overlapped partially (Wyder et al., 2007; Cowie & Barger, 2008; Brammer et al., 2009). Despite the UVJ diagrams demonstrated to be a reliable method to split quiescent from star-forming galaxies, these diagrams present a level of contamination in the selection of quiescent galaxies that depends on redshift and stellar mass (Williams et al., 2009; Moresco et al., 2013), for which the number of star-forming outliers may

reach 30 % at certain redshift and mass regime, or at least a 15 % after imposing a more restrictive $U - V$ colour limit than the one defined originally (Moresco et al., 2013).

Alternative methods for splitting galaxies comprise colours and stellar masses (Peng et al., 2010), but these are quasi-equivalent to the colour magnitude diagrams, as absolute magnitudes or luminosities are tightly linked to stellar mass. Therefore, colour-stellar mass diagrams present similar non-negligible contaminations of dusty star-forming galaxies in the red part, as they are not able to distinguish the influence of dust. Moustakas et al. (2013) introduced star formation rates (SFR), along with stellar masses, as a criterion for separating both quiescent and star-forming galaxies. This diagram has the disadvantage that it is necessary a previous estimation of the mentioned stellar population parameters, which in many cases are not available or they could be calculated with great difficulty. In some cases, SFR and specific star formation rates (sSFR, defined as SFR/$M_\star$) can be also used as an additional (or the unique criterion) for selecting passive or quiescent galaxies (e. g. Ilbert et al., 2010; Pozzetti et al., 2010; Domínguez Sánchez et al., 2011, 2016).

1.2 Galaxy formation and evolution

In spite of the great advances of the modern astronomy along the last centuries, there is no a clear consensus about the precise scenario where galaxies were assembled. Traditionally, many authors tried to favours different formation scenarios basing their results on the galaxy morphology and its evolution. On the other hand, studies about the evolution of the stellar populations of galaxies can shed light on this topic as well. Complementing both morphological and stellar content results can also reveal some hints regarding the evolution and assembly of galaxies (e. g. by the spatially distribution of stellar populations or line-strength gradients, evolution of colour gradients, or by correlations with the size of the galaxy Ferreras et al., 2005; Sánchez-Blázquez et al., 2007; Ferreras et al., 2009; Shankar & Bernardi, 2009; La Barbera et al., 2011; Sánchez et al., 2012; González Delgado et al., 2014b; Belli et al., 2015; Bundy et al., 2015; González Delgado et al., 2015; McDermid et al., 2015; Martín-Navarro et al., 2015a; Williams et al., 2016; Gargiulo et al., 2016; Goddard et al., 2017), as the assembly of the internal structures of galaxies is related with the star formation processes in them. Nevertheless, both morphological and stellar population changes can occur in different time scales (e. g. Poggianti et al., 1999; Fasano et al., 2000).

1.2.1 Historical scenarios of galaxy formation

Historically, we distinguish two (still) competing scenarios of formation for early-type galaxies.

- Monolithic collapse (Larson, 1969, 1974a; Kodama & Arimoto, 1997; Chiosi & Carraro, 2002; Romano et al., 2002; Kaviraj et al., 2005). This scenario assumes that all the parts of early-type galaxies were formed at very high redshift and at the same time, during an intense episode of star formation through the collapse of a cloud of primordial gas. Within this scenario, there are two theories that differs in the treatment of the mechanisms involved during the collapse of gas: (i) Dissipative-less (stellar dynamical) collapse (Gott, 1973, 1975; Aarseth & Binney, 1978; McGlynn, 1984), in this theory the collapse of gas during the initial formation epoch was rapid enough as to suffer a subsequent violent relaxation. Thereby, the initial angular momentum of gas would be the responsible of the rotation curves and isophotes of early-type galaxies, although this theory does not explain metallicity gradients for instance. (ii) Dissipative (monolithic) collapse (Larson, 1969, 1974a,b, 1975; Carlberg, 1984a,b; Arimoto & Yoshii, 1987), these models are like the dissipative-less ones but also including a colliding scenario of gas clouds, galactic winds, dissipation of the gas energy, star formation, enrichment of metals, or supernova explosions. In this scenario the stars do not experiment significant displacements to the inner parts of the early-type galaxies, unlike the gas enriched in metals by massive stars, which is dissipated towards the inner regions. However, this scenario does not support the morphological variation of massive galaxies (Buitrago et al., 2013).

- Hierarchical merging (Davis et al., 1985; White et al., 1987; Kauffmann et al., 1993; Somerville & Primack, 1999; Cole et al., 2000; Hatton et al., 2003; Khochfar & Burkert, 2003; De Lucia et al., 2006). In this scenario, galaxies are supposed to be formed by a continuous merging of smaller structures (e. g. globular clusters), that then merge with even larger systems until assembling massive galaxies. According to the Cold Dark Matter cosmology and merger fractions (see e. g. López-Sanjuan et al., 2013), the merger rates increase at higher redshifts, supporting a hierarchical scenario. Observations at high redshift show that there are a larger percentage of disturbed and interacting galaxies (e. g. Glazebrook et al., 1995; Abraham et al., 1996), which agrees with this scenario. The presence of shells around early-type galaxies at low redshifts is also a hint to favour this hypothesis. However, the presence of massive passive galaxies at high redshifts (Papovich et al., 2006; Arnouts et al., 2007; Conselice et al., 2011; Domínguez Sánchez et al., 2011; Ilbert et al., 2013) is usually used for supporting the idea of an anti-hierarchical scenario.

In late-type or disk galaxies is also discussed the secular evolution (e. g. Sheth et al., 2005; Debattista et al., 2006; Martinez-Valpuesta et al., 2006), which it is though that is negligible in early-type galaxies. Secular evolution is usually defined as a slow and steady dynamical evolution owing to either internal processes (e. g. interactions with spiral arms, galactic winds, bars, etc.) or environment (e. g. gas accretion, galaxy harassment or high-speed "fly-bys",etc.). For instance, under the secular evolution scenario bars in spiral galaxies can perturb and extend the outskirts of the bulge, or to explain the creation of stars in spiral arms. In addition, satellite galaxies can drastically modify its morphology or even inducing star formation by galaxy harassment.

1.2.2 The cessation of star formation

Quenching is a relevant stage during the life of a galaxy, as after quenching, a galaxy suffers a quick reddening by ageing, experimenting a transition from the sequence of star-forming galaxies to the sequence of passive/quiescent galaxies. Nowadays, it is still matter of debate many of the aspects that involves quenching, such as the trigger of quenching, the influence of environment, or typical quenching timescales. In fact, it is far from clear which is the primary responsible mechanism of quenching or the cessation of star formation (Faber et al., 2007; Peng et al., 2010; Ilbert et al., 2013; Peng et al., 2015). Several mechanisms have been proposed as candidates for explaining the shutting down of star formation, but we distinguish two main categories or families (see Peng et al., 2015): sudden removal of gas and "strangulation". Both categories are based on a common framework in which galaxies are subject to gas inflows and there is a continuous star formation, increasing the mass of the galaxy and the metal content of the ISM. Under this assumption, the inflows of gas partially diluted the metallicity of the ISM, that is, the enrichment in metals of the ISM via stellar evolution and winds is delayed by gas inflows.

In the sudden gas removal scenario, the mechanism triggering quenching removes the reserves of gas in the affected galaxy, as well as the inflows of gas. This process is more violent than "strangulation" and the star formation is suddenly ceased. Thereby, quiescent galaxies affected by sudden gas removal present the same stellar mass and metallicity than its progenitor. We distinguish two types of sudden gas removal:

- Outflows (e. g. Di Matteo et al., 2008; Hopkins et al., 2006; Maiolino et al., 2012; Diamond-Stanic et al., 2012; Cicone et al., 2014). Some of the mechanisms proposed are feedback processes (AGN or super massive black holes) or the expulsion of gas by strong winds. In particular, AGN feedbacks is one of the most debated mechanisms for shutting down star formation (Silk & Rees, 1998; Dekel & Birnboim, 2006; Nandra et al., 2007; Bundy et al., 2008), as there exist a remarkable presence of AGNs in galaxies with host-galaxy colours between the passive and star-forming galaxy populations, in the so-called green valley, (Nandra et al., 2007; Bundy et al., 2008; Georgakakis et al., 2008; Silverman et al., 2008; Hickox et al., 2009; Schawinski et al., 2009). Even AGN feedback is a good candidate for preventing the gas cooling and new star forming processes (Croton et al., 2006; Bower et al., 2006). As quiescent galaxies were already present at $z \sim 3$, presence of AGN driven outflows

must be at epochs close to the reionization epoch and it must extend along the whole galaxy to efficiently expel the gas (Maiolino et al., 2012). Other mechanisms as mergers of gas-rich galaxies provide inflows of gas producing strong starbursts and feeding supermassive black holes, whose feedbacks expel the gas from the galaxy (Hopkins et al., 2006). Diamond-Stanic et al. (2012) found a star forming galaxy presenting outflows only driven by both radiation (massive stars) and ram pressures (super novae), and stellar winds without the presence of AGNs.

- Stripping (Gunn & Gott, 1972; Abadi et al., 1999; Quilis et al., 2000). Satellite galaxies falling into a massive halo or in a rich cluster can be strongly affected by ram pressure stripping, which efficiently removes and truncates the diffuse gas in the galaxy. Some studies predicts that in poorer clusters this mechanism is not efficient enough for removing all the gas, and ram pressure stripping is insufficient itself for quenching star formation. Although it may morphologically transforms spiral galaxies into lenticular galaxies (Abadi et al., 1999).

Regarding "strangulation" (Larson et al., 1980; Balogh et al., 2000; Kereš et al., 2005; Dekel & Birnboim, 2006; Peng et al., 2015), this category implies a quenching process less severe than the proposed in the sudden gas removal scenario. Once the inflow of gas is over, whatever was the responsible mechanism, the galaxy continues forming stars by the available gas in the galaxy. As the inflow of gas diluted the metal content of the ISM, subsequent population of stars will be more rich in metals increasing both the stellar mass and metallicity of the galaxy (see Peng et al., 2015). "Strangulation" would also explain the morphological transformation of disk systems to lenticular galaxies (Larson et al., 1980), after losing the gas-rich envelop and consuming the remaining gas by star formation. Under this scenario, passive and star-forming galaxies would exhibit systematics differences between typical ages and metallicities of both populations. Peng et al. (2015) showed that there is a systematic shift of 4 Gyr between the ages of passive and star-forming galaxies at the nearby Universe. In addition, there were systematics differences between metallicities, which are more remarkable at decreasing redshift, but compatible under a "strangulation" scenario for stellar masses of $\log_{10} M_\star < 11$. In addition, by the use of a closed box model, Peng et al. (2015) estimated that since the inflow of gas is stopped, galaxies expend 4 Gyr until reaching the passive population via "strangulation", which matches with the ages differences between quiescent and star-forming galaxies, favouring "strangulation" as the main scenario for explaining quenching mechanisms.

There are also evidences for supporting that quenching mechanisms differ depending of the stellar mass of the galaxy (Peng et al., 2010; Ilbert et al., 2013). Massive galaxies would suffer a more efficient quenching, referred as "mass quenching", at redshift $1 < z < 3$ when they experienced a steep increase in number. This will also explain the maximum density of the stellar mass function of quiescent galaxies at $\log_{10} M_\star \sim 10.8$, supporting that the quenching mechanism for ceasing star formation is more efficient at $\log_{10} M_\star \gtrsim 10.8$ (Ilbert et al., 2013). However, less-massive quiescent galaxies would suffer a different quenching mechanism that is more related to environment, or "quenching environment", because there are evidences for supporting that low-mass quiescent galaxies appear in high density environments (see Peng et al., 2010; Gabor & Davé, 2012; Scoville et al., 2013). The quenching of low mass systems must be present at $z \lesssim 1$, when the stellar mass function of quiescent galaxies becomes flatter. Moreover, this flattening would involve a little fraction of star forming galaxies ($\sim$ 1–10 %, see Bezanson et al., 2012), supporting the "environmental" quenching as this conciliates with the number of quiescent galaxies in dense environments.

1.2.3 Evolution and formation of quiescent galaxies

As mentioned above, galaxies tend to present bimodal distributions of red and blue galaxies (e. g. Bell et al., 2004; Baldry et al., 2004; Williams et al., 2009; Ilbert et al., 2010; Peng et al., 2010; Arnouts et al., 2013; Moresco et al., 2013; Fritz et al., 2014), where red galaxies present more evolved stellar populations with lower star formation levels, for which they are usually referred as passive or quiescent. The formation and evolution of the so-called quiescent/passive galaxies is still today a challenge, as these galaxies started to

form stars at very early epochs, to later shut down their star formation by a mechanism that is still today matter of debate (see Sect. 1.2.2). Amongst the topics involving quiescent galaxies, there are two lines of study in which many authors are devoting a great deal of effort: the evolution of the stellar content of quiescent galaxies and the growth in size of quiescent galaxies.

1.2.3.1 The stellar content of quiescent galaxies

Many authors tried to established the evolution or star formation history of galaxies from the study of their local stellar populations. This methodology is usually referred as "archaeological" approach or fossil record methods, and it has been extensively used for determining the stellar content of galaxies through their integrated properties or by their spatially-resolved stellar populations (e. g. Cid Fernandes et al., 2005; Gallazzi et al., 2005; Thomas et al., 2005; Ferré-Mateu et al., 2013; Trujillo et al., 2014; Belli et al., 2015; McDermid et al., 2015; González Delgado et al., 2015; Citro et al., 2016; Zheng et al., 2016; Goddard et al., 2017). These predictions are based on the SED reconstruction of galaxies, as well as spectral indices sensitive to stellar population parameters (such as age, metallicity, α enhancement, IMF, etc.), usually using stellar population models with different SFH or including burst of various durations. Alternatively, the comparison between the stellar populations of similar samples at higher and nearby redshifts, "look-back" studies, provides complementary constraints in order to explain how galaxies evolved from the past until building-up their present stellar content (e. g. Schiavon et al., 2006; Sánchez-Blázquez et al., 2009; Choi et al., 2014; Gallazzi et al., 2014; Fagioli et al., 2016; Gargiulo et al., 2016; Siudek et al., 2016). Whilst the "look-back" studies constitute a direct comparison of the galaxy evolution, any interpretation of the results is limited by the "progenitor" bias (van Dokkum & Franx, 2001). In fact, recent studies point out that there is an increasing number of quiescent galaxies since $z \sim 3$ (e. g. Drory et al., 2009; Pozzetti et al., 2010; Ilbert et al., 2010; Cassata et al., 2011; Davidzon et al., 2013; Ilbert et al., 2013; Moustakas et al., 2013; Moresco et al., 2013; Tomczak et al., 2014) that support an scenario in which quiescent galaxies are largely affected by the "progenitor" bias. Other recent results advocate for a reduction in the number of massive star-forming galaxies (Bell et al., 2007; Davidzon et al., 2013; Ilbert et al., 2013; Moustakas et al., 2013), which also explains the observational growth in size of massive quiescent galaxies (e. g. Shankar & Bernardi, 2009; Belli et al., 2015; Fagioli et al., 2016; Gargiulo et al., 2016; McDermid et al., 2015; Williams et al., 2016) and the scatter in the red sequence (Harker et al., 2006; Ruhland et al., 2009).

Some of these quiescent galaxies are really old (with ages slightly below ~ 1 Gyr respect the age of the Universe) and they should suffer very efficient process of star formation, and a subsequently fast quenching, because the sequence of quiescent galaxies is already in place at $z \sim 3$ (Whitaker et al., 2011; Ilbert et al., 2013). Some authors have dedicated large efforts in study their evolution in a long period of time, amongst others, through the study of their SFR or sSFR (Papovich et al., 2006; Martin et al., 2007; Zheng et al., 2007; Pérez-González et al., 2008; Damen et al., 2009), studying the evolution of their number density with cosmic time (Ilbert et al., 2010; Pozzetti et al., 2010; Ilbert et al., 2013), or attempting to reconstruct their star formation history with fossil record methods (Heavens et al., 2004; Thomas et al., 2005; Jimenez et al., 2007; McDermid et al., 2015, see Fig. 1.2 to illustrate). Overall, there is a good agreement in that, these galaxies present a strong dependence in their evolution with the stellar mass (largely studied in the local Universe, e. g. Kauffmann et al., 2003; Gallazzi et al., 2005; Thomas et al., 2005; Sánchez-Blázquez et al., 2006a; Jimenez et al., 2007; Panter et al., 2008; González Delgado et al., 2014a; Peng et al., 2015) and more slight with environment (e. g. Thomas et al., 2005; Rogers et al., 2010; La Barbera et al., 2014; McDermid et al., 2015), being the more massive galaxies formed at earlier epochs and presenting a more efficient and quicker process of star formation, usually called "downsizing" scenario (Cowie et al., 1996). Additionally, the more massive the quiescent galaxy, the more metal rich is (Gallazzi et al., 2005, 2014; González Delgado et al., 2014a; Peng et al., 2015).

Mergers are an efficient mechanism for the creation of spheroid-like galaxies by the merging of gas-rich disks (Toomre, 1977; Schweizer & Seitzer, 1992; Barnes & Hernquist, 1996), as well as to modify colours of galaxies. In addition, many authors suggest that massive early-type galaxies were assembled by

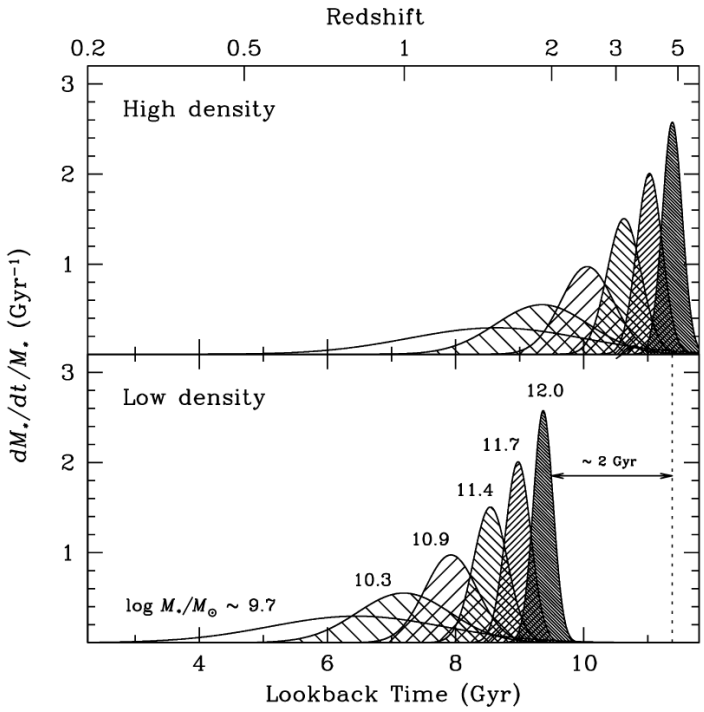

Figure 1.2: Cartoon of the star formation history (SFH) of early-type galaxies as a function of the stellar mass and environment (see labels). Picture taken from Thomas et al. (2005).

major mergers, in which a temporary quasar activity can be also present (Benson et al., 2003; Croton et al., 2006; Somerville et al., 2008; Hopkins et al., 2008b, 2009c; van der Wel et al., 2009; López-Sanjuan et al., 2013). Some results agree with an scenario in which the bulk of stars, specially in massive galaxies, were built up to $z \sim 1$, and then these galaxies have suffered numerous merger events in a hierarchical context (Bundy et al., 2007; White et al., 2007; Wake et al., 2008; Skelton et al., 2012; Ferreras et al., 2014), which can alter their stellar content. One of the limitations to explore the influence of mergers is that the time scale of a merger is dependent of the properties of the progenitor galaxies, as well as the orbit (Lotz et al., 2010a,b), although recent cosmological simulations (e. g. Springel et al., 2005; Kitzbichler & White, 2008) are facilitating these issues. In the early attempt by Skelton et al. (2012), authors showed that the presence of mergers reconstruct better the evolution of the RS than a passive evolution of galaxies in the RS. In the same work, the evolution of both mass and luminosity functions since $z \sim 1$ are better reproduced when mergers are included in their model of evolution. The predictions rather agree when wet mergers and the "progenitor" bias are also accounted (see also Faber et al., 2007), specially the predictions on their color-magnitude evolution. Furthermore, recent studies based on the radial stellar population profiles in early-type galaxies (González Delgado et al., 2014b, 2015; Wilkinson et al., 2015; Goddard et al., 2017; Zheng et al., 2016) show flat age and shallow negative metallicity radial profiles, which agree with an assembly of these galaxies via major mergers (using smoothed particle hydrodynamics or SPH and cosmological simulations Kobayashi, 2004; Hirschmann et al., 2015). Nevertheless, the common presence of mergers, specially in the quiescent population (López-Sanjuan et al., 2012), are not properly treated for studying the impact that have this mechanism on the stellar population parameters or on their integrated properties, such age and metallicity. Generally, the impact of mergers is only mentioned for the interpretation of the results, as an external contribution (rather when the rest of mechanism cannot explain the evolution of galaxies), but without estimating its impact on the results.

1.2.3.2 Evolution in size of quiescent galaxies

During the last decade, many authors found out evidences for a continuous and generalised increase in size of both spheroidal-like/quiescent and late-type/star-forming galaxies with cosmic time (e. g. Trujillo et al., 2004; Daddi et al., 2005; McIntosh et al., 2005; Trujillo et al., 2006a; Toft et al., 2007; Trujillo et al., 2007; Zirm et al., 2007; Buitrago et al., 2008; van Dokkum et al., 2008; Damjanov et al., 2011; Newman et al., 2012; van der Wel et al., 2014, see also Fig. 1.3). In particular, since $z \sim 2$ ($z \sim 1$) spheroidal-like/quiescent galaxies have rapidly increased in size a factor of ~ 4 (1.5–2) up to the current days. The main mechanism responsible of this fast growth is not clear yet.

First attempts for disentangling how galaxies grow in size proposed that the influence of AGNs can play a role. This scenario, usually referred as the "puffing-up" scenario (Fan et al., 2008, 2010; Damjanov et al., 2009), proposed that AGNs or quasar feedbacks would produce a removal of cold gas from the inner regions of the galaxy, that would redistribute the stellar populations of the inner regions in a time scale of ~ 2 Gyr. Although it is a plausible mechanism, this would imply that: (i) less compact quiescent galaxies would present older ages in the local Universe; and (ii) the dispersion of the stellar mass-size relation would increase (Fan et al., 2010) with cosmic time. Previous studies (e. g. Cenarro & Trujillo, 2009; Shankar & Bernardi, 2009; Trujillo et al., 2009, 2011; McDermid et al., 2015; Gargiulo et al., 2016) obtained that observations differ from the predictions of this scenario.

Alternatively, mergers were proposed as an efficient mechanism for producing a generalised growth in size (Naab et al., 2009). In this scenario, galaxies firstly formed their compact and dense cores, which are proposed to be the so called red nuggets observed at at $z > 2$ (Damjanov et al., 2009). These systems could be the result of mergers between gas-rich disks (which yields compact starbursts of small radii, Hopkins et al., 2008a) or of the accretion of cold streams (which forms compact massive bulges and suppresses star formation Kereš et al., 2005; Dekel et al., 2009). Once the core is assembled, a continuous fall of pieces at lower redshifts via mergers (with ex-situ stellar populations) would populate the surroundings of these dense cores via an "inside-out" formation scenario (e. g. de la Rosa et al., 2016). This scenario would be mainly driven by minor mergers on parabolic orbits (Khochfar & Burkert, 2006a; Khochfar & Silk, 2006b; Bezanson et al., 2009; Hopkins et al., 2009b; Naab et al., 2009; Trujillo et al., 2011), because the number of major mergers is not large enough as to reproduce the evolution in size observed since $z \sim 1$ (Bundy et al., 2009; de Ravel et al., 2009; López-Sanjuan et al., 2010, 2012). Díaz-García et al. (2013) shows that mergers do not involve necessarily smaller galaxies, and therefore, under this scenario the growth in size via mergers must be generalised for all galaxies in the stellar mass–size plane. If this is the case, the number of compact galaxies will reduce towards larger cosmic times (Cassata et al., 2013; Quilis & Trujillo, 2013; Trujillo et al., 2014; van der Wel et al., 2014), despite other studies show that the number of compact galaxies remain almost constant (Saracco et al., 2010; Damjanov et al., 2014, 2015; Gargiulo et al., 2016) or experiment only a slight decrease in number (Valentinuzzi et al., 2010; Poggianti et al., 2013). A reliable estimation of the evolution in number of compact (massive) galaxies along redshift is therefore needed to discard or favour the merger scenario as the responsible mechanism for the growth in size of quiescent or spheroidal-like galaxies.

In the last years, the "progenitor" bias scenario is gaining force in this topic. It proposes that the first galaxies formed in the earliest epochs of the Universe were also the densest ones, as they resided in denser halos. Consequently, galaxy sizes would reflect the density of the Universe at the epoch in which they were formed. At the same time, they would evolve and quench their star-formation processes earlier. Any galaxy formed at later epochs will therefore be larger, evolving later on until they reach enough stellar mass as to do not support more star forming processes. This would imply that less dense quiescent galaxies (less compact or extended) are also younger, as they reach a state of quenching in later epochs (Valentinuzzi et al., 2010; Carollo et al., 2013; Belli et al., 2015). At the same time, this would imply that the number density of compact galaxies would be constant, or at least this would suffer mild and increasing modifications with cosmic time. Under this scenario, we would expect a correlation between the size of a galaxy and their stellar content age, where denser galaxies exhibit older ages (Shankar & Bernardi, 2009; Poggianti et al.,

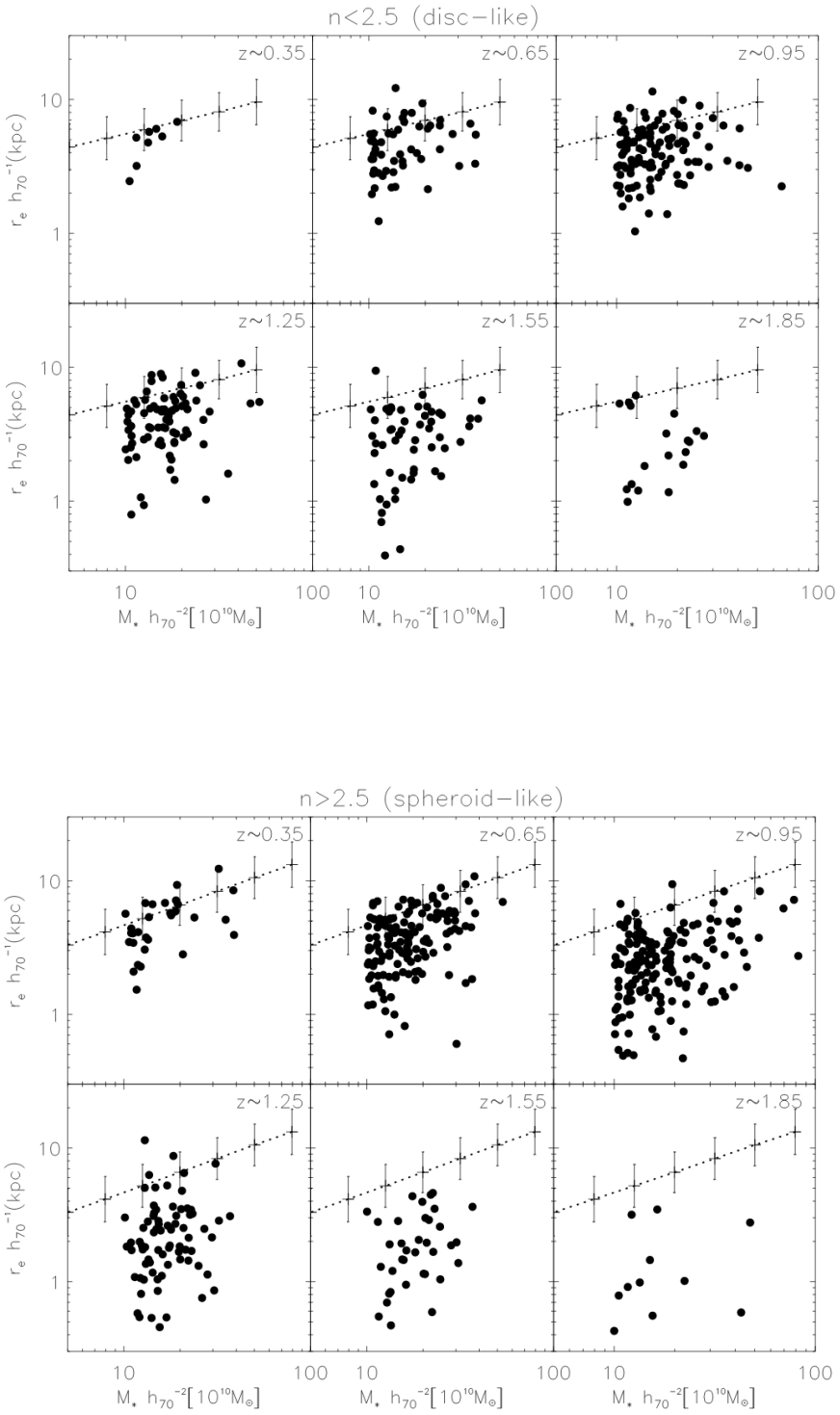

Figure 1.3: Stellar mass (X–axis) versus size (Y–axis) distribution for disc-like (*top panels*) and spheroid-like (*bottom panels*) galaxies. Picture taken from Trujillo et al. (2007).

2013; Fagioli et al., 2016; Gargiulo et al., 2016; Williams et al., 2016) or large quiescent galaxies will reach the red sequence later than their compact counterparts (Belli et al., 2015).

1.3 Tracing the stellar content of galaxies

Nowadays, the set of analysis techniques is tightly linked to the type of data used for retrieving the stellar population parameters (also the spectral type of the source, e. g. emission line galaxies). Mainly, we distinguish two main methodologies that stand out respect the rest of them: photo-spectral fitting and line absorption features. Nevertheless, the determination of the stellar populations of galaxies has suffered continuous changes along the last decades. These changes do not only affect the methodologies for retrieving the different parameters involved in the star formation history of galaxies, but also in the set of models or "chronometers" used for calibrating these parameters in an homogeneous scale of values, such as age, metallicity, abundances of α-elements, etc. These techniques, along with the models used during the process of analysis, have become indispensable for studying the stellar content of galaxies, tracing their evolutive pathways since they started to form their first populations of stars at high redshift. In fact, techniques and models are the key ingredients for the determination of the stellar content in any galactic source. Any result is strictly linked to both aspects, and an adequate integration of both elements is essential for the success of any research. Despite the strong efforts and advances achieved in this topic during the last decades, it still remains as one of the most challenging and promising ways to understand galaxy evolution. Both techniques and models are still being modified and improved, implementing the most recent results and the most modern techniques (e. g. by the use of empirical stellar libraries in larger spectral ranges or implementing statistical methods for supporting the results and uncertainties).

1.3.1 Methodologies for determining stellar population parameters

In the 1960s, pioneer studies for retrieving stellar population parameters of extragalactic sources involved photometric data through non-so primitive wide and narrow filters (Baum, 1959; Tifft, 1963; Wood, 1966; McClure & van den Bergh, 1968; Faber, 1973). These studies supposed a great challenge for the epoch, as they comprised integrated stellar populations and rudimentary stellar population models. Despite these drawbacks, they achieved the goal of retrieving ages and metallicities of some nearby early-type galaxies only using photometry. This kind of analysis was the origin of the modern photo-spectral fitting, although it was gradually displaced by techniques based on more specific features (Faber, 1973; Pritchet, 1977). The increment of spectral resolution via photometers (resolution ranging from 15 Å to 50 Å) were key to move the bulk of stellar population studies of extragalactic sources from photometry to spectroscopy. These more specific features, defined in narrow spectral ranges, demonstrated to be sensitive to certain stellar parameters, e. g. metallicity.

The arrival of absorption line-strength indices to study the stellar content of galaxies (Burstein et al., 1984; Faber et al., 1985) brought a significant breakthrough in the field. On this front, it is worth noting the Lick system of indices (Gorgas et al., 1993; Worthey et al., 1994b), which for the past decades has been the standard for most spectroscopic studies in stellar populations in the optical (e. g. Trager et al., 1998; Jørgensen, 1999; Kuntschner et al., 2001; Thomas et al., 2005; Bernardi et al., 2006; Sánchez-Blázquez et al., 2006b; Gorgas et al., 2007). This system allows us to measure the spectral features of a source, star or galaxy, through the definition of three fluxes. These fluxes are determined in three spectral ranges or bandpass: the central bandpass comprising the parameter-sensitive feature (e. g. metallicity or the age for a galactic case); and the continuum bandpass composed of two fluxes defined at the contiguous spectral range of the stellar population parameter feature, used for defining a continuum or reference level. By construction, line-strength indices involve narrow spectral ranges and the influence of extinction is therefore negligible, making it an effective method for determining stellar population parameters in which extinction is present (specially in galaxies or integrated stellar populations). Line-strength indices are very sensitive to stellar population parameters (e. g. ages, metallicities, IMF, or [α/Fe]), but they also present degeneracies amongst

stellar population parameters (Worthey, 1994a). To solve this problem, the use of index-index diagrams (e. g. Balmer lines for age; whereas for metallicity, the traced ones by elements such as Fe , Mg , Ti , C , Ca , and Na), the fine-tuning of the bandpass of sensitive features, as well as the fitting to multiple indices were key to diminish the bias introduced by degeneracies (typically between age and metallicity, but also with other stellar population parameters as [α/Fe]; e. g. Vazdekis & Arimoto, 1999b; Proctor et al., 2004; Thomas et al., 2003; Gallazzi et al., 2005; Cervantes & Vazdekis, 2009). In spite of all these considerations, there are still discrepancies between the ages and metallicities when different sets of line-strength indices are used for deriving the stellar population parameters (e. g. age estimations varies when Hδ is used instead of either Hγ or Hβ), even when the same set of SSP models is used. This is usually attributed to the use of SSP models for calibrating indices, as galaxies experienced more complex star formation histories than the predicted by a SSP model. This implies that, for instance, age and metallicity indices are the combination of the fluxes of different star formation episodes, where the contribution of young populations have a larger impact on the blue indices than in the red ones (see e. g. Schiavon et al., 2004; Serra & Trager, 2007; Rogers et al., 2010).

1.3.2 Stellar population synthesis models: a brief look

Stellar population synthesis models allow us to interpret the integrated flux coming from extragalactic sources, converting them into stellar population properties (e. g. ages, metallicities, mass-to-light ratios, redshifts). Stellar population synthesis models are as essential as the methodologies performed for retrieving stellar population parameters. If models are not built properly, any parameter derived from them will be invalid. For this reason, several efforts were carried out for developing the stellar population models that we enjoy today. Historically, we can distinguish three types of stellar population synthesis models: empirical synthesis models, evolutionary synthesis models, and chemo-evolutionary population synthesis models.

Empirical synthesis models were mainly involved in very early works for deriving the stellar populations of galaxies, as they were designed for reproducing the colours of galaxies. These models followed a set of recipes for mixing the flux contributions of stars, in order to reproduce the colours and magnitudes of galaxies. Whilst the main feature of empirical models is that they include very few physical constraints, they were used successfully in the past (Spinrad & Taylor, 1971; Faber, 1972; O'Connell, 1976, 1980; Pickles, 1985).

On the other hand, evolutionary synthesis models were initially performed by Tinsley (1968, 1972); Searle et al. (1973); Tinsley & Gunn (1976); Tinsley (1978); Whitford (1978); Gunn et al. (1981). These work were the origin of the modern stellar population models, which involved numerous constraints for reproducing the light coming from a stellar population after modelling its evolution. One of the main characteristics of evolutionary synthesis models is the use of isochrones (also called stellar evolutionary tracks) or Hertzsprung–Russell (HR) diagrams. Since these early work, stellar population models have suffered numerous improvements and modifications concerning their main ingredients (e. g. Aragon et al., 1987; Guiderdoni & Rocca-Volmerange, 1987; Peletier & Valentijn, 1989; Bruzual & Charlot, 2003; González Delgado et al., 2005; Coelho et al., 2007; Schiavon, 2007; Maraston et al., 2009; Vazdekis et al., 2012; Röck et al., 2015; Vazdekis et al., 2015, 2016). The goal of these models is to reproduce the integrated light of a galaxy by a unique spectrum, which contains many contributions from stars with different ages, metallicities, α-element abundances, etc. The most modern stellar population models provide single stellar populations (SSP), that assumes that a population of stars is originated at the same time with the same metallicity. For a SSP model, the flux at wavelength λ with age t and metallicity [M/H] is expressed as,

$$S_\lambda(t, [\mathrm{M/H}]) = \int_{m_{\mathrm{low}}}^{m_{\mathrm{up}}} S_\lambda(m, t, [\mathrm{M/H}])\, N(m, t)\, \mathrm{d}m \,, \tag{1.1}$$

where m_{low} and m_{up} are the lower and upper limits of the mass range of stars respectively; $S_\lambda(m, t, [\mathrm{M/H}])$ is the flux at λ of a star of mass m, age t and metallicity [M/H]; and $N(m, t)$ the number of these stars. All the modern SSP models or the evolutionary synthesis models include as basic ingredients:

i) Stellar libraries. This can be considered as the main ingredient of any evolutionary synthesis or SSP model. This consists of a collection or set of stellar spectra, whose range in stellar types, spectral resolution, spectral range, and flux calibration determine the quality of the SSP models. Stellar libraries must cover wide ranges of stellar parameters, i. e. effective temperature, $T_{\rm eff}$; gravity, $\log g$; and metallicity [M/H]. These libraries can be theoretical or empirical (e. g. Pickles, 1998; Lejeune et al., 1998; Cenarro et al., 2001a,b; Prugniel & Soubiran, 2001; Westera et al., 2002; Le Borgne et al., 2003; Valdes et al., 2004; Coelho et al., 2005; Martins et al., 2005; Sánchez-Blázquez et al., 2006c; Cenarro et al., 2007). Although empirical stellar libraries are more trustworthy than the theoretical stellar libraries, they are limited to the observational values of the involved stars. Therefore, when used empirical stellar libraries, an interpolation amongst the stellar spectra is usually necessary.

ii) Isochrones of stars. Isochrones are the element that provides the evolutionary aspect to the models. Isochrones provide the distribution of stars on a HR diagram for a given age and composition (metallicity). For this reason, they must contain all the stellar parameters (temperature and gravity, the metallicity is fixed for each isochrone) at any age along the isochrone, as well as the initial mass and the mass at the moment of interest. Since the original HR diagram carried out in the beginning of the 20$^{\rm th}$ century, isochrones have experimented significant modifications to cover wider ranges of age and star masses (at least spanning ranges of 0.005–17 Gyr, and masses from 0.5 $M_\odot$ to 70 $M_\odot$), to carry out more reliable predictions and to cover all the evolutionary stellar stages (from the zero age main sequence or ZAMS to the white dwarf stage), where for later phases such as the asymptotic giant branch, or AGB, and post-AGB this is specially tricky, see e. g. Alongi et al. (1993); Bressan et al. (1993); Bertelli et al. (1994); Fagotto et al. (1994a,b,c); Girardi et al. (1996, 2000); Lejeune & Schaerer (2001); Yi et al. (2003); Pietrinferni et al. (2004); Marigo et al. (2008)

iii) Initial mass functions (IMF). The initial mass function describes the initial distribution of masses of a population of stars. This function can be also empirical or theoretical (e. g. Salpeter, 1955; Vazdekis et al., 1996; Kroupa, 2001; Chabrier, 2003). By definition, the IMF is related with the relative number of stars belonging to an instant burst of star formation or SSP, that is, it is related to $N(m,t)$ (see Eq. 1.1). Following Vazdekis et al. (1996), the IMF can be formally included as

$$N(m,t) = \frac{\Phi(m)}{m} M_{\rm G}\, \delta m\ , \tag{1.2}$$

where $\Phi(m)$ is the IMF, and $M_{\rm G}$ the mass of the galaxy or region.

In addition, SSP models can be used as building blocks for the composition of more complex models, in which different generations of stars with different metallicities can appear at different epochs. The construction of composite stellar populations from SSP models can be driven using different analytical functions for the SFH, such as: exponentially declining (the most extended one and usually referred as τ-models), single bursts of a τ duration, linearly declining, or delayed exponentially declining SFHs. The inclusion of composite stellar populations will open the possibility for exploring other interesting topics, as the formation timescales (duration of the main star formation episodes that built the bulk of stars). The abundance of α-elements (mainly Mg , Ne , and O ; but also N , Na , Si , S , and C) is also a problem during the determination of reliable synthesis models, as the "lockstep" hyphotesis (the rate of elements in stars changes in the same proportion than in the sun) is compromised by the measurements of abundances during the last 20 years (Edvardsson et al., 1993; Tolstoy et al., 2009). It is though that these α-overabundances are related with an enrichment of the ISM mostly driven by SN-type II (massive stars) as opposed to SN-type Ia, which are efficient enriching the interstellar medium with these elements (see also Thomas et al., 1999; Pipino & Matteucci, 2004; Thomas et al., 2005; de La Rosa et al., 2011). Modern synthesis models are also including different abundances for the α-elements (see e. g. Thomas et al., 2003; Coelho et al., 2007; Vazdekis et al., 2015), which would imply an inclusion of stellar libraries including different α-element abundances or to estimate how a stellar library changes with different abundances.

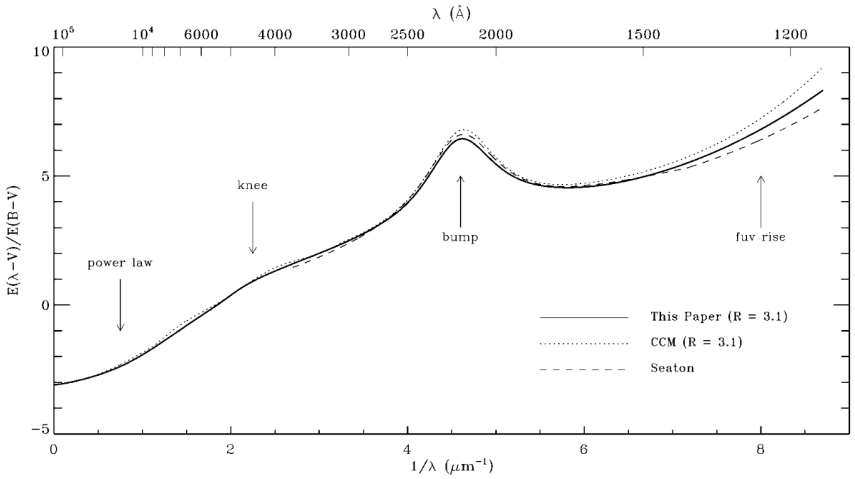

Figure 1.4: Parametrization of the reddening by dust (Y–axis) as a function of wavelength (X–axis). Picture taken from Fitzpatrick (1999).

Finally, the chemo-evolutionary models (e. g. Arimoto & Yoshii, 1986, 1987; Matteucci & Tornambe, 1987; Tosi, 1988; Casuso, 1991; Theis et al., 1992; Bressan et al., 1994; Vazdekis et al., 1996) are evolutionary synthesis models in which the chemical enrichment of the gas of the galaxy is also taken into account. Consequently, for the derivation of these models, there are involved various isochrones of different metallicities. Notice that a more complex enrichment of the interstellar medium can include different α-element abundances, rather than the total metallicity of the isochrone ([M/H]).

In addition, the interstellar medium (ISM) of galaxies is supposed to be partly populated by elements produced and ejected out during the life of stars. Part of these elements are reprocessed constituting dust grains that are the main source of extinction in the ISM (Draine, 2003a,b). Dust grains scatter the light and absorb ultraviolet (UV) and optical photons, whose energy is re-radiated at infrared (IR) wavelengths. Flux at the UV regime is more affected by extinction than at redder wavelengths, introducing a colour term in the continuum of the sources affected by extinction. This can also affect the colours of stellar populations, and therefore, when an analysis is based on colours their effects can be remarkable, specially in the cases of high extinction. There exist numerous parametrizations in the literature of dust reddening effects or extinction (e.g. Prevot et al., 1984; Massa, 1987; Mathis, 1990; Cardelli et al., 1989; Calzetti et al., 2000; Charlot & Fall, 2000; O'Donnell, 1994; Fitzpatrick, 1999), that can be easily computed in typical rest-frame spectral ranges (from $\lambda\lambda$ 1 000–1 200Å to $\lambda\lambda$ 2–3 μm). Extinction effects can be easily introduced in synthesis stellar population models, which will reinforce any stellar population predictions in which colours are involved, e. g. colour diagrams or photo-spectral fitting techniques of galaxies. Extinctions are typically parametrized by the total absorption in magnitudes at V (A_V) and the ratio of total to selective absorption at V (R_V, see Fig. 1.4 for the parametrization by Fitzpatrick, 1999). The latter varies between 2.2 and 5.8 depending on the environmental characteristics of the diffuse ISM, whose reference value in almost the totality of extragalactic studies is $R_V = 3.1$, which is the mean value in the diffuse ISM of the MW (Cardelli et al., 1989; Schlafly & Finkbeiner, 2011).

1.3.3 Large scale multi-filter surveys

At present, there is an increasing number of modern and future multi-filter surveys (see references in Díaz-García et al., 2015, or Sect. 6.1), including a vast volume of high-quality multi-filter data. These kinds of surveys are composed of several top-hat and/or broad-band filters that mainly cover the optical range, although sometimes the near-infrared (NIR) is also included. This allows to sample all the sources of the imaged sky in a very wide spectral range with multiple bands, that is, the spectral energy distribution (SED) of galaxies and stars are sampled with a spectral resolution equal to the width of each band (low-resolution

spectrum or photo-spectrum, see Hickson et al., 1994). The potential data of this kind of surveys are opening new pathways for exploring many topics in Astronomy and Cosmology, as well as they are promoting the development of new analysis techniques (e. g. including Bayesian methods) and the fine-tuning of others such as SED-fitting techniques. In fact, multi-filter surveys are already demonstrating to be an excellent set of data to study stellar populations of galaxies at intermediate and high-redshift (e. g. Mathis et al., 2006; Koleva et al., 2008; Ilbert et al., 2010; Walcher et al., 2011; Hernán-Caballero et al., 2013; Oteo et al., 2013; Ferreras et al., 2014; Moustakas et al., 2013; Marchesini et al., 2014; Cava et al., 2015; Díaz-García et al., 2015; Ruiz-Lara et al., 2015; Viironen et al., 2015; Domínguez Sánchez et al., 2016; Gargiulo et al., 2016), which largely contributes to advance in our understanding of galaxy evolution. Even though the data from multi-filter surveys suffer from the lack of high spectral resolution, they present a set of interesting advantages that can motivate future studies about stellar populations only using this kind of data:

i) There is no sampling bias. The galaxy samples of multi-filter surveys do not suffer from selection criteria other than the photometric depth in the detection band of the survey, because all the objects in the field of view are observed.

ii) Great photometric calibration. The SED of galaxies observed in multi-filter surveys does not suffer from the typical uncertainties in the flux calibration that lead to systematic colour terms, since the photometric calibration of each individual band is independent of the rest.

iii) The photometric depth. With similar telescopes, the depth of multi-filter surveys is usually much greater than for spectroscopic surveys, since direct imaging is much more efficient than spectroscopy. The state-of-the-art multi-filter surveys can easily reach galaxies at intermediate redshifts ($z \sim 1$–2), allowing us to set milestones on the evolution of galaxies.

iv) Multi-filter surveys provide spatially resolved photo-spectra. Multi-filter surveys allow to perform 2D stellar population studies in galaxies whose apparent sizes are not dominated by the point spread function (PSF) of the system.

v) Photometry is not affected by aperture bias. Unlike spectroscopic studies using fibers, the photometric apertures defined in these surveys are not fixed to constant values, that is, dynamical apertures are defined using more deep images for detection purposes in order to retrieve the fluxes of galaxies.

1.4 Goals of this work

This thesis aims at improving our understanding of the evolution of quiescent galaxies since $z \sim 1$, with the ultimate goal of providing a general picture for the formation and evolution of these objects along the history of the Universe. Making use of data from the Advanced Large Homogeneous Area Medium-Band Redshift Astronomical (ALHAMBRA) survey, this Ph. D. thesis is novel at facing for the first time an extensive, observational study that comprises the time evolution of the number density of quiescent galaxies, as well as their masses, stellar populations (ages, metallicities and extinctions) and sizes, to ultimately build up a phenomenological evolutionary model based on the merger, "frosting" and "progenitor bias" scenarios that tries to reconcile the observed trends in the above parameters.

There are a lot of objectives that should be properly accounted for in order to achieve our aims. These ones are listed below:

- **Reliable determination of stellar population parameters via SED-fitting and only using data from large scale multi-filter surveys**. In particular, the code MUFFIT, developed as part of this work, is devoted for determining the stellar population parameters using any photometric dataset. Although we exclusively use the ALHAMBRA data throughout this work for determining stellar populations of galaxies, we planned to span all the methodologies to other multi-filter surveys. It

is noteworthy that the ALHAMBRA dataset is an excellent test bench for the performing of these techniques. Once the large-scale surveys J-PLUS (Cenarro et al., in prep.) and J-PAS (Benítez et al., 2014) start the observations, all the methodologies performed under the ALHAMBRA dataset will be directly applied on these fruitful surveys.

- **Extraction of a pure sample of quiescent galaxies**. There exist several diagnostic diagrams to select samples of quiescent galaxies (see Sect. 1.1), some of them with interesting advantages with respect to others. The combination of optimal diagnostic diagrams with the stellar population determinations for each galaxy in the parent dataset can provide a reliable sample of quiescent galaxies, where typical sources of contamination (e. g. reddened-by-dust star forming galaxies) may be successfully mitigated.

- **Evolution of the stellar population parameters of quiescent galaxies with redshift**. In particular, we aim to determine the evolution of ages, metallicities, and extinctions of quiescent galaxies via SED-fitting, through their distributions of values at different redshifts and stellar masses. The evolution of these parameters will be key to trace how these galaxies have evolved up to present days.

- **Quantifying and discerning the likely mechanisms affecting the evolution of quiescent galaxies**. Once galaxies quench star formation, its evolution is suitable to other mechanisms less representative than starbursts or efficient star formation. Other effects, such as the proper ones of a hierarchical merging, are suitable candidates to drive the evolution of galaxies that do not experiment a significant star formation.

- **Correlations between size and the stellar content of quiescent galaxies and implications for their growth in size**. During the past and present decade, many efforts were performed for quoting the responsible mechanisms of the increase in size of galaxies. Owing to the large set of quiescent galaxies that we can retrieve from ALHAMBRA and it is wide range in redshift, we are able to explore the mechanisms driving the increase in size of galaxies through the study of the stellar content of quiescent galaxies.

On the basis of all the above pieces of information, in many case unique and unprecedented due to the amount and type of data, as well as to the analysis techniques, this work is ultimately expected to shed light on a global view on the formation and evolution of red sequence galaxies, being this overall consistent with all the observables in play.

Notice the both Chapter 2 and Chapter 6 were actually published in referred journals under references Díaz-García et al. 2015, A&A, 582A, 14D and Díaz-García et al. 2013, MNRAS, 433, 60D respectively.

2

MUFFIT: a MUlti-Filter FITting code for stellar population diagnostics

> *A pessimist sees the difficulty in every opportunity; an optimist sees the opportunity in every difficulty.*
>
> Winston Churchill

This chapter has been published as
Díaz-García et al. 2015, A&A, 582A, 14D

Introducción al artículo

A lo largo de este artículo se presenta una de las partes más largas y difíciles de desarrollar, y al mismo tiempo indispensables, para alcanzar los objetivos de esta tesis doctoral: el código genérico MUFFIT. Éste ha sido cuidadosamente y específicamente desarrollado con el objetivo de extraer los parámetros de las poblaciones estelares de galaxias mediantes datos fotométricos de cartografiados multifiltro (fotoespectros). Al mismo tiempo, se comprueba su fiabilidad y viabilidad con galaxias reales procedentes del cartografiado ALHAMBRA y con simulaciones, con un resultado satisfactorio en todos los casos. A pesar de existir múltiples herramientas disponibles para la comunidad científica para llevar a cabo ajustes de fotoespectros, SED-fitting, éstos carecían de los detalles técnicos para cubrir todas las necesidades para llevar a cabo el análisis de poblaciones estelares con el nivel de detalle necesario para este tipo de estudios. Entre las características más llamativas de MUFFIT podemos destacar:

i) La libertad de incluir diferentes modelos de poblaciones simples (SSP) para llevar a cabo el SED-fitting de galaxias. Modelos que han sido cuidadosamente elaborados con múltiples restricciones físicas para predecir de la forma más fiable la evolución de una población estelar, determinando parámetros que pueden ser interpretados físicamente como edad y metalicidad. Esto marca una diferencia respecto otros códigos que simplemente incluyen conjuntos de modelos que, o bien, han sido calculados empíricamente y que por tanto sus parámetros de poblaciones estelares son de difícil calibración o interpretación; o bien, modelos que han sido seleccionados con el único objetivo de determinar otros parámetros que difieren de las edades y metalicidades que describen una población estelar (por ejemplo, desplazamientos al rojo o masas estelares).

ii) MUFFIT ha sido diseñado para lidiar con todo tipo de cartografiados multi-filtro, incluyendo J-PAS y J-PLUS que incluyen multitud de filtros lo suficientemente estrechos ($FWHM \sim 125$ Å) como para ser sensibles a líneas de emisión. Esto supone un reto para otro tipo de códigos debido a la presencia

de líneas emisión, las cuales pueden perjudicar drásticamente los ajustes a modelos, como los SSP (que habitualmente no las incluyen y cuya contribución es de difícil estimación).

iii) MUFFIT ha sido analizado y calibrado detalladamente para lidiar con datos fotométricos de la forma más precisa posible, comparando con otros estudios de la literatura (incluyendo estudios espectroscópicos).

MUFFIT está basado en un test de χ^2 pesado con errores, donde se comparan los flujos de las diferentes bandas de la galaxia con la fotometría sintética de modelos mezcla de dos poblaciones estelares simples, a diferentes desplazamientos al rojo y con diferentes extinciones, para obtener el rango probable de sus parámetros de poblaciones estelares (mayormente edad y metalicidad), extinción, desplazamiento al rojo y masa estelar. Para mejorar la fiabilidad del análisis, MUFFIT identifica y descarta del proceso de análisis aquellas bandas con indicios de contener lineas de emisión de intensidad significativa. Los parámetros finales junto con sus incertidumbres son derivados a partir de una metodología Monte Carlo, usando las incertidumbres de la fotometría de cada banda.

A lo largo de este trabajo se concluye que MUFFIT es un código preciso y fiable para derivar los parámetros de las poblaciones estelares de las galaxias de ALHAMBRA. Es más, hacemos un análisis exhaustivo y detallado de todos los problemas que pueden acarrear este tipo de análisis, detallando en todo momento la capacidad para determinar particularmente edad, metalicidad y extinción, y de forma complementaria, masa estelar y desplazamientos al rojo fotométricos. Parte de estas conclusiones son obtenidas a partir de simulaciones que incluyen diferentes valores de señal-ruido, las cuales también demuestran que estos tipos de análisis basados en los colores del continuo son lo suficientemente sensibles a este conjunto de parámetros estelares. Al mismo tiempo, podemos cuantificar los tipos de incertidumbres intrínsecos a esta metodología, así como los tipos de degeneraciones que podemos esperar entre los parámetros involucrados. Por otro lado, complementamos estas pruebas para comprobar la fiabilidad de MUFFIT utilizando galaxias reales de ALHAMBRA. Utilizando predicciones de desplazamientos al rojo fotométricos como datos de entrada, MUFFIT es capaz de mejorar la precisión de éstos en un $\sim$ 10–20 %. Además, MUFFIT es capaz de detectar emisiones nebulares en galaxias y suministrar predicciones físicas de su intensidad. Las medidas de masa estelar calculadas por MUFFIT muestran un acuerdo excelente con los valores dados por COSMOS y SDSS para casos en común. También obtenemos que los mapas de edad–metalicidad para una muestra de galaxias de tipo temprano a $z \leq 0.22$ están en acuerdo con las obtenidas en diagnósticos espectroscópicos de SDSS. La comparación uno a uno entre desplazamientos al rojo, edades, metalicidades y masas estelares, derivadas con espectroscopía en SDSS y por MUFFIT en ALHAMBRA, muestran un buen acuerdo cualitativo entre todas ellas, reforzando así el potencial de los cartografiados multifiltro cuando son analizados con las técnicas de análisis apropiadas, como MUFFIT, para llevar a cabo estudios de poblaciones estelares de forma correcta.

Lamentablemente, las técnicas y metologías de este tipo han sido pobremente explotadas en cartografiados multifiltro. Habitualmente no van más allá de tareas como determinar desplazamientos al rojo fotométricos o masas estelares, mientras que para edades y metalicidades son injustamente despreciados porque en muchos casos no han sido calibrados debidamente. En ciertos casos también han sido utilizadas como un soporte para corroborar los propios resultados espectroscópicos, centrados en zonas del espectro más sensibles a ciertos parámetros poblacionales como edad (e. g. Fagioli et al., 2016; Gargiulo et al., 2016). Es más, los resultados demuestran que las incertidumbres típicas con las que se recuperan los valores de metalicidad en cartografiados tipo ALHAMBRA pueden llegar a ser más fiables que ciertas estimaciones de metalicidades espectroscópicas, y que además reforzamos mediante la estadística del gran número de galaxias con los que cuentan los cartografiados multifiltro.

Stellar populations of galaxies in the ALHAMBRA survey up to $z \sim 1$: I. MUFFIT a MUlti-Filter FITting code for stellar population diagnostics

Díaz-García et al. 2015, A&A, 582A, 14D

ABSTRACT: We present MUFFIT, a new generic code optimized to retrieve the main stellar population parameters of galaxies in photometric multi-filter surveys, and check its reliability and feasibility with real galaxy data from the ALHAMBRA survey.

Making use of an error-weighted χ^2-test, we compare the multi-filter fluxes of galaxies with the synthetic photometry of mixtures of two single stellar populations at different redshifts and extinctions, to provide the most likely range of stellar population parameters (mainly ages and metallicities), extinctions, redshifts, and stellar masses. To improve the diagnostic reliability, MUFFIT identifies and removes from the analysis those bands that are significantly affected by emission lines. The final parameters and their uncertainties are derived by a Monte Carlo method, using the individual photometric uncertainties in each band. Finally, we discuss the accuracies, degeneracies, and reliability of MUFFIT using both simulated and real galaxies from ALHAMBRA, comparing with results from the literature.

MUFFIT is a precise and reliable code to derive stellar population parameters of galaxies in ALHAMBRA. Using the results from photometric-redshift codes as input, MUFFIT improves the photometric-redshift accuracy by $\sim$ 10–20 %. MUFFIT also detects nebular emissions in galaxies, providing physical information about their strengths. The stellar masses derived from MUFFIT show excellent agreement with the COSMOS and SDSS values. In addition, the retrieved age–metallicity locus for a sample of $z \leq 0.22$ early-type galaxies in ALHAMBRA at different stellar mass bins are in very good agreement with the ones from SDSS spectroscopic diagnostics. Moreover, a one-to-one comparison between the redshifts, ages, metallicities, and stellar masses derived spectroscopically for SDSS and by MUFFIT for ALHAMBRA reveals good qualitative agreements in all the parameters, hence reinforcing the strengths of multi-filter galaxy data and optimized analysis techniques, like MUFFIT, to conduct reliable stellar population studies.

2.1 Introduction

Studying the stellar content of galaxies is crucial to understanding their star formation histories (SFH), which in turn provides us with valuable information about the possible evolutive paths from their formation at high redshift down to the present time. Despite the strong efforts and advances achieved in this topic during the past decades, it still remains as one of the most challenging and promising ways to understand galaxy evolution.

Early attempts to study the stellar content of early-type galaxies were based on colours from wide and narrow band photometry (Baum, 1959; Tifft, 1963; Wood, 1966; McClure & van den Bergh, 1968; Faber, 1973) and on empirical synthesis of the populations using the observed colours of nearby early-types as basis. These early methods can be considered as the pioneers of the current photo-spectral fitting techniques, which are the main topic of the present paper. The above methods were gradually displaced by techniques based in more specific features (Faber, 1973; Pritchet, 1977) that were defined in narrow spectral ranges.

The arrival of absorption line-strength indices to study the stellar content of galaxies (Burstein et al., 1984; Faber et al., 1985) brought a significant breakthrough in the field. On this front, it is worth noting

the Lick system of indices (Gorgas et al., 1993; Worthey et al., 1994b), which for the past decades has been the standard for most spectroscopic studies in stellar populations in the optical (e. g. Trager et al., 1998; Jørgensen, 1999; Kuntschner et al., 2001; Thomas et al., 2005; Bernardi et al., 2006; Sánchez-Blázquez et al., 2006b; Gorgas et al., 2007). The combination of a certain number of absorption lines mainly sensitive to age, such as the Balmer lines, or to the metallicity, as traced by certain elements such as Fe , Mg , Ti , C , Ca , and Na were proven to be an efficient way to break the well known degeneracy between these two parameters, at least to some extent (Worthey, 1994a). The way to measure these features is delicately chosen to be very sensitive to a parameter of interest, focusing its study on narrow spectral ranges. By construction, line-strength indices are quite insensitive to the influence of extinction, and by fine-tuning their definition or combining the sensitivities of different indices, some of them may end up being almost independent of other parameters, such as metallicity (Vazdekis & Arimoto, 1999b; Cervantes & Vazdekis, 2009) and α-element overabundances (Thomas et al., 2003).

In the past fifteen years, the development of stellar libraries in spectral ranges other than the optical has driven the definition of new indices that allowed this kind of study to be extended to other regions with unexplored sensitivities (Cenarro et al., 2002; Mármol-Queraltó et al., 2008). In addition, the index system of reference in the optical spectral range has been revisited and improved (see e. g. Vazdekis et al., 2010) thanks to the availability of much better stellar libraries at much better spectral resolution.

It was with the arrival of improved stellar libraries, such as CaT (Cenarro et al., 2001a,b), ELODIE (Prugniel & Soubiran, 2001), STELIB (Le Borgne et al., 2003), INDO-US (Valdes et al., 2004), Martins et al. (2005), and MILES (Sánchez-Blázquez et al., 2006c; Cenarro et al., 2007), and the consequent evolutionary stellar population synthesis models (e. g. Bruzual & Charlot, 2003; Vazdekis et al., 2003; González Delgado et al., 2005; Maraston et al., 2009; Vazdekis et al., 2010; Conroy & van Dokkum, 2012; Vazdekis et al., 2012), that fitting techniques over the full spectral energy distribution of galaxies appeared as an alternative to line-strength indices. SED-fitting can also be used to derive several physical properties of galaxies (Mathis et al., 2006; Koleva et al., 2008; Coelho et al., 2009; Walcher et al., 2011; Liu et al., 2013). In fact, there is a growing number of public codes specifically devoted to carrying out SED-fitting with different procedures, such as hyperz (Bolzonella et al., 2000), LE PHARE (Arnouts et al., 2002; Ilbert et al., 2006), STARLIGHT (Cid Fernandes et al., 2005), STECKMAP (Ocvirk et al., 2006), VESPA (Tojeiro et al., 2007), ULYSS (Koleva et al., 2009), FAST (Kriek et al., 2009), and SEDfit (Sawicki, 2012).

Nowadays, there is an increasing number of present and future multi-filter surveys, including COMBO-17 (Wolf et al., 2003), MUSYC (Gawiser et al., 2006), COSMOS (Scoville et al., 2007), ALHAMBRA (Moles et al., 2008), CLASH (Postman et al., 2012), SHARDS (Pérez-González et al., 2013), J-PAS (Benítez et al., 2014), and J-PLUS (Cenarro et al., in prep.), each of them with a vast volume of high-quality multi-filter data. These kinds of surveys pursue diverse goals with a common feature: sampling the SEDs of galaxies using top-hat and/or broad-band filters that mainly cover the optical range. Owing to this configuration, the retrieved SEDs are half-way between classical photometry and spectroscopy, because in practice they are like a low-resolution spectrum whose resolution depends on the filter system (e. g. $R \sim 20$ for ALHAMBRA; $R \sim 50$ for J-PAS).

Although multi-filter observing techniques suffer from the lack of high spectral resolution, their advantages over standard spectroscopy are worth noting: (i) the galaxy samples of multi-filter surveys do not suffer from selection criteria other than the photometric depth in the detection band of the survey, because all the objects in the field of view are observed. For a fixed observational time and similar telescopes, this leads to much larger galaxy samples than in multi-object spectroscopy, where achieving multiplexities greater than ~ 1000 is a challenge at present. (ii) Unlike standard spectroscopy, the SED of galaxies observed in multi-filter surveys does not suffer from the typical uncertainties in the flux calibration that lead to systematic colour terms, since the photometric calibration of each individual band is independent of the rest. This advantage is crucial, because it is the overall continuum of the stellar population that in most cases dominates the diagnostic with SED-fitting techniques. (iii) With similar telescopes, the depth of multi-filter surveys is usually much greater than for spectroscopic survey, since direct imaging is much more efficient than spectroscopy. (iv) Multi-filter surveys provide spatially resolved photo-spectra, similar to an integral

field unit (IFU), allowing us to perform 2D stellar population studies in galaxies whose apparent sizes are not dominated by the PSF of the system.

It is therefore clear that multi-filter surveys open a profitable way to advance in our understanding of galaxy evolution by providing complete and homogeneous sets of galaxy SEDs down to a certain magnitude depth. Although there are several SED-fitting codes available, to cope with the calibration particularities of multi-filter surveys (see e. g. Molino et al., 2014), and given the vast amount of high-quality photometric data already available in the literature and still to come in the next years, in this paper we present MUFFIT (MUlti-Filter FITting for stellar population diagnostics), a code specifically designed for analysing the stellar content of galaxies with available multi-filter data.

This paper mainly aims to describe the code and its functionalities, set the accuracy and typical uncertainties in the retrieved stellar population parameters, and demonstrate its reliability compared with already existing stellar population results in the literature. MUFFIT was developed within the framework of the ALHAMBRA survey (see Sect. 2.2), so even though the code is generic and can be easily employed for any kind of photometric system, many sections in this paper are specific to the ALHAMBRA dataset. This allows us to show the code's performance on real galaxy data, which is ultimately the best sanity check for any stellar population code. Even though in this paper we use galaxy data from ALHAMBRA, it is not our intention to scientifically exploit the dataset here. In subsequent papers in this series, we will provide and exploit the stellar population parameters retrieved for the whole galaxy sample in the ALHAMBRA survey.

This paper is organized as follows. Section 2.2 presents a quick overview of the ALHAMBRA survey, that is, the photometric dataset employed to develop the present work. In Sect. 2.3, we summarise the main technical aspects of our code, MUFFIT, as well as the processes for obtaining photometric colour predictions from models of SSP and the MW extinction corrections. We show the accuracy and reliability of the stellar population parameters retrieved with our code, together with the uncertainties and degeneracies expected for ALHAMBRA data in Sec. 2.4. Section 2.5 presents a comparison study of the results retrieved from ALHAMBRA galaxy data using MUFFIT with previous studies, including spectroscopic ones and data from the literature, thereby testing the reliability of our results. Finally, we provide the summary and conclusions of this research in Sect. 2.6.

Throughout this paper we assume a ΛCDM cosmology with $H_0 = 71$ km s^{-1}, $\Omega_M = 0.27$, and $\Omega_\Lambda = 0.73$.

2.2 The ALHAMBRA survey

The stellar population code that we present in this paper is generically designed for all types of multi-filter surveys. However, we make use of the data in the ALHAMBRA survey[1] to prove and test the reliability of our techniques, as in fact this code will be employed to analyse the stellar population properties of ALHAMBRA galaxies in forthcoming papers (Díaz-García et al., in prep.). Throughout this work, therefore, we mainly present results from both simulations and real observations that are based either on the ALHAMBRA data or on its technical setup. In the following paragraphs we present a short summary of the ALHAMBRA survey.

The ALHAMBRA survey provides a photometric dataset of 20 contiguous, medium-band ($FWHM \sim 300$ Å), top-hat filters, that cover the complete optical range $\lambda\lambda$ 3 500–9 700 Å (see Aparicio Villegas et al., 2010, for further details) over eight non-contiguous regions of the northern hemisphere, amounting to a total area of 4 deg^2 of the sky (including areas in common with other cosmological surveys such as COSMOS, see Molino et al., 2014, for other overlapping areas). All filters in the optical range have very steep side transmission slopes, close to zero overlap in wavelength, a flat top, and transmissions of 80–95 % (Moles et al., 2008). The magnitude limit is $m_{AB} \sim 24$ (5-sigma, measured on 3″) for the 14 filters ranging from 3 500 to 7 700 Å, decreasing smoothly in the six reddest filters reaching down to $m_{AB} \sim 21.5$ in the reddest one (Molino et al., 2014), which is centred at 9 550 Å. The optical coverage is supplemented with the

[1] http://www.alhambrasurvey.com

standard NIR J, H, and K_s filters, which have a 50 % detection efficiency depth (point-like sources, AB magnitudes) of $J \sim 22.4$, $H \sim 21.3$, and $K_s \sim 20.0$, analysed in Cristóbal-Hornillos et al. (2009). The ALHAMBRA filter set[2] is designed to optimize the accuracy of photometric redshifts (photo-z, Benítez et al., 2009), but due to their characteristics, it also provides low-resolution photo-spectra composed of 23 bands, corresponding to a resolving power $R \sim 20$ in the optical. All the observations were done under a quality criterion of seeing $< 1.6''$ and airmass < 1.8, using the 3.5 m telescope in the Calar Alto Observatory[3] (CAHA) with two cameras, the imager LAICA in the optical range and Omega-2000 for the NIR filters. The actual area for this work is 2.8 deg^2 with a total on-target exposure time of ~ 700 h (~ 608 h were dedicated for the optical bands, and ~ 92 h for the NIR ones) because part of the ALHAMBRA fields have not been imaged yet, although the rest of the fields will be completed reaching the expected total area of 4 deg^2.

The ALHAMBRA Gold catalogue[4] (Molino et al., 2014, hereafter Gold catalogue), is the reference catalogue for this work. As explained in Molino et al. (2014), synthetic $F814W$ images were created, as a linear combination of individual filters, to be used for both detection and completeness purposes, emulating the $F814W$ band of the ACS camera in the HST telescope. Therefore, the Gold catalogue provides 23 + 1 photometric AB magnitudes (Oke & Gunn, 1983) and errors for $\sim 95\,000$ bright galaxies ($17 < m_{F814W} \leq 23$), which are complete up to $m_{F814W} = 23$. Throughout this work, the synthetic $F814W$ photometry is removed from the analysis. Due to the existence of a PSF variability among different filters, the photometry is corrected for PSF and aperture effects. In addition, and for the specific ALHAMBRA case, we quadratically add an extra uncertainty of ~ 0.025 (AB magnitudes) in each photometric measurement to account for potential calibration issues or uncertainties.

For further details of the ALHAMBRA survey, we refer readers to (Moles et al., 2008) and (Molino et al., 2014).

2.3 The code

Although there are many public codes devoted to carrying out SED fitting in many different ways, e. g. hyperz, STARLIGHT, ULySS, VESPA, LE PHARE, FAST, or SEDfit; we are performing our own analysis techniques to retrieve stellar population parameters from photometric SEDs, specifically designed for analysing the stellar content of galaxies from the ALHAMBRA survey, but being generic and easily adaptable to any multi-photometric survey. Secondarily, there is an increasing number of large-scale multi-filter surveys; e. g. ALHAMBRA, J-PLUS and J-PAS, SHARDS, CLASH, MUSYC, COSMOS, or COMBO-17. They offer a huge amount of photometric data that we can exploit to study the evolution of galaxies, opening a new path to exploring the stellar population of galaxies, overall at intermediate and high redshifts. Although these photometric data are like low-resolution spectra, these techniques present remarkable advantages in comparison with spectroscopy. They can go deeper with a better flux calibration (the calibration of each filter is independent of the rest of them), we can study the stellar content in each resolution element (similar to IFU techniques) with one exposure, and we can work with larger galaxy samples; as a result, it would be a pity not to take advantage of these studies and not exploit all the opportunities that they offer.

The collection of analysis techniques, routines, and other tools that we are using, are collected under the code name MUFFIT, which is written in `Python` language, and it mainly focuses on retrieving the stellar populations of galaxies whose SEDs are dominated by their stellar content.

This section is subdivided in two extended sections. On the one hand, we show in Sect. 2.3.1 the main ingredients or inputs required to develop the analysis. These preliminary elements are basically composed of the SSP models, the photometric system, and the selection of a dust extinction law to treat the impact of dust on the model SEDs properly. On the other hand, the code is described in Sect. 2.3.2, emphasizing the description of some specific tasks.

[2] `http://svo2.cab.inta-csic.es/theory/fps3/`
[3] `www.caha.es`
[4] `http://cosmo.iaa.es/content/alhambra-gold-catalog`

In Fig. 2.1, we outline the main structure of the code by a brief flowchart that summarises the main features of the followed processes to set constraints on the stellar populations. We caution that the purposes of the flowchart are to help the reader follow the development of Sects. 2.3.1 and 2.3.2 and to support the schematic comprehension of the several stages.

The reader who is primarily interested either in the reliability of the code or in the comparison with results retrieved from the literature may skip this section to continue with the self-contained Sects. 2.4 and 2.5.

2.3.1 Main ingredients of the stellar population code

In this section we describe the main input ingredients and preparatory tasks that are considered for developing the stellar population analysis code that is presented in this paper. In particular, our code requires an input set of reference SSP models (Sect. 2.3.1.1), the photometric system of the data (Sect. 2.3.1.2), along with a set of recipes to take the intrinsic and MW extinction into account (Sect. 2.3.1.3). The redshifts of the target galaxy data can be managed as an input ingredient or an output of the code, as explained in Sect. 2.3.1.4. The flowchart on the left-hand side of Fig. 2.1 particularly illustrates the main ingredients and preliminary work carried out by the code before starting with the analysis of the data.

2.3.1.1 The SSP models

The code has been designed to use SSP models as input templates for the comparative analysis of the stellar populations of galaxies. Currently, the code is ready to account for the Bruzual & Charlot (2003, hereafter BC03)[5] and MIUSCAT[6] (Vazdekis et al., 2012; Ricciardelli et al., 2012) SSP models, although any other SSP spectral dataset can be easily implemented.

BC03 is perfectly suited to SED fitting given the large spectral coverage of the models, from 91 Å to 160 μm, allowing us to cope with most kinds of multi-filter galaxy data, irrespective of the redshift. For the present work, we assume ages up to 14 Gyr and metallicities [Fe/H]= −1.65, −0.64, −0.33, 0.09, and 0.55, Padova 1994 tracks (for further details and references, see Bruzual & Charlot, 2003), and a Chabrier (2003) IMF.

MIUSCAT provides a sample of SEDs with a spectral range $\lambda\lambda$ 3 465–9 469 Å and a resolution of $FWHM \sim 2.5$ Å, almost constant with wavelength (Falcón-Barroso et al., 2011). Despite the great colour calibration of these models, its spectral range is not enough for galaxies at intermediate redshift and further, missing the observed ALHAMBRA colours in the UV range. For this purpose, we extend the lower end of MIUSCAT models up to 1 860 Å(A. Vazdekis 2015, priv. comm.), using the Next Generation Spectral Library (NGSL, Heap & Lindler, 2007). In addition, we complement these models with their photometric predictions for J, H, and K, which are adapted to predict the ALHAMBRA NIR bands. Throughout this work, we use the models up to 14.13 Gyr with metallicities [Fe/H]= −1.31, −0.71, −0.40, 0.0, and 0.22. We assume a Kroupa Universal-like initial mass function (Kroupa, 2001), even though its universality is a current matter of debate (see, e. g. Ferreras et al., 2013). In future works, we will shed light on the systematic variation of the IMF for the more massive galaxies in the ALHAMBRA database.

By construction, the code can also use not only any other set of SSP models, but also any other kind of reference template spectra; for example, as long as their main stellar population parameters (age, metallicity, IMF, extinction, and over-abundances), the spectra of real galaxies are assigned by the user. Throughout this paper we do not present this possibility, but concentrate on the performance of the code on the basis of the two SSP model sets mentioned above.

[5] http://bruzual.org/
[6] http://miles.iac.es/

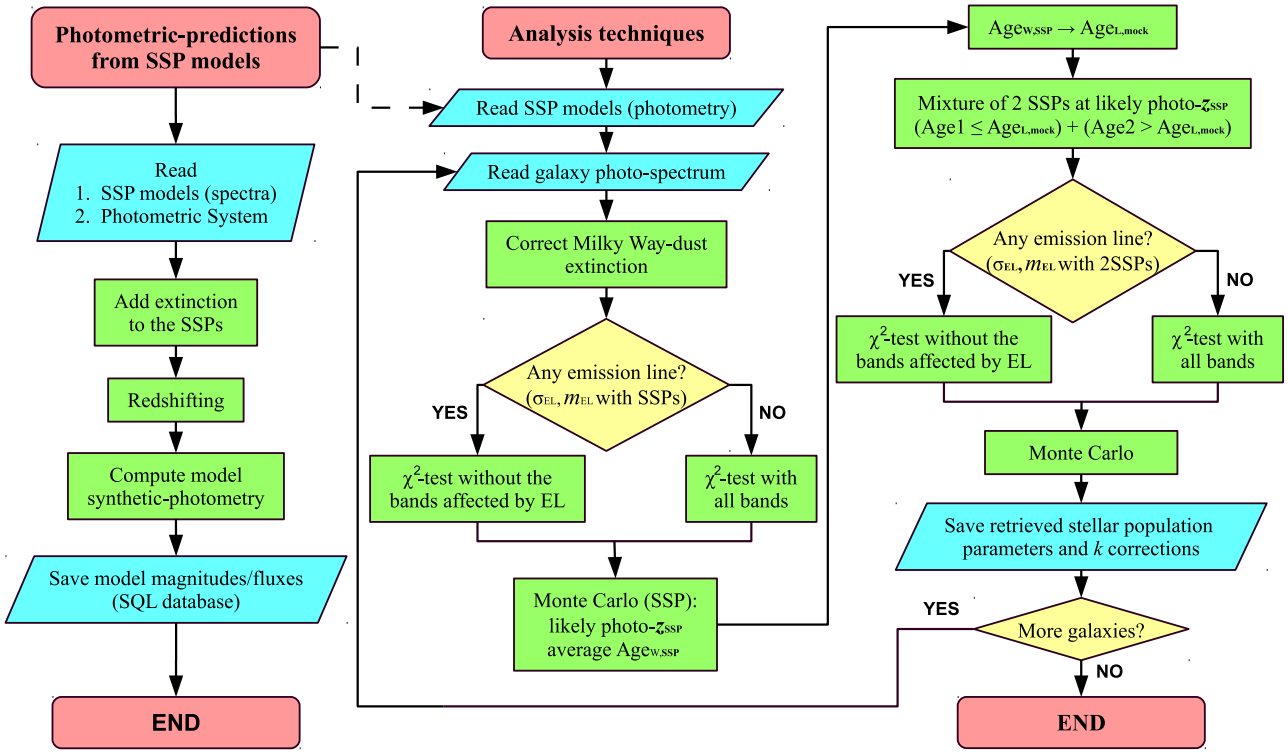

Figure 2.1: Flowcharts of the photometric model predictions (*left*) and the analysis techniques (*right*). A more detailed explanation of each step can be found in Sects. 2.3.1.2, 2.3.1.3, and 2.3.2. The dashed row indicates where both processes are related. Flowchart symbols represent standard tasks: ovals, start/end of a process (red); arrows, the direction of logic flow in the process; parallelograms, input/ouput operation (cyan); diamonds, a decision or branch to be made (yellow); and rectangles, a processing step (green).

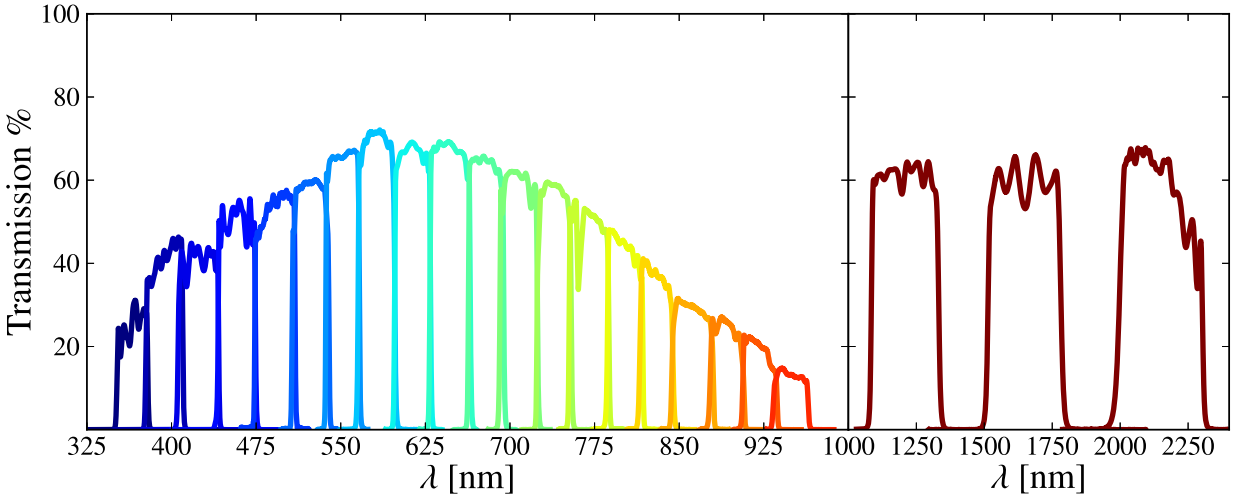

Figure 2.2: Response curves of the ALHAMBRA filter set for the CCD 1 in the optical range (LAICA camera; one colour from blue to red per band), together with the ALHAMBRA J, H, and K_s filters (Omega-2000 camera; dark red) to make the model synthetic photometry.

2.3.1.2 Photometric system and synthetic photometry

For a proper comparison between input SSP models and galaxy data, it is essential to build a reliable estimation of the synthetic magnitudes (or integrated fluxes) of the SSP template models in the same photometric system of the galaxies as the one that needs to be analysed. This is computed by convolving the SSP model or galaxy reference spectra with the response functions of the photometric system. In addition to taking the empirical filter transmission curves into account, in order to obtain a reliable photometric prediction it is advisable to account for specific characteristics of the observing conditions and the instrumental setup employed for the photometric observations of the galaxies to be analysed, for example, the transmittance of the optical system and/or the sky absorption spectrum where the observations were done. The wavelength dependence of the quantum efficiency of charge-coupled devices (CCDs) is remarkable, since typically less sensitive in the bluer and redder ends. If not accounted for properly, this effect modifies the effective wavelength of such filter bandpasses, creating a fictitious colour term in the synthetic photometry of the reference models. Figure 2.2 presents the response functions of the ALHAMBRA photometric system. It consists of 20 optical bands (left-hand side) and the ALHAMBRA J, H, and K_s NIR-bands (right-hand side). In this figure, all the effects explained above are already embedded.

We compute the synthetic photometry following the methodology described in Pickles & Depagne (2010), which is based on the HST `synphot`[7] package and in Bessell (2005). Since current detectors are photon-counting detectors, the number of photons detected across a pass-band X is

$$N_X^{\rm ph} = \int \frac{\lambda}{\rm hc} F_\lambda R_X(\lambda)\, {\rm d}\lambda \,, \tag{2.1}$$

where F_λ is the spectrum to convolve, and $R_X(\lambda)$ is the response function of the filter X (also called sensitivity function in some previous work). Normalizing Eq. 2.1, we get the weighted mean photon flux density,

$$\overline{F_X^{\rm ph}} = \frac{\int \lambda F_\lambda R_X(\lambda)\, {\rm d}\lambda}{\int \lambda R_X(\lambda)\, {\rm d}\lambda}. \tag{2.2}$$

Some catalogues provide photometry in AB magnitudes, defined as

$$m_{\rm AB} = -2.5 \log_{10} f_\nu - 48.6 \,, \tag{2.3}$$

[7] `http://www.stsci.edu/institute/software_hardware/stsdas/synphot`

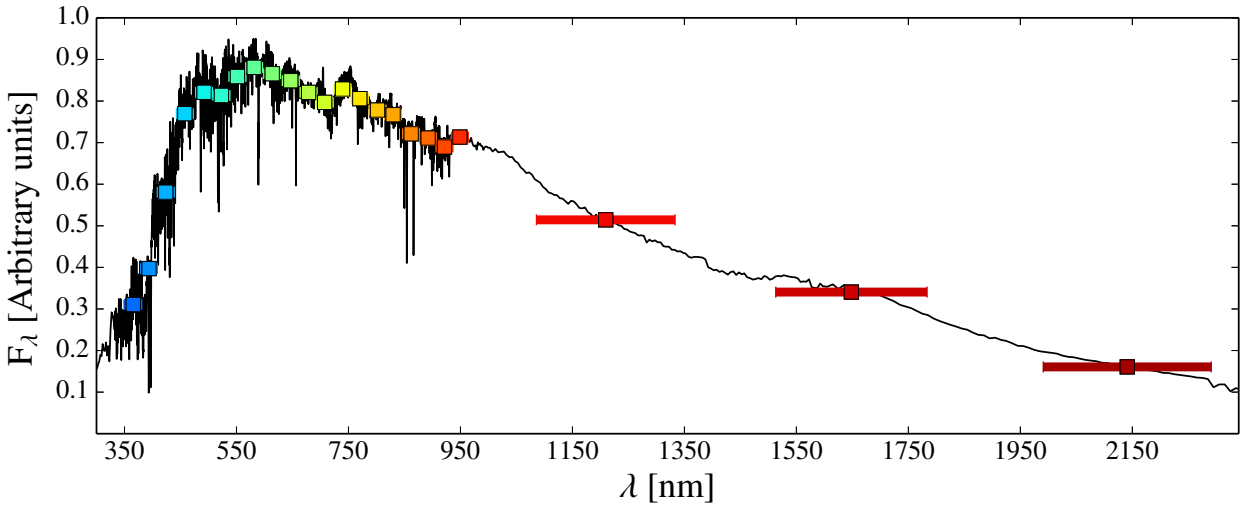

Figure 2.3: Synthetic photometry of a SSP using the ALHAMBRA photometric system. The black line is the SSP flux, the colour squares are the expected passbands, and the horizontal bars represent the FWHM of each filter.

where f_ν is the flux in ergs cm^{-2} Hz^{-1} s^{-1}. To transform the weighted mean photon flux density into AB magnitudes, we compute the magnitude of the flux in the STMAG system (system for calibrating HST stars, Stone, 1996), which can be easily transformed to the AB magnitude system (Eq. 2.5). This intermediate step is necessary because the weighted mean photon flux density is established per unit wavelength, whereas the AB magnitude system is given per unit frequency. The magnitude across the bandpass X in the STMAG system, $m_{\mathrm{ST},X}$, and in the AB system, $m_{\mathrm{AB},X}$, is

$$m_{\mathrm{ST},X} = -2.5 \log_{10} \overline{F_X^{\mathrm{ph}}} - 21.1 \,, \tag{2.4}$$

$$m_{\mathrm{AB},X} = m_{\mathrm{ST},X} - 5 \log_{10} \lambda_{\mathrm{pivot}} + 18.692 \,, \tag{2.5}$$

To illustrate this, Fig. 2.3 shows an example of a SSP spectrum taken from the model set of BC03 (rest frame, solar metallicity, intermediate age of 5 Gyr, Chabrier IMF, and no intrinsic extinction) along with its synthetic photometry using the ALHAMBRA filter set. The spectrum synthetic photometry was computed following the process explained above, where each bandpass is centred at their effective wavelengths ($\lambda_{\mathrm{eff}} = \int \lambda R_X(\lambda)\, \mathrm{d}\lambda / \int R_X(\lambda)\, \mathrm{d}\lambda$) and the horizontal bars represent the FWHM of each filter. This example is also useful for showing that the main, broader spectral features are easily distinguished after convolving, emphasizing the power of the ALHAMBRA photo-spectra as halfway between classical photometry and spectroscopy.

For the specific case of ALHAMBRA, and because of the configuration of LAICA, we computed four photometric databases for the optical bands, one per CCD, because there are discrepancies among CCD sensitivities and each CCD has its own set of filters. For the NIR-filters J, H, and K_{s}, we repeat this process taking the Omega-2000 configuration (only one detector plate). In both optical and NIR synthetic photometry, we take the filter transmission curves into account, the quantum efficiency of every CCD/camera, the sky absorption spectrum at CAHA, and the reflectivity of the 3.5 m-telescope primary mirror with the transmittance of the optical system.

Owing to both the large number of input model parameters (ages, metallicities, extinctions, IMF slopes, and redshifts) and the intermediate-high spectral resolution of current SSP models, it is in general more efficient to build up our set of convolved models once at the beginning, rather than recomputing the model synthetic photometry every time the code is run. After computing the synthetic photometry of all models, the photometric predictions (fluxes and magnitudes), along with the main characteristics of each model,

are stored in a structured query language (SQL) database. A straightforward flowchart of the process for estimating photometric predictions is shown on the left-hand side of Fig. 2.1.

2.3.1.3 Dust-extinction

Stellar population diagnostic techniques based on SED fitting over a broad spectral coverage, as in this case, require the reddening by extinction to be thoroughly considered to avoid potential misinterpretations of the integrated colours of the population, e. g. older ages or higher metallicities, as well as to derive reliable stellar masses.

Many authors have tried to parametrize the shape of the dust extinction curve (e. g. Prevot et al., 1984; Massa, 1987; Mathis, 1990; Cardelli et al., 1989; Calzetti et al., 2000; O'Donnell, 1994; Fitzpatrick, 1999), overall on the bluer parts where the dust reddening is more complex. The dust extinction curve is reproduced well using the parameter $R_V \equiv A_V/E(B-V)$ (Cardelli et al., 1989), which varies between 2.2 and 5.8 depending on the environmental characteristics of the diffuse ISM. Although the values of R_V may change depending of the line of sight, throughout this work we assume that the value of this parameter is $R_V = 3.1$, which is the mean value in the diffuse ISM of the MW (Cardelli et al., 1989; Schlafly & Finkbeiner, 2011). Amongst the available extinction laws in our code (Prevot et al., 1984; Cardelli et al., 1989; Fitzpatrick, 1999; Calzetti et al., 2000), throughout this work we have chosen the Fitzpatrick reddening law (Fitzpatrick, 1999) because it reproduces the extinction observed for MW stars well with a preferred mean value around $R_V = 3.1$ (Schlafly & Finkbeiner, 2011).

For extragalactic objects, there are two main sources of extinction to account for: on the one hand, the dust intrinsic to the observed galaxy, which is redshifted with the galaxy system; on the other, the foreground dust of the MW, which redden the observed galaxy SED in the observer's reference system. It is important to note that this local MW extinction cannot be corrected with the intrinsic galaxy reddening as the emitted flux is redshifted before being scattered by the dust in our galaxy. As we present below, we separately deal with both extinction effects.

Following a given extinction law, the intrinsic extinction is applied to the SSP template models before they are redshifted and convolved with the photometric system. Throughout this work the values of A_V range from 0.0 to 3.1 (in bins of 0.1 in the range 0.0–1.0, and in bins of 0.3 from 1.0–3.1). The intrinsic extinction can be added as

$$F_\lambda = F_{\lambda,0} \times 10^{-0.4A_\lambda} \,, \tag{2.6}$$

where $F_{\lambda,0}$ is the SSP-model/template flux at rest frame F_λ, and A_λ is determined by the extinction law, which can be chosen by the user. Since it is not clear how R_V varies within a host galaxy and amongst different types of galaxies, we keep the value to $R_V = 3.1$ constant, i. e. the mean value in the MW. This helps to avoid degeneracies and to reduce the number of free parameters, which is already very high and time consuming. Even though the different reddening laws have intrinsic differences (see Fitzpatrick, 1999), we do not assume errors in the SSP template models owing to such uncertainties.

We use the dust maps of Schlegel et al. (1998), in order to deal with the MW reddening in the line of sight of each galaxy in our sample. The SFD dust maps provide $E(B-V)$ values in different positions of the sky by estimating the dust column density. These estimations were calibrated using galaxies and assuming a standard reddening law to infer the existence of galactic dust between the observer and the sources beyond the MW limits. Since the spatial resolution of SFD is low, $FWHM \sim 6.1'$ and pixel size $(2.372')^2$, MUFFIT makes a bilinear interpolation in the $E(B-V)$ grid for all the galaxy coordinates in the sample.

MUFFIT applies a foreground extinction correction for each individual galaxy photo-spectrum using an extinction law for a value of $E(B-V)$ and R_V. The simplest way to deredden the photo-spectrum of a given galaxy is to compute the extinction in the effective wavelengths of the different filters and then correct the source photometry using the equation

$$F_{\lambda,\mathrm{c}} = F_{\lambda,\mathrm{red}} \times 10^{0.4A_\lambda} \,, \tag{2.7}$$

where $F_{\lambda,c}$ is the flux corrected for MW extinction for a given wavelength, $F_{\lambda,red}$ is the observed flux (reddened), and A_λ the extinction factor given for a extinction law. Since the transmission curves of the filters are not completely flat and the shape of the continuum is source dependent, this approximation may be inappropriate for those filters that exhibit a gradient in their transmission curves (e. g. the lower and upper ends of the ALHAMBRA optical bands, see Fig. 2.2), especially in the spectral ranges where the observed spectrum is not flat. This effect would be interpreted as a shift in the filter effective wavelength (Fitzpatrick, 1999) and, finally, as a colour term in the spectral regions with strong gradients in flux, such as the 4000 Å-break. To get a more reliable correction in this sense, the code carries out the dereddening process of the data in three steps:

- First, we pick up a set of models from BC03 (29 ages, from 0.1 to 10 Gyr, four metallicities, [Fe/H]= −0.64, −0.33, 0.09, and 0.56, and a Chabrier IMF) to be redshifted (redshift bin 0.01) and convolved with the survey photometric system. Before redshifting and computing the synthetic photometry, we add the intrinsic extinction (A_V from 0.0 to 1.0, in bins of 0.2) to the rest-frame BC03 models. Then, we carry out an error-weighted χ^2 test to find the best fit between the above models and the observed galaxy photometry. The aim of this step is not to derive physical parameters from the best fitting, but to set constraints on the shape of the continuum.

- Second, we re-normalize the BC03 spectroscopic model associated to the best-fitting photo-spectrum. The synthetic photometry of this re-normalized model has to reproduce all the observed photometric bands exactly.

- Finally, we apply Eq. 2.7 to the re-normalized model derived in the previous step, in order to obtain a dereddened spectrum that we convolve with its related filter response curve. We use the Fitzpatrick (1999) extinction laws to calculate A_λ, the value $E(B-V)$ provided by SFD and $R_V = 3.1$, to deredden all the galaxies of our sample.

In particular, the Fitzpatrick (1999) extinction law was built from the superposition of the extinction curves derived for a set of stars. Consequently, this extinction law contains intrinsic uncertainties, although we would accurately know the values of R_V and $E(B-V)$. We account for the particular uncertainties of this law, adding an error to the dereddened photometry of MW dust, $F_{\lambda,c}$, following the methodology explained in Fitzpatrick (1999) and assuming $\sigma_{R_V} = 0$.

Cosmological fields, often the targets of multi-filter photometric surveys, used to be regions of the sky with low extinction values. In the particular case of ALHAMBRA, our main galaxy sample has MW extinction values of $E(B-V)$ down to 0.04 ($A_V < 0.12$ for $R_V = 3.1$) in all the cases. The colour term due to the MW dust in the ALHAMBRA survey may reach a maximum of $\Delta m_{AB} \sim 0.15$, and the stellar masses may be underestimated by 3 % (8 %) if we use the K_s (R) filter to estimate it. Although the stellar mass is not primarily affected by MW extinction in these fields, the colour term might change the retrieved stellar populations and consequently the derived stellar mass (see Sect. 2.3.2.3). In ALHAMBRA there are no galaxies at low Galactic latitudes, $| b | < 5$, where the MW temperature structures are not duly resolved in the SFD maps (Schlegel et al., 1998).

2.3.1.4 Redshifts

Together with the mass and the stellar population parameters of the galaxy, the code is generically prepared to provide an estimation of the photo-z. It is worth noting, however, that this code is not intended to be a photo-z code. The large number of potential model parameters that the code plays with when the redshift is set as a completely free parameter in the fitting process, means that there is a slight degeneracy with other parameters (like extinction; see Sect. 2.4.4) that tends to overestimate the derived photo-z. To overcome this effect, the code is also prepared to accept a list of redshift values for each target galaxy as initial constraint: either a list of nominal redshift values, so that the code only performs the fitting process at exactly these

redshifts, or complete probability distribution functions (PDF) of redshifts. Then the code only accounts for the model redshifts within the PDF interval. Because of the good results we obtain, we use the photo-z PDFs provided by the ALHAMBRA Gold catalogue as input redshift constraints using BPZ2.0 throughout this work (Molino et al., 2014). It is noteworthy that the combination of our code with the ALHAMBRA photo-z constraints improves the quality of the input photo-z (see Sect. 2.4.3).

2.3.2 The core of the MUFFIT analysis techniques

This section is devoted to the main technical features and processes carried out by our code to constrain the stellar population parameters of galaxies in multi-filter data samples. We first describe the way in which the χ^2 minimization is performed in Sect. 2.3.2.1, with the addition of a mixture of SSPs giving remarkable improvement, which was specifically computed for each galaxy, in order to set more precise constraints on the stellar populations. In Sect. 2.3.2.2 we explain the process of detecting those bands that may be affected by strong emission lines in detail, helping to understand the overall fitting process. Section 2.3.2.3 explains how the stellar masses are calculated from the fittings. In addition, a Monte Carlo approach is used to set constraints on the confidence intervals of the parameters provided by the code, detailed in Sect. 2.3.2.5. Finally, we describe how we manage the k-corrections as a result of the fittings in Sect. 2.3.2.6. The content of this section is outlined on the right-hand side of the flowchart (see Fig. 2.1).

2.3.2.1 The χ^2 minimization and mixture of SSPs

Our stellar population analysis technique is based on error-weighted χ^2 tests between the multi-filter galaxy data and the template SSP models of choice. Since SSP models are usually normalized to a initial stellar mass and both the galaxy distance and its luminosity are uncertain in a general case (in fact these are parameters generally derived from the fit), it is required to add a normalization term, ε, in the classical χ^2 equation. This term minimises the χ^2 value for every model-galaxy pair and it takes all observed bands and associated errors into account, so that the result is only colour dependent. It is more robust for multi-filter surveys because, at most, they only contain a few dozen filters (e. g. 23 in ALHAMBRA). This way, all the meaningful filters contribute to determining the best solution of the fitting (without giving up one of the best bands in order to normalise), and there is no risk that the normalisation band is affected by emission lines or cosmetic defects.

Because the number of reliable bands in each source may be different from one object to the next (for some objects, some filters may be rejected for observational, cosmetic, or calibration problems), in general we divide every χ^2 by the number of available, safe filters in each case. Depending on whether we are working with bandpass fluxes or magnitudes, the χ^2 definition can be expressed as

$$\chi^2_{\rm m} = \frac{1}{N_{\rm p}} \sum_{X=1}^{N_{\rm p}} \left[\frac{O^{\rm m}_X - (\varepsilon_{\rm m} + m_X)}{\sigma^{\rm m}_X} \right]^2 , \text{and} \tag{2.8}$$

$$\chi^2_{\rm f} = \frac{1}{N_{\rm p}} \sum_{X=1}^{N_{\rm p}} \left[\frac{O^{\rm f}_X - \varepsilon_{\rm f} f_X}{\sigma^{\rm f}_X} \right]^2 , \tag{2.9}$$

where $N_{\rm p}$ is the number of available filters in an observed galaxy, $O^{\rm m,f}_X$ is the observed X-filter (magnitude or flux), $\sigma^{\rm m,f}_X$ its error, m_X (f_X) the X-filter model prediction (single SSP or SSP mixture, more details below) and $\varepsilon_{\rm m}$ ($\varepsilon_{\rm f}$) the normalization term. For our purposes, $\varepsilon_{\rm m}$ and $\varepsilon_{\rm f}$ are written as

$$\varepsilon_{\rm m} = \left(\sum_{X=1}^{N_{\rm p}} \frac{O^{\rm m}_X - m_X}{\sigma^{\rm m\,2}_X} \right) \times \left(\sum_{X=1}^{N_{\rm p}} \frac{1}{\sigma^{\rm m\,2}_X} \right)^{-1} , \text{and} \tag{2.10}$$

$$\varepsilon_{\rm f} = \left(\sum_{X=1}^{N_{\rm p}} \frac{O_X^{\rm f} f_X}{{\sigma_X^{\rm f}}^2} \right) \times \left(\sum_{X=1}^{N_{\rm p}} \frac{f_X^2}{{\sigma_X^{\rm f}}^2} \right)^{-1} , \tag{2.11}$$

which correspond respectively to minimizing Eqs. 2.8 and 2.9 for each galaxy, i. e., $\partial\chi^2_{\rm m,f}/\partial\varepsilon_{\rm m,f} = 0$. As we show later (Sect. 2.3.2.3), by finding the best stellar population solutions for each galaxy, we can estimate its stellar mass from the ε values.

Equation 2.8 (the equation used throughout this work) assumes that the distribution of errors is Gaussian, when the distribution of magnitudes is generally not Gaussian since these are logarithmic measurements of flux. From certain signal-to-noise ratios, $S/N \gtrsim 5$ (or uncertainties $\sigma_X^m \lesssim 0.22$), the magnitude uncertainties are quasi-normally distributed, and therefore, this approach is valid. Consequently, we encourage potential MUFFIT users to take fluxes instead of magnitudes when several galaxy bands are compromised by very low signal-to-noise ratios, $S/N \lesssim 4$–5. It must be also taken into account that a certain minimum signal-to-noise ratio is required for determining reliable stellar population parameters without being dominated by degeneracies, as shown later in this paper.

Once we have defined how to compute the fitting goodness, the next step is to compare our set of models to retrieve the most likely stellar population parameters. We carry out this process in two different steps.

- First, we run the χ^2-test described above with the set of SSP models selected by the user (base models), making a first determination of the bands that may be affected by strong emission lines. In short, for each redshift step of the SSP models, the code looks for a flux excess in the galaxy SED with respect to the SSP model SEDs, for all those bands that could be affected by emission lines at the given redshift. A more extensive explanation of our technique of detection of emissions lines in multi-filter galaxy data is presented in Sect. 2.3.2.2. When this is the case, those bands potentially affected by emission lines are removed from the fitting process, and the χ^2-test is repeated again without the affected bands. In addition, rather than taking the parameters of the best SSP fitting, we carry out a Monte Carlo simulation using the proper signal-to-noise ratios in each filter (further details in Sect. 2.3.2.5). From the set of parameters retrieved during the Monte Carlo approach, we map the parameter space of compatible solutions (overall age, metallicity, extinction, redshift, stellar mass, and IMF), although at this stage we only focus on the retrieved distributions of age and redshift to carry out the next step: the mixture of two SSPs and its subsequent SED-fitting process.

- Second, according to the age and redshift distributions derived from the initial SSP analysis, we make a new database of models consisting of a mixture of two individual base SSP models. The mixture is only computed for the best redshift solutions determined in the previous step. For each redshift value, the two-model mixture is constrained to combine two SSPs, younger and older than a certain age threshold, $\mathrm{age_T}$, that is related to the most likely age, $\mathrm{age_{SSP}}$, inferred from the Monte Carlo analysis performed in the previous step. This is a reasonable assumption given that the stellar content of galaxies are usually the result of complex SFHs with multiple stellar populations (Ferreras & Silk, 2000; Kaviraj et al., 2007; Lonoce et al., 2014), and the age solutions derived from comparisons with single SSPs can be considered to be, in first order, luminosity-weighted means of the ages of the individual, true populations. To determine the $\mathrm{age_T}$ value that allows us to define the limit between younger and older SSP mixtures for each galaxy, we have studied the empirical relation between the luminosity-weighted ages of mock galaxies made of random mixtures of two SSPs, $\mathrm{age_{L,\,mock}}$, and the best age determination for such mock galaxies derived from a single SSP fitting, $\mathrm{age_{SSP}}$. In Fig. 2.4 we present the result of this study. As expected, we observe that $\mathrm{age_{SSP}}$ underestimates the real age, in particular for $\mathrm{age_{L,\,mock}} \lesssim 6$ Gyr. The yellow curve in Fig. 2.4 represents $\mathrm{age_T}$ as a function of $\mathrm{age_{SSP}}$. Once the age threshold is established, we generate all the possible SSP combinations (younger and older than $\mathrm{age_T}$), including the stellar mass weight of each component as a new degree of freedom. For a general case with n components per mixture, each magnitude in the band X of the new mixture

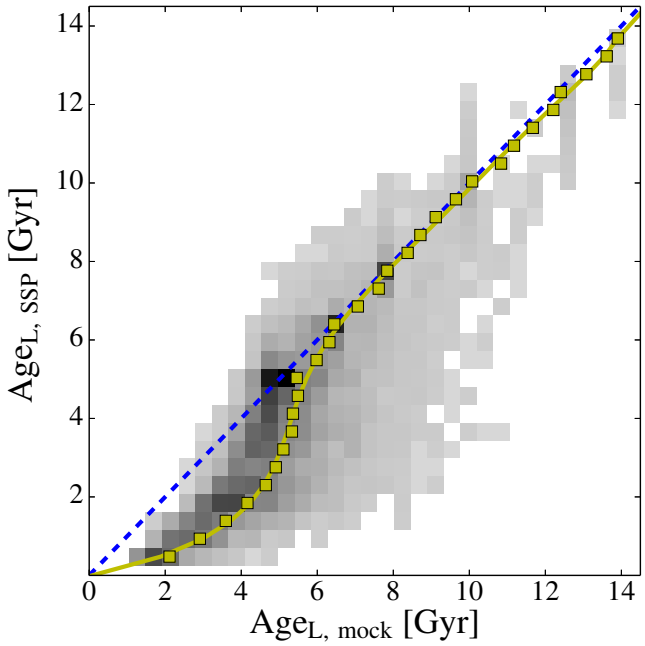

Figure 2.4: Empirical relation between the luminosity-weighted ages of mock galaxies made of random mixtures of two SSPs, $\mathrm{Age}_{\mathrm{L,\ mock}}$, and the best age determination for such mock galaxies derived from a single SSP fitting, $\mathrm{Age}_{\mathrm{SSP}}$. The yellow curve is the $\mathrm{Age}_{\mathrm{L,\ mock}}$ median for a given value of $\mathrm{Age}_{\mathrm{SSP}}$, and it represents the typical offset in age that one may expect when interpreting the SED of a mixture of two SSPs by fitting a unique SSP.

model is expressed as

$$m_{X,\mathrm{mix}} = -2.5 \log_{10} \left(\sum_{i=1}^{n} \alpha_i 10^{-0.4\ m_X^i} \right) , \tag{2.12}$$

$$f_{X,\mathrm{mix}} = \sum_{i=1}^{n} \alpha_i f_X^i , \tag{2.13}$$

where m_X^i (f_X^i) is the magnitude (flux) in the band X for the ith SSP model, and α_i the relative flux contribution of the SSP model in the ith component, with $\sum_{i=1}^{n} \alpha_i = 1$ and $0 \leq \alpha_i \leq 1$. In our case, we are mixing two SSPs and consequently $n = 2$.

After mixing the SSP models as explained above, the code again searches for the best-fitting solution, repeating the detection of emission lines with the mixture of models as explained in Sect. 2.3.2.2. As in the first step using a single SSP, we not only provide the best solution but also map the compatible stellar-population parameters by a Monte Carlo approach, treating the errors properly in each band. This provides an extra advantage when carrying out a statistical treatment of the results. We devote Sect. 2.3.2.5 to explaining in detail how we explore the compatible space of derived parameters for each galaxy.

With this method and two SSPs, one database of mixed SSPs is particularly created for each galaxy, because it is more adequate and realistic than a single SSP fitting. As shown above, for a non-parametric SFH, this represents a substantial improvement over using only one SSP, which is not able to reproduce the colour of an underlying main red population plus less massive and later events of star formation. The mixture of two populations is a reasonable compromise that significantly improves the reliability of determining the

stellar population parameters of multi-filter galaxy data (Ferreras & Silk, 2000; Kaviraj et al., 2007; Lonoce et al., 2014). In fact, it has been demonstrated (e. g. Rogers et al., 2010) that the mixture of two SSPs turns out to be the most reliable approach to describing the stellar populations of young early-type galaxies, as well as a very reasonable approach for older galaxies where the latter case is only slightly surpassed by the use of chemically enriched exponential models. The two SSP model fitting approach may therefore be generally considered as a reasonable method for analysing the stellar populations of most kinds of galaxies in a consistent way. Moreover, given that MUFFIT does not impose constraints on the metallicities of the two-SSP mixture, this can provide hints not only of age evolution but also of a metallicity build-up. That being said, future versions of MUFFIT will also account for the use of different sets of SSP or τ-models for the best choice of the user.

2.3.2.2 Emission lines

Nebular emission lines appear frequently in the SEDs of galaxies, even if these are dominated by the light contribution of their stellar content. In particular, dealing with multi-filter galaxy data, filters affected by emission lines may present a substantial excess in flux with respect to any combination of SSP models, because the latter typically do not account for the nebular emission physics. To guarantee the accuracy and reliability of the stellar population parameters derived during the fitting process, it is crucial to detect and remove those bands that can be significantly affected by emission. Not only because they are not comparable to SSP models, but also since filters contaminated by strong emission lines tend to exhibit much higher luminosities and lower photonic errors than the rest of bands, and therefore, these bands would dominate our error-weighted SED-fitting techniques (see Eqs. 2.8 and 2.9). On the other hand, it is worth recalling that the presence of strong emission lines may also provide fruitful information, since they contribute to restricting the feasible redshift intervals of the galaxy. The redshift constraints due to nebular emissions are also considered during the analysis.

The emission line detection process of our code depends on the specific photometric system of the galaxy sample, because it only accounts for those emission lines that are typically strong enough to affect the photometry of the given filter set. It is obvious that the broader the spectral filter width, the larger the equivalent width (hereafter EW) of the line that may be potentially detected at a fixed signal-to-noise. In this sense, the code is initially fed with a list of target emission lines that depends particularly on the filter set, customizable by the user, with emission lines, such as [O II] $\lambda\lambda$3 726, 3 729, [O III] $\lambda\lambda$4 959, 5 007, H Balmer's series, and [S II] $\lambda\lambda$6 717, 6 731.

Thanks to the design of MUFFIT, we can also provide a list of typical AGN emission lines to reduce their effects on the fittings, but broad AGN lines may affect two or more ALHAMBRA filters, so the AGN emission line detection criteria in MUFFIT might fail or be inaccurate. It is very important to note that an excessive list of emission lines, mostly when they are spread in the broad wavelength ranges, will eventually derive incorrect results, since too many bands might be removed. It is therefore advisable to restrict this list to the lines that can present a measurable excess in flux, which mainly depends on both the filter widths and the line intensity. For this reason, some bands can be forced by the user to remain in the SED-fitting analysis irrespective of whether they can be potentially affected by emission lines. For instance, in ALHAMBRA we expect that the NIR bands are too wide to be sensitive to the presence of emission lines, so they are never removed during the fitting process even if the code detects a flux excess in any of them.

Once we specify the emission line list in the code, the emission line detection process is carried out in two steps. First, taking the model redshift into account, we fit our models (single SSP or SSP mixture) without all the bands that could be potentially affected by the specified emission lines, and explore the residuals of the best fitting. If the residuals of any of the potentially affected bands present an excess in flux/magnitude greater than a limit value provided by the code user, $\Delta m_{\rm EL}$, and these residuals are deviated beyond a band-error factor, $\sigma_{\rm EL}$, the bands are considered to be affected by emission lines and are removed from the fitting process. Both constraints, $\Delta m_{\rm EL}$ and $\sigma_{\rm EL}$, are required: the latter to assure that the excess in flux is not due to photometric uncertainties, and the former to avoid removing those bands with tiny

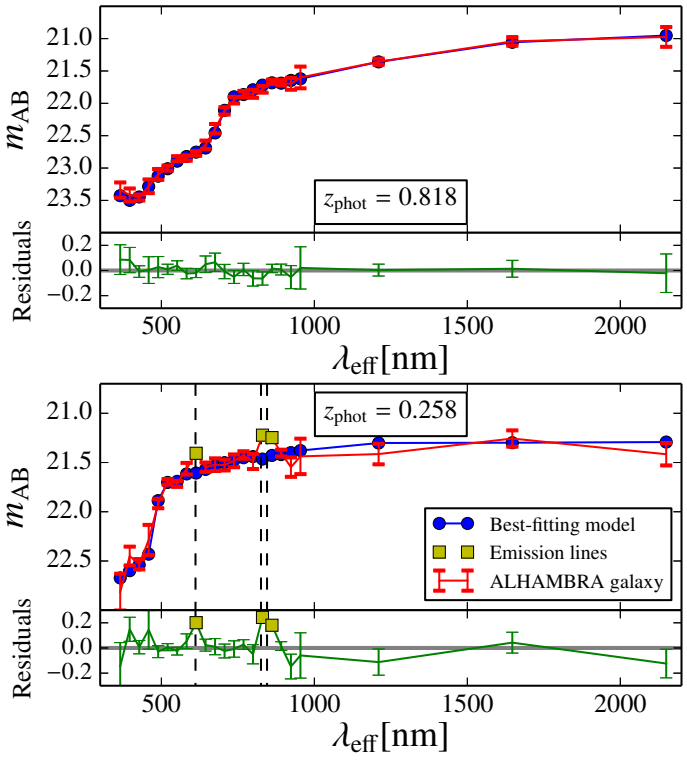

Figure 2.5: Spectral fitting examples for galaxies from the ALHAMBRA survey using MUFFIT and the MIUSCAT SSP models. The galaxy photo-spectra and their errors are given in red, whereas the best-fitting models are given in blue. The *top panel* corresponds to a quiescent galaxy for which no emission lines are detected. The *bottom panel* illustrates the case of a star-forming galaxy for which MUFFIT detects three bands affected by emission lines, in yellow. The dashed black lines indicate the wavelengths for Hβ, Hα, and [S II]. Photometric redshifts are given in the insets in the figure.

observational errors that present little discrepancies with respect to the models. Finally, we repeat the fitting without the bands identified in the previous step, getting a new set of reliable χ^2 values, free of nebular contributions.

For the ALHAMBRA case, we use $\Delta m_{EL} = 0.1$, because for lower contributions, the affected bands do not significantly affect the SED-fitting results retrieved with MUFFIT. In addition, we set $\sigma_{EL} = 2.5$ as a reasonable statistical threshold to detect emission lines over the noise. Figure 2.5 illustrates two SED-fitting examples of two galaxies from ALHAMBRA. The top panel of Fig. 2.5 illustrates a fitting of a quiescent galaxy in ALHAMBRA without strong nebular emissions, whereas the bottom panel shows a galaxy for which MUFFIT detects that some bands may be affected by emission lines (yellow squares). The red curves represent the observed photo-spectra, while the blue curve is the best-fitting model after the detection of emission lines process. The yellow squares are the bands where the influence of an emission line is ticked, in this particular case Hβ, Hα+[N II], and [S II]. The dashed black lines point out the wavelengths for Hα, Hβ, and [S II] at the galaxy photo-z. For this case, the detection of the emission lines contribute particularly to strongly constraining the redshift range. Despite the ALHAMBRA resolution ($FWHM \sim 300$ Å), we note that strong emission lines can modify the fitting results. In some cases, even Hβ shows significant contributions in the ALHAMBRA dataset.

Since we are providing both those bands that may be affected by strong emission lines and the residuals from the SED fittings, we can easily estimate the flux excesses in order to later transform them to EWs. The advantage of this method is that our best SED-fittings are mixtures of SSPs that already include the

corresponding stellar absorptions, so the residuals can be directly related to the absolute nebular emission. The main limitation, in general, comes from the low resolution of the data, because in many cases some filters can be affected by more than one emission line, such as H α and [N II]. Still, as presented in Sect. 2.5.2, this technique opens new paths for future work on emission-line galaxies with multi-filter data.

2.3.2.3 Stellar masses

As we explain in Section 2.3.2.1, both the normalization term ε introduced in the χ^2 minimization equation and the intrinsic luminosities of the two best-fitted SSPs are directly related to the total stellar mass of the galaxy. SSP models are usually normalized to an initial stellar mass of $1M_\odot$, but this decreases with time, thereby accounting for the evolution of the most massive stars. This effect is properly taken into account for determining the final galaxy mass by applying a correction term to each SSP, $\kappa_{\rm SSP}$, which is usually provided by the models.

When taking the above considerations into account, the total stellar mass, $M_{\star,\rm T}$, of a mixture of n SSPs (for this work $n = 2$) can be expressed as

$$\begin{aligned} M_{\star,\rm T} = \sum_{i=1}^{n} M_{\star,\,i} &= 10^{-0.4\,\varepsilon_{\rm m}} \times 4\pi d_{\rm L}^2 \times \sum_{i=1}^{n} \kappa_{i,\,\rm SSP}\,\alpha_i\,, \\ &= \varepsilon_{\rm f} \times 4\pi d_{\rm L}^2 \times \sum_{i=1}^{n} \kappa_{i,\,\rm SSP}\,\alpha_i\,, \end{aligned} \tag{2.14}$$

where $M_{\star,\,i}$ is the stellar mass of each population in the mixture, $\varepsilon_{\rm m}$ is the normalization term defined in Eq. 2.11, $d_{\rm L}$ the luminosity distance in cm units (see Hogg, 1999), $\kappa_{i,\,\rm SSP}$ the relative stellar mass correction for the ith component in the SSP mixture, and α_i the relative flux contribution of the SSP model in the ith component (see Eqs. 2.12 and 2.13). Throughout this work, the derived stellar masses are quoted including stellar remnants through $\kappa_{i,\,\rm SSP}$, but for a more general case, this parameter may not include remnants.

2.3.2.4 Stellar population parameters of the SSP mixture

The stellar-population parameters of the mixture of SSPs are estimated from the parameters of each component in the mixture. This can be done in different ways, which mainly depend of the weights assigned to the parameters of the different components. The most common definitions, provided by MUFFIT and employed in this paper, are luminosity-weighted and mass-weighted. The latter provides more realistic information since it accounts for the total mass of stars in each population, hence assigning larger weights to the more abundant or dominant stellar populations. However, these populations may have very different luminosities. In this sense, luminosity-weighted parameters are more representative of the populations that dominate the observed spectrum, since the galaxy SEDs are predominantly led by the brighter populations, even if they are not dominant in relative mass.

Throughout this work, the luminosity-weighted and mass-weighted stellar population parameters of a mixture of n SSPs (for this work $n = 2$), $p_{\rm L}$ and $p_{\rm M}$, respectively, are defined from the stellar population parameters of each i-th component (p_i; age, metallicity, extinction, IMF slope, or [α/Fe]) as

$$p_{\rm L} = \frac{\sum\limits_{i=1}^{n} \alpha_i \times L_i \times p_i}{\sum\limits_{i=1}^{n} \alpha_i \times L_i}\,, \tag{2.15}$$

$$p_{\rm M} = \sum_{i=1}^{n} \frac{M_{\star,\,i}}{M_{\star,\rm T}} p_i = \frac{\sum\limits_{i=1}^{n} \alpha_i \times \kappa_{i,\,\rm SSP} \times p_i}{\sum\limits_{i=1}^{n} \alpha_i \times \kappa_{i,\,\rm SSP}}\,, \tag{2.16}$$

where α_i is the relative flux-contribution of the SSP model in the ith component, $\kappa_{i,\,\mathrm{SSP}}$ the relative stellar mass correction for the ith component in the SSP mixture, and L_i the luminosity of the SSP model in the observed spectral range. Both definitions agree when the parameter value is the same in each component.

2.3.2.5 Determining the space of best solutions

Because of the well known degeneracies among stellar population parameters, it is essential to perform a reliable analysis of the possible solutions (as mixtures of two SSPs) for each galaxy according to the uncertainties of the data. For this reason, rather than providing only the best-fitting solution for each galaxy (it is well known that the most likely parameters are not always the best-fitting model parameters), our code accounts for the photometric errors of the multi-filter galaxy data to provide a set of the best-fitting solutions, thereby providing a set of probable values of redshifts, stellar masses, extinctions, and stellar population parameters (ages, metallicities, and IMFs) for each object. These values can ultimately be averaged according to their weights and frequencies to derive the average final parameters assigned to each galaxy and their errors. In this section we explain the processes and the applied criterion used to carry out this analysis.

The determination of the best solution space is based on a Monte Carlo method that, using the proper signal-to-noise ratio of each filter, seeks to find which parameter values are compatible within the photometric errors of the data. Since photometric uncertainties usually follow a normal distribution (or Gaussian), we assume an independent Gaussian distribution in each filter, centred on the band flux/magnitude, with a standard deviation equal to its photometric error. It is worth noting that each filter is observed and calibrated independently of the remaining ones, so the errors of different filters are not expected to be correlated.

For each galaxy, on the basis of the above Gaussian error distributions for its multi-filter data, MUFFIT generates Monte Carlo simulations (the number of realizations is defined by the user), ending up with a set of multi-filter data realisations for the same galaxy, all of them compatible within the errors. Ideally, the next step would be to run the χ^2 test individually for each realisation of the galaxy using the complete set of models, but this is extremely time-consuming since the code plays with million of models for each fitting (for the present research: 21 ages, 5 metallicities, 18 extinctions, 1 IMFs, 300 redshifts, and solar [α/Fe]). Instead, to speed up this computational process, for each galaxy we perform a preliminary selection of SSP and mixture models that can play an important role in the fitting given the specific SED and errors of the galaxy. This pre-selection of models is carried out as follows:

i) After having run our code for a certain galaxy SED and having obtained the χ^2 values for all the possible mixture of two SSP models (χ^2_{mix}), we take the χ^2_{mix} value of the best-fitting model (BFM), χ^2_{BFM}, i. e. the mixture of two SSPs with the greatest probability of being the solution, which corresponds to the lowest χ^2_{mix} value.

ii) Since the parameter space of best solutions depends not only on the filter photometric uncertainties but also on the shape of the SED, the next step is to determine, for each individual galaxy SED, the range of plausible χ^2 values that are expected according to the set of photometric uncertainties. To do this, MUFFIT performs 10 000 Monte Carlo realisations of the BFM bands according to the Gaussian error distributions of the real galaxy multi-filter data. The corresponding 10 000 χ^2 values between these realisations and the BFM, namely χ^2_{M}, represent the range of χ^2 values that one would expect just due to the photometric uncertainties of the real galaxy data. This range can be very different among different galaxies. In MUFFIT, the limiting plausible value, χ^2_{phot}, is set to the value that encloses the 68.27 % (a Gaussian 1 σ) of the cumulative distribution function of the χ^2_{M} values.

iii) Finally, the subsample of possible solutions for a given galaxy SED is composed of those models that fulfil the criterion $\chi^2_{\mathrm{mix}} \leq \chi^2_{\mathrm{BFM}} + \chi^2_{\mathrm{phot}}$. This subsample is consequently restricted to those models whose colours are statistically compatible within the galaxy photon errors.

This way, the set of compatible best solutions for each galaxy is determined by generating N_{m} Monte Carlo realizations of the galaxy SED data (throughout this work $N_{\mathrm{m}} = 100$) according to their errors and

then running our χ^2 minimization test for each galaxy realisation using the subsample of preselected models as input. In each realisation, we get a new BFM whose parameters are ultimately weighted (ω_j) with its χ^2 value to provide the most likely stellar population parameters together with their errors. Formally,

$$\omega_j = \frac{1/\chi^2_{\mathrm{MC},j}}{\sum_{j=1}^{N_\mathrm{m}} 1/\chi^2_{\mathrm{MC},j}}, \tag{2.17}$$

$$< p >= \sum_{j=1}^{N_\mathrm{m}} \omega_j p_j \tag{2.18}$$

$$\sigma_{<p>} = \sqrt{\sum_{j=1}^{N_\mathrm{m}} \omega_j \left(< p > - p_j\right)^2}, \tag{2.19}$$

where $< p >$ and $\sigma_{<p>}$ are, respectively, the average stellar population parameters (age, metallicity, extinction, redshift, stellar mass, IMF, and [α/Fe], in a general case) and their errors, and p_j are the stellar population parameters associated to each BFM in the Monte Carlo realisation with a χ^2 value equal to $\chi^2_{\mathrm{MC,j}}$. In addition, the essential stellar parameters of each BFM obtained in the N_m Monte Carlo iterations are also provided.

Finally, we note that the uncertainties of the parameters retrieved in this stage comprise not only the main parameters of the models, such as ages, metallicities, and IMFs, but also the extinction, the redshift (if it is the case, within the interval provided by an external photo-z code), and the stellar mass.

2.3.2.6 K-corrected luminosities

Once we have computed the best-fitting models, we end up with a combination of SSP models that reproduce the colours of the galaxy photometric SED. As a result, the luminosity of the galaxy, its absolute magnitudes at any band, and the mass-luminosity relation are estimated from exactly the same combination of SSP models taken at rest frame. Independently of the physical parameters linked to the best combination of models, the k-correction is model-independent since it properly reproduces the colours of a galaxy SED at a given cosmological distance, as long as the redshift is well constrained. If we compute the magnitudes for the different bands following this method, the main parameter that determines the k-correction goodness of fitting is the photo-z accuracy. Since the set of SSP models does not contain emission line templates, and our code removes them automatically during the fitting process, the provided k-corrections and luminosities only contain rest-frame predictions about the stellar continuum, not about the nebular content.

To determine rest-frame magnitudes with the corresponding errors, for each galaxy we take all the best-fitting models recovered in the Monte Carlo approach (see Sect. 2.3.2.5), average them, and provide the average rest-frame magnitudes and their standard deviations, so that we can consider the uncertainties in the photometry thanks to the Monte Carlo approach. It is noteworthy that, at low redshifts, the uncertainties of rest-frame magnitudes may be very high, since the apparent magnitudes depend on the luminosity distance ($\propto \ d_\mathrm{L}^{-2}$), which diverges at $z = 0$. This suggests that more accurate photo-z are needed to have better k-corrections in the most local Universe. Despite this, the colour terms among different filters are not so affected by this effect, because the major impact is on the source luminosity and not on the rest-frame colours. To minimise this effect, we provide a second k-correction, for which we study the variability of the colours with respect to an anchor band. In short, once we have all the rest-frame models recovered during the Monte Carlo method, the anchor band is the one that presents the lowest variability at rest frame. In ALHAMBRA, this anchor band is usually a band in the red optical part (higher signal-to-noise ratios). This approach turns out to be very useful, for example, for making reliable CMD at low redshift.

2.4 Intrinsic uncertainties and degeneracies with ALHAMBRA galaxy data

After having presented the main technical aspects of our SED fitting code in Sect. 2.3, and before presenting a comparison study between our stellar population results and similar previous data from the literature (see Sect. 2.5), the goal of this section is to study the accuracy and reliability of the stellar population parameters retrieved with our code. Since this strongly depends on the photometric system of the data under study, it is important to note that, throughout this section, all the tests and predictions about uncertainties, degeneracies, etc. are performed especially for the ALHAMBRA filter system.

Since the code presented in this paper is particularly suited to studying the stellar populations of galaxies whose SEDs are dominated by their stellar content, we begin to build the CMD of the ALHAMBRA galaxy data in Sect. 2.4.1, which allows us to properly select our target of galaxies and to compare our results with those published in the literature (Sect. 2.5). In Sect. 2.4.2 we check how the intrinsic uncertainties in the photometry of the ALHAMBRA filter system affect the typical errors of the derived parameters, using a set of mock galaxies with well known input parameters. Furthermore, the impact that the uncertainties of the input ALHAMBRA photo-z, Sect. 2.4.3, have on the derived stellar population parameters is analysed in Sect. 2.4.4. Finally, we quantify the expected degeneracies among the derived galactic parameters of typical red-sequence galaxies for the ALHAMBRA photometric system and different signal-to-noise ratios.

2.4.1 Selection criteria of ALHAMBRA red sequence galaxies

It is well known that the CMD of galaxies exhibits a bimodal distribution with two main populations, usually referred to as the "red sequence" (RS) and the "blue cloud" (Bell et al., 2004; Baldry et al., 2004; Faber et al., 2007; Fritz et al., 2014). A large number of RS galaxies are mainly composed of early types (Strateva et al., 2001; Cassata et al., 2007), but since the RS definition is clearly based on the observed galaxy colours, there is also a fraction of star-forming dusty galaxies that may lie on the RS (Williams et al., 2009). To break the degeneracies between quenched galaxies and dusty star-forming galaxies, there are colour–colour diagnostics that use NIR bands (Williams et al., 2009; Arnouts et al., 2013), and even methods that split the CMD into three populations ("red", "blue", and "green") by fitting to a set of SED type classes (Fritz et al., 2014). For the aims of this work, we just follow the classical method of the CMD (Bell et al., 2004; Faber et al., 2007; Fritz et al., 2014). A more detailed study of the contamination of star-forming, reddened galaxies in the RS will be given in a forthcoming paper (Díaz-García et al., in prep.).

To build the sample of RS galaxies, we firstly chose all the galaxies from the Gold catalogue[8] with a statistical STAR/GALAXY discriminator parameter that is lower than or equal to 0.5 (`Stellar_flag` ≤ 0.5) and that is imaged with 70 % photometric weight on the detection image (`PercW` ≥ 0.7), to avoid photometric errors in the galaxies close to the image edges. Secondly, we applied our analysis techniques over the full sample of ALHAMBRA galaxies, using the set of MIUSCAT SSP models and the photo-z predictions included in the Gold catalogue, to automatically get their k corrections (see Sect. 2.3.2.6). From the k corrections and the stellar masses, we can easily estimate their absolute magnitudes, which together with the rest-frame colours, compose the CMD. We note that our CMD does not change significantly if we use another set of models, e. g. BC03, instead of MIUSCAT. In fact, this method is roughly model-independent as we are reproducing the luminosity and colours of the galaxy through the best mixture of two SSP models, irrespective of their parameters, so that the key here is to have a well-constrained photo-z (see Sect. 2.4.4).

The RS and the blue cloud appear to be clearly separated when the CMD is constructed using the Johnson-like filters U and V (Johnson & Morgan, 1953). In our case, we selected the ALHAMBRA filters *F365W* and *F582W* for simplicity, because these are the ones whose effective wavelengths are like U and V, respectively. The CMD of the ALHAMBRA galaxies based on the *F365W* and *F582W* filters is presented in Fig. 2.6, where redder colours indicate higher and bluer colours and lower galaxy densities, respectively. Following the equation provided in Bell et al. (2004), which is compatible with the relation obtained in Fritz

[8] `http://cosmo.iaa.es/content/alhambra-gold-catalog`

et al. (2014), we define the RS as those galaxies redder than the following colour–magnitude relation:

$$m_{F365W} - m_{F582W} = 1.15 - 0.3z - 0.08(M_{F582W} - 5\log h + 20), \tag{2.20}$$

where m and M indicate apparent and absolute magnitudes in the Vega system. By simple visual inspection, it is clear that Eq. 2.20, illustrated in Fig. 2.6, splits the RS from the blue cloud properly, which already constitutes a first-order check of the goodness of the SED fitting.

2.4.2 Photon-noise uncertainties

To analyse the intrinsic uncertainties in the derived stellar population parameters of the galaxies due to the photon-noise errors of the ALHAMBRA photometry, we created mock galaxies consisting of a mixture of two random SSPs, in which we add photon noise according to the sensitivity of the ALHAMBRA filters and to the SED of the mock galaxies. By construction, this test is fairly representative of the performance of RS galaxies. After adding noise, we ran our code in order to derive the stellar population parameters of these mock galaxies, treating them as observed galaxies, but as ones for which we know the real values of their parameters. The comparison between the input and the output parameters, as a function of the signal-to-noise ratio of the filters, allows us to conclude something about the main topic of this section.

We took the extended version of the MIUSCAT models (see Sect. 2.3.1.1) with the Kroupa IMF to develop these simulations. After adding different extinction values (Fitzpatrick's law, A_V values ranging from 0.0 to 0.8 in steps of 0.1) at different redshifts (from 0 to 1 and a step of 0.01), we randomly mixed two SSPs with a series of constraints:

- The weight of the younger population should not be more than 30 % in mass, and its age not be larger than 4 Gyr. The mass limit is required to avoid luminosity-weighted ages that are too low, which is unlikely in RS galaxies (Kaviraj et al., 2007), and to guarantee the presence of old galaxies at all redshifts.
- The age of the random SSPs cannot be much older than the age of the Universe at that redshift. Since the ages of SSP models are a discrete set of values, we state the limit to the first model that surpasses the age of the universe at each redshift.
- The extinction of both SSPs is the same. Although this may not necessarily be the case in general, it is a reasonable assumption because we are studying integrated stellar populations, which translates to an average intrinsic extinction that affects the projected incoming light from different populations.

To properly sample the galaxy mass range, we assigned random stellar masses in the range $9.5 \leq \log_{10}(M_\star/\mathrm{M}_\odot) \leq 12.5$. We repeated this process 2 000 times per interval of redshift from 0 to 1 in bins of 0.2, getting 10 000 mock galaxies. As we explain below, we study the impact of the signal-to-noise ratio for three cases (S/N = 10, 20, and 50). In each case, we constructed a new random sample of mock galaxies, with the total number of simulations 30 000.

After having built the set of toy mock galaxies, it is important to accurately model the way the galaxies are seen by the ALHAMBRA photometric system. It is at this point where the ALHAMBRA configuration plays an important role. The ALHAMBRA characteristics (see Fig. 2.2 and Sect. 2.3.1.2) are such that the reddest bands are not as deep as the rest of the LAICA filters. On the other hand, the SED of typical RS galaxies, even the youngest ones, exhibit a clear flux drop in the blue region, with a prominent 4 000 Å-break in the middle. Therefore, we cannot assume either that all the filters present the same signal-to-noise ratio or that the signal-to-noise ratio among filters does not depend on the redshift.

To carry out a realistic simulation, we take all the galaxies from the ALHAMBRA Gold catalogue for which the best-fitting corresponds to a RS galaxy (see Sect. 2.4.1), and compute, for every galaxy, the signal-to-noise ratios in each filter relative to the $F799W$ filter, which is on average the band with the maximum signal-to-noise ratio at any redshift. By repeating this process in different redshift bins, we determine how

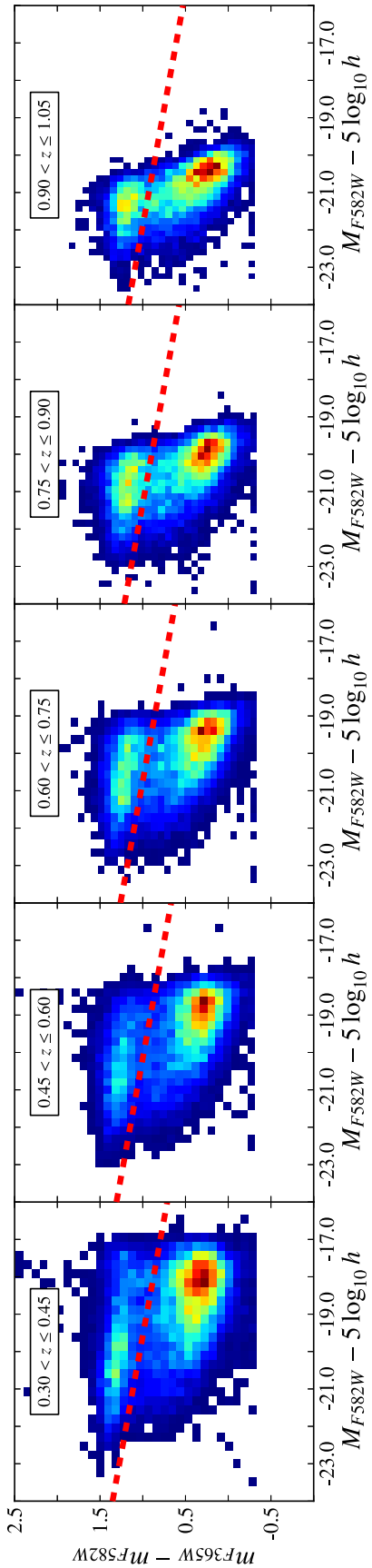

Figure 2.6: Colour–magnitude diagram (CMD) of the ALHAMBRA galaxies at different redshift bins. The filters *F365W* and *F582W*, both in Vega magnitudes, are used as a proxy for the Johnson filters U and V. Redder and bluer colours indicate regions of the CMD with higher and lower galaxy densities, respectively. The dashed red line is the colour–magnitude relation that splits the RS from the blue cloud for the mean redshift of the bin, as expressed in Eq. 2.20.

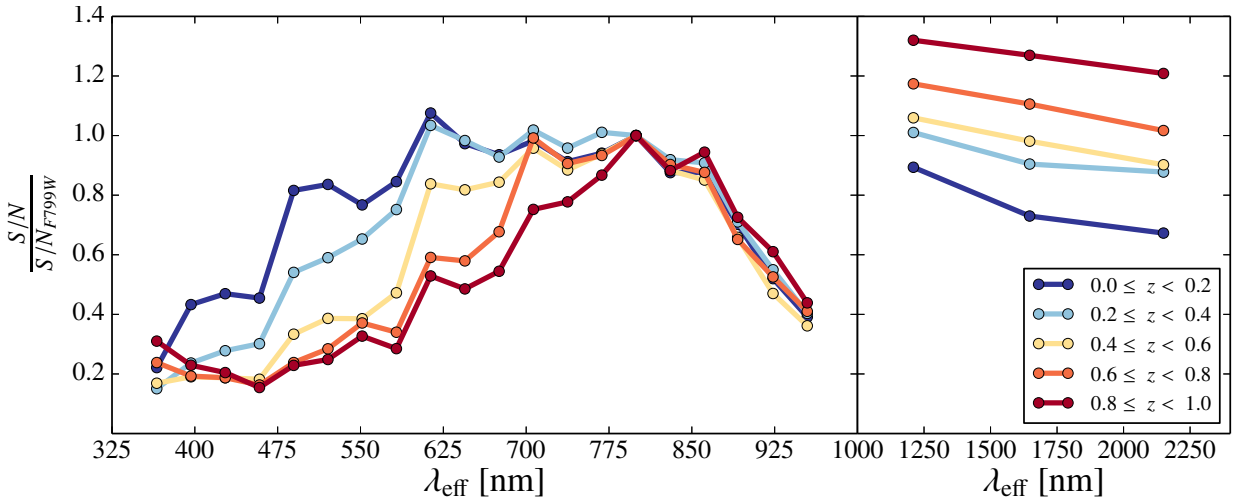

Figure 2.7: Typical signal-to-noise ratios per filter for real ALHAMBRA red sequence galaxies in different redshift bins. The signal-to-noise ratios are normalized to that of the $F799W$ filter. The observed data points account for the effective throughput of the telescope plus camera system and for the average SEDs of red sequence galaxies.

the signal-to-noise ratio changes along the SED as a function of the signal-to-noise in the anchor band $F799W$. These curves are shown in Fig. 2.7, and they account for the effective throughput of the telescope plus camera system, and for the average SEDs of RS galaxies. The signal-to-noise ratios of the reddest filters up to $z = 1$ are strongly affected by technical features of the survey (mainly the depth in these bands), whereas the bluest filters are also affected by the SED shape. From the curves in this figure, it is easy to see how the 4 000 Å-break moves from blue to red wavelengths when the redshift increases. Interestingly, at higher redshifts, the signal-to-noise ratio of the bluest filters starts to grow, indicating larger fluxes in these bands, probably due to the presence of young populations in the galaxy (Ferreras & Silk, 2000), which are easily observable at higher redshifts. Regarding the NIR filters, we checked that typical RS galaxies become redder, on average, when they are observed at higher redshifts.

To study the impact of different signal-to-noise ratios on the derived stellar population parameters, we added noise to the mock galaxies, in each case taking the suitable signal-to-noise ratio curve depending on its redshift. We built three samples of 10 000 mock galaxies, and in each sample we forced the mean signal-to-noise ratio per mock photo spectrum to be $S/N = 10$, 20, and 50, respectively; that is, for a galaxy with $S/N = 20$ at redshift 0.5, the mean signal-to-noise for the 23 filters is 20, but in the bluest filter $S/N_{F365W} \sim 6$, and in the anchor band (maximum) $S/N_{F799W} \sim 30$. The values of $S/N = 10$, 20, and 50 correspond to median apparent magnitudes for the detection band of $m_{F814W} \sim 22.6$, 21.4, and 19.8, respectively (ALHAMBRA RS galaxies and AB magnitudes). For the anchor band $F799W$, these values are almost identical. In ALHAMBRA, typical errors in the zero points due to calibration issues are ~ 0.025 (AB magnitudes), which correspond to a signal-to-noise ratio of ~ 50. Furthermore, most ($\gtrsim 80$ %) of our ALHAMBRA RS subsample has a mean signal-to-noise ratio over 10, whereby these values ($S/N = 10$, 20, and 50) are suitable for our simulations.

Although for the mock galaxies we take models with $0.0 \leq A_V \leq 0.8$ and $0.0 \leq z \leq 1.0$, for the mock analysis we use SSP models with redshifts up to 1.2 and extinctions up to 1.0 to avoid border effects in the parameter estimation. Concerning the age estimation, we use the same constraint as in the mocks; i. e., depending on the redshift, the oldest ages are not allowed.

Figure 2.8 illustrates the comparison between the input parameters of the mock galaxies and the output parameters retrieved with MUFFIT, for the case $S/N = 20$ and all redshifts. The left-hand panels present one-to-one comparisons for the input and output photometric redshifts, extinctions, luminosity-weighted ages and metallicities, and stellar masses. Right-hand panels illustrate the distributions of the differences

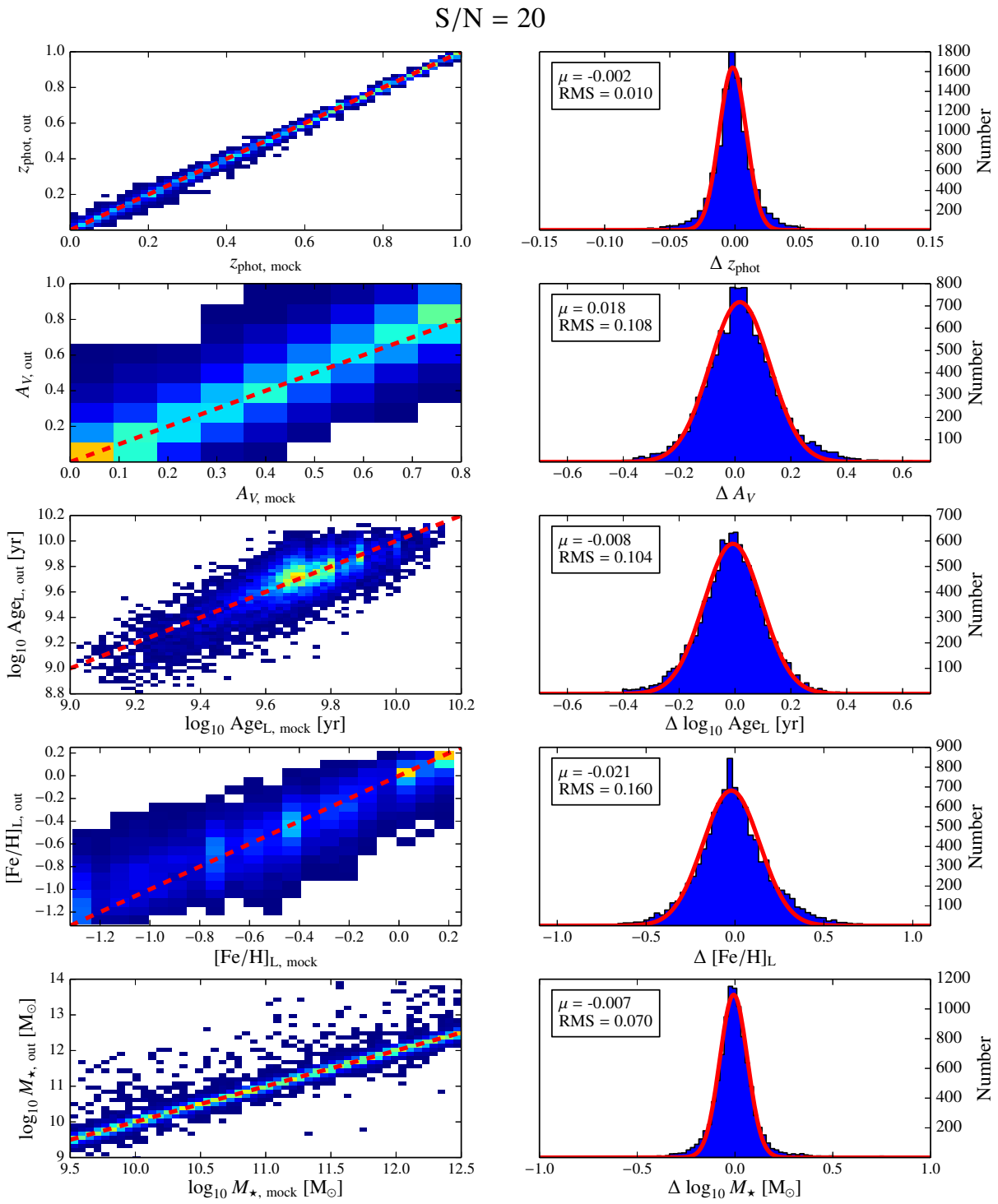

Figure 2.8: Comparison between the input parameters of mock ALHAMBRA galaxies, consisting of random mixtures of two SSP models, and the output parameters retrieved with MUFFIT. The mock galaxies (RS-like galaxies) have average signal-to-noise ratios per filter of 20, according to the typical signal-to-noise ratio distribution presented in Fig. 2.7. *Left panels* show, *from top to bottom*, the one-to-one comparisons in redshift, extinction, luminosity-weighted age, luminosity-weighted metallicity, and stellar mass. Redder and bluer colours indicate regions with higher and lower solution densities, respectively. The red dashed line indicates the one-to-one relationship. *Right panels* present the distributions of the differences between the input and output values in each case, fitted to a Gaussian function (in red) whose mean and root mean square (RMS) are indicated within the box.

between the input and output values in each case, fitted to a Gaussian function (in red) whose mean and root mean square (RMS) are therein indicated. In addition, Table 2.1 provides the typical mean differences and their RMS for different redshift bins and $S/N = 10$, 20, and 50.

As expected, overall there is a very good agreement between the input stellar-population parameters of the mock galaxies and the ones provided by MUFFIT after applying the correspond noise curve on the preceding mock galaxies. This is not surprising since we are analysing mock galaxies made of mixtures of two SSP models, with the same SSP models as input for our code. In this sense, this test must be considered as a lower limit to the parameter uncertainties that we can expect for the forthcoming analysis of ALHAMBRA galaxies, only because of the photon-noise photometric errors. As a matter of fact, the total errors in the derived parameters are expected to be larger, owing to potential differences between the spectro-photometric systems of the ALHAMBRA data and the models, independently of the SSP models of choice. In addition, real galaxies may be affected by ISM emissions or AGNs, which modify their SEDs with respect to a classical mixture of SSPs.

Looking at the stellar mass plot in Fig. 2.8, there seems to be a slight overestimation of the stellar mass. These cases correspond to galaxies with $z \lesssim 0.02$, for which small variations in the redshift cause big changes in the luminosity distance, hence in the retrieved stellar mass (see Eq. 2.14). This result suggests that in the very local Universe, more accurate redshifts are required to provide reliable stellar masses using the analysis techniques explained above. Fortunately, the very few local galaxies in the ALHAMBRA survey have a very high signal-to-noise ratio as well, so that this overestimation is negligible in our case.

Another case that is worth being explained is the one of mock galaxies with low extinctions and low metallicities. According to Fig. 2.8, we are getting higher values on average. However, this is an artefact of the simulations since there are no lower values in our set of SSP models. The important result in these plots is that we are still retrieving the right trend in the parameters, despite the border effects in the parameter space.

The results in Table 2.1 are divided into different redshift bins because old ages are not allowed at high redshifts. It is noteworthy that all the parameters are determined better at high redshifts than at low redshifts at the same mean signal-to-noise ratio. First, because at higher redshifts the galaxy SEDs are sampled with an equivalent higher spectral resolution at rest frame, so that both redshift and age, which are sensitive to the 4 000 Å-break, are better established (and consequently, the rest of parameters as well). Also, at high redshift the range of possible ages is shorter, and are in turn younger with lower degeneracies than their older counterparts. Finally, the bluest parts of the $z \gtrsim 0.5$ SEDs have higher signal-to-noise ratios. These filters act as anchoring bands to constrain blue-sensitive parameters (like extinction or metallicity). This growth in the signal may be due to an underlying young and less massive population in the galaxy (Ferreras & Silk, 2000) that is not strong enough to contribute in the optical range, but that dominates the flux in the NUV rest-frame regime (being visible at $z \gtrsim 0.5$ in ALHAMBRA), reinforcing the necessity of using two components in the fittings.

To conclude, these simulations are key for giving us an idea of the typical issues that may appear in this kind of study and the uncertainties that we expect from photon-noise photometric uncertainties. These results show that one can robustly explore the stellar populations of galaxies in the ALHAMBRA dataset by using the MUFFIT code presented here.

2.4.3 Photometric redshifts in the ALHAMBRA survey

Although the main aim of our code is not to determine redshifts, it is very important to check whether, for a general case in which the galaxies do not have any redshift information, the code is self-sufficient for estimating photo-z properly, at least to some extent. Otherwise, the derived galaxy parameters may be estimated incorrectly.

To do this, we ran our code on the subsample of RS galaxies with spectroscopic redshifts in ALHAMBRA, from Molino et al. (2014), to set the accuracy of the ALHAMBRA photo-z. This subsample is built by the publicly available data of the spectroscopic surveys that overlap with ALHAMBRA (zCOSMOS,

Table 2.1: Typical uncertainties in the determination of redshifts, luminosity-weighted ages and metallicities, extinctions, and stellar masses, expected from running our code on ALHAMBRA RS galaxies at different redshift bins and for different S/N (10, 20, and 50).

Parameters	$0.0 \leq z \leq 0.2$	$0.2 \leq z \leq 0.4$	$0.4 \leq z \leq 0.6$	$0.6 \leq z \leq 0.8$	$0.8 \leq z \leq 1.0$
$S/N = 10$					
$z_{\rm phot}$	0.01 ± 0.03	0.00 ± 0.04	0.00 ± 0.03	0.00 ± 0.02	0.00 ± 0.02
A_V	0.10 ± 0.22	0.08 ± 0.20	0.04 ± 0.17	0.04 ± 0.15	0.02 ± 0.14
$\log_{10}$ Age$_{\rm L}$ [yr]	-0.01 ± 0.19	-0.03 ± 0.17	-0.03 ± 0.14	0.00 ± 0.11	0.03 ± 0.10
[Fe/H]$_{\rm L}$	-0.09 ± 0.29	0.01 ± 0.30	0.03 ± 0.26	0.00 ± 0.23	0.03 ± 0.22
$\log_{10} M_\star$ [M$_\odot$]	0.10 ± 0.28	0.02 ± 0.12	0.01 ± 0.10	0.01 ± 0.08	-0.01 ± 0.06
S/N = 20					
$z_{\rm phot}$	0.00 ± 0.01	0.00 ± 0.01	0.00 ± 0.01	0.00 ± 0.01	0.00 ± 0.01
A_V	0.06 ± 0.15	0.04 ± 0.13	0.01 ± 0.10	0.02 ± 0.09	0.00 ± 0.08
$\log_{10}$ Age$_{\rm L}$ [yr]	-0.03 ± 0.14	-0.03 ± 0.13	-0.01 ± 0.11	0.00 ± 0.09	0.01 ± 0.07
[Fe/H]$_{\rm L}$	-0.06 ± 0.20	-0.03 ± 0.19	-0.01 ± 0.16	-0.01 ± 0.14	0.00 ± 0.12
$\log_{10} M_\star$ [M$_\odot$]	0.02 ± 0.15	0.01 ± 0.09	0.00 ± 0.07	0.00 ± 0.06	-0.01 ± 0.05
S/N = 50					
$z_{\rm phot}$	0.00 ± 0.00	0.00 ± 0.00	0.00 ± 0.00	0.00 ± 0.00	0.00 ± 0.00
A_V	0.01 ± 0.08	0.00 ± 0.06	0.00 ± 0.05	0.00 ± 0.03	0.00 ± 0.02
$\log_{10}$ Age$_{\rm L}$ [yr]	-0.02 ± 0.11	-0.02 ± 0.09	0.00 ± 0.08	0.00 ± 0.06	0.00 ± 0.05
[Fe/H]$_{\rm L}$	-0.03 ± 0.08	-0.02 ± 0.08	-0.02 ± 0.07	-0.02 ± 0.06	-0.01 ± 0.05
$\log_{10} M_\star$ [M$_\odot$]	0.00 ± 0.08	0.01 ± 0.06	0.00 ± 0.05	0.00 ± 0.04	0.00 ± 0.03

Notes. The random errors in the parameters are given as the mean and RMS of the best Gaussian function that reproduces the distribution of the differences between the input and output parameter values, as illustrated in the right panels of Fig. 2.8.

Lilly et al. 2009; AEGIS, Davis et al. 2007; and GOODS-N, Cooper et al. 2011), amounting to $\sim$ 900 RS galaxies up to magnitude $m_{F814W} < 22.5$. For the purpose of this test, we used the photo-z predictions provided by BPZ2.0 in the Gold catalogue. In addition, we also took the photo-z constraints provided by EAZY (Brammer et al., 2008) with the default configurations and templates, to assess whether MUFFIT also works similarly when the input photometric redshifts come from an external source.

To provide a numerical value for the quality and accuracy of the photo-z, we simultaneously use definitions, which can be more or less useful depending on our purposes for both accuracy and catastrophic outliers. Brammer et al. (2008) propose the normalized median absolute deviation, $\sigma_{\rm NMAD}$, as a measurement of the photo-z uncertainties, since it estimates the deviation of the photo-z distribution without being affected by catastrophic errors. It is defined as

$$\sigma_{\rm NMAD} = 1.48 \times median\left(\frac{|\Delta z - median(\Delta z)|}{1 + z_{\rm spec}}\right), \tag{2.21}$$

where $\Delta z = z_{\rm phot} - z_{\rm spec}$. Furthermore, we provide the RMS of the distribution $\Delta z/(1 + z_{\rm spec})$, which in the following, we denote as $\sigma_z/(1 + z_{\rm spec})$. Additionally, we use two definitions for the rate of photo-z catastrophic outliers, as in Molino et al. (2014), formally expressed as

$$\eta_1 = \frac{\Delta z}{1 + z_{\rm spec}} > 0.2, \text{and} \tag{2.22}$$

Table 2.2: Quality of the photo-z retrieved for a subsample of RS galaxies in ALHAMBRA, when different method are applied: our code alone, BPZ2.0, EAZY, and our code using BPZ2.0 and EAZY as input values of redshift.

	$\sigma_{\rm NMAD}$	$\sigma_z/(1+z_{\rm s})$	η_1	η_2
MUFFIT	0.0157	0.0105	1.6 %	5.8 %
BPZ2.0	0.0104	0.0076	0.9 %	7.7 %
EAZY	0.0102	0.0083	0.8 %	4.0 %
MUFFIT + BPZ2.0	0.0087	0.0070	0.9 %	6.3 %
MUFFIT + EAZY	0.0092	0.0071	0.7 %	5.5 %

Notes. Details on the definition of the quality values are given in Eqs. 3.3, 3.4, and 3.5.

$$\eta_2 = \frac{\Delta z}{1+z_{\rm spec}} > 5 \times \sigma_{\rm NMAD}. \tag{2.23}$$

On the basis of the above equations, Table 2.2 presents the quality of the photo-z determined for the subsample of RS galaxies with different methods. First, we analysed the reliability and accuracy of the photo z derived from our own code alone, that is, not using any photo-z value as input to constrain the solution. This case can be directly compared with the values directly derived from the BPZ2.0 and EAZY codes, showing, as expected, that photo-z codes do a better job of determining redshifts from scratch. In addition, we analysed the quality of the photo z derived in the same way from our code when the redshift PDFs of BPZ2.0 are used as input parameters. MUFFIT explores the plausible stellar population parameters, managing the photo z as another free parameter inside the redshift range of choice for the user. For the present work, we used the 1 σ PDF range provided in the Gold catalogue, hence all the photo-z weights equal to 1 inside the provided range (1 σ) and 0 beyond this range. According to Eqs. 3.3, 3.4, and 3.5, we obtained $\sigma_{\rm NMAD} \sim 0.0087$, yielding a rate of catastrophic outliers $\eta_1 = 0.97$ % and $\eta_2 = 6.26$ %. For this specific case, the resulting photo z were compared with their spectroscopic counterparts in Fig. 2.9. Similarly, using the photo-z constrains from EAZY as an input to our code (also 1 σ, for consistency in the comparison), we find $\sigma_{\rm NMAD} = 0.0092$, $\eta_1 = 0.76$ %, and $\eta_2 = 5.51$ %. From these results we conclude that, at least for RS galaxies, our stellar population code improves the redshift accuracy of classical photo-z codes, when these are used as input for our technique. This can be explained as our method plays with mixtures of much larger numbers (million) of SSP models, allowing flexible SED fittings to be performed, hence providing a fine-tuned, second-order correction to the redshift values of photo-z codes. In addition, the number of catastrophic outliers, η_1 and η_2, is also marginally decreased on average. The shifts between photo-z and spectroscopic values are statistically insignificant ($\lesssim 0.002$), as we see in Sect. 2.4.4, on our stellar population results. As we show in Sect. 2.4.4, devoted to setting constraints on the uncertainties of the stellar population parameters due to the photo-z uncertainties, it is more important for our aims for the stellar population to minimise the number of outliers, rather than decreasing $\sigma_{\rm NMAD}$ a little.

2.4.4 Impact of the photometric-redshift uncertainties

One of the most critical parameters for determining reliable stellar populations and masses for a galaxy is the redshift. If the redshift is unknown or uncertain, it is obvious that the rest of the derived parameters will not be reliable either. In this section, we aim to quantify the impact of the typical redshift uncertainties on the reliability of the retrieved parameters and the maximum redshift errors allowed to reach our goals.

To answer these questions, we again focus on the ALHAMBRA data. To determine the direct impact of redshift uncertainties over the rest of derived parameters, we compared the results obtained from our code for the spectroscopic subsample of RS galaxies (see Sect. 2.4.3) using the redshift PDFs of BPZ2.0 as input, with the results that we obtained with our code for the same galaxy sample assuming exactly their spectroscopic redshifts. It is worth noting that, in contrast to the previous simulations (e. g. Sect. 2.4.2), we

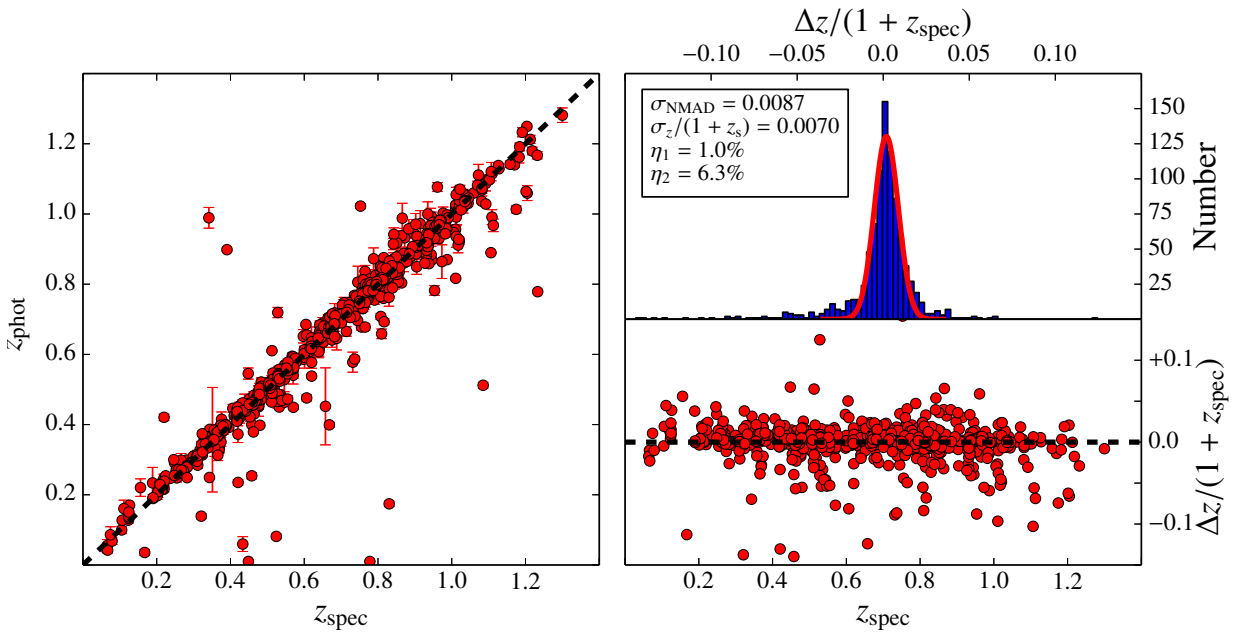

Figure 2.9: Comparison of the photo-z retrieved with our code using the redshift PDFs of BPZ2.0 as input values. The data correspond to a subsample of RS galaxies from ALHAMBRA with spectroscopic redshifts in the literature. *Left panel* illustrates the one-to-one redshift comparison for every galaxy, with the dashed line being the one-to-one relation. The *bottom-right* panel presents the differences between the photo-z and their spectroscopic counterparts for each galaxy, normalized by (1+z_{spec}). The *top-right* panel shows the obtained distribution $\Delta z/(1+z_{spec})$, indicating the accuracy parameters and the rate of outliers (Eqs. 3.3, 3.4, and 3.5) at the inner box.

were using real galaxies to estimate these uncertainties.

Figure 2.10 summarises the results of this test. Left-hand panels present the one-to-one comparison for the redshift, extinction, luminosity-weighted age, luminosity-weighted metallicity, and stellar mass. To facilitate the visual interpretation of the comparison and observe the direct effect of the worst estimated photo-z on the stellar population parameters, we plot each galaxy with a colour depending on the discrepancy level of its photo-z using the above definitions of catastrophic outliers (η_1 and η_2, see Eqs. 3.4 and 3.5). This is clearly seen in the top left-hand panel of Fig. 2.10, where the redshift values are compared. From the data in Fig. 2.10 and the RMS of the differences, we observe that, overall, the stellar population parameters present very minor changes due to typical redshift uncertainties and all the distributions are centred close to zero. On average, such uncertainties account for $\sigma^z_{A_V} = 0.03$, $\sigma^z_{\rm Age} = 0.18$ Gyr (0.03 dex), $\sigma^z_{\rm [Fe/H]} = 0.04$ dex, and $\sigma^z_{M_\star} = 0.03$ dex, which are all negligible when we compare them with the uncertainties introduced by the typical photon noise (see Sect. 2.4.2). As expected, catastrophic outliers ($|z_{phot} - z_{spec}| \geq 0.044$) exhibit a larger spread in most parameters.

To conclude, the typical uncertainties on the redshifts present a negligible impact on the main stellar population parameters, except if the galaxy is a catastrophic outlier. The uncertainties on the ALHAMBRA photometry and the model systematics are more crucial uncertainties in the present work.

2.4.5 Degeneracies

In addition to estimating the uncertainties, it is crucial to know which kind of degeneracy may alter our results, to avoid unveiling a finding that really is a degeneracy aftermath. To interpret the output properly, we must keep these degeneracies under control, reducing their impact as much as possible.

Unlike stellar population diagnostic techniques based on local absorption features, such as classical

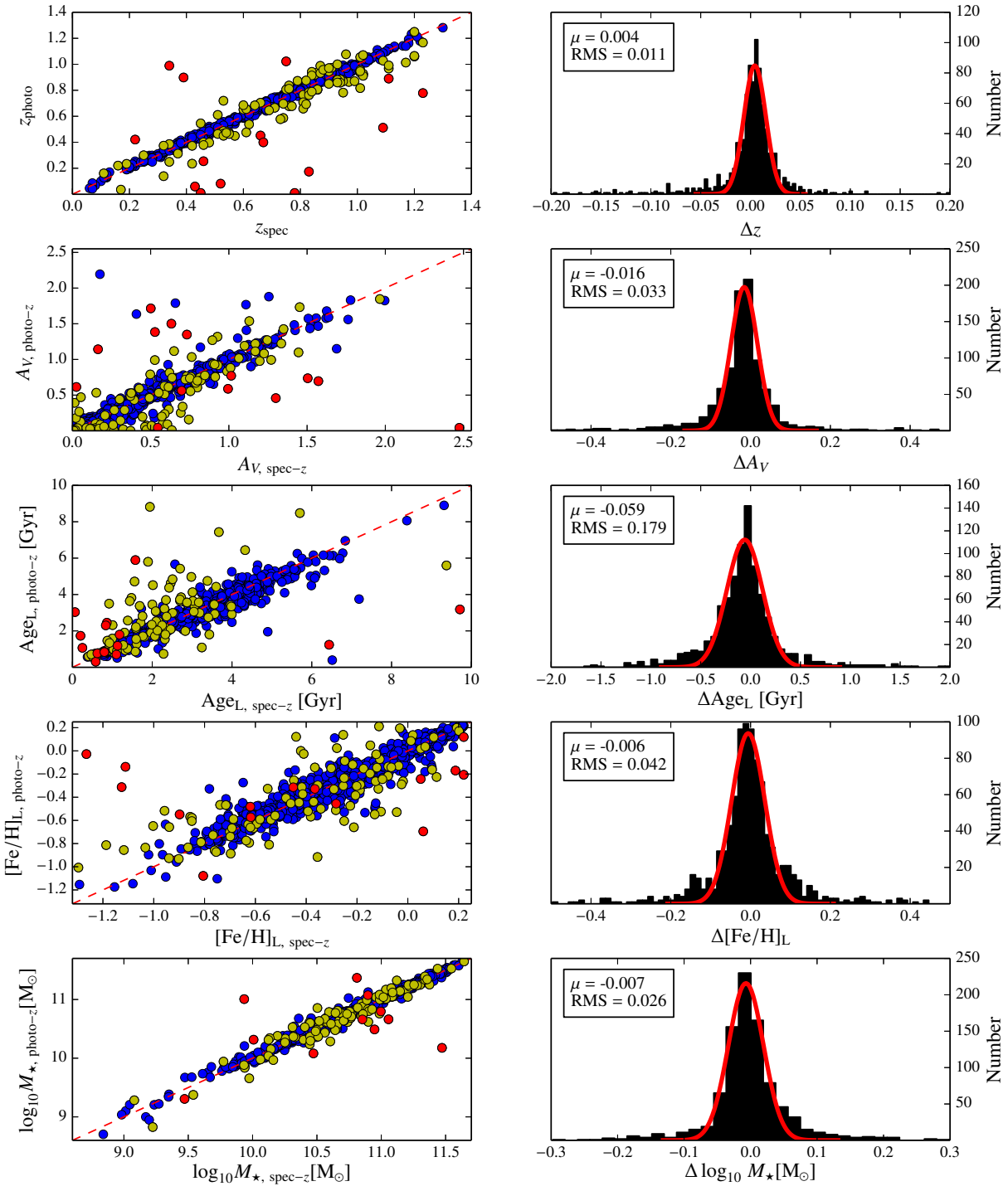

Figure 2.10: Impact of a redshift uncertainty $\sim$ 1 % on the stellar population parameters. On the *left panels*, we present the comparative one-to-one of the obtained parameters without any constrain in the photo z (Y–axis) versus the results forcing the redshift to its spectroscopic value (X–axis). The dashed red line represents the one-to-one relationship. Red, yellow, and blue dots are galaxies for which $|z_{\rm spec} - z_{\rm phot}| > 0.2$, $0.044 \leq |z_{\rm phot} - z_{\rm spec}| < 0.2$, and $|z_{\rm phot} - z_{\rm spec}| < 0.044$, respectively. On the *right panels*, we have the histograms of the differences between the obtained results with and without the spectroscopic constraint. The solid red line is the best fit of the distribution to a Gaussian function, and the boxes show both Gaussian mean and RMS. *From top to bottom*, we show redshift, extinction, age, metallicity, and stellar mass.

line strength indices, which also present the well known age–metallicity degeneracy (Worthey, 1994a), our multi-filter stellar population code depends on colour, because it tries to reproduce the galaxy SED by mixing SSPs over a wide wavelength range. Therefore, considering only the age–metallicity degeneracy may not be enough, since we must evaluate any parameter that can modify the colour in a wide wavelength range; that is, we also have to include the intrinsic extinction as another degenerated parameter in our analysis. As we mention above, in this paper we assume a universal IMF. Otherwise, this parameter should be considered for the degeneracies as well, as bottom-heavy IMFs exhibit redder colours than top-heavy ones. Moreover, since the degeneracies amongst parameters strongly depend on the number and width of the filters, the total spectral coverage, etc., it is worth noting that the results presented in this section only apply to the use of our code on ALHAMBRA data.

To address the degeneracy questions in the most realistic way, we take all the ALHAMBRA RS galaxies as targets (see Sect. 2.4.1) with mean signal-to-noise ratios of $\sim$ 20 and in certain ranges of age and metallicity. These results come up after having run MUFFIT with the ALHAMBRA galaxies using the MIUSCAT SSP models. The degeneracy estimation is done by taking all the stellar population values recovered during the Monte Carlo approaches at different stellar population bins (detailed below), and then stacking each retrieved distribution to build a whole distribution per bin, getting distributions among pairs of parameters (age, metallicity, and extinction). We characterise each distribution by setting confidence ellipses (2D confidence intervals) that enclose the results provided during the Monte Carlo process. These ellipses are obtained by the covariance matrix of each distribution, and they allow parametrising the degeneracies through two parameters: by the ellipticity, denoted as e, and by θ, the angle between the X–axis and the ellipse semi-major axis.

The angle θ is determined by the eigenvectors of the covariance matrix, as well as the eigenvalues of the covariance matrix determine the axis lengths. If e is close to zero, this implies that the degeneration between the two parameters is not very significant, irrespective of the value of θ. On the other hand, if θ is a multiple of $\pi/2$ (lies on any of the two axes), both parameters are uncorrelated, consequently there is no degeneracy between them. Consequently, both parameters are necessary to confirm whether a degeneracy exists or not. In fact, we can quantify the level of degeneracy between parameters via the Pearson's correlation coefficient, which mathematically reflects both e and θ effects. Formally,

$$r_{xy} = \frac{\sum_{i=1}^{n}(x_i - \bar{x})(y_i - \bar{y})}{\sqrt{\sum_{i=1}^{n}(x_i - \bar{x})^2 \sum_{i=1}^{n}(y_i - \bar{y})^2}}, \tag{2.24}$$

where x_i and y_i denote the value pairs of the parameters (age, metallicity, extinction) with means $\bar{x}$ and $\bar{y}$, respectively. The closer r_{xy} is to 1 (to -1), the larger the correlation (anti-correlation), meaning the degeneracy between parameters; in contrast, a value close to 0 ($-0.1 \lesssim r_{xy} \lesssim 0.1$) suggests that the parameters are uncorrelated, and there would be no degeneracy.

Regarding the parameter ranges, we take bins in age of $0.5 \leq \mathrm{Age_L} \leq 1.0$, $3.0 \leq \mathrm{Age_L} \leq 4.5$, and $7.0 \leq \mathrm{Age_L} \leq 10.0$ Gyr, whereas for metallicity we take $-0.8 \leq [\mathrm{Fe/H}]_\mathrm{L} \leq -0.6$, $-0.4 \leq [\mathrm{Fe/H}]_\mathrm{L} \leq -0.2$, and $-0.1 \leq [\mathrm{Fe/H}]_\mathrm{L} \leq 0.1$. These bins have been chosen to evaluate how the degeneracies vary along different stellar population parameters. We do not establish any extinction bin, because we have previously checked that the degeneracies in different extinction bins present negligible differences in e and θ. We also studied whether different redshifts can alter the degeneracy effects, since the redshift determines the observed spectral range of the ALHAMBRA SEDs. We find that at higher redshift some degeneracies tend to decrease, especially for young and low-metallicity galaxies, but in general the degeneracies remain alike (less dispersion as well, see Sect. 2.4.2). Thus, the three bins in age and in metallicity define the nine intervals where the degeneracies of our parameters are explored. In each interval, we compare the age–metallicity, age–extinction, and metallicity–extinction degeneracies.

In Fig. 2.11 we present the covariance error ellipses (in blue) that enclose, at the 95 % confidence level, the distribution of the provided parameters during the Monte Carlo approach for all the ALHAMBRA RS

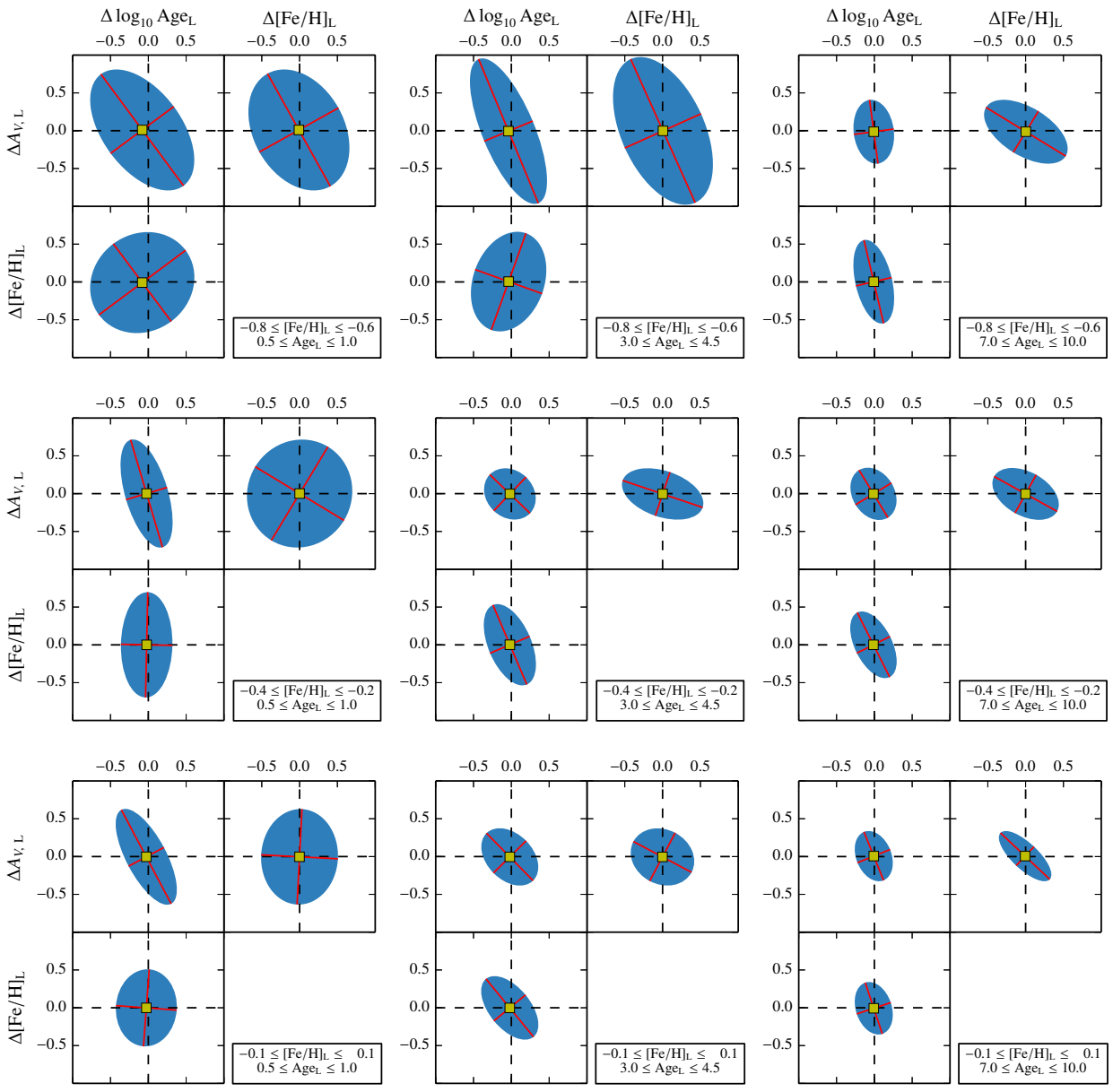

Figure 2.11: Covariance error ellipses, at the 95 % confidence level, of the stellar population parameters provided by the Monte Carlo approach in MUFFIT with respect to their most probable values, for different age and metallicity bins (see *inner panels*). Yellow squares indicate the ellipse centres, and the red lines illustrate the minor and major axes of each ellipse.

Table 2.3: Summary of the confidence error ellipses in Fig. 2.11 for different parameter bins and MIUSCAT models.

		0.5 ≤ Age [Gyr] ≤ 1.0			3.0 ≤ Age [Gyr] ≤ 4.5			7.0 ≤ Age [Gyr] ≤ 10.0		
		r_{xy}	θ	e	r_{xy}	θ	e	r_{xy}	θ	e
MIUSCAT	$\Delta\log_{10}$ Age vs Δ[Fe/H]									
	$-0.8 \leq$ [Fe/H] ≤ -0.6	0.11	36	0.11	0.24	70	0.31	−0.40	103	0.58
	$-0.4 \leq$ [Fe/H] ≤ -0.2	0.03	88	0.52	−0.49	113	0.51	−0.51	116	0.50
	$-0.1 \leq$ [Fe/H] ≤ 0.1	0.04	85	0.22	−0.55	129	0.46	−0.26	108	0.35
	Δ[Fe/H] vs ΔA_V									
	$-0.8 \leq$ [Fe/H] ≤ -0.6	−0.30	119	0.30	−0.46	114	0.47	−0.54	148	0.49
	$-0.4 \leq$ [Fe/H] ≤ -0.2	0.05	58	0.05	−0.37	161	0.46	−0.41	150	0.40
	$-0.1 \leq$ [Fe/H] ≤ 0.1	0.02	87	0.20	−0.16	152	0.18	−0.76	136	0.63
	$\Delta\log_{10}$ Age vs ΔA_V									
	$-0.8 \leq$ [Fe/H] ≤ -0.6	−0.50	126	0.44	−0.69	112	0.67	−0.13	97	0.38
	$-0.4 \leq$ [Fe/H] ≤ -0.2	−0.53	106	0.63	−0.18	136	0.17	−0.25	121	0.25
	$-0.1 \leq$ [Fe/H] ≤ 0.1	−0.70	117	0.63	−0.37	134	0.32	−0.28	111	0.34
BC03	$\Delta\log_{10}$ Age vs Δ[Fe/H]									
	$-0.8 \leq$ [Fe/H] ≤ -0.6	−0.07	93	0.42	−0.24	104	0.38	−0.19	96	0.53
	$-0.4 \leq$ [Fe/H] ≤ -0.2	0.01	89	0.39	−0.46	112	0.49	−0.32	120	0.31
	$-0.1 \leq$ [Fe/H] ≤ 0.1	−0.05	91	0.54	−0.57	118	0.53	−0.48	136	0.41
	Δ[Fe/H] vs ΔA_V									
	$-0.8 \leq$ [Fe/H] ≤ -0.6	−0.63	145	0.55	−0.22	118	0.23	−0.77	150	0.68
	$-0.4 \leq$ [Fe/H] ≤ -0.2	−0.58	141	0.49	−0.16	167	0.31	−0.34	158	0.40
	$-0.1 \leq$ [Fe/H] ≤ 0.1	−0.59	144	0.51	−0.10	174	0.37	−0.25	104	0.39
	$\Delta\log_{10}$ Age vs ΔA_V									
	$-0.8 \leq$ [Fe/H] ≤ -0.6	−0.45	118	0.43	−0.62	114	0.60	−0.16	104	0.28
	$-0.4 \leq$ [Fe/H] ≤ -0.2	−0.50	117	0.48	−0.43	126	0.38	−0.46	144	0.41
	$-0.1 \leq$ [Fe/H] ≤ 0.1	−0.46	108	0.53	−0.40	140	0.35	−0.44	116	0.44

Notes. θ is the angle between the X–axis and the semi-major axis a in degrees (counter clockwise), whereas e is the ellipticity. To quantify the degeneracy between parameters, we provide the Pearson's correlation coefficient, r_{xy}, where values close to 0 correspond to uncorrelated parameters.

galaxies in the nine age and metallicity ranges (see inner panels), and at redshift $z \leq 0.4$. The semi-minor and semi-major axes of each ellipse are shown in red, whereas their centres are represented with a yellow square. Table 2.3 provides θ, e, and r_{xy} for the same age and metallicity regimes.

As intuitively expected, age and extinction are anti-correlated in all cases, in the sense that a reddening by extinction can mimic an older age, and vice versa. However, the behaviour of the age–metallicity and metallicity–extinction degeneracies is not so immediate. This is clearly a consequence of the role that extinction plays in the analysis as a third degree of freedom, partially absorbing the weight of metallicity in the classical age–metallicity degeneracy problem. Whilst older galaxies exhibit, as expected, clear anti-correlated age–metallicity and metallicity–extinction degeneracies, such anti-correlations may turn into very mild or even positive correlations depending on the range of age and metallicity. For instance, at the lower

metallicity range, young and intermediate-age galaxies exhibit a positive degeneracy between age and metallicity, turning mild or negligible for young galaxies with intermediate and high metallicities. Interestingly, young metal-rich galaxies are essentially only subject to the extinction-age degeneracy.

Finally, we checked that the general degeneracy trends presented in this section do not vary qualitatively when computed on the basis of the BC03 models (see Table. 2.3). For ages lower than $\sim$ 1 Gyr, there is a clear degeneracy of both age and metallicity with extinction, and for older ages, there is also an age–metallicity degeneracy.

2.5 Testing the perfomance of the code with ALHAMBRA galaxy data

Once the technical details of MUFFIT have been described in detail and the typical uncertainties and degeneracies amongst the derived parameters have been studied for the case of the ALHAMBRA survey, in this section we apply the code to different subsamples of galaxies in ALHAMBRA. The ultimate goal of this section is not to provide a thorough study of the stellar populations of ALHAMBRA galaxies, but rather to test the reliability of the stellar populations, emission line equivalent widths (EW), stellar masses, and redshifts derived from our code in comparison with those published in previous work for either similar or identical galaxy samples. A forthcoming paper (Díaz-García et al., in prep.) will present a complete analysis of the stellar populations of galaxies in ALHAMBRA making use of MUFFIT.

2.5.1 Stellar masses and photo z in the COSMOS survey

Since Field 4 in the ALHAMBRA survey partly overlaps with the COSMOS field, we can construct a subsample of RS galaxies (see Sect. 2.4.1) in common between both surveys. After removing all the sources labelled as stars in COSMOS (point-like sources, Ilbert et al., 2009) and in ALHAMBRA, we end up with a subsample of 767 common galaxies up to redshift $z \leq 1.6$.

This galaxy subsample indeed has an important added value for our testing goals, because it has spectroscopic data in the zCOSMOS 10k-bright catalogue (Lilly et al., 2007, 2009), allowing for a calibration of the derived photo z using the LE PHARE code. In addition, using broad and medium bands and following a SED-fitting technique with BC03 models, Ilbert et al. (2010) estimated the stellar masses of the COSMOS galaxies. They assumed a fixed Chabrier IMF (similar to the IMF of Kroupa, 2001), a star formation rate $\propto e^{-t/\tau}$ (with $0.1 \leq \tau \leq 30$ Gyr), a unique solar metallicity, an age grid of 0.1–14.5 Gyr, and the Calzetti et al. (2000) extinction law with $0.0 \leq E(B-V) \leq 0.5$. (high extinction values are only allowed for galaxies with high star formation).

For analysing this sample we used MUFFIT, which imposes a mixture of two SSPs rather than an exponential star formation rate. We selected MIUSCAT models with a Kroupa IMF (which slightly differs from the Chabrier IMF), for a wider range in metallicity ($-1.31 \leq$ [Fe/H] ≤ 0.22). For our analysis we used the Fitzpatrick (1999) extinction law rather than the Calzetti et al. (2000) law, because the latter is generally more appropriate to central star-forming regions (Calzetti, 1997).

In Fig. 2.12 we present a one-to-one comparison of the photo-z and stellar masses obtained with our code on the ALHAMBRA data and those presented in the above work on the COSMOS data (Ilbert et al., 2009, 2010) for the subsample of 767 RS galaxies in common. Having already constrained the reliability and accuracy of the ALHAMBRA photo z with respect to available spectroscopic redshifts (see Sects. 2.4.3 and 2.4.4), in the top panels of Fig. 2.12, we compare our outcomes with the COSMOS photo z, not only because of the qualitative similarity of both techniques, but also to check that there are systematics in our photo-z measurements that might cause any kind of systematic in the retrieved ALHAMBRA stellar masses. From these plots we can see that both photo-z estimations are in very good agreement, with one-to-one differences having an RMS of just 0.015, and not finding statistically significant differences between both samples. The bottom panels of Fig. 2.12 are devoted to the stellar mass comparison. We find that the mean value of the one-to-one stellar mass differences is 0.04 dex, with a dispersion of 0.15 dex.

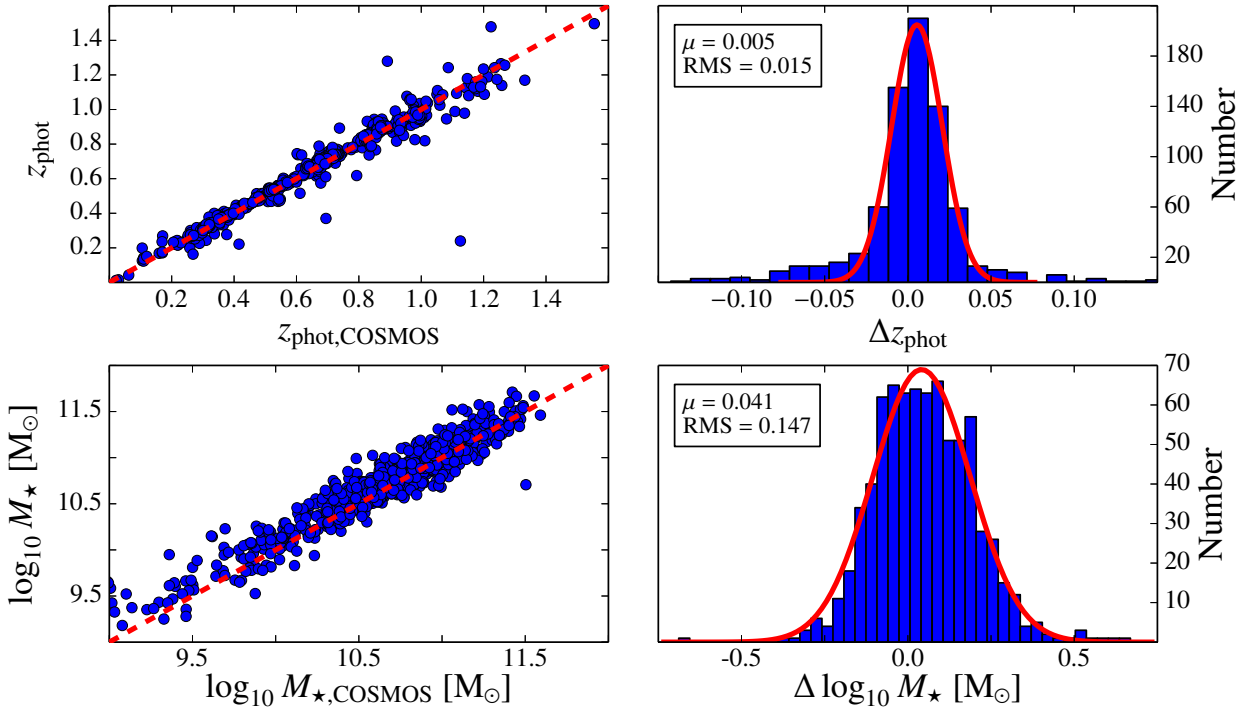

Figure 2.12: Differences between the photo-z (*top panels*) and stellar masses (*bottom panels*), computed with MUFFIT (Y–axis) and the values provided in COSMOS catalogues (X–axis; Ilbert et al., 2009, 2010), for a subsample of RS galaxies. On the *right panel*, we show the histograms of the differences, which are fitted to a Gaussian distribution.

As we explained in Sect.2.4.4, the typical uncertainties of our ALHAMBRA photo z may have an impact on the dispersion of the retrieved stellar masses of up to 0.026 (see Fig. 2.10), well below the observed value. On the other hand, the offset between masses cannot be completely explained by the mild offset between redshifts ($\mu = 0.005$), since when using Eq. 2.14, this difference implies a shift in mass $\lesssim 0.015$ dex. Previous work have already reported the non-negligible effect of using different model sets on the absolute values of the derived stellar masses (see e. g. Pozzetti et al., 2007; Ilbert et al., 2010). To check this in our particular case, we have repeated the above analysis for the same subsample of galaxies with the BC03 models, instead of MIUSCAT. The new mean difference between the stellar masses of ALHAMBRA and COSMOS galaxies is now -0.03 dex, with a similar dispersion of RMS $= 0.15$ dex. Consequently, the mild systematic between stellar masses is probably due to the SSP model choice. Irrespective of the input set of SSP models, the dispersion between the stellar masses provided by COSMOS and the retrieved from ALHAMBRA data after running MUFFIT remains RMS ~ 0.15 dex. This can be easily explained as the quadratic sum of the stellar mass uncertainties retrieved from both COSMOS and our proper technique in the common sample, where ~ 0.09 dex in COSMOS and ~ 0.11 dex in ALHAMBRA.

As a general conclusion, despite the differences in the analysis techniques presented in this paper for ALHAMBRA galaxies and those performed by previous work for the COSMOS data, we find remarkable agreement between the photo-z and the stellar masses derived for galaxies in common, showing the reliability and robustness of our code. We confirm that the choice of SSP models and extinction laws has an impact on the absolute values of the derived stellar masses. In particular, we find that the stellar masses derived using the MIUSCAT models lead to mean values of 0.07 dex that are higher than when using BC03 models.

2.5.2 Photometric EWs of emission lines

During the SED fitting process, the detection and subsequent removal of the bands affected by nebular emission lines may be crucial for determining reliable properties of the underlying stellar content of the galaxy under study. The way in which the affected bands are detected and removed from the analysis is already described in Sect.2.3.2.2. Here we analyse to what extent the emission line residuals retrieved from our fittings, based on photometric data, are reliable and still keep meaningful information on the true EWs of the nebular lines derived from classical spectroscopy.

To build up a comparison galaxy sample, we first take all the ALHAMBRA galaxies that i) are in common with the data catalogues of the MPA/JHU [9] (hereafter MPA/JHU catalogues) and ii) present nebular emission lines in their spectra (Brinchmann et al., 2004; Tremonti et al., 2004). This catalogue contains EWs and flux measurements of nebular lines for galaxies in the SDSS DR7 (Abazajian et al., 2009). Such measurements already account for their corresponding underlying stellar absorptions, because they were calculated after subtracting appropriate SSP models.

Since our stellar population code is focused on the analysis of galaxies whose SEDs are dominated by their stellar content, for a fair comparison we systematically remove all the AGNs and QSOs from the sample (*AGN*, *AGN_BROADLINE*, *QSO*, and *T2* types in SDSS), even if some of them could still be interpreted by our code. In addition, galaxies with a signal-to-noise ratio lower than 5 in the EW continuum are removed, as are those galaxies in the redshift ranges $0.112 < z < 0.114$, $0.123 < z < 0.125$, and $0.146 < z < 0.148$, to avoid EW contaminations due to the sky line O I λ 5 577, and all the galaxies larger than 4″ (the SDSS fibres have 3″ diameter) to minimise strong aperture effects in the photometry. Under the above constraints, there are 92 galaxies in common between ALHAMBRA and the MPA/JHU catalogues of SDSS.

The detection and classification of emission lines in multi-filter surveys is clearly limited by the low spectral resolution of the data. For instance, at the ALHAMBRA resolution, and depending on the redshift, the emission line pairs Hβ–[O III], Hα–[N II], and even Hα–[S II] can be unresolved because of their proximity in wavelength. To try to overcome this intrinsic limitation, rather than comparing the EWs of individual lines, we compare the total flux in excess along the observed spectral-range ($\lambda\lambda$ 3 500–9 700 Å for ALHAMBRA) with the total sum of the EWs measured in the MPA/JHU catalogues for the following strong nebular lines: Hβ λ 4 861, [O III] λ 4 959, [O III] λ 5 007, Hα λ 6 563, [N II] λ 6 548, [N II] λ 6 584, [S II] λ 6 717, and [S II] λ 6 731. We do not account for weaker lines because they might not be detected under the ALHAMBRA resolution. As explained in Section 2.3.2.2, we set the detection limits of emission lines in ALHAMBRA to a flux excess of $\Delta m_{\rm EL} = 0.1$ and a signal-to-noise ratio with respect to the photometric error of the filter of $\sigma_{\rm EL} = 2.5$. Out of the 92 galaxies in common, there are 44 galaxies in ALHAMBRA for which our code detects an emission line in at least one filter, hence constituting the final galaxy subsample for the sake of EW comparisons.

Since our SED-fitting technique is based on a χ^2 minimization technique between the filter fluxes of models and real galaxies over the full spectral range of the data, we must be aware that the best fitting solution may not match the local continuum around the emission lines perfectly, leading to random over- or under-estimations of the flux line. To minimise this effect for the sake of this study, given the filter that contains the emission line, f_l, we define a local continuum for this band, f_l^c, as the mean value of the flux in the contiguous bands not affected by the emission line. For the model band that contains the modelled corresponding stellar absorption, t_l, we similarly define a continuum for the model, t_l^c, in the same bands as where f_l^c is calculated. Following the formalism for spectroscopic EWs, the equation for photometric EWs (in Å) is

$$EW_{\rm T,phot} = \sum_X \left(\frac{f_l}{f_l^c} - \frac{t_l}{t_l^c} \right) \Delta\lambda_l \,, \tag{2.25}$$

where $\Delta\lambda_l$ is the width of the band ($\sim$ 300 Å for the optical filters in ALHAMBRA) that contains the emission line, and the sum applies to all the bands affected by strong emission lines, X.

[9] www.mpa-garching.mpg.de/SDSS/

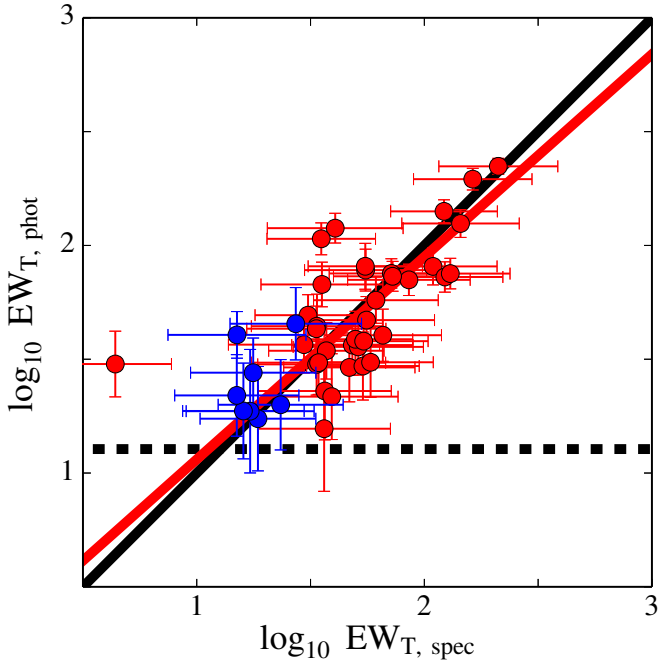

Figure 2.13: Comparison between the emission line EWs measured in galactic SDSS spectroscopic data taken from the MPA/JHU catalogues, $EW_{\mathrm{T,\ spec}}$, and the emission line EWs derived from the residuals of our fitting code on the same galaxies in ALHAMBRA, $EW_{\mathrm{T,\ phot}}$. Blue dots indicate galaxies with only one strong emission line in their spectra, i. e. with a reasonably specific or individual emission line measurement in ALHAMBRA, whereas red dots illustrate galaxies with more than one emission line. The black line is the one-to-one relationship, whereas the red line is a linear regression to all the points. The dashed black line is the minimum $EW_{\mathrm{T,\ phot}}$ that we can detect when imposing $\Delta m_{\mathrm{EL}} = 0.1$ for a unique emission line in one ALHAMBRA filter. See more details in the text.

In Fig. 2.13 we present the photometric $EW_{\mathrm{T,\ phot}}$ derived with our spectral-fitting techniques on ALHAMBRA data versus the spectroscopic $EW_{\mathrm{T,\ spec}}$ computed from MPA/JHU catalogues, for the 44 galaxies in common that fulfilled the above selection criteria. Overall, we obtain good agreement between photometric and spectroscopic EWs considering both photometric and spectroscopic uncertainties (see the red line), where the bias between both measurements is $\mu = 0.018$ dex and RMS = 0.234 dex , demonstrating the feasibility and reliability of our code for determining the EWs of emission lines above a certain strength ($\gtrsim$ 13 Å). We highlight that the concordance with our photometric EW predictions is good independently if the galaxies only present one strong emission line in their spectra (blue dots) or they present more than one emission line (red dots) in SDSS. It is interesting that under the imposed detection limit $\Delta m_{\mathrm{EL}} = 0.1$ (dashed black line), there is no detection of emission lines either. In fact, our method can provide more robust determinations under certain conditions. This is the case, for instance, for the galaxy that deviates on the left-hand side of the panel. The SDSS spectrum of this galaxy, at redshift $z = 0.299$, exhibits both Hα and Hβ in emission. Hβ emission is too weak to be detected in ALHAMBRA with our criteria, whilst Hα, at λ 8 526, falls in a very noisy region of the spectrum plenty of sky emission line residuals and telluric bands, which are hardly corrected in the SDSS data. This is not the case for the ALHAMBRA data, for which the continuum is better determined and where the absolute flux excess, for this particular case, becomes more reliable.

Finally we pay attention to the 48 galaxies for which our code does not detect any emission line in the ALHAMBRA data with the detection limits set in this paper. We find that 35 galaxies ($\sim$ 75 %) present $\log_{10} EW_{\mathrm{T,\ spec}} \leq 1.11$ ($\sim$ 13 Å), which corresponds to our detection limit $\Delta m_{\mathrm{EL}} = 0.1$, i. e. that indeed

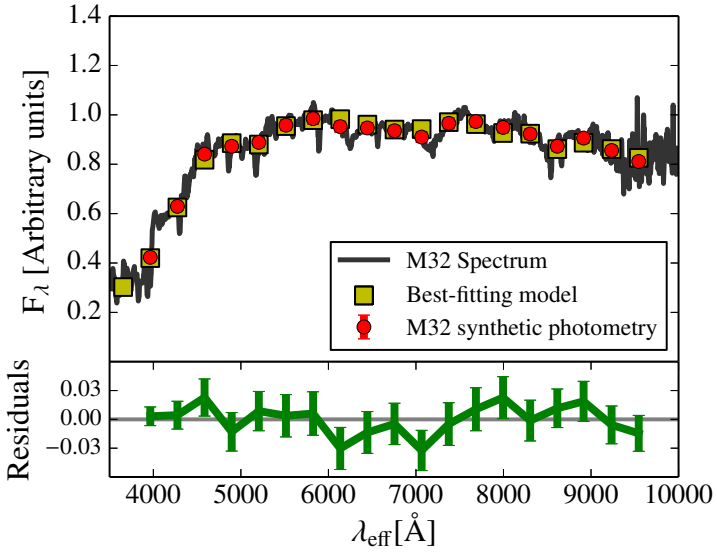

Figure 2.14: Spectral fitting of M32 as seen by ALHAMBRA using the MIUSCAT SSP SEDs as template models with the analysis explained above. The synthetic photometry of M32 is plotted in red, whereas the best fit of a mixture of two SSPs to the spectrum of M32 is plotted in yellow. The *bottom pannel* shows the residuals of the best fit.

remain imperceptible under our detection constrain. Of the remaining 13 galaxies, ten have $\log_{10} EW_{\rm T,\ spec} > 1.11$, but distributed along different lines, where all the lines individually are under the detection limit. Finally, for three galaxies we did not properly detect the emission lines for two reasons: first, since one of the emission lines (in this particular case Hα) is right between two filters and the flux is split into both of them, not fulfilling the detection criteria in any of the filters. Second, there was an incorrect determination of the $z_{\rm phot}$, which prevents the code from looking for emission lines in the right filters, besides the fact that a wrong redshift determination affects the quality of the derived continuum, yielding a line residual under $\Delta m_{\rm EL} = 0.1$.

To conclude, we demonstrate that despite MUFFIT being mainly optimized for the analysis of the stellar populations of galaxies dominated by their stellar content, it is still reliable for detecting and characterising the strength of strong emission lines under certain conditions that depend on the type of the multi-filter data we are working with (e. g. filter width, signal-to-noise ratios per filter). In future versions of the code, we expect to improve the algorithms of detection of emission lines with additional techniques and criteria (e. g. assuming intrinsic relations among lines), but this is beyond the scope of the present paper.

2.5.3 The stellar populations of M32

As a first step in testing the reliability of the stellar populations derived with our code, we analysed the stellar content of M32, because this is one of the best known galaxies in terms of its resolved and unresolved stellar populations. The spectrum of M32 used for this study was taken from the compilation of Santos et al. (2002), and it had been convolved with the ALHAMBRA filter set for the sake of this test, as if it had been observed in ALHAMBRA. Since the spectral range of this spectrum, $\lambda\lambda$ 3 500–10 000 Å, is shorter than the filter coverage of ALHAMBRA, both the bluest optical filter and the three NIR filters were rejected from the whole fitting procedure described in Sect. 2.3. In addition, to be able to explore the parameter space that is compatible with the best solution due to uncertainties in the photometry, and given that we had created a fake ALHAMBRA spectrum from a higher resolution spectrum, we added a synthetic error of $\sigma_{\rm AB} = 0.025$ in each filter, which is the expected error in the photometric calibration of ALHAMBRA (equivalent to a signal-to-noise ratio $\sim$ 40).

In Fig. 2.14 we present the complete spectrum of M32, in black, the M32 spectrum at the ALHAMBRA resolution and the best fit derived from our code with a mixture of two MIUSCAT SSPs and a Kroupa IMF to the M32 ALHAMBRA spectrum. As consequence of the spectral range ($\lambda\lambda$ 3 500–10 000 Å), the bluest and NIR ALHAMBRA filters were rejected in the analysis. The obtained residuals are shown in the lower panel.

It is clear from Fig. 2.14 that the best fit derived from our code reproduces the observed spectrum well at both low and high frequencies. The best fitting solution to a single SSP, as derived from our code in the first step, corresponds to a MIUSCAT model of 3.7 ± 1.3 Gyr and around solar metallicity ([Fe/H]= 0.02 ± 0.14 dex). When the code was run completely for the mixture of two SSPs, we obtained a luminosity-weighted age of 6.8 ± 2.2 Gyr, a slightly sub-solar metallicity ([Fe/H]=−0.08 ± 0.14 dex), and extinction $A_V = 0.28 \pm 0.08$. Looking at the individual results for the two SSPs, we find that the spectrum of M32 is appropriately reproduced by an intermediate-age population of 2.1 ± 0.5 Gyr and an older population of 11.5 ± 3.4 Gyr. We find that the weight on the stellar mass of the young population is ∼ 20 %. Previous work, such as from Coelho et al. (2009) and Monachesi et al. (2012), arrive at similar results in the sense that M32 is not composed of a unique SSP of intermediate age, but its stars were formed in at least two episodes of star formation, one ancient and the other one at intermediate ages.

Even though we are using 19 filters (instead of 23 in a typical ALHAMBRA photo-spectrum), we still get good agreement between the retrieved parameters and those derived by previous work when making use of detailed spectroscopic studies, showing the power of this kind of multi-filter survey for stellar population studies.

2.5.4 Ages and metallicities of early-types in the local Universe

Disentangling the stellar populations of early-type galaxies and their assembling histories is a key question for our understanding of galaxy evolution; however, it is not our intention to address this point in this section. The aim of this section is only to explore the stellar content of a subsample of early-type galaxies in the nearby Universe from the ALHAMBRA survey, making use of MUFFIT, and to compare our results with previous findings in the literature. Once again, this is an additional check to assess the reliability of the stellar populations derived from our techniques. In a forthcoming paper (Díaz-García et al., in prep.), we will carry out a more complete and systematic analysis of all the galaxies in ALHAMBRA, allowing us to face these and other related questions.

Our reference work is the paper by Gallazzi et al. (2005, in the following G05) and, in particular, the ages and metallicities derived from spectroscopic analysis techniques for a sample of early-type galaxies located at $z < 0.22$ in SDSS. Their spectra were drawn from the SDSS DR4 (3″ diameter fibres, Adelman-McCarthy et al., 2006) spanning the full range of galaxy types (from actively star-forming to early-type galaxies) and covering the range $\lambda\lambda$ 3 800–9 200 Å with a resolution of $R \sim 1\,800$, and Petrosian magnitudes in the r-band range $14.5 < r < 17.77$. To construct our subsample of early-types galaxies in ALHAMBRA we have used the morphological catalogue provided by Pović et al. (2013), built using the code galSVM (designed to deal with low-resolution images at low and high redshifts, Huertas-Company et al., 2008) that, following a Bayesian approach, classifies the galaxies morphologically. This catalogue contains more than ∼ 1 500 early-type galaxies with redshifts down to $z \lesssim 0.5$ and a contamination lower than 10 %, up to magnitude $m_{F613W} \leq 22$. To guarantee a fair comparison study, we only select those early-type galaxies in ALHAMBRA with $z \leq 0.22$ from the above catalogue, so in the same redshift interval as in G05. With this constraint in redshift, we end up with a reliable subsample of ∼ 400 early-type galaxies (mean signal-to-noise ratios $S/N > 14$ in all cases), in which a significant part (∼ 65 %) also reside in the RS.

Following Figure 12 in G05, in Fig.2.15 we present the density contours of our results on luminosity-weighted ages, $\mathrm{Age_L}$, and metallicities, $[\mathrm{Fe/H}]_\mathrm{L}$, derived for our subsample of early-type galaxies in ALHAMBRA up to $z = 0.22$ using BC03 models and the photo-z constraints provided by the Gold catalogue. As in G05, the galaxy sample is split in stellar mass bins as indicated in the top labels of Fig.2.15. For each galaxy, rather than using the weighted values retrieved from the simulations, the whole set of results from

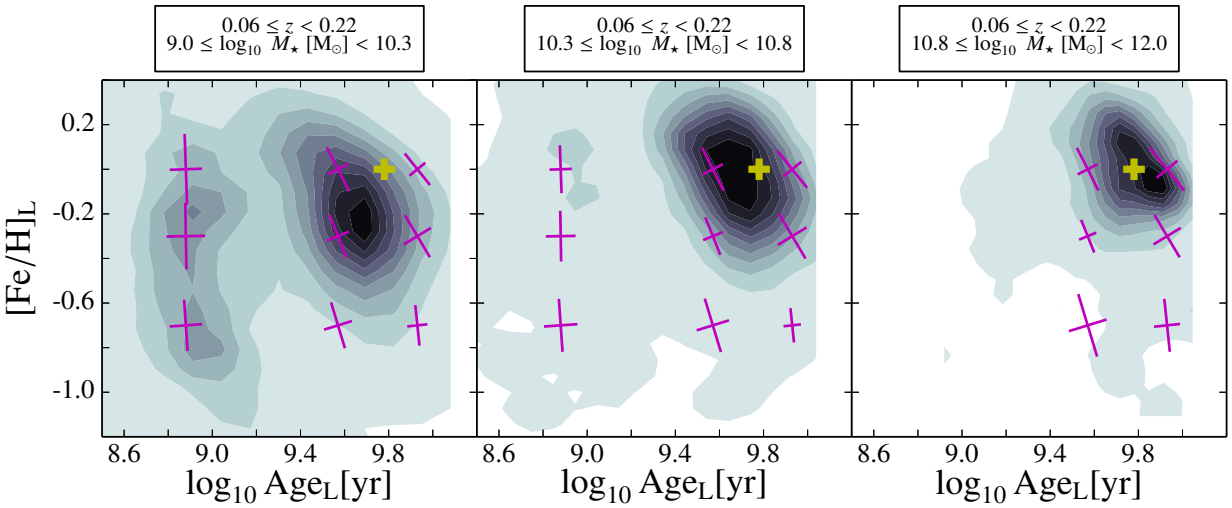

Figure 2.15: Luminosity-weighted ages and metallicities derived from MUFFIT and the BC03 models, for a subsample of ALHAMBRA early-type galaxies at different stellar mass bins and up to $z \leq 0.22$. Purple crosses illustrate the semi-axes of the degeneracy ellipses for 1 σ confidence level for the BC03 SSP models, as computed in Sect. 2.4.5, in the same age and metallicites ranges. To guide the eye, yellow crosses illustrate an age of 6 Gyr with solar metallicity.

the Monte Carlo simulations (see Sect. 2.3.2.5) are included in the plot. Darker colours correspond to the ages and metallicity regions with higher population densities. To see the influence of the age–metallicity degeneracy on the results, we also include the semi-axes of the degeneracy ellipses for 1 σ confidence level for the BC03 SSP models, as computed in Sect. 2.4.5, in the same age and metallicity ranges.

From Fig.2.15 we infer that low-mass early types, $\log_{10} M_\star \lesssim 10.3$ dex, show a bimodal distribution in their stellar populations. There is a population of younger early types with slightly lower metallicities that does not seem to exist at higher masses. On the other hand, there is a main population of older and, on average, more metal-rich galaxies at the same stellar mass bin. The set of younger early types of mild metallicities may be contaminated by lenticular galaxies (Poggianti et al., 2001), and they are also found in G05. Using the rest-frame colours (see Sect. 2.3.2.6), we check that almost the totality of these "young" galaxies corresponds to galaxies that reside in the blue cloud, and they are probably composed mainly of star-forming bulge-dominated galaxies.

It is worth noticing that, even though this analysis is based on photometric data, using MUFFIT and ALHAMBRA allows us to be sensitive to this population and to characterise their stellar populations quite well by not only obtaining close agreement with spectroscopic studies, but also opening the possibility of extending the mass limit up to lower stellar masses than typical spectroscopic surveys. We reinforce this result by repeating the analysis using the MIUSCAT SSP models instead of the BC03, getting the same result. Since the detailed analysis of the stellar populations is beyond the scope of this paper, this point will be addressed in a forthcoming work (Díaz-García et al., in prep.).

For intermediate stellar masses ($10.3 \lesssim \log_{10} M_\star[\mathrm{M}_\odot] \lesssim 10.8$), the "young" population tends to disappear, and consequently, the number of youngish and less metal-rich galaxies decreases, because they negligible for the higher stellar masses ($10.8 \lesssim \log_{10} M_\star[\mathrm{M}_\odot] \lesssim 12.0$), for which there is a clear predominance of old and metal-rich galaxies. For the lowest stellar masses, the spread in age and metallicity is apparently larger than for the most massive cases. Overall, our results suggest that massive galaxies are on average more metal-rich than less massive ones (Tremonti et al., 2004; Gallazzi et al., 2005, 2006), therefore the abundance of metals in a galaxy is related or linked to its stellar mass, showing a wider spread at the low-mass end (also found in G05), except for the young metal-poor population. We also observe that the mean ages of massive early types tend to be slightly older than their less massive counterparts, so they were

formed at earlier epochs (higher redshifts) than the low-mass galaxies, in agreement with the "downsizing" scenario (Cowie et al., 1996; Jimenez et al., 2007). The increase in the mean ages and metallicities for massive early types was also found in G05 (equivalent results with very similar age-metallicity relations using SDSS spectroscopy). Even though these stellar population differences are quite mild for the early-type galaxies (at least in comparison with late-type galaxies, see G05), it is worth pointing out that when running on the ALHAMBRA data, MUFFIT is still sensitive to the subtle changes in age and metallicity. On average, for the whole galaxy population in Fig.2.15, we find that the increase in age from the low-mass galaxies ($9.0 \lesssim \log_{10} M_\star[\mathrm{M}_\odot] \lesssim 10.3$) up to the most massive ones ($10.8 \lesssim \log_{10} M_\star[\mathrm{M}_\odot] \lesssim 12.0$) is ~ 3 Gyr, with mean ages of 3 and 6 Gyr, respectively. Similarly, the mean metallicity progressively increases from -0.35 to about solar metallicity.

We performed several tests to assess whether the bi-modality in the populations of the less massive galaxies, $9.0 \leq \log_{10} M_\star < 10.3$ dex, is driven by age-metallicity degeneracies. First, we observed the degeneracies on the age-metallicity parameters for the whole sample of RS galaxies in ALHAMBRA at the parameter ranges of both distributions (Sect. 2.4.5, see Fig. 2.11 and Table 2.3). For both sub-populations ($\mathrm{Age_L} \sim 0.8$ Gyr with $[\mathrm{Fe/H}]_\mathrm{L} \sim -0.7$ dex; $\mathrm{Age_L} \sim 4$ Gyr with solar metallicity), the degeneracy contours do not present bi-modalities, and they are well constrained by a unique ellipse (illustrated in Fig. 2.15). In addition, we confirmed that all the Monte Carlo realisations of each individual galaxy in the left-hand panel of Fig. 2.15 clearly belong to only one of the two galaxy sub-populations, proving that degeneracies are not responsible for the younger and less metal-rich population at the low-mass regime. Moreover, we added noise ($\sigma_\mathrm{AB} = 0.05$–$0.20$, corresponding to a signal-to-noise ratio $S/N \sim 20$–5) to the high-mass galaxy sample and analysed them again with MUFFIT to see if there is any hint of bi-modality driven by degeneracies in low signal-to-noise regimes. Even in the worst case ($S/N \sim 5$), fewer than 3 % of the galaxies end up in the young and metal poor sub-population region, without exhibiting any bimodal pattern in the distribution. We conclude that there is a true sub-population of "young" early-type galaxies in the stellar mass regime $9.0 \leq \log_{10} M_\star < 10.3$ dex, which is not a consequence of parameter degeneracies and the use of probability distribution functions.

2.5.5 Comparison with spectroscopic stellar-population studies

A definitive step forward in the above analysis rests on the one-to-one comparison of spectroscopic galaxy ages and metallicities with the ones derived from MUFFIT. Interestingly, there is a sub-sample of galaxies in the MPA/JHU catalogues for which individual spectroscopic estimations of ages and metallicities are provided (obtained following the methodology explained in G05), and also imaged in the ALHAMBRA fields. G05 performed an age and metallicity diagnostic method based on a simultaneous fitting to five absorption line strength indices, most of them in the Lick system (Gorgas et al., 1993; Worthey et al., 1994b). They are made up of age-sensitive indices like D4000 (Balogh et al., 1999), Hβ and Hδ_A+Hγ_A, and by metal-sensitive indices like [$\mathrm{Mg_2Fe}$] (Bruzual & Charlot, 2003) and [MgFe]$'$ (Thomas et al., 2003), the latter weakly dependent on non-solar [α/Fe] abundances. Each set of five spectral features is compared, through a χ^2-test, with the values provided by a set of models randomly generated from BC03, with different bursts of star formation and different fractions relative to the total stellar mass in a velocity dispersion range, to finally construct the PDF of the parameters being the weight of each model $\propto \exp(-\chi^2/2)$ (see details in G05).

By crossmatching the ALHAMBRA galaxy catalogue with the above work, we find 80 RS galaxies (not spectroscopically classified as either *BROADLINE* or *AGN*) in common between both studies, with a mean signal-to-noise ratio per pixel in SDSS greater than nine. (Under this constraint, the signal-to-noise ratio of the common ALHAMBRA galaxies is more than 18 in all cases.) We establish this as a minimum threshold for obtaining meaningful stellar population results from spectroscopic diagnostics based on line-strength indices. Even if G05 stated that metallicity is well constrained for spectra whose signal-to-noise ratio is higher than 20, this more permissive restriction in the SDSS signal-to-noise ratio increases the number of common galaxies, allowing us to explore the age compatibility of both methods for a larger number of RS

galaxies, where the age accuracy is not as affected by the signal-to-noise ratio of the SDSS spectra. (These details are extensively tested in G05.)

To keep the model consistent with G05, we fed MUFFIT with the SSP models of BC03 to explore, via ALHAMBRA data, the stellar content of these 80 RS galaxies in common. In addition, to explore the impact of different SSP models on the retrieved parameters, we repeated the same analysis with the MIUSCAT SSP models instead (see the end of this section).

Figure 2.16 presents a one-to-one comparison of the spectroscopic redshifts, luminosity-weighted ages, luminosity-weighted metallicities, and stellar masses given in the work by G05 for the subsample of 80 SDSS galaxies in common with ALHAMBRA and the photometric values determined from MUFFIT using the BC03 SSP models for the same galaxies and the ALHAMBRA data. The error bars at different parameter ranges indicate the typical 1σ uncertainties in the parameters from both methods. Different colours indicate different extinction ranges ($A_V < 0.3$; $0.3 \leq A_V < 0.6$; $A_V > 0.6$), as inferred from our code. In addition, to discuss aperture effects (SDSS spectra were taken in a $3''$ aperture, while ALHAMBRA photo-spectra are not restricted to a fixed aperture, which is determined by the synthetic band *F814W*), star-shape markers are assigned to galaxies with apertures below $4''$ in ALHAMBRA, which are, a priori, less affected by any potential aperture bias.

Except for two galaxies, which have been removed from the plots since their ALHAMBRA photometry has been confirmed to be affected by nearby and bright stars, the spectroscopic redshifts in Fig. 2.16*a* show excellent agreement with our photo-z, with an RMS of ~ 0.008. As we expect from Sect. 2.4.3, we rule out that any difference in the stellar populations between the two sources can be due to uncertainties in the photo z (see Sect. 2.4.4).

Concerning the luminosity-weighted age comparison, in Fig. 2.16*b* we find good qualitative agreement between both methods given the uncertainties of both methods (see black crosses in Fig. 2.16), in the sense that lower (higher) spectroscopic ages correspond, respectively, with lower (higher) photometric ages from MUFFIT. Interestingly, according to MUFFIT, young galaxies also tend to be more reddened by dust than old galaxies. From our results in this test sample, the mean age (luminosity-weighted) of the dusty galaxies ($A_V > 0.6$) is 1.8 Gyr, increasing to 3.9 Gyr for the intermediate extinction range and rising up to 5.4 Gyr for galaxies for which we retrieve low dust contents ($A_V \leq 0.3$). This is an expected result, since it is well known that younger galaxies may still have remnants of gas and dust from recent star formation events, whereas older/quiescent galaxies use to have less dust content.

We notice that this trend could in principle be explained by the age-extinction degeneracy (Section 2.4.5). However, if this were the case we would not find any qualitative relation with the spectroscopic ages, because the line indices, by construction, are not significantly affected by extinction. In addition, we emphasize that the galaxies in ALHAMBRA for which MUFFIT retrieves young stellar populations, for ages down to 2.6 Gyr, are also classified as *STARFORMING* in SDSS. This also supports the idea that the retrieved extinctions with MUFFIT are very robust and that they are not dominated by the degeneracy with age, because star-forming galaxies may present young populations with significant amounts of dust. In fact, previous and similar work (e. g. Fontana et al., 2006; Pozzetti et al., 2007; Ilbert et al., 2010) assumed in their codes that models with large extinctions are only allowed for star-forming galaxies. The key point from this result is that MUFFIT is able to intrinsically retrieve the extinction of the stellar populations without assuming any prior on the models or the galaxy type. Despite the qualitative agreement between MUFFIT and spectroscopic ages, with an RMS of ~ 1.6 Gyr, we also notice an offset between the ages of the two samples, with the spectroscopic ages being ~ 2 Gyr older than the ones derived from our code for the ALHAMBRA data. We discuss possible reasons for this offset at the end of this section.

In Fig. 2.16*c* we can see that the metallicities present qualitatively good agreement (despite the metallicity being more affected by uncertainties, see black crosses in Fig. 2.16), with an RMS of ~ 0.22 dex, although there is also a very small shift in the sense that our retrieved metallicities in ALHAMBRA tend to be smaller (Δ[Fe/H] ~ -0.08 dex) than the spectroscopic ones derived for SDSS galaxies in G05. It is noticeable that the metallicities of ALHAMBRA galaxies within an aperture of $4''$ (star-shape markers) present

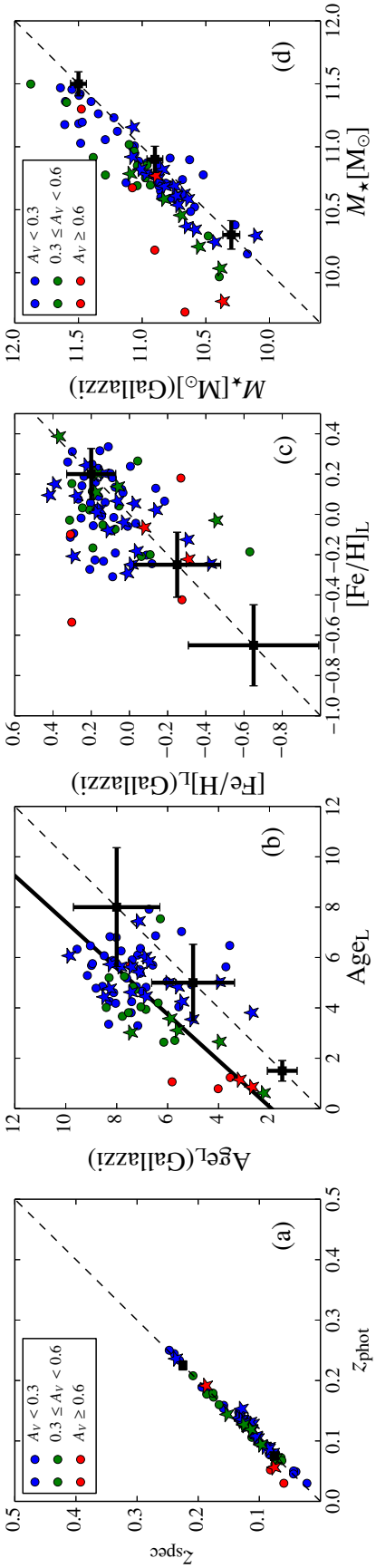

Figure 2.16: Comparison of redshifts, ages, metallicities, and stellar masses between the spectroscopic study of Gallazzi et al. (2005), Y–axis, and the stellar populations retrieved from ALHAMBRA with BC03 models, X–axis. In red, we present the galaxies for which our techniques establish that they may have large extinctions: intermediate extinctions in green and low extinctions in blue. The dashed black line indicates the one-to-one relationship. The solid black line shows the fit between spectroscopic and photometric ages, accounting for the uncertainties in both measurements. The black crosses represent the average uncertainties of both techniques at different ranges. The star-shape markers are the galaxies with a radial size below 2″.

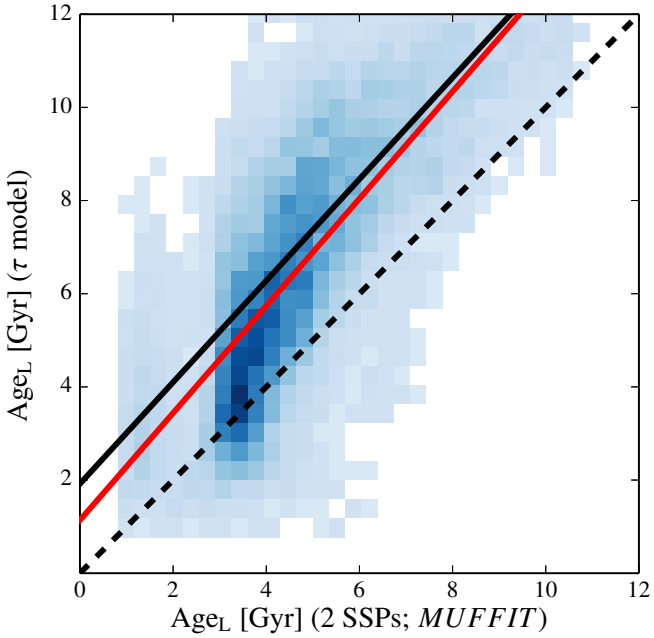

Figure 2.17: Comparison between the luminosity-weighted ages of a subset of RS τ-models from SSAG and the ones derived by MUFFIT for the same models employing a mixture of 2 SSPs. The dashed black line represents the one-to-one relationship, while the red line is the simple linear regression of the data points. The solid black line illustrates the fit between the ages provided by G05 and the ones provided by MUFFIT using ALHAMBRA data (see Fig. 2.16b).

better agreement with the spectroscopic measurements (Δ[Fe/H] $\lesssim -0.05$ dex) than the galaxies with larger apertures (dot markers; Δ[Fe/H] ~ -0.15 dex). As shown in G05, aperture effects and typical metallicity gradients can lead to up to $\sim$ 0.15–0.20 dex differences in metallicity for galaxies with $\gtrsim 10^{10}$M$_\odot$. This reinforces the consistency and good agreement between both metallicity predictions (from SDSS and ALHAMBRA), since MUFFIT retrieves lower metallicities on average with respect to SDSS, and not higher, with a similar difference to those measured by G05 ($\sim$ 0.17 dex) owing to possible aperture effects.

Interestingly, as pointed out by G05, a signal-to-noise ratio greater than 20 is required for a reliable constraint on the metallicity in SDSS spectra. Unfortunately, the adopted signal-to-noise ratio limit substantially restricts our sample, by excluding low-luminosity galaxies with potential sub-solar metallicities. Moreover, in G05 it is also mentioned that low-metallicity galaxies are more affected by uncertainties coming from their weak absorption features of [Mg$_2$Fe] and [MgFe]$'$. Indeed, in our subsample, the lower the metallicity, the greater the dispersion in the spectroscopic metallicity, as illustrated by the error bars. Instead, the metallicities provided by MUFFIT using ALHAMBRA data at the same regime are slightly better constrained, because in the end, it is the overall stellar continuum that mainly determines the retrieved stellar populations.

Figure 2.16*d* exhibits good agreement between the stellar masses of the two methods, with an RMS of $\sim$ 0.19 dex, even with an offset of $\sim$ 0.18 dex. This offset in the stellar mass can be explained mainly by the systematic differences of $\sim$ 2 Gyr between the ages of both methods, since this implies a shift in the mass-luminosity relation in the sense that older galaxies, at the same apparent magnitude, are also more massive galaxies.

Before concluding, we intend to investigate the potential origin of the $\sim$ 2 Gyr offset in age derived in Fig. 2.16*b*. There are several potential reasons that could explain this offset: i) the age–extinction degeneracy, ii) the way to compute luminosity-weighted ages, iii) aperture effects, and iv) intrinsic systematic differences between both analysis techniques.

i) Unlike SED fitting techniques, absorption line-strength indices are basically not sensitive to extinction, because they are defined in short wavelength ranges. If the ages derived from MUFFIT were severely affected by the age–extinction degeneracy, we would expect galaxies with very low extinction values, $A_V < 0.05$, to present better agreement in the age comparison of Fig. 2.16*b*. However, this is not the case. By exploring the ages and metallicities of the galaxies with low extinction values ($A_V < 0.05$, according to MUFFIT and the ALHAMBRA data), checking that both metallicities, spectroscopic and photometric, remain in agreement without great differences, we find that the age difference is still ~ 2 Gyr. This rejects the potential impact of the age–metallicity degeneracy, as well as the influence of using different extinction laws.

ii) In G05, luminosity-weighted ages are computed according to the total *r*-band flux, whereas in MUFFIT this is done using the whole flux in all the ALHAMBRA bands. To explore whether this normalisation difference could drive the age offset, we recomputed the MUFFIT luminosity-weighted ages using the ALHAMBRA *F644W* band, which has the most similar effective wavelength to the SDSS *r*-band. The results are essentially the same, so do not explain the observed age offset.

iii) It is well known that early-type galaxies may show radial variations in their stellar population properties, showing gradients in metallicity and/or age. We already discussed above how the combination of different photometric apertures and the existence of metallicity gradients has an impact on the metallicity comparison of Fig. 2.16*c*). It is worth noting, however, that age gradients generally used to be shallower than metallicity gradients (Wu et al., 2005; Sánchez-Blázquez et al., 2007; La Barbera et al., 2012; Eigenthaler & Zeilinger, 2013), so aperture effects are expected to be less as well. Nevertheless, shallow gradients in all the parameters can also be found (González Delgado et al., 2015). To assess this effect, we focus on galaxies whose photometric apertures in ALHAMBRA are down to $4''$ (Fig. 2.16), not far from the SDSS fibre aperture. We observe that the age offset is significant even for these galaxies, so aperture effects are rejected to explain the age offset, too.

iv) After the negative results of the three previous tests, the existence of intrinsic systematic differences between the two methods seems to be the most plausible reason for the different absolute values of the derived ages. The discrepancies between the analysis of spectral features versus colours, together with the assumptions of different SFHs (exponentially declining tau models in G05, versus a mixture of young+old SSPs in this work), may be responsible for the age offset. To shed light on this last item, we aim at constraining a purely mathematical problem: the potential differences between the luminosity ages derived from parametric τ-models and the ones derived from a non-parametric mixture of two SSPs. To do this, we made use of the set of τ-model Synthetic Spectral Atlas of Galaxies (SSAG, Magris C. et al., 2015), which is very similar to the τ models employed in G05. SSAG models are based on the recipes described in Chen et al. (2012) and have been constructed following exponentially declining SFH and BC03 models, which may randomly suffer an instantaneous and random burst during different periods of time. The SSAG also includes intrinsic extinctions, following the dust model of Charlot & Fall (2000), and different velocity dispersions.

To create a subsample of RS galaxies, we selected all the SSAG galaxy models whose colours satisfy $U - V \gtrsim 2.0$ (AB-system). After convolving SSAG models with the ALHAMBRA filter set, we ran MUFFIT using the same BC03 models as input, in concordance with SSAG, and compared derived luminosity-weighted ages with the input SSAG ones. The result of the comparison is exhibited in Fig. 2.17. There appears to be a systematic offset between ages of $\Delta\mathrm{Age}_\mathrm{L} \sim 1.8 \pm 1.7$ Gyr, which fully explains (qualitatively and quantitatively) the $\sim 2 \pm 1.6$ Gyr offset found in the previous comparison between the spectroscopic ages of G05 and the ones retrieved using MUFFIT and ALHAMBRA data, as due to the mathematical differences in the diagnostic input models (mixture of SSP models vs exponentially declining SFH models).

Finally, we have also investigated the impact of using a different set of SSP models for the stellar population comparison. In Fig. 2.18 we present the same comparison of Fig. 2.16, but in this case having

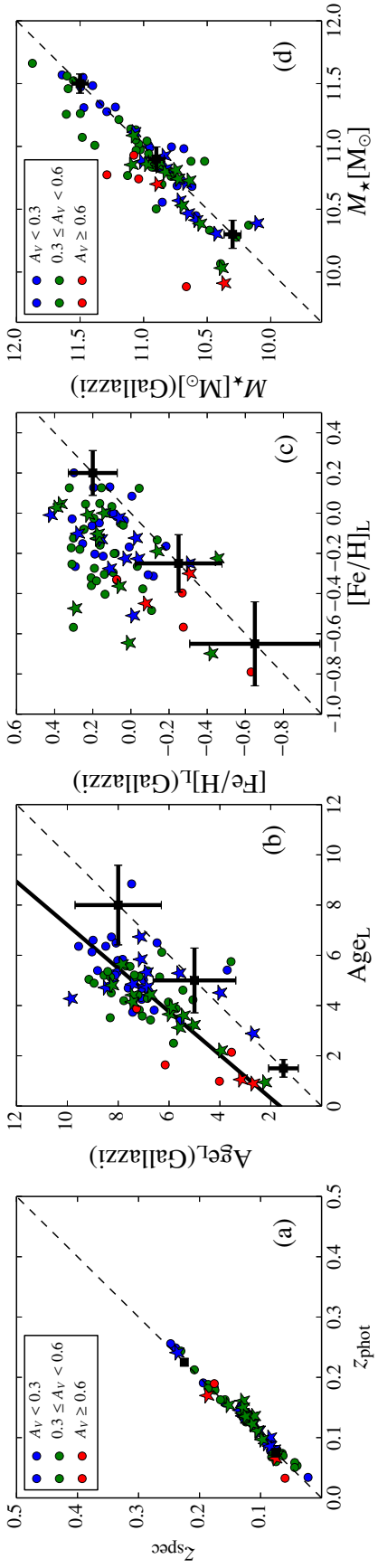

Figure 2.18: As in Fig. 2.16 but using the MIUSCAT SSP models instead of the BC03 ones.

used the MIUSCAT SSP models, instead of BC03, to analyse the ALHAMBRA data with MUFFIT. Except for a slightly larger difference in metallicity, in the sense that MIUSCAT models tend to predict lower metallicities, the rest of the parameters are similar to Fig. 2.16. This is important for assessing the impact of different SSP models on the absolute values of the derived parameters.

2.6 Summary and conclusions

The arrival of present and future large-scale multi-filter surveys (e. g. COMBO-17, COSMOS, ALHAMBRA, SHARDS, J-PLUS, and J-PAS) promises that formidable datasets for many purposes in Cosmology and Astrophysics will be available. These photometric surveys, based on the mapping of different regions of the sky with a set of contiguous intermediate- and narrow-band filters, provide low-resolution photo spectra for each region of the sky (hence performing like a low-resolution IFU with PSF-limited spatial resolution), with the survey depth as the only selection criterion and without the typical spectroscopic uncertainties in the flux calibration. This opens an unprecedented way to progress in our understanding about galaxy evolution through studying millions of homogeneous galaxy SEDs, both spatially resolved in the closer Universe and integrated.

This paper was devoted to presenting MUFFIT (MUlti-Filter FITting for stellar population diagnostics), a generic code specifically designed to analyse the stellar content of galaxies with available multi-filter data (dealing with the technical peculiarities and the big amount of high-quality photometric data available in multi-filter surveys), as well as to show its functionalities, set the accuracy and typical uncertainties in the retrieved stellar population parameters, and ultimately test it with real data. In this way, we made use of the ALHAMBRA database as a test bench for MUFFIT, not with the aim of performing a thorough stellar population analysis of the galaxies in ALHAMBRA (which constitutes the matter of the next papers in this series), but to compare the stellar population results derived from MUFFIT with similar studies in the literature, allowing us to assess its reliability and the feasibility of this kind of technique to accurately explore the stellar content of galaxies.

In the following items the main conclusions of this work are summarised:

- Using a set of SSP models that explores different stellar population parameters as input, MUFFIT builds photometric predictions of bands at different redshifts and extinctions. For the present work, the stellar population parameters that were considered are only age and metallicity, although in a general case even the IMF slope and the α-enhancement can also be retrieved if SSP models properly account for them. In addition, the survey photometry was corrected for MW dust effects, as the colour terms introduced by MW dust may play an important role not only in the stellar masses derived using SED-fitting techniques, but also in the retrieved stellar population parameters.

- MUFFIT compares the multi-filter fluxes of a given galaxy with the photometric predictions of a reasonable mixture of two SSPs, one younger and one older than the mean age provided by a single SSP fitting. The mixture of two SSPs determined by the last prior, specific for each individual galaxy, is a relevant improvement over the fitting of only one SSP, since it represents an underlying main red population plus a less massive and later episode of star formation. The stellar population parameters provided by MUFFIT (in this work the age and metallicity weighted by both luminosity and mass, extinction, redshift, and stellar mass) are constrained by the use of an error-weighted χ^2 test. During the fitting process, MUFFIT removes those bands that are affected by emission lines, improving the quality of the fitting and restricting the plausible redshift space, as in a general case the redshift of the galaxy is treated as another free parameter to be determined. MUFFIT is not limited to providing the parameters of the best-fitting model, but also explores the parameter space using the proper photometric uncertainties in each band by a Monte Carlo method, reinforcing the parameter predictions because it provides their statistical uncertainties, too. MUFFIT also computes and provides the k corrections of each galaxy from the same mixture of models in rest frame.

- Specifically for the ALHAMBRA data, we studied the intrinsic uncertainties in redshift, extinction, age, metallicity, and stellar mass that appear when diagnosed by MUFFIT. Using the typical distribution of errors for the RS galaxies in ALHAMBRA, we constructed mock galaxies with an average S/N per filter of 20, obtaining typical uncertainties (RMS) of $\sigma_z \sim 0.01$, $\sigma_{A_V} \sim 0.11$, $\sigma_{\rm Age} \sim 0.10$ dex, $\sigma_{\rm [Fe/H]} \sim 0.16$ dex, and $\sigma_{M_\star} \sim 0.08$ dex. In no case were there systematic errors that are statistically significant.

- Even though MUFFIT is not a generic photo-z code, using the redshift PDFs provided by external photo-z codes as input, MUFFIT returns fine-tuned redshift values whose accuracy is improved by $\sim$ 10–20 %. We also found that the photo-z accuracy reached in ALHAMBRA, $\sigma_{\rm NMAD} \lesssim 0.009$, has a negligible impact on the main stellar population parameters retrieved using MUFFIT, where the typical uncertainties in the photometry are more crucial.

- We studied the age–metallicity–extinction degeneracy of the ALHAMBRA data with MUFFIT at different parameter ranges, after having fixed the IMF slope. The age-extinction anti-correlation is present in all ranges of age and metallicity. However, the well known age–metallicity anti-correlation may turn into a positive correlation for young and/or metal-poor populations due to the role of the extinction in reddening the spectral energy distributions of galaxies.

- The stellar-mass predictions provided by MUFFIT for a common sample of RS galaxies in ALHAMBRA are in wonderful agreement with the stellar masses computed for the same galaxies in COSMOS. The dispersion of the comparison, with an RMS of $\Delta \log_{10} M_\star \sim 0.15$ dex, can be fully explained by the intrinsic uncertainties of both methods.

- MUFFIT offers a reliable way to explore emission lines in multi-filter surveys. Using a set of emission line galaxies shared by SDSS and ALHAMBRA, we demonstrate that the residuals provided by MUFFIT for the filters affected by emission lines in ALHAMBRA are correlated with the strengths of the main emission lines.

- The age–metallicity loci provided by MUFFIT for a sample of $z \leq 0.22$ early-type galaxies in ALHAMBRA in different stellar mass bins are in very good agreement with the ones determined from SDSS data on the basis of spectroscopic diagnostics. When we analysed the stellar content of these galaxies in ALHAMBRA using their photometric data and MUFFIT, our results showed that the more massive early types ($\gtrsim 10^{11} M_\star[\mathrm{M}_\odot]$) were formed in an earlier epoch than their low-mass counterparts ($\lesssim 10^{10} M_\star[\mathrm{M}_\odot]$) with a larger content of metals with differences of ΔAge $\sim$ 3 Gyr and Δ[Fe/H] $\sim$ 0.3 dex. This result agrees with the "downsizing" scenario as well.

- For a subsample of galaxies shared by ALHAMBRA and SDSS, a one-to-one comparison between the redshifts, ages, metallicities, and stellar masses derived spectroscopically for the SDSS data (provided by Gallazzi et al., 2005) and those determined from MUFFIT and ALHAMBRA reveal good qualitative agreement in all the parameters given the uncertainties of both methods, with typical RMS for the distribution of differences between both diagnostics of $\sigma_z^{\rm SDSS} \sim 0.008$, $\sigma_{\rm Age}^{\rm SDSS} \sim 1.6$ Gyr, $\sigma_{\rm [Fe/H]}^{\rm SDSS} \sim 0.2$ dex, and $\sigma_{M_\star}^{\rm SDSS} \sim 0.19$ dex, thus reinforcing the strengths of multi-filter galaxy data and optimised analysis techniques, like MUFFIT, to conduct reliable stellar population studies. Despite the qualitative agreement between ages, in the sense that young (old) spectroscopic ages in SDSS are also found to be young (old) photometric ages in ALHAMBRA using MUFFIT, there is a systematic difference of $\sim$ 2 Gyr between the two samples that is explained by the differences between using mixtures of SSPs instead of τ models. And even though there is good agreement between metallicities, it is noticeable that the metallicities of ALHAMBRA galaxies within an aperture of $\leq 4''$ offer better agreement with the spectroscopic measurements (Δ[Fe/H] $\lesssim$ 0.05 dex) than the galaxies with larger apertures (Δ[Fe/H] $\lesssim$ 0.15 dex), pointing towards the possibility that aperture differences between SDSS and ALHAMBRA and the existence of metallicity gradients drive the observed differences (in

agreement with G05). There is also good agreement between stellar masses, with a minor shift of ~ 0.18 dex that can be explained by the observed offset in age.

To conclude, we demonstrate that MUFFIT is a reliable stellar population code for multi-filter galaxy data, which is suited to and optimized for analysing the stellar content of galaxies in ALHAMBRA-like surveys. This opens a new way to explore and address stellar population studies of galaxies with multiple photometric bands or colours, as long as the effective spectral resolution is at least the one of ALHAMBRA, allowing us to accurately extract the stellar content of thousands of galaxies at higher redshifts, benefited by the large-number statistics in comparison with typical spectroscopic datasets at the same redshift. With the arrival of the new-generation large-scale multi-filter surveys, such as J-PLUS and J-PAS, codes like MUFFIT will contribute to shedding light on our understanding of the formation and evolution of galaxies.

Acknowledgements

We thank the referee for the valuable suggestions and comments that reinforced part of our results. L. A. D. G. acknowledges support from the "Caja Rural de Teruel" for developing this research. A. J. C. is a Ramón y Cajal Fellow of the Spanish Ministry of Science and Innovation. This work has been supported by the "Programa Nacional de Astronomía y Astrofísica" of the Spanish Ministry of Economy and Competitiveness (MINECO) under grant AYA2012-30789, as well as by FEDER funds and the Government of Aragón, through the Research Group E103. L. A. D. G. also thanks the Mullard Space Science Laboratory (MSSL) and Royal Astronomical Society (RAS) for offering the opportunity to support and develop part of this research in collaboration with I.F. MINECO grants AYA2010-15081, AYA2010-15169, AYA2010-22111-C03-01, AYA2010-22111-C03-02, AYA2011-29517-C03-01, AYA2013-40611-P, AYA2013-42227-P, AYA2013-43188-P, AYA2013-48623-C2-1, AYA2013-48623-C2-2, and AYA2014-58861-C3-1 are also acknowledged, together with Generalitat Valenciana projects Prometeo 2009/064 and PROMETEOII/2014/060, and Junta de Andalucía grants TIC114, JA2828, and P10-FQM-6444. MP acknowledges financial support from the JAE-Doc programme of the Spanish National Research Council (CSIC), co-funded by the European Social Fund. The Max Planck Institute for Astrophysics A14, page 29 of 31 A&A 582, A14 (2015) and the Johns Hopkins University are acknowledged for making their catalogues (MPA/JHU catalogues) publicly available with the physical properties for galaxies in SDSS employed in this work. Throughout this research, we made use of the Matplotlib package (Hunter, 2007), a 2D graphics package used for Python which is designed for interactive scripting and quality image generation.

3

The stellar content of the quiescent galaxy population during the last ∼ 8 Gyr

“Blue is the male principle, stern and spiritual. Yellow the female principle, gentle, cheerful and sensual. Red is matter, brutal and heavy and always the colour which must be fought and vanquished by the other two.”

Franz Marc

Once the methodology for retrieving stellar population parameters from multi-filter photometric data is performed (see Chapter 2), we carry out a complete and detailed analysis of the stellar populations of the quiescent galaxies from the ALHAMBRA survey that is the main goal of the present chapter. The study of the stellar populations of quiescent galaxies since $z \sim 1$, as well as the determination of a reliable sample of quiescent galaxies are a great challenge, whose results will shed light on how these galaxies have evolved during the last 8 Gyr. This is also an opportunity for analysing alternative mechanisms that are able to alter the stellar content of galaxies, e. g. mergers, as some of these mechanisms may remain unnoticed under the in-situ star formation of the host galaxy. If star formation is quenched, their effects will emerge, or at least they will be more easily detected.

3.1 Introduction

Galaxies tend to present bimodal distributions of red and blue galaxies (e. g. Bell et al., 2004; Baldry et al., 2004; Williams et al., 2009; Ilbert et al., 2010; Peng et al., 2010; Arnouts et al., 2013; Moresco et al., 2013; Fritz et al., 2014), where red galaxies present more evolved stellar populations with lower star formation levels, for which they are usually referred as passive or quiescent. The formation and evolution of the so-called quiescent/passive galaxies (even sometimes "dead") is still today a challenge, as these galaxies started to form stars at very early epochs, to later shut down their star formation by a mechanism that is still today matter of debate (e. g. ram pressure stripping, "strangulation", heating of galaxy’s gas by AGN, Silk & Rees, 1998; Balogh et al., 2000; Dekel & Birnboim, 2006; Hopkins et al., 2006; Nandra et al., 2007; Bundy et al., 2008; Di Matteo et al., 2008; Diamond-Stanic et al., 2012; Peng et al., 2015). Some of these galaxies are really old (with ages slightly below ∼ 1 Gyr respect the age of the Universe) and they should suffer very efficient process of star formation, and a subsequently fast quenching, because the sequence of quiescent galaxies is already in place at $z \sim 3$ (Whitaker et al., 2011; Ilbert et al., 2013). Some authors have dedicated large efforts in studying their evolution in a long period of time, using several methods, namely the study of their SFR or sSFR (Papovich et al., 2006; Martin et al., 2007; Zheng et al., 2007; Pérez-González et al., 2008; Damen et al., 2009), studying the evolution of their number density with cosmic time (Ilbert

et al., 2010; Pozzetti et al., 2010; Ilbert et al., 2013), or attempting to reconstruct their star formation history with fossil record methods (Heavens et al., 2004; Thomas et al., 2005; Jimenez et al., 2007; McDermid et al., 2015). Overall, there is a good agreement in that, these galaxies present a strong dependence in their evolution with the stellar mass (largely studied in the local Universe, e. g. Kauffmann et al., 2003; Gallazzi et al., 2005; Thomas et al., 2005; Sánchez-Blázquez et al., 2006a; Jimenez et al., 2007; Panter et al., 2008; González Delgado et al., 2014a; Peng et al., 2015), being the more massive galaxies formed at earlier epochs and presenting a more efficient and quicker process of star formation, usually called "downsizing" scenario (Cowie et al., 1996).

In this situation, the state-of-the-art multi-filter surveys, e. g COMBO-17, COSMOS, ALHAMBRA, SHARDS , J-PAS, can provide an alternative and complementary way for exploring the stellar content of galaxies through the SED-fitting techniques (Mathis et al., 2006; Koleva et al., 2008; Walcher et al., 2011; Díaz-García et al., 2015; Ruiz-Lara et al., 2015), further than the local Universe. These photometric surveys, usually deeper than spectroscopy, can easily reach galaxies at intermediate redshifts ($z \sim 1$–2), allowing us to set milestones on the assembly of the stellar content of quiescent galaxies, offering a more continuous point of view of the building up of a galaxy than fossil record methods as they offer a sequence of "pictures" along the cosmic time.

In Sect. 3.2, we describe the basic aspects to select the galaxies from the ALHAMBRA catalogue, and the parameters and models selected in order to carry out the stellar population analysis of the ALHAMBRA data by MUFFIT. The criteria to select the quiescent sample is detailed in Sec. 3.3. We present the methodology to study the SFR of quiescent galaxies through the results provided by MUFFIT and its analysis in Sec. 3.4. The distribution of the stellar population parameters and its dependency with the $U - V$ and $V - J$ colours is studied in Sect. 3.5. The number density of quiescent galaxies is explored in Sec. 3.6. Sects. 3.7 and 3.8 detail the stellar population distributions of galaxies (mass-weighted age, metallicity, and extinction) since $z = 1.1$ using the BC03 and EMILES as input SSP models respectively. In Sect. 3.9, we study the systematics introduced in the stellar population distribution after assuming various star SFHs constraints. We discuss and summarize our results in Sects. 3.10 and 3.11 respectively.

Along this chapter we assume a ΛCDM cosmology with $H_0 = 71$ km s^{-1}, $\Omega_M = 0.27$, and $\Omega_\Lambda = 0.73$. All magnitudes are in AB-system (Oke & Gunn, 1983). The stellar masses are given in solar mass units [$M_\odot$].

3.2 The ALHAMBRA data

As in Chapter 2, the reference catalogue is again the ALHAMBRA Gold catalogue (more details about ALHAMBRA in Sect. 2.2 and Moles et al., 2008; Cristóbal-Hornillos et al., 2009; Aparicio Villegas et al., 2010; Molino et al., 2014), that contains ~ 95 000 galaxies imaged in 20 + 3 optical and NIR bands respectively. This catalogue provides an accurate enough photometry (non-fixed aperture) as for developing stellar population studies of galaxies (see above Chapter 2 or Díaz-García et al., 2015), complemented with precise photo-z predictions ($\sigma_z \sim 0.012$). In order to build the galaxy set from the Gold catalogue, we took all the sources classified as galaxies (STAR/GALAXY discriminator parameter `Stellar_flag` ≤ 0.5); and also imaged with 70% photometric weight on the detection image (`PercW` ≥ 0.7), the latter to avoid photometric errors in the galaxies close to the image edges. This catalogue also provides the synthetic AB-magnitude m_{F814W}, which is mainly employed for detection purposes and that sets the Gold catalogue selection as $m_{F814W} \leq 23$. This synthetic band is not used during the SED-fitting process anytime.

3.2.1 Stellar-population parameters in ALHAMBRA

Along this chapter, we focus on the evolution and assembly of the so-called quiescent galaxy population (galaxies without dominant star formation processes, which predominantly present red colours), as well as on the role of the stellar mass, studying how their stellar populations evolved along the cosmic time. For exploring this topic, we only employed the photometric data of each galaxy in ALHAMBRA and a set of

the SED-fitting techniques that were specifically and carefully developed for setting constraints on their stellar population parameters. These techniques are powerful and present high capabilities for this kind of surveys, despite the inferred results may deviate from the classical methods based on index-index diagrams of line-strength indices sensitive to age and metallicity (e. g. the Lick index system, Gorgas et al., 1993; Worthey et al., 1994b).

In order to retrieve the stellar population parameters of our galaxies, we ran the generic code MUFFIT (detailed above in Chapter 2), since this code demonstrated to be a reliable tool for exploring the stellar content of galaxies from multi-filter photometric data and it is specifically optimised to deal with multi-photometric data. We include in our analysis the iterative process for removing those bands that may be affected by strong emission lines, to carry out a detailed analysis of the galaxy SED even when strong nebular or AGN emission lines are present. The results are complemented by the Monte Carlo simulations available in MUFFIT, in order to explore the kind of errors and uncertainties that affect the retrieved stellar population parameters. From MUFFIT analysis, we retrieved ages and metallicities (both luminosity- and mass-weighted), photo z (treated as another free parameter in the 1 σ confidence level provided by the Gold catalogue), stellar masses, rest-frame luminosities or k-corrections, and extinctions.

For the analysis, we firstly selected the public BC03 SSP models (Padova 1994 tracks, ages from 0.06 to 14 Gyr, and metallicities [M/H] = −1.65, −0.64, −0.33, 0.09, 0.55) with a Chabrier (2003) initial mass function, because its wide spectral coverage, $\lambda\lambda$ 91 Å–160 μm, allows us to perform our analysis in an extensive redshift range, as in the present case of ALHAMBRA where the population of galaxies easily extends up to redshift $z \sim 1.5$. As we show in Sect. 3.8, we explore the influence on the results using other sets of SSPs, particularly we make use of the set of MIUSCAT SSP models, which are an extension of the Vazdekis et al. (2003, 2010) models and are built from empirical stellar spectra. Owing to the variety of spectral wavelength-ranges and stellar population parameters handled for this family of models (see e. g. `http://miles.iac.es`), we select various sets to cover our needs during the analysis and interpretation of stellar population results. More precisely, we chose the UV and NIR extension of MIUSCAT models (EMILES, $\lambda\lambda$ 1 680 Å–5 μm; Vazdekis et al., 2016) taking the two sets of theoretical isochrones: the scaled-solar isochrones of Girardi et al. (2000, hereafter Padova00) and Pietrinferni et al. (2004, BaSTI in the following). It is noteworthy that this set includes the optical MIUSCAT SSP predictions (Vazdekis et al., 2012; Ricciardelli et al., 2012), the NIR ones of MIUSCATIR (Röck et al., 2015), and the UV extension from the NGSL stellar library. For EMILES, we took 22 ages in the range 0.05–14 Gyr and metallicities [M/H] = −1.31, −0.71, −0.40, 0.00, 0.22 for Padova00 and [M/H] = −1.26, −0.96, −0.66, −0.35, 0.06, 0.26, 0.40 for BaSTI, with Kroupa Universal IMF.

For the whole set of SSP models, we added extinctions to the SSPs with values in the range A_V = 0.0–3.1 (assuming a constant value $R_V = 3.1$), following the extinction law of Fitzpatrick (1999). This extinction law ranges a wider spectral range than the observed in ALHAMBRA since $z \sim 2$, and it is suitable for dereddening any photospectroscopic data, such as ALHAMBRA, after exploring various methodologies and accounting for uncertainties robustly (further details in Fitzpatrick, 1999). Previously to the SED-fitting analysis, the photometry of the galaxies was also corrected of the Milky Way dust using MUFFIT. Although the discrepancies among the CCDs of the LAICA[1] camera (4 CCDs of 4096 × 4096 pixels and pixel scale 0.225″ pixel^{-1}) are mild, each galaxy was analysed with the SSP model set after convolving it with the precise photometric system/CCD in which was imaged. For the Omega-2000[2] camera (1CCD with 2048 × 2048 pixels and plate scale 0.45″ pixel^{-1}), this process is not necessary as it only contains a unique CCD. Noteworthy, the ages provided by MUFFIT through its 2-SSP SED-fitting may differ systematically up to $\lesssim$ 2 Gyr younger when we compare them with the ages obtained assuming alternative SFH, such as τ-models (see Sect. 2.5.5).

Throughout this work, the mass-weighted ages and metallicities are preferred to the luminosity ones, because of the mass-weighted parameters are more representative of the total stellar content of the galaxy

[1] `http://www.caha.es/CAHA/Instruments/LAICA`
[2] `http://www.caha.es/CAHA/Instruments/O2000`

Table 3.1: Stellar-population parameters of the sample of quiescent galaxies using BC03 SSP models. From left to right: ALHAMBRA source ID, right ascension, declination, magnitude in the detection band, photometric redshift, stellar mass, extinction, mass weighted age and metallicity, $m_{F365} - m_{F551}$ and $m_{F551} - J$ rest-frame colours (labeled as $U - V$ and $V - J$ respectively) and their values after dust correction (intrinsic colours), and average signal-to-noise ratio. The parameter uncertainties are attached below each quantity.

SourceID 814−	RA [deg]	DEC [deg]	m_{F814W} [AB]	z	$\log_{10} M_\star$ [$M_\odot$]	A_V [AB]	$\mathrm{Age_M}$ [Gyr]	$[\mathrm{M/H}]_\mathrm{M}$ [dex]	$U-V$ [AB]	$V-J$ [AB]	$(U-V)_\mathrm{int}$ [AB]	$(V-J)_\mathrm{int}$ [AB]	$< S/N >$
62402442	214.4301	52.3397	16.71	0.119	10.66	0.27	4.5	−0.24	1.88	1.24	1.73	1.09	40.64
			±0.02	±0.003	±0.05	±0.07	±1.3	±0.15	±0.04	±0.02	±0.04	±0.05	
62300829	213.5037	52.3945	16.53	0.100	10.64	0.08	6.0	−0.05	1.91	1.20	1.87	1.16	39.73
			±0.02	< 0.001	±0.08	±0.08	±2.4	±0.17	±0.02	±0.02	±0.05	±0.05	
74405663	243.0770	54.1213	17.10	0.119	10.55	0.15	4.1	−0.20	1.78	1.19	1.68	1.10	39.52
			±0.02	±0.003	±0.04	±0.16	±0.5	±0.10	±0.04	±0.02	±0.20	±0.09	
22202797	36.8434	1.1945	17.31	0.104	10.33	0.10	5.2	−0.15	1.86	1.14	1.80	1.09	38.77
			±0.02	±0.007	±0.10	±0.08	±1.9	±0.20	±0.06	±0.03	±0.06	±0.05	
74103404	243.0550	54.6608	17.14	0.230	11.31	0.02	5.4	0.12	1.89	1.24	1.87	1.22	38.69
			±0.02	< 0.001	±0.04	±0.05	±0.9	±0.16	±0.02	±0.02	±0.04	±0.03	
21205253	37.0285	1.1497	17.37	0.136	10.66	0.07	7.8	−0.05	1.96	1.18	1.93	1.14	38.66
			±0.02	±0.005	±0.08	±0.09	±2.0	±0.16	±0.04	±0.03	±0.05	±0.06	
74401062	243.1835	54.2408	18.02	0.140	10.33	0.13	4.8	−0.12	1.86	1.12	1.79	1.05	38.64
			±0.02	±0.001	±0.06	±0.09	±1.5	±0.13	±0.02	±0.02	±0.05	±0.06	
74405753	243.1381	54.1192	17.97	0.151	10.47	0.11	5.0	0.03	1.94	1.23	1.88	1.17	38.61
			±0.02	±0.004	±0.06	±0.10	±1.6	±0.13	±0.03	±0.02	±0.06	±0.06	
74406006	243.2873	54.1121	17.14	0.144	10.80	0.13	7.1	0.02	1.99	1.23	1.92	1.16	38.59
			±0.02	±0.006	±0.10	±0.11	±2.2	±0.15	±0.05	±0.03	±0.07	±0.07	
51406997	189.5499	61.7978	16.77	0.108	10.59	0.15	6.7	−0.04	1.97	1.20	1.88	1.11	38.57
			±0.02	±0.007	±0.09	±0.10	±2.4	±0.14	±0.06	±0.03	±0.07	±0.07	
74101458	243.4018	54.7131	17.64	0.140	10.58	0.02	5.3	−0.22	1.74	1.18	1.73	1.17	38.41
			±0.02	< 0.001	±0.03	±0.04	±0.8	±0.14	±0.02	±0.02	±0.02	±0.03	
51210550	188.7010	62.2081	17.53	0.110	10.26	0.02	5.3	−0.19	1.79	1.14	1.78	1.13	38.31
			±0.02	±0.002	±0.05	±0.04	±1.1	±0.23	±0.04	±0.02	±0.04	±0.03	
74104138	243.0991	54.6405	17.40	0.206	11.16	0.11	7.2	0.07	2.04	1.21	1.98	1.15	38.30
			±0.02	±0.006	±0.07	±0.11	±2.2	±0.10	±0.05	±0.03	±0.07	±0.06	

Notes. Continued on next page.

Table 3.1: continued.

SourceID	RA	DEC	m_{F814W}	z	$\log_{10} M_\star$	A_V	$\mathrm{Age_M}$	$[\mathrm{M/H}]_\mathrm{M}$	$U-V$	$V-J$	$(U-V)_\mathrm{int}$	$(V-J)_\mathrm{int}$	$< S/N >$
41401013	150.4250	2.0662	15.98	0.133	11.02	0.17	4.1	0.13	1.88	1.26	1.79	1.16	38.26
			±0.02	±0.006	±0.11	±0.07	±2.4	±0.19	±0.04	±0.02	±0.05	±0.05	
74406197	243.3334	54.1071	17.96	0.156	10.48	0.06	4.6	0.10	1.88	1.19	1.85	1.16	38.25
			±0.02	±0.005	±0.07	±0.08	±1.1	±0.16	±0.05	±0.03	±0.04	±0.05	
73400609	243.4698	54.2539	17.54	0.142	10.64	0.04	7.0	−0.11	1.92	1.18	1.91	1.16	38.12
			±0.02	±0.005	±0.06	±0.07	±1.8	±0.12	±0.05	±0.04	±0.04	±0.04	
74408909	243.4100	54.0274	16.64	0.145	11.03	0.06	7.6	−0.18	1.92	1.17	1.88	1.14	38.06
			±0.02	±0.006	±0.07	±0.09	±1.9	±0.13	±0.06	±0.04	±0.06	±0.07	
74104674	243.3939	54.6296	18.24	0.220	10.73	0.05	5.1	0.08	1.93	1.12	1.90	1.10	38.04
			±0.02	±0.001	±0.10	±0.08	±2.0	±0.12	±0.02	±0.02	±0.06	±0.05	
22102185	37.3262	1.2085	18.41	0.250	10.74	0.12	4.0	0.16	1.96	1.22	1.89	1.15	38.00
			±0.02	±0.004	±0.08	±0.10	±1.5	±0.13	±0.04	±0.03	±0.06	±0.06	
74108616	243.0808	54.5163	18.12	0.120	10.23	0.02	6.1	−0.43	1.71	1.12	1.70	1.10	37.98
			±0.02	±0.001	±0.03	±0.04	±0.8	±0.11	±0.02	±0.02	±0.03	±0.04	
74103640	243.1188	54.6574	18.35	0.217	10.82	0.09	7.1	0.07	2.03	1.18	1.98	1.14	37.87
			±0.02	±0.006	±0.05	±0.10	±1.5	±0.09	±0.04	±0.03	±0.07	±0.06	
22106868	37.2473	1.0738	18.06	0.187	10.71	0.08	6.3	0.07	2.01	1.27	1.97	1.23	37.84
			±0.02	±0.005	±0.06	±0.09	±1.8	±0.16	±0.04	±0.02	±0.06	±0.06	
82208557	356.1854	15.8722	16.50	0.106	10.75	0.20	6.8	−0.00	1.98	1.24	1.87	1.14	37.81
			±0.02	±0.006	±0.09	±0.11	±2.5	±0.22	±0.06	±0.04	±0.07	±0.08	
51401954	189.3063	61.9076	17.59	0.125	10.32	0.14	3.8	−0.16	1.77	1.16	1.69	1.08	37.73
			±0.02	±0.015	±0.10	±0.13	±0.8	±0.16	±0.11	±0.06	±0.06	±0.06	
61100980	214.6721	52.8711	16.63	0.109	10.65	0.06	4.5	−0.23	1.73	1.15	1.70	1.12	37.63
			±0.02	±0.008	±0.08	±0.05	±0.5	±0.13	±0.07	±0.04	±0.04	±0.05	
41401300	150.3795	2.0625	17.61	0.170	10.62	0.08	4.9	0.05	1.83	1.18	1.78	1.14	37.63
			±0.02	< 0.001	±0.10	±0.09	±2.1	±0.23	±0.03	±0.02	±0.06	±0.06	

Notes. Additional columns and galaxies will be available at `http://archive.cefca.es/alhambra/quiescent_galaxies_query.html` . Only a portion of the table is shown in the printed version for illustrating purposes.

and they are not linked to a definition luminosity weight (which may differ among different work easily); although luminosity-weighted parameters are also estimated. In fact, in some cases a young population can dominate the luminosity of a galaxy, and consequently its luminosity weighted age, even when its contribution in mass is very low (Trager et al., 2000; Conroy, 2013). Lookback times were established following the recipes of Hogg (1999) with the cosmological parameters presented in Sect. 3.1. Hereafter, we define formation epoch as the addition of the mass-weighted age ($\mathrm{Age_M}$) and lookback time (t_{LB}).

Table 3.1 illustrates part of the stellar-population parameters and uncertainties derived by MUFFIT using BC03 for the sample of 8 547 quiescent galaxies (see Sect. 3.3 below) used throughout this research. A more complete catalogue with additional columns will be available via query submission at `http://archive.cefca.es/alhambra/quiescent_galaxies_query.html`.

3.3 Definition of the quiescent sample

The definition of a reliable sample of quiescent galaxies with low levels of contamination may be a sensitive and tricky process, because both dusty star-forming galaxies and cool stars in ground-based surveys present colours similar to those of the quiescent galaxy population. The contamination of these sources can represented a substantial part of the sample at certain redshift and mass ranges and their effects should be removed or minimised at least (see Sects. 3.3.1 and Sect. 3.3.3). Even though multi-filter photometric surveys with the prominent advantage that they are not biased by selection effects other than the photometric depth, the definition of a complete sample in stellar mass (Sect. 3.3.4) with accurate enough photo-z predictions (Sect. 3.3.5) is key to reliable drive this study, because as we mention above, the stellar mass is tightly related to the star formation history of each galaxy.

3.3.1 The dust corrected UVJ-diagram

There are many similar relations that define a sample of quiescent galaxies based in colour–magnitude diagrams (CMD, Bell et al., 2004; Baldry et al., 2004; Brown et al., 2007), in SFR-mass relations (Moustakas et al., 2013), in colour–mass relations (Peng et al., 2010), or in colour–colour diagrams (Daddi et al., 2004; Williams et al., 2009; Arnouts et al., 2013) usually defined at rest-frame. During the last years, the UVJ colour–colour diagram (Williams et al., 2009) has become one of the most extended methods for separating the quiescent galaxy population from the galaxies that lie on the blue cloud or star forming population (also referred as the *main sequence* of star formation, Noeske et al., 2007). The most remarkable advantage of this colour–colour diagram is the inclusion of the colour $V - J$, that mitigates the problem of their predecessors ($U - V$ mainly based diagrams or CMD), because of quiescent and dust-obscured star-forming galaxies are empirically separated occupying different loci in the UVJ-diagram besides they present similar red $U - V$ colours (Wyder et al., 2007; Cowie & Barger, 2008; Brammer et al., 2009). Despite the UVJ diagrams demonstrated to be a reliable method to split quiescent (low sSFR) from star-forming galaxies (high sSFR), these diagrams present a level of contamination in the selection of quiescent galaxies that depends on redshift and stellar mass (Williams et al., 2009; Moresco et al., 2013), for which the number of star-forming outliers may reach 30 % at certain redshift and mass regime, or at least a 15 % after imposing a more restrictive $U - V$ colour limit than the defined one originally (Moresco et al., 2013).

For the aims of this work, it is therefore crucial to diminish the contamination of dust-reddened star-forming galaxies in our sample. Otherwise, the sample would contain a subset of younger and obscured galaxies, that differs from the largely evolved quiescent galaxies. To make a more reliable sample selection, we took advantage of the stellar population results provided by MUFFIT, more specifically we used the k corrections along with the extinction values to build a new and improved version of the UVJ-diagram free of dust colour effects, which allows us to clean the quiescent sample of obscured star-forming galaxies. Basically, MUFFIT retrieves a set of SSP mixtures with different weights and parameters after fitting the SED of each galaxy from the ALHAMBRA dataset, in which the extinction is included. From these mixtures, it is straightforward to rebuild the same combination of models (in a general case age, metallicity, stellar

initial mass function, over-abundances, stellar mass, and the weight of each SSP component in the mixture), at rest-frame and null extinction ($A_V = 0.0$).

Instead of using the rest-frame $U - V$ and $V - J$ colours in order to build the UVJ-diagram, we took the bands $F365W$, $F551W$, and J from ALHAMBRA to compute the rest-frame colours $m_{F365} - m_{F551}$ and $m_{F551} - J$, which are the most similar bands to the U, V, and J effective wavelengths (the empirical bimodality is also present using these bands). In Fig. 3.1, we present the UVJ-diagram made with the ALHAMBRA bands mentioned previously for all the galaxies at $0.1 \leq z \leq 1.1$ in the ALHAMBRA Gold catalogue (complete down to $m_{F814W} = 23$) and corrected of reddening. By looking at the distribution of the rest-frame intrinsic colour $(m_{F365} - m_{F551})_{\rm int}$ (see top inner panels in Fig. 3.1), we can easily set the limit for quiescent galaxies as $(m_{F365} - m_{F551})_{\rm int} \geq 1.5$, that is roughly constant with redshift, at least up to $z \sim 1.1$. Although this colour limit is not strictly located in the minimum between the red and blue peaks (corresponding to the quiescent and star-forming population respectively), its value was defined to agree with the limit established in Moresco et al. (2013, see Eq. 3.1 below) and to be slightly larger as to avoid the (now) poorly populated green valley, whose limits are difficult to define due to the low number of sources. In fact, after the definition of a quiescent sample complete in stellar mass (Sect. 3.3.4 below), the sample remains almost unaltered. For comparison reasons, we present the UVJ-diagram without the extinction correction in the bottom panels of Fig. 3.1. The range of colours in the UVJ-diagram to select the quiescent sample defined by Moresco et al. (2013) is also plotted, which is less contaminated of obscured star-forming galaxies than the proposed by Williams et al. (2009). Formally,

$$\begin{cases} (m_{F365} - m_{F551}) > & 0.88 \times (m_{F551} - J) + 0.69, \text{ for } z \leq 0.5 \\ (m_{F365} - m_{F551}) > & 0.88 \times (m_{F551} - J) + 0.66, \text{ for } z > 0.5 \end{cases} \tag{3.1}$$

where $m_{F365} - m_{F551} > 1.6$ ($m_{F365} - m_{F551} > 1.5$) at $z \leq 0.5$ ($z > 0.5$) and $m_{F551} - J < 1.6$, all quantities at rest-frame and in AB-magnitudes.

The simple extinction correction applied on the UVJ colours yields striking results:

- As expected, removing dust effects makes clearer the colour bimodality of galaxies in the UVJ-diagram (see Fig. 3.1). This is because a very considerable part of the galaxies that reside in the green valley (the bridge between red and blue galaxies) are obscured star-forming galaxies (~ 65 %). Their intrinsic colour $(m_{F365} - m_{F551})_{\rm int}$ unveils that these galaxies really lie on the star-forming population, although they also present a large dust content that redden their observed colours (Brammer et al., 2009; Whitaker et al., 2010, obtained a similar result for $U - V$). Thereby, the green valley is largely depopulated after accounting for extinction (inner panels in Fig. 3.1; see also Bell et al., 2005; Cowie & Barger, 2008; Brammer et al., 2009; Cardamone et al., 2010).

- At least for a sample complete down to $m_{F814W} = 23$, the histogram of the $(m_{F365} - m_{F551})_{\rm int}$ colour exhibits a local minimum at ~ 1.45 that can be imposed as the bluest colour limit to fairly select the quiescent sample. This limit to separate quiescent from star-forming galaxies also remains roughly constant since $z \leq 1.1$, and it does not present any remarkable evolution. In spite of there is a bridge between the bulk of intrinsic red and blue galaxies at $(m_{F365} - m_{F551})_{\rm int} \sim 1.45$, this colour range is not largely populated by many galaxy and it looks to be restricted for a few ones only.

- Additionally, we can see that the galaxies labelled as quiescent by Eq. 3.1 and that belong to the star-forming sample after the dust correction (intrinsic $m_{F365} - m_{F551} < 1.5$, black dots in Fig. 3.1) are typically concentrated close to the edges of Eq. 3.1, supporting the reliability of the extinction values provided by MUFFIT. Otherwise, the distribution of reddened-by-dust galaxies would uniformly populate the red part of the UVJ diagram as a consequence of degeneracies, where the effects of age, metallicity and extinction on the stellar continuum were not properly differentiated.

- Dusty star forming galaxies comprise the ~ 20 % of the quiescent sample defined through Eq. 3.1. Our results clearly established that more massive quiescent galaxies are less biased by dusty star forming

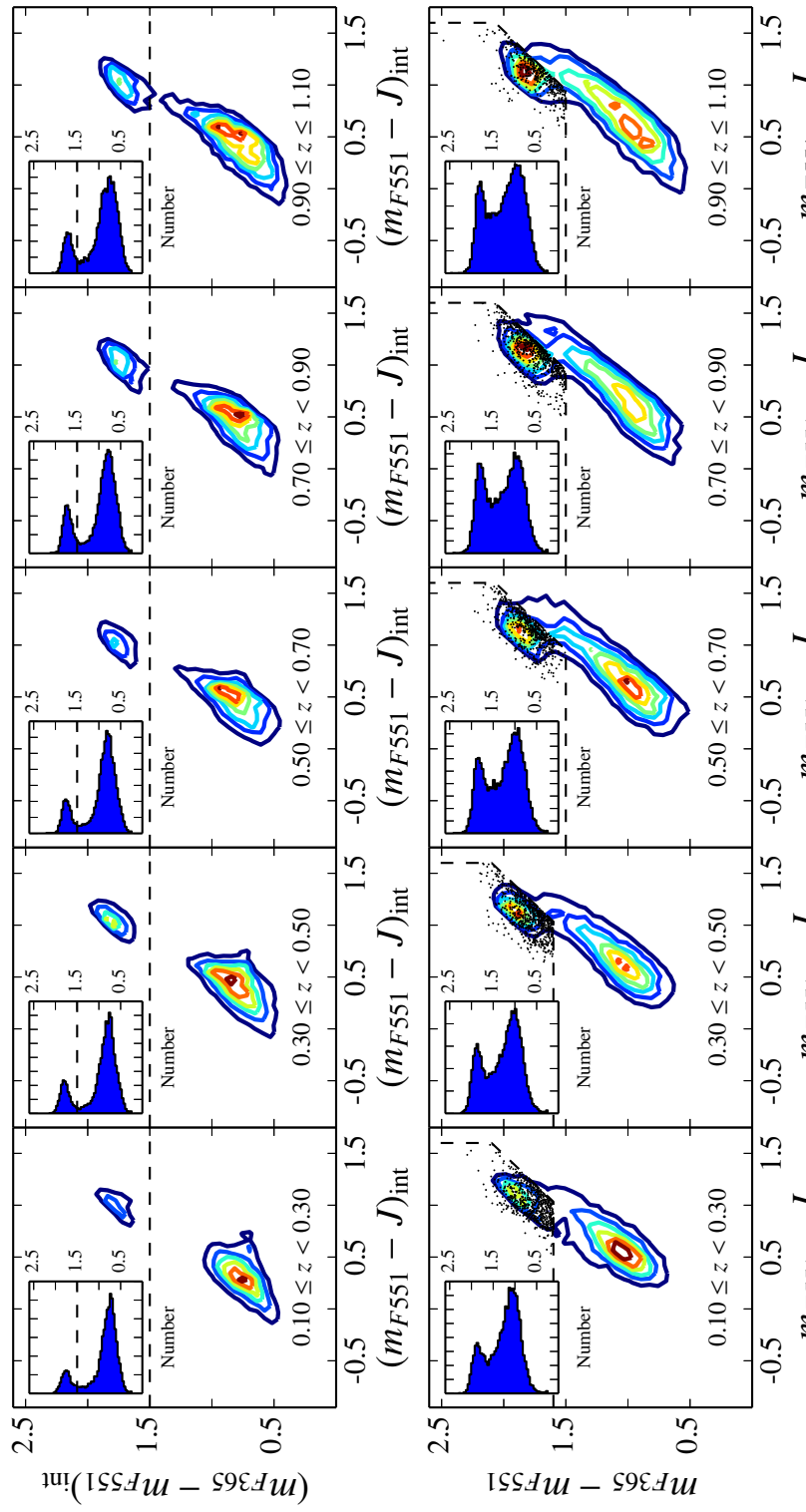

Figure 3.1: *Top panels* illustrate the density surface of rest-frame intrinsic colours $m_{F551} - J$ (X-axis) and $m_{F365} - m_{F551}$ (Y-axis) after correcting for extinction at different redshifts, whereas *bottom panels* are rest-frame colours without removing dust effects. Redder (bluer) density-curve colours are related to high (low) densities. *Inner panels*, histograms of the intrinsic (*top*) and observed (*bottom*) rest-frame colour $m_{F365} - m_{F551}$. Dashed lines in *top panels* illustrate our limiting value $(m_{F365} - m_{F551})_{\rm int} = 1.5$ for quiescent galaxies, and in the *bottom panel* the quiescent UVJ-sample defined by Moresco et al. (2013, Eq. 3.1). Black dots are galaxies defined as quiescent with the UVJ-criteria of Moresco et al. (2013) that lie in the star-forming region after taking their extinctions into account.

galaxies than the less massive ones. More precisely, the most massive part of the sample is weakly contaminated by dusty star-forming galaxies when they are defined by Eq. 3.1 ($\log_{10} M_\star \geq 11$, 2–8 % from $z \sim 0.1$ to $z \sim 1.1$), while the low mass ones may be significantly biased by them (e. g. $\sim$ 40 % for $9.2 \leq \log_{10} M_\star \leq 9.6$ at $0.1 \leq z \leq 0.3$).

In addition to the colour cut $(m_{F365} - m_{F551})_{\rm int} \geq 1.5$, we restrict this study to the redshift interval $0.1 \leq z \leq 1.1$ because: i) the stellar mass completeness constraint largely reduces the number of quiescent galaxies further than $z > 1.1$; ii) at $z < 0.1$, the number of quiescent galaxies in ALHAMBRA is also very low, specially for the most massive ones, which are substantially less frequent. The total number of quiescent galaxies at this point is 14 944.

3.3.2 Visual inspection

For increasing the purity of the sample, we also carried out a one-by-one visual inspection on the $\sim$ 15k galaxies with intrinsic red colours retrieved above (Sect. 3.3.1) and in the interval $0.1 \leq z \leq 1.1$. We removed from the sample those galaxies for which their photometry presented significant irregularities or that were compromised by really nearby sources, imaged in bad CCD regions, or spurious detections. To develop this process, we simultaneously checked one-by-one all the galaxy stamps, the adequacy of the photometric aperture (mainly the efficiency on the detection-deblending of sources and surroundings), and that the photo-spectrum did not present strong irregularities as the presented by time-variable sources or sources close to stellar spikes, which cannot be reproduced by SSPs. Finally, we removed from the quiescent sample $\sim$ 5 % of sources after the visual inspection, remaining 14 235 quiescent galaxies at this stage.

3.3.3 Faint star removal

The ALHAMBRA Gold catalogue provides a statistical star/galaxy classification for discerning if each source in the catalogue is either a galaxy or a star (`Stellar_flag`, more detailed in Molino et al., 2014). This parameter was originally used to define our sample of galaxies (see Sect. 3.2) and it accounts for the geometry, apparent magnitude, and two colours to provide a statistical approach to carry out the star/galaxy separation for each detection. Unfortunately, this parameter is less effective at decreasing signal-to-noise-ratio, and consequently, for sources fainter than $m_{F814W} = 22.5$ this classification is uncertain and a value `Stellar_flag`= 0.5 is assigned. Although we do not expect a large number of contamination from stars at $22.5 \leq m_{F814W} < 23$ for the full sample, the ALHAMBRA fields may contain stars from the Milky Way halo, which are mainly composed of cool red stars. Our quiescent sample, composed of red sources, may be therefore partly contaminated by stars that were analysed as galaxies.

This problem is faced through a new MUFFIT module devoted to analysing stars, which carries out a similar SED-fitting process to the galactic version but using the Coelho et al. (2005) star models instead. This methodology ends up reducing the contamination of faint stars in ALHAMBRA from 24 % to 4 % after comparing our faint star detection predictions with the star/galaxy classification provided by COSMOS (classified as point-like sources thanks for its tiny PSF; Leauthaud et al., 2007), in a shared subsample of sources at $22.5 \leq m_{F814W} < 23$. It is worth mentioning that owing to the spectral coverage of the Coelho et al. (2005) stellar models (300 nm – 1.8μm), the $K_{\rm s}$ photometry of the ALHAMBRA band is not used for the stellar analysis. A more detailed explanation about the whole process is provided in Appendix A, as well as the comparison with COSMOS to check the reliability of the methodology.

After removing 439 star candidates from the sample in the range $22.5 \leq m_{F814W} < 23$, the number of quiescent galaxies is reduced to 13 796.

3.3.4 Stellar mass completeness

We model the stellar mass completeness, C, through a Fermi-Dirac distribution (see Eq. B.2) that is parametrised by two redshift-dependent parameters, $M_{\rm F}$ and $\Delta_{\rm F}$. We find out that this kind of distribution reproduces the

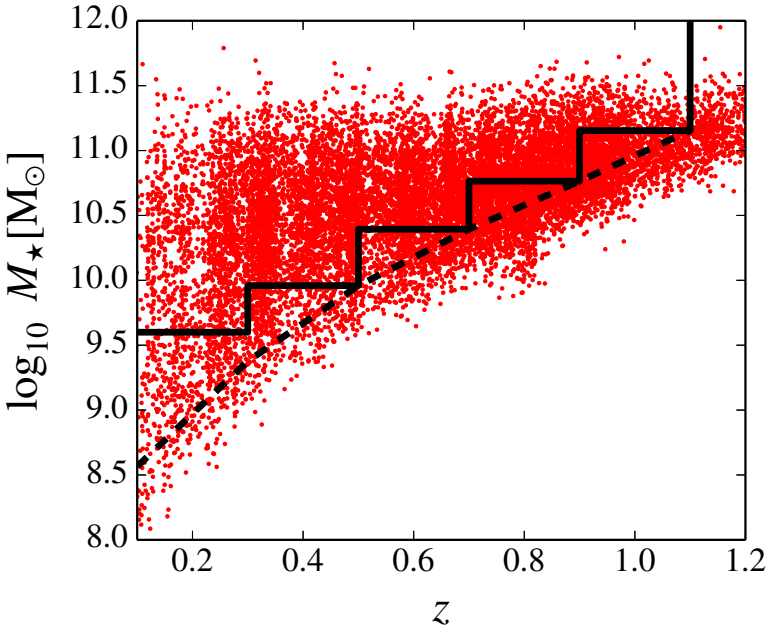

Figure 3.2: Redshifts (X–axis) and stellar masses (Y–axis) of the sample of ALHAMBRA quiescent galaxies. The dashed line shows the 95 % stellar mass completeness level of quiescent galaxies from the ALHAMBRA Gold catalogue (complete down to $m_{F814W} = 23$). The solid line illustrates the limits assumed in this work to define our sample of galaxies complete in stellar mass at different redshift bins (see Sect.3.3).

decay on the less massive galaxies of our flux-limited sample ($m_{F814W} \leq 23$) at any redshift properly (see Appendix B.1). Briefly, $M_{\rm F}$ is the stellar mass value in dex units for which the completeness reaches 50 % ($C = 0.5$), while $\Delta_{\rm F}$ is related with the rate of decrease on the number of galaxies. The process for deriving these parameters takes advantage of stellar mass functions from deeper surveys (for further details, see Appendix B.2), in particular from the COSMOS survey, which specifically provides them for quiescent galaxies (Ilbert et al., 2010) and partly overlaps with ALHAMBRA. In this process, we assume that any discrepancy between the low-mass end of the ALHAMBRA stellar mass function and the COSMOS one is leaded by the mass incompleteness. These differences allow us to determine both $M_{\rm F}$ and $\Delta_{\rm F}$, that are directly related to the stellar mass limit, $\log_{10} M_C$, at certain redshift z and completeness level by

$$\log_{10} M_C(z) = \Delta_{\rm F}(z) \ln [(1 - C) - 1] + M_{\rm F}(z) \, . \tag{3.2}$$

For this work, we require a conservative stellar mass completeness of at least $C = 0.95$ at any redshift slice (see Fig. 3.2 and values in Table 3.2). From Table 3.2, we derive that ALHAMBRA is complete down to $\log_{10} M_\star \geq 9.4$ dex at $z = 0.3$. However, to develop this work, we rise the low-mass limit down to $\log_{10} M_\star \geq 9.6$ dex, with the only aim of having a set of equal-size stellar mass bins of ~ 0.4 dex. In Appendix B, there is a more detailed and complete explanation of the full process to determine the ALHAMBRA completeness.

Finally, the total balance of galaxies for this study, including the stellar mass completeness constraint, comprises a total of 8 547 quiescent galaxies (all the galaxies in our sample are enclosed by the black solid line in Fig. 3.2). The number of quiescent galaxies per stellar mass and redshift bin is detailed in Table 3.3.

3.3.5 The photo-z accuracy of the quiescent sample

An accurate photo-z determination is essential to properly drive a stellar population study, otherwise any stellar-population prediction may be erroneous. As we mention above, we came from the great photo-z constraints provided in the ALHAMBRA Gold catalogue (computed using BPZ2.0, Benítez, 2000; Molino

Table 3.2: The parameters $M_{\rm F}$ and $\Delta_{\rm F}$ at different redshift, and the stellar mass limit at the completeness level $C = 0.7$, 0.8, 0.9, and 0.95 for the quiescent sample.

Redshift	0.3	0.5	0.7	0.9	1.1
$M_{\rm F}$	8.99	9.64	10.08	10.44	10.84
$\Delta_{\rm F}$	0.132	0.108	0.105	0.110	0.108
$\log_{10} M_{C=0.7}$	9.10	9.73	10.17	10.53	10.93
$\log_{10} M_{C=0.8}$	9.17	9.79	10.23	10.59	10.99
$\log_{10} M_{C=0.9}$	9.28	9.88	10.31	10.68	11.07
$\log_{10} M_{C=0.95}$	9.38	9.96	10.39	10.76	11.15

Table 3.3: Number of quiescent galaxies per stellar mass and redshift bin. Last column summarizes the total number of galaxies per stellar mass bin. Last row presents the total number of quiescent galaxies per redshift bin. All the cells include redshift and stellar mass bins complete at the level $C = 0.95$, otherwise appear dashed.

	$0.1 \leq z < 0.3$	$0.3 \leq z < 0.5$	$0.5 \leq z < 0.7$	$0.7 \leq z < 0.9$	$0.9 \leq z \leq 1.1$	Total
$9.6 \leq \log_{10} M_\star < 10.0$	289	–	–	–	–	289
$10.0 \leq \log_{10} M_\star < 10.4$	433	996	–	–	–	1429
$10.4 \leq \log_{10} M_\star < 10.8$	403	1035	1088	–	–	2526
$10.8 \leq \log_{10} M_\star < 11.2$	238	663	800	1480	–	3181
$\log_{10} M_\star \geq 11.2$	51	140	157	357	417	1122
Total	1414	2834	2045	1837	417	8547

et al., 2014), to subsequently run MUFFIT in the photo-z intervals provided in this catalogue, that is, treating the redshift as another free parameter to determine in our stellar population analysis. Despite MUFFIT is not a photo-z code, the combined use of both photo-z constraints from dedicated photo-z codes and MUFFIT has demonstrated to be a reliable method that improves the photo-z predictions $\sim$ 15 % (see Díaz-García et al., 2015, Chapter 2 in this thesis), and it is necessary to check its reliability and accuracy.

As in Sect. 4.3 of Díaz-García et al. (2015), also Sect. 2.4.3 in this thesis, the methodology to establish the level of accuracy for the photo-z predictions provided by MUFFIT (after using as priors the photo-z constraints from the Gold catalogue), is based on all the galaxies in our final sample with publicly available spectroscopic redshifts from surveys (zCOSMOS, Lilly et al. 2009; AEGIS, Davis et al. 2007; and GOODS-N, Cooper et al. 2011) that overlap with ALHAMBRA (from the catalogue of Molino et al., 2014). As there is no a unique method to set numerical values of the photo-z accuracy, we turned to various methods already used in the literature. One of the most extended is the normalised median absolute deviation ($\sigma_{\rm NMAD}$, Brammer et al., 2008), since this is less affected of catastrophic errors or outliers. Formally,

$$\sigma_{\rm NMAD} = 1.48 \times median\left(\frac{|\Delta z - median(\Delta z)|}{1 + z_{\rm spec}}\right), \tag{3.3}$$

where $\Delta z = z_{\rm phot} - z_{\rm spec}$. Moreover, we complement our results proposing another photo-z accuracy estimator: the RMS of the Gaussian distribution built from the values $\Delta z/(1 + z_{\rm spec})$, which in the following, we denote as $\sigma_{{\rm photo}-z}$. The number of catastrophic outliers is also a noted factor to take into account, so we include two estimators for them

$$\eta_1 = \frac{|\Delta z|}{1 + z_{\rm spec}} > 0.2, \text{and} \tag{3.4}$$

$$\eta_2 = \frac{|\Delta z|}{1 + z_{\rm spec}} > 5 \times \sigma_{\rm NMAD}. \tag{3.5}$$

Amongst the 8 547 quiescent galaxies in our sample complete in luminosity ($m_{F814W} \leq 23$) and in stellar mass (see Sect. 3.3.4 above), there are 576 quiescent galaxies with spectroscopic redshift measurements.

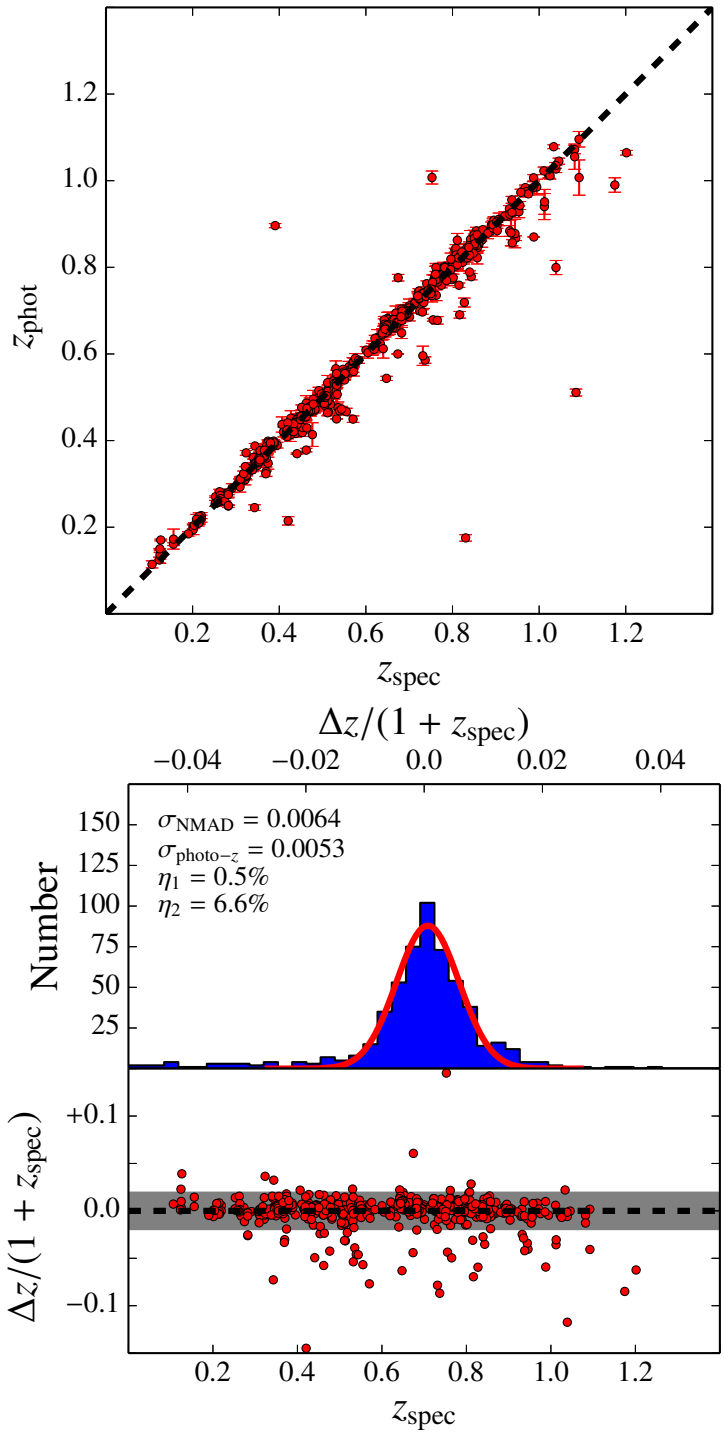

Figure 3.3: Comparison of the photo-z provided by MUFFIT ($z_{\rm phot}$) with their spectroscopic values ($z_{\rm spec}$) for 576 quiescent galaxies in our sample. *Top panel*, comparison one-to-one of the redshifts, where the dashed black line is the one-to-one relation. *Middle panel* shows the histogram of values $\Delta z/(1+z_{\rm spec})$, along with the Gaussian that best fits this distribution (red solid line) and the photo-z accuracy estimators defined in the text (Eqs. 3.3–3.5). *Bottom panel* illustrates the differences $\Delta z/(1+z_{\rm spec})$ as a function of the spectroscopic redshift (X-axis). Shaded region illustrates $3\times\sigma_{\rm NMAD}$ uncertainty.

Figure 3.3 illustrates the one-to-one comparison (top panel) of the 576 quiescent galaxies, showing the excellent agreement between our photometric predictions and the spectroscopic ones. For this subsample of 576 galaxies and according to Eqs. 3.3–3.5, we obtained $\sigma_{\rm NMAD} = 0.0064$, $\eta_1 = 0.5$ %, and $\eta_2 = 6.6$ % respectively; whereas for the $\Delta z/(1 + z_{\rm spec})$ distribution we carried out a good fit to a Gaussian function (red solid line in middle panel in Fig. 3.3) centred at 0.0006 (i. e. closely centred to zero and without a systematic shift) and with a RMS or $\sigma_{{\rm photo}-z} = 0.0053$.

If we compare the photo-z values provided by BPZ in the ALHAMBRA Gold catalogue with the spectroscopic ones, we obtain an accuracy of $\sigma_{\rm NMAD} = 0.0080$, $\sigma_{{\rm photo}-z} = 0.0062$, $\eta_1 = 0.5$ %, and $\eta_2 = 7.1$ %. Thereby, treating the photo z as another free parameter for MUFFIT, in the ranges provided by BPZ, improves the photo-z accuracy $\sim 15 - 20$ %. As checked by Díaz-García et al. (2015), a photo-z uncertainty at this level, 0.6 %, has a minimum impact on the stellar population parameters that are determined via SED-fitting in ALHAMBRA: age, metallicity, and extinction.

3.4 Star formation rates via SED-fitting

By means of combination of two SSPs, we cannot estimate the SFR of galaxies directly, unlike SED-fitting analyses based in τ-models or in more complex SFH (e. g. Cid Fernandes et al., 2005; Moustakas et al., 2013). In order to retrieve SFRs from the SED-fitting results provided by MUFFIT, it is necessary the definition of a tracer or parameter that allow us to estimate them (Sect. 3.4.1). Although the SFR of quiescent galaxies are typically low, they can also be used to complement and reinforce the reliability of the results obtained in Sect. 3.3.1, opening an alternative process or criterion in order to support that the reddened by dust star-forming galaxies that exhibit UVJ-colours of quiescent galaxies (hereafter DSF, see Eq. 3.1) also show other features proper of star-forming galaxies, and therefore, they were removed from the quiescent sample properly. Specifically, we focus on the SFRs of the DSF to check that they present SFR values in the range of star-forming galaxies.

On the one hand, we present the methodology for computing SFRs using the SED-fitting results provided by MUFFIT using the ALHAMBRA data (Sect. 3.4.1), taking the luminosity at 2 800 Å as SFR tracer, to subsequently compare the SFR of DSF with the rest of the sample. On the other hand, we studied the dust emission at 24 μm of all the DSF removed from the quiescent sample, that is, a tracer separated from SED-fitting results, such as MUFFIT, which is also independent of the ALHAMBRA data (Sect. 3.4.2).

3.4.1 Star formation rates in ALHAMBRA: dusty star-forming galaxies

By means of model predictions of stellar populations, the UV continuum in the range $\lambda\lambda$ 1 500–2 800 Å is a good tracer of SFR in galaxies with on-going star formation, because this range is mainly dominated by the light emitted by late-O and early-B stars (see e. g. Madau et al., 1998). In particular, we chose the SFR tracers proposed by Madau et al. (1998), which are based in stellar population models with exponential declining SFRs, or τ models, and Salpeter (1955) IMF. Even though the SFR derived from luminosities at 1 500 Å and τ-models is slightly less-dependent of the duration of the star-formation burst, the SFR rates derived along this section were computed by the rest-frame luminosity at 2 800 Å, $L^{z=0}_{2800\text{Å}}$. Formally,

$$SFR_{2800\text{Å}} = 1.27\ 10^{-28} \times L^{z=0}_{2800\text{Å}}\ , \tag{3.6}$$

where $L^{z=0}_{2800\text{Å}}$ is in units of ergs s^{-1} Hz^{-1}, and $SFR_{2800\text{Å}}$ in M$_\odot$ yr^{-1}. Notice that Eq. 3.6 is not taking dust effects into account. The election of the SFR tracer at 2 800 Å is motivated by the observational wavelength-frame of ALHAMBRA, because this starts at $\sim$ 3 500 Å (band $F365$, $FWHM \sim 300$ Å and effective wavelength $\lambda_{\rm eff} = 3\,650$ Å), and therefore, the SFR tracer based on the luminosity at 2 800 Å is only matched at redshifts $z > 0.25$, whereas for 1 500 Å is at $z > 1.3$, which reduces our sample dramatically. Actually, for redshifts $z < 0.25$ we are able to obtain a prediction of the luminosity at 2 800 Å, but this prediction would be an extrapolation of the SED-fitting carried out by MUFFIT. For this section, we preferred a more

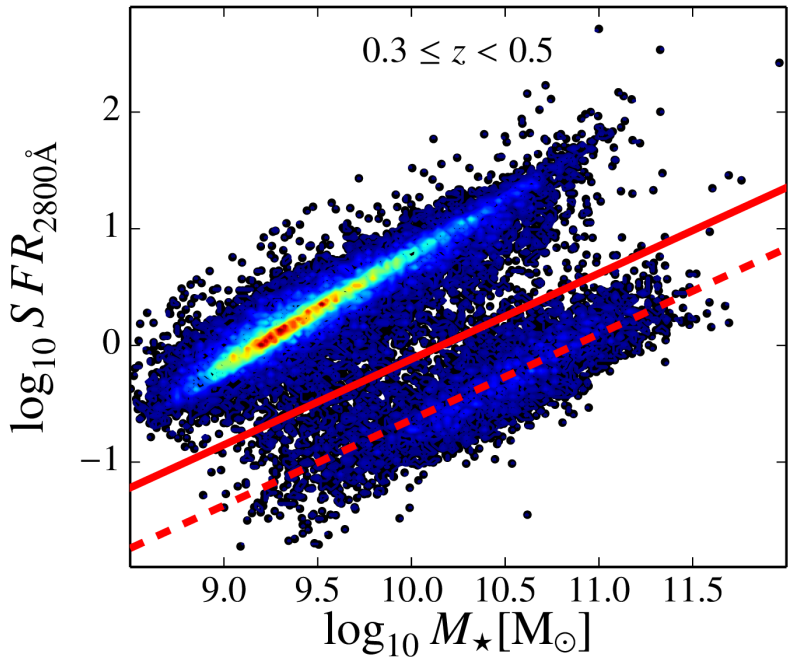

Figure 3.4: Stellar mass (X-axis) versus star formation rate tracer $SFR_{2800Å}$ (Y-axis) defined by Madau et al. (1998, see Eq. 3.6) of the ALHAMBRA galaxies at $0.3 \leq z < 0.5$. Higher densities are presented by redder colours, whereas the lower ones by bluer colours. Dashed and solid red lines show the fit to the quiescent sequence and the limiting $SFR_{2800Å}$ values for star-forming galaxies respectively.

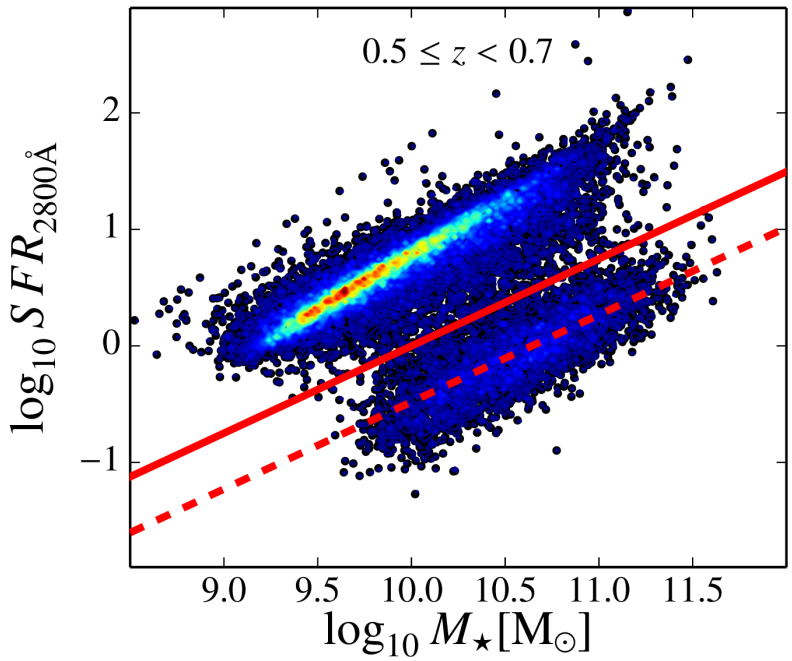

Figure 3.5: As Fig. 3.4, but at redshift $0.5 \leq z < 0.7$.

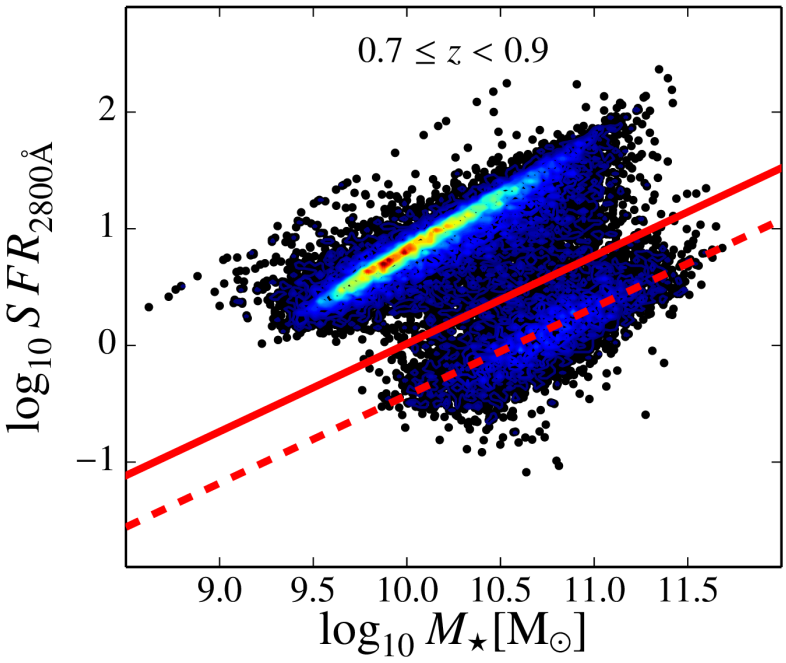

Figure 3.6: As Fig. 3.4, but at redshift $0.7 \leq z < 0.9$.

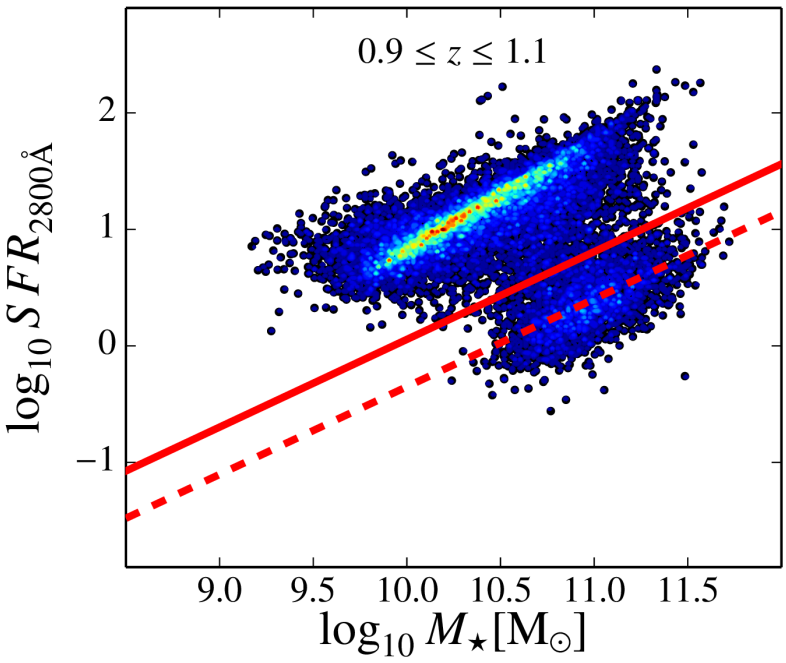

Figure 3.7: As Fig. 3.4, but at redshift $0.9 \leq z \leq 1.1$.

conservative treatment in which the rest-frame flux at 2 800 Å must be included in the observational frame ($z \gtrsim 0.25$).

The rest-frame luminosity $L^{z=0}_{2800\text{Å}}$, also free of dust attenuation, is calculated from the SED-fitting results provided by MUFFIT. Similarly to the process of removing the dust effects on colours (Sect. 3.3.1), we rebuilt the combination of best-fitting models retrieved during the Monte Carlo approach without extinction and for all the galaxies in ALHAMBRA. From these combination of models, we integrated the flux emitted in the rest-frame range $\lambda\lambda$ 2 750–2 850 Å in order to compute $L^{z=0}_{2800\text{Å}}$ with its uncertainty and $SFR_{2800\text{Å}}$ using Eq. 3.6.

In order to characterize the range of $SFR_{2800\text{Å}}$ values of star-forming galaxies, as well as its dependency with redshift and stellar mass, we plotted the distribution $SFR_{2800\text{Å}}$ versus stellar mass at different redshift bins. When viewed the full sample of ALHAMBRA galaxies in the SFR versus stellar mass plane, taking the stellar masses provided by MUFFIT, the already observed bimodality of star-forming and passive galaxies (e. g. Ilbert et al., 2010; Moustakas et al., 2013; Choi et al., 2014) appears, see Figs. 3.4–3.7. These figures also exhibit that there is a tight correlation between the stellar mass and the SFR of the galaxy: the more massive, the larger is the SFR of the galaxy independently of the spectral type (Daddi et al., 2007; Elbaz et al., 2007; Noeske et al., 2007; Moustakas et al., 2013). In order to separate both quiescent and star-forming populations, i. e. setting limiting $SFR_{2800\text{Å}}$ values for quiescent and star-forming galaxies, we followed the process detailed below:

i) We took all the ALHAMBRA galaxies at the redshift range in which the rest-frame luminosity $L^{z=0}_{2800\text{Å}}$ is in the observational wavelength-frame of ALHAMBRA, $0.3 \leq z \leq 1.1$. We plotted their distribution in the $SFR_{2800\text{Å}}$ versus stellar mass plane in redshift bins of $\Delta z = 0.2$. For each redshift bin, the quiescent population is separated by a straight line that was established between both populations by eye.

ii) From all the galaxies with $SFR_{2800\text{Å}}$ below the limit established in the previous step or quiescent galaxies, we carried out an analytical fit of the population in each redshift bin assuming a linear dependency with stellar mass. Our results point out that the correlation between $\log_{10} SFR_{2800\text{Å}}$ and stellar mass is compatible with no evolution in redshift. From lower to upper redshift bins, the slope of the $\log_{10} SFR_{2800\text{Å}}$–$\log_{10} M_\star$ relation is 0.745 ± 0.022, 0.745 ± 0.037, 0.752 ± 0.032, and 0.769 ± 0.069 respectively. In the following, a relation of the form $\log_{10} SFR_{2800\text{Å}} \propto 0.75 \log_{10} M_\star$ is assumed for any redshift providing that the $\log_{10} SFR_{2800\text{Å}}$–$\log_{10} M_\star$ relation of quiescent galaxies in our sample (see also dashed lines in Figs. 3.4–3.7) is well expressed by:

$$\log_{10} SFR^{\text{Q}}_{2800\text{Å}} = (0.75 \pm 0.02) \log_{10} M_\star - (8.00 \pm 0.24). \tag{3.7}$$

iii) To determine the $SFR_{2800\text{Å}}$ upper limiting values of quiescent galaxies (defined by $SFR_{2800\text{Å}}$), or the lower ones of star-forming, we assumed that this frontier between both populations is also of the form $SFR_{2800\text{Å}} \propto M_\star^{0.75}$. Under this assumption, the plane $\log_{10} SFR_{2800\text{Å}}$ versus $\log_{10} M_\star$ can be rotated by Eq. 3.7 easily, as

$$\log_{10} SFR^{\text{rot}}_{2800\text{Å}} = \log_{10} SFR_{2800\text{Å}} - \log_{10} SFR^{\text{Q}}_{2800\text{Å}} \, . \tag{3.8}$$

The distribution of $\log_{10} SFR^{\text{rot}}_{2800\text{Å}}$ for the different redshift bins can be fitted by Gaussian functions, see Fig. 3.9, where the typical uncertainties for $SFR_{2800\text{Å}}$ are in average 0.16 dex for the most local bin and ~ 50 % larger (~ 0.23 dex) at $0.9 \leq z \leq 1.1$. Motivated by the differences among uncertainties, we again take advantage of the MLE methodology presented in Appendix D for both removing the uncertainty effects on the distributions of $\log_{10} SFR^{\text{rot}}_{2800\text{Å}}$ and retrieving the redshift dependency of the distribution shape. For the MLE method, we assumed a linear dependency ($\sigma_2 = \mu_2 = 0$) of the median and width of the distribution, $\mu(z)$ and $\sigma^{\text{int}}(z)$ respectively. From the fits provided by the MLE method, we can set the range of $\log_{10} SFR^{\text{rot}}_{2800\text{Å}}$ at the redshift range $0.3 \leq z \leq 1.1$, to subsequently set

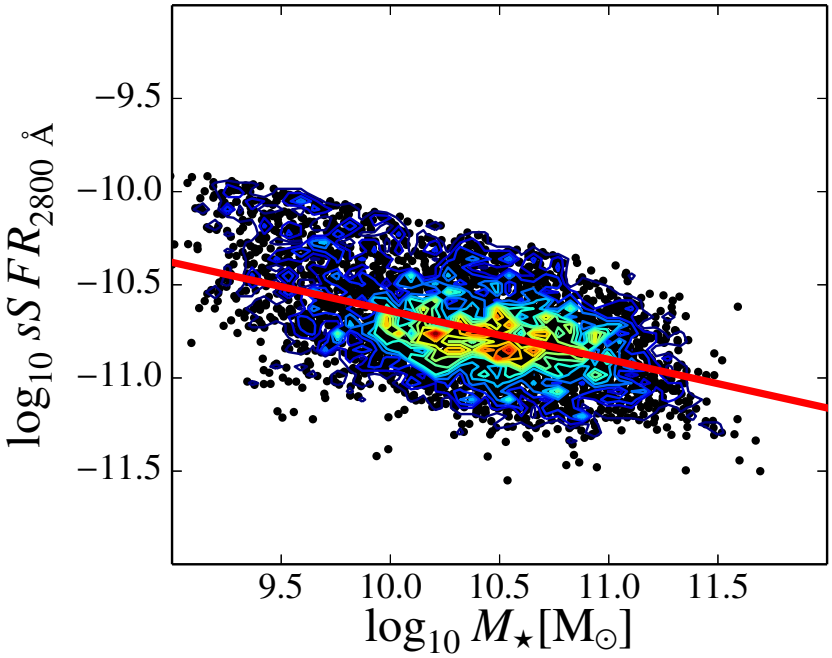

Figure 3.8: Stellar mass (X-axis) versus specific star formation rate $sSFR_{2800Å}$ (Y-axis) of the ALHAMBRA galaxies at $0.3 \leq z \leq 0.5$. Higher densities are presented by redder colours, whereas the lower ones by bluer colours. Solid red line shows the fit to the quiescent sequence.

limits in the $SFR_{2800Å}$ values of quiescent and star-forming galaxies. We established the maximum value of quiescent galaxies (defined by $SFR_{2800Å}$) as the upper 3 σ limit of the distribution of values derived from the MLE (redshift dependent, see dashed lines in Fig. 3.9), which is also close to the limits established by eye in the first step. By Eq. 3.8 and the 3 σ limits of the distributions derived by the MLE, the limiting value between populations (solid lines in Figs. 3.4–3.7) is expressed as follows:

$$\log_{10} SFR^{\rm lim}_{2800Å} = 0.75(\log_{10} M_\star - 10) - 0.18(z - 0.1) + 0.11\ . \tag{3.9}$$

To illustrate, we plot in Fig. 3.8 the stellar mass versus sSFR for all the galaxies classified as quiescent based in their SFR values (see Eq. 3.9). In spite of the more massive quiescent galaxies present larger SFRs, after comparing the relative mass of new stars, our results point out that this contribution is less significant in more massive quiescent galaxies, that is, the larger the mass of quiescent galaxies the lower its sSFR is. This result is also in agreement with previous work in the literature (e. g. Papovich et al., 2006; Zheng et al., 2007; Pérez-González et al., 2008; Damen et al., 2009), which favours the results of the present section.

There are 828 DSF galaxies that were removed from the complete in stellar mass quiescent sample (defined by the dust corrected UVJ-diagram in Sect. 3.5) between redshifts $0.3 \leq z \leq 1.1$. Their $SFR_{2800Å}$ measurements were confronted with Eq. 3.9 for determining whether they present proper values of star-forming galaxies or not. Around $\sim$ 90 % of the 828 DSF galaxies have $SFR_{2800Å}$ above Eq. 3.9, and consequently, their SFR values are in the range of star-forming galaxies. Indeed, when we take the SFR uncertainties into account, the fraction increases up to $\sim$ 97 %, that is, almost the totality of DSF galaxies, with intrinsic blue colours that were removed from the sample of this work, exhibit SFRs in the range of values of star-forming galaxies for a 1 σ uncertainty level. Moreover, we found out that $\sim$ 98.2 % of quiescent galaxies (defined by colours in Sect. 3.5) have SFR below Eq. 3.9, which increases up to $\sim$ 99.8 % at 1 σ uncertainty level.

These results additionally supports the MUFFIT predictions about DSF and the necessity of removing these galaxies, which comprise $\sim$ 10 % of the sample, when a UVJ-selection is performed without removing

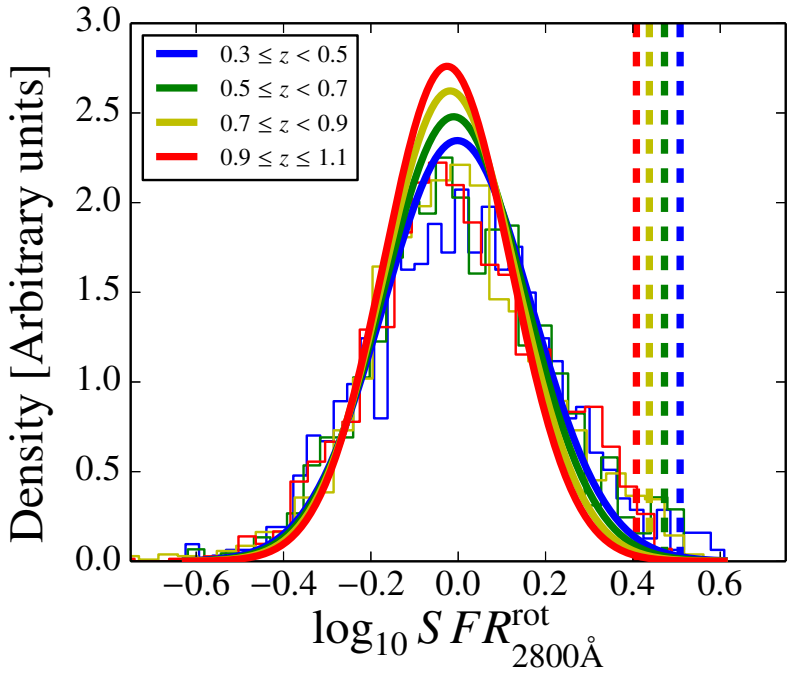

Figure 3.9: Histogram of the $\log_{10} SFR^{\rm rot}_{2800\text{Å}}$ (see Eq. 3.8) values for the quiescent sample defined by their star formation rates $SFR_{2800\text{Å}}$ (see Eq. 3.6) at different redshifts. Solid lines illustrates the MLE best-fitting of the $\log_{10} SFR^{\rm rot}_{2800\text{Å}}$ distributions at their average redshifts. Dashed coloured lines show the upper 3 σ limit of the distributions provided by the MLE method (see details in text).

the dust effects on colours. Notice that $SFR_{2800\text{Å}}$ are also based in SED-fitting predictions carried out by MUFFIT because it is necessary to estimate the luminosity at ~ 2800 Å removing their dust effects, but it differs respect the selection process developed in Sect. 3.5 which is based in a colour criterion and not in a luminosity-based SFR tracer.

3.4.2 Star formation rates and dust emission at 24 μm

The dust emission at 24 μm is an additional tracer to confirm the predictions of MUFFIT and the above Sect. 3.4.1. Furthermore, the SFRs predicted from 24 μm are fully separated from the SED-fitting results provided by MUFFIT and ALHAMBRA data.

The ALHAMBRA field number four, ALHAMBRA-4 in the following, is specially adequate for the purpose of this section. The main feature of ALHAMBRA-4 is that partly overlaps with the COSMOS field, and consequently with S-COSMOS (Sanders et al., 2007). As part of the *Spitzer* Legacy Program, S-COSMOS is a deep infrared survey imaged with the *Spitzer* Space Telescope that covers the entire COSMOS field (2 deg^2) with the IRAC and MIPS cameras. As starting infrared catalogue, we chose the S-COSMOS MIPS 24 μm Photometry Catalog October 2008[3], ~ 90 % (~ 75 %) complete above a 24 μm flux of $S_{24\mu\text{m}} \sim 80$ μJy ($S_{24\mu\text{m}} \sim 60$ μJy) where the FWHM of the MIPS 24 μm PSF is ~ 6″ (Le Floc'h et al., 2009). After cross-correlating the 24 μm MIPS catalogue with all the galaxies in ALHAMBRA-4, we found a total of 1261 common galaxies at $0.2 \leq z \leq 1.2$, both quiescent and star-forming.

In brief (for further details, see López-Comazzi, 2015), the model of Dale & Helou (2002) is performed in order to obtain the k corrected fluxes $S^{z=0}_{24\mu\text{m}}$ and rest-frame luminosities $L^{z=0}_{24\mu\text{m}}$ making use of the photo-z constraints provided by MUFFIT for these galaxies. In Dale & Helou (2002), the model SED for the ISM is built from combinations of different dust masses heated by a radiation field, with a contribution α for each

[3] http://irsa.ipac.caltech.edu/data/COSMOS/

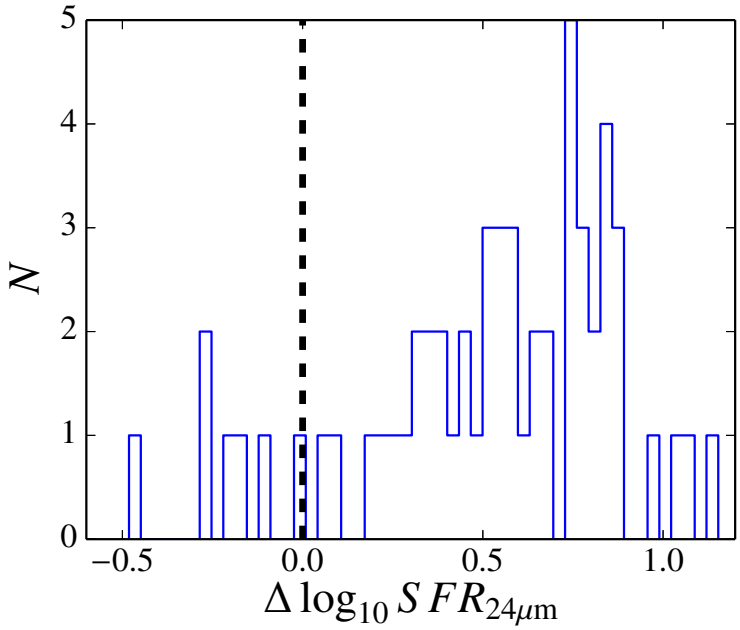

Figure 3.10: Histogram of the differences between the star formation rate (SFR) derived from the 24 μm MIPS catalogue, $\log_{10} SFR_{24\mu m}$, and the SFR low limit of main sequence galaxies $\log_{10} SFR^{lim}_{2800Å}$ (see Eq. 3.9) for the 58 dusty star-forming galaxies. The dashed black line illustrates the equality between $SFR_{24\ \mu m}$ and $SFR^{lim}_{2800Å}$. Positive values belong to galaxies with $SFR_{24\mu m}$ in the main sequence.

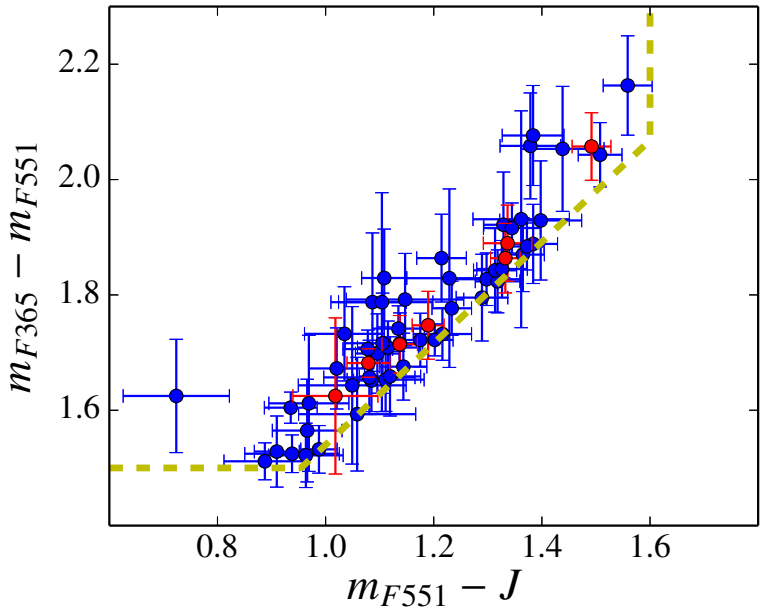

Figure 3.11: Rest-frame colours $m_{F365} - m_{F551}$ and $m_{F551} - J$ of dusty star-forming galaxies in ALHAMBRA with MIPS measurements at 24μm. Blue dots are those galaxies that present SFR values in the range of star-forming galaxies, while red dots are for galaxies with SFRs below of the main sequence ones.

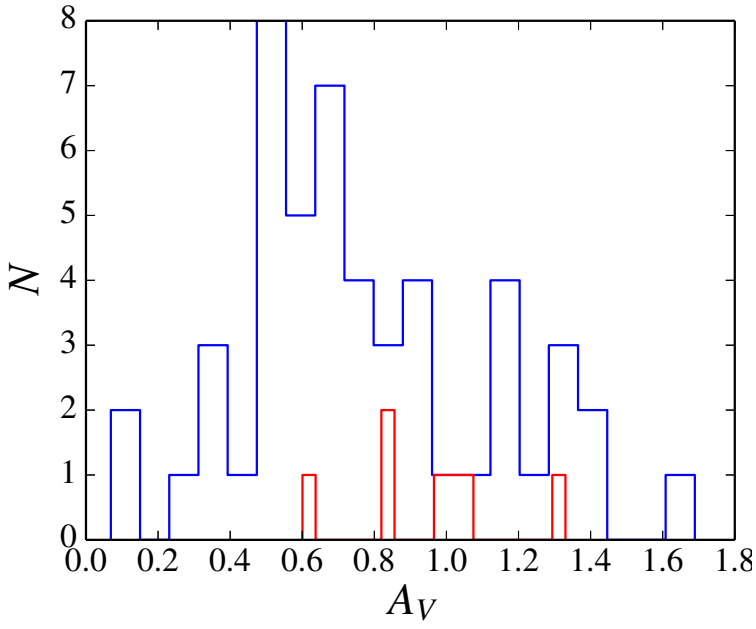

Figure 3.12: Distribution of extinction values, A_V, for the ALHAMBRA galaxies classified as dusty star-forming by MUFFIT with MIPS measurements at 24μm. Red lines are for galaxies with $SFR_{24\mu m} < SFR^{lim}_{2800Å}$ (see Eqs. 3.9 and 3.10), and the blue ones for $SFR_{24\mu m} \geq SFR^{lim}_{2800Å}$.

component. For obtaining $L^{z=0}_{24\mu m}$, we assumed the α range $1.0 \leq \alpha \leq 2.5$ ($\alpha = 1.0$ is the typical value for active galaxies, whereas for the passive ones is $\alpha = 2.5$). Finally, to convert rest-frame luminosities $L^{z=0}_{24\mu m}$ into SFRs, we used the relation provided by Calzetti et al. (2007) and expressed as:

$$SFR_{24\mu m} = 1.31\ 10^{-38} \times {L^{z=0}_{24\mu m}}^{0.885}\ . \tag{3.10}$$

Amongst the 1261 galaxies with MIPS measurements at 24 μm, there are 58 DSF. Using Eq. 3.9, we are able to determine whether these 58 galaxies also present SFRs in the order of star-forming galaxies or not. We found out that 51 of 58 galaxies (i. e. the 88 ± 12 %) present SFR values using Eq. 3.10 larger than the lower limit established by Eq. 3.9, see Fig. 3.10 for the differences with Eq. 3.9. Consequently, the SFR of these galaxies is more proper of star-forming galaxies than quiescent, which strongly favours that MUFFIT is pointing out that these galaxies are actually reddened by dust star-forming galaxies.

In addition, we checked that the 58 galaxies identified as DSF galaxies lies on the box edges that delimits the quiescent sample in a UVJ-diagram without dust corrections, see Fig. 3.11. Through Fig. 3.12, we also confirmed that the DSF that do not present large 24 μm flux emissions show large extinctions above $A_V > 0.6$, for which their $SFR_{2800Å}$ values are in the range of star-forming galaxies.

3.5 Stellar population analysis within the intrinsic UVJ diagram

The empirical bimodality of galaxies in the UVJ-diagram presents a range of colours, both in the $U - V$ and $V - J$, that are related to their stellar populations (mainly age and metallicity, e. g. Bower et al., 1992; Gallazzi et al., 2006; Whitaker et al., 2010) and extinctions. In this work, we are in a privileged position because we are able to estimate the extinction, and thus, discerning what are the main stellar-population parameters that lead the distribution of colours.

In Figs. 3.13 and 3.14, we present the distribution of stellar population parameters for quiescent galaxies on the rest-frame UVJ-diagram (non dust-corrected and intrinsic colours respectively). To guide the eye, we

also plot the typical selection of quiescent galaxies (dotted black line in Fig. 3.14, see Eq. 3.1 in this work and Moresco et al., 2013). Rather than plotting the individual measurements with their uncertainties, we carried out a bidimensional and locally weighted regression method (LOESS, Cleveland, 1988; Cleveland & Devlin, 1979). The LOESS method allows us to model the trends of our quiescent sample and minimize the uncertainty effects on the UVJ-plane through a regression method. Specifically, we used the LOESS implementation for `Python` language [4] (Cappellari et al., 2013a), where the regularization factor is set to $f = 0.6$ and a local linear approximation is assumed (this method dropped satisfactory results in previous work, as Cappellari et al., 2013a; McDermid et al., 2015) in which the uncertainties in stellar mass, extinction, age, and metallicity were taking into account too. The same diagrams than Figs. 3.13 and 3.14 but without applying the LOESS methodology, i. e. plotting the individual measurements of each galaxy in the sample, are illustrated in Figs. C.1 and C.2 in Appendix C.

Interestingly, the only selection criterion $(m_{F365} - m_{F551})_{\rm int} \geq 1.5$ (dashed black line in Fig. 3.13) provides a quiescent sample whose observed colour ranges are well delimited by Eq. 3.1 (see Fig. 3.14). In our sample of quiescent galaxies, we only find a 1 % of galaxies with $m_{F365} - m_{F551}$ and $m_{F551} - J$ colours out of the box delimited by Eq. 3.1. Below, we rather analyse the UVJ-distribution of stellar population parameters, which constitutes the main result of this section:

- From the first rows of Figs. 3.13 and 3.14, less massive quiescent galaxies tend to populate the bluest parts of the UVJ-diagram, whereas at increasing red colours $(m_{F365} - m_{F551})_{\rm int}$ and $(m_{F551} - J)_{\rm int}$ quiescent galaxies continuously present larger stellar masses. The most massive galaxies are also the reddest ones and they are concentrated in the upper part of the UVJ-diagram at decreasing redshift ($(m_{F365} - m_{F551})_{\rm int} \sim 2.0$). Nevertheless, most massive galaxies are scattered in a larger $(m_{F365} - m_{F551})_{\rm int}$ range when we explore the highest redshift panels ($1.5 \leq (m_{F365} - m_{F551})_{\rm int} \leq 2.0$), which has been extensively observed in the last years (e. g. Bower et al., 1992; Kauffmann et al., 2003; Gallazzi et al., 2005; Baldry et al., 2006; Peng et al., 2010). Notice that each panel comprises different stellar mass ranges, as indicated in the upper labels and according to Fig. 3.2, hence the less massive galaxies are only present in the local redshift bins.

- The whole sample shows an expected low dust content (96 % of galaxies present $A_V \leq 0.6$), where the more obscured quiescent galaxies lie on the bluer $(m_{F365} - m_{F551})_{\rm int}$ and $(m_{F551} - J)_{\rm int}$ intrinsic colour regions of the diagram (see Fig. 3.13). On the other hand, if dust effects on the colours are not corrected (observational rest-frame colours, Fig. 3.14), dusty galaxies populate the red parts of the diagram. As sanity check, the colour changes owing to a dust reddening case with $A_V = 0.5$ and $R_V = 3.1$ and the extinction law of Fitzpatrick (1999) are $\Delta(m_{F365} - m_{F551}) \sim 0.28$ and $\Delta(m_{F551} - J) \sim 0.29$ (illustrated in Figs. 3.13 and 3.14), showing the good agreement between the colour changes predicted by an extinction law and the direction of the distribution of increasing extinction values retrieved at any redshift. This also remarks that the extinction values provided by MUFFIT are properly decoupled and not significantly affected by degeneracies with the rest of stellar-population parameters: age and metallicity. Otherwise, the extinction distribution in the UVJ-diagram would be randomly distributed or it would show another colour dependences.

- Regarding ages (third row in Figs. 3.13 and 3.14), older quiescent galaxies in the sample are concentrated in the upper part of the UVJ-diagram, and they therefore tend to populate the intrinsic redder colours $(m_{F365} - m_{F551})_{\rm int}$. Likewise young quiescent galaxies lie on the bluest colours in concordance with the less massive systems in the sample. From Fig. 3.13, we find evidences that the variety of ages presented by quiescent galaxies is linked with the scatter of $(m_{F365} - m_{F551})_{\rm int}$ partly, but not fully linked to this colour. In the rest-frame UVJ-diagram, we also find a non-negligible dependency of the age with $(m_{F551} - J)_{\rm int}$, although milder than the other intrinsic colour. Consequently, our results match with previous findings (e. g. Whitaker et al., 2010) in which the $(m_{F365} - m_{F551})_{\rm int}$ colour is

[4] http://www-astro.physics.ox.ac.uk/~mxc/software/

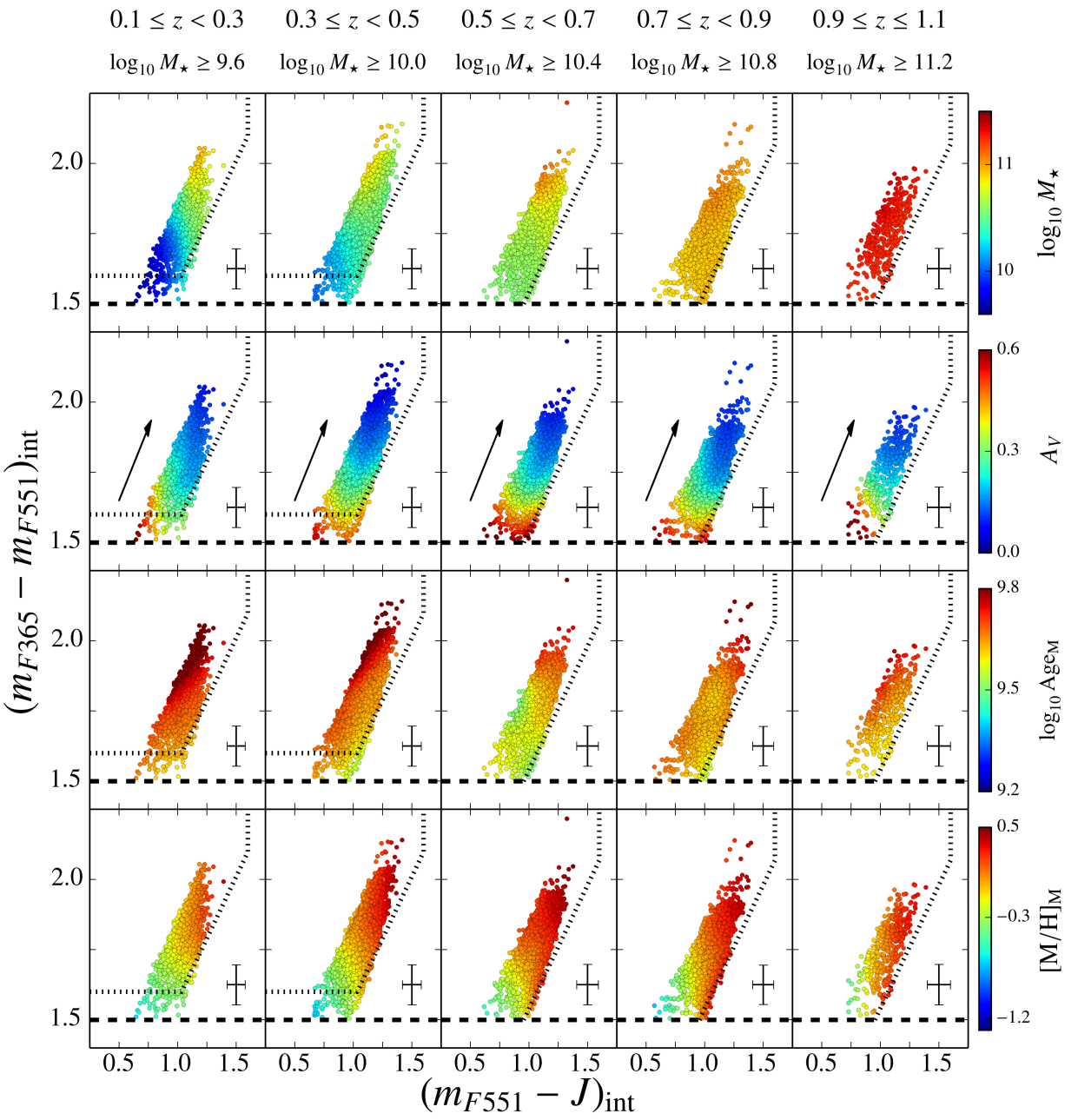

Figure 3.13: The stellar-population parameters in the rest-frame UVJ-diagram. At different redshift bins, we present the intrinsic colours $(m_{F551} - J)_{\rm int}$ (X-axis) and $(m_{F365} - m_{F551})_{\rm int}$ (Y-axis) after correcting for extinction for the mass complete sample of quiescent galaxies (see stellar mass completeness on the top). The different stellar-population parameters are colour coded in function of their values, see the inset colour bars in each panel. *From top to bottom*, stellar mass, extinction, and both mass-weighted age and metallicity. All the parameters were spatially averaged through a LOESS method. Black crosses illustrate the median uncertainties in both $(m_{F551} - J)_{\rm int}$ and $(m_{F365} - m_{F551})_{\rm int}$ intrinsic colours. Dashed black line encloses the rest-frame colour ranges assumed for selecting quiescent galaxies in Moresco et al. (2013, see Eq. 3.1), while dotted line illustrates our colour limit for selecting quiescent galaxies $(m_{F365} - m_{F551})_{\rm int} > 1.5$. We illustrate the colour variations owing to a reddening of $A_V = 0.5$ (black arrow), assuming the extinction law of Fitzpatrick (1999).

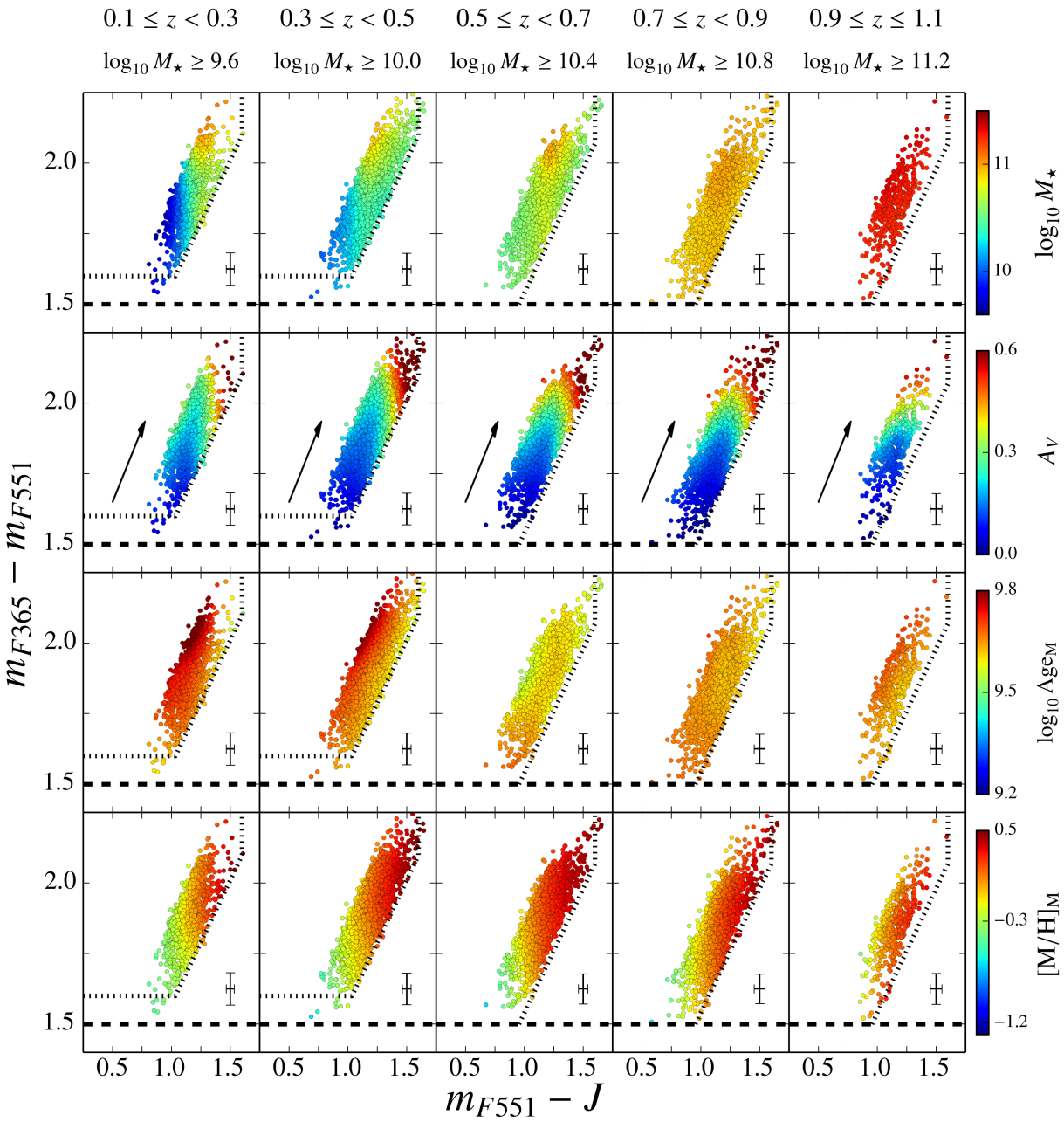

Figure 3.14: As Fig. 3.13, but we plot the rest-frame colours $m_{F551} - J$ (X-axis) and $m_{F365} - m_{F551}$ (Y-axis) instead.

scattered by the ages in the quiescent population. This is not surprising because the $(m_{F365} - m_{F551})_{\rm int}$ colour ranges the 4 000 Å-break that is sensitive to age (e. g. Bruzual A., 1983; Balogh et al., 1999), even though this is also degenerated with the metallicity (Worthey, 1994a; Peletier, 2013). On the contrary, the observed UVJ-diagram (instead of using the dust-free colours, see Fig. 3.14) shows that the observed colour $m_{F365} - m_{F551}$ is not driven by the age. In fact, in some panels of Fig. 3.14, the trends of age with $m_{F365} - m_{F551}$ are not so clear as in the intrinsic ones, or they looks inverted. Thereby, extinction is also playing an important role in this aspect masking and blurring the relation between $(m_{F365} - m_{F551})_{\rm int}$ and age.

- Exploring the metallicity distribution in the UVJ-diagram, see last row in Fig. 3.13, we find out that there is a tight correlation between metallicity and the intrinsic $(m_{F551} - J)_{\rm int}$ colour. There is a clear trend in which larger metallicity contents ($[{\rm M/H}]_{\rm M} > 0.1$ dex) present redder $(m_{F551} - J)_{\rm int} > 1.1$ colours. In this sense, the most metal rich quiescent galaxies lie on the right-hand side of the UVJ-diagram and this trend remains at least up to redshift $z \sim 1$. For a fixed $(m_{F551} - J)_{\rm int}$ colour, the influence of the metal content on the $(m_{F365} - m_{F551})_{\rm int}$ is almost negligible in a wide range of the colour $(m_{F551} - J)_{\rm int}$, but it is not null. Whilst the age distribution is distorted by extinction, the metallicity trend with the colour $m_{F551} - J$ is still prominent (last row in Fig. 3.14). The main extinction effect over metallicity distribution is that at the high redshift panels (or the most massive galaxies, $\log_{10} M_\star > 10.8$ dex), the metallicity exhibits a more remarkable dependence with the $m_{F365} - m_{F551}$ colour respect to its intrinsic counterpart (see Fig. 3.13) and it is substantially less affected than the age.

As we mention above, this is a qualitative analysis since different column panels encompass different stellar mass ranges. A further analysis of the distribution of stellar population parameters on the UVJ-diagram is left for future work (see also Sect. 9.2).

3.6 Number density of quiescent galaxies

To derive the number densities of our sample, $\rho_{\rm N}$, we made use of the $1/V_{\rm max}$ formalism (Schmidt, 1968) in the subsamples that are complete in stellar mass (see Sect. 3.3.4). The errors of $\rho_{\rm N}$ are estimated by the error propagation of the $1/V_{\rm max}$ method, that is associated with Poisson errors (in accordance with similar previous assumptions, e. g. Marshall, 1985; Ilbert et al., 2005). It is worth mentioning that additional uncertainties owing to cosmic variance are also included in the error budget (see also López-Sanjuan et al., 2015a), for which we followed the recipe detailed in Moster et al. (2011). Our estimations point out that the relative cosmic variance for ALHAMBRA is only 5–7 %.

The number density measurements of quiescent galaxies are summarised in Table 3.4 and illustrated in Fig. 3.17 (coloured dots). It is noticeable that there exist a generalised lack of galaxies at $z \sim 0.6$, which is independent of the stellar mass. In order to ensure that this lack of galaxies is not a systematic or bias introduced by our techniques, we check that the number density of the whole population of galaxies in ALHAMBRA also present a lack of galaxies. To support this idea and as sanity check, we studied the distribution of photo-z provided by the parent Gold catalogue instead of the provided by MUFFIT, and those provided making use of other independent photo-z codes, as EAZY and LE PHARE. For EAZY, we allowed the combination of its default templates; whereas for LE PHARE we chose the COSMOS SED templates, which includes dust extinction. As BPZ (Benítez, 2000), both codes can apply constraints on the redshift distribution during the χ^2 fitting procedure, which have demonstrated to improve the photo-z predictions (e. g. Benítez, 2000; Ilbert et al., 2006; Brammer et al., 2008). We therefore assumed the default priors of each code: for EAZY the prior is on R band (Brammer et al., 2008), and for LE PHARE on I (Ilbert et al., 2006). After running EAZY and LE PHARE, the retrieved photo-z distributions are analysed separately for quiescent and star-forming galaxies, in order to discard that the galaxy deficit in the distribution is not driven by a selection bias either. The photo-z distribution for our quiescent sample, see Fig. 3.15, shows

Table 3.4: Logarithm of the number density, $\log_{10}\rho_N[h^3\ \mathrm{Mpc}^{-3}]$, for the quiescent galaxies in our sample at different stellar mass and redshift bins.

	$0.1 \leq z < 0.3$	$0.3 \leq z < 0.5$	$0.5 \leq z < 0.7$	$0.7 \leq z < 0.9$	$0.9 \leq z \leq 1.1$
$9.6 \leq \log_{10} M_\star < 10.0$	-2.75 ± 0.04	–	–	–	–
$10.0 \leq \log_{10} M_\star < 10.4$	-2.57 ± 0.04	-2.71 ± 0.03	–	–	–
$10.4 \leq \log_{10} M_\star < 10.8$	-2.60 ± 0.04	-2.69 ± 0.03	-2.93 ± 0.03	–	–
$10.8 \leq \log_{10} M_\star < 11.2$	-2.83 ± 0.04	-2.88 ± 0.03	-3.06 ± 0.03	-2.95 ± 0.02	–
$\log_{10} M_\star \geq 11.2$	-3.50 ± 0.08	-3.56 ± 0.05	-3.77 ± 0.05	-3.57 ± 0.04	-3.60 ± 0.04

Notes. These values were measured through the $1/V_{\mathrm{max}}$ formalism of each bin. All the bins are complete in stellar mass, $C = 0.95$, otherwise appear dashed. All the values were obtained setting $h = 1$.

Table 3.5: Values ρ_0 and γ that best fit our number density quantification (see Eq. 3.11) at different stellar mass bins.

	$\log_{10}\rho_0$	γ
$10.0 \leq \log_{10} M_\star < 10.4$	-2.36 ± 0.10	-2.40 ± 0.80
$10.4 \leq \log_{10} M_\star < 10.8$	-2.48 ± 0.10	-1.45 ± 0.79
$10.8 \leq \log_{10} M_\star < 11.2$	-2.78 ± 0.05	-0.67 ± 0.26
$\log_{10} M_\star \geq 11.2$	-3.49 ± 0.08	-0.35 ± 0.33

Notes. There is no ρ_0 and γ fitting values for the lowest stellar mass bin, $9.6 \leq \log_{10} M_\star < 10.$, because this subsample is only available at the lowest redshift bin, $0.1 \leq z < 0.3$. All the values were obtained setting $h = 1$.

a remarkable agreement among the three different photo-z codes. In fact, the three codes find a prominent lack of galaxies at $0.5 < z < 0.7$ (see grey region in Fig. 3.15), and the rest of structures are also similar independently of the code used. Regarding the star-forming photo-z distribution, Fig. 3.16, there are more subtle discrepancies among the output codes. Although at $0.5 < z < 0.7$ BPZ2.0 (from Gold catalogue) and EAZY also retrieve a lack of galaxies, indeed milder than the quiescent case, for LE PHARE this decrement in number may be restricted at only $0.5 < z < 0.6$ but it also exists. Consequently, the lack of red galaxies at $0.5 < z < 0.7$ is real and it is not associated to MUFFIT systematics or a biased selection. This shows that even though ALHAMBRA comprises seven uncorrelated fields on the sky, some large scale structures escape from this survey.

The number density trends are quantified through a redshift-dependent power-law function (solid lines in Fig. 3.17) of the form:

$$\rho_N(z) = \rho_0\ (1+z)^\gamma\ . \tag{3.11}$$

For the different stellar mass bins, we provide the values ρ_0 and γ that best fit our number density values in Table 3.5 (all the number density estimations at $0.5 \leq z < 0.7$ were removed from the fit). From Fig. 3.17, we visualize three remarkable results:

- The number density evolution is well fitted by the power-law function Eq. 3.11.
- There is a general and clear trend in which the number density of quiescent galaxies tends to increase with time up to the present.
- At decreasing stellar mass, quiescent galaxies show a more prominent increasing in their number density. Thus, the most massive quiescent galaxies present γ values close to zero, and the least massive galaxies larger values than indicate a larger evolution in number.

The least massive bin in our sample ($9.6 \leq \log_{10} M_\star < 10.0$) greatly reflects the stellar mass range in which the stellar mass function of quiescent galaxies present a local minimum or valley (Drory et al., 2009;

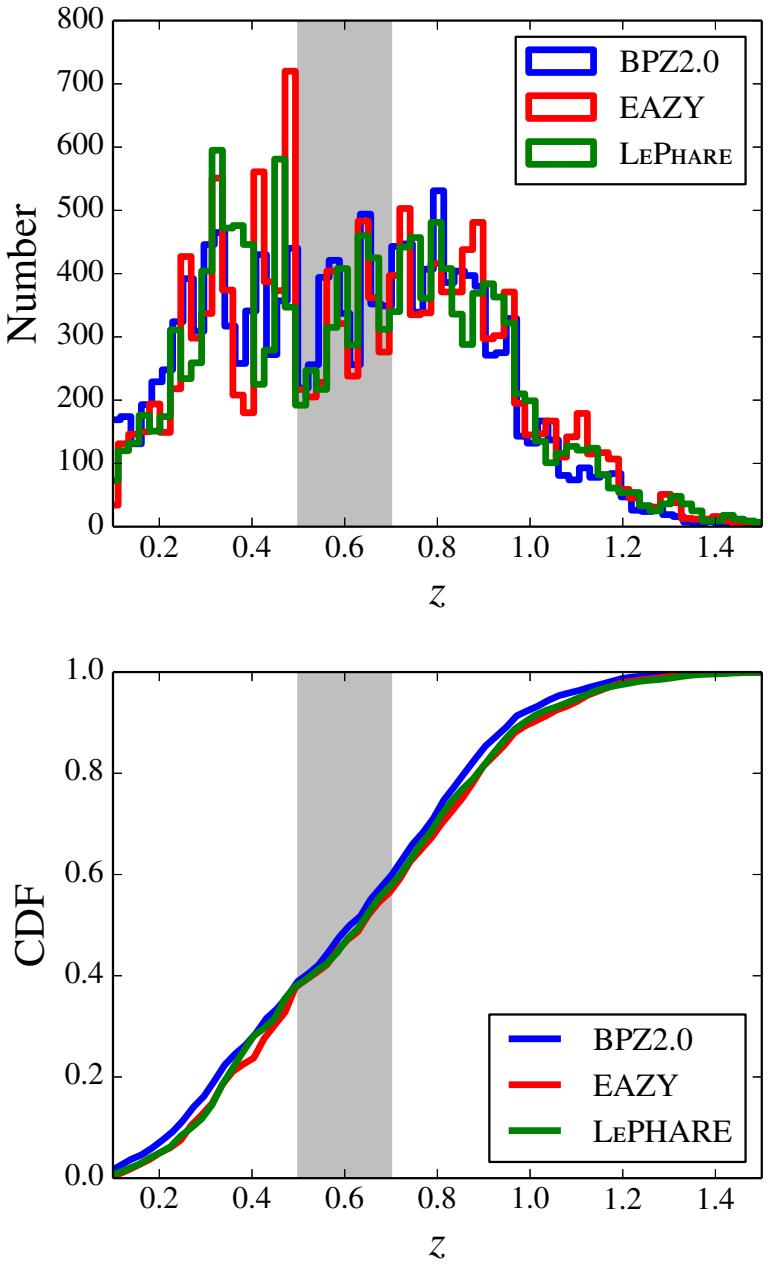

Figure 3.15: Photometric-redshift distribution and cumulative distribution function (CDF) of quiescent galaxies from the ALHAMBRA Gold catalogue down to $0.1 \leq z \leq 1.5$ using the codes BPZ2.0, EAZY, and LE PHARE. To guide the eye, grey area encloses the redshift bin $0.5 \leq z \leq 0.7$.

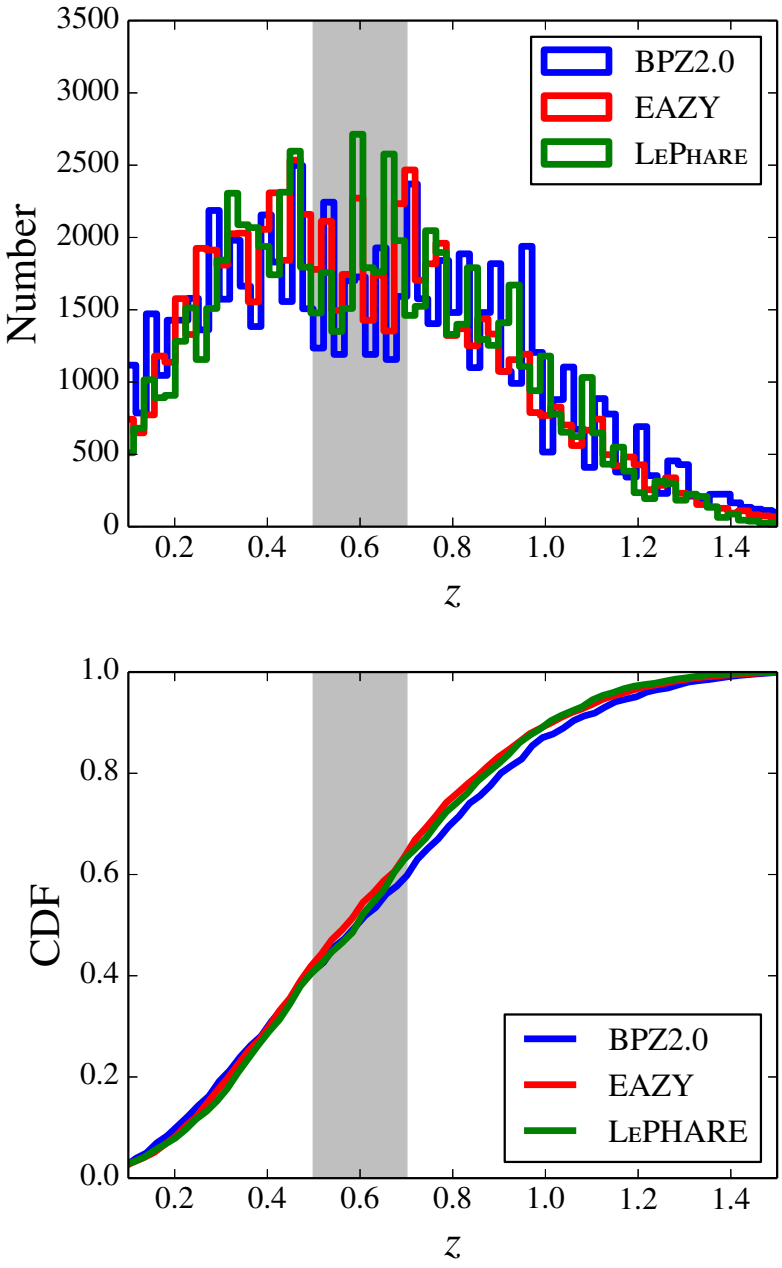

Figure 3.16: Photometric-redshift distribution and cumulative distribution function (CDF) of star-forming galaxies from the ALHAMBRA Gold catalogue down to $0.1 \leq z \leq 1.5$ using the codes BPZ2.0, EAZY, and LE PHARE. To guide the eye, grey area encloses the redshift bin $0.5 \leq z \leq 0.7$.

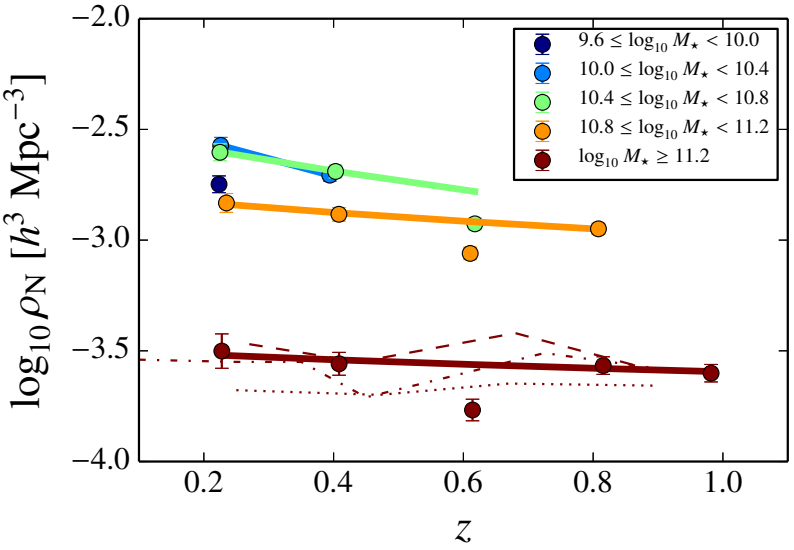

Figure 3.17: Evolution of the number density of quiescent galaxies in ALHAMBRA (solid lines) with redshift (X–axis), for different stellar mass bins (see *inner-panel* colours). Over-plotted, we show the evolution on the number density of massive quiescent galaxies, $\log_{10} M_\star \geq 11$, with redshift from the previous work of Pozzetti et al. (2010, dashed line), Moresco et al. (2013, dotted line), and Moustakas et al. (2013, dash-dot line). In all cases, the number densities at the 0.5<z<0.7 bin are excluded from the fit as explained in the text.

Tomczak et al., 2014), but owing to completeness reasons we cannot stablish the variation on its number density. For larger galaxy masses, our fit establishes that the number density of quiescent galaxies $\rho_N(z)$ systematically grows ~ 50, 25, 10, 5 % (from the $10.0 \leq \log_{10} M_\star < 10.4$ bin to the $\log_{10} M_\star > 11.2$ bin, respectively) $\Delta z = 0.2$ (see Table 3.5), at least wherever our sample is complete in stellar mass. Thereby, the number density for the case $\log_{10} M_\star \geq 11.2$ shows the least steep growth in number density with a value of 0.1 dex in the redshift range $z = 0.1$–1.1.

Ilbert et al. (2013) reported that massive quiescent galaxies, stellar masses of $\log_{10} M_\star > 11.2$ dex, suffer a rapid and efficient increase in number at $1 < z < 3$. However, they do not exhibit a prominent evolution since $z \sim 1$, where the great number density variations of quenched galaxies are more focused to the less massive systems (also observed by e. g. Davidzon et al., 2013), in agreement with our results (see Table 3.5). In the work by Pozzetti et al. (2010), the authors found that the number density evolution of quiescent galaxies ($\log_{10} M_\star > 11.$ dex) is not significant, ~ 0.1 dex, since $z \sim 0.85$ up to $z \sim 0.25$; while in this work this variation is ~ 0.12 dex. Moresco et al. (2013) retrieved that quiescent galaxies ($\log_{10} M_\star \sim 10.5$ dex) increase their number density by a factor of ~ 80 % between $z \sim 0.65$ and $z \sim 0.2$ compatible with ours (60 %), and the massive ones ($\log_{10} M_\star > 11.$ dex) were compatible with no evolution. Finally and with a different selection criteria, Moustakas et al. (2013) found out that quiescent galaxies in the mass range $10.0 < \log_{10} M_\star < 10.5$ increase a factor of 60 % ± 20 % between redshift 0.2 and 0.6; for $10.5 < \log_{10} M_\star < 11.0$ around 40 % ± 10 % between $z = 0.2$–0.8 , and for $11.0 < \log_{10} M_\star < 11.5$ the increment is 20 % ± 10 % at $z = 0.2$–1.0. For the same redshift and stellar mass bins than Moustakas et al. (2013), we obtained number density variations of 90 % ± 40 %, 60 % ± 20 %, 40 % ± 20 % respectively, that is, a slightly larger evolution of the density number respect them and where both results are close to an agreement after accounting for the uncertainties. In Fig. 3.17, we illustrate the number density for the most massive bin, $\log_{10} M_\star > 11.2$, in this research along with those mentioned above.

In the "downsizing" scenario more massive systems were formed at higher redshifts than their less massive counterparts. For observations at $z \lesssim 1$, a direct consequence of the "downsizing" is that the number of less massive systems would increase up to the present days, since the more massive galaxies were mainly

formed at an early formation epoch $z_f \gtrsim 1.0$ and the bulk of less massive systems is still being assembled ($z_f < 1.0$, see Thomas et al., 2005). An increment in number of less massive systems, and independently of the quenching mechanism that move star-forming galaxies to the quenched sequence, would imply also a growth in number of less massive quiescent galaxies, and therefore, our results favour a "downsizing" scenario. This continuous arrival of new quenched galaxies additionally shows that less massive systems are more largely affected by the "progenitor" bias, whereas in the more massive ones the inclusion of new members is not so significant a priori.

3.7 The stellar populations of quiescent galaxies since $z \sim 1$

This section includes the main results of this research, mainly focused on the evolution of the stellar population distribution of ages, metallicities, and extinctions that mainly constitute this kind of systems (Sects. 3.7.2– 3.7.4), which were obtained using MUFFIT and mixtures of two SSPs from the BC03 SSP model set (see Sect. 3.2.1 for a brief summary).

3.7.1 Probability distribution functions of stellar population parameters

Previously to the distribution analysis of the different stellar population parameters, we should consider that we are fitting galaxies scattered in a wide redshift range, where their stellar population uncertainties also depend on redshift. Moreover, certain ranges of stellar-population parameters are intrinsically more subject to SED-fitting errors (see fig. 11 in Díaz-García et al., 2015); for instance, old stellar populations (~ 9 Gyr) are more uncertain than young stellar populations, which are better constrained under similar signal-to-noise ratio conditions. To illustrate this, the median of the age, metallicity, and extinction uncertainties obtained by MUFFIT and the ALHAMBRA dataset is showed in Fig. 3.18. Apparently, the age uncertainties decrease at increasing redshift, although at higher redshifts these are also younger, i. e. better determined, and the relative errors are larger. In addition, at higher redshifts the age range of SSP models cannot be much larger than the age of the Universe and a wider wavelength range of the rest-frame NUV regime is observed allowing us to better constraint their stellar population parameters. This behaviour was also observed by simulations (Díaz-García et al., 2015). As expected, the metallicity uncertainties are larger at higher redshifts and at decreasing stellar masses. Regarding the extinction, the median uncertainty does not present great dependencies with redshift, although the most uncertainty extinctions are only present at the highest redshifts (see vertical bars in Fig. 3.18).

Consequently, the effects of uncertainties are able to modify some distribution parameters, such as its median or width (ω, defined as the difference of the percentiles 84^{th} and 16^{th} of the distribution), making difficult both a direct comparison among the distribution of the stellar-population parameters at different redshifts and a precise reconstruction of the intrinsic distribution shape without noise effects.

For dealing with the above drawbacks and minimizing the impact of uncertainties on the distributions of stellar population parameters, we made use of a maximum likelihood estimator method (MLE), which constraints the most likely set of parameter values that maximizes the probability distribution describing our sample. In particular, we adapted the MLE developed by López-Sanjuan et al. (2014) for removing the observational errors from the intrinsic distributions of stellar population parameters in this work, that is equivalent to deconvolve the observational errors from our desired stellar-population distributions, or at least for minimizing their effects. As a result, we obtained a set of functional and analytical distributions (distributions of age, metallicity, and extinction) fitted by log-normal distributions properly, that we re-normalize with their number densities (see Sect. 3.6) in order to build the PDFs of age, metallicity, and extinction for the first time. For a detailed presentation of the whole process to obtain the PDFs of the stellar population parameters (including the MLE method specifically performed for the present research) and its parametrization, we refer readers to Appendix D.

In Figs. 3.19 and 3.20, we illustrate the PDFs of mass-weighted formation epochs, ages, metallicities, and extinctions for the quiescent galaxy population, taking the values obtained from the MLE at different

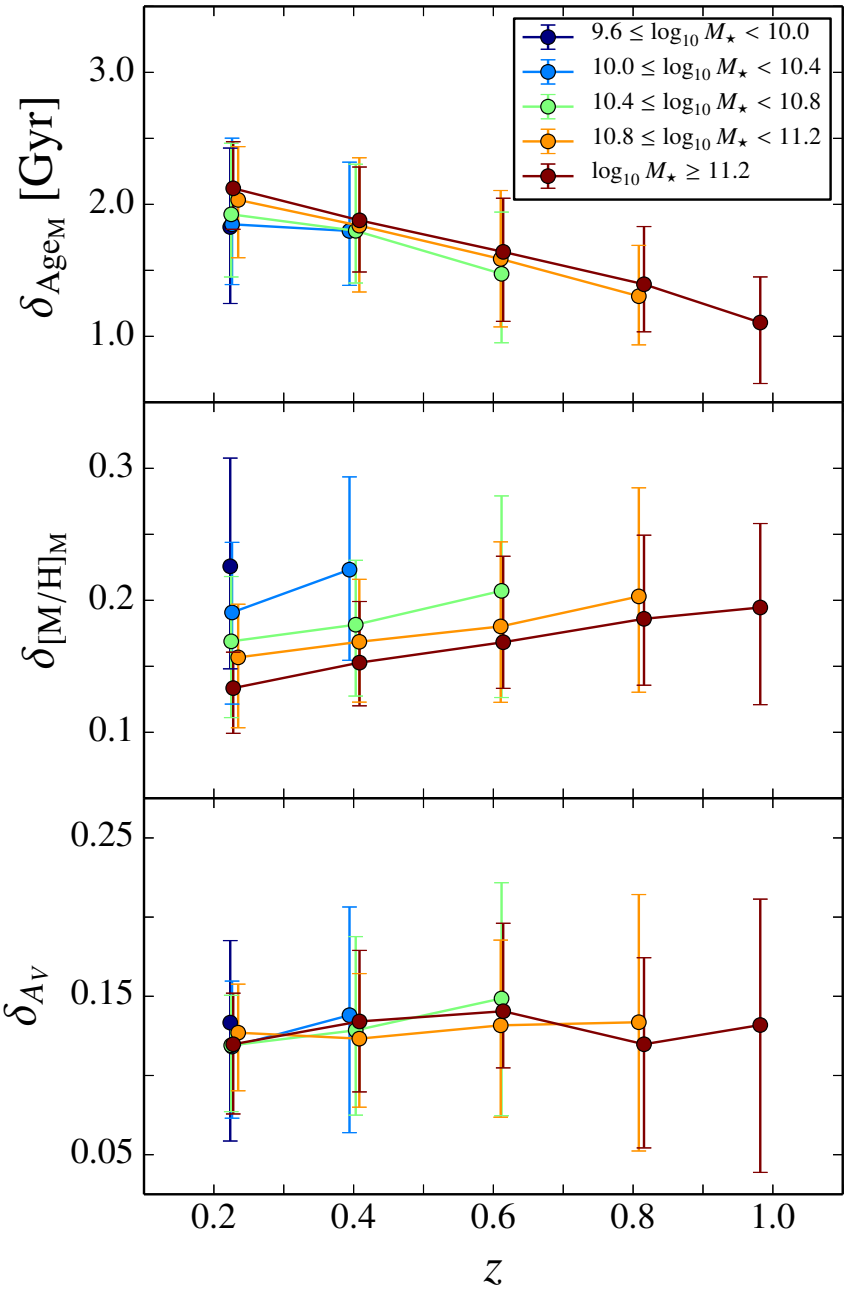

Figure 3.18: *From top to bottom*, median of the age, metallicity, and extinction uncertainties at different redshifts and stellar mass bins (see inner panel). Vertical bars enclose the 68 % confidence level of the distribution of uncertainty values.

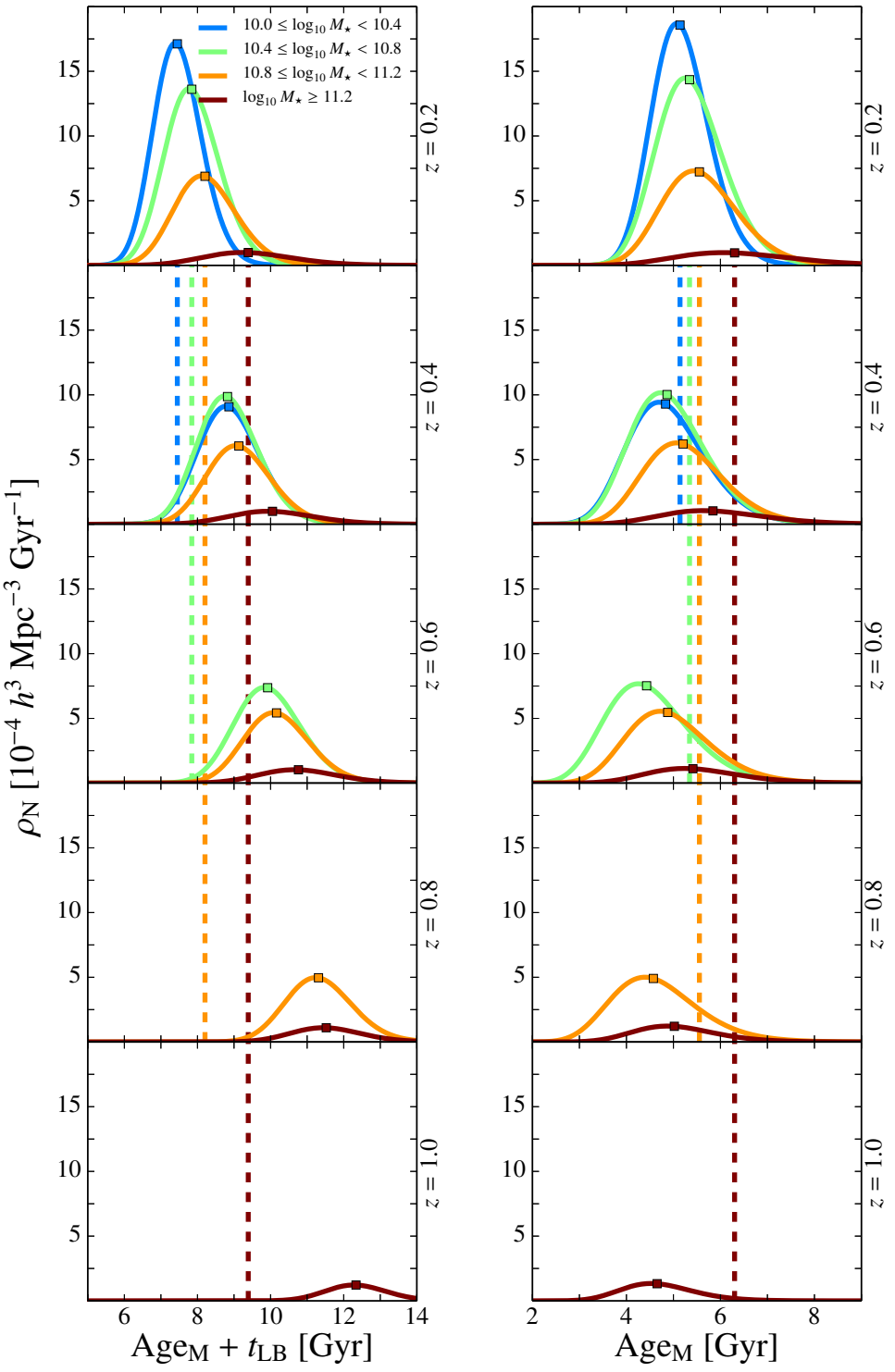

Figure 3.19: Probability distribution functions (PDF) of mass-weighted formation epochs (*left panels*) and ages derived (*right panels*) from the MLE (details in the text) for the quiescent galaxy population at different redshift bins and stellar masses (see colours in legend). Square-shape markers set the median of the distributions. Dashed coloured lines illustrate the median of the distributions at the lowest redshift bin ($z = 0.2$) for comparing purposes. All the distributions correspond to the ranges in which our sample is complete in stellar mass.

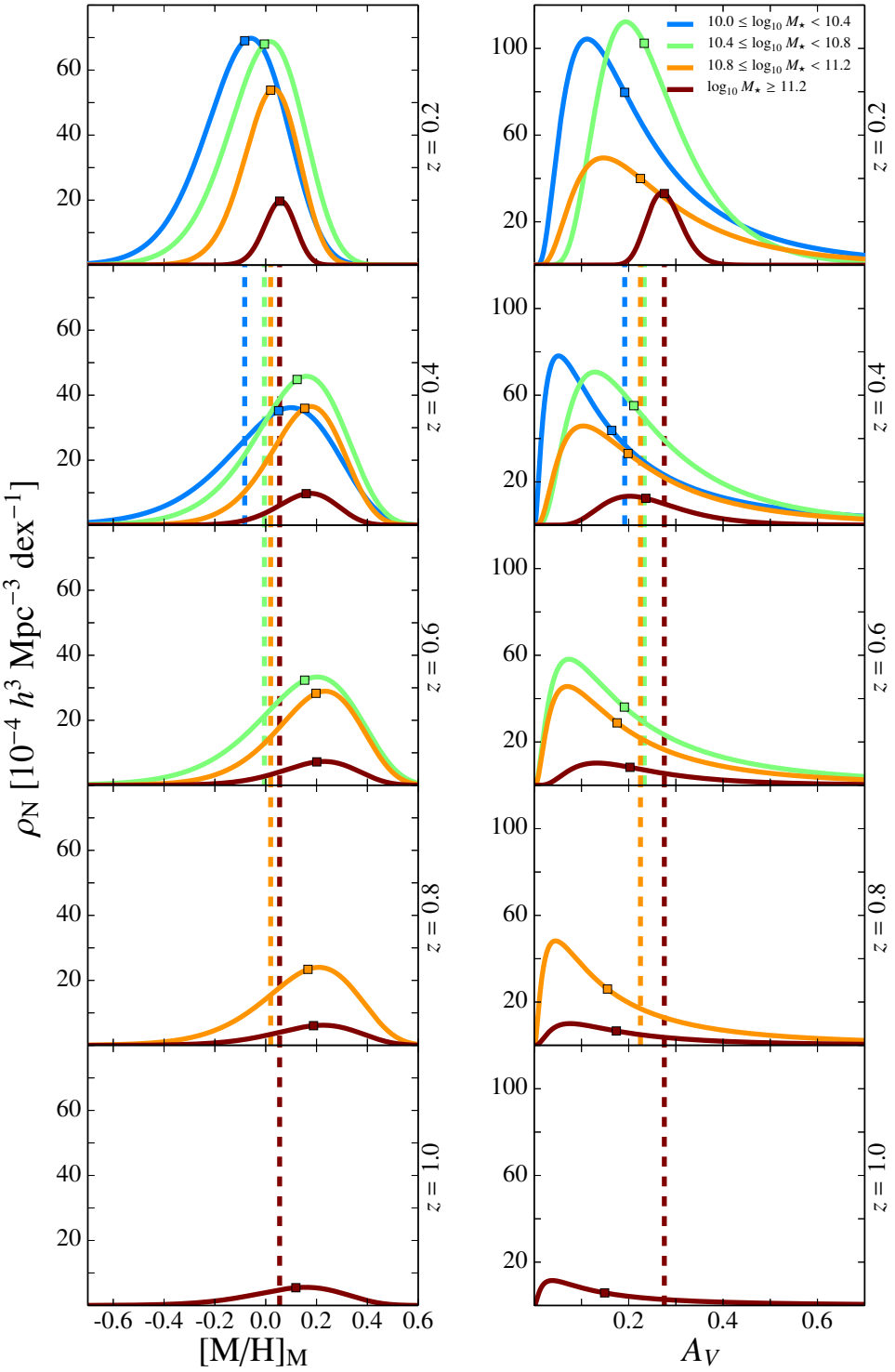

Figure 3.20: As Fig. 3.19, but for the mass-weighted metallicities (*left panels*) and extinctions (*right panels*).

Table 3.6: Medians of the mass-weighted age PDFs for quiescent galaxies, binned in stellar mass and redshift. Top (bottom) numbers stablish the 84^{th} (16^{th}) percentile for each distribution.

Age_{M} [Gyr]	$z = 0.2$	$z = 0.4$	$z = 0.6$	$z = 0.8$	$z = 1.0$
$9.6 \leq \log_{10} M_\star < 10.0$	$5.04^{+0.92}_{-0.78}$	–	–	–	–
$10.0 \leq \log_{10} M_\star < 10.4$	$5.14^{+0.64}_{-0.57}$	$4.83^{+0.91}_{-0.77}$	–	–	–
$10.4 \leq \log_{10} M_\star < 10.8$	$5.34^{+0.76}_{-0.67}$	$4.86^{+0.89}_{-0.75}$	$4.43^{+0.99}_{-0.81}$	–	–
$10.8 \leq \log_{10} M_\star < 11.2$	$5.56^{+0.88}_{-0.76}$	$5.21^{+0.93}_{-0.79}$	$4.88^{+0.97}_{-0.81}$	$4.57^{+1.01}_{-0.83}$	–
$\log_{10} M_\star \geq 11.2$	$6.32^{+1.39}_{-1.14}$	$5.85^{+1.23}_{-1.01}$	$5.42^{+1.08}_{-0.90}$	$5.02^{+0.95}_{-0.80}$	$4.65^{+0.83}_{-0.70}$

Notes. All the bins are complete in stellar mass, $C = 0.95$, otherwise appear dashed. For the $9.6 \leq \log_{10} M_\star < 10.0$ case, these values were obtained by the MLE methodology assuming $\mu_2 = \mu_1 = \sigma_2 = \sigma_1 = 0$ owing to the low number of galaxies.

Table 3.7: As Table 3.6, but for the mass-weighted formation epoch PDFs.

$\text{Age}_{\text{M}} + t_{\text{LB}}$ [Gyr]	$z = 0.2$	$z = 0.4$	$z = 0.6$	$z = 0.8$	$z = 1.0$
$9.6 \leq \log_{10} M_\star < 10.0$	$7.53^{+0.88}_{-0.79}$	–	–	–	–
$10.0 \leq \log_{10} M_\star < 10.4$	$7.45^{+0.69}_{-0.63}$	$8.86^{+0.89}_{-0.81}$	–	–	–
$10.4 \leq \log_{10} M_\star < 10.8$	$7.84^{+0.79}_{-0.72}$	$8.82^{+0.87}_{-0.79}$	$9.92^{+0.95}_{-0.87}$	–	–
$10.8 \leq \log_{10} M_\star < 11.2$	$8.21^{+0.90}_{-0.81}$	$9.13^{+0.92}_{-0.84}$	$10.16^{+0.93}_{-0.85}$	$11.31^{+0.94}_{-0.87}$	–
$\log_{10} M_\star \geq 11.2$	$9.39^{+1.31}_{-1.14}$	$10.05^{+1.22}_{-1.09}$	$10.76^{+1.12}_{-1.01}$	$11.52^{+1.00}_{-0.92}$	$12.33^{+0.86}_{-0.80}$

redshifts and stellar masses (see Eqs.D.2–D.4 and Tables D.1–D.3 for the analytical expressions and their parameters respectively). Notice that we do not provide the redshift-dependent PDFs of quiescent galaxies in the stellar mass range $9.6 \leq \log_{10} M_\star < 10.0$, because the reliability of the MLE method is compromised owing to the low number of sources. Instead, and only for the least massive case, we applied the MLE method assuming a non-redshift dependency of the PDF parameters (i. e. $\mu_2 = \mu_1 = \sigma_2 = \sigma_1 = 0$, see Appendix D), to set the average values of the median and width of the stellar population parameter distributions in the redshift bin $0.1 \leq z < 0.3$ (see values in Tables 3.7–3.9). We treat the detailed analysis of each PDF (mass-weighted formation epoch, age, metallicity, and extinction) more intensively in the subsequent Sects. 3.7.2, 3.7.3, and 3.7.4 respectively.

3.7.2 Formation epochs and ages

The aim of this section is to unveil the typical ages and formation epochs of quiescent galaxies in order to constraint and discern the different scenarios or processes that are able to explain the evolution of these galaxies with redshift. We mostly focus on the changes of both median and width (defined as the difference between the 84^{th} and 16^{th} percentiles of the distribution) of the mass-weighted formation epoch and age PDFs. In Fig. 3.21, we present these values during the last 8 Gyr (from $z \sim 1.1$), which compose the main results of this section. It is worth reminding that throughout this work, the mass-weighted formation epoch is defined as the addition of the mass-weighted age (Age_{M}) and lookback time (t_{LB}), which does not strictly match with the definition of formation epoch in previous works (it is a proxy actually).

From Fig. 3.21 (panel *a* and *c*) and Tables 3.7 and 3.6, we observe that the medians of the mass-weighted formation epoch and age PDFs are correlated with the stellar mass of quiescent galaxies as well, showing

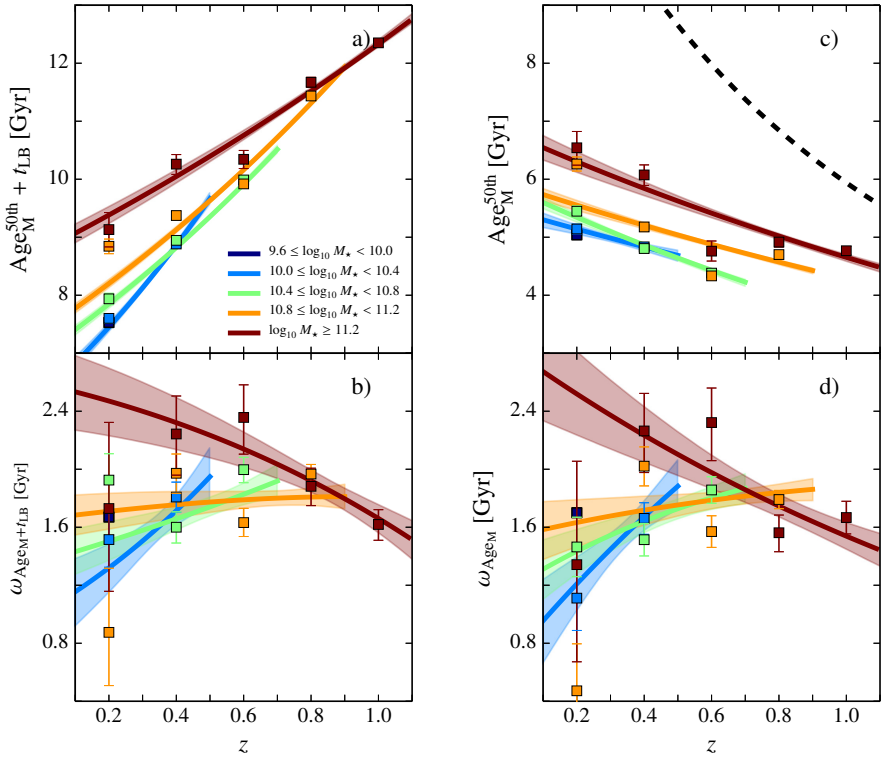

Figure 3.21: Evolution of the medians (*top panels*) and widths (ω, *bottom panels*) of the mass-weighted formation epoch (*left column*) and age (*right column*) PDFs of the quiescent population along the sample cosmic time for different stellar mass bins. The shaded regions delimit the 1 σ uncertainties of both parameters. The square-shape markers illustrate the average median and width assuming for the MLE deconvolution $\mu_2 = \mu_1 = \sigma_2 = \sigma_1 = 0$. Dashed black line illustrates the age of the Universe at different redshifts assuming a ΛCDM cosmology with $H_0 = 71$ km s^{-1}, $\Omega_M = 0.27$, and $\Omega_\Lambda = 0.73$.

systematic variations that depends of the stellar mass. Our results evidence that more massive quiescent galaxies present a larger stellar content of older stars than the less massive quiescent systems, which are preferentially formed at more recent epochs showing younger stellar populations on average. In this sense, the formation epoch and age PDFs built from the results provided by MUFFIT using the ALHAMBRA dataset also agree with the "downsizing" scenario. Moreover, the redshift coverage and wide mass range of galaxies in our sample allow us to track back the "downsizing" scenario of quiescent galaxies further than the local Universe (up to $z \sim 1.0$).

If quiescent galaxies had evolved passively (without any remain of star formation or completely quenched) since they entered in the quiescent sample, the redshift at which the stellar mass was assembled would not present any variation (z_f constant) and the median in Fig. 3.21 would be constant. The median of the formation epoch PDFs of quiescent galaxies exhibits a continuous and general decrement towards lower redshifts for all the stellar masses. For the most massive case, $\log_{10} M_\star \geq 11.2$ which extends in the largest redshift range too, the formation epoch at $z \sim 1.0$ was ~ 12 Gyr (equivalent to a redshift formation $z_f \sim 4.5$), whereas at $z = 0.2$ the median decreases up to ~ 9 Gyr (i. e. at a redshift formation $z_f \sim 1.5$). As we can infer from our results (see Fig. 3.21 and Table 3.7), the evolution of the median formation epochs is generalised for the whole sample independently of the stellar mass range: the lower the stellar mass, the more dramatic the evolution of the median formation epoch is. For the most massive quiescent sample the evolution of the median is around 2.9 Gyr between $z = 0.2$ and $z = 1.0$, while this change would be of 3.1, 2.1, and 1.4 Gyr at decreasing stellar masses from $z = 0.8$, 0.6, and 0.4 down to $z = 0.2$ respectively. Regarding the

Table 3.8: As Table 3.6, but for the mass-weighted metallicity PDFs.

$[M/H]_M$	$z = 0.2$	$z = 0.4$	$z = 0.6$	$z = 0.8$	$z = 1.0$
$9.6 \leq \log_{10} M_\star < 10.0$	$-0.21^{+0.2}_{-0.24}$	–	–	–	–
$10.0 \leq \log_{10} M_\star < 10.4$	$-0.08^{+0.15}_{-0.18}$	$0.05^{+0.20}_{-0.25}$	–	–	–
$10.4 \leq \log_{10} M_\star < 10.8$	$-0.00^{+0.14}_{-0.16}$	$0.12^{+0.17}_{-0.20}$	$0.15^{+0.18}_{-0.24}$	–	–
$10.8 \leq \log_{10} M_\star < 11.2$	$0.02^{+0.10}_{-0.12}$	$0.15^{+0.14}_{-0.16}$	$0.20^{+0.15}_{-0.19}$	$0.17^{+0.17}_{-0.22}$	–
$\log_{10} M_\star \geq 11.2$	$0.05^{+0.06}_{-0.07}$	$0.16^{+0.11}_{-0.13}$	$0.20^{+0.14}_{-0.17}$	$0.19^{+0.16}_{-0.19}$	$0.12^{+0.17}_{-0.21}$

ages (Fig. 3.21 and Table 3.6), the quiescent population presents older stellar populations at lower redshifts independently of the stellar mass bin, as expected for passive or quenched systems. From the most massive case $\log_{10} M_\star \geq 11.2$ down to $10 \leq \log_{10} M_\star < 10.4$, the increment of ages are 1.7, 1.0, 0.9, and 0.3 Gyr since $z = 0.2$ to $z = 1.0$, 0.8, 0.6, and 0.4 respectively.

Regarding the width of these distributions (panel *b* and *d* in Fig. 3.21 and Tables 3.7 and 3.6), all the PDF exhibit similar width values fairly constrained in the range $\sim$ 1.0–2.5 Gyr, where the preferred or likely value is close to 1.6 Gyr. Only the most massive bin ($\log_{10} M_\star \geq 11.2$) slightly exhibits a more prominent difference with the rest of masses, with width values larger than $\sim$ 1.8 Gyr.

Our results point out that the evolution with redshift of the widths of the age/formation epoch PDFs is mild. The widths of the mass-weighted age/formation epoch PDFs decrease at larger cosmic times, with values in the range $\omega_M \sim$ 1–2.5 Gyr. There are subtle differences about the evolution of the width of the mass-weighted age/formation epoch PDFs amongst different stellar mass bins; except for the most massive bin, $\log_{10} M_\star \geq 11.2$, where results are compatible with an increment of the width since $z \sim 1.1$ ($\omega_M \sim$ 1.6–2.5 Gyr).

3.7.3 Evolution of the metal content

The metal content in quiescent galaxies also contributes to understand how these galaxies were formed and how they have evolved since they quenched their star formation. Both the median and width of the mass-weighted metallicity PDFs, see Fig. 3.22 and Table 3.8, shed light on the amount of metals that quiescent galaxies typically present, as well as on how they have evolved from $z = 1.1$.

From the results in Fig. 3.22 (panel *e*) and Table 3.8, it is immediate to infer that there is a clear relation between stellar mass and metallicity, in the sense that, at any redshift, the larger the galaxy mass, the larger the metal content. This relation is usually referred as the stellar mass-metallicity relation (MZR), which has been observed in previous and recent studies usually without distinction between quiescent and star forming galaxies (Trager et al., 2000; Tremonti et al., 2004; Gallazzi et al., 2005; Panter et al., 2008; González Delgado et al., 2014a). Our results agree with the MZR and confirm that this relation also exists for pure quiescent galaxies. In addition, we can confirm that the MZR of quiescent galaxies is present not only at low redshift but also at earlier times in the Universe. In general, quiescent galaxies present median metallicities around solar and super-solar values. Only the least massive galaxies at the lowest redshift in our sample exhibit sub-solar metallicities.

The median of the mass-weighted metallicity PDF also exhibits a dependency with redshift (see panel *e* in Fig. 3.22 and Table 3.8). For the most massive galaxies, for which the redshift evolution can be evaluated properly, we find that median metallicity increases from the earliest times up to a certain redshift, reaching a maximum, after which the metallicity decreases again up to the present time. For instance, for galaxies with $\log_{10} M_\star \geq 10.8$, there is an increase of their $[M/H]_M^{50th}$ from 0.1 dex at $z \sim 1$ to a maximum value of $[M/H]_M^{50th} \sim 0.2$ dex at $z \sim$ 0.60–0.65, to subsequently decrease reaching solar metallicity values at $z = 0.1$.

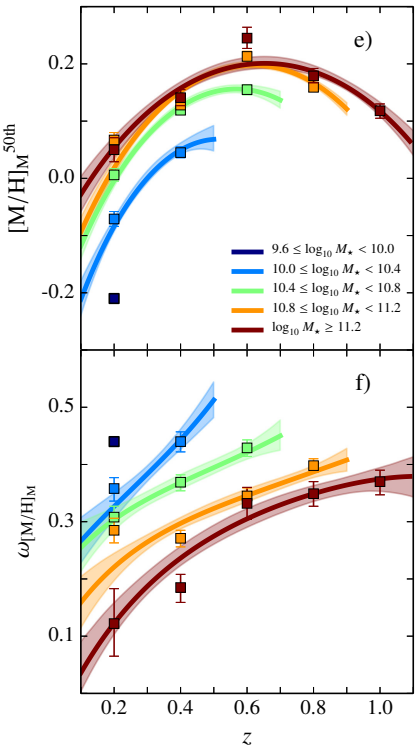

Figure 3.22: Same as Fig. 3.21, but showing the probability distribution function (PDF) of the mass-weighted metallicity.

For lower stellar masses, $\log_{10} M_\star < 10.8$, there is also a general tendency in which the median metallicity increases by $\Delta[M/H]_M^{50th} \sim 0.25$ dex from $z = 0.1$ up to $z \sim 0.55$. Whether or not these galaxies decrease their metallicities at larger redshifts cannot be confirmed due to the completeness of our galaxy sample. Nevertheless, our results suggest that the position of the maximum median-metallicity is also correlated with the stellar mass, in the sense that the larger the galaxy stellar mass the higher the redshift of the maximum median-metallicity. From Table D.2, we easily derive the redshift of the maximum as $z_{[M/H]_M} = -\mu_1/(2\mu_2)$ with values 0.66 ± 0.14, 0.62 ± 0.09, 0.57 ± 0.12, and 0.52 ± 0.26 at decreasing stellar masses respectively.

Regarding the width of the metallicity PDFs (panel f of Fig. 3.22 and Table 3.8), there are evidences that the metallicity distribution of quiescent galaxies is wider at lower mass regimes, whereas for the more massive ones the range of metallicity values is narrower. Therefore, the width of the metallicity PDF is anti-correlated with the stellar mass, again in agreement with the local MZR. This behaviour is clearly observed at any redshift in our sample up to $z \lesssim 1.1$. The width of the metallicity PDFs also present an evolution with redshift, in the sense that the higher the redshift the wider the metallicity PDF. We do not appreciate that the variation of the width is correlated with the stellar mass. At $z \sim 0.3$ the width evolves $\Delta\omega_{[M/H]_M} \sim 0.1$ dex every $\Delta z = 0.2$, while at $z \sim 0.7$ is $\Delta\omega_{[M/H]_M} \sim 0.05$ dex independently of the stellar mass range. It is worth reminding that the widths of the PDFs that we present here have been corrected from the data uncertainties that tend to broaden the observed distributions. In this sense, the widths of the PDFs should reflect the intrinsic, real values of the population.

3.7.4 The extinction in the quiescent population

Although the extinction is not strictly a stellar population parameter, this is usually related with the star formation processes that occur in the galaxy, and at the same time, it masks the colours of the underlying stellar populations. Overall, the extinction PDF of quiescent galaxies derived in this research, see Fig. 3.23

Table 3.9: As Table 3.6, but for the extinction PDFs.

A_V	$z = 0.2$	$z = 0.4$	$z = 0.6$	$z = 0.8$	$z = 1.0$
$9.6 \leq \log_{10} M_\star < 10.0$	$0.17^{+0.13}_{-0.07}$	–	–	–	–
$10.0 \leq \log_{10} M_\star < 10.4$	$0.19^{+0.21}_{-0.10}$	$0.16^{+0.32}_{-0.11}$	–	–	–
$10.4 \leq \log_{10} M_\star < 10.8$	$0.23^{+0.13}_{-0.08}$	$0.21^{+0.22}_{-0.11}$	$0.19^{+0.32}_{-0.12}$	–	–
$10.8 \leq \log_{10} M_\star < 11.2$	$0.22^{+0.21}_{-0.11}$	$0.20^{+0.25}_{-0.11}$	$0.17^{+0.28}_{-0.11}$	$0.15^{+0.32}_{-0.10}$	–
$\log_{10} M_\star \geq 11.2$	$0.27^{+0.04}_{-0.04}$	$0.23^{+0.12}_{-0.08}$	$0.20^{+0.19}_{-0.10}$	$0.17^{+0.26}_{-0.10}$	$0.15^{+0.33}_{-0.10}$

and Table 3.9, show predominant low extinctions irrespectively of the stellar mass or redshift. The extinction values of our quiescent galaxies are typically below $A_V \lesssim 0.6$, despite for our analysis with MUFFIT we allowed extinction values as large as $A_V = 3.1$. Indeed, the median extinctions for all the stellar masses and redshifts do not exceed the value $A_V^{50\text{th}} = 0.3$.

From Fig. 3.23 (panel *g*), we infer a subtle relation between the stellar mass and the extinction, so that the median of the extinction PDF increases slightly with the stellar mass. This accounts for up to $\Delta A_V^{50\text{th}} \lesssim 0.1$ over the galaxy mass range of the sample, remaining approximately the same with along the cosmic time under study. Regarding the evolution with redshift, we find that quiescent galaxies at higher redshifts tend to exhibit extinctions lower than their counterparts at low redshift, reaching medians of the extinction PDF of $A_V^{50\text{th}} \lesssim 0.2$ for $z \geq 0.6$.

The width of the extinction PDF is anticorrelated with the stellar masses: the lower the stellar mass the larger the width of the PDF is, except for the case $10.8 \leq \log_{10} M_\star < 11.2$. At increasing redshift the width of the extinction PDF gets larger for all the stellar mass ranges, where less massive quiescent galaxies present broader probability distributions at any redshift, and consequently present a larger range of likely extinction values than the more massive ones. As in the metallicity case, there are evidences that the distribution of extinction in quiescent galaxies suffer a process of "narrowing" when quiescent galaxies are observed at more local redshifts. The rate of "narrowing" does not show a great dependence with the stellar mass range under study. This broadening may be noticeable, and depending of the redshift range, it can be doubled its width. Note that at $0.1 \leq z < 0.2$ and $\log_{10} M_\star \geq 11.2$, the assumption of linearity for $\sigma^{\text{int}}(z)$ and $\mu(z)$ in the extinction case is too strict, and we impose $\sigma^{\text{int}}(0.1 \leq z < 0.2) = \sigma^{\text{int}}(z = 0.2) = 0.14 \pm 0.03$ and $\mu(0.1 \leq z < 0.2) = \mu(z = 0.2) = -1.29 \pm 0.09$ (details in Appendices D and D.1).

3.8 The stellar content of quiescent galaxies using alternative SSP models

Any stellar population model is built from complex set of recipes that comprises stellar tracks or isochrones, IMF assumptions, an either empirical or theoretical library of stars, etc. A direct consequence is that the stellar population predictions retrieved from them can differs amongst different set of SSP models. Obviously, our results are firstly constrained to the colour predictions established by the chosen set of SSPs, BC03 in this work. In this section we explore how our stellar population predictions would change when another set of SSPs is used instead. More precisely, the model set of EMILES (for a brief presentation see Sect. 3.2.1) is a good candidate for this test as their large spectral coverage covers the ALHAMBRA spectral range. In order to challenge both set of models and to discern how much the solutions can be altered only due to different assumptions in their construction, we re-analysed the full ALHAMBRA data set using the SSP model set EMILES and MUFFIT. The selection of the quiescent sample was also repeated with the same criteria than in Sect. 3.3, but with the EMILES stellar population predictions. In this section the universal Kroupa (2001) IMF was selected along with BaSTI and Padova00 stellar isochrones. The results obtained for both theoretical isochrones are analysed in parallel. For further details of the PDF construction using

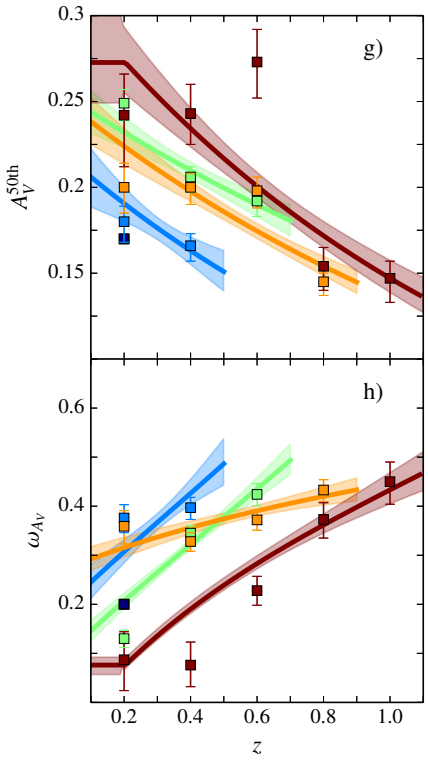

Figure 3.23: As Fig. 3.21, but for the extinction probability distribution function (PDF).

EMILES SSP models, see Appendices D, D.2, and D.3

3.8.1 Formation epochs and ages with EMILES

The median of the mass-weighted age PDF points out that the correlation between the age of quiescent galaxies and their stellar masses persists when the sample of EMILES SSP models is used, independently of the isochrone election (see Table 3.10 and Fig. 3.24). The larger the mass of the galaxy, the older the galaxy is. This correlation also agrees with the "downsizing" scenario and the results obtained using BC03 SSP models (see Sect. 3.7.2). Moreover, the ages of these galaxies are older at lower redshifts, as expected in this kind of galaxies in which the processes of star formation are specially low. We retrieved that the median age of quiescent galaxies is about 5 Gyr at $z \sim 1$ (for both isochrones and only confirmed for $\log_{10} M_\star \geq 11.2$ owing to completeness), whereas for $z \sim 0.2$ these ones present older ages in the range 7.5–9.0 and 7.0–8.0 Gyr for BaSTI and Padova00 isochrones respectively. It is worth noting that BaSTI isochrones provide ages older than those from Padova00, as the BASTI isochrones are bluer than the Padova00 ones (A. Vazdekis 2016, priv. comm.). The mass-weighted ages retrieved from the model set of EMILES are also older than the obtained for BC03, these differences can reach up to 2–3 Gyr (BaSTI) and 1.5–2 Gyr (Padova00) at $z = 0.2$ in comparison with the results for BC03 (Sect. 3.7.2). This constitutes an indication that there is a strong dependency of the absolute values of the age on the SSP model set, at least when these ages are retrieved using SED-fitting techniques based in colours.

The formation epochs retrieved from EMILES SSP models and MUFFIT (age plus lookback-time, see Table 3.11, Fig. 3.25 and Sect. 3.7.2) show that quiescent galaxies are not consistent with a passive evolution. In particular, the deviation from passiveness is more remarkable for BC03, whereas for EMILES the BaSTI isochrones provide predictions closer to a passive evolution. Note that for a strict passive scenario, the formation epoch would remain constant along the cosmic time. Under the EMILES colour predictions, the bulk of stars in massive quiescent galaxies observed at $z \sim 1$ ($\log_{10} M_\star \geq 11.2$) were formed at a formation

Table 3.10: Medians of the mass-weighted age PDFs for quiescent galaxies using EMILES for both BaSTI (top) and Padova00 (bottom) isochrones, binned in stellar mass and redshift. Top (bottom) numbers stablish the 84^{th} (16^{th}) percentile for each distribution.

Age_{M} [Gyr]	$z = 0.2$	$z = 0.4$	$z = 0.6$	$z = 0.8$	$z = 1.0$
$9.6 \leq \log_{10} M_\star < 10.0$	$7.69^{+0.98}_{-0.88}$	–	–	–	–
$10.0 \leq \log_{10} M_\star < 10.4$	$7.34^{+0.96}_{-0.85}$	$6.99^{+0.88}_{-0.78}$	–	–	–
$10.4 \leq \log_{10} M_\star < 10.8$	$7.75^{+0.92}_{-0.83}$	$6.93^{+0.80}_{-0.72}$	$6.20^{+0.69}_{-0.62}$	–	–
$10.8 \leq \log_{10} M_\star < 11.2$	$8.26^{+0.74}_{-0.68}$	$7.20^{+0.66}_{-0.61}$	$6.27^{+0.59}_{-0.54}$	$5.47^{+0.53}_{-0.48}$	–
$\log_{10} M_\star \geq 11.2$	$8.63^{+0.90}_{-0.81}$	$7.49^{+0.75}_{-0.68}$	$6.50^{+0.62}_{-0.56}$	$5.64^{+0.51}_{-0.47}$	$4.90^{+0.42}_{-0.39}$
$9.6 \leq \log_{10} M_\star < 10.0$	$8.05^{+1.59}_{-1.33}$	–	–	–	–
$10.0 \leq \log_{10} M_\star < 10.4$	$6.96^{+1.52}_{-1.24}$	$6.56^{+1.11}_{-0.95}$	–	–	–
$10.4 \leq \log_{10} M_\star < 10.8$	$6.92^{+1.07}_{-0.92}$	$6.40^{+0.92}_{-0.81}$	$5.93^{+0.79}_{-0.70}$	–	–
$10.8 \leq \log_{10} M_\star < 11.2$	$7.36^{+0.92}_{-0.82}$	$6.59^{+0.80}_{-0.72}$	$5.90^{+0.70}_{-0.62}$	$5.28^{+0.61}_{-0.54}$	–
$\log_{10} M_\star \geq 11.2$	$7.67^{+0.94}_{-0.84}$	$6.93^{+0.78}_{-0.70}$	$6.26^{+0.64}_{-0.58}$	$5.66^{+0.52}_{-0.48}$	$5.12^{+0.42}_{-0.39}$

Notes. All the bins are complete in stellar mass, $C = 0.95$, otherwise appear dashed. For the $9.6 \leq \log_{10} M_\star < 10.0$ case, these values were obtained by the MLE methodology assuming $\mu_2 = \mu_1 = \sigma_2 = \sigma_1 = 0$ owing to the low number of galaxies.

redshift $z_{\text{f}} \sim 6$, as shown by the median of the formation epoch PDF, whereas the observed ones at $z \sim 0.2$ is $z_{\text{f}} \sim 2.5$–3. For decreasing stellar masses, the variation of the formation epochs is more remarkable.

Using EMILES, the width of the mass-weighted age PDFs does not present a great dependency with the stellar mass of quiescent galaxies. Although we retrieved that less massive systems also present wider age distributions (see Figs. 3.24 and 3.25), the differences are very mild ($\Delta\sigma^{\text{int}}_{\text{Age}_{\text{M}}} < 1$ Gyr, specially lower at higher redshifts) and all the distributions present widths of the PDF in the range 1–2 Gyr. We do not find great discrepancies after comparing the widths of the PDFs obtained with BaSTI and those obtained with Padova00.

Finally, our results suggest that the width of the mass-weighted age PDFs is anti-correlated with redshift. The lower the redshift, the wider the PDF distribution of the age. There is no significant evidence that this result depends on the stellar mass range and EMILES isochrone. Consequently, all the stellar mass ranges present a similar increase in width of ~ 1 Gyr since $z \sim 1$. After comparing with the results obtained for BC03 (see dashed lines in Figs. 3.24 and 3.25), both model results show similar width ranges ($\sigma^{\text{int}}_{\text{Age}_{\text{M}}} \sim 1$–2 Gyr), but the BC03 ones are correlated with redshift and the width of the PDFs decreases at lower redshifts, i. e. the opposite to the obtained using EMILES.

3.8.2 The metallicity evolution through EMILES SSP models

From the results obtained with MUFFIT and EMILES (including both isochrones), there is a clear correlation between the stellar mass and the mass-weighted metallicity of quiescent galaxies (see Table 3.12 and Fig. 3.26). The more massive the quiescent galaxy is, the more metal-rich it is. The results point out that the MZR of pure quiescent galaxies is present since earlier epochs, with hints for a variation of its slope with redshift (in agreement with BC03 predictions in Sect. 3.7.3).

At $z \sim 0.7$–0.9, the differences in the median of the metallicity PDF for different galaxy masses is almost negligible, quoting values of $\Delta[\text{M/H}]^{50\text{th}}_{\text{M}} \lesssim 0.03$ dex approximately. However, at lower redshifts of $z \sim 0.1$,

Table 3.11: As Table 3.10, but for the mass-weighted formation epoch PDFs.

$\mathrm{Age_M} + t_{\mathrm{LB}}$ [Gyr]	$z = 0.2$	$z = 0.4$	$z = 0.6$	$z = 0.8$	$z = 1.0$
$9.6 \leq \log_{10} M_\star < 10.0$	$10.08^{+1.17}_{-1.04}$	–	–	–	–
$10.0 \leq \log_{10} M_\star < 10.4$	$9.65^{+0.99}_{-0.90}$	$11.04^{+0.94}_{-0.87}$	–	–	–
$10.4 \leq \log_{10} M_\star < 10.8$	$10.20^{+0.95}_{-0.87}$	$10.93^{+0.87}_{-0.80}$	$11.71^{+0.76}_{-0.71}$	–	–
$10.8 \leq \log_{10} M_\star < 11.2$	$10.85^{+0.82}_{-0.77}$	$11.28^{+0.74}_{-0.70}$	$11.73^{+0.65}_{-0.62}$	$12.19^{+0.55}_{-0.53}$	–
$\log_{10} M_\star \geq 11.2$	$11.35^{+0.88}_{-0.81}$	$11.66^{+0.77}_{-0.72}$	$11.98^{+0.66}_{-0.62}$	$12.31^{+0.54}_{-0.52}$	$12.64^{+0.41}_{-0.40}$
$9.6 \leq \log_{10} M_\star < 10.0$	$10.52^{+1.70}_{-1.45}$	–	–	–	–
$10.0 \leq \log_{10} M_\star < 10.4$	$9.33^{+1.50}_{-1.29}$	$10.61^{+1.18}_{-1.06}$	–	–	–
$10.4 \leq \log_{10} M_\star < 10.8$	$9.48^{+1.06}_{-0.95}$	$10.41^{+0.99}_{-0.91}$	$11.44^{+0.90}_{-0.84}$	–	–
$10.8 \leq \log_{10} M_\star < 11.2$	$10.17^{+0.84}_{-0.78}$	$10.76^{+0.76}_{-0.71}$	$11.39^{+0.67}_{-0.64}$	$12.05^{+0.57}_{-0.54}$	–
$\log_{10} M_\star \geq 11.2$	$10.75^{+0.84}_{-0.78}$	$11.24^{+0.75}_{-0.71}$	$11.75^{+0.66}_{-0.63}$	$12.28^{+0.56}_{-0.54}$	$12.84^{+0.45}_{-0.44}$

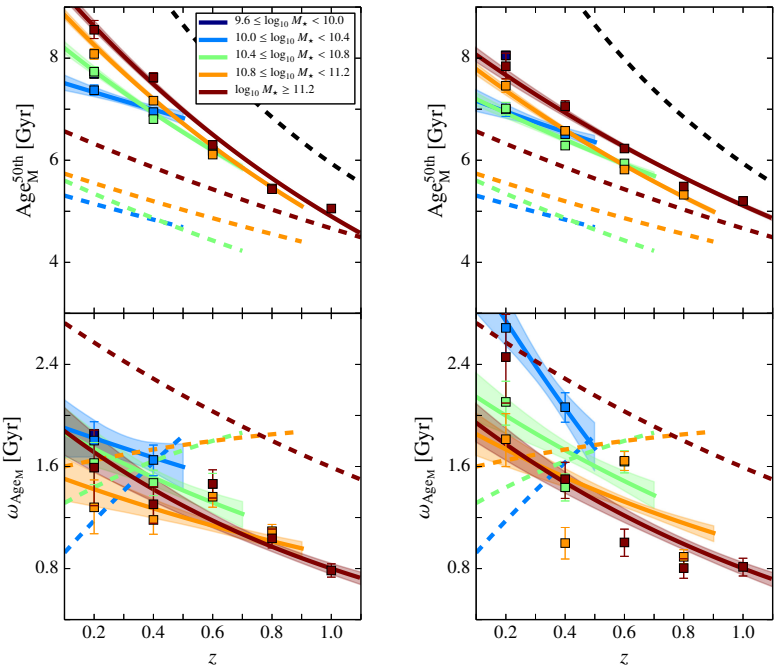

Figure 3.24: Evolution of the median (*top panels*) and width (ω, *bottom panels*) of the mass-weighted age PDF using EMILES with BaSTI (*left column*) and Padova00 isochrones (*right column*) of the quiescent population along the sample cosmic time for different stellar mass bins. The shaded regions delimit the 1 σ uncertainties of both parameters. The square-shape markers illustrate the average median and width assuming for the MLE deconvolution $\mu_2 = \mu_1 = \sigma_2 = \sigma_1 = 0$. Dashed coloured lines are the same parameters obtained using BC03 SSP models (see Sect. 3.7). Dashed black line illustrates the age of the Universe at different redshifts.

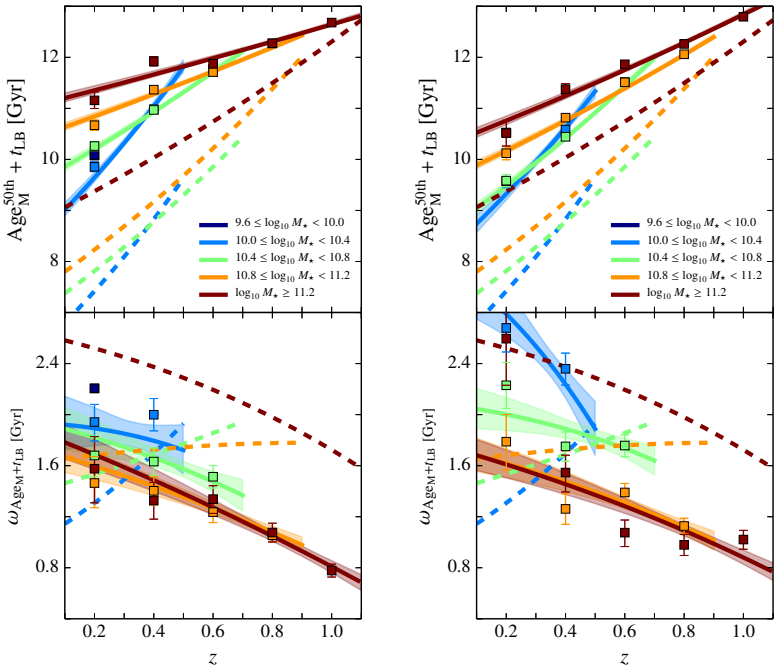

Figure 3.25: As Fig. 3.24, but for the mass-weighted formation epoch distributions.

the median of the metallicity PDF spans the range $\Delta[\mathrm{M/H}]_{\mathrm{M}}^{50\mathrm{th}} \sim 0.1$–$0.4$ dex depending of the stellar mass bin, differences being more significant at lower masses. Consequently, these results, qualitatively consistent for both BaSTI and Padova00 isochrones, suggest that the MZR of quiescent galaxies at earlier epochs was flatter than in the present time. Noteworthy, BaSTI isochrones provide larger metallicities than the Padova00 ones ($\Delta[\mathrm{M/H}]_{\mathrm{M}}^{50\mathrm{th}} \sim 0.1$ dex, see Table 3.12 and Fig. 3.26), which is a direct consequence of the use of different stellar isochrones even though the rest of ingredients of the SSP models are exactly the same (BaSTI tracks are bluer than the Padova00 ones). To illustrate and for $\log_{10} M_\star \geq 11.2$, BaSTI (Padova00) isochrones return solar and super-solar (sub-solar and solar) metallicities at any redshift, while for $10.0 \leq \log_{10} M_\star < 10.4$ are $[\mathrm{M/H}]_{\mathrm{M}}^{50\mathrm{th}} \sim -0.35$ dex ($[\mathrm{M/H}]_{\mathrm{M}}^{50\mathrm{th}} \sim -0.25$ dex). Concerning the BC03 metallicities, these are typically more rich in metals than the predicted by EMILES (see dashed line in Fig. 3.26 and Sect. 3.7.3) at any redshift, whose isochrones are also different (BC03 uses Padova 1994 tracks). Although the most metal-rich BC03 models have metallicities of [M/H] = 0.55 dex, this value may be overestimated owing to the poor coverage of the stellar library STELIB (the library feeding BC03 SSP models, see Vazdekis et al., 2010) in the super-solar metallicity range, and the metallicity for these BC03 models may be lower consequently.

As for BC03 SSP models (Sect. 3.7.3), there are evidences of a decrease in the median of the mass-weighted metallicity PDF of quiescent galaxies since $z \sim 1$. This behaviour is intrinsic to the whole quiescent population and independent of the stellar mass, although at decreasing stellar mass this is steeper. For quiescent galaxies of $\log_{10} M_\star \geq 10.8$, the median of the metallicity PDF shows larger variations for the BaSTI isochrones ($\Delta[\mathrm{M/H}]_{\mathrm{M}}^{50\mathrm{th}} \sim 0.2$ dex) than for the Padova00 ones ($\Delta[\mathrm{M/H}]_{\mathrm{M}}^{50\mathrm{th}} \sim 0.1$ dex) from $z = 1.1$ to $z = 0.1$ (see also Table 3.12 and Fig. 3.26). Unlike BC03 SSP models, there are no hints for a maximum in metallicity at intermediate redshift $z \sim 0.5$–0.6, and the metallicity variations with redshift retrieved with EMILES are milder than those obtained with BC03.

The values obtained for the width of the mass-weighted metallicity PDF are independent of the EMILES isochrone. The less massive bins ($\log_{10} M_\star < 10.8$) present widths in the range $\omega_{[\mathrm{M/H}]_{\mathrm{M}}} \sim 0.3$–$0.5$ dex up to $z \sim 0.5$ and they are compatible with the BC03 ones (see dashed lines in Fig. 3.26); whereas for $\log_{10} M_\star \geq 10.8$ these are mainly lower with values $\omega_{[\mathrm{M/H}]_{\mathrm{M}}} \sim 0.3$ dex. In addition, the width of the metallicity PDF

Table 3.12: As Table 3.10, but for the mass-weighted metallicity PDFs.

$[\mathrm{M/H}]_\mathrm{M}$	$z = 0.2$	$z = 0.4$	$z = 0.6$	$z = 0.8$	$z = 1.0$
$9.6 \leq \log_{10} M_\star < 10.0$	$-0.45^{+0.19}_{-0.16}$	–	–	–	–
$10.0 \leq \log_{10} M_\star < 10.4$	$-0.33^{+0.15}_{-0.17}$	$-0.16^{+0.23}_{-0.28}$	–	–	–
$10.4 \leq \log_{10} M_\star < 10.8$	$-0.18^{+0.16}_{-0.18}$	$-0.08^{+0.19}_{-0.22}$	$0.01^{+0.21}_{-0.26}$	–	–
$10.8 \leq \log_{10} M_\star < 11.2$	$-0.08^{+0.14}_{-0.17}$	$-0.01^{+0.14}_{-0.17}$	$0.05^{+0.14}_{-0.17}$	$0.10^{+0.14}_{-0.17}$	–
$\log_{10} M_\star \geq 11.2$	$-0.02^{+0.15}_{-0.17}$	$0.03^{+0.14}_{-0.16}$	$0.07^{+0.13}_{-0.15}$	$0.12^{+0.12}_{-0.14}$	$0.16^{+0.11}_{-0.13}$
$9.6 \leq \log_{10} M_\star < 10.0$	$-0.55^{+0.22}_{-0.26}$	–	–	–	–
$10.0 \leq \log_{10} M_\star < 10.4$	$-0.44^{+0.16}_{-0.18}$	$-0.29^{+0.21}_{-0.25}$	–	–	–
$10.4 \leq \log_{10} M_\star < 10.8$	$-0.27^{+0.12}_{-0.14}$	$-0.20^{+0.17}_{-0.19}$	$-0.13^{+0.20}_{-0.24}$	–	–
$10.8 \leq \log_{10} M_\star < 11.2$	$-0.16^{+0.15}_{-0.17}$	$-0.12^{+0.15}_{-0.17}$	$-0.09^{+0.15}_{-0.17}$	$-0.06^{+0.15}_{-0.17}$	–
$\log_{10} M_\star \geq 11.2$	$-0.08^{+0.15}_{-0.18}$	$-0.06^{+0.14}_{-0.16}$	$-0.04^{+0.13}_{-0.15}$	$-0.02^{+0.12}_{-0.14}$	$0.00^{+0.11}_{-0.12}$

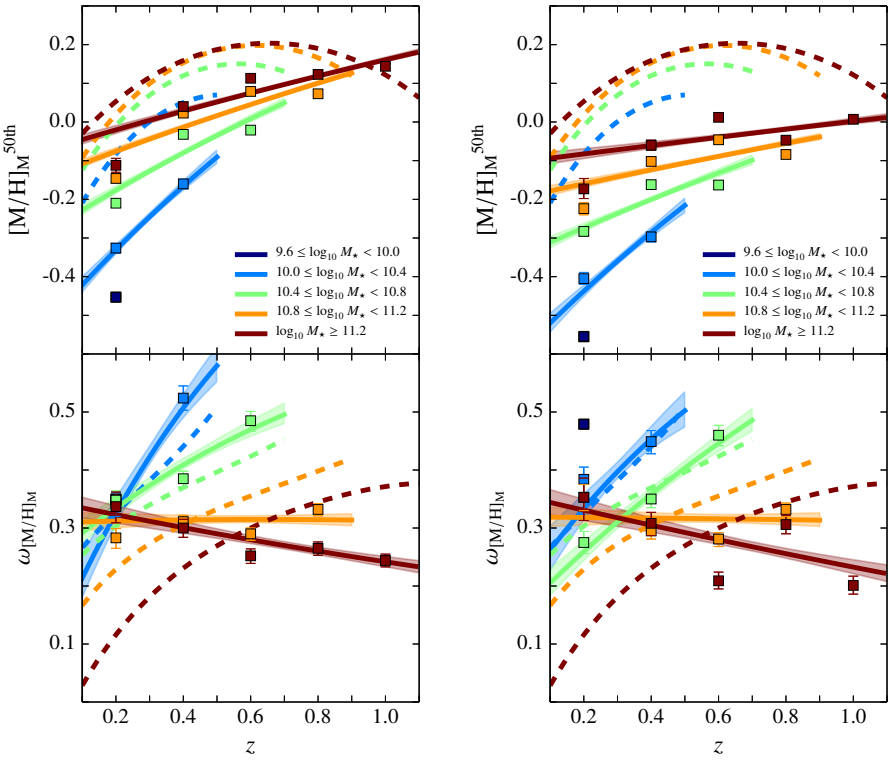

Figure 3.26: As Fig. 3.24, but for the mass-weighted metallicity PDFs.

Table 3.13: As Table 3.10, but for the extinction PDFs.

A_V	$z = 0.2$	$z = 0.4$	$z = 0.6$	$z = 0.8$	$z = 1.0$
$9.6 \leq \log_{10} M_\star < 10.0$	$0.24^{+0.14}_{-0.12}$	–	–	–	–
$10.0 \leq \log_{10} M_\star < 10.4$	$0.25^{+0.18}_{-0.10}$	$0.20^{+0.36}_{-0.13}$	–	–	–
$10.4 \leq \log_{10} M_\star < 10.8$	$0.22^{+0.25}_{-0.12}$	$0.21^{+0.33}_{-0.13}$	$0.20^{+0.42}_{-0.13}$	–	–
$10.8 \leq \log_{10} M_\star < 11.2$	$0.27^{+0.16}_{-0.10}$	$0.25^{+0.22}_{-0.12}$	$0.23^{+0.29}_{-0.13}$	$0.21^{+0.36}_{-0.13}$	–
$\log_{10} M_\star \geq 11.2$	$0.23^{+0.19}_{-0.10}$	$0.22^{+0.23}_{-0.11}$	$0.22^{+0.27}_{-0.12}$	$0.21^{+0.32}_{-0.13}$	$0.20^{+0.36}_{-0.13}$
$9.6 \leq \log_{10} M_\star < 10.0$	$0.22^{+0.27}_{-0.12}$	–	–	–	–
$10.0 \leq \log_{10} M_\star < 10.4$	$0.21^{+0.22}_{-0.11}$	$0.19^{+0.39}_{-0.13}$	–	–	–
$10.4 \leq \log_{10} M_\star < 10.8$	$0.23^{+0.27}_{-0.12}$	$0.21^{+0.33}_{-0.13}$	$0.19^{+0.40}_{-0.13}$	–	–
$10.8 \leq \log_{10} M_\star < 11.2$	$0.20^{+0.27}_{-0.11}$	$0.19^{+0.32}_{-0.12}$	$0.19^{+0.38}_{-0.13}$	$0.18^{+0.44}_{-0.13}$	–
$\log_{10} M_\star \geq 11.2$	$0.18^{+0.26}_{-0.11}$	$0.18^{+0.28}_{-0.11}$	$0.18^{+0.30}_{-0.11}$	$0.18^{+0.31}_{-0.12}$	$0.18^{+0.33}_{-0.12}$

for $\log_{10} M_\star < 10.8$ exhibits a correlation with redshift (as for the BC03 case). Nevertheless, for quiescent galaxies of $\log_{10} M_\star \geq 10.8$, this is not the case and they present a constant width of $\omega_{[\mathrm{M/H}]_\mathrm{M}} \sim 0.3$ dex.

3.8.3 The evolution of extinction using EMILES

We do not appreciate significant differences in the medians of the extinction PDFs amongst the stellar mass bins of quiescent galaxies (see Table 3.13 and Fig. 3.27), where all the values retrieved are compatible at a 1 σ confidence level for both BaSTI and Padova00 results. The medians of extinction PDFs range values of $A_V^{50\mathrm{th}} \sim 0.2$–$0.3$ up to $z = 1.1$ with maximum extinction values of $A_V \lesssim 0.6$, in agreement with BC03 predictions (see Sect. 3.7.4). We also find out that there is a subtle increment of extinction for the less massive bins in our sample ($\log_{10} M_\star \leq 10.8$) at decreasing redshifts, while for the massive ones ($\log_{10} M_\star \geq 10.8$) the median extinction remains constant $A_V^{50\mathrm{th}} \sim 0.2$. The results obtained for BC03 SSP models (see dashed lines in Fig. 3.27 and Sect. 3.7.4) present a correlation between the stellar mass of the quiescent galaxy and the median of the extinction PDF, which also evolves with redshift, unlike EMILES where these values are more similar amongst stellar mass bins and almost constant with redshift.

Moreover, the lower the stellar mass, the wider the extinction PDF. Thereby, the less massive quiescent galaxies exhibit a wider range of extinctions, which agrees with the BC03 predictions. Moreover, the extinction distributions are narrower at lower redshifts, although this correlation is slightly less remarkable at larger stellar masses. For BC03, we also obtain that the extinction distributions of quiescent galaxies are narrower at lower redshifts, but this trend does not depend of the stellar mass.

3.9 Constraints on the SFH

The large number of degrees of freedom involved in stellar population studies increases the difficulty of retrieving the stellar population parameters of galaxies. Frequently, many authors constrain some of them basing their assumptions in previous studies in order to reduce the uncertainties in the rest of parameters. In this section, we explore the consequences of several assumptions often used in the literature (e. g. constant solar metallicity or low extinction priors) on the stellar-population results retrieved in Sects. 3.7 and 3.8.

As three sets of SSPs with different recipes are involved, we study the consequences of different SFH assumptions on the results of each SSP model set separately. The impact of these SFH assumptions was

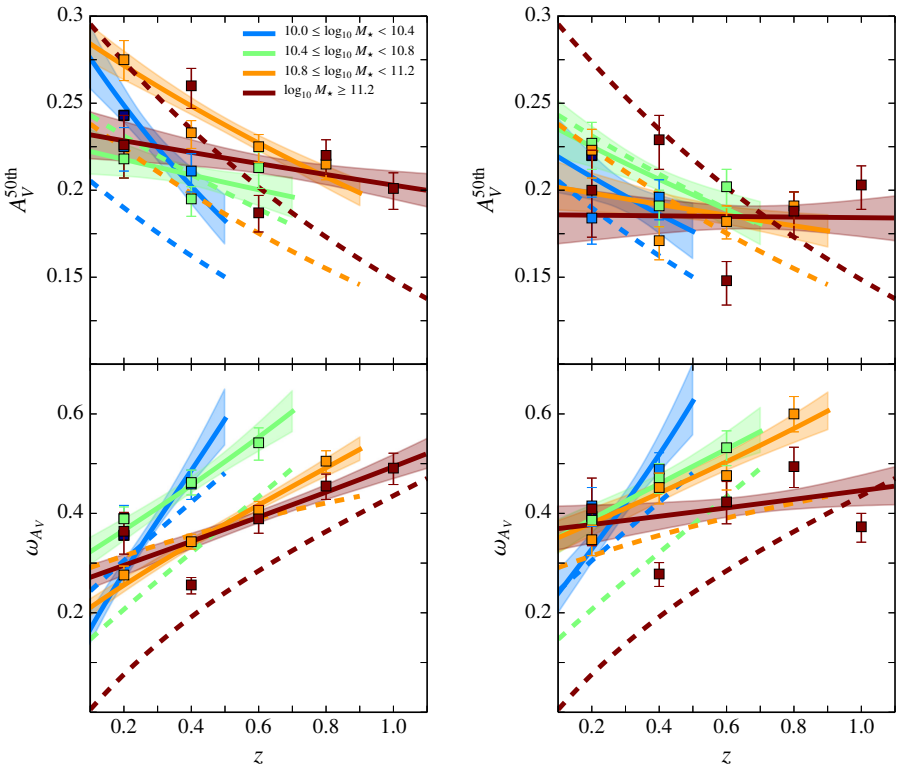

Figure 3.27: As Fig. 3.24, but for the extinction PDFs.

determined rerunning MUFFIT with all the galaxies from the ALHAMBRA survey, and repeating the selection of the quiescent sample (except in some cases, details below) as described in Sect. 3.3 for each model set, but with the SFH constraints detailed below:

i) Constant values of extinction. Under this constraint, we assume that all the quiescent galaxies present similar extinction values, independently of their stellar masses and redshift.

ii) Fixed metallicity values. All the quiescent galaxies have a constant solar metallicity.

iii) Closed-box enrichment of metals. We assume a continuous enrichment of metals in the ISM of all the galaxies. For addressing this assumption, the young component in the mixture of the two SSP models of MUFFIT has to be more rich in metals than the one of the old component.

iv) Constant metallicity during the assembly of the galaxy. For this case, the metallicity of the young and old components in the mixture of SSPs is the same.

v) Fall of metal-poor cold gas from the cosmic web. There is a continuous fall of cold gas from the cosmic web, which is more poor in metals than the one in the ISM. Consequently, the young component in the mixture of SSPs is more metal poor than the old component.

vi) Stellar population predictions assuming a constant and local MZR. At any redshift, we assume that quiescent galaxies exhibit a metallicity equal to the observed one in the local Universe, determined by the MZR as a function of the stellar mass. This test is only performed for EMILES with BaSTI isochrones.

Note that just for cases (i), (ii), and (vi) these constraints were only applied on those galaxies classified as quiescent in Sects. 3.7 and 3.8. Otherwise, the SFH constraints may be too severe.

After studying the impact of these constraints on the SFH, we shed interesting results:

- The main qualitative insights obtained in Sects. 3.7 and 3.8 remain unaltered after setting the SFH constraints presented above, that is, the evolution of quiescent galaxies is not compatible with a passive evolution and there is a continuous decrease in metallicity since $z \sim 1$.
- Different SFH constraints can introduce non-negligible systematics that produce quantitative alterations of the values of age, metallicity, and extinction of quiescent galaxies.
- The constraints on the SFH are a source of (quantitative) uncertainties that can have a larger impact than the proper uncertainties during the determination of the stellar population parameters in multifilter surveys like ALHAMBRA.

For further details, we refer readers to Appendix E, where we detail the changes on the stellar-population parameters for quiescent galaxies using BC03 (Appendix E.1) and EMILES (Appendix E.2) under the SFH constraints mentioned above. The whole set of figures of the present section is collected in Appendix E.3.

3.10 Comparison with previous studies

The main goal of this chapter is to present how quiescent galaxies evolve since $z \sim 1$. Although this topic has been addressed in the past, it was mainly performed through spectroscopic techniques. Actually, these previous studies were mainly carried out by stacked spectra, where the intrinsic dispersion in the distributions of stellar population parameters cannot be explored. In addition, metallicity predictions by spectroscopic data at intermediate redshifts ($z \sim 1$) are usually biased to provide uncertain values. For the first time, we explore the evolution of the quiescent population only using photometric data to determine PDFs of age, metallicity, and extinction since $z \sim 1$. Therefore, and whenever possible, the ages and metallicities of quiescent galaxies from previous studies (see Table 3.14) are compared with ours at different stellar mass and redshift ranges. Below, we describe the data, analysis techniques, and stellar population results of several previous work to compare with the results achieved in this thesis.

- In the work by **Vergani et al. (2008)**, the authors studied the influence of the stellar mass in the age of galaxies beyond the local Universe by a complete sample of 4 048 galaxies from the VIMOS VLT Deep Survey (VVDS, Le Fèvre et al., 2003) in the redshift interval $0.5 \leq z \leq 1.3$. This sample differs from ours in that there exists no colour pre-selection of galaxies, while in our work we focus on the quiescent sample. Through the spectroscopic data in the VVDS-F02 field, they retrieved stellar masses, redshifts and the $D4000$ values (interpreted as age indicator).

  Larger $D4000$ values were retrieved for high-mass galaxies (interpreted as older stellar populations), whereas less massive galaxies show lower $D4000$ values. As in this thesis, these results evidence that the stellar populations of more massive galaxies were formed at earlier epochs in the Universe. In both studies, the results are compatible with the "downsizing" assembly, and in agreement with the fossil record method predictions at $z < 0.1$ (e. g. Gallazzi et al., 2005; Jimenez et al., 2007). Thanks to MUFFIT and the ALHAMBRA features, we are in a privileged position to complement the results of Vergani et al. (2008) setting milestones in the formation epochs of these galaxies since $z = 1$ up to the present days.

  In Vergani et al. (2008), the authors also obtained that both redder and massive galaxies presented lower EW[O II] values suggesting that contain a relative low star formation, and the most efficient star formation episodes are restricted to be in the less massive systems, as we derive from the results in Sect. 3.4.1 in which the SFR per unit of mass, or sSFR (see Fig. 3.8), of massive quiescent galaxies are also the lowest ones (also in agreement with previous work, e. g. Papovich et al., 2006; Zheng et al., 2007; Pérez-González et al., 2008; Damen et al., 2009). Consequently, we are also getting proves that

Table 3.14: Brief description of papers trying to constraint the stellar population parameters of quiescent galaxies.

References	Redshift	Stellar mass	Number	Parameters
Vergani et al. (2008)†	$0.5 \leq z \leq 1.3$	$M_\star > 10^{9.6}$	4 048	Age
Siudek et al. (2016)†	$0.4 < z < 1.0$	$10^{10} < M_\star < 10^{12}$	3 991	Age
Sánchez-Blázquez et al. (2009)††	$0.4 < z < 0.8$	$\sigma > 100$	215	Age, [M/H]
Schiavon et al. (2006)††	$0.7 < z < 1.0$	$\sigma \gtrsim 170$	1 160	Age, [M/H]
Choi et al. (2014)	$z < 0.7$	$10^{9.6} < M_\star < 10^{11.8}$	2 400	Age, [M/H]
Gallazzi et al. (2014)	$z \sim 0.7$	$M_\star > 10^{10.5}$	33	Age, [M/H]
Belli et al. (2015)	$1.0 < z < 1.12$	$M_\star > 10^{11.1}$	12	Age
Peng et al. (2015)	$0.05 < z < 0.09$	$M_\star > 10^{9.5}$	22 168	Age, [M/H]
Citro et al. (2016)	$0.02 < z < 0.3$	$M_\star > 10^{10.8}$	24 488	Age, [M/H], A_V
Fumagalli et al. (2016)	$0.5 < z < 2.0$	$M_\star > 10^{10.8}$	248	Age

Notes. From left to right, reference of the work, redshift bin, stellar mass range of the sample, number of galaxies, and stellar population parameters explored. All the stellar masses (velocity dispersion, σ) are in solar units [$M_\odot$] (km s^{-1}). All the work involve spectroscopic data.
(†) In the work by Vergani et al. (2008); Siudek et al. (2016), line strength indices are used as age proxy.
(††) In the work by Schiavon et al. (2006); Sánchez-Blázquez et al. (2009), velocity dispersions are used as stellar mass proxy.

the more efficient star formation episodes (higher SFRs) in quiescent galaxies are taking place in less massive systems.

- Using a subset of 3 991 quiescent galaxies from VIMOS Public Extragalactic Survey (VIPERS, Guzzo et al., 2014, effective area of 24 deg^2 and $i'_{AB} < 22.5$), the work by **Siudek et al. (2016)** constrained the evolution and SFHs of this kind of galaxies at $0.4 < z < 1.0$. These galaxies were observed with the spectrograph VIMOS (Le Fèvre et al., 2003, spectral coverage $\lambda\lambda$ 5 500–9 500 Å, $1''$ slit, $R = 230$, and mounted on the ESO very large telescope), to subsequently perform a stacking in stellar mass and redshift bins. Quiescent galaxies were chosen through an evolving colour cut $U - V$ (Fritz et al., 2014) and without visually detected emission-lines ([O II]λ 3 727 and/or Hδ_A), reaching stellar masses down to $\log_{10} M_\star \sim 10.0$ in the lowest redshift bin. Although the selection process of quiescent galaxies differs from ours, the results may be compatible as there is a colour criterion along with a removal of galaxies with emission lines, which are related to dusty star-forming galaxies.

  The authors obtained that the low mass quiescent galaxies always present lower $D4000$ and higher Hδ_A indices (i. e. younger populations) as compare to the more massive ones in the whole redshift range ($0.4 < z < 1.0$). This mainly implies a tight correlation between the age and stellar mass in quiescent galaxies up to $z \sim 1.0$, in agreement with our results and the "downsizing" scenario. After estimating the equivalent ages and formation epochs, and having rejected the influence of metallicity on the results, they also found that the formation epochs of quiescent galaxies vary depending on the redshift in which quiescent galaxies are observed. In agreement with our results (further details in Secs. 3.7 and 3.8), the larger the redshift of these galaxies, the earlier their formation epochs, which is more prominent at lower stellar masses. Consequently, they also agree that the quiescent galaxy population is suffering modifications in their average stellar content via "frosting" (remains of star formation processes), mergers, the "progenitor" bias, or other mechanisms.

- **Sánchez-Blázquez et al. (2009)** focused on the stellar populations of RS galaxies belonging to 24

cluster and group environments at $0.4 < z < 0.8$. Their parent dataset was composed of 215 spectra from the ESO Distant Cluster Survey (1″-wide slit and spectral range $\lambda\lambda$ 3 670–4 150 Å) complemented with photometric data. These RS galaxies were defined as those with secure spectroscopic redshifts, without strong emission lines (equivalent widths [O II]λ 3 727 $EW < 7$ Å), and colours between ±0.3 mag to the best-fitting linear relation (slope −0.09) to the red part of the colour-magnitude relation ($V - I$ versus I). As the signal-to-noise is low individually, the authors stacked the spectra in three different redshift bins (z = 0.45, 0.55, and 0.75) and velocity dispersions ($\sigma < 175$ km s^{-1} and $\sigma > 175$ km s^{-1}). To retrieve ages and metallicities from the stacked spectra, they carried out a simultaneous fit through a χ^2-test of the Lick indices Fe4383, CN2, H$\delta_{\rm A}$, and H$\gamma_{\rm F}$. For more massive galaxies ($\sigma \sim 230$ km s^{-1} or $\log_{10} M_\star \sim 11.3$ using eq. 2 in Thomas et al., 2005), the authors found that quiescent galaxies have larger ages at lower redshifts, in qualitative accordance with our results (see top panels in 3.28–3.30). They claim this can be compatible with a passive evolution at 1 σ uncertainty level (formation redshift $z_{\rm f} > 1.4$), but given the uncertainties they do not confirm it.

Regarding metallicity, the work by Sánchez-Blázquez et al. (2009) concludes that their measurements are compatible with no variation with redshift given their uncertainties. Interestingly, the most massive galaxies in their sample exhibit hints for a decrease in metallicity with the decreasing redshift, which would be in qualitative agreement with our results. For less massive systems ($\sigma \sim$ 120–150 km s^{-1}, i. e. $\log_{10} M_\star \sim 10.3$), they show neither age or metallicity evolution within the errors. Overall, they concluded that massive red galaxies are compatible with a passive evolution, whereas the low mass systems of the sample need either a continuous level of star formation to maintain a constant age or the RS is in a continuous build-up adding new and younger galaxies. In this framework, this thesis supports a non constant metallicity in massive and red systems (largely populated by quiescent galaxies) and the necessity of a process for including younger stars in these galaxies, specially in lower mass systems. Nevertheless, it is noteworthy that the work by Sánchez-Blázquez et al. (2009) might differ from ours in some aspects,as environment plays a role on the stellar population properties of galaxies (e. g. Sánchez-Blázquez et al., 2003; Eisenstein et al., 2003; Thomas et al., 2005; Trager et al., 2008; Thomas et al., 2010).

- As part of the DEEP2 galaxy survey, **Schiavon et al. (2006)** analysed stacked spectra of field RS galaxies at $z \sim 0.9$ from the *Keck* DEIMOS (Faber et al., 2003) spectrograph to retrieve ages and metallicities. The field RS galaxies were selected through a CMD, $U - B \geq 0.25$ and M_B = [−21.76, −20.76] (both in Vega system), where the colour $U - B$ and absolute magnitude M_B were derived from the CFHT photometry (Willmer et al., 2006). In addition, all red galaxies with emission larger than [O II]λ 3 727 $EW \geq -5$ Å were removed from the sample minimizing the contamination due to reddened late-type galaxies (contamination at the 5 % level), which is almost equivalent to our sample selection.

  The ages and metallicities in this paper were derived from the absorption line strengths H$\delta_{\rm F}$ and Fe4383, using Schiavon (2007) models with different [α/Fe] values. For a fair comparison, we performed a similar sample selection of quiescent galaxies through the photometric conversions from the Vega to the AB system in DEEP2 (Willmer et al., 2006), for establishing the equivalent range of stellar masses. It corresponds to quiescent galaxies with $1.06 \leq U - B \leq 1.41$ (AB system) and absolute magnitudes in the range M_B = [−21.87, −20.87] (AB system). To convert the ALHAMBRA magnitudes to the rest-frame UB ones, as in Schiavon et al. (2006), we followed the process explained in Sect. 2.3.2.6, that is, we rebuilt the combination of best-fitting models retrieved during the MUFFIT analysis and we convolved them (rest-frame) with the UB bands instead.

  The bulk of ALHAMBRA quiescent galaxies in the range $1.06 \leq U - B \leq 1.41$ and M_B = [−21.87, −20.87] at $0.75 \leq z \leq 0.95$ have stellar masses of $\log_{10} M_\star \sim$ 10.7–11.1 dex (16th and 84th percentiles respectively). If we split the sample in the same three colour bins as in Schiavon et al. (2006, $U - V$ = 1.06–1.16, 1.16–1.26, and 1.26–1.41), we observe that the redder the quiescent galaxy, the higher the stellar mass (median values of $\log_{10} M_\star \sim$ 10.8, 10.9, and 11.0 dex respectively). So, the

most representative stellar mass bin in our sample for comparing with our age and metallicity predictions is $10.8 \leq \log_{10} M_\star < 11.2$. The main result obtained by Schiavon et al. (2006) is that the ages of RS galaxies at $z \sim 0.9$ are not compatible with a passive evolution, after comparing them with the local SDSS counterpart (spectroscopic catalogue of Eisenstein et al., 2003). In particular in their work, RS galaxies at $z \sim 0.9$ present luminosity-weighted SSP ages of $\sim$ 1.2 and 1.7 Gyr, the latter for SSP models of $[\alpha/\mathrm{Fe}] = +0.4$, which are significantly younger than the ones obtained by MUFFIT for the ALHAMBRA quiescent galaxies (see Figs. 3.28–3.30, mass-weighted ages of 4.5–5 Gyr for BC03 and EMILES respectively). To explain qualitatively these differences, we must take into account that luminosity-weighted ages are systematically younger than mass-weighted ones, and the fact that the use of one SSP leads to ages younger than the ones derived from the mixture of two or several SSPs, as in this thesis. Regarding metallicities, there is a reasonable agreement between the iron abundances obtained by Schiavon et al. (2006) ([Fe/H] = [0, +0.3] dex) and the ones by MUFFIT (0.12, 0.13, −0.04 dex for BC03, BaSTI, and Padova00).

The stellar populations of SDSS RS galaxies ($z \sim 0.15$) obtained by Schiavon et al. (2006) are from $\sim$ 3 to 5 Gyr and super-solar metallicities, whereas assuming a passive evolution this value should be over 6 Gyr. The non-passive evolution of RS galaxies reported by Schiavon et al. (2006) is in perfect agreement with this thesis, which is obtained with all the different SSP models used in this work, being stronger for BC03 and milder for EMILES. In particular, Schiavon et al. (2006) concluded that it is necessary the inclusion of young/intermediate-age stars in RS galaxies in order to explain the evolution in age in this kind of galaxies by at least two scenarios: the so-called "frosting" models (e. g. Trager et al., 2000), with remains of in-situ star formation; and the "progenitor" bias or "quenching" models, by the incorporation of new galaxies to the quiescent population later on (e. g. Bell et al., 2004; Faber et al., 2007).

- **Choi et al. (2014)** analysed the stellar populations of stacked spectra of quiescent galaxies up to $z < 0.7$. The spectroscopic data were obtained from the AGN and Galaxy Evolution Survey (AGES, Kochanek et al., 2012), which was extended up to $9.6 < \log_{10} M_\star < 11.8$ dex to be complete in mass at the lowest redshift bin. Instead of a colour-colour selection, the quiescent sample was defined from the individual sSFR and stellar mass values. From a parent sample of 2 400 quiescent galaxies, the authors stacked the spectra in different bins of redshift and stellar mass, to perform an analysis of their stellar population parameters. They computed SSP equivalent ages and abundances of elements such as [Fe/H] through a full SED-fitting of continuum-normalised spectra in the wavelength range $\lambda\lambda$ 4 000–5 500 Å.

  As in this thesis, there exists a clear influence of the stellar mass on the age, in the sense that quiescent galaxies are older at lower redshifts, and, at fixed redshift the most massive ones are older. On the other hand, the authors did not find evidences in favour of a variation of the metallicity with redshift or stellar mass. From the derived SSP-equivalent ages, Choi et al. (2014) proposed that quiescent galaxies present little modifications in their ages since $z < 0.7$ due to a composed passive evolution (or a continuous process of low star formation). Albeit for less massive systems, where their sample is more limited, their age evolution is shallower. Less massive systems show a better the agreement with our results. Differences in the set of models and the use of SSP-equivalent ages could drive the observed differences.

  Regarding metallicities, unlike the predictions in this thesis, the authors do not clearly retrieve the MZR at different redshifts, including the local Universe (Gallazzi et al., 2005; Sánchez-Blázquez et al., 2009; Gallazzi et al., 2014). Besides, they state that they are potentially affected by aperture effects. Therefore, we do not consider their metallicity estimations are reliable enough.

- Another work dealing with stellar populations of quiescent galaxies at the redshift range of ALHAMBRA is **Gallazzi et al. (2014)**. In this paper, the authors explore the stellar content of 33 quiescent galaxies at $z \sim 0.7$ with stellar masses $M_\star > 3 \times 10^{10}$ $\mathrm{M}_\odot$ from the E-CDFS (Wolf et al., 2004, Vega

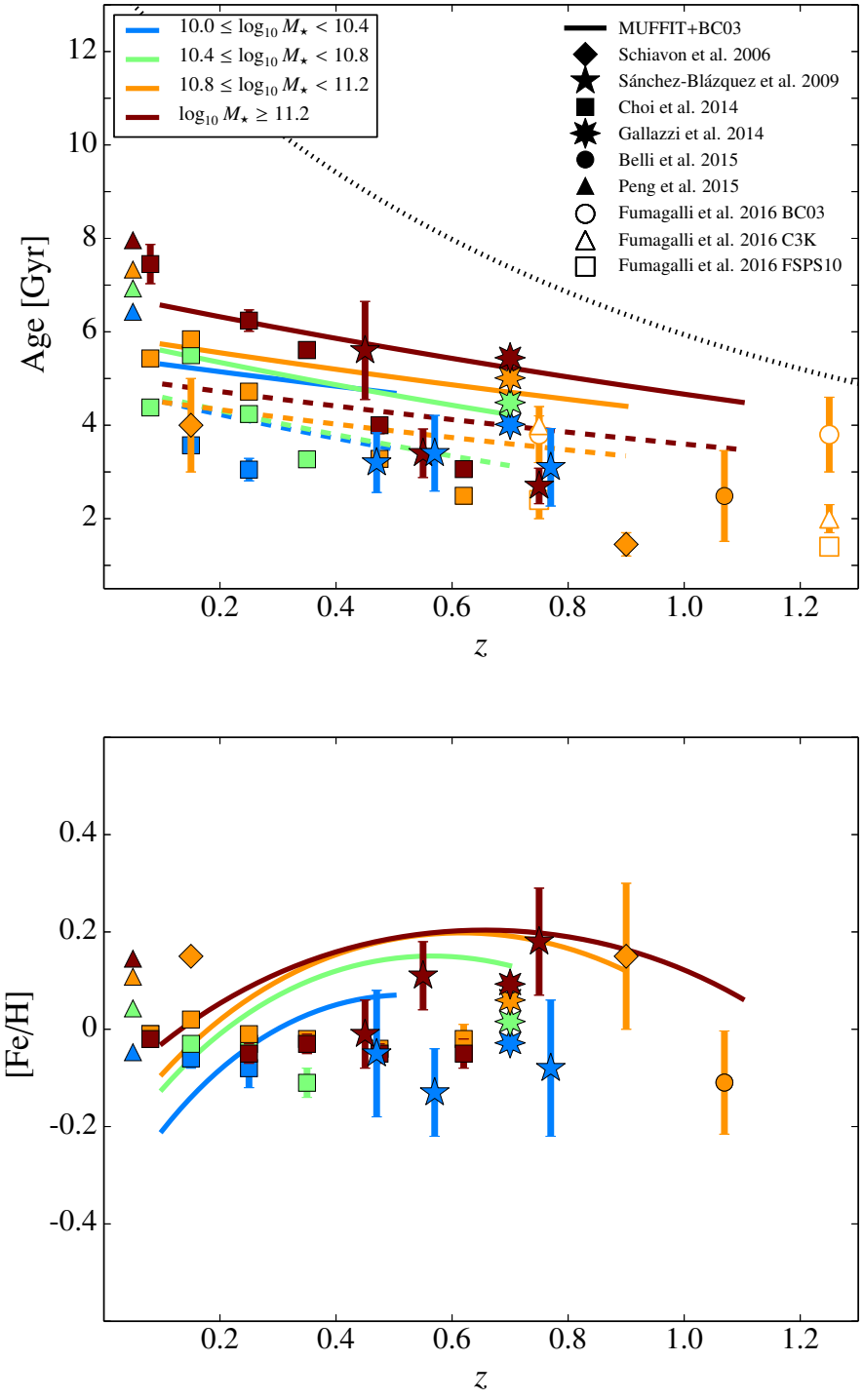

Figure 3.28: Comparison of ages (*top panel*) and metallicities (*bottom panel*) of quiescent galaxies from several work (details in the text, see legend for references) and our results (BC03 SSP models) at the redshift range $0 < z < 1.2$. The mass-weighted ages and metallicities retrieved using MUFFIT and ALHAMBRA data are illustrated with solid lines, whereas the coloured dashed lines correspond to luminosity weighted ages. The ages and metallicities retrieved from other work are colour coded in concordance with their proximity to the stellar mass bins of our quiescent sample (see inset). Dotted line shows the Universe age.

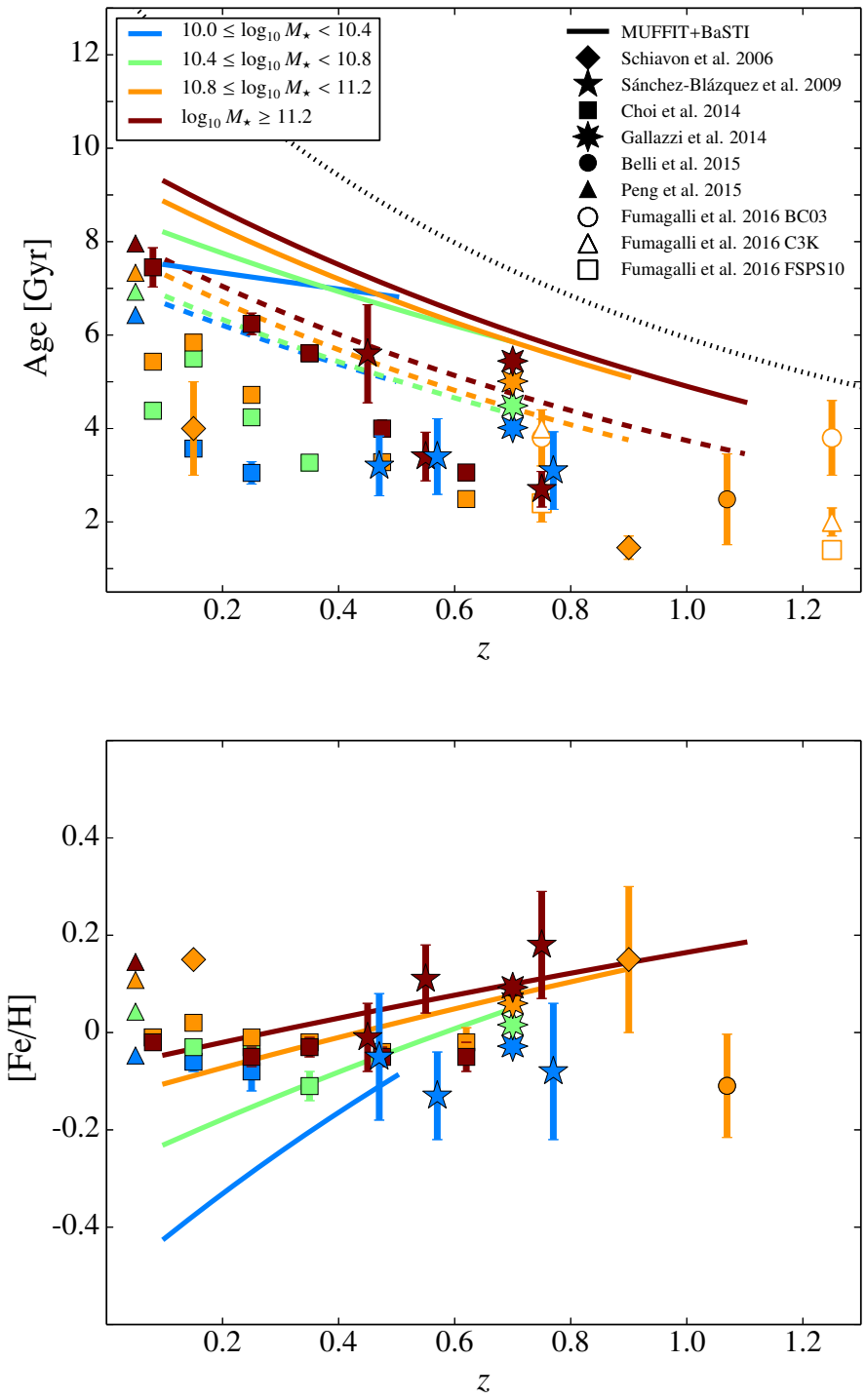

Figure 3.29: As Fig. 3.28, but for our results using EMILES SSP models and BaSTI isochrones.

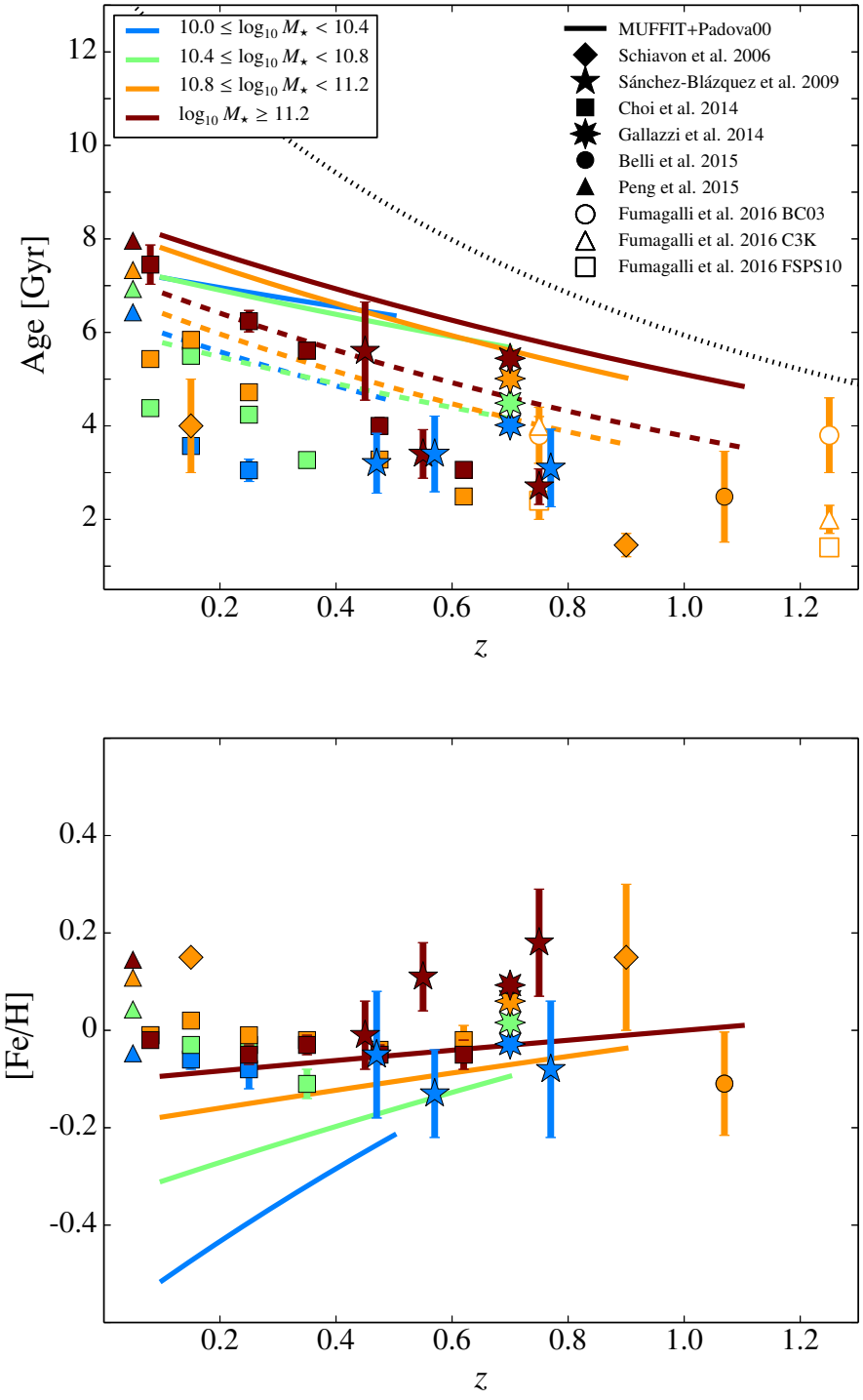

Figure 3.30: As Fig. 3.28, but for our results using EMILES SSP models and Padova00 isochrones.

magnitudes $R < 22.7$ and spectroscopy with IMACS in the spectral range $\lambda\lambda$ 6 500–9 500 Å). The age and metallicity of each galaxy was derived by a Bayesian statistical approach based on a multiple fit to age- (D4000, Hβ, and Hδ_A+Hγ_A; Worthey & Ottaviani, 1997, for the last one) and metallicity-sensitive ([Mg_2Fe] and [MgFe]$'$) absorption features, and a Monte Carlo library of models built from BC03 SSP models and various SFHs (same metallicity in the SFH of each model).

Gallazzi et al. (2014) found out that the age-stellar mass relation is also present for quiescent galaxies at $z \sim 0.7$. Furthermore, the ages were non-compatible with a simple passive evolution because they are ~ 2 Gyr lower than the obtained with a similar methodology in the local SDSS counterpart (more precisely in Gallazzi et al., 2005). This strongly favours our conclusions in this aspect, not only quiescent galaxies are older at larger cosmic times, but the ageing that they would suffer with respect to a complete passive scenario is delayed too. Moreover, they obtained that the age-stellar mass relation is also compatible with the slope retrieved for quiescent galaxies in SDSS.

The authors found that there is a relation between metallicity and stellar mass at $z \sim 0.7$ as well, but this one is slightly lower than the obtained for the local Universe (~ 0.04 dex from Gallazzi et al., 2005), which would suggest an enrichment of metals in quiescent populations. In addition, the slope of the metallicity at $z \sim 0.7$ is slightly lower (0.11 ± 0.1) in comparison to the local one (0.15 ± 0.003), but it is compatible with no evolution within the uncertainties (even larger). However, as we already discussed above, the combination of different photometric apertures and the existence of metallicity gradients has an impact on the Gallazzi et al. (2005) local metallicities (see Sect. 2.5.5), which may affect the conclusions about the evolution of metallicity in Gallazzi et al. (2014). Gallazzi et al. (2005) estimated than the SDSS aperture effects that typical metallicity gradients can lead to metallicity differences of $\sim$ 0.15–0.2 dex for $\log_{10} M_\star \gtrsim 10$, that if confirmed would make the metallicity of quiescent galaxies to lie on slightly lower metallicities as we obtained from BC03 and EMILES SSP models in this thesis. Age gradients use to be shallower than metallicity ones (Wu et al., 2005; Sánchez-Blázquez et al., 2007; La Barbera et al., 2012; Eigenthaler & Zeilinger, 2013), and therefore, it is not expect a large impact on age due to aperture effects. Notice that in Fig. 3.28 the mass-weighted age predictions of MUFFIT+BC03 are in very good agreement with those provided by Gallazzi et al. (2014, also BC03 models), however we obtain larger super-solar metallicities of Δ[Fe/H] ~ 0.1 dex. For EMILES models (Figs. 3.29 and 3.30), the ages provided by MUFFIT are $\sim$ 1.5 Gyr older. For BaSTI isochrones the agreement with metallicity is remarkable, but for the Padova00 ones we retrieved lower metallicities of Δ[Fe/H] ~ 0.15 dex.

- From *Keck* LRIS spectra and photometric data, the stellar population parameters of 51 quiescent galaxies at $1 < z < 1.6$ were retrieved by **Belli et al. (2015)**. They estimated ages, metallicities, and extinctions of each galaxy via SED-fitting techniques by the Bayesian code `pyspecfit` (Newman et al., 2014) and BC03 τ-models (metallicity fixed around solar values). At $1.0 < z < 1.12$, there are 12 galaxies (with median stellar mass of $\log_{10} M_\star \sim 11.1$) overlapping with the redshift upper-limit of our sample, whose median stellar populations allow us to compare with our massive galaxies at the redshift upper-limit $z \sim 1.1$ (see Figs. 3.28–3.30).

  For these 12 massive quiescent galaxies, the median age, metallicity, and extinction are 2.3 Gyr, -0.1 dex, and 0.36 respectively. At the redshift upper-limit, MUFFIT retrieved that massive quiescent galaxies in the range $10.8 \leq \log_{10} M_\star < 11.2$ exhibit ~ 4.2 Gyr of age, metallicities [Fe/H] = -0.05, 0.0, and 0.18 dex (BC03, EMILES+Padova00, and EMILES+BaSTI respectively), and extinctions of $A_V \sim 0.2$. The discrepancies in age and extinction with Belli et al. (2015) can be partly explained by the assumption of metallicities around solar values. As we analyse in Sects. E.1.2 and E.2.2 (see also Figs. E.3, E.4, E.27, and E.28), this assumption alters the stellar population parameters getting younger ages and larger extinction values at $z \sim 1.1$, which would support our stellar population predictions.

- Aimed at exploring the responsible mechanisms for quenching galaxies, **Peng et al. (2015)** built sam-

ples of star-forming and quiescent galaxies to study both the metallicity- and age-stellar mass relations in the local Universe. These relations were derived through galaxies from SDSS at $0.05 \leq z \leq 0.085$ and the quiescent sample was composed of 22 618 galaxy spectra (signal-to-noise ratios larger than 20 per spectral pixel), with red $U - B$ colours and without Hα emission. Ages and metallicities for common galaxies with the parent sample were taken from Gallazzi et al. (2005). Thereby, we may expect aperture effects on metallicities. Peng et al. (2015) results differ with Gallazzi et al. (2005) conclusions in that these ones were obtained for quiescent and star-forming galaxies separately and not only for the total population. The authors determined that the metallicity- and age-stellar mass relations are also present in the more local Universe for quiescent galaxies (and for star-forming as well), even when both red and blue populations are studied separately.

After comparing the age estimations provided by MUFFIT and BC03 (EMILES+BaSTI) SSP models with the Peng et al. (2015) ones, the latter are $\sim$ 1.5 Gyr older (younger) with a similar slope in the age-stellar relation for $\log_{10} M_\star \geq 10$ (Figs. 3.28 and 3.29). In Fig. 3.30, the EMILES+Padova00 age-stellar mass relation is steeper and less prominent, but the range of ages for quiescent galaxies is qualitatively the same than the provided in Peng et al. (2015). Regarding metallicity, there is a shift of ~ -0.2 dex between our BC03 and EMILES+BaSTI values and the provided by Peng et al. (2015). For the Padova00 ones, with the lowest metallicity values, this shift is even larger (Δ[Fe/H] ~ -0.3 dex). Although if we account for the aperture effects (0.15–0.2 dex, Gallazzi et al., 2005), these differences are much relaxed and the metallicity predictions provided by MUFFIT and ALHAMBRA for quiescent galaxies agree well with the Peng et al. (2015) ones.

- Recently, **Citro et al. (2016)** focused on the SFH of massive and red early-type galaxies through the "archaeological" approach of SDSS galaxies. They selected a sample of 24 488 massive galaxies ($\log_{10} M_\star > 10.75$) with redshift $0.02 < z < 0.3$, red colours (matching the early-type template colours of Ilbert et al., 2006), and without strong emission lines ([O II]λ 3 727 $EW > -5$ Å and Hα $EW > -5$ Å). The stellar population parameters of this population were retrieved through stacked spectra in different bins of stellar mass and redshift, using STARLIGHT with BC03 and Maraston & Strömbäck (2011) SSP models.

  The authors retrieved from their SED-fitting results that the mass-weighted ages increases with stellar mass and these are systematically older at lower redshifts with values between $\sim$ 10–13 Gyr at $z \sim 0.02$ and $z \sim 0.3$ respectively. The less massive quiescent galaxies ($10.75 < \log_{10} M_\star < 11$) are younger than the most massive ones ($\log_{10} M_\star > 11.5$) by 0.4 Gyr and 0.2 Gyr using BC03 and Maraston & Strömbäck (2011) models respectively. These ages are substantially older in comparison with ours, in the range 7–9 Gyr, although the age–stellar mass relation is also present. They also obtained that the local passive galaxies have mass-weighted super-solar metallicities of [M/H] $\sim$ 0.16 (0.13) dex using BC03 (Maraston & Strömbäck, 2011) SSP models with little differences among contiguous stellar mass bins. These metallicities are also larger than ours at $z \sim 0.1$ that are around solar values. The discrepancies between the use of BC03 models instead of the Maraston & Strömbäck (2011) increases for the extinction predictions. While for BC03 they obtained typical extinction values of $A_V \sim 0.08$ ($A_V < 0.2$), for Maraston & Strömbäck (2011) these values increases up to $A_V \sim 0.16$ ($A_V < 0.25$), that is, these extinction values are lower than the ones obtained in this thesis. For both model sets, they retrieved an increase of extinction since $z \sim 0.3$ up to $z \sim 0.1$ of $\Delta A_V \sim 0.1$, where for BC03 it is remarkable that at increasing stellar masses the extinction is lower than the less massive ones, but this is not the case for Maraston & Strömbäck (2011) for which all the stellar masses present compatible dust extinctions.

- Making use of spectroscopic data from the 3D-HST survey, **Fumagalli et al. (2016)** estimated the ages of quiescent galaxies at $0.5 < z < 2.0$. They used 248 quiescent spectra from the low-resolution Wide Field Camera (WFC3, grism onboard *HST* and spectral coverage $\lambda\lambda$ 11 000–16 000 Å). They defined their quiescent sample using a rest-frame UVJ-diagram, although without extinction corrections as

in the present thesis. Only the more massive galaxies ($\log_{10} M_\star > 10.8$) were selected in order to stack all the spectra in three redshift bins. Every stacked spectra was normalised by its proper continuum for avoiding degeneracies with extinction, focusing the analysis on the absorption spectral lines. Three different sets of SSP models were challenged for claiming the ages and results of the spectrum stacks: BC03, Flexible Stellar Population Synthesis (FSPS10, Conroy & Gunn, 2010), and C3K (Conroy, Kurucz, Cargile, & Castelli, in prep.) models. The age estimation was performed for every normalised stack carrying out a least-square minimization of the 3 model sets (to SSPs) and forcing solar metallicities.

As a result, the ages of quiescent galaxies present a large spread in age due to the use of different model sets, although they are usually below half of the age of the Universe in the explored redshift ranges. Our analysis at the same redshift ranges yields older mass-weighted ages, but the luminosity weighted ages provide a good agreement with our predictions for both BC03 and EMILES SSP models. It is remarkable that the extrapolation at $z = 1.25$ of the mass-weighted ages (BC03 and EMILES) also match with the ages derived by Fumagalli et al. (2016) and BC03 models. Although, as we studied in Sect. 3.9, the solar metallicity constraint imposed by Fumagalli et al. (2016) can produce systematics in the retrieved ages.

In summary, there is a general consensus since $z \sim 1$, in good agreement with our results, in which quiescent galaxies get older with cosmic time independently of their stellar masses. In addition, the "downsizing" scenario is well reproduced by several of the studies in this section, as well as the results obtained by MUFFIT using the ALHAMBRA dataset and different sets of SSP models (BC03 and EMILES). Despite the good agreement among studies, there is large spread on the age values that are strongly related to the use of different techniques, stellar population models, and SFH assumptions. Concerning metallicities, there are less estimations and with larger uncertainties, but most results point out that quiescent galaxies have around solar and super-solar metallicities (the more metal-rich ones are also the most massive), with hints for the MZR being in place since earlier epochs. The difficulty to disentangle the evolution with redshift of the metal content in quiescent galaxies comes, primarily, by the fact that for these galaxies it is expected to be mild (~ 0.1 dex) during the last 8 Gyr, provided that most of their star formation seemed to happen at high redshifts. In addition, measuring a precise metallicity evolution through spectroscopic data has technical limitations, like (i) the need of high signal-to-noise ratio spectra at high redshifts, (ii) the existence of large data sets of galaxies along redshift, and (iii) the fact that the reference metallicity at the local Universe is based on SDSS data, which may be affected by aperture effects. We believe that the combination of MUFFIT and the ALHAMBRA data in this thesis provides unique advantages: we are not affected by the aperture bias and there is a large number of galaxies to fully populate the different bins in redshift and stellar mass, which along with an homogeneous analysis all over the redshift range, allows us to be sensitive to this little variations and perform an statistical analysis of the sample properly.

3.11 Summary and conclusions

Using the dataset provided by the ALHAMBRA multi-filter photometric survey and our optimised SED-fitting tool MUFFIT (extensively detailed in Chapter 2) with both BC03 and EMILES SSP models, we explore the stellar content of quiescent galaxies since $z = 1.1$, or during the last 8 Gyr (60 % of the age of the Universe), as well as how these galaxies have evolved and assembled their stellar populations.

The selection of the quiescent sample is carried out carefully in order to minimize as much as possible the number of contaminants, mainly faint stars and dusty star-forming galaxies. In brief, we improve the colour-colour UVJ diagram taking the extinction estimations provided by MUFFIT into account for generating a dust-corrected UVJ diagram, which minimizes the contamination of dusty star-forming galaxies. Moreover, we carry out a one-by-one visual inspection to remove those sources whose photometry can be compromised (e. g. bad CCD regions or bad photometric apertures) and spurious detections. Using the stellar version

of MUFFIT, we remove the faint stars of the ALHAMBRA catalogue with magnitudes ranging $22.5 \leq m_{F814W} \leq 23$. After comparing with the morphological classification of COSMOS for a common sample of sources, the contamination due to faint stars is reduced from 24 % to 4 %. Finally, we estimate the stellar mass completeness of our sample of quiescent galaxies in ALHAMBRA applying a novel method for defining an analytic function for the stellar mass completeness that yields a final sample of 8 547 galaxies at $0.1 \leq z \leq 1.1$ with a photo-z accuracy of $\sigma_{\rm NMAD} = 0.006$.

We also develop a reliable methodology to take advantage of our SED-fitting results (based on mixture of two SSPs) and make predictions of SFR and sSFR. The exploration of the distribution of SFR and sSFR values in the stellar mass plane reveals a bimodality, where the main sequence of galaxies (star-forming galaxies) populate the upper SFR and sSFR values. In addition, the more massive quiescent galaxies exhibit larger SFRs than their lower mass counterparts. However, the most efficient process of star formation in the quiescent population reside in the low mass systems, whereas the massive ones present the lowest sSFR of the quiescent population. We confront our SFR predictions based in the UV luminosity at around 2 800 Åwith an independent SFR tracer based in the 24 μm luminosity or dust emission, getting a satisfactory agreement that supports that the DSF of the sample were removed properly.

From the dust-corrected UVJ-diagram, we find out striking results:

- A significant part of the galaxies that reside in the green valley are actually obscured star-forming galaxies ($\sim$ 65 %). These reveal intrinsic colours $(m_{F365} - m_{F551})_{\rm int}$ proper of the star-forming population, although their great dust content redden their colours. This also implies that the green valley is less populated than expected.

- Down to $m_{F814W} = 23$, the histogram of the $(m_{F365} - m_{F551})_{\rm int}$ colour exhibits a local minimum at ~ 1.45 that can be imposed as the bluest colour limit to fairly select the quiescent sample, which remains roughly constant since $z \leq 1.1$. Consequently, galaxies with intrinsic colours at $(m_{F365} - m_{F551})_{\rm int} \sim 1.45$ are less frequent, constituting what can be considered as the true green valley.

- Red galaxies that belong to the star-forming sample after the dust correction (intrinsic $m_{F365} - m_{F551} < 1.5$) are typically concentrated close to the edges of UVJ diagrams (e. g. Williams et al., 2009; Moresco et al., 2013), supporting the reliability of the extinction values provided by MUFFIT.

- Quiescent galaxies selected through a classical UVJ diagram (not corrected from dust effects) are typically contaminated by a $\sim$ 20 % of dusty star forming galaxies. Our results clearly establish that this contamination is less severe for massive galaxies ($\log_{10} M_\star \geq 11$, 2–8 % from $z \sim 0.1$ to $z \sim 1.1$) than for the least massive ones (40 %, for $9.2 \leq \log_{10} M_\star \leq 9.6$ at $0.1 \leq z \leq 0.3$).

The analysis of the distribution of stellar population parameters of quiescent galaxies on a dust-corrected UVJ-diagram reveals that there exist a close correlation between the position of each galaxy in this diagram and its age, metallicity, extinction, and stellar mass. We conclude that:

- The more massive quiescent galaxies lie on the redder parts of the UVJ-diagram at larger cosmic times. At larger redshifts, $z \sim 1$, massive quiescent galaxies present a larger spread of $(m_{F365} - m_{F551})_{\rm int}$ colours ($1.5 \leq (m_{F365} - m_{F551})_{\rm int} \leq 2.0$) than at $z \sim 0.2$, where they lie on the upper and redder parts of the UVJ-diagram $(m_{F365} - m_{F551})_{\rm int} \sim 2.0$.

- The whole quiescent sample shows an expected low dust content (96 % of galaxies present $A_V \leq 0.6$), where quiescent galaxies with bluer intrinsic colours, $(m_{F365} - m_{F551})_{\rm int} \lesssim 1.7$ and $(m_{F551} - J)_{\rm int} \lesssim 1.2$, are also the galaxies with larger extinction values ($A_V \gtrsim 0.4$).

- We find out a correlation of the colour $(m_{F365} - m_{F551})_{\rm int}$ with the age of quiescent galaxies. The older ages present the redder $(m_{F365} - m_{F551})_{\rm int}$ colours, populating the upper parts of the UVJ-diagram ($(m_{F365} - m_{F551})_{\rm int} > 1.8$). On the other hand, the younger quiescent galaxies present the bluer colour

of the diagram. Although there is a correlation with the $(m_{F365}-m_{F551})_{\rm int}$ colour, age is also dependent of the $(m_{F551}-J)_{\rm int}$ colour. Thus, to carry out an accurate determination of the age, it is necessary both $(m_{F365}-m_{F551})_{\rm int}$ and $(m_{F551}-J)_{\rm int}$ colours.

- The metallicity distribution in the UVJ-diagram is tightly correlated to the colour $(m_{F551}-J)_{\rm int}$ and weakly to $(m_{F365}-m_{F551})_{\rm int}$. The most metal rich quiescent galaxies ($[{\rm M/H}]_{\rm M} > 0.1$ dex) also present the reddest colours $(m_{F551}-J)_{\rm int} > 1.1$.

- Dust corrections play an important role in understanding how quiescent galaxies distribute inside the UVJ diagram as a function of their parameters: mass, age, metallicity and extinction. Without dust corrections, quiescent galaxies with large dust contents are in the upper parts of the UVJ-diagram as predicted by extinction laws. The correlation between age and the colour $(m_{F365}-m_{F551})$ is weaker than with $(m_{F365}-m_{F551})_{\rm int}$, whereas metallicity still correlates with $(m_{F551}-J)$ but also with $(m_{F365}-m_{F551})$.

It is well known that there is an increasing number of quiescent galaxies from high redshift to the present time. After exploring the number densities of quiescent galaxies at $0.1 \leq z \leq 1.1$, we confirm this result, as well as the variation of their number densities are well reproduced by a power-law function (as proposed by Moustakas et al., 2013). Moreover, the increasing number density for less massive galaxies is more striking than for the most massive ones ($\sim$ 50 % and 5 % every $\Delta z = 0.2$ for $10 \leq \log_{10} M_\star < 10.4$ and $\log_{10} M_\star \geq 11.2$ respectively). The above numbers agree within a "downsizing" picture in which less massive galaxies were formed in more recent epochs than the massive ones.

Finally, we shed light on the stellar population parameters of quiescent galaxies, along with its evolution, since $z = 1.1$ through the stellar population distributions built from the analysis results provided by MUFFIT. Indeed, we construct the probability distribution functions (PDF) of mass-weighted age/formation epoch, metallicity, and extinction during the last 8 Gyr, using a maximum likelihood estimator in order to deconvolve the uncertainty effects from these distributions and to parametrize them as function of redshift and stellar mass. This allows us to determine the evolution of the typical parameters (age, metallicity, and extinction), as well as to explore the intrinsic dispersion of the distributions of parameters. As expected, we find that the PDFs of the galaxy ages, metallicities and extinctions are strongly dependent on the SSP models used during the diagnostic SED-fitting process (BC03 and EMILES), although we still retrieve very interesting and striking results in common for both model sets:

- Quiescent galaxies are older at larger cosmic times, but these values are not compatible with a simple passive evolution, that is, there must be an incoming of new galaxies from the blue cloud and/or a mechanism including new stars of young and intermediate ages in their stellar populations (e. g. mergers, frosting, fall of cold gas, etc.) that slows down their ageing. In addition, the larger the galaxy mass the older the stellar population at any redshift, supporting the "downsizing" scenario up to $z \sim 1$. Regarding the widths of the mass-weighted age PDFs (intrinsic dispersions), these present values of $\omega_{{\rm Age}_{\rm M}} \sim$ 1–2 Gyr and a slight correlation with the stellar mass and redshift dependency.

- For BC03 and EMILES SSP models, quiescent galaxies show predominantly solar and super-solar metallicities, except for the local and less massive quiescent galaxies, which reveal sub-solar metallicities. Furthermore, the galaxy mass-metallicity relation seems to be present since earlier times, with hints of being steeper at lower redshifts.

- We find evidences for a decrease of the median of the metallicity PDF of quiescent galaxies since $z \sim$ 0.6–1.1, depending on the SSP models (BC03 and EMILES respectively). This decrement amounts to 0.1–0.2 dex and it is consistently recovered irrespective of the SSP models and isochrones employed during the analysis. At decreasing stellar masses the range of mass-weighted metallicities increases, and therefore, there is a dependency of the width of this PDF with stellar mass. The width of the mass-weighted metallicity PDF is broader at larger redshifts, where more massive galaxies present the narrower PDFs.

- All the quiescent galaxies present low extinction values $A_V < 0.6$, with median values in the range $A_V = 0.15$–0.3. For BC03 SSP models, there is a dependency with stellar mass and redshift, in the sense that more massive galaxies also present larger extinctions by dust and the extinction increases at lower redshifts. However for EMILES SSP models, all the quiescent galaxies exhibit extinction values of $A_V \sim 0.2$ independently of the stellar mass bins explored or redshift. As in the metallicity case, the width of the extinction PDF becomes larger at higher redshifts, i. e. a lower spread of extinction values in the local Universe, specially in the more massive galaxies.

The consistency of these results are studied imposing different constraints on the SFH of the models as well, such as constant extinction, constant solar metallicity, a closed-box enrichment of metals, fall of metal-poor cold gas, etc. In addition, we determine the systematics effects and the modifications of the stellar population predictions as a result of these constraints. In some cases, these ones can alter well studied relations as the MZR or the "downsizing" scenario. All the results are compared with the obtained from previous studies, including spectroscopic data and different analysis techniques (e. g. Lick indices), providing a good agreement with many of the conclusions and aspects treated in this chapter. The decrease in metallicity since high redshift up to the present time obtained for quiescent galaxies in this thesis cannot be assessed from current spectroscopic work as metallicity uncertainties are typically very large and, in addition, aperture effects can drive the spectroscopic results obtained for SDSS data.

4

The impact of mergers, "frosting" and the "progenitor" bias on the global populations of quiescent galaxies

In greatness, life and death merge.

Dejan Stojanovic

In this chapter, we aim at shedding light on the impact of mergers, "frosting" (remnants of star formation), and "progenitor" bias in the evolution of quiescent galaxies, both number density and stellar population properties. In particular, we focus on the evolution of the massive quiescent population. For the present work, we define massive quiescent population to those galaxies with stellar masses above the stellar mass limit $M_{\star,\mathrm{lim}}$. This stellar mass limit is an arbitrary limit and it is fixed at $\log_{10} M_{\star,\mathrm{lim}} = 11.2$ (the stellar mass bin that is complete in stellar mass up to $z \sim 1$ in ALHAMBRA), although we developed our methodology for a generic mass limit and other stellar mass limit would be able to be imposed. Making use of the results obtained in Chapter 3, we carried out a phenomenological model, in which the distributions of stellar population parameters (both mass-weighted age and metallicity) of massive quiescent galaxies are evolved since $z = 1$ down to $z = 0.2$ under the only effects of mergers, "frosting", and the "progenitor" bias. Moreover, as we determined the distributions of stellar populations of this subsample (see Sects. 3.7 and 3.8), we compare at any redshift ($0.2 \leq z \leq 1.0$) whether our phenomenological model reproduces the observations, which also constitutes a challenge for the proper SSP models used for determining stellar population properties (both BC03 and EMILES) discerning whether they are self-consistent with their predictions. Consequently, this novel phenomenological model is half way between the "archaeological" and the "look-back" approaches (see below). As we detail below, mergers and "progenitor" bias are observationally determined, and therefore, we are able to set upper-limit constraints on the level of "frosting", because the evolution in number with redshift (stellar population distributions as well) of massive quiescent sample is continuously confronted along the whole redshift range explored $0.2 \leq z \leq 1.0$.

4.1 Introduction

During the last decade, many authors tried to established the evolution or star formation history of galaxies from the study of their local stellar populations. This methodology is usually referred as "archaeological" approach or fossil record methods, and it has been extensively used for determining the stellar content of galaxies through their integrated properties or by their spatially-resolved stellar populations (e. g. Cid Fernandes et al., 2005; Gallazzi et al., 2005; Thomas et al., 2005; Ferré-Mateu et al., 2013; Trujillo et al., 2014; Belli et al., 2015; McDermid et al., 2015; González Delgado et al., 2015; Citro et al., 2016; Zheng et al., 2016; Goddard et al., 2017). These predictions are based on the SED reconstruction of galaxies, as well

as spectral indices sensitive to stellar population parameters (such as age, metallicity, α enhancement, IMF, etc.), usually using stellar population models with different SFH or including burst of various durations. Alternatively, the comparison between the stellar populations of similar samples at higher and nearby redshifts, "look-back" studies, provides complementary constraints in order to explain how galaxies evolved from the past until building-up their present stellar content (e. g. Schiavon et al., 2006; Sánchez-Blázquez et al., 2009; Choi et al., 2014; Gallazzi et al., 2014; Fagioli et al., 2016; Gargiulo et al., 2016; Siudek et al., 2016). Whilst the "look-back" studies constitute a direct comparison of the galaxy evolution, any interpretation of the results is limited by "progenitor" bias (van Dokkum & Franx, 2001). In fact, recent studies point out that there is an increasing number of quiescent galaxies since $z \sim 3$ (see Sect. 3.6, e. g. Drory et al., 2009; Pozzetti et al., 2010; Ilbert et al., 2010; Cassata et al., 2011; Davidzon et al., 2013; Ilbert et al., 2013; Moustakas et al., 2013; Moresco et al., 2013; Tomczak et al., 2014) that support an scenario in which quiescent galaxies are largely affected by "progenitor" bias. Other recent results advocate for a reduction in the number of massive star-forming galaxies (Bell et al., 2007; Davidzon et al., 2013; Ilbert et al., 2013; Moustakas et al., 2013), which also explains the observational growth in size of massive quiescent galaxies (see also Chapter 5, e. g. Shankar & Bernardi, 2009; Belli et al., 2015; Fagioli et al., 2016; Gargiulo et al., 2016; McDermid et al., 2015; Williams et al., 2016) and the scatter in the red sequence (Harker et al., 2006; Ruhland et al., 2009), which also supports the necessity for including their effects.

Mergers are an efficient mechanism for the creation of spheroid-like galaxies by the merging of gas-rich disks (Toomre, 1977; Schweizer & Seitzer, 1992; Barnes & Hernquist, 1996), as well as to modify colours of galaxies. In addition, many authors suggest that massive early-type galaxies were assembled by major mergers, in which a temporary quasar activity can be also present (Benson et al., 2003; Croton et al., 2006; Somerville et al., 2008; Hopkins et al., 2008b, 2009c; van der Wel et al., 2009; López-Sanjuan et al., 2013). Some results agree with an scenario in which the bulk of stars, specially in massive galaxies, were built up to $z \sim 1$, and then these galaxies have suffered numerous merger events in a hierarchical context (Bundy et al., 2007; White et al., 2007; Wake et al., 2008; Skelton et al., 2012; Ferreras et al., 2014), which can alter their stellar content. One of the limitations to explore the influence of mergers is that the time scale of a merger is dependent of the properties of the progenitor galaxies, as well as the orbit (Lotz et al., 2010a,b), although recent cosmological simulations (e. g. Springel et al., 2005; Kitzbichler & White, 2008) are facilitating these issues. In the early attempt by Skelton et al. (2012), authors showed that the presence of mergers reconstruct better the evolution of the RS than a passive evolution of galaxies in the RS. In the same work, the evolution of both mass and luminosity functions since $z \sim 1$ are better reproduced when mergers are included in their model of evolution. The predictions rather agree when wet mergers and "progenitor" bias are also accounted (see also Faber et al., 2007), specially the predictions on their color-magnitude evolution. Furthermore, recent studies based on the radial stellar population profiles in early-type galaxies (González Delgado et al., 2014b, 2015; Wilkinson et al., 2015; Goddard et al., 2017; Zheng et al., 2016) show flat age and shallow negative metallicity radial profiles, which agree with an assembly of these galaxies via major mergers (using SPH methodologies and cosmological simulations Kobayashi, 2004; Hirschmann et al., 2015). Nevertheless, the common presence of mergers, specially in the quiescent population (López-Sanjuan et al., 2012), are not properly treated for studying the impact that have this mechanism on the stellar population parameters or on their integrated properties, such age and metallicity. Generally, the impact of mergers is only mentioned for the interpretation of the results, as an external contribution (rather when the rest of mechanism cannot explain the evolution of galaxies), but without estimating its impact on the results.

This chapter is organized as follows. Sections 4.2, 4.3, and 4.4 detail the inclusion and methodology for treating mergers, "frosting", and "progenitor" bias in our phenomenological model respectively. In Sect. 4.5, the stellar mass loss due to intrinsic stellar evolution is also treated. Along Sect. 4.6, the individual effects of mergers, "frosting", and "progenitor" bias on the massive quiescent population are detailed, whereas in Sect. 4.7 the global effect of these mechanisms is described. A brief summary of the chapter, as well as the conclusions, are presented in Sect. 4.8.

Along this chapter we assume a ΛCDM cosmology with $H_0 = 71$ km s^{-1}, $\Omega_M = 0.27$, and $\Omega_\Lambda = 0.73$. All magnitudes are in AB-system (Oke & Gunn, 1983). The stellar masses are given in solar mass units

[$M_\odot$].

4.2 Mergers as mechanism to alter the stellar population distributions of quiescent galaxies

There are two main ways in which a merger can alter the stellar populations of the massive quiescent population. The first one is by the modification of the stellar populations of the already quiescent galaxies through accretion of the stellar content from satellite galaxies. On the other hand, the resultant increase in stellar mass by merger events can promote galaxies below $M_{\star,\mathrm{lim}}$, with other stellar populations or SFHs, towards the most massive bin, which also modifies the number of galaxies in the massive sample. Consequently, there are several channels of merger or scenarios that can contribute to modifying the stellar content of quiescent galaxies since $z = 1.0$.

We distinguish three merger contributions or main channels:

i) Galaxies that without belonging to the massive quiescent sample ($M_\star < M_{\star,\mathrm{lim}}$, for this work the mass limit is established at $\log_{10} M_{\star,\mathrm{lim}} = 11.2$) after a merger exceed this mass limit and they are also quiescent galaxies, that is, increasing the number density of the massive ones and adding members with a different stellar content (hereafter the channel "new"). For instance, 2 galaxies of $\log_{10} M_\star = 11$ ($< M_{\star,\mathrm{lim}}$) merge into 1 new galaxy of $\log_{10} M_\star = 11.3$ ($> M_{\star,\mathrm{lim}}$). The net balance in the number counts of the population under study is adding a new galaxy to the sample.

ii) Massive quiescent galaxies that experiment a merger event with galaxies outside this subpopulation (quiescent galaxies with stellar masses below $M_{\star,\mathrm{lim}}$ or star-forming galaxies) modifying their stellar content without altering the number density (referred as channel "in"). For instance, 2 galaxies of $\log_{10} M_\star = 11$ ($< M_{\star,\mathrm{lim}}$) and $\log_{10} M_\star = 11.3$ ($> M_{\star,\mathrm{lim}}$ and quiescent galaxy) merge into 1 new galaxy of $\log_{10} M_\star = 11.5$ ($> M_{\star,\mathrm{lim}}$). The net balance in the number counts of the population under study remains unaltered.

iii) Mergers amongst massive quiescent galaxies (in the following channel "out"), which will not substantially alter the stellar content, but decreasing in number the population of quiescent with $M_\star \geq M_{\star,\mathrm{lim}}$. For instance, 2 quiescent galaxies of $\log_{10} M_\star = 11.3$ ($> M_{\star,\mathrm{lim}}$) merge into 1 new galaxy of $\log_{10} M_\star = 11.6$ ($> M_{\star,\mathrm{lim}}$). The net balance in the number counts of the population under study is loosing 1 member.

In all cases, the stellar populations of the new galaxy will be determined by the ones of its progenitors and the type of merger event. The basic definitions and parameters concerning mergers in our phenomenological model are briefly explained in Sect. 4.2.1. The determination of the contributions of mergers to the massive quiescent sample via channels "new", "in", and "out" are detailed in Sects. 4.2.2, 4.2.3, and 4.2.4 respectively. The methodology for determining the impact of mergers on the stellar population distributions of the massive quiescent sample is presented in Sect. 4.2.5.

4.2.1 Basic definitions and some parameters involved in mergers

We introduce the numerous factors that are taken into account in order to estimate the influence of mergers on the massive quiescent population, as well as the concepts and receipts from previous work in order to support these assumptions.

4.2.1.1 The merger rate of galaxies

Many authors have studied the merger fraction of galaxies departing from both spectroscopic and photometric data from cosmological surveys (e. g. Conselice, 2006; Bluck et al., 2009; López-Sanjuan et al., 2009,

2010; Xu et al., 2012; López-Sanjuan et al., 2015b), in which the definition of merger fraction for major and minor mergers, $f_{\rm MM}$ and $f_{\rm mm}$ respectively, is not universal. For instance, in López-Sanjuan et al. (2013) authors defined the merger fraction as the number of close pairs, $N_{\rm m}$, divided by the number of galaxies targeted, $N_{\rm g}$. Formally,

$$f_{\rm MM,mm} = \frac{N_{\rm m}}{N_{\rm g}} \, , \tag{4.1}$$

where a close pair is defined as a couple of galaxies separated by a projected radius in the sky-plane $r_{\rm p}^{\rm min} \leq r_{\rm p} \leq r_{\rm p}^{\rm max}$ (e. g. $r_{\rm p}^{\rm min} = 0$ and $r_{\rm p}^{\rm max} = 20$–$30\ h^{-1}$ kpc), and the relative velocity between candidates, Δv, has to satisfy that $\Delta v \leq \Delta v^{\rm max}$ (e. g. $\Delta v^{\rm max} = 500$ km s^{-1}). In addition, the mass or luminosity ratios in close pairs (for this work defined as the stellar mass ratio between the principal and the companion galaxies in the pair, $\mu = M_{\rm p}/M_{\rm c}$) is defined for distinguishing between major ($\mu_{\rm MM}$) and minor mergers ($\mu_{\rm mm}$), and for its definition there is no consensus either. Throughout this work, we refer as major merger to those mergers in which the mass ratio between the companion and principal galaxies in the pair satisfies $1/4 \leq \mu_{\rm MM} \leq 1$; whereas for minor merger mergers this range is $1/10 \leq \mu_{\rm mm} \leq 1/4$. Consequently, the definition of $f_{\rm MM,mm}$ may change, as the values for $r_{\rm p}^{\rm min}$, $r_{\rm p}^{\rm max}$, $\Delta v^{\rm max}$, and $\mu_{\rm MM,mm}$ can differ amongst different studies. For solving this drawback, López-Sanjuan et al. (2013) proposed a quantification of the fraction merger rate that allows us to convert $f_{\rm MM}$ and $f_{\rm mm}$ to different definitions. Formally,

$$f_{\rm MM}(20, 1/4) = C_{\rm p} \times F(\mu_{\rm MM}) \times \left(\frac{20 h^{-1}\ {\rm kpc}}{r_{\rm p}^{\rm max}} \right)^{0.95} \times f_{\rm MM}(r_{\rm p}^{\rm max}, \mu_{\rm MM}) \, , \tag{4.2}$$

where the factor $C_{\rm p} = \frac{r_{\rm p}^{\rm max}}{r_{\rm p}^{\rm max} - r_{\rm p}^{\rm min}}$ accounts for the missing close companions at $r_{\rm p}^{\rm min} \neq 0$, $F(\mu_{\rm MM})$ converts merger fractions to alternative definitions of mass ratio ranges, and $f_{\rm MM}$ is normalised to $r_{\rm p}^{\rm max} = 20\ h^{-1}$ for a mass ratio $1/4 \leq \mu_{\rm MM} \leq 1$. The function $F(\mu_{\rm MM})$ was observationally derived as $F(\mu) \propto \mu^s$ and established by López-Sanjuan et al. (2011) as

$$F(\mu_{\rm MM}) = f_{\rm MM} \left(\frac{\mu}{\mu_{\rm MM}} \right)^s \, . \tag{4.3}$$

The parameter s for this work is fixed to $s = -0.9 \pm 0.4$, which was derived observationally (López-Sanjuan et al., 2011, 2012; Xu et al., 2012). From the results obtained in López-Sanjuan et al. (2011), Eq. 4.2 is also valid for minor mergers. It is noteworthy mentioning that Eq. 4.2 demonstrated to conciliate merger fractions from various surveys properly, such as Lin et al. (2008); de Ravel et al. (2009); López-Sanjuan et al. (2011); Xu et al. (2012).

Although $f_{\rm MM}$ and $f_{\rm mm}$ are observationally constrained, there exist the necessity of a physical parameter in order to quantify the influence of mergers on the quiescent population. Note that each close pair resides in a different potential well, and the distance between them is also a parameter that determines when a close pair of galaxies will finally merge. Consequently, the definition of a major and minor merger rate per galaxy and Gyr ($R_{\rm MM}$ and $R_{\rm mm}$ respectively) is necessary for our aims. $R_{\rm MM}$ and $R_{\rm mm}$ must take all the factors mentioned above into account, as well as the efficiency of mergers because part of the close pairs will not finally merge (fly-by). For obtaining $R_{\rm MM,mm}$ through $f_{\rm MM,mm}$, we followed de Ravel et al. (2009)

$$R_{\rm MM} = f_{\rm MM} C_{\rm MM} T_{\rm MM}^{-1} \, , \tag{4.4}$$

$$R_{\rm mm} = f_{\rm mm} C_{\rm mm} T_{\rm mm}^{-1} \, , \tag{4.5}$$

where $C_{\rm MM}(C_{\rm mm})$ is the fraction of the observed close pairs that finally merge in a typical time scale $T_{\rm MM}(T_{\rm mm})$. The typical time scales can be determined from the cosmological simulations of Kitzbichler & White (2008), which are based on the Millenium simulation (Springel et al., 2005). Actually, these time scales also include the factors $C_{\rm MM}$ and $C_{\rm mm}$, so in the following we can assume $C_{\rm MM} = C_{\rm mm} = 1$. To illustrate, the typical time scale for early-type galaxies is $T_{\rm MM} = 1.0 \pm 0.2$ Gyr for $r_{\rm p}^{\rm max} = 30 h^{-1}$ kpc, $\Delta v^{\rm max} = 500$ km s^{-1} and $\log_{10} M_\star = 11.2$ dex.

For our model of mergers and its influence in the quiescent population, we assumed the major and minor merger rate prescriptions retrieved in López-Sanjuan et al. (2012, 2013) from COSMOS-zCOSMOS and MASSIV projects respectively (which also includes a compilation of various merger fractions at different redshifts from other surveys). These merger rates were also parametrised by a redshift power-law, making easy their application in our redshift range, and separated in early and late types. Our first assumption is that the merger rate of early-type galaxies should be quite similar to the quiescent ones. For major mergers, the merger rates of star-forming and quiescent galaxies are respectively,

$$R^{\rm SF}_{\rm MM} = (1.37 \pm 0.8)10^{-3}(1+z)^{3.95\pm0.12}\ [{\rm Gyr}^{-1}]\ , \tag{4.6}$$

$$R^{\rm Q}_{\rm MM} = (3.0 \pm 0.6)10^{-2}(1+z)^{1.8\pm0.3}\ [{\rm Gyr}^{-1}]\ , \tag{4.7}$$

whereas for minor mergers, the merger rate is compatible with constant values since $z = 1$ of the form:

$$R^{\rm SF}_{\rm mm} = (2.3 \pm 1.0)10^{-2}\ [{\rm Gyr}^{-1}]\ , \tag{4.8}$$

$$R^{\rm Q}_{\rm mm} = (6.0 \pm 0.8)10^{-2}\ [{\rm Gyr}^{-1}]\ . \tag{4.9}$$

Note that Eqs. 4.6–4.9 are defined as the merger rate per galaxy and Gyr, where the only distinction is that the principal galaxy is star-forming or quiescent.

4.2.1.2 Number density of mergers

The number of minor and major mergers that an individual galaxy suffers along a period of cosmic time ($N_{\rm mm}$ and $N_{\rm MM}$ respectively) can be easily obtained from the merger rate as:

$$N_{\rm MM,mm}(z_1, z_2) = \int_{z_1}^{z_2} \frac{R_{\rm MM,mm}\ {\rm d}z}{(1+z)\,H_0\,\sqrt{\Omega_\Lambda + \Omega_{\rm K}(1+z)^2 + \Omega_{\rm M}(1+z)^3}}\ . \tag{4.10}$$

The number of minor and major mergers undergone by a quiescent galaxy at the redshift range $0.2 \leq z \leq 1.0$, using the merger rates in Eqs. 4.9 and 4.7, are respectively $N_{\rm mm} = 0.32 \pm 0.05$ and $N_{\rm MM} = 0.35 \pm 0.09$. Consequently, almost one third of quiescent galaxies at $z = 1.0$ will suffer at least one major and one minor merger. This striking result points out that mergers can significantly contribute to the build-up of the nowadays quiescent population, as well as modifying the stellar content of these galaxies through the incorporation of ex-situ stellar populations or gas from less massive systems. Note that quiescent galaxies are expected to have stellar populations that correlate with stellar mass, i. e. the well known MZR and "downsizing", and therefore, pieces of younger and more metal poor systems will fall from less massive galaxies during the merger. The impact is stronger after accounting for those galaxies with stellar masses below $M_{\star,\rm lim}$, which are able to suffer merger events as well, but also increasing in mass as to exceed this mass limit (we treat all these effects in Sects. 4.2.2–4.2.4).

In order to estimate the relative contribution of mergers in the massive quiescent sample (or the number density of galaxies affected), we based our estimations on the parent model by López-Sanjuan et al. (2013). The number density of sources affected by mergers, $\rho_{\rm ch}$, at the redshift range $z_1 \leq z < z_2$ is formally expressed as

$$\rho_{\rm ch} = \int_{z_1+\Delta z_1}^{z_2+\Delta z_2} \int_{M_{\star,1}}^{M_{\star,2}} \Phi(z, M_\star) R_{\rm MM,mm}(z)\ E_{\rm ch}(M_\star, \mu)\ {\rm d}M_\star {\rm d}z\ , \tag{4.11}$$

where the subindex "ch" is referred to the merger channel (further detailed in Sects. 4.2.2–4.2.4), Φ is the stellar mass function (MF) of the principal galaxy in the merger (quiescent or star-forming), $E_{\rm ch}$ the merger efficiency function of the merger channel (related with the range of stellar masses that contributes to the massive sample and based in Eqs. 4.2 and 4.3; e. g. for quiescent galaxies with $\log_{10} M_\star = 10.9$, these increase the density number of quiescent galaxies with $M_\star \geq M_{\star,\rm lim}$ only for major mergers with $\mu_{\rm MM} = 1$ and the major merger rate is defined for mass ratios $1/4 \leq \mu_{\rm MM} \leq 1$ in Eq. 4.7), $M_{\star,1}$ and $M_{\star,2}$ limit

the stellar mass range that contributes in the channel (e. g. when exploring the number density of galaxies above $M_{\star,\mathrm{lim}}$ that experiment a minor merger, we set $M_{\star,1} = M_{\star,\mathrm{lim}}$ and $M_{\star,2} = \infty$), and $\Delta z_{1,2}$ reflects the coalescence time of the merger (i. e. the cosmic time after the merger event to consider that the merger remnant belong to the sample under study) that for this work is null, because the selection criteria is based in colours and it is therefore supposed to be instantaneous (superposition of the stellar population luminosities in the pair).

4.2.1.3 Fraction of red and blue companions

The merger rates proposed for this work, Eqs. 4.6–4.9, do not distinct the spectral type of the companion galaxy in the merger, that is, there is no distinction whether the companion galaxy is red or blue. To convert these merger rates in which the companion galaxy is quiescent or star-forming, we resorted to the observational results by López-Sanjuan et al. (2012), where the authors determined that the fraction of red (blue) companion galaxies in mergers is 65 % (35 %) for both minor and major mergers. This result is also independent whether the principal galaxy is quiescent ($f_{\mathrm{Q,Q}} = 0.65$ and $f_{\mathrm{Q,SF}} = 0.35$) or star-forming ($f_{\mathrm{SF,Q}} = 0.65$ and $f_{\mathrm{SF,SF}} = 0.35$). To convert Eqs. 4.6–4.9 for a case in which the companion galaxy in the close pair is a certain spectral type, we multiply them by these factors. For instance, for obtaining the major merger rate between quiescent galaxies (both the principal and the companion belong to the quiescent population), we must multiply Eq. 4.7 by $f_{\mathrm{Q,Q}} = 0.65$.

4.2.1.4 Wet and dry mergers: the gas fraction

The common presence of red galaxies in mergers (see Eqs. 4.6–4.9 and Sect. 4.2.1.3) implies that the majority of mergers are "dry" mergers or with low gas content, whereas "wet" mergers, which contains larger reserves of gas, are less frequent. In spite of mergers that provide new amount of gas are less frequent, we account for this accretion of new gas.

Based on the simulations by Hopkins et al. (2009a), a merger of two close galaxies induced star formation processes, in which part of the cold gas belonging to the involved galaxies is transformed into stars. Owing to the proper evolution of galaxies, these fractions of gas vary with redshift and stellar mass (e. g. Bell, 2003; Kannappan, 2004; Erb et al., 2006; Reddy et al., 2006; Dalcanton, 2007). For quiescent galaxies, in which the star formation process has been quenched, we assumed that the fraction of gas is negligible or null in any case, $f^{\mathrm{Q}}_{\mathrm{gas}}(z, M_\star) = 0$. For star-forming galaxies, we used the parametrization provided by Rodrigues et al. (2012) for estimating its gas fraction, $f^{\mathrm{SF}}_{\mathrm{gas}}(z, M_\star)$, which is a function of the stellar mass and cosmic time of the form:

$$f^{\mathrm{SF}}_{\mathrm{gas}}(z, M_\star) = \frac{M_{\mathrm{gas}}}{M_\star + M_{\mathrm{gas}}} = \frac{1}{1 + (M_\star / 10^{A(t)})^{B(t)}} \,, \tag{4.12}$$

where t is the cosmic time between redshift z and the present, and

$$A(t) = 9.15 + 0.13t \,, \tag{4.13}$$

$$B(t) = 0.5 + 13.36 \times \exp -38.02/t \,. \tag{4.14}$$

The assumption of that all the expected gas in the close pair is transformed into stars may result quite strong. For this reason, we assumed the prescription by Hopkins et al. (2009a), which is analytically expressed and estimated from simulations. Thus, the fraction of initial gas that will finally be transformed into stars is

$$f_{\mathrm{burst}} = \frac{2\mu}{1+\mu} f_{\mathrm{T,gas}} (1 - f_{\mathrm{T,gas}}) \,, \tag{4.15}$$

where μ is the mass ratio between the close pair components and $f_{\mathrm{T,gas}}$ is the total mass gas fraction in the pair.

Combining both Eqs. 4.12 and 4.16, we obtain that the fraction of mass created into new stars ($f_{\rm sf}$) respect the total stellar mass involved in the merger (both principal and companion galaxies) is

$$f_{\rm sf}(z, M_\star) = \frac{f_{\rm burst}\, M_{\rm gas}}{M_\star} = \frac{2\mu}{1+\mu} f_{\rm T,gas}^2 \,, \tag{4.16}$$

where $f_{\rm T,gas}$ is null when both galaxies in the pair are quiescent and for the star-forming ones is expressed by Eq. 4.12. Note that in those mergers in which both galaxies are quiescent $f_{\rm sf} = 0$, in the rest of cases there is at least one star-forming galaxy with gas available to increase the stellar mass of the initial close pair. Moreover, each galaxy in the close pair can present different stellar mass values and spectral types, which allow us to distinguish the fraction of mass from new stars created during a merger for the principal and the companion galaxy in the pair.

4.2.2 Number density of mergers via channel "new"

The channel "new" is specially important as this increases the number of quiescent massive galaxies and the members of the pairs contain different stellar populations ("downsizing" and MZR) associated to different SFH. For the present channel, we can distinguish two scenarios: mergers between two already quiescent galaxies (Sect. 4.2.2.1), and mergers between a quiescent and a star-forming galaxy (Sect. 4.2.2.2). Taking advantage of Eq. 4.11 and dealing with minor and major mergers separately, we estimate the increment in number density by the "new" channel.

4.2.2.1 Mergers of quiescent galaxies below $M_{\star,\rm lim}$

As both galaxies in the pair are below $M_{\star,\rm lim}$ and the fraction of gas is negligible ($f_{\rm T,gas} = 0$), the merger efficiency function in Eq. 4.11 will account for the stellar mass of the principal galaxy in the pair and the range of μ values that are able to exceed $M_{\star,\rm lim}$, and thus increasing in number the massive quiescent sample. Formally,

$$E_{\rm new}^{\rm Q,Q}(M_\star, \mu, M_{\star,\rm lim}) = \begin{cases} 0, & \text{if } M_\star < M_1, \\ f_{\rm Q,Q} \times \left(\frac{\mu_1}{\mu_{\rm min}}\right)^s, & \text{if } M_1 \leq M_\star < M_2, \\ f_{\rm Q,Q}, & \text{if } M_\star \geq M_2, \end{cases} \tag{4.17}$$

where $f_{\rm Q,Q}$ reflects the fraction of red companions in the pair ($f_{\rm Q,Q} = 0.65$ for this work), $\mu_{\rm min}$ and $\mu_{\rm max}$ are the limit mass ratios of the merger rate (for minor mergers $\mu_{\rm min} = 1/10$ and $\mu_{\rm max} = 1/4$, whereas for the major ones $\mu_{\rm min} = 1/4$ and $\mu_{\rm max} = 1$), and

$$M_1 = \frac{M_{\star,\rm lim}}{1+\mu_{\rm max}} \,, \tag{4.18}$$

$$M_2 = \frac{M_{\star,\rm lim}}{1+\mu_{\rm min}} \,, \tag{4.19}$$

$$\mu_1 = \frac{M_{\star,\rm lim}}{M_\star} - 1 \,. \tag{4.20}$$

The number density of new sources owing to mergers between quiescent galaxies is,

$$\rho_{\rm new}^{\rm Q,Q} = \rho_{\rm new,MM}^{\rm Q,Q} + \rho_{\rm new,mm}^{\rm Q,Q} = \int_{z_1}^{z_2} \int_0^{M_{\star,\rm lim}} \Phi_{\rm Q} R_{\rm MM}^{\rm Q}\, E_{\rm new}^{\rm Q,Q}(\mu_{\rm min} = 1/4, \mu_{\rm max} = 1)\, {\rm d}M_\star {\rm d}z + \\ + \int_{z_1}^{z_2} \int_0^{M_{\star,\rm lim}} \Phi_{\rm Q} R_{\rm mm}^{\rm Q}\, E_{\rm new}^{\rm Q,Q}(\mu_{\rm min} = 1/10, \mu_{\rm max} = 1/4)\, {\rm d}M_\star {\rm d}z \,, \tag{4.21}$$

where $\Phi_{\rm Q}$ refers to the MF of quiescent galaxies. Note that the derivation of MF is key for determining the number of galaxies at any stellar mass and redshift. We devote Appendix F to describing the novel methodology developed in this work for deriving Schechter-like MFs that are also redshift dependent.

4.2.2.2 Mergers between star-forming and quiescent galaxies below $M_{\star,\mathrm{lim}}$

As above, there are quiescent galaxies with stellar masses below $M_{\star,\mathrm{lim}}$ that after the merger will increase in mass as to exceed this limit, but where the companion is a blue or star-forming galaxy. In the same sense, there are star-forming galaxies that after a merger with a quiescent galaxy becomes as red as to incorporate the merger remnant in the massive quiescent population.

When a quiescent galaxy with stellar mass below $M_{\star,\mathrm{lim}}$ experiments a merger with a star-forming one, the efficiency function is expressed as follow,

$$E^{\mathrm{Q,SF}}_{\mathrm{new}}(M_\star,\mu,M_{\star,\mathrm{lim}}) = \begin{cases} 0, & \text{if } M_\star < M_3, \\ f_{\mathrm{Q,SF}} \times \epsilon_{\mathrm{c}}^{\mathrm{Q,SF}} \times \left(\frac{\mu_2}{\mu_{\mathrm{min}}}\right)^s, & \text{if } M_3 \leq M_\star < M_4, \\ f_{\mathrm{Q,SF}} \times \epsilon_{\mathrm{c}}^{\mathrm{Q,SF}}, & \text{if } M_\star \geq M_4, \end{cases} \tag{4.22}$$

where $f_{\mathrm{Q,SF}}$ reflects the fraction of blue companions in the pair ($f_{\mathrm{Q,SF}} = 0.35$ for this work), $\epsilon_{\mathrm{c}}^{\mathrm{Q,SF}}$ the efficiency of the colour in the merger (which accounts that a merger of a blue and a red galaxy can provide either a red or a blue more massive galaxy), and

$$M_3 = \frac{M_{\star,\mathrm{lim}}}{(1+\mu_{\mathrm{max}})(1+f_{\mathrm{sf}})}\,, \tag{4.23}$$

$$M_4 = \frac{M_{\star,\mathrm{lim}}}{(1+\mu_{\mathrm{min}})(1+f_{\mathrm{sf}})}\,, \tag{4.24}$$

$$\mu_2 = \frac{M_{\star,\mathrm{lim}}}{M_\star(1+f_{\mathrm{sf}})} - 1\,, \tag{4.25}$$

where f_{sf} is the fraction of stellar mass transformed into stars during the merger (as in this case there is a star forming galaxy which contributes with gas to the merger remnant, see Sect. 4.2.1.4).

The factor $\epsilon_{\mathrm{c}}^{\mathrm{Q,SF}}(z, M_\star, \mu)$ is observationally derived by our sample of galaxies from ALHAMBRA. For each redshift, stellar mass, and mass ratio involved in Eq. 4.11, we built the dust-corrected m_{F365} and m_{F551} luminosity distributions of red galaxies (principal galaxy in the pair) and the blue ones (companion). The dust-corrected m_{F365} and m_{F551} luminosities are obtained from the k corrections provided by MUFFIT. Finally, we explore the percentage of combinations between both luminosity distributions (red and blue) that are able to present redder colours than the colour limit imposed for selecting the quiescent sample $(m_{F365} - m_{F551})_{\mathrm{int}} \geq 1.5$, that is, the observationally percentage of minor and major mergers whose final colour will be redder than 1.5 in a hypothetical case in which a merger successes.

The number density of new members due to mergers between quiescent galaxies below $M_{\star,\mathrm{lim}}$ and star-forming ones is therefore

$$\begin{aligned} \rho^{\mathrm{Q,SF}}_{\mathrm{new}} = \rho^{\mathrm{Q,SF}}_{\mathrm{new,MM}} + \rho^{\mathrm{Q,SF}}_{\mathrm{new,mm}} = &\int_{z_1}^{z_2}\int_0^{M_{\star,\mathrm{lim}}} \Phi_{\mathrm{Q}} R^{\mathrm{Q}}_{\mathrm{MM}}\, E^{\mathrm{Q,SF}}_{\mathrm{new}}(\mu_{\mathrm{min}}=1/4, \mu_{\mathrm{max}}=1)\,\mathrm{d}M_\star \mathrm{d}z + \\ &+ \int_{z_1}^{z_2}\int_0^{M_{\star,\mathrm{lim}}} \Phi_{\mathrm{Q}} R^{\mathrm{Q}}_{\mathrm{mm}}\, E^{\mathrm{Q,SF}}_{\mathrm{new}}(\mu_{\mathrm{min}}=1/10, \mu_{\mathrm{max}}=1/4)\,\mathrm{d}M_\star \mathrm{d}z\,, \end{aligned} \tag{4.26}$$

Similarly, there are star-forming galaxies that after adding new populations from quiescent galaxies, these will present typical red colours as the quiescent ones. The efficiency merger function is quiet similar to Eq. 4.22 and expressed as

$$E^{\mathrm{SF,Q}}_{\mathrm{new}}(M_\star,\mu,M_{\star,\mathrm{lim}}) = \begin{cases} 0, & \text{if } M_\star < M_3, \\ f_{\mathrm{SF,Q}} \times \epsilon_{\mathrm{c}}^{\mathrm{SF,Q}} \times \left(\frac{\mu_2}{\mu_{\mathrm{min}}}\right)^s, & \text{if } M_3 \leq M_\star < M_4, \\ f_{\mathrm{SF,Q}} \times \epsilon_{\mathrm{c}}^{\mathrm{SF,Q}}, & \text{if } M_\star \geq M_4, \end{cases} \tag{4.27}$$

where $f_{\mathrm{SF,Q}}$ is the fraction of red companions when the principal galaxy is star-forming ($f_{\mathrm{SF,Q}} = 0.65$ in the present research), and $\epsilon_{\mathrm{c}}^{\mathrm{SF,Q}}$ is obtained following the process described above (although now the principal galaxy is the blue one).

The number density of star-forming galaxies that experiment a merger with a quiescent one, getting as a result a new massive quiescent galaxy with stellar mass larger than $M_{\star,\mathrm{lim}}$ is

$$\rho_{\mathrm{new}}^{\mathrm{SF,Q}} = \rho_{\mathrm{new,MM}}^{\mathrm{SF,Q}} + \rho_{\mathrm{new,mm}}^{\mathrm{SF,Q}} = \int_{z_1}^{z_2}\int_{0}^{\infty} \Phi_{\mathrm{SF}} R_{\mathrm{MM}}^{\mathrm{SF}}\, E_{\mathrm{new}}^{\mathrm{SF,Q}}(\mu_{\mathrm{min}} = 1/4, \mu_{\mathrm{max}} = 1)\, \mathrm{d}M_\star \mathrm{d}z + \\ + \int_{z_1}^{z_2}\int_{0}^{\infty} \Phi_{\mathrm{SF}} R_{\mathrm{mm}}^{\mathrm{SF}}\, E_{\mathrm{new}}^{\mathrm{SF,Q}}(\mu_{\mathrm{min}} = 1/10, \mu_{\mathrm{max}} = 1/4)\, \mathrm{d}M_\star \mathrm{d}z\,, \tag{4.28}$$

where Φ_{SF} is the MF of star-forming galaxies (see Appendix F).

4.2.3 Number density of mergers via channel "in"

Massive quiescent galaxies also suffer merger events, that without modifying the density number of their population, it alters their stellar content adding stellar populations from less massive systems. This scenario, or channel "in", can play an important role because it modifies their stellar contents. Likewise, the merger efficiency function for estimating the number density of massive galaxies that experiment merger events with quiescent galaxies is

$$E_{\mathrm{in}}^{\mathrm{Q,Q}}(M_\star, \mu, M_{\star,\mathrm{lim}}) = \begin{cases} f_{\mathrm{Q,Q}}, & \text{if } M_\star = M_{\star,\mathrm{lim}}, \\ f_{\mathrm{Q,Q}} \times \left(1 - \frac{\mu_3}{\mu_{\mathrm{min}}}\right)^s, & \text{if } M_{\star,\mathrm{lim}} \leq M_\star < M_5, \\ 0, & \text{if } M_\star \geq M_5, \end{cases} \tag{4.29}$$

where

$$M_5 = \frac{M_{\star,\mathrm{lim}}}{\mu_{\mathrm{min}}} \tag{4.30}$$

$$\mu_3 = \frac{M_{\star,\mathrm{lim}}}{M_\star}\,. \tag{4.31}$$

The number density of massive quiescent galaxies that merges with other quiescent galaxies is therefore

$$\rho_{\mathrm{in}}^{\mathrm{Q,Q}} = \rho_{\mathrm{in,MM}}^{\mathrm{Q,Q}} + \rho_{\mathrm{in,mm}}^{\mathrm{Q,Q}} = \int_{z_1}^{z_2}\int_{M_{\star,\mathrm{lim}}}^{\infty} \Phi_{\mathrm{Q}} R_{\mathrm{MM}}^{\mathrm{Q}}\, E_{\mathrm{in}}^{\mathrm{Q,Q}}(\mu_{\mathrm{min}} = 1/4, \mu_{\mathrm{max}} = 1)\, \mathrm{d}M_\star \mathrm{d}z + \\ + \int_{z_1}^{z_2}\int_{M_{\star,\mathrm{lim}}}^{\infty} \Phi_{\mathrm{Q}} R_{\mathrm{mm}}^{\mathrm{Q}}\, E_{\mathrm{in}}^{\mathrm{Q,Q}}(\mu_{\mathrm{min}} = 1/10, \mu_{\mathrm{max}} = 1/4)\, \mathrm{d}M_\star \mathrm{d}z\,. \tag{4.32}$$

Furthermore, quiescent galaxies exceeding $M_{\star,\mathrm{lim}}$ also accrete star-forming galaxies via merger, rather modifying their stellar content. Its merger efficiency function is

$$E_{\mathrm{in}}^{\mathrm{Q,SF}}(M_\star, \mu, M_{\star,\mathrm{lim}}) = \begin{cases} f_{\mathrm{Q,SF}} \times \epsilon_{\mathrm{c}}^{\mathrm{Q,SF}}, & \text{if } M_\star = M_{\star,\mathrm{lim}}, \\ f_{\mathrm{Q,SF}} \times \epsilon_{\mathrm{c}}^{\mathrm{Q,SF}} \times \left(1 - \frac{\mu_3}{\mu_{\mathrm{min}}}\right)^s, & \text{if } M_{\star,\mathrm{lim}} \leq M_\star < M_5, \\ 0, & \text{if } M_\star \geq M_5. \end{cases} \tag{4.33}$$

Thereby, the number density of massive quiescent galaxies affected by channel "in" for this case is

$$\rho_{\mathrm{in}}^{\mathrm{Q,SF}} = \rho_{\mathrm{in,MM}}^{\mathrm{Q,SF}} + \rho_{\mathrm{in,mm}}^{\mathrm{Q,SF}} = \int_{z_1}^{z_2}\int_{M_{\star,\mathrm{lim}}}^{\infty} \Phi_{\mathrm{Q}} R_{\mathrm{MM}}^{\mathrm{Q}}\, E_{\mathrm{in}}^{\mathrm{Q,SF}}(\mu_{\mathrm{min}} = 1/4, \mu_{\mathrm{max}} = 1)\, \mathrm{d}M_\star \mathrm{d}z + \\ + \int_{z_1}^{z_2}\int_{M_{\star,\mathrm{lim}}}^{\infty} \Phi_{\mathrm{Q}} R_{\mathrm{mm}}^{\mathrm{Q}}\, E_{\mathrm{in}}^{\mathrm{Q,SF}}(\mu_{\mathrm{min}} = 1/10, \mu_{\mathrm{max}} = 1/4)\, \mathrm{d}M_\star \mathrm{d}z\,. \tag{4.34}$$

4.2.4 Number density of mergers via channel "out"

A natural mechanism to reduce the number density of massive quiescent galaxies is a merger between two massive quiescent galaxies. A major or minor merger between two galaxies of stellar mass larger than $M_{\star,\mathrm{lim}}$ will produce an even more massive quiescent galaxy that is the product of a merger of two of them, decreasing the number of quiescent massive galaxies in one unit. For this scenario, and following the same process than in sections above, the merger efficiency function for this scenario in the channel "out" is

$$E_{\mathrm{out}}^{\mathrm{Q,Q}}(M_\star, \mu, M_{\star,\mathrm{lim}}) = \begin{cases} 0, & \text{if } M_\star < M_6, \\ f_{\mathrm{Q,Q}} \times \left(\frac{\mu_4}{\mu_{\mathrm{min}}}\right)^s, & \text{if } M_6 \leq M_\star < M_7, \\ f_{\mathrm{Q,Q}}, & \text{if } M_\star \geq M_7, \end{cases} \tag{4.35}$$

where the gas fraction of these galaxies is assumed null, and

$$M_6 = \frac{M_{\star,\mathrm{lim}}}{\mu_{\mathrm{max}}} \tag{4.36}$$

$$M_7 = \frac{M_{\star,\mathrm{lim}}}{\mu_{\mathrm{min}}} \tag{4.37}$$

$$\mu_4 = \frac{M_{\star,\mathrm{lim}}}{M_\star} \, . \tag{4.38}$$

Consequently, the decrease in number of the quiescent massive sample owing to mergers among them is formally expressed as

$$\rho_{\mathrm{out}}^{\mathrm{Q,Q}} = \rho_{\mathrm{out,MM}}^{\mathrm{Q,Q}} + \rho_{\mathrm{out,mm}}^{\mathrm{Q,Q}} = \int_{z_1}^{z_2} \int_{M_{\star,\mathrm{lim}}}^{\infty} \Phi_{\mathrm{Q}} R_{\mathrm{MM}}^{\mathrm{Q}} \, E_{\mathrm{out}}^{\mathrm{Q,Q}}(\mu_{\mathrm{min}} = 1/4, \mu_{\mathrm{max}} = 1) \, \mathrm{d}M_\star \mathrm{d}z + \\ + \int_{z_1}^{z_2} \int_{M_{\star,\mathrm{lim}}}^{\infty} \Phi_{\mathrm{Q}} R_{\mathrm{mm}}^{\mathrm{Q}} \, E_{\mathrm{out}}^{\mathrm{Q,Q}}(\mu_{\mathrm{min}} = 1/10, \mu_{\mathrm{max}} = 1/4) \, \mathrm{d}M_\star \mathrm{d}z \, . \tag{4.39}$$

In addition, we take into account that quiescent galaxies with larger stellar masses than $M_{\star,\mathrm{lim}}$ can suffer mergers of blue galaxies with large amounts of younger stellar populations, that can affect their colours moving them towards the main sequence, and reducing their number too. For this scenario, the merger efficiency function is

$$E_{\mathrm{out}}^{\mathrm{Q,SF}}(M_\star, \mu, M_{\star,\mathrm{lim}}) = \begin{cases} 0, & \text{if } M_\star < M_3, \\ f_{\mathrm{Q,SF}} \times (1 - \epsilon_{\mathrm{c}}^{\mathrm{Q,SF}}) \times \left(\frac{\mu_2}{\mu_{\mathrm{min}}}\right)^s, & \text{if } M_3 \leq M_\star < M_4, \\ f_{\mathrm{Q,SF}} \times (1 - \epsilon_{\mathrm{c}}^{\mathrm{Q,SF}}), & \text{if } M_\star \geq M_4, \end{cases} \tag{4.40}$$

where the factor $(1 - \epsilon_{\mathrm{c}}^{\mathrm{Q,SF}})$ accounts for the galaxies that after merging present colours bluer than $(m_{F365} - m_{F551})_{\mathrm{int}} < 1.5$, and estimated as in Sect. 4.2.2.2. The decrement in the number density of massive quiescent galaxies for this scenario is expressed as

$$\rho_{\mathrm{out}}^{\mathrm{Q,SF}} = \rho_{\mathrm{out,MM}}^{\mathrm{Q,SF}} + \rho_{\mathrm{out,mm}}^{\mathrm{Q,SF}} = \int_{z_1}^{z_2} \int_{M_{\star,\mathrm{lim}}}^{\infty} \Phi_{\mathrm{Q}} R_{\mathrm{MM}}^{\mathrm{Q}} \, E_{\mathrm{out}}^{\mathrm{Q,SF}}(\mu_{\mathrm{min}} = 1/4, \mu_{\mathrm{max}} = 1) \, \mathrm{d}M_\star \mathrm{d}z + \\ + \int_{z_1}^{z_2} \int_{M_{\star,\mathrm{lim}}}^{\infty} \Phi_{\mathrm{Q}} R_{\mathrm{mm}}^{\mathrm{Q}} \, E_{\mathrm{out}}^{\mathrm{Q,SF}}(\mu_{\mathrm{min}} = 1/10, \mu_{\mathrm{max}} = 1/4) \, \mathrm{d}M_\star \mathrm{d}z \, . \tag{4.41}$$

4.2.5 Treating the evolution of the stellar populations in the merger scenario

We restrict the implications of mergers only for ages and metallicities, as there is no much information in the literature in order to constraint the correlations of extinction with stellar mass and redshift for star forming galaxies. Moreover, we are not able to establish the evolution of extinction due to the evolution of the stellar

populations inside the host galaxy. This is mainly hard to handle for star forming galaxies, in which the process of star formation and quenching mechanisms can modify the intrinsic extinction (also in quiescent galaxies by "frosting" mechanisms). Although these processes will be analysed in future work, once the evolution of star forming galaxies was properly treated in ALHAMBRA via SED-fitting techniques and their reliability was checked.

To treat the evolution of the stellar populations of the massive quiescent population in this phenomenological model, we distinguish three categories of stellar populations or PDFs: (i) the stellar populations of the massive quiescent sample (Sect. 4.2.5.1), (ii) the ones of quiescent galaxies below $M_{\star,\mathrm{lim}}$ (Sect. 4.2.5.2), and (iii) the ages and metallicities of star-forming galaxies (Sect. 4.2.5.3).

4.2.5.1 The stellar populations of quiescent galaxies with stellar mass above $M_{\star,\mathrm{lim}}$

As one of the main aims is to clarify how evolve the massive quiescent sample by determining the impact of mergers amongst others, the initial stellar population distribution for massive quiescent galaxies are the ones obtained along Chapter 3 at redshift $z = 1$ and for the different SSP model sets (BC03 and EMILES PDFs, see Sects. 3.7 and 3.8). From these initial PDFs, mass-weighted age and metallicity, we continuously added the stellar populations of accreted less massive systems, both quiescent and star-forming galaxies, with the densities of the observed merger rates in the Universe at each redshift and estimated for each channel in Sects. 4.2.2–4.2.4. Note that at this point no evolution of the initial PDFs is assumed rather than the ones introduced by this phenomenological model. For each of the members in the merger, we combined their stellar population PDFs of mass-weighted age and metallicity by a Monte Carlo approach. In any case in which a massive quiescent galaxy is involved in the merger, we used the current state of the mass-weighted age and metallicity PDFs (the PDFs evolved since $z = 1$).

4.2.5.2 The stellar populations of quiescent galaxies with stellar mass below $M_{\star,\mathrm{lim}}$

For non massive quiescent galaxies, we used the stellar population predictions obtained in Sects. 3.7 and 3.8 to be self-consistent with our results. For each stellar mass, the redshift dependent parameters $\mu_p(z)$ and $\sigma_p^{\mathrm{int}}(z)$ for building the stellar population PDFs (mass-weighted age and metallicity) are linearly interpolated and computed at the merger redshift. Therefore, the evolution of the PDF width is also estimated in this phenomenological model, and the effects of mergers on the evolution of the PDF width of massive quiescent galaxies since $z = 1$ is also confronted.

4.2.5.3 The stellar populations of star-forming galaxies

When there is a star-forming galaxy in the merger, we carried out a rough approach for their stellar population distributions, basing their PDF predictions in the mean values observed by Gallazzi et al. (2014, see also Sect. 3.10 for additional details). The authors by Gallazzi et al. (2014) determined that the stellar mass–age and –metallicity relation of star forming galaxies at $z = 0.7$ are compatible with those obtained at the nearby Universe. We also assumed the non-variability with redshift of the stellar mass-age and -metallicity relations along the whole redshift range of this simulation ($0.2 \leq z \leq 1.0$). In addition, Gallazzi et al. (2014) obtained that star-forming galaxies are 2.2 Gyr younger and 0.2 dex more metal poor than quiescent galaxies with stellar masses $\log_{10} M_\star = 11$ at both $z = 0.1$ and $z = 0.7$. This implies that the shift between both mean ages and metallicities of star-forming and quiescent galaxies (with $\log_{10} M_\star = 11$) are roughly constant along a wide redshift range. This fact allows us to predict the dependency of the medians of the star-forming PDFs with redshift. As we detailed in Sect. 3.8, different SSP models bring different stellar population predictions. In order to adapt the stellar population predictions of star-forming galaxies for the BC03 and EMILES ones, we assumed that at any redshift there are the same shifts than the observed in Gallazzi et al. (2014, 2.2 Gyr younger and 0.2 dex more metal poor at $\log_{10} M_\star = 11$) between star-forming and quiescent galaxies, where the reference values for quiescent galaxies are the ones provided by MUFFIT

Table 4.1: Parameter $\sigma^{\rm int}(z, M_\star)$ of the mass-weighted age and metallicity probability distribution functions of star-forming galaxies, which were derived using BC03 SSP models.

$\mathrm{Age_M}$ [Gyr]	$N_{\rm gal}$	$\sigma^{\rm int}_{\mathrm{Age_M}}$ [Gyr]		$\sigma^{\rm int}_{\mathrm{[M/H]_M}}$ [dex]		
		σ_1	σ_0	σ_2	σ_1	σ_0
$9.6 \leq \log_{10} M_\star < 10.0$	966	$-0.75^{+0.25}_{-0.26}$	$0.61^{+0.06}_{-0.06}$	$0.00^{+0.00}_{-0.00}$	$0.27^{+1.38}_{-1.36}$	$0.27^{+0.14}_{-0.14}$
$10.0 \leq \log_{10} M_\star < 10.4$	2942	$-0.04^{+0.07}_{-0.07}$	$0.35^{+0.03}_{-0.02}$	$0.00^{+0.00}_{-0.00}$	$0.26^{+0.06}_{-0.06}$	$0.26^{+0.02}_{-0.02}$
$10.4 \leq \log_{10} M_\star < 10.8$	2941	$-0.02^{+0.04}_{-0.04}$	$0.35^{+0.02}_{-0.02}$	$-0.72^{+0.24}_{-0.23}$	$0.76^{+0.21}_{-0.23}$	$0.18^{+0.05}_{-0.05}$
$10.8 \leq \log_{10} M_\star < 11.2$	1838	$-0.07^{+0.05}_{-0.05}$	$0.40^{+0.04}_{-0.04}$	$-0.60^{+0.28}_{-0.26}$	$0.86^{+0.34}_{-0.36}$	$0.09^{+0.11}_{-0.10}$
$\log_{10} M_\star \geq 11.2$	236	$-0.08^{+0.21}_{-0.21}$	$0.61^{+0.21}_{-0.20}$	$-0.60^{+0.41}_{-0.39}$	$0.85^{+0.55}_{-0.61}$	$0.09^{+0.24}_{-0.18}$

Notes. The top and bottom numbers stablish the 1 σ confidence level of the parameters. Notice that for $\mathrm{[M/H]_M}$, we repeat the same assumption for BC03 SSP models than in Chapter 3 (see also Appendix D), i. e. $\sigma^{\rm int}_{\mathrm{[M/H]_M}} = \sigma_2 \times z^2 + \sigma_1 \times z + \sigma_0$ for $\log_{10} M_\star \geq 10.4$.

Table 4.2: As Table 4.1, but using EMILES+BaSTI SSP models.

$\mathrm{Age_M}$ [Gyr]	$N_{\rm gal}$	$\sigma^{\rm int}_{\mathrm{Age_M}}$ [Gyr]		$\sigma^{\rm int}_{\mathrm{[M/H]_M}}$ [dex]	
		σ_1	σ_0	σ_1	σ_0
$9.6 \leq \log_{10} M_\star < 10.0$	1146	$1.96^{+0.22}_{-0.22}$	$-0.03^{+0.05}_{-0.05}$	$-0.20^{+0.14}_{-0.14}$	$0.31^{+0.03}_{-0.03}$
$10.0 \leq \log_{10} M_\star < 10.4$	3686	$-0.30^{+0.06}_{-0.06}$	$0.55^{+0.02}_{-0.02}$	$-0.27^{+0.05}_{-0.05}$	$0.38^{+0.02}_{-0.02}$
$10.4 \leq \log_{10} M_\star < 10.8$	4279	$-0.32^{+0.05}_{-0.05}$	$0.51^{+0.03}_{-0.03}$	$-0.25^{+0.02}_{-0.02}$	$0.32^{+0.01}_{-0.01}$
$10.8 \leq \log_{10} M_\star < 11.2$	4005	$-0.16^{+0.03}_{-0.03}$	$0.39^{+0.02}_{-0.02}$	$-0.06^{+0.02}_{-0.01}$	$0.23^{+0.01}_{-0.01}$
$\log_{10} M_\star \geq 11.2$	1008	$-0.15^{+0.05}_{-0.06}$	$0.38^{+0.05}_{-0.05}$	$-0.16^{+0.03}_{-0.03}$	$0.30^{+0.03}_{-0.03}$

and ALHAMBRA data for each SSP model set. Thus, the medians of the mass-weighted age and metallicity PDFs for the star-forming case are

$$\mathrm{Age(SF)}^{\rm 50th}_{\rm M} = 10^{(0.375\times\log_{10} M_\star - 3.8)} + O_{\rm SSP}(z, M_\star = 10^{11}) \tag{4.42}$$

$$\mathrm{[M/H](SF)}^{\rm 50th}_{\rm M} = 10.3 \times \log_{10} M_\star - 3.4 + \hat{O}_{\rm SSP}(z, M_\star = 10^{11}) \tag{4.43}$$

where $O_{\rm SSP}$ and $\hat{O}_{\rm SSP}$ are the offset respect the quiescent values in order to convert the equivalent quiescent ages and metallicities from the Gallazzi et al. (2014) system to our each SSP model prediction. From the values obtained in Eqs. 4.42 and 4.43, the values for $\mu_p(z)$ can be easily computed by Eqs. D.5 and D.7. This approach for the medians of the PDFs of star-forming galaxies is motivated by two aspects: (i) The analysis of the stellar population parameters of star-forming galaxies is carried out by combinations of two SSPs, that in some cases this may be not accurate enough, because there are additional contributions to the SED owing to active and ongoing processes of star formation (e. g. nebular contributions in the continuum) that affects the derivation of the right ages and metallicities. (ii) Basic correlations, such as the stellar mass–age and –metallicity, are compromised in some cases (mainly in BC03). Anyway, these correlations are properly obtained for EMILES, specially for EMILES+Padova00. In future work, we will determined the reliability of the stellar population parameters for star-forming galaxies using two SSPs for its inclusion in the present phenomenological model.

Table 4.3: As Table 4.1, but using EMILES+Padova00 SSP models.

$\mathrm{Age_M}$ [Gyr]	N_{gal}	$\sigma^{\mathrm{int}}_{\mathrm{Age_M}}$ [Gyr]		$\sigma^{\mathrm{int}}_{\mathrm{[M/H]_M}}$ [dex]	
		σ_1	σ_0	σ_1	σ_0
$9.6 \leq \log_{10} M_\star < 10.0$	1323	$-0.01^{+0.24}_{-0.24}$	$0.50^{+0.06}_{-0.06}$	$-0.10^{+0.09}_{-0.10}$	$0.19^{+0.02}_{-0.02}$
$10.0 \leq \log_{10} M_\star < 10.4$	3845	$0.08^{+0.05}_{-0.05}$	$0.40^{+0.02}_{-0.02}$	$-0.09^{+0.04}_{-0.04}$	$0.23^{+0.01}_{-0.01}$
$10.4 \leq \log_{10} M_\star < 10.8$	4170	$-0.03^{+0.04}_{-0.04}$	$0.41^{+0.02}_{-0.02}$	$-0.15^{+0.02}_{-0.02}$	$0.23^{+0.01}_{-0.01}$
$10.8 \leq \log_{10} M_\star < 11.2$	3464	$-0.09^{+0.03}_{-0.03}$	$0.39^{+0.02}_{-0.02}$	$-0.02^{+0.01}_{-0.01}$	$0.16^{+0.01}_{-0.01}$
$\log_{10} M_\star \geq 11.2$	960	$-0.10^{+0.05}_{-0.05}$	$0.38^{+0.04}_{-0.04}$	$-0.04^{+0.02}_{-0.02}$	$0.17^{+0.02}_{-0.01}$

Regarding the widths of the PDFs of star-forming galaxies, there is no available information in the literature. Instead, we carried out an analysis of the stellar populations of star forming galaxies using MUFFIT and ALHAMBRA data. We ran MUFFIT paying attention to the range of stellar population values rather than their median values, which were calibrated using the spectroscopic results by Gallazzi et al. (2014). As we highlighted in Sect. 3.5, the range of stellar population values is closely related with the range of $m_{F365} - m_{F551}$ and $m_{F551} - J$ colours, and this analysis can provides the dispersion of colours, and consequently, the range of ages and metallicities. From the distributions obtained for star forming galaxies and each SSP model set (BC03 and EMILES), we again applied the MLE for deconvolving observational errors from the stellar population distributions. As a result, the σ_p^{int} used for the phenomenological model and star-forming galaxies are listed in Tables 4.1–4.3.

As remarked in Sect. 4.2.1.4, when there is a star forming galaxy involved in a merger, a fraction of the available gas is converted into stars. The introduction of this effect is straightforwardly treated assuming that, during the burst, the new stars have in average the same metallicity than the host galaxy (principal or companion), and therefore, the effect on metallicity is rather negligible and the main consequence is a little inclusion of younger stars.

4.3 "Frosting" in quiescent galaxies

A low amount of star formation or "frosting" can be allowed to slow down the ageing of red galaxies even for stellar masses of $\log_{10} M_\star > 11$ (e. g. Ferreras & Silk, 2000; Trager et al., 2000; Kaviraj et al., 2007; Schiminovich et al., 2007; Serra & Trager, 2007; Lonoce et al., 2014; Vazdekis et al., 2016). For this purpose, we introduced bursts that will form a percentage in mass of new stars. For the creation of this new stellar populations via "frosting", we assume that the metallicity do suffer a negligible alteration respect the mass-weighted metallicity of the host galaxy, that is, we assume a non-variability of the host galaxy metallicity by "frosting" mechanisms owing to the low SFR present in the most massive quiescent galaxies. The resultant mass-weighted age of a host galaxy evolving under a "frosting" process between redshifts z and $z + \Delta z$ can be expressed as

$$\mathrm{Age_{M,host}}(z + \Delta z) = \frac{\mathrm{Age_{M,host}}(z)}{1 + \tau_{\mathrm{f}} \times t_{\mathrm{c}}(z, z + \Delta z)} + t_{\mathrm{c}}(z, z + \Delta z)\,, \tag{4.44}$$

where τ_{f} is the percentage of stellar mass created per Gyr via "frosting", $t_{\mathrm{c}}(z, z + \Delta z)$ is the cosmic time elapsed between z and $z + \Delta z$, and $\mathrm{Age_{M,host}}(z)$ the age of the host galaxy at redshift z. We assume a constant value for τ_{f}, in part motivated for the results obtained in Sect. 3.4.1 where the main values of SFR remain almost constant since $z \sim 1$ in the massive quiescent part. Note that $\mathrm{Age_{M,host}}(z + \Delta z) - t_{\mathrm{c}}(z, z + \Delta z)$ reflects the ageing term that differs respect a simple passive evolution, and that the stellar mass at $z + \Delta z$ would be $M_{\star,\mathrm{host}}(1 + \tau_{\mathrm{f}} \times t_{\mathrm{c}}(z, z + \Delta z))$.

When assumed a "frosting" mechanism, quiescent galaxies with stellar masses slightly lower than $M_{\star,\mathrm{lim}}$ will also increase in stellar mass becoming part of the massive sample under study ($\log_{10} M_\star \geq 11.2$). The density number of these galaxies can be easily estimated from the MF as

$$\rho_\mathrm{f}(z, z + \Delta z) = \int_{M_{\star,\mathrm{f}}}^{M_{\star,\mathrm{lim}}} \Phi_\mathrm{Q}(z, M_\star)\, \mathrm{d}M_\star \ , \tag{4.45}$$

where $M_{\star,\mathrm{f}}$ is the lower stellar mass limit of quiescent galaxies that after "frosting" with efficiency τ_f reaches $M_{\star,\mathrm{lim}}$. For a constant and redshift independent value of τ_f, this lower mass limit is expressed as

$$M_{\star,\mathrm{f}} = \frac{M_{\star,\mathrm{lim}}}{1 + \tau_\mathrm{f} \times t_\mathrm{c}(z, z + \Delta z)} \ . \tag{4.46}$$

As we assume a generalised "frosting" independently of any stellar population parameter or stellar mass, "frosting" acts as a shift in the age PDF. As mentioned above, we assume that the inclusion of new stars in quiescent galaxies via "frosting" does not modify the metallicity of each galaxy. For those quiescent galaxies below $M_{\star,\mathrm{lim}}$ that become part of the massive sample via "frosting", quiescent galaxies with $M_{\star,\mathrm{f}} \leq M_\star < M_{\star,\mathrm{lim}}$, the mass-weighted age and metallicity PDFs are included taking their number densities (through the MF in the range $M_{\star,\mathrm{f}} \leq M_\star < M_{\star,\mathrm{lim}}$) into account. It is worth mentioning that although the metallicity content of individual quiescent galaxies is not altered by "frosting" processes, quiescent galaxies less massive than $M_{\star,\mathrm{lim}}$ that promote to the massive sample have lower metallicity contents due to the observed stellar mass–metallicity relation. This can modify the median metallicity values of the whole massive quiescent population, but not the individual metallicities in each galaxy member affected of "frosting".

4.4 Accounting for the new quenched galaxies or "progenitor" bias

Since $z = 1$, we find out a general decrement in number of massive star-forming galaxies, whereas the number of massive quiescent galaxies increases ($\log_{10} M_\star \gtrsim 11$,e. g. Faber et al., 2007; Ilbert et al., 2010, 2013; Moustakas et al., 2013). The typical and rational assumption is that star-forming galaxies are quenching their star formation processes, whatever was the responsible mechanism of quenching, getting typical colours of quiescent galaxies. This means that there is also an increasing number of massive quiescent galaxies owing to massive blue galaxies are also quenching their star formation.

As the mechanism for quenching the star formation is rather unknown, we explore various mechanisms or approaches that are able to predict the likely effects of "progenitor" bias on the massive quiescent population. On the one hand, mergers trigger star formation processes (Sect. 4.4.1), which expends the reserves of available gas in galaxies producing a subsequently (plausible) state of quenching. On the other hand, the evolution in number density of massive star-forming galaxies (Sect. 4.4.2) can shed light around the minimum level of recent quenched galaxies that shut down their star formation processes.

4.4.1 Mergers as mechanism of quenching

Mergers are a natural mechanism to trigger star formation processes, or bursts, expending and decreasing the reserves of gas in the pair, which may accelerate the incorporation of new members into the quiescent sequence (van der Wel et al., 2009). There are also mergers in which star-forming galaxies are involved. This might be an efficient mechanism to accelerate the built-up of the stellar populations in the merger remnant, as well as to quenched its star formation earlier. At this point and to estimate a ground level of the number of star-forming galaxies that quenched their star formation (moving from the main sequence to the quiescent sample), we are able to assume that major mergers of blue massive galaxies induces a state of quenching. In order to account the arrival of new quiescent massive galaxies owing to quenching, we assume that all the galaxies that suffer both a merger with at least one star-forming galaxy involved and its merger remnant is

bluer than $(m_{F365} - m_{F551})_{\rm int} < 1.5$, starts a process of quenching. After this quenching, we assume that the merger of the pair gets redder colours owing to a complete passive evolution or ageing. After a certain time that depends of the initial conditions of the progenitors, the merger of the pair will belong to the quiescent sample as it is explained in Sect. 4.4.1.2.

4.4.1.1 Mergers of star-forming galaxies

Strictly, after merging two star-forming galaxies, the colour of the resultant galaxy is going to be blue. So, a remnant of two star-forming galaxies will not be incorporated into the quiescent sequence immediately. A priori, this scenario is not contributing to the build-up of the massive quiescent population. Mergers are a channel to trigger star formation (Hopkins et al., 2009a), which decreases the reserves of gas rapidly. Depending of the stellar populations previous to the merger event, and the amount of gas available in each member of the pair, the incorporation of these galaxies will succeed sooner or later.

Even though this scenario does not modify the quiescent population immediately, we will account for it. More precisely, we use it in order to estimate the incorporation of new quenched massive galaxies, in which the quenching mechanism in this case would be mergers, as these induce star formation processes spending gas. Note that in this scenario both members in the pair contain gas that, as consequence of mergers, will be partly transformed into stars increasing additionally the stellar mass of the merger remnant and adding young stellar populations. Notice that after quenching and for including them in the massive quiescent sample, the resultant galaxy of the merger should excess $M_{\star,\rm lim}$. The number density of mergers between star-forming galaxies is also derived from Eq. 4.11, where the efficiency merger function for this case is

$$E_{\rm PB}^{\rm SF,SF}(M_\star, \mu, M_{\star,\rm lim}) = \begin{cases} 0, & \text{if } M_\star < M_3, \\ f_{\rm SF,SF} \times \left(\frac{\mu_2}{\mu_{\rm min}}\right)^s, & \text{if } M_3 \leq M_\star < M_4, \\ f_{\rm SF,SF}, & \text{if } M_\star \geq M_4, \end{cases} \tag{4.47}$$

where $f_{\rm SF,SF}$ is the fraction of blue companions when the principal galaxy is star-forming ($f_{\rm SF,SF} = 0.35$ in this work), and M_3, M_4, and μ_2 are expressed by Eqs. 4.23, 4.24, and 4.25 respectively.

Thus, the number density of mergers between star-forming galaxies is

$$\rho_{\rm PB}^{\rm SF,SF} = \rho_{\rm PB,MM}^{\rm SF,SF} = \int_{z_1}^{z_2} \int_0^\infty \Phi_{\rm SF} R_{\rm MM}^{\rm SF}\, E_{\rm PB}^{\rm SF,SF}(\mu_{\rm min} = 1/4, \mu_{\rm max} = 1)\, {\rm d}M_\star {\rm d}z\,. \tag{4.48}$$

4.4.1.2 Inclusion of mergers with a remnant blue colour

The stellar population parameters of the merger progenitors are key to estimate the quenching time, $t_{\rm q}$, necessary to reach the quiescent sequence (or redder colours than 1.5). After the merger, we assume that these galaxies create a new fraction of stars (see Sect. 4.2.1.4) to subsequently truncate their star formation. After fixing the metallicity of each merger remnant, we compute the colour $(m_{F365} - m_{F551})_{\rm int}$ of older stellar population SSP models, as to reach the colour limit imposed for selecting quiescent galaxies $(m_{F365} - m_{F551})_{\rm int} \geq 1.5$, which we checked that is constant since $z \sim 1.1$ (see Sect. 3.3.1). Thus, the time expended between the mass-weighted age of the merger remnant and the model with colours redder than 1.5, both with the same mass-weighted metallicity of the remnant, is assumed as the (SSP-scaled) quenching time $t_{\rm q}$. This means that a merger of massive star-forming galaxies at z', or cosmic time t', will belong to the quiescent sample at cosmic time $t' + t_{\rm q}$ due to quenching. There are therefore mergers further than $z > 1$ (outside of our redshift bin under study) that also contribute in the massive quiescent sample at $0.2 \leq z \leq 1.0$.

In practise, we compute the number density of mergers between star forming and quiescent galaxies, with colours $(m_{F365} - m_{F551})_{\rm int} < 1.5$, and between star-forming galaxies since $z = 2$. From the stellar populations previous to merger and the gas converted into stars, we compute SSP-scaled $t_{\rm q}$ and the redshift in which will be incorporated to the quiescent sample. Note that owing to the range of ages of metallicities that present galaxies with similar mass (the width of the stellar population PDFs), the mergers that take

place at z' will contribute in number to the quiescent sample at different redshifts, as $t_{\rm q}$ depends of the initial colour of the pair. The merger efficiency function and the density numbers for mergers between star-forming galaxies are already expressed by Eqs. 4.47 and 4.48. The efficiency merger function and density numbers from the later contribution via quenching of galaxies from mergers between a massive quiescent galaxy (stellar mass larger than $M_{\star,\rm lim}$) and star-forming galaxies is already expressed by Eqs. 4.40 and 4.41. Finally, for the rest of cases, i. e. quiescent galaxies below $M_{\star,\rm lim}$ and a star-forming one, their equations are the same than Eqs. 4.22, 4.26, 4.27, and 4.28 after replacing the colour efficiency in each scenario $\epsilon_{\rm c}$ by $1-\epsilon_{\rm c}$.

4.4.2 Decrement of massive star-forming galaxies and the "progenitor" bias

The decrement in number of massive star-forming galaxies can be assumed as a hint for the arrival of new massive quiescent galaxies owing to the quenching mechanisms, whatever was the responsible mechanism for the shutting down of star formation. Consequently, the number of new massive quiescent galaxies via "progenitor" bias is the decrement in number of massive star-forming galaxies minus those massive star-forming galaxies that already merge with a quiescent galaxy and belong to the quiescent sample ($\rho_{\rm PB}^{\rm Q,SF}$ and $\rho_{\rm PB}^{\rm SF,Q}$, when the principal galaxy in the pair is quiescent and star-forming respectively), and minus the number of massive star-forming galaxies that experiment a merge between them ($\rho_{\rm PB}^{\rm SF,SF}$). Formally, the number of massive star-forming galaxies that quench their star-formation, $\rho_{\rm PB}$, in a redshift interval is the following

$$\rho_{\rm PB} = \int_{M_{\star,\rm lim}}^{\infty} \left(\Phi_{\rm SF}(z+\Delta z, M_\star) - \Phi_{\rm SF}(z, M_\star)\right)\, {\rm d}M_\star \; - \rho_{\rm PB}^{\rm SF,SF} - \rho_{\rm PB}^{\rm Q,SF} - \rho_{\rm PB}^{\rm SF,Q}\,. \tag{4.49}$$

As above, the number densities $\rho_{\rm PB}^{\rm SF,SF}$, $\rho_{\rm PB}^{\rm Q,SF}$, and $\rho_{\rm PB}^{\rm SF,Q}$ are derived through Eqs. 4.2 and 4.3. The number density $\rho_{\rm PB}^{\rm SF,SF}$ is

$$\begin{aligned}\rho_{\rm PB}^{\rm SF,SF} = \rho_{\rm PB,MM}^{\rm SF,SF} + \rho_{\rm PB,mm}^{\rm SF,SF} = &\int_{z_1}^{z_2}\int_{M_{\star,\rm lim}}^{\infty} \Phi_{\rm SF} R_{\rm MM}^{\rm SF}\, E_{\rm PB}^{\rm SF,SF}(\mu_{\rm min}=1/4, \mu_{\rm max}=1)\, {\rm d}M_\star {\rm d}z + \\ &+ \int_{z_1}^{z_2}\int_{M_{\star,\rm lim}}^{\infty} \Phi_{\rm SF} R_{\rm mm}^{\rm SF}\, E_{\rm PB}^{\rm SF,SF}(\mu_{\rm min}=1/10, \mu_{\rm max}=1/4)\, {\rm d}M_\star {\rm d}z\,,\end{aligned} \tag{4.50}$$

where the merger efficiency rate for this case is expressed as

$$E_{\rm PB}^{\rm SF,SF}(M_\star, \mu, M_{\star,\rm lim}) = \begin{cases} 0, & \text{if } M_\star < M_3, \\ f_{\rm SF,SF} \times \left(\frac{\mu_2}{\mu_{\rm min}}\right)^s, & \text{if } M_3 \leq M_\star < M_4, \\ f_{\rm SF,SF}, & \text{if } M_\star \geq M_4, \end{cases} \tag{4.51}$$

where $f_{\rm SF,SF}$ is the fraction of blue companions when the principal galaxy is star-forming ($f_{\rm SF,SF}=0.35$ in this work), and M_3, M_4, and μ_2 are expressed by Eqs. 4.23, 4.24, and 4.25 respectively. Notice that these equations are quite similar to Eqs. 4.47 and 4.48, except for the integration limits.

In the same sense, $\rho_{\rm PB}^{\rm SF,Q}$ and $\rho_{\rm PB}^{\rm Q,SF}$ are respectively expressed as

$$\begin{aligned}\rho_{\rm PB}^{\rm SF,Q} = \rho_{\rm PB,MM}^{\rm SF,Q} + \rho_{\rm PB,mm}^{\rm SF,Q} = &\int_{z_1}^{z_2}\int_{M_{\star,\rm lim}}^{\infty} \Phi_{\rm SF} R_{\rm MM}^{\rm SF}\, E_{\rm PB}^{\rm SF,Q}(\mu_{\rm min}=1/4, \mu_{\rm max}=1)\, {\rm d}M_\star {\rm d}z + \\ &+ \int_{z_1}^{z_2}\int_{M_{\star,\rm lim}}^{\infty} \Phi_{\rm SF} R_{\rm mm}^{\rm SF}\, E_{\rm PB}^{\rm SF,Q}(\mu_{\rm min}=1/10, \mu_{\rm max}=1/4)\, {\rm d}M_\star {\rm d}z\,,\end{aligned} \tag{4.52}$$

$$\rho_{\rm PB}^{\rm Q,SF} = \rho_{\rm PB,MM}^{\rm Q,SF} + \rho_{\rm PB,mm}^{\rm Q,SF} = \int_{z_1}^{z_2}\int_{M_{\star,\rm lim}}^{\infty} \Phi_{\rm Q} R_{\rm MM}^{\rm Q}\, E_{\rm PB}^{\rm Q,SF}(\mu_{\rm min}=1/4, \mu_{\rm max}=1)\, {\rm d}M_\star {\rm d}z + \\ + \int_{z_1}^{z_2}\int_{M_{\star,\rm lim}}^{\infty} \Phi_{\rm Q} R_{\rm mm}^{\rm Q}\, E_{\rm PB}^{\rm Q,SF}(\mu_{\rm min}=1/10, \mu_{\rm max}=1/4)\, {\rm d}M_\star {\rm d}z\,, \quad (4.53)$$

whose efficiency functions are

$$E_{\rm PB}^{\rm SF,Q}(M_\star, \mu, M_{\star,\rm lim}) = \begin{cases} 0, & \text{if } M_\star < M_3, \\ f_{\rm SF,Q} \times \epsilon_{\rm c}^{\rm SF,Q} \times \left(\frac{\mu_2}{\mu_{\rm min}}\right)^s, & \text{if } M_3 \le M_\star < M_4, \\ f_{\rm SF,Q} \times \epsilon_{\rm c}^{\rm SF,Q}, & \text{if } M_\star \ge M_4, \end{cases} \quad (4.54)$$

$$E_{\rm PB}^{\rm Q,SF}(M_\star, \mu, M_{\star,\rm lim}) = \begin{cases} 0, & \text{if } M_\star < M_6, \\ f_{\rm Q,SF} \times \epsilon_{\rm c}^{\rm Q,SF} \times \left(\frac{\mu_4}{\mu_{\rm min}}\right)^s, & \text{if } M_6 \le M_\star < M_7, \\ f_{\rm Q,SF} \times \epsilon_{\rm c}^{\rm Q,SF}, & \text{if } M_\star \ge M_7, \end{cases} \quad (4.55)$$

where M_3, M_4, μ_2 and M_6, M_7, μ_4 are expressed by Eqs. 4.23, 4.24, 4.25 and Eqs. 4.36, 4.37, 4.38 respectively.

It is worth mentioning that, as we explore the number density of quenched galaxies by the differences in number provided by their MFs, there is also a contribution of new massive star-forming galaxies that pass unnoticed. Consequently, the number of massive star-forming galaxies quenching their star formation may be higher, and $\rho_{\rm PB}$ should be considered as a lower limit.

For the definition of the stellar population PDFs of the massive star-forming galaxies that quench their star formation forming part of the massive quiescent sample, we carried out three approaches and we explored their effects. Firstly, the PDFs for massive star-forming galaxies (the general sample, not the distributions of the quenched massive star-forming galaxies) were derived from the stellar population predictions defined in Sect. 4.2.5, which are defined for every stellar mass and redshift, as:

$${\rm PDF_{SF}}({\rm Age_M}, z, M_\star \ge M_{\star,\rm lim}) = \frac{\int_{M_{\star,\rm lim}}^{\infty} {\rm PDF_{SF}}({\rm Age_M}, z, M_\star)\Phi_{\rm SF}(z, M_\star)\, {\rm d}M_\star}{\int_{M_{\star,\rm lim}}^{\infty} \Phi_{\rm SF}(z, M_\star)\, {\rm d}M_\star}\,, \quad (4.56)$$

$${\rm PDF_{SF}}([{\rm M/H}]_{\rm M}, z, M_\star \ge M_{\star,\rm lim}) = \frac{\int_{M_{\star,\rm lim}}^{\infty} {\rm PDF_{SF}}([{\rm M/H}]_{\rm M}, z, M_\star)\Phi_{\rm SF}(z, M_\star)\, {\rm d}M_\star}{\int_{M_{\star,\rm lim}}^{\infty} \Phi_{\rm SF}(z, M_\star)\, {\rm d}M_\star}\,, \quad (4.57)$$

where ${\rm PDF_{SF}}({\rm Age_M}, z, M_\star)$ and ${\rm PDF_{SF}}({\rm Age_M}, z, M_\star)$ are derived from Eqs. 4.42 and 4.43 (see also Eqs. D.5 and D.7) and from Tables 4.1–4.3 (see also Eq. D.8).

From Eqs. 4.56 and 4.57, which actually correspond to the whole sample of massive star-forming galaxies, we carried out our three assumptions to determine the stellar population PDFs of the massive star-forming galaxies that shut down their star formation to subsequently form part of the massive quiescent sample. These assumptions are:

i) The "random" assumption. We assume that the mechanism that quenches star formation processes acts randomly along the massive star-forming population. Therefore, the stellar population PDFs have the same shape that the ones expressed by Eqs. 4.56 and 4.57, where the number density is equal to $\rho_{\rm PB}$ (Eq. 4.49).

ii) The "reddest" assumption. This approach assumes that the reddest star-forming galaxies are the most likely candidates to form part of the massive quiescent population. From the PDFs of massive star-forming galaxies, Eqs. 4.56 and 4.57, we randomly create (by a Monte Carlo approach) combinations of age and metallicity. Amongst all the retrieved combinations, we selected only those $\rho_{\rm PB}$ combinations with the reddest rest-frame intrinsic colours $(m_{F365} - m_{F551})_{\rm int}$, where the intrinsic colour of the age and metallicity combination is established by a bilinear interpolation in the SSP models.

iii) The "phenomenological" assumption. This is based in the assumption that the changes with redshift of the star-forming PDFs are mainly related with the star-forming galaxies that leave the "blue cloud" or main sequence. Those stellar population parameters that present a decrement in their number density of massive star-forming galaxies are assumed as the stellar populations of the massive star-forming galaxies that constitute the core of the "progenitor" bias. Again, the number density is assumed equal to $\rho_{\rm PB}$. For comparing contiguous mass-weighted age PDFs in redshift, we assumed passive evolution. It is worth mentioning that these discrepancies between contiguous PDFs are also log-normal like functions.

4.5 Evolution and loss of stellar mass

Stars evolve following evolutionary tracks ejecting gas to the ISM. The more massive the star, the larger the ejection of gas to the ISM and the faster its evolution. Therefore, there is a continuous loss of stellar mass owing to the proper evolution of stellar populations, which can be more important when we take non-universal IMFs into account. Consequently, in addition to mergers, "frosting", and "progenitor" bias, we must account for the stellar population mass loss due to its intrinsic evolution to estimate how many galaxies decrease their stellar masses below $M_{\star,\rm lim}$.

This effect is already estimated by the authors of the proper SSP models and it is closely related to the mass–luminosity relation of each model. Indeed, this factor is taken into account by MUFFIT to estimate stellar masses (see Sect. 2.3.2.3). So, making use of the quiescent MFs, and given the stellar population values of the massive quiescent population above $M_{\star,\rm lim}$ (stellar population PDFs), we have determined, at first order, the number of galaxies that after certain cosmic time leave the massive quiescent sample, as long as there is no star formation processes incorporating new stars.

4.6 The individual effects of mergers, "frosting", and "progenitor" bias on the evolution of the massive quiescent sample

In order to quantify the impact that the different merger channels have, as well as to discern which is the mass fraction, i. e. major or minor mergers, playing a more fundamental role in the variation of the stellar populations in quiescent massive galaxies, we study their effects separately (Sect. 4.6.1). In addition, we explore the consequences of a remnant of continuous star formation or "frosting" (Sect. 4.6.2), and of the "progenitor" bias (Sect. 4.6.3). The loss of stellar mass due to the intrinsic stellar evolution (which alters the number density of the massive quiescent sample, see Sect. 4.5) is not included in the present section. It is worth reminding that the initial stellar population distribution for massive quiescent galaxies (more massive than $\log_{10} M_{\star,\rm lim} = 11.2$ for this work) are the mass-weighted age and metallicity PDFs obtained along Chapter 3 at redshift $z = 1$ (for the both BC03 and EMILES SSP models), and that no evolution of these initial PDFs is assumed rather than the ones introduced by this phenomenological model (ageing, mergers, "frosting", and "progenitor" bias).

4.6.1 The impact of mergers on the stellar populations of massive quiescent galaxies

The first consequence of mergers is the alteration of the number density of quiescent galaxies with stellar masses above $M_{\star,\rm lim}$ (Sect. 4.6.1.1), as the accretion of less massive systems efficiently increases the stellar mass of galaxies below $M_{\star,\rm lim}$. Different merger channels can contribute at different levels, as well as the mass ratios will have a different impact or weight on the massive quiescent population. As commented above, the presence of a stellar mass–age and –metallicity correlation suggests that mergers are a mechanism to modify the stellar content of massive quiescent galaxies. Our goal is to determine what is the impact due to the observational rate of mergers. These predictions actually set, for the first time, observational constraints to the variations of the average stellar populations of the massive quiescent population, ages and

metallicities, via mergers (Sects. 4.6.1.2 and 4.6.1.3). We subsequently compare whether these predictions agree with the observations of quiescent stellar populations until $z = 0.2$ (Chapter 3).

In brief, Figs. 4.1 and 4.2 illustrate the impact of mergers on the number density of massive quiescent galaxies for BC03 and EMILES SSP models, see also Table 4.4. While in Figs. 4.3 and 4.4, we present the impact of mergers on the mass-weighted age and metallicity PDFs respectively, see also Tables 4.5 and 4.6. Details are given in captions and subsections below.

4.6.1.1 Evolution of the number density by mergers

The total balance between the new quiescent massive galaxies (channel "new", see Sect. 4.2.2) owing to mergers and those that leave the massive quiescent sample (channel "out", see Sect. 4.2.4) will shed light on whether mergers play a role in the number density increment observed in the quiescent massive sample since $z = 1$ (see Sect. 3.6). It is worth recalling again that the merger rates are observationally constrained and they do not follow any theoretical assumption.

In general, there is a good agreement amongst the three SSP model predictions assumed in this work (i. e. BC03 and EMILES with both BaSTI and Padova00 isochrones) in which the channel "new" presents a remarkable contribution to the increase in number of massive quiescent galaxies (see top panels in Figs. 4.1 and 4.2). The largest contribution to the massive quiescent sample of "new" galaxies correspond to major mergers between two quiescent galaxies, where the number density variation varies among SSP models around 0.1–0.2 dex since $z = 1$. This result is not surprising since the merger rate of quiescent galaxies (principal galaxy in the pair, see Eqs. 4.7 and 4.9) is the largest at $z < 1$. In addition, the fraction of red companions is also larger than the blue ones (respectively 65 and 35 %, see Sect. 4.2.1.3), which also contributes to be the most efficient scenario for the inclusion of new massive quiescent galaxies. Major mergers (mass ratio $1 \leq \mu_{\rm MM} < 1/4$) between two quiescent galaxies, whose final stellar mass exceeds the mass limit of the massive quiescent sample, are more frequent than minor mergers ($1/4 \leq \mu_{\rm mm} \leq 1/10$), whose number density variation does not surpass 0.05 dex.For the "new" channel and mergers between galaxies of different spectral types (quiescent as principal and star-forming as companion, and vice versa), the contribution to the number of massive quiescent galaxies is more subtle, lower than 0.03 dex, independently whether this is via major or minor merger (see top panels in Figs. 4.1 and 4.2). Only for EMILES and Padova00 isochrones, major mergers between star-forming and quiescent galaxies show a non-negligible contribution.

The channel "out", or the channel responsible for the decrease in the number density of the massive quiescent sample (mergers between quiescent galaxies with stellar masses above $M_{\star,\rm lim}$ and mergers with star-forming galaxies with bluer intrinsic colours than $m_{F365} - m_{F551} < 1.5$ as a result), present a non-negligible contribution to the variation in its number density (see top panels in Figs. 4.1 and 4.2). Major mergers in channel "out" play an important role for diminishing the number density for both merger scenarios: between massive quiescent galaxies and with a different spectral type. For both cases, major mergers reduce the number density of the massive quiescent sample $\sim$ 0.07 dex. As expected, minor mergers in channel "out" do not modify drastically the number density of quiescent galaxies above $M_{\star,\rm lim}$, as these variations are below 0.05 dex since $z \sim 1$. This is due to the fact that minor mergers with star-forming galaxies do not largely modify the colours of massive quiescent galaxies, and consequently these are still red. On the other hand, minor mergers between massive quiescent galaxies are restricted to the massive-end of the MF, that is, the more restricted in number quiescent galaxies. In fact, minor mergers between massive quiescent galaxies is the least efficient scenario for reducing the number of massive quiescent galaxies.

Regarding those massive quiescent galaxies that suffer a merger and they still belong to the massive quiescent sample, or channel "in", there is a larger number of galaxies that experience mergers with other quiescent galaxies (see middle panel in Figs. 4.1 and 4.2) than those with a star-forming one, as expected from the fraction of blue and red galaxy companions. This means that the variations in the stellar populations of massive quiescent galaxies owing to mergers in channel "in" are mainly driven by the accretion of other less massive quiescent galaxies. Analysing the percentage of massive quiescent galaxies that suffer a merger event since $z = 1$, we find that minor mergers are slightly more frequent than major mergers. After taking

the predictions of BC03 and EMILES SSP models into account for the merger channel "in", 20–25 % (15–20 %) of massive quiescent galaxies suffer a minor (major) merger with another quiescent galaxy, whereas this percentage reduces down to 4–12 % (3–10 %) when the companion is a star-forming galaxy. EMILES+Padova00 and BC03 present the largest and smallest percentages respectively. In both scenarios and model predictions massive quiescent galaxies suffer a larger number of major mergers at $z \gtrsim 0.6$, however at lower redshifts, the number of minor mergers dominates.

Focusing in the overall contribution of mergers to the increase in number of massive quiescent galaxies, see bottom panel in Figs. 4.1 and 4.2 and Table 4.4, we observe that the main mass ratios responsible for the changes in density number are major merger. The impact of minor mergers in the number density is less remarkable since $z \sim 1$. Notice that minor mergers do not largely alter the number densities of massive quiescent galaxies, since the number of new galaxies compensates those going out from the massive quiescent sample. This means that there a mild flow of galaxies entering and exiting that can modify the global stellar populations of this massive sample (not accounting for the effects of channel "in") without altering their number density. In major mergers, the channel "new" is more dominant than the "out" one, driving to the increase in the number density. For BC03 and EMILES+Padova00, the evolution in number density is entirely explained by the merger rates observed in the Universe within the uncertainties. For EMILES+BaSTI, there are not enough mergers to explain the evolution in their number density.

4.6.1.2 Variations in the age PDFs by mergers

Minor and major mergers are expected to have a non-negligible impact in the global stellar populations of massive quiescent galaxies. For the first time, we explore this effect, which partly remain unnoticed owing to the continuous flow of galaxies with low alterations in the number density. In fact, the influence of the use of different SSP models for retrieving stellar population parameters via SED-fitting will be more remarkable in the ages and metallicities than in the number density (Sect. 4.6.1.1), where the dependence of the use of different SSP models was limited to the retrieved MFs.

As expected from the stellar mass-age relation, the new members coming from the merge of two less massive systems with younger stellar populations produces a general rejuvenation of massive quiescent galaxies, as long as the number of mergers is large enough. We confirm from the three sets of SSP models, see Table 4.5 and Fig. 4.3, that there are enough mergers as to modify the median age of the whole massive quiescent population by 0.5–1.2 Gyr since $z = 1.0$ up to $z = 0.2$. In addition, the variety of merger channels (channels "new", "out", and "in") with diverse stellar masses and spectral types also induces an increase of the width of the distributions of mass-weighted ages, and therefore, the distribution of ages becomes wider at lower redshifts. Both effects, a systematic rejuvenation and a wider range of ages, are determined in this thesis using the ALHAMBRA data and the results provided by MUFFIT (Sects. 3.7 and 3.8), although the delay in the ageing (respect a passive evolution) is greater than the predicted by our merger model. While the analysis of the stellar populations of these galaxies in the same redshift range, $0.2 \leq z \leq 1.0$, presents stellar populations younger by 3.7, 1.6, and 2.8 Gyr than the expectations for a passive evolution (BC03, EMILES+BaSTI, and Padova00 respectively), these are much larger than the predicted by the merger model, which are around $\sim$ 1 Gyr. Therefore, the merger mechanism by itself does not seem to be able to explain the rejuvenation of massive quiescent galaxies according to the three SSP model predictions. However, the evolution of the width of the mass-weighted age PDF owing to mergers, 1–2 Gyr, is compatible with the one measured by MUFFIT in ALHAMBRA, 1 Gyr.

We are in a privilege position to discern the role of the mass ratio in the process of rejuvenation via mergers, because a priori more massive systems are more efficient to modify the stellar content of a massive galaxy but these contain more similar stellar populations. On the other hand, the accretion of a less massive systems has a lower impact in mass, but their stellar populations differ more from the ones of the massive galaxies owing to the stellar mass-age relation. We find that the variation of the median values of mass-weighted ages are weaker for the case of minor mergers (< 0.5 Gyr) than for the major ones (< 1 Gyr), although the differences are very subtle (see Table 4.5 and Fig. 4.3). EMILES+BaSTI predictions present

the lowest modifications in the median age, and the major and minor contribution are basically the same. Regarding the width of the distribution of age values, major mergers imprint larger variations than minor ones do, although these differences are minimal. The increase in width of the mass-weighted age PDF, splitting major from minor merger effects, are around ~ 1.5 Gyr.

Thereby, we conclude that mergers drive a slightly process of rejuvenation of 1 Gyr from $z = 1$ to $z = 0.2$ and increase the range of mass-weighted age values in the population of massive quiescent galaxies. Despite this, the rejuvenation observed from ALHAMBRA data cannot be fully explained by mergers, and it is necessary the inclusion of other mechanism to reproduce its evolution. Nevertheless, the evolution in the width of the age PDF can be reproduced in an scenario in which mergers are present.

4.6.1.3 Variations in the metallicity PDFs by mergers

We study the global effects of major and minor mergers in the evolution of metallicities in massive quiescent galaxies. In this case, there are larger discrepancies in the metallicity predictions of quiescent galaxies owing to the use of different SSP models (see Sects. 3.7 and 3.8).

The effects of mergers on the mass-weighted metallicity PDF is a general decrement of the median values (see Table 4.6 and Fig. 4.4) since $z = 1.0$. In particular, BC03 SSP models present the lower decrement in metallicity, whereas the EMILES predictions show a more prominent evolution due to mergers. In fact, the evolution of the median of the mass-weighted metallicity PDF derived from BC03 SSP models in Chapter 3, exhibits a maximum at $z \sim 0.6$ that is at odds with the mild trend obtained for mergers. Notice that the presence of a maximum in the median metallicity at $z \lesssim 0.6$, makes the merger model to predict a very soft increase in metallicity. For EMILES, the decrement in the median of metallicity is more remarkable and continuous, ~ 0.10 dex in both cases, than in BC03. In addition, the predictions about the evolution of the median of the mass-weighted metallicity PDF obtained with the merger model agree better with the observed ones by MUFFIT and ALHAMBRA data (a decrement of 0.1–0.2 dex). In particular, Padova00 isochrones ask for a variation in the median metallicity slightly larger than observed. Consequently, mergers are able to reproduce the decrement in the medians of the metallicity PDFs without the necessity of extra mechanisms. Except for BC03, in which the width of the mass-weighted metallicity PDF remains almost constant, mergers also increase the width of the distributions of metallicity values of massive quiescent galaxies since $z = 1$. Indeed, the increase in the width of the metallicity PDF predicted by our merger model ($\lesssim 0.1$ dex) is in good agreement with those obtained observationally by MUFFIT and ALHAMBRA (~ 0.1 dex).

Treating the effects of major and minor mergers separately (see Table 4.6 and Fig. 4.4), we find that major mergers show similar contributions to modify both the medians and widths of mass-weighted metallicity PDFs. For the medians this is ~ 0.1 dex for both EMILES isochrones, and almost negligibles for BC03. The same result is obtained for minor mergers. In the same sense, the effect of mergers with BC03 SSP models on the widths of the metallicity PDFs persists unnoticed, whereas for EMILES these are ~ 0.1 dex for both isochrones and for major and minor mergers. Consequently, minor and major mergers contribute similarly to the global metallicity evolution since $z = 1$ to $z = 0.2$. Notice that the effects of minor mergers is more remarkable at lower redshifts, and at the larger ones major mergers played a slightly greater role.

To conclude, mergers can naturally explain the slight decrease in the observed metallicity distributions of massive quiescent galaxies in ALHAMBRA (not for BC03) since $z = 1$.

4.6.2 The impact of "frosting" on the stellar populations of massive quiescent galaxies

A direct mechanism for including younger stellar populations and delaying the ageing of a galaxy is formation of new stars through the reserves of gas available in each galaxy. This mechanism could a priori support the evolution in age observed with ALHAMBRA and MUFFIT, that mergers are not able to reproduce by themselves. We firstly study the effects of "frosting" assuming the absence of both mergers and "progenitor" bias effects in order to explore its consequences on the number density and stellar population distributions

Table 4.4: Expected variations in the number density owing to the effect of both major and minor mergers, only major and only minor mergers, in comparison with the observed variation in the number density of massive quiescent galaxies using ALHAMBRA data and MUFFIT from $z = 1$ to $z = 0.2$.

	BC03	EMILES+BaSTI	EMILES+Padova00
	$\Delta \log_{10} \rho_{\rm N}$	$\Delta \log_{10} \rho_{\rm N}$	$\Delta \log_{10} \rho_{\rm N}$
Major + Minor	0.15	0.10	0.26
Major merger	0.13	0.07	0.21
Minor merger	0.03	0.04	0.06
MUFFIT+ALH	0.11	0.25	0.31

Notes. The estimations were obtained for the three SSP model sets (BC03 and both EMILES isochrones: BaSTI and Padova00). All the number densities are obtained assuming $h = 0.71$. Positive modifications in $\Delta \log_{10} \rho_{\rm N}$ illustrates an increment in the number density owing to mergers.

Table 4.5: As Table 4.4, but for both the median and width of the mass-weighted age PDFs ($\Delta{\rm Age}_{\rm M}^{\rm 50th}$ and $\Delta\omega_{{\rm Age}_{\rm M}}$ respectively).

	BC03		EMILES+BaSTI		EMILES+Padova00	
	$\Delta{\rm Age}_{\rm M}^{\rm 50th}$	$\Delta\omega_{{\rm Age}_{\rm M}}$	$\Delta{\rm Age}_{\rm M}^{\rm 50th}$	$\Delta\omega_{{\rm Age}_{\rm M}}$	$\Delta{\rm Age}_{\rm M}^{\rm 50th}$	$\Delta\omega_{{\rm Age}_{\rm M}}$
Major + Minor	1.1	1.8	0.5	0.8	1.1	2.0
Major merger	0.8	1.6	0.3	0.7	0.8	1.9
Minor merger	0.3	0.5	0.2	0.3	0.3	0.7
MUFFIT+ALH	3.7	1.0	1.6	0.9	2.8	1.0

Notes. All the ages are in Gyr units. Positive modifications in $\Delta{\rm Age}_{\rm M}^{\rm 50th}$ illustrates a delay in ageing respect a complete passive evolution owing to mergers. Positive modifications in $\Delta\omega_{{\rm Age}_{\rm M}}$ illustrates a widening of the mass-weighted age PDF owing to mergers.

Table 4.6: As Table 4.4, but for both the median and width of the mass-weighted metallicity PDF ($\Delta[{\rm M/H}]_{\rm M}^{\rm 50th}$ and $\Delta\omega_{[{\rm M/H}]_{\rm M}}$ respectively).

	BC03		EMILES+BaSTI		EMILES+Padova00	
	$\Delta[{\rm M/H}]_{\rm M}^{\rm 50th}$	$\Delta\omega_{[{\rm M/H}]_{\rm M}}$	$\Delta[{\rm M/H}]_{\rm M}^{\rm 50th}$	$\Delta\omega_{[{\rm M/H}]_{\rm M}}$	$\Delta[{\rm M/H}]_{\rm M}^{\rm 50th}$	$\Delta\omega_{[{\rm M/H}]_{\rm M}}$
Major + Minor	−0.02	−0.06	−0.10	0.07	−0.11	0.08
Major merger	−0.01	−0.04	−0.06	0.07	−0.10	0.07
Minor merger	−0.01	−0.02	−0.04	0.03	−0.04	0.03
MUFFIT+ALH	−0.07	−0.26	−0.19	0.09	−0.10	0.09

Notes. All the metallicities are in dex units. Negative modifications in $\Delta[{\rm M/H}]_{\rm M}^{\rm 50th}$ illustrates a decrement in metallicity owing to mergers. Positive modifications in $\Delta\omega_{[{\rm M/H}]_{\rm M}}$ illustrates a widening of the mass-weighted metallicity PDF owing to mergers.

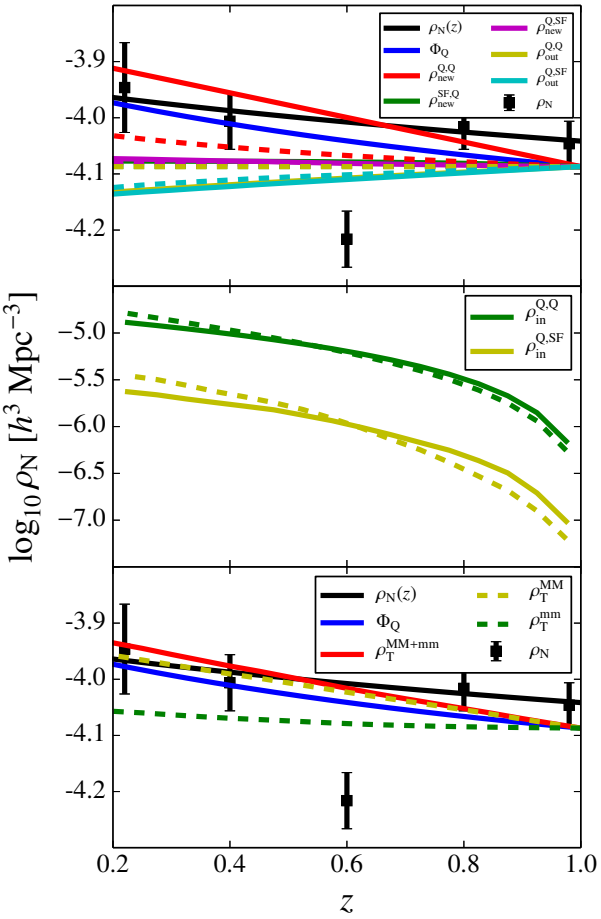

Figure 4.1: Contributions of the different merger channels to the number density of the massive quiescent sample using BC03 SSP models. Black square-shape markers illustrates the number density for quiescent galaxies ($\log_{10} M_\star \geq 11.2$) in ALHAMBRA by a V_{max} method, solid black line its power-law fitting, and solid blue line the predicted by the stellar mass function (MF). In *top panel*, the increase and decrease in number density of quiescent massive galaxy members (channels "new" and "out", see details in Sects. 4.2.2 and 4.2.4) owing to mergers are presented (see inset for the different scenarios in each channel). Solid and dashed lines of the same colour distinguish the case of major and minor mergers respectively. *Middle panel* shows the density of quiescent massive galaxies that have experimented a merger event since $z = 1.0$ (channel "in", see details in Sect. 4.2.3). *Bottom panel* shows the global number density contribution of mergers (red), the one for major mergers (yellow), and for the minor merger one (green). All densities are presented assuming $h = 0.71$.

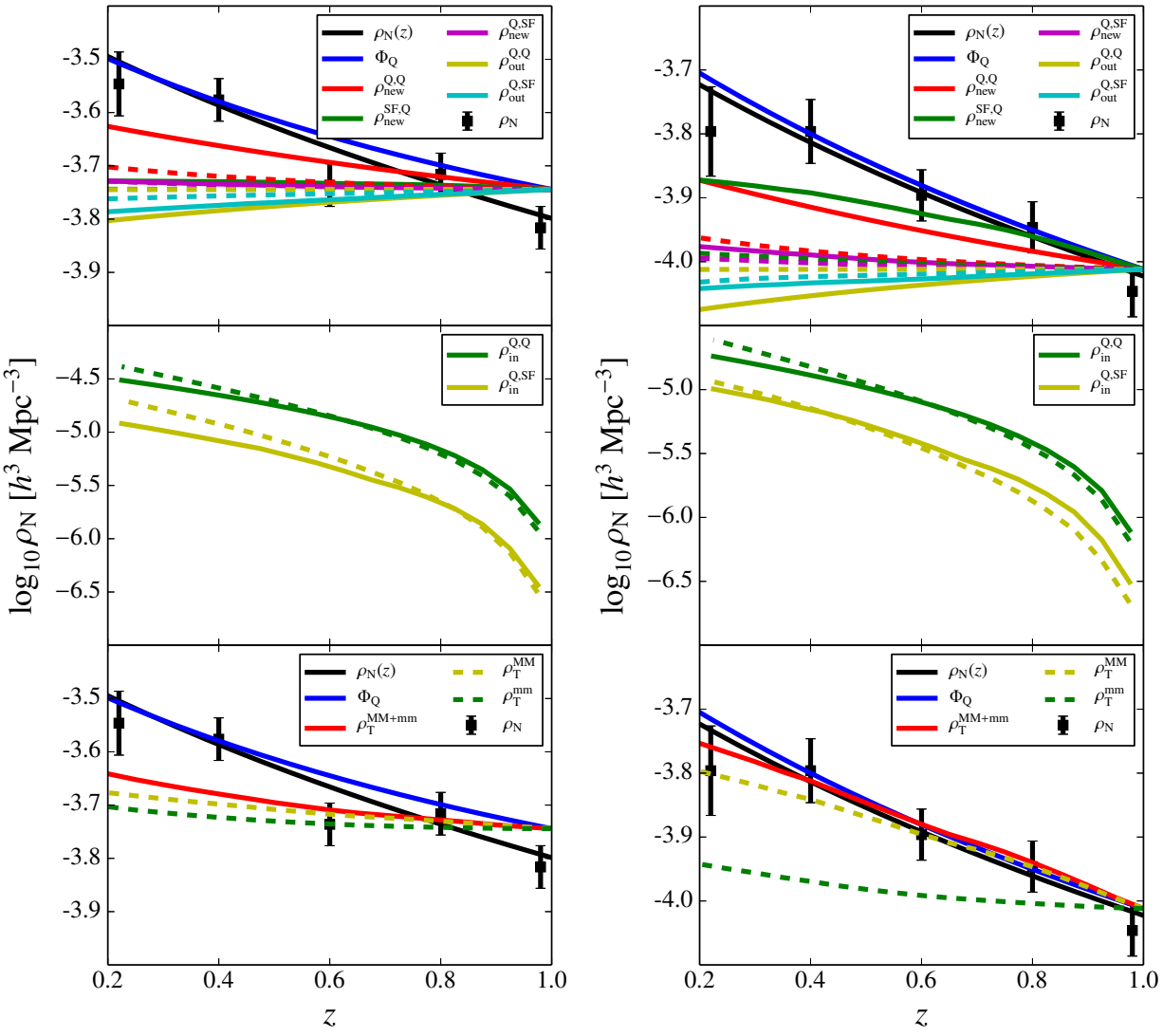

Figure 4.2: As Fig. 4.1 but using EMILES SSP models with BaSTI isochrones (*left panels*) and Padova00 isochrones (*right panels*).

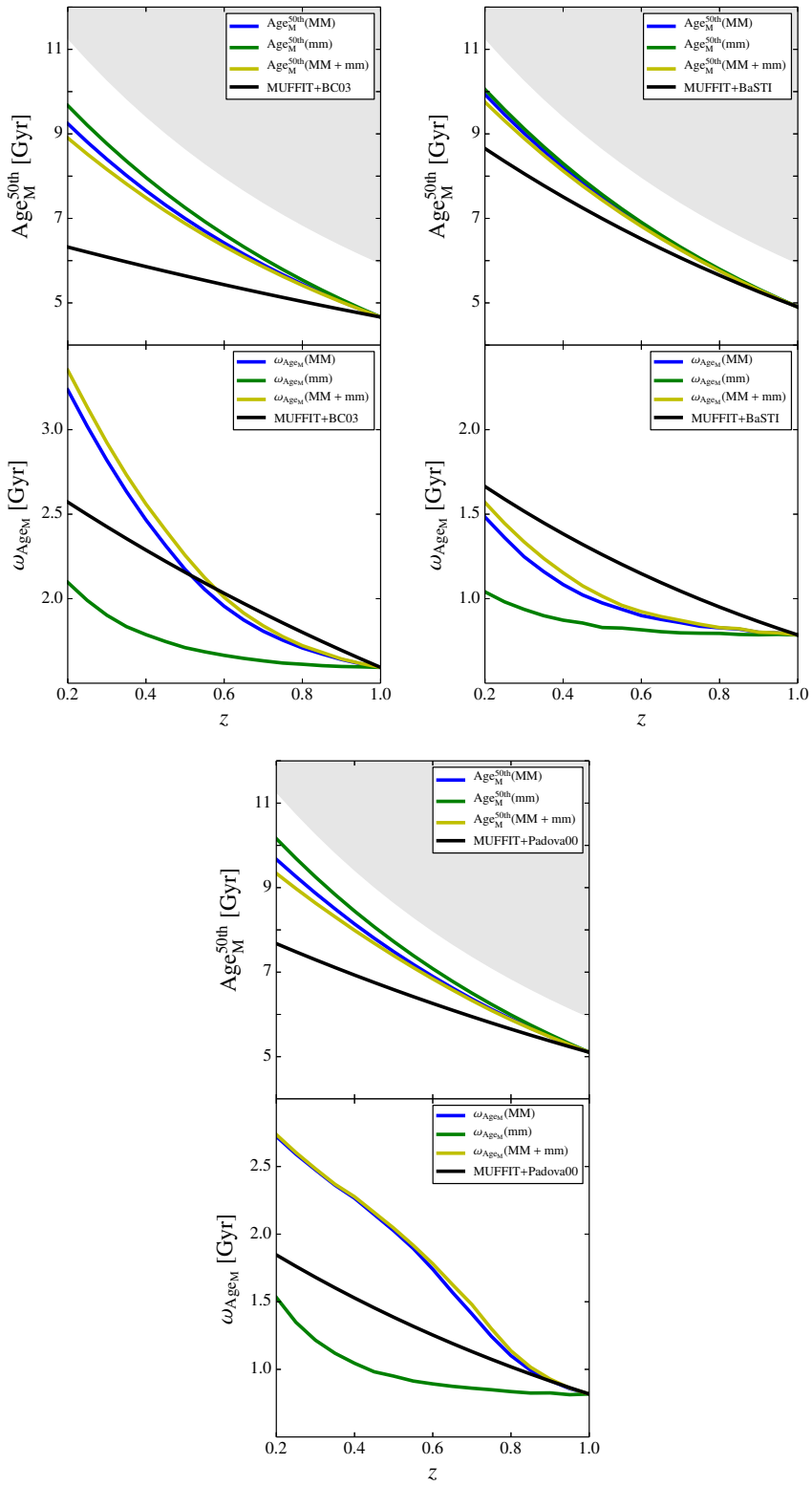

Figure 4.3: Contribution of mergers to the median and width of the mass-weighted age PDF of the massive quiescent sample using BC03 (*top-left panels*) and EMILES SSP models with BaSTI (*top-right panels*) and Padova00 (*bottom panels*) isochrones. Solid blue lines present the individual effects of major mergers, solid green lines the minor merger ones, and solid yellow lines the global effects of mergers (both major and minor contributions).

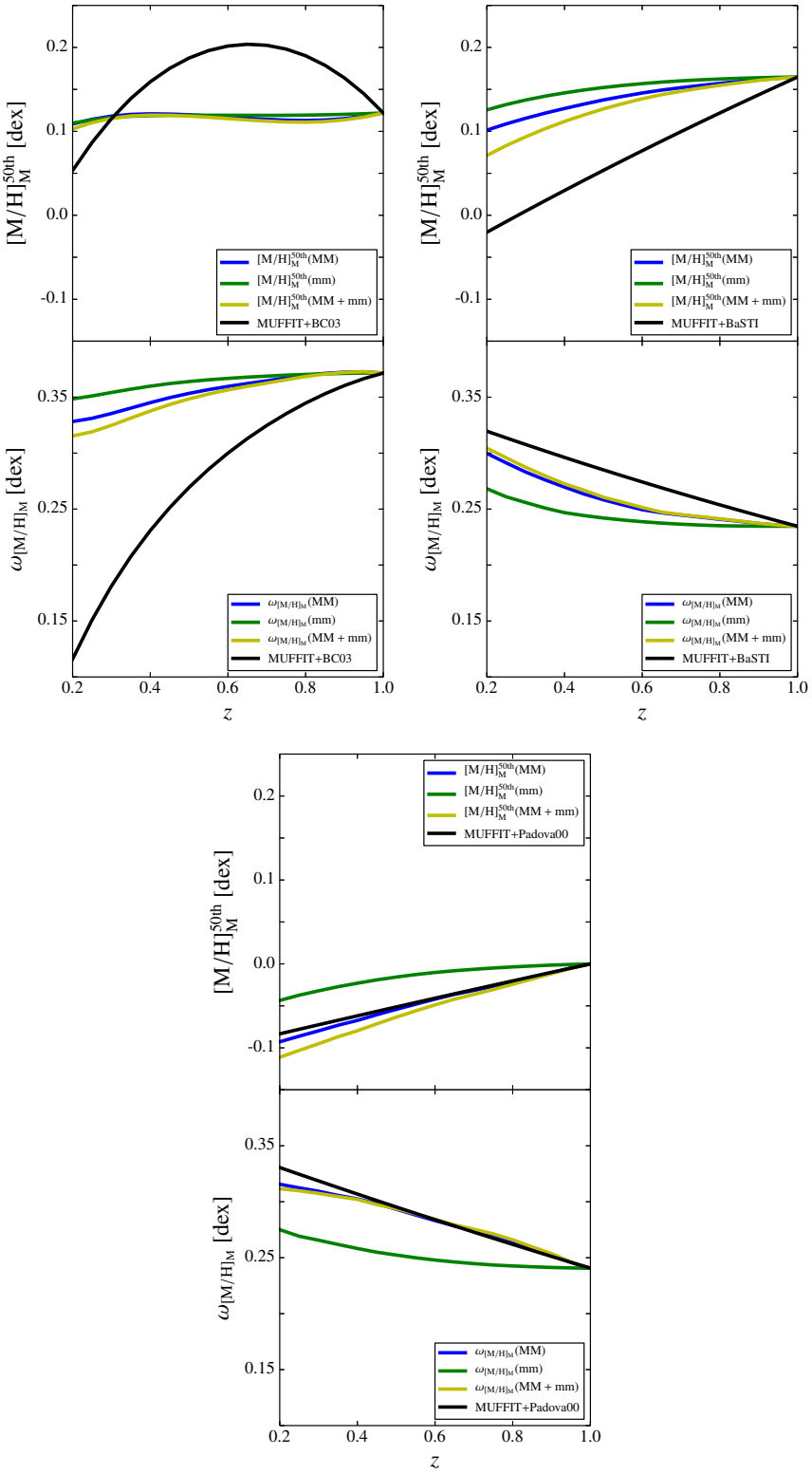

Figure 4.4: As Fig. 4.3, but for the mass-weighted metallicity PDFs.

of massive quiescent galaxies.

Figure 4.5 illustrates the impact of "frosting" on the number density of massive quiescent galaxies for BC03 and EMILES SSP models, see also Table 4.7. In Fig. 4.6, we present the impact of "frosting" on the mass-weighted age and metallicity PDFs, see also Tables 4.8 and 4.9. Details are given in captions and subsections below.

4.6.2.1 Evolution of the number density by "frosting"

Although the primal effect of "frosting" is the creation of new stars getting younger stellar populations than the expected one for a pure passive evolution, it also affects the number density of massive quiescent galaxies. By the "frosting" mechanisms, a certain number of quiescent galaxies below $M_{\star,\mathrm{lim}}$ will increase in stellar mass so as to enter in the massive quiescent sample. Only for this section, we impose a constant τ_f = 0.10, 0.04, and 0.08 Gyr^{-1} for BC03, EMILES+BaSTI, and EMILES+Padova00 SSP models respectively, as we show below these are the percentages of stellar mass created per Gyr necessary to reproduce the evolution in age observed in ALHAMBRA for the different SSP models since $z = 1$ in absence of other mechanisms. As presented in Fig. 4.5 and Table 4.7, there is a large impact on the density number of massive quiescent galaxies above $M_{\star,\mathrm{lim}}$ independently of the SSP model set used. As expected, the larger τ_f, the larger the increase in number. The predictions for BC03 present the most remarkable evolution in number, with $\tau_\mathrm{f} = 0.10$ implying a number density evolution larger than the observed one in ALHAMBRA (see also Sect. 3.6). We observe that for these τ_f values and EMILES models, the proposed level of "frosting" would imply an evolution in the density number as the measured from ALHAMBRA, without the necessity of a mergers, specially in EMILES+Padova00. Consequently, the assumption of a remain of low star-formation in this kind of galaxies is limited by the evolution in number density, specially for BC03 SSP models, and in turn restricts their values of τ_f, which is an important factor for taking into account in future studies.

4.6.2.2 Variations in the age PDFs by "frosting"

In Fig. 4.6 (left panels) and Table 4.8, we illustrate how the inclusion of the factors τ_f modifies the medians of the mass-weighted age PDFs. It is clear that the variation of the ages are much more sensitive to "frosting" effects than to mergers, where the variations in age since $z = 1$ are ~ 1 Gyr (Sect. 4.6.1.2). It is remarkable that the trends of age are properly reproduced at any redshift since $z = 1$. Note that all the evolution in age is not completely driven by the creation of new stars in those galaxies with stellar masses larger than $M_{\star,\mathrm{lim}}$, but that part of this evolution also comes from the younger galaxies with stellar masses below this limit (stellar mass-age relation). Nevertheless, the "frosting" mechanism does not modify the width of the mass-weighted age PDF substantially, even though from real data we obtained the contrary effect: an increase in the range of mass values towards lower redshifts.

4.6.2.3 Variations in the metallicity PDFs by "frosting"

In spite of we assume that "frosting" does not largely modify the metallicity of the host galaxy, the inclusion of galaxies below $M_{\star,\mathrm{lim}}$ (which increase in mass owing to "frosting") will also modify the metallicity of the massive quiescent sample owing to the relation between stellar mass and metallicity (see Table 4.9). Figure 4.6 (right panels) shows that these levels of "frosting" can also diminish the global metallicities (~ 0.05 dex since $z = 1$ up to $z = 0.2$) of the massive sample for the inclusion of new members, although in a less efficient way than mergers. This means that "frosting" is not able to explain the evolution in metallicity observed in ALHAMBRA of massive quiescent galaxies since $z = 1$ itself, although it also reproduces a decrement of their metal content. Concerning the widths of the mass-weighted metallicity PDFs, given τ_f their evolution is less significant than the produced by mergers and the real data advocates for a larger evolution in the width of the metallicity PDF.

Table 4.7: Expected variation of the number density owing to the effect of "frosting" in comparison with the observed number density of massive quiescent galaxies using ALHAMBRA data and MUFFIT from $z = 1$ to $z = 0.2$.

	BC03	EMILES+BaSTI	EMILES+Padova00
	$\Delta \log_{10} \rho_{\rm N}$	$\Delta \log_{10} \rho_{\rm N}$	$\Delta \log_{10} \rho_{\rm N}$
"Frosting"	0.43	0.19	0.35
MUFFIT+ALH	0.11	0.25	0.31

Notes. The estimations were obtained for the three SSP model sets (BC03 and both EMILES isochrones: BaSTI and Padova00). All the number densities are obtained assuming $h = 0.71$. Positive modifications in $\Delta \log_{10} \rho_{\rm N}$ illustrates an increment in the number density owing to "frosting".

Table 4.8: As Table 4.7, but for the mass-weighted age PDFs (median and width, $\Delta{\rm Age}_{\rm M}^{\rm 50th}$ and $\Delta\omega_{{\rm Age}_{\rm M}}$ respectively).

	BC03		EMILES+BaSTI		EMILES+Padova00	
	$\Delta{\rm Age}_{\rm M}^{\rm 50th}$	$\Delta\omega_{{\rm Age}_{\rm M}}$	$\Delta{\rm Age}_{\rm M}^{\rm 50th}$	$\Delta\omega_{{\rm Age}_{\rm M}}$	$\Delta{\rm Age}_{\rm M}^{\rm 50th}$	$\Delta\omega_{{\rm Age}_{\rm M}}$
"Frosting"	3.6	0.02	1.4	0.01	2.7	0.07
MUFFIT+ALH	3.7	1.0	1.6	0.9	2.8	1.0

Notes. All the ages are in Gyr units. Positive modifications in $\Delta{\rm Age}_{\rm M}^{\rm 50th}$ illustrates a delay in ageing respect a complete passive evolution owing to "frosting". Positive modifications in $\Delta\omega_{{\rm Age}_{\rm M}}$ illustrates a widening of the mass-weighted age PDF owing to "frosting".

Table 4.9: As Table 4.7, but for the mass-weighted metallicity PDFs (median and width, $\Delta[{\rm M/H}]_{\rm M}^{\rm 50th}$ and $\Delta\omega_{[{\rm M/H}]_{\rm M}}$ respectively).

	BC03		EMILES+BaSTI		EMILES+Padova00	
	$\Delta[{\rm M/H}]_{\rm M}^{\rm 50th}$	$\Delta\omega_{[{\rm M/H}]_{\rm M}}$	$\Delta[{\rm M/H}]_{\rm M}^{\rm 50th}$	$\Delta\omega_{[{\rm M/H}]_{\rm M}}$	$\Delta[{\rm M/H}]_{\rm M}^{\rm 50th}$	$\Delta\omega_{[{\rm M/H}]_{\rm M}}$
"Frosting"	0.01	−0.06	−0.04	0.05	−0.04	0.04
MUFFIT+ALH	−0.07	−0.26	−0.19	0.09	−0.10	0.09

Notes. All the metallicities are in dex units. Negative modifications in $\Delta[{\rm M/H}]_{\rm M}^{\rm 50th}$ illustrates a decrement in metallicity owing to "frosting". Positive modifications in $\Delta\omega_{[{\rm M/H}]_{\rm M}}$ illustrates a widening of the mass-weighted metallicity PDF owing to "frosting".

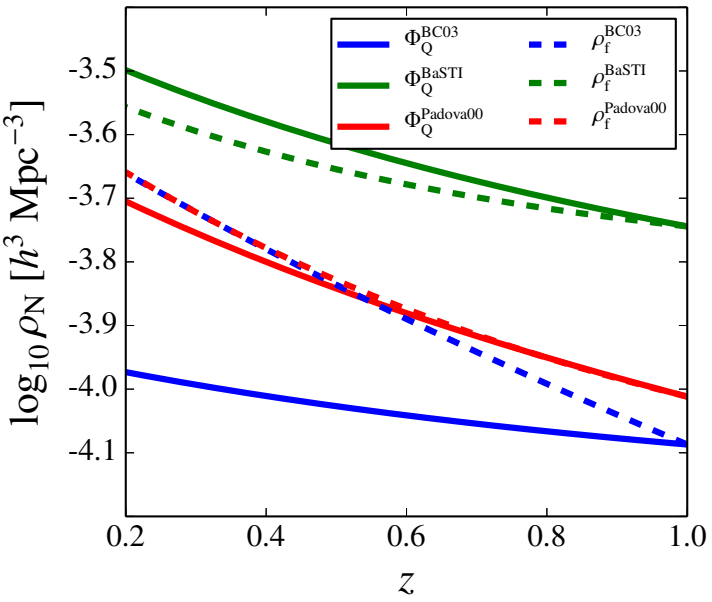

Figure 4.5: Contributions of "frosting" to the number density of the massive quiescent sample ($\log_{10} M_\star \geq 11.2$). Solid lines illustrate the number density evolution observed for massive quiescent galaxies in ALHAMBRA by the stellar mass functions (MF) for BC03 (blue), EMILES+BaSTI (green), and EMILES+Padova00 (red) SSP models. Dashed coloured lines are the number density evolution expected for "frosting" processes of efficiency $\tau_f = 0.10$, 0.04, and 0.08 Gyr^{-1} for BC03 (blue), EMILES+BaSTI (green), and EMILES+Padova00 (red) SSP models respectively. All densities are presented assuming $h = 0.71$.

"Frosting" is therefore a mechanism that has a large impact in the evolution of the number density of quiescent galaxies and it greatly explains the evolution of the median of the age PDF. The evolution of the median of the metallicity PDF, as well as the evolution of the widths of the age and metallicity PDFs, are not reproduced by a basic "frosting" scenario properly.

4.6.3 The impact of the "progenitor" bias on the stellar populations of massive quiescent galaxies

As explained in Sect. 4.4, the decrement in the number density of massive star-forming galaxies reveals that there must be a flow of massive galaxies towards the quiescent sample that can modify in part the average values or PDFs of massive quiescent galaxies.

Figure 4.7 illustrates the impact of the "progenitor" bias on the number density of massive quiescent galaxies for BC03 and EMILES SSP models, see also Table 4.10. In Figs. 4.8 and 4.9, we present the impact of "frosting" on the mass-weighted age and metallicity PDFs respectively, see also Tables 4.11 and 4.12. Details are given in captions and subsections below.

4.6.3.1 Evolution of the number density by the "progenitor" bias

After exploring mergers as a mechanism to shut down star formation in massive star-forming galaxies (details in Sect. 4.4.1), we obtained that its number density is largely below the observed variation in number of star-forming galaxies (lower than 0.1 %). In fact, the contribution of mergers as quenching mechanism is negligible (below 0.1 %), hence remaining unnoticed for the massive quiescent population. The number of star-forming galaxies that experiment a merger event is much lower than for quiescent galaxies and also than the decrease in number observed at $0.2 \leq z \leq 1.0$. From this result, we discard mergers as an efficient mechanism for quenching star formation. In the following, we rather focus on the "progenitor" bias alternative based in the descend of the number density of star-forming galaxies (Sect. 4.4.2).

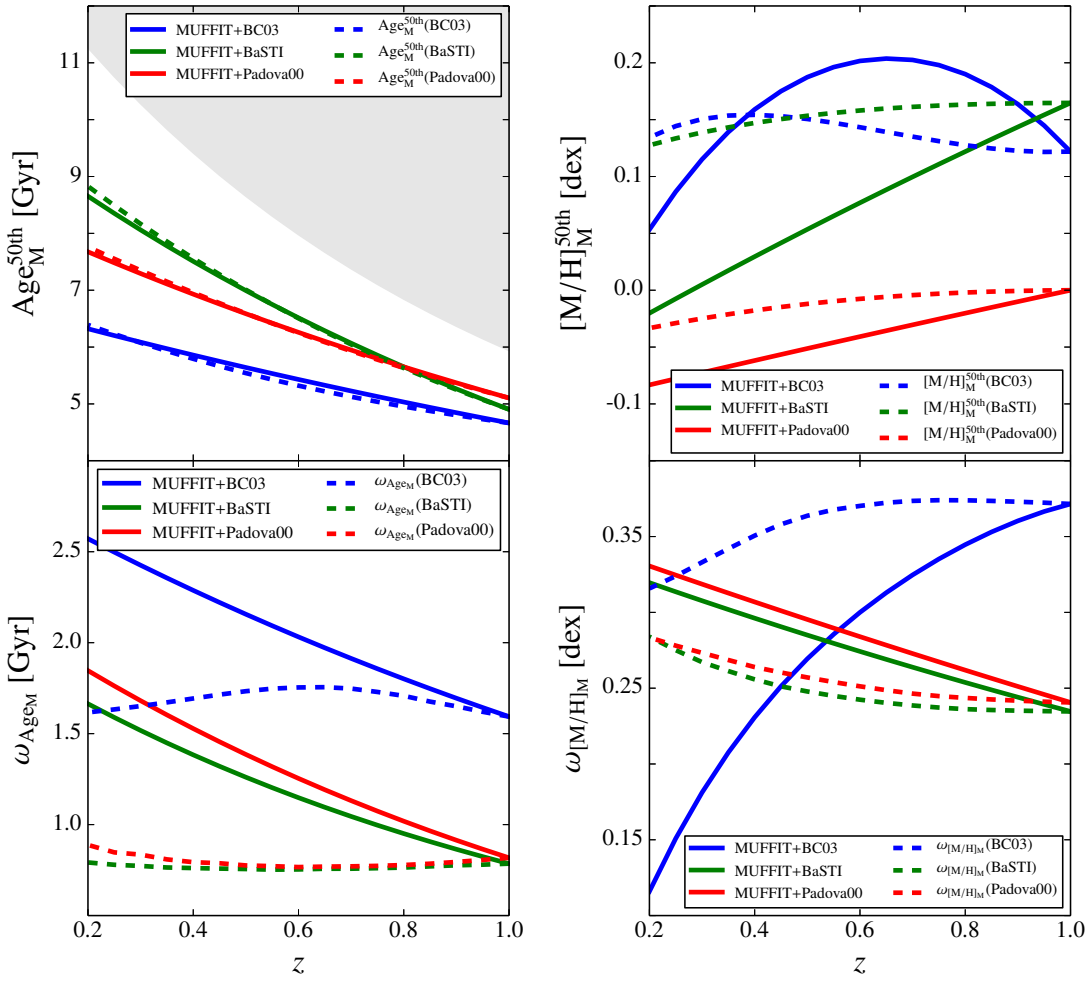

Figure 4.6: Contributions of "frosting" to the median and width of the mass-weighted age (*left panels*) and metallicity (*right panels*) PDF of the massive quiescent sample using BC03 (blue), EMILES+BaSTI (green), EMILES+Padova00 (red) SSP models with "frosting" efficiencies of $\tau_f = 0.10$, 0.04, and 0.08 Gyr^{-1} respectively. Solid lines illustrate the observed changes in the median and width of the mass-weighted age PDF in ALHAMBRA using BC03 and EMILES, whereas the dashed ones are the predicted ones under a "frosting" scenario assumption.

The variations observed in the number density of massive star-forming galaxies change with the SSP model chosen during the SED-fitting analysis of ALHAMBRA galaxies, as the MF are different amongst models. For BC03 and EMILES+BaSTI isochrones, the decrease in number of massive star-forming galaxies, $\rho_{\rm PB}$, is compatible with the variation in number observed for massive quiescent galaxies (0.1–0.25 dex, see Fig. 4.7 and Table 4.10). Particularly for EMILES+BaSTI, we observe a significant decrease in the number of massive star-forming galaxies at $0.7 \lesssim z \lesssim 1.0$, which provokes a larger impact in the number density of massive quiescent galaxies. However, for EMILES+Padova00 this variation is more subtle (0.05 dex) between redshift $z = 1$ and $z = 0.2$, which implies a lower impact of the "progenitor" bias on the average stellar populations of the quiescent sample.

4.6.3.2 Variations in the age PDFs by the "progenitor" bias

The "progenitor" bias effects on the mass-weighted age PDFs of the massive quiescent sample (see Fig. 4.8 and Table 4.11) are different for each of the assumptions presented in Sect. 4.4.2. In general, we observe that the "random" assumption has the largest impact. This assumption brings ages younger than the ones present in the quiescent sample, therefore, reducing the median of the mass-weighted age PDF and increasing the range of age values that they can exhibit (a width increment in the mass-weighted age PDF). On the other hand, the "reddest" assumption selects the reddest galaxies in the massive star-forming sample, whose ages are comparable to the typical ages of the massive quiescent sample. Consequently, the modifications introduced by the "reddest" assumption on the mass-weighted age PDF of the quiescent sample (both median and width) are the lowest ones. Finally, the effects of the "phenomenological" assumption are half-way between the "reddest" and "random" assumptions. This assumption is more self-consistent than the other two, because it intrinsically contains the evolution of the star-forming populations that is observed. Moreover, the stellar population distributions derived in the "phenomenological" assumption are also log-normal like functions, where the younger ages of massive star-forming galaxies are not included, but these ones are not restricted to the oldest ages either.

As expected from the evolution in the number density of massive star-forming galaxies (Fig. 4.7 and Table 4.10), the Padova00 predictions are the less affected by the "progenitor" bias for all their assumptions ("reddest", "random", and "phenomenological"). The estimated variations of the median of the age PDF are below 0.1 Gyr, which is negligible in comparison with the evolution observed using MUFFIT and ALHAMBRA data. The impact on the width of the age PDF is also negligible, lower than 0.2 Gyr. For BC03, the impact of the "progenitor" bias on the mass-weighted age distributions is larger than EMILES+Padova00, mainly because there is a larger inclusion of quenched massive galaxies from the main sequence, although these are also very mild (changes lower than 0.3 Gyr in the median and $\sim$ 1 Gyr in the width). The largest impact of the "progenitor" bias appears in EMILES+BaSTI, specially at $0.7 \lesssim z \lesssim 1.0$ where the contribution of $\rho_{\rm PB}$ is more prominent. Despite this, the alteration of the median of the mass-weighted age PDF of quiescent galaxies is still very mild, $\sim$ 0.3 Gyr, while for the width is more remarkable $\sim$ 1 Gyr. Therefore, we conclude that the role of the "progenitor" bias is a very mild rejuvenation of the median age, lower than 0.4 Gyr, and an increase in the range of likely age values of the massive quiescent sample, 0.2–1.5 Gyr.

4.6.3.3 Variations in the metallicity PDFs by the "progenitor" bias

Concerning metallicities, the "random", "reddest", and "phenomenological" assumptions have a similar interpretation than in the age case. The "random" assumption for a the "progenitor" bias scenario has a the largest impact on the metallicity PDF (both median and width) of quiescent galaxies, because there are star-forming galaxies less metal rich than in the quiescent sample, which modifies the median and width. The "reddest" assumption implies that the massive star-forming galaxies that quenches their star formation present as large metallicities as the the ones in the quiescent sample, and its inclusion does not modify prominently the mass-weighted metallicity PDF of the quiescent ones. As above, the "phenomenological" assumption is half-way between the "random" and the "reddest" ones.

Table 4.10: Expected variation of the number density owing to "progenitor" bias in comparison with the observed number density of massive quiescent galaxies using ALHAMBRA data and MUFFIT from $z = 1$ to $z = 0.2$.

	BC03	EMILES+BaSTI	EMILES+Padova00
	$\Delta \log_{10} \rho_{\rm N}$	$\Delta \log_{10} \rho_{\rm N}$	$\Delta \log_{10} \rho_{\rm N}$
"Progenitor" bias	0.11	0.23	0.05
MUFFIT+ALH	0.11	0.25	0.31

Notes. The estimations were obtained for the three SSP model sets (BC03 and both EMILES isochrones: BaSTI and Padova00). All the number densities are obtained assuming $h = 0.71$. Positive modifications in $\Delta \log_{10} \rho_{\rm N}$ illustrates an increment in the number density owing to the "progenitor" bias. The number densities $\rho_{\rm PB}$ are the same for the three "progenitor" bias approaches "random", "reddest", and "phenomenological".

Table 4.11: As Table 4.10, but for the mass-weighted age PDFs (median and width, $\Delta{\rm Age}_{\rm M}^{\rm 50th}$ and $\Delta\omega_{{\rm Age}_{\rm M}}$ respectively).

	BC03		EMILES+BaSTI		EMILES+Padova00	
	$\Delta{\rm Age}_{\rm M}^{\rm 50th}$	$\Delta\omega_{{\rm Age}_{\rm M}}$	$\Delta{\rm Age}_{\rm M}^{\rm 50th}$	$\Delta\omega_{{\rm Age}_{\rm M}}$	$\Delta{\rm Age}_{\rm M}^{\rm 50th}$	$\Delta\omega_{{\rm Age}_{\rm M}}$
Random	0.3	1.3	0.3	1.8	0.06	0.19
Reddest	0.2	0.6	0.2	0.8	0.02	0.12
Phenomenological	0.3	0.7	0.4	1.2	0.06	0.18
MUFFIT+ALH	3.7	1.0	1.6	0.9	2.8	1.0

Notes. All the ages are in Gyr units. Positive modifications in $\Delta{\rm Age}_{\rm M}^{\rm 50th}$ illustrates a delay in ageing respect a complete passive evolution. Positive modifications in $\Delta\omega_{{\rm Age}_{\rm M}}$ illustrates a widening of the mass-weighted age PDF.

Table 4.12: As Table 4.10, but for the mass-weighted metallicity PDFs (median and width, $\Delta[{\rm M/H}]_{\rm M}^{\rm 50th}$ and $\Delta\omega_{[{\rm M/H}]_{\rm M}}$ respectively).

	BC03		EMILES+BaSTI		EMILES+Padova00	
	$\Delta[{\rm M/H}]_{\rm M}^{\rm 50th}$	$\Delta\omega_{[{\rm M/H}]_{\rm M}}$	$\Delta[{\rm M/H}]_{\rm M}^{\rm 50th}$	$\Delta\omega_{[{\rm M/H}]_{\rm M}}$	$\Delta[{\rm M/H}]_{\rm M}^{\rm 50th}$	$\Delta\omega_{[{\rm M/H}]_{\rm M}}$
Random	−0.02	0.07	−0.06	0.12	−0.02	0.04
Reddest	0.06	0.03	−0.01	−0.01	0.01	0.00
Phenomenological	−0.03	0.18	−0.03	0.00	−0.01	0.01
MUFFIT+ALH	−0.07	−0.26	−0.19	0.09	−0.10	0.09

Notes. All the metallicities are in dex units. Negative modifications in $\Delta[{\rm M/H}]_{\rm M}^{\rm 50th}$ illustrates a decrement in metallicity. Positive modifications in $\Delta\omega_{[{\rm M/H}]_{\rm M}}$ illustrates a widening of the mass-weighted metallicity PDF.

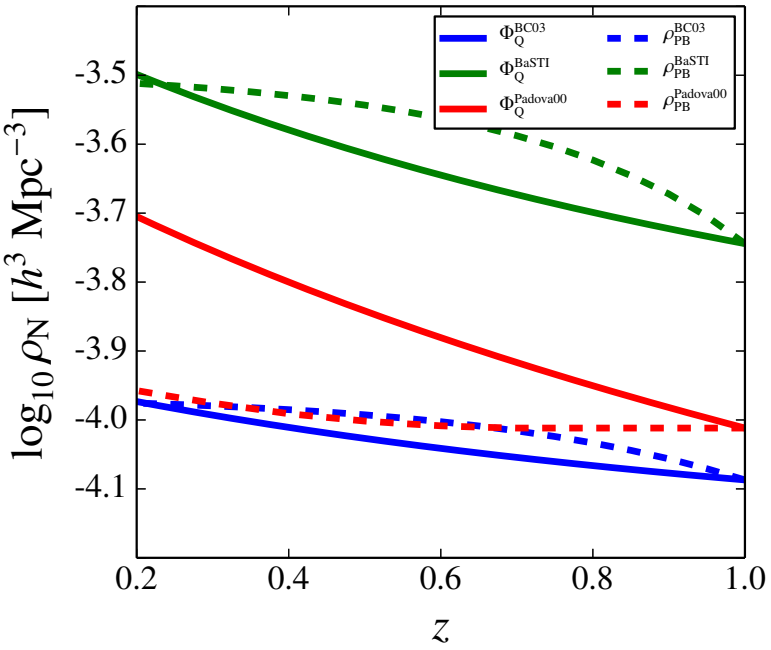

Figure 4.7: Contribution of the "progenitor" bias (dashed lines) to the number density of the massive quiescent sample for BC03 (blue), EMILES+BaSTI (green), and EMILES+Padova00 (red) SSP models. Solid lines illustrate the evolution with redshift of the number density measured by stellar mass functions (MF) in ALHAMBRA.

The complex evolution of the median of the mass-weighted metallicity PDF using BC03 SSP models largely differs from the modifications produced by the "progenitor" bias, which remains constant or even increases in the "reddest" assumption. The width of the metallicity PDF increases as well, owing to the new metallicity values contributed by the massive recently quenched galaxies. From EMILES+BaSTI results, the median of the metallicity PDF experiments a decrement of ~ 0.05 dex; whereas the width of the PDF remains constant except for the "random" assumption, which produces a widening in the metallicity distribution of 0.1 dex. This increase is even more remarkable at $0.7 \lesssim z \lesssim 1.0$, where the ρ_{PB} is more prominent and the contribution of "progenitor" bias using EMILES+BaSTI is more significant. As for the age case, the effects of "progenitor" bias are unnoticed for EMILES+Padova00 predictions. Along $0.2 \leq z \leq 1.0$, the values of ρ_{PB} are negligible as to modify the mass-weighted metallicity PDFs of quiescent galaxies, and therefore, the median and width of the metallicity PDF are not altered. In conclusion, the effects of "progenitor" bias on the mass-weighted metallicity PDFs is to diminish their medians and increasing their widths.

4.7 The role of mergers, "frosting" and the "progenitor" bias in the evolution of the quiescent galaxy population

After exploring the individual effects of mergers, "frosting" and the "progenitor" bias (each one with a different impact level and affecting particular parameters such as the medians of the PDFs or density number, see Sects. 4.6.1–4.6.3), we explore their joint consequences on the quiescent massive population in a common frame. In fact, their effects are not additive, but a combination of them. For instance, "frosting" increases in number the quiescent population through the inclusion of less massive quiescent galaxies (younger) and these galaxies also experiment mergers (which is proportional to the number density) that modify the distribution of stellar populations in the massive part. As the "frosting" efficiency parameter, τ_f, is actually a free parameter, it is fixed for reproducing the evolution of the median of the mass-weighted age PDF in

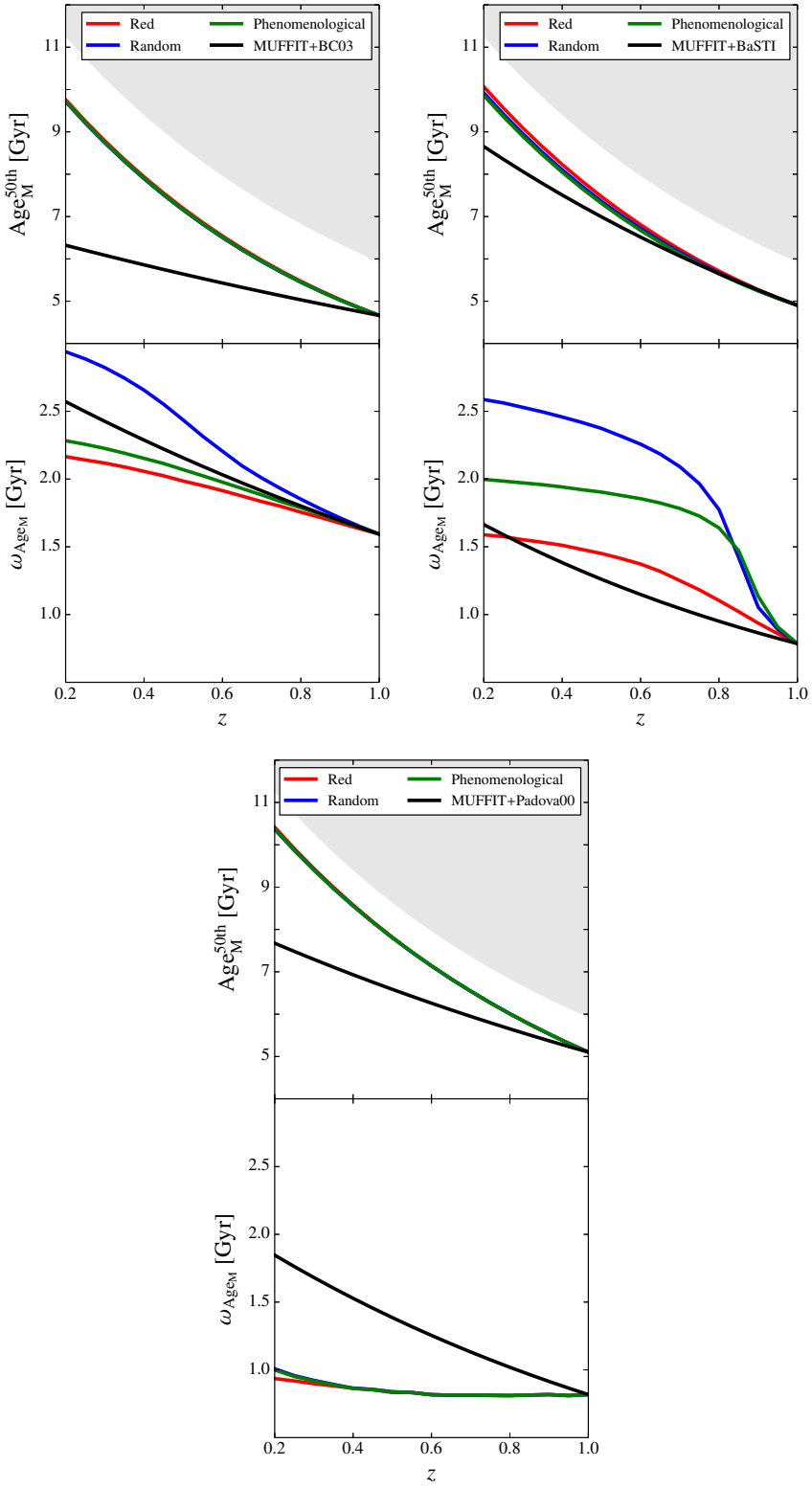

Figure 4.8: Contribution of the "progenitor" bias to the median and width of the mass-weighted age PDF of the massive quiescent sample for BC03 (*top-left panels*), EMILES+BaSTI (*top-right panels*), and EMILES+Padova00 (*bottom panels*) SSP models. Blue, red, and green solid lines show the effects of the "progenitor" bias with the assumptions for quenching "random", "reddest", and "phenomenological" respectively. Black solid line illustrates the evolution with redshift of the median and width of the mass-weighted age PDF measured in ALHAMBRA and their respective SSP models.

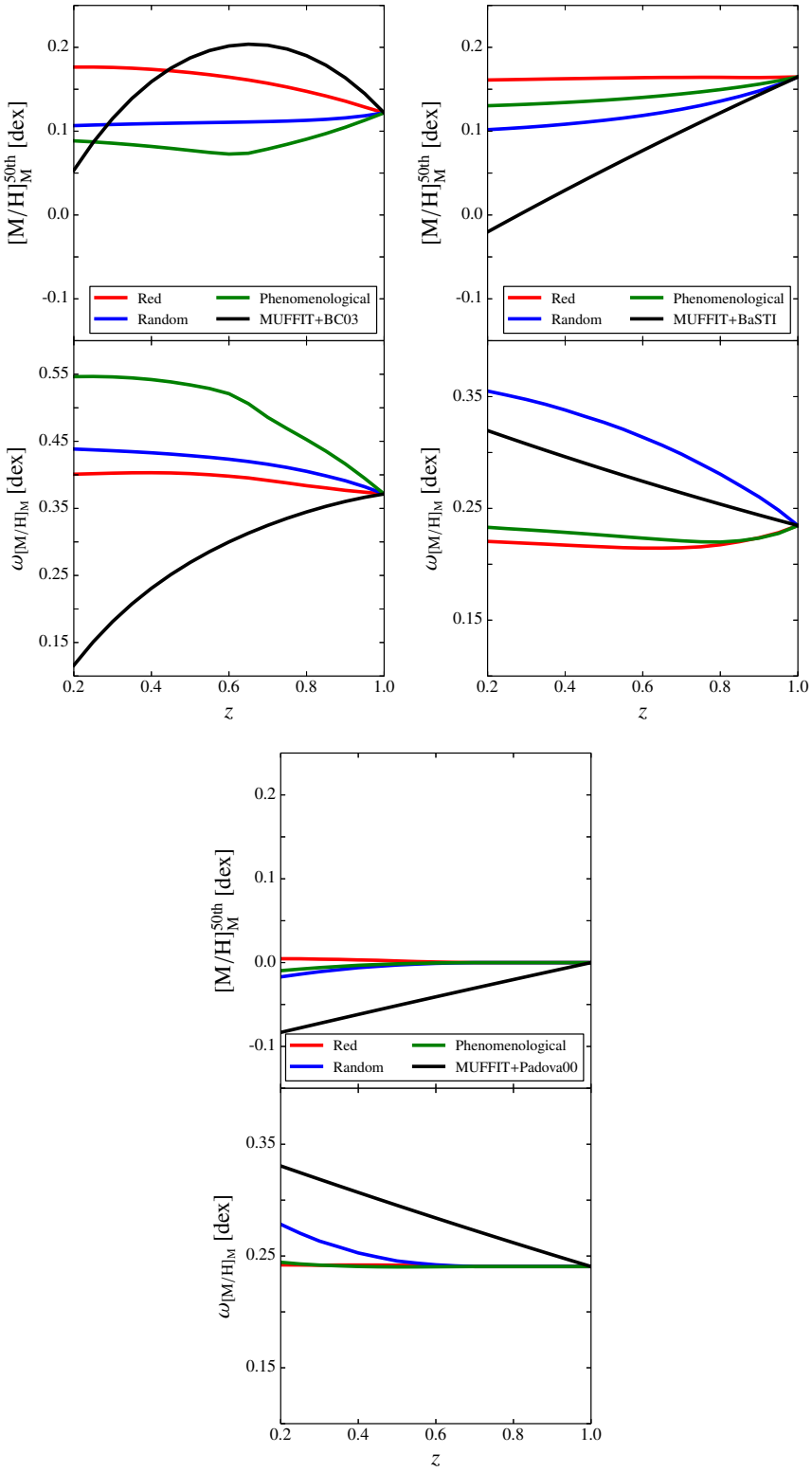

Figure 4.9: As Fig. 4.8, but for the mass-weighted metallicity PDFs.

combination with the effects of mergers and the "progenitor" bias for the different SSP model predictions. Therefore, we fixed $\tau_f = 0.08$, 0.02, and 0.06 for BC03, EMILES+BaSTI, and EMILES+Padova00 respectively. To be self-consistent with our proper stellar population predictions, in the following we assume the "phenomenological" assumption for the "progenitor" bias approach, which also yields intermediate alterations of the stellar population PDFs (see Tables 4.11 and 4.12). In the results detailed below, the loss of stellar mass due to the intrinsic stellar evolution (Sect. 4.5) is taken into account.

From our phenomenological model, we study the overlapped effects of these three mechanisms, where the first affected parameters is the number density. Mergers, "frosting", and the "progenitor" bias increase in number the quiescent massive population, and when the three scenarios take place its impact is even greater. From Table 4.13 and Fig. 4.10, we conclude that the increase in number density observed for massive quiescent galaxies is explained through the three mechanisms. For BC03 and EMILES+Padova00, the larger contribution to the number density comes from "frosting", in part owing to their large "frosting" efficiency ($\tau_f = 0.08$ and 0.06 respectively), which has a great impact on age but also in the increase in number. There is also a non-negligible impact on the number density via mergers. The lower contribution in number for both models is the "progenitor" bias. However for BaSTI, the larger contribution in number is the "progenitor" bias owing to the great decrease in number of star-forming galaxies at $z \gtrsim 0.7$ (obtained from their MFs). The contribution via "frosting" to the EMILES+BaSTI predictions reveals that it also has an impact even though their "frosting" efficiency is low ($\tau_f = 0.02$). Despite mergers also increase in number the population, they are not able to explain by themselves the evolution in number observed in ALHAMBRA. This means that although "frosting" is necessary for explaining the evolution of the mass-weighted age distribution, the number densities suffer a large impact as consequence of its effects (see below for the impact on age and metallicity). As a result of all the mechanisms, the number density predictions from BC03 SSP models show a much larger increase in number ($\Delta \log_{10} \rho_N = 0.46$ dex) than the observed one ($\Delta \log_{10} \rho_N = 0.11$ dex) impossible to reconcile with observations as implies a number density two times larger than the observed. For EMILES predictions, there is also a prediction in excess of the number density of massive quiescent galaxies from our phenomenological model, although this is more subtle than for the BC03 one. This excess is fairly constrained between 20–38 % for BaSTI and Padova00 isochrones respectively. For BaSTI it is dominated by the "progenitor" bias at $z \gtrsim 0.7$, whereas for Padova00 is owing to "frosting". Despite this, the agreement for EMILES is reasonably adequate given the several assumptions and uncertainties embedded in our phenomenological model (merger rates, MFs, stellar masses uncertainties, etc.). Notice that for the "progenitor" bias, ρ_{PB} is actually a low limit and this number density may be larger. This would imply a larger impact on the stellar population distributions by the "progenitor" bias, which would contribute to reduce the "frosting" efficiency necessary for explaining the mass-weighted age PDF evolution.

As mentioned above, the level of "frosting" included in our model was set in order to reproduce the median of the mass-weighted age PDF. Since mergers and the "progenitor" bias are not able to account for this evolution, the inclusion of "frosting" is therefore indispensable. From our model, "frosting" is largely the most efficient mechanism for delay the ageing of massive quiescent galaxies (see also Sects. 4.6.1–4.6.3). In fact, the "progenitor" bias is not a good mechanism for the inclusion of younger stellar populations in the massive quiescent sample; whereas mergers predict a non negligible support of 0.5–1 Gyr. When the three mechanisms act together, the evolution with redshift of the median mass-weighted age can be reproduced satisfactorily, see Table 4.14 and Fig. 4.11, recalling that "frosting" is essential at this point. Regarding the widths of the mass-weighted age PDF, mergers, "frosting" and the "progenitor" bias are efficient mechanisms for increasing it. Mergers are in general the most efficient one for the width increment of age, while "frosting" does not alter significantly their widths, remaining almost constant. The "progenitor" bias also alters the width of the age PDF, but it depends of the number density of quenched star-forming galaxies. For BC03 predictions, we do not appreciate a substantial evolution of the width of the age distribution, because the level of "frosting" introduced is strong and dominates the evolution (actually the no evolution) of the width of the age PDF, which remains unaltered. Nevertheless, for EMILES the increase in width of the age PDF is properly reproduced by mergers. In the predictions using BaSTI isochrones, we find that the strong evolution in the "progenitor" bias at $z \gtrsim 0.7$ produces a larger and dominant evolution of the width of the

Table 4.13: Expected variation of the number density owing to mergers, "frosting", and the "progenitor" bias in comparison with the observed number density of massive quiescent galaxies using ALHAMBRA data and MUFFIT from $z = 1$ to $z = 0.2$.

	BC03	EMILES+BaSTI	EMILES+Padova00
	$\Delta \log_{10} \rho_{\rm N}$	$\Delta \log_{10} \rho_{\rm N}$	$\Delta \log_{10} \rho_{\rm N}$
Mergers+"frosting"+ +"progenitor" bias	0.46	0.33	0.45
MUFFIT+ALH	0.11	0.25	0.31

Notes. The estimations were obtained for the three SSP model sets (BC03 and both EMILES isochrones: BaSTI and Padova00). All the number densities are obtained assuming $h = 0.71$. Positive modifications in $\Delta \log_{10} \rho_{\rm N}$ illustrates an increment in the number density.

Table 4.14: As Table 4.13, but for the mass-weighted age PDFs (median and width, $\Delta{\rm Age}_{\rm M}^{\rm 50th}$ and $\Delta\omega_{{\rm Age}_{\rm M}}$ respectively).

	BC03		EMILES+BaSTI		EMILES+Padova00	
	$\Delta{\rm Age}_{\rm M}^{\rm 50th}$	$\Delta\omega_{{\rm Age}_{\rm M}}$	$\Delta{\rm Age}_{\rm M}^{\rm 50th}$	$\Delta\omega_{{\rm Age}_{\rm M}}$	$\Delta{\rm Age}_{\rm M}^{\rm 50th}$	$\Delta\omega_{{\rm Age}_{\rm M}}$
Mergers+"frosting"+ +"progenitor" bias	3.5	0.14	1.3	0.80	2.5	0.73
MUFFIT+ALH	3.7	1.0	1.6	0.9	2.8	1.0

Notes. All the ages are in Gyr units. Positive modifications in $\Delta{\rm Age}_{\rm M}^{\rm 50th}$ illustrates a delay in ageing respect a complete passive evolution. Positive modifications in $\Delta\omega_{{\rm Age}_{\rm M}}$ illustrates a widening of the mass-weighted age PDF.

Table 4.15: As Table 4.13, but for the mass-weighted metallicity PDFs (median and width, $\Delta[{\rm M/H}]_{\rm M}^{\rm 50th}$ and $\Delta\omega_{[{\rm M/H}]_{\rm M}}$ respectively).

	BC03		EMILES+BaSTI		EMILES+Padova00	
	$\Delta[{\rm M/H}]_{\rm M}^{\rm 50th}$	$\Delta\omega_{[{\rm M/H}]_{\rm M}}$	$\Delta[{\rm M/H}]_{\rm M}^{\rm 50th}$	$\Delta\omega_{[{\rm M/H}]_{\rm M}}$	$\Delta[{\rm M/H}]_{\rm M}^{\rm 50th}$	$\Delta\omega_{[{\rm M/H}]_{\rm M}}$
Mergers+"frosting"+ +"progenitor" bias	−0.01	−0.02	−0.09	0.04	−0.1	0.07
MUFFIT+ALH	−0.07	−0.26	−0.19	0.09	−0.10	0.09

Notes. All the metallicities are in dex units. Negative modifications in $\Delta[{\rm M/H}]_{\rm M}^{\rm 50th}$ illustrates a decrement in metallicity. Positive modifications in $\Delta\omega_{[{\rm M/H}]_{\rm M}}$ illustrates a widening of the mass-weighted metallicity PDF.

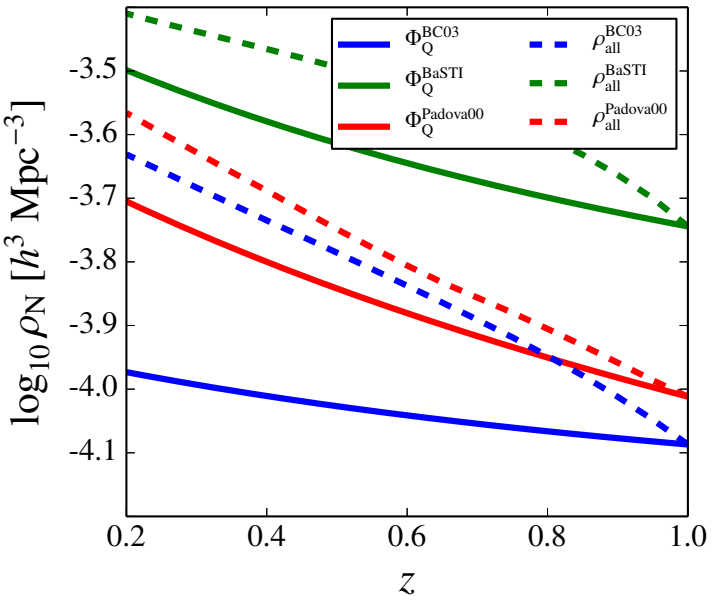

Figure 4.10: Contribution of mergers,"frosting" and the "progenitor" bias to the number density of the massive quiescent sample ($\log_{10} M_\star \geq 11.2$). Solid lines illustrate the number density evolution observed for massive quiescent galaxies in ALHAMBRA by the stellar mass functions (MF) for BC03 (blue), EMILES+BaSTI (green), and EMILES+Padova00 (red) SSP models. Dashed coloured lines are the number density evolution expected for mergers, "frosting" and the "progenitor" bias ("phenomenological" assumption). The "frosting" efficiency is $\tau_f = 0.08$, 0.02, and 0.06 Gyr^{-1} for BC03, EMILES+BaSTI, and EMILES+Padova00 SSP models respectively. All densities are presented assuming $h = 0.71$.

age distribution that diverges of its observed evolution in ALHAMBRA, with a more subtle contribution of the "progenitor" bias this evolution will be reproduced in good agreement with observations (see Fig. 4.3 and Table 4.5). Regarding Padova00 isochrones, where the "progenitor" bias has a low impact, the evolution of the width of the age PDF is in agreement with observations when mergers, "frosting", and the "progenitor" bias are accounted for.

The evolution of the mass-weighted metallicity PDF is mainly driven by mergers, whereas "frosting" and the "progenitor" bias play a secondary role (see also Sects. 4.6.1–4.6.3). For BC03, which also presents the more complex variation of metallicity PDF, the evolution with redshift of the median of the mass-weighted metallicity PDF is not self-consistent with their stellar population predictions. From the results of our phenomenological model, both EMILES isochrones reproduced the decrease on the median of the mass-weighted metallicity PDF (~ 0.1 dex) observed in ALHAMBRA as a consequence of the effects of mergers, "frosting", and the "progenitor" bias, specially the isochrone of Padova00, which greatly matches with the real observations. Concerning the widths of the mass-weighted metallicity PDFs, the main responsible for its evolution with redshift is again mergers. The predictions from our model for BC03 do not match with the evolution of the width of the metallicity PDF, although they also show a slight decrement in their values (see Table 4.15 and Fig. 4.11). EMILES reaches a good agreement with the evolution of the width of the mass-weighted metallicity PDF. In particular, EMILES with Padova00 isochrones achieve the best agreement with the ALHAMBRA observations. Part of the differences of the evolution of the width of the metallicity PDF with BaSTI isochrones are driven by the "progenitor" bias at $z \gtrsim 0.7$, otherwise there would be an excellent agreement with BaSTI predictions.

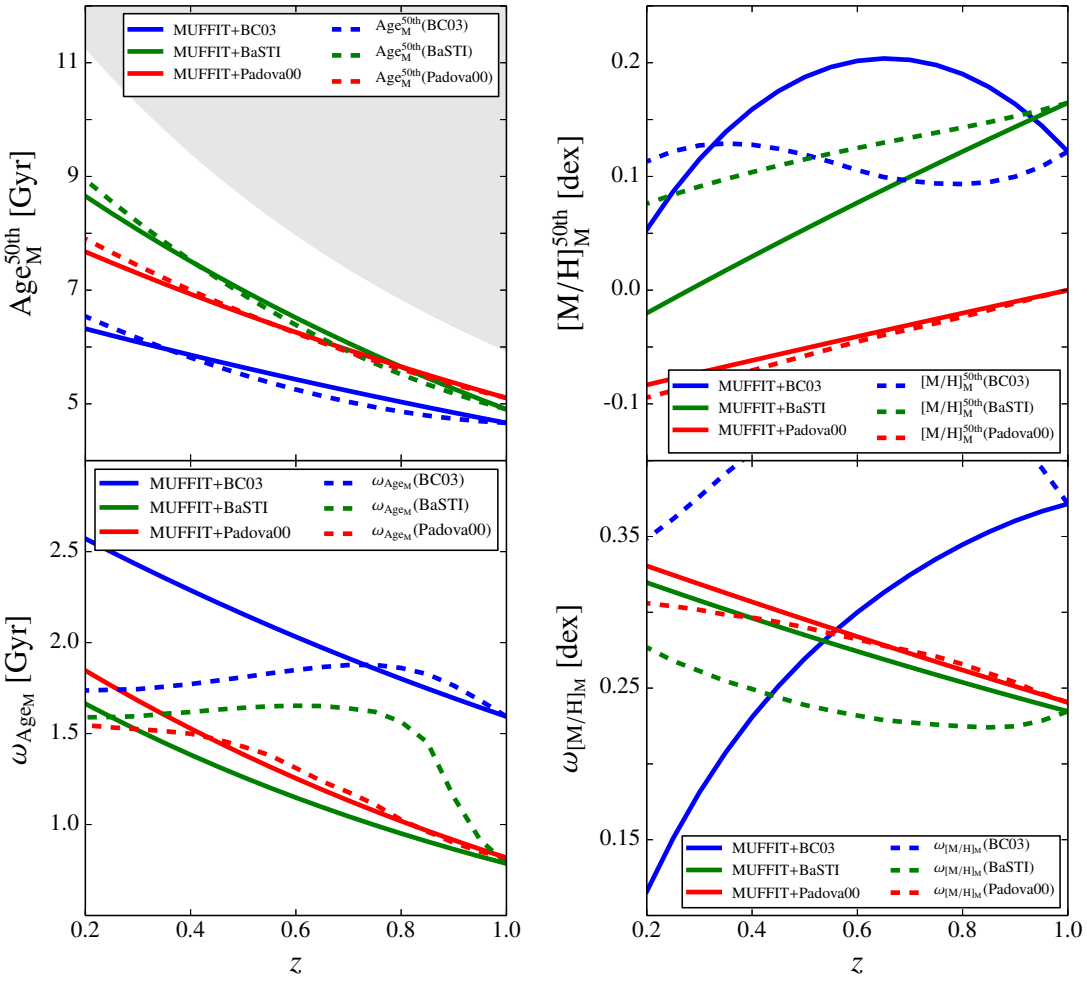

Figure 4.11: Contribution of mergers, "frosting" and the "progenitor" bias to the medians and widths of the mass-weighted age (*left panels*) and metallicity (*right panels*) PDFs of the massive quiescent sample using BC03 (blue), EMILES+BaSTI (green), EMILES+Padova00 (red) SSP models with "frosting" efficiencies of τ_f = 0.08, 0.02, and 0.06 Gyr^{-1} respectively. Solid lines illustrate the observed changes in the medians and widths of the mass-weighted age and metallicity PDFs in ALHAMBRA using BC03 and EMILES, whereas the dashed ones are the predicted ones for a common scenario including mergers, "frosting" and the "progenitor" bias ("phenomenological" assumption).

4.8 Summary and conclusions

Through a novel phenomenological model, we present, for the first time, a meta-analysis aimed at reconciling the observed evolution of both the density number and the stellar populations of massive quiescent galaxies since $z = 1$ down to $z = 0.2$, discerning the role that different mechanisms such as mergers, "frosting", and the "progenitor" bias play in this game. The predictions from the phenomenological model are also confronted with the observational results obtained in Chapter 3 using the SSP models of BC03 and EMILES, as a support for the proper model and for explaining the variations observed on the massive quiescent population in ALHAMBRA. Several contributions from mergers based in observational constraints from photometric and spectroscopic cosmological surveys are included for exploring a reliable scenario, supplemented with the assumption of a remnant star-formation process intrinsic to each quiescent galaxy, or "frosting", and accounting for the arrival of new quenched galaxies from the massive star-forming sample, or the "progenitor" bias through several assumptions.

In the above framework, we get the following conclusions:

- We find out evidences for supporting that mergers play a remarkable role in the evolution of massive quiescent galaxies since $z = 1$. Estimations from merger rates involving massive quiescent galaxies points out that around a third of this population suffers at least one major merger (mass ratio $1 \geq \mu_{\rm MM} \geq 1/4$) and one minor merger (mass ratio $1/4 \geq \mu_{\rm MM} \geq 1/10$) since $z = 1$. Mergers alter the number of massive quiescent galaxies, where major mergers contribute more efficiently than the minor ones. The impact on number density varies depending of the SSP model used. Mergers increase the number density of massive quiescent galaxies around $\Delta \log_{10} \rho_{\rm N} \sim 0.1$–$0.25$ dex (0.07–0.21 dex is due to major mergers, whereas for the minor ones is 0.03–0.06 dex) depending of the SSP model. Moreover, the continuous inclusion of new stars from less massive galaxies via mergers is large enough as to modify the stellar population PDFs of mass-weighted age and metallicity. Mergers are responsible for part of the evolution in the median age of massive quiescent galaxies, 0.5–1 Gyr, which partly explains the non passive evolution of the massive quiescent population observed using ALHAMBRA data. Mergers can explain the increase of the width of the mass-weighted age PDF observed since $z = 1$, whose impact is $\Delta\omega_{\rm Age_M} = 1$–$2$ Gyr. Regarding metallicity, mergers induce a continuous decrease of $\lesssim 0.1$ dex in the median metallicity of the massive quiescent population, whereas the width of the metallicity PDF increases less than 0.1 dex. The evolution of the metallicity PDF using BC03 SSP models is not self-consistent, owing to its complex shape. However, using EMILES SSP models all the stellar population trends observed in ALHAMBRA are qualitatively in agreement with the predictions provided by mergers in our phenomenological model.

- One of the main results retrieved from our model is that the inclusion of "frosting" is necessary to explain the evolution of the age distributions of massive quiescent galaxies. The main impact of "frosting" resides in an efficient mechanism to increase in number the massive quiescent population, as well as to rejuvenate these galaxies through the creation of new in-situ stars without altering the width of the mass-weighted age PDF. Whilst we assume that the metallicity of the new stars do not modify the metallicity of the host galaxy, "frosting" is able to reduce with time the median metallicity of the massive population (< 0.05 dex), owing to the quiescent galaxies below $M_{\star,\rm lim}$ (younger and less metal rich due to the mass metallicity relation) also increase in mass contributing to modify the PDFs of the massive counterpart. For EMILES predictions, "frosting" increases the width of the mass-weighted metallicity PDF (~ 0.05 dex), whereas for BC03 it decreases a similar factor. In addition, this phenomenological model can be used to constraint the level of "frosting", as large "frosting" efficiency values trigger the evolution in number.

- As the mechanism for quenching the star formation is rather unknown, we assumed various scenarios for accounting for the "progenitor" bias in our phenomenological model, confronting their effects with the massive quiescent population evolution. Our estimation of merger rates reveals that there

are not enough mergers to explain the variation in number of massive star-forming galaxies since $z = 1$, discarding mergers as the only mechanism for shutting down the star formation in main-sequence massive galaxies. Using BC03 and EMILES+BaSTI SSP models, the number density evolution of the massive quiescent sample can be fully explained by the "progenitor" bias, whereas for EMILES+Padova00 this contribution is negligible (lower than 0.05 dex). It is worth mentioning that for EMILES+BaSTI the number density is mainly driven by a quick decrease in the number of massive star-forming galaxies at $z \gtrsim 0.7$ and it should be revised, otherwise this contribution would be like the Padova00 ones. The "progenitor" bias tends to reduce the median age of the massive quiescent population without altering the width of the age PDF. In fact, these modifications are less efficient than the other mechanisms involved in our phenomenological model (mergers and "frosting"), but contributing to the evolution of the number density. The modification of the mass-weighted metallicity PDFs of massive quiescent galaxies are not very much affected by the "progenitor" bias either, which acts reducing the median metallicity (lower than 0.03 dex) and without increasing its width substantially.

- When mergers, "frosting", and the "progenitor" bias are taken into account, the observed number density and stellar population evolution of the massive quiescent population agree with the predictions from the phenomenological model when EMILES SSP models are used. The number densities are fairly reproduced except for an excess in number of 20–38 %, and the evolution of the stellar population PDFs (mass-weighted age and metallicity, including medians and widths of the PDFs) are explained by mergers, "frosting" ($\tau_f = 0.02$ and 0.06 for BaSTI and Padova00 respectively), and the "progenitor" bias. They together reconcile the non-passive age evolution and the decrease in metallicity with time by ~ 0.15 dex. Nevertheless, for BC03 SSP models the number density and the evolution of the metallicity cannot be reconciled within the framework proposed in this work.

5

Stellar populations of quiescent galaxies on the stellar mass–size plane

“It’s not the size of the nose that matters, it’s what’s inside that counts.”

Steve Martin

In this chapter, we aim at performing a comprehensive study of the stellar populations of our set of quiescent galaxies as a function of their sizes, masses and redshifts, with the ultimate goal of finding the most plausible evolutive scenarios that can explain their growth in size. It is worth noting that the galaxy sizes employed in this thesis are not derived from the ALHAMBRA data, hence being fully independent on the stellar populations derived from MUFFIT for the ALHAMBRA galaxy sample. This, in turn, constitutes an additional opportunity to confront the reliability of the results obtained in Chapter 3.

5.1 Introduction

During the last decade, many authors found out evidences for a continuous and generalised increase in size of both spheroidal-like/quiescent and late-type/star-forming galaxies with cosmic time (e. g. Trujillo et al., 2004; Daddi et al., 2005; McIntosh et al., 2005; Trujillo et al., 2006a; Toft et al., 2007; Trujillo et al., 2007; Zirm et al., 2007; Buitrago et al., 2008; van Dokkum et al., 2008; Damjanov et al., 2011; Newman et al., 2012; van der Wel et al., 2014). In particular, since $z \sim 2$ ($z \sim 1$) massive spheroidal-like/quiescent galaxies have rapidly increased in size a factor of ~ 4 (1.5–2) up to the current days. The main mechanism responsible of this fast growth is not clear yet.

First attempts for disentangling how galaxies grow in size proposed that the influence of AGNs can play a role. This scenario, usually referred as the "puffing-up" scenario (Fan et al., 2008, 2010; Damjanov et al., 2009), proposed that AGNs or quasar feedbacks would produce a removal of cold gas from the inner regions of the galaxy, that would redistribute the stellar populations of the inner regions in a time scale of ~ 2 Gyr. Although it is a plausible mechanism, this would imply that: (i) less compact quiescent galaxies would present older ages in the local Universe; and (ii) the dispersion of the stellar mass-size relation would increase (Fan et al., 2010) with cosmic time. Previous studies (e. g. Cenarro & Trujillo, 2009; Shankar & Bernardi, 2009; Trujillo et al., 2009, 2011; McDermid et al., 2015; Gargiulo et al., 2016) obtained that observations differ from the predictions of this scenario.

Alternatively, mergers were proposed as an efficient mechanism for producing a generalised growth in size (Naab et al., 2009). In this scenario, galaxies firstly formed their compact and dense cores, which are proposed to be the so called red nuggets observed at at $z > 2$ (Damjanov et al., 2009). These systems could be the result of mergers between gas-rich disks (which yields compact starbursts of small radii, Hopkins

et al., 2008a) or of the accretion of cold streams (which forms compact massive bulges and suppresses star formation Kereš et al., 2005; Dekel et al., 2009). Once the core is assembled, a continuous fall of pieces at lower redshifts via mergers (with ex-situ stellar populations) would populate the surroundings of these dense cores via an "inside-out" formation scenario (e. g. de la Rosa et al., 2016). This scenario would be mainly driven by minor mergers on parabolic orbits (Khochfar & Burkert, 2006a; Khochfar & Silk, 2006b; Bezanson et al., 2009; Hopkins et al., 2009b; Naab et al., 2009; Trujillo et al., 2011), because the number of major mergers is not large enough as to reproduce the evolution in size observed since $z \sim 1$ (Bundy et al., 2009; de Ravel et al., 2009; López-Sanjuan et al., 2010, 2012). Díaz-García et al. (2013, or Chapter 6) shows that mergers do not involve necessarily smaller galaxies, and therefore, under this scenario the growth in size via mergers must be generalised for all galaxies in the stellar mass–size plane. If this is the case, the number of compact galaxies will reduce towards larger cosmic times (Cassata et al., 2013; Quilis & Trujillo, 2013; Trujillo et al., 2014; van der Wel et al., 2014), despite other studies show that the number of compact galaxies remain almost constant (Saracco et al., 2010; Damjanov et al., 2014, 2015; Gargiulo et al., 2016) or experiment only a slight decrease in number (Valentinuzzi et al., 2010; Poggianti et al., 2013). A reliable estimation of the evolution in number of compact (massive) galaxies along redshift is therefore needed to discard or favour the merger scenario as the responsible mechanism for the growth in size of quiescent or spheroidal-like galaxies.

In the last years, the "progenitor" bias scenario is gaining force in this topic. It proposes that the first galaxies formed in the earliest epochs of the Universe were also the densest ones, as they resided in denser halos. Consequently, galaxy sizes would reflect the density of the Universe at the epoch in which they were formed. At the same time, they would evolve and quench their star-formation processes earlier. Any galaxy formed at later epochs will therefore be larger, evolving later on until they reach enough stellar mass as to do not support more star forming processes. This would imply that less dense quiescent galaxies (less compact or extended) are also younger, as they reach a state of quenching in later epochs (Valentinuzzi et al., 2010; Carollo et al., 2013; Belli et al., 2015). At the same time, this would imply that the number density of compact galaxies would be constant, or at least this would suffer mild and increasing modifications with cosmic time. Under this scenario, we would expect a correlation between the size of a galaxy and their stellar content age, where denser galaxies exhibit older ages (Shankar & Bernardi, 2009; Poggianti et al., 2013; Fagioli et al., 2016; Gargiulo et al., 2016; Williams et al., 2016) or large quiescent galaxies will reach the red sequence later than their compact counterparts (Belli et al., 2015).

Studying the stellar populations of compact and extended quiescent galaxies will allow us to shed light on the scenarios or mechanisms responsible for the prominent growth in size that these galaxies have undergone since high redshifts. Extended galaxies being older than their compact counterparts would favour an "inside-out" formation, whereas the opposite case could be consistent with the merging and "progenitor" bias scenarios. In fact, probing the stellar content of these galaxies along a large period of cosmic time will also provide valuable information to test more complex scenarios in which there is not a unique mechanism acting in favour of a growth in size. For instance, Belli et al. (2015) showed that the "progenitor" bias contribution at $1 < z < 1.6$ can only explain half of the average size evolution that quiescent galaxies exhibit during $1.25 < z < 2$. In addition, for the generalised evolution of the median metallicity of massive quiescent galaxies reported in Sects. 3.7.3 and 3.8.2, the presence of mergers is also necessary (see Sect. 4.7).

The definition of the quiescent sample with reliable sizes is presented in Sect. 5.2. In Sect. 5.3 we explore the correlations between the sizes and the ages, metallicities, extinctions and SFRs of the galaxies. The comparison of our results with previous work is detailed in Sect. 5.4, and a brief summary of the results is presented in Sect. 5.5.

Along this chapter we assume a ΛCDM cosmology with $H_0 = 71$ km s^{-1}, $\Omega_M = 0.27$, and $\Omega_\Lambda = 0.73$. The stellar masses are given in solar mass units [$M_\odot$].

5.2 Retrieval of sizes and stellar populations of quiescent galaxies

As the ALHAMBRA survey is a ground-based survey, the measurement of galaxy sizes is biased to those galaxies with sizes larger than the spatial resolution of the survey (which includes atmospheric "seeing", instrumental resolution, etc.). In addition, the stellar mass–size relation makes the measurement of galaxy sizes to be even more biased at larger redshifts. A rough and fair estimation of the sizes that we can resolve in ALHAMBRA, see Fig. 5.1, can be done assuming that a galaxy is spatially resolved when this one presents at least a projected size equivalent to the image PSF. Therefore, the minimum size that is spatially resolved at redshift z, $r_{\rm min}(z)$, for a ΛCDM cosmology is expressed as

$$r_{\rm min} = {\rm PSF} \times \frac{c}{(1+z)H_0} \int_0^z \frac{{\rm d}z'}{\sqrt{\Omega_{\rm M}(1+z')^3 + \Omega_\Lambda}} \,, \tag{5.1}$$

where the PSF is in arcsec, c is the speed of light, and the term in the right-hand side of the equation is the angular diameter distance assuming a flat Universe ($\Omega_{\rm k} = 0.0$, for the general expression see Hogg, 1999). For ALHAMBRA, the typical PSF size in the synthetic $F814W$ band is $1''$. In addition, we took the typical sizes of quiescent galaxies through the fits provided by Díaz-García et al. (2013, or Chapter 6) of the stellar mass–size relation for stellar masses $\log_{10} M_\star = 10.0$, 10.4,10.8, and 11.2. This allow us to see the impact of the PSF limitations for estimating reliable sizes of quiescent galaxies in ALHAMBRA. Figure 5.1 reveals that the measurement of reliable effective radii, or half-light radius, for the ALHAMBRA dataset is only possible for those galaxies located in the nearby Universe or the most massive ones at $z \lesssim 0.3$. Note that the measurement of sizes in ALHAMBRA is more biased when we assume that the stellar mass–size relation has an intrinsic dispersion. This fact largely limits the retrieval of galaxy sizes from the ALHAMBRA images (or photometric catalogues), even after carrying out a detailed PSF correction. To overcome this drawback, we took advantage of the ALHAMBRA fields that overlap with HST fields, where these limitations do not exist up to $z = 2$ and beyond.

From the ALHAMBRA galaxy sample presented in Chapter 3, we constructed a subset of quiescent galaxies with accurate effective radius measurements derived from HST data. From the ACS general catalogue of structural parameters (Griffith et al., 2012), we cross-correlated all our sources to obtain 1 411, 1 412, and 1070 quiescent galaxies (for BC03, EMILES+BaSTI, and EMILES +Padova00 respectively) with reliable effective radii in the redshift range $0.1 \leq z \leq 0.9$. Even though we explored the stellar populations of (massive) quiescent galaxies beyond $z > 0.9$, the number of sources with ACS size measurements is small when splitting into different stellar mass ranges, and hence they will not be used for this analysis. We constrained this sample to be complete in stellar mass at a completeness level of 95 %, finally providing 870, 830, and 631 quiescent galaxies for BC03, EMILES+BaSTI, and EMILES+Padova00 respectively (further details in Table 5.1).

The galaxy projected sizes taken from the ACS general catalogue of structural parameters (Griffith et al., 2012) were computed as it is explained below. All the sources in the ACS were fitted to a Sérsic profile (Sersic, 1968) with the tool GALAPAGOS (Häußler et al., 2011) in order to compute their effective radii $r_{\rm eff}$. Moreover, all the galaxies were selected following the guidelines recommended by the authors in Griffith et al. (2012) to avoid both compact (surface brightness $\mu_{F814W} \geq 18$ mag arcsec^{-2} and effective radius $r_{\rm eff} > 0.03''$given the ACS pixel scale) and low surface brightness sources $\mu < 26$ (only 7 sources did not satisfy these criteria); where all the galaxies with the flag value `FLAG_GALFIT= 1` were rejected as well (unreliable fit). Table 5.1 presents a very brief summary of the characteristics of this subsample, including the selected filter in which the Sérsic profile fitting was carried out. In closing, the effective radius were circularized using the axis ratio provided by the ACS catalogue (b/a, column `BA_GALFIT_HI`), $r_{\rm e} = r_{\rm eff}\sqrt{b/a}$, to subsequently converting it into physical units (in kpc) assuming a ΛCDM cosmology ($H_0 = 71$ km s^{-1}, $\Omega_{\rm M} = 0.27$, and $\Omega_\Lambda = 0.73$). In the following, our reference measurement for size is the circularized effective radius $r_{\rm e}$.

All the quiescent galaxies in these subsamples were analysed by MUFFIT (see Chapter 3), getting their individual stellar population parameters, as well as all the solutions retrieved by the SED-fitting analysis

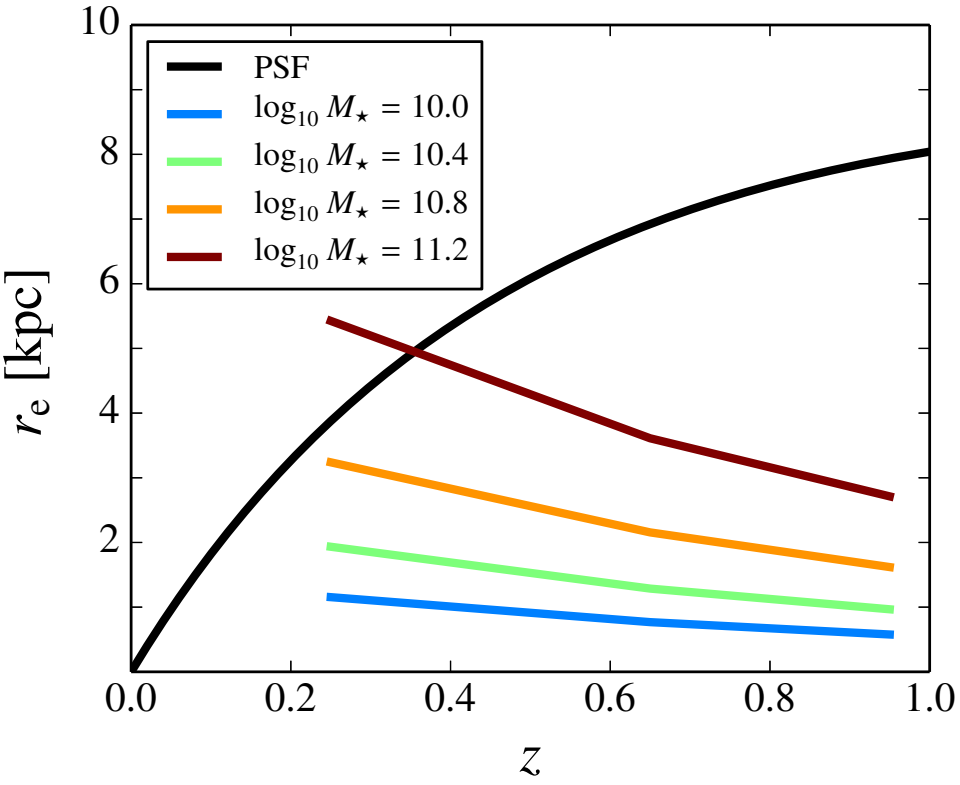

Figure 5.1: Lower limit sizes of galaxies in order to be spatially resolved in the ALHAMBRA survey (black solid line) and typical sizes of quiescent galaxies from Díaz-García et al. (2013, coloured solid lines) at different redshifts and stellar masses (see inset).

Table 5.1: Number of quiescent galaxies with reliable sizes obtained from ACS/HST fields in common with ALHAMBRA for a stellar mass completeness level of 95 %.

ACS field	ALHAMBRA field	Number (BC03)	Number (BaSTI)	Number (Padova00)	Filter	ACS pixel scale [pixel^{-1}]
COSMOS[1]	ALH-4	715	677	493	$F814W$	0.05″
HDF-N[2,3]	ALH-5	41	42	44	$F775W$	0.03″
AEGIS[4]	ALH-6	114	111	88	$F814W$	0.03″
Total		870	830	625		

Notes. (1) Scoville et al. (2007); (2) Dickinson et al. (2003); (3) Giavalisco et al. (2004); (4) Davis et al. (2007)

during the Monte Carlo approach. In the following, we use the individual stellar population values rather than the PDFs. For SFR and sSFR, we used the retrieved values in Sect. 3.4.1 using the luminosity at 2 800 Å as SFR tracer for BC03 SSP models, repeating the same process for deriving SFR and sSFR for EMILES predictions. It is worth noting that the SFR tracer is based in the luminosity at 2 800 Å expected from a τ model. This means that even when there is not any star formation in the galaxy, the stellar continuum provides a non null SFR value.

5.3 Correlations between size and stellar population parameters of quiescent galaxies

It is well known that galaxies show correlations between stellar mass and stellar population parameters such as age, metallicity, and SFR. In this section, we explore whether for a fixed stellar mass there are also correlations with the size of the galaxy, what could shed light in the growth in size mechanisms that experiment massive galaxies since $z = 1$.

For studying the distribution of the stellar population parameters on the stellar mass–size plane, we took advantage of the bidimensional and locally weighted regression method or LOESS (previously used in Sect. 3.5). To account for the crosscorrelation of uncertainties in the stellar mass–size plane (the stellar masses depends on the redshifts, ages, metallicities and extinctions, whilst the sizes do depend on redshift too), we ran the LOESS methodology with a regularization factor of $f = 0.6$ for all the solutions retrieved during the Monte Carlo approach. This properly takes all the correlations and uncertainties involved in the analysis into account, obtaining the uncertainties of the LOESS fit. We carried out the process for mass-weighted age/formation epoch (Sect. 5.3.1), metallicity (Sect. 5.3.2), extinction (Sect. 5.3.3), and SFR/sSFR (Sect. 5.3.4).

The distribution of ages, metallicities, extinctions, SFRs and sSFRs in the stellar mass–size plane are presented in Figs. 5.2–5.7 for the different SSP models employed in this thesis and several redshift bins. The interpretation of these figures is given in the next subsections.

Moreover, from the LOESS fits we are able to quantify the variation of the different stellar population parameters with size. This relation is expressed as a function of the median circularized radius, $r_{\rm e}^{\rm 50th}$, observed at each redshift and stellar mass ranges in order to diminish differences in median sizes amongst stellar masses. Thereby, we assumed a linear relation of the form

$$p_{\rm s}(z, M_\star, r_{\rm e}) = (\log_{10} r_{\rm e} - \log_{10} r_{\rm e}^{\rm 50th}) \times \bar{m}_{\rm s}(z, M_\star) + \bar{n}_{\rm s}(z, M_\star)\,, \tag{5.2}$$

where $p_{\rm s}$ represents the stellar population parameters (mass-weighted age/formation epoch, metallicity, extinction, SFR, and sSFR), $\bar{m}_{\rm s}$ the slope or the correlation with size, and $\bar{n}_{\rm s}$ the zero point. Note that Eq. 5.2 can be used to estimate, for the first time, the stellar population parameters of a galaxy when redshift, stellar mass and size are known. Figures 5.5–5.7 illustrate the results of the above fits. In addition, Tables 5.2–5.4 summarize the coefficients derived for Eq. 5.2 in different redshift bins.

5.3.1 Ages and formation epochs in the stellar mass–size plane

The results in Figs. 5.2–5.7 and Tables 5.2–5.4 point out that there is a tight correlation between the size of a quiescent galaxy and its mass-weighted age. This result is confirmed independently of the three sets of SSP models (BC03 and EMILES with isochrones BaSTI and Padova00) used for the stellar population predictions. We find out a clear trend in which more compact galaxies are systematically older at the same stellar mass range further than $\log_{10} M_\star \sim 9.6$ dex, whereas younger quiescent galaxies lie on the upper parts of the stellar mass–size relation. This correlation is extended beyond the nearby Universe up to the maximum redshift in our sample ($z = 0.9$). From Figs. 5.5–5.7, there are no strong evidences for a dependency of the size-age correlation with stellar mass, $\langle \bar{m}_{\rm s,Age_M} \rangle \sim -1.9$ at $\log_{10} M_\star \gtrsim 9.6$ dex. In addition, there is no evidence for an evolution of the size-age relation with cosmic time. We obtain that the common

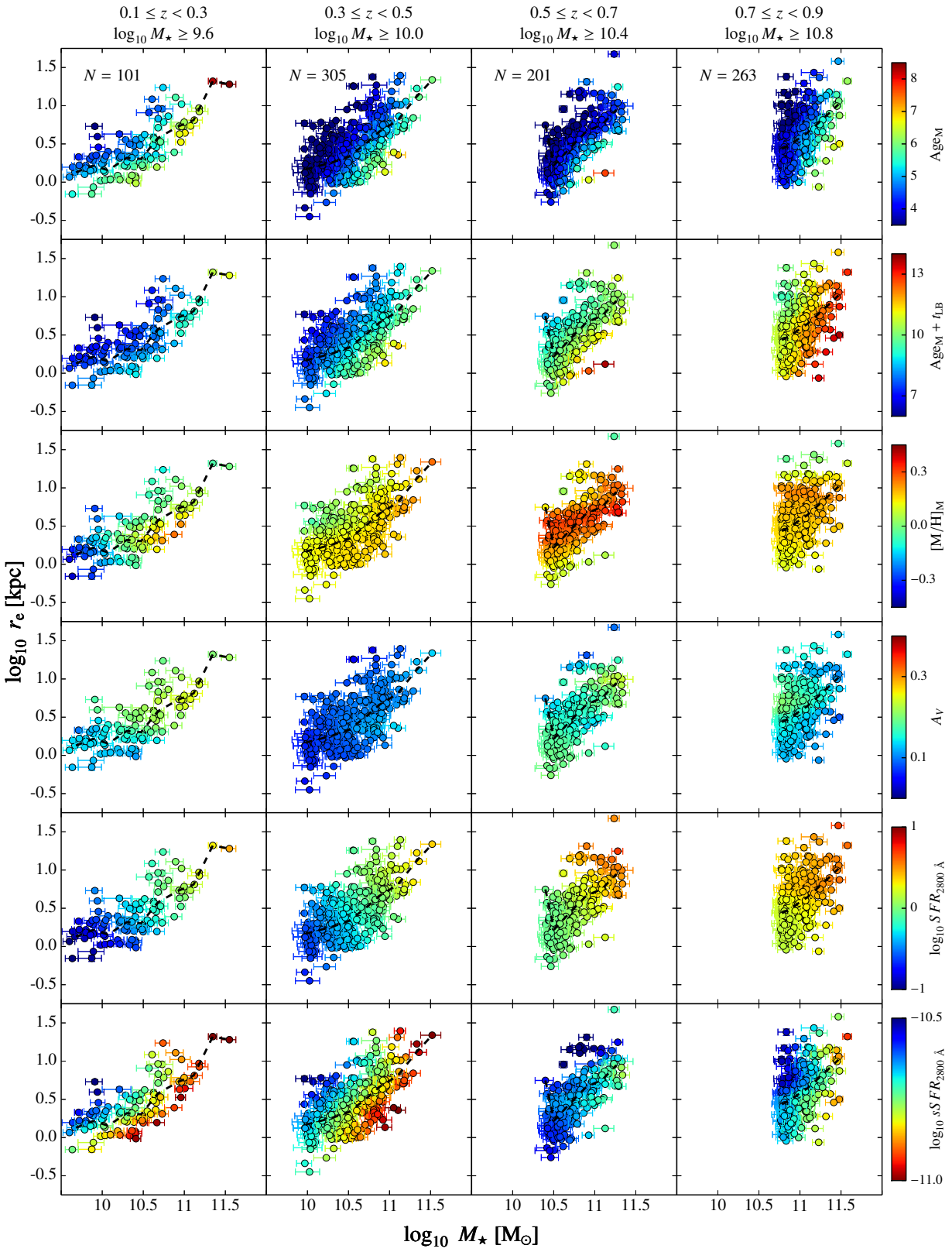

Figure 5.2: *From top to bottom*, the mass-weighted age, formation epoch, metallicity, extinction, star formation rate (SFR), and specific star formation rate (sSFR) of quiescent galaxies using BC03 models plotted on the circularized radius versus stellar mass plane down to $z = 0.9$. All values are colour-coded as indicated by the colour bar and averaged by LOESS methodology (details in text). Dashed line illustrates the median circularized radius. The number of galaxies in each panel is pointed out on the first row.

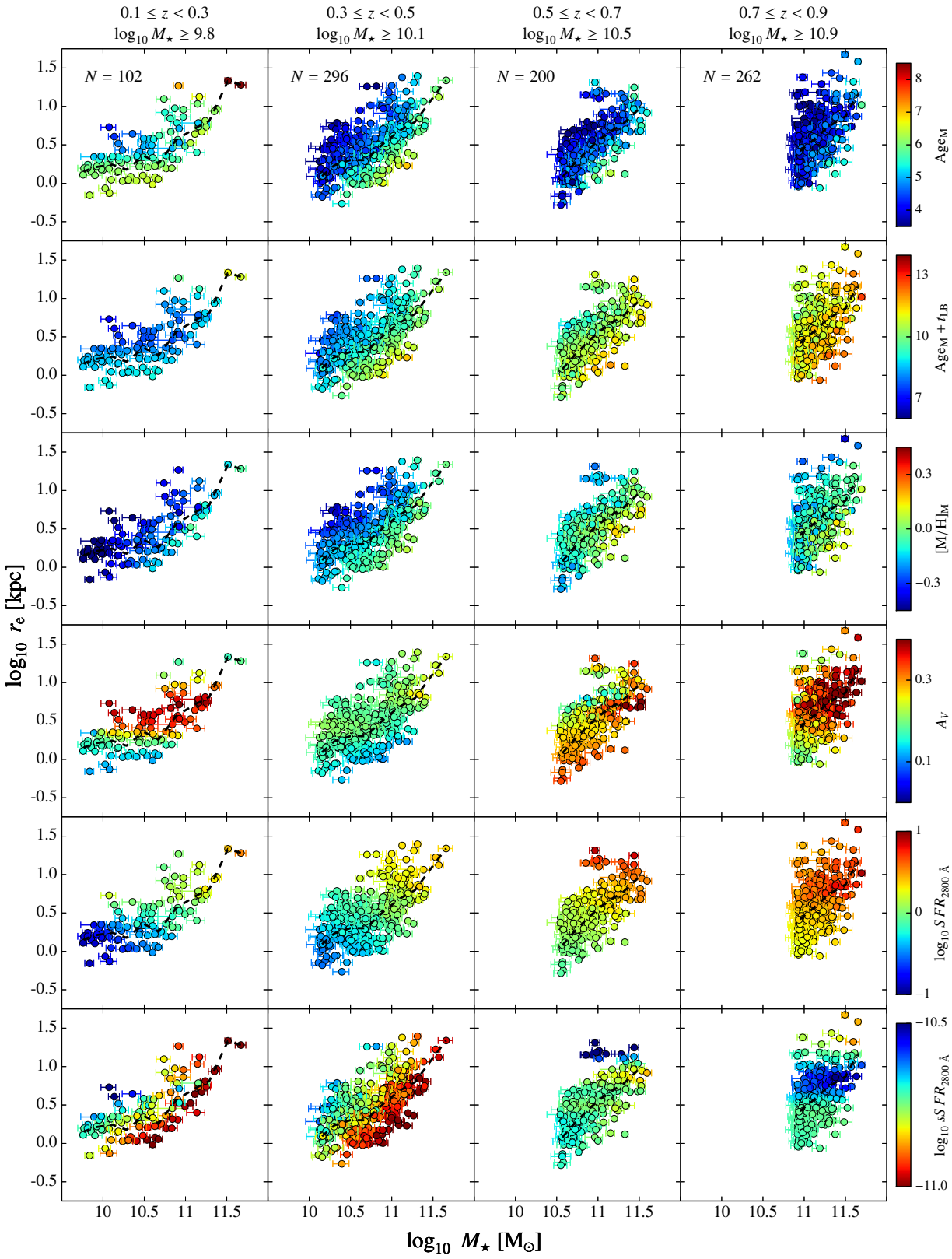

Figure 5.3: As Fig. 5.2, but using EMILES+BaSTI SSP models.

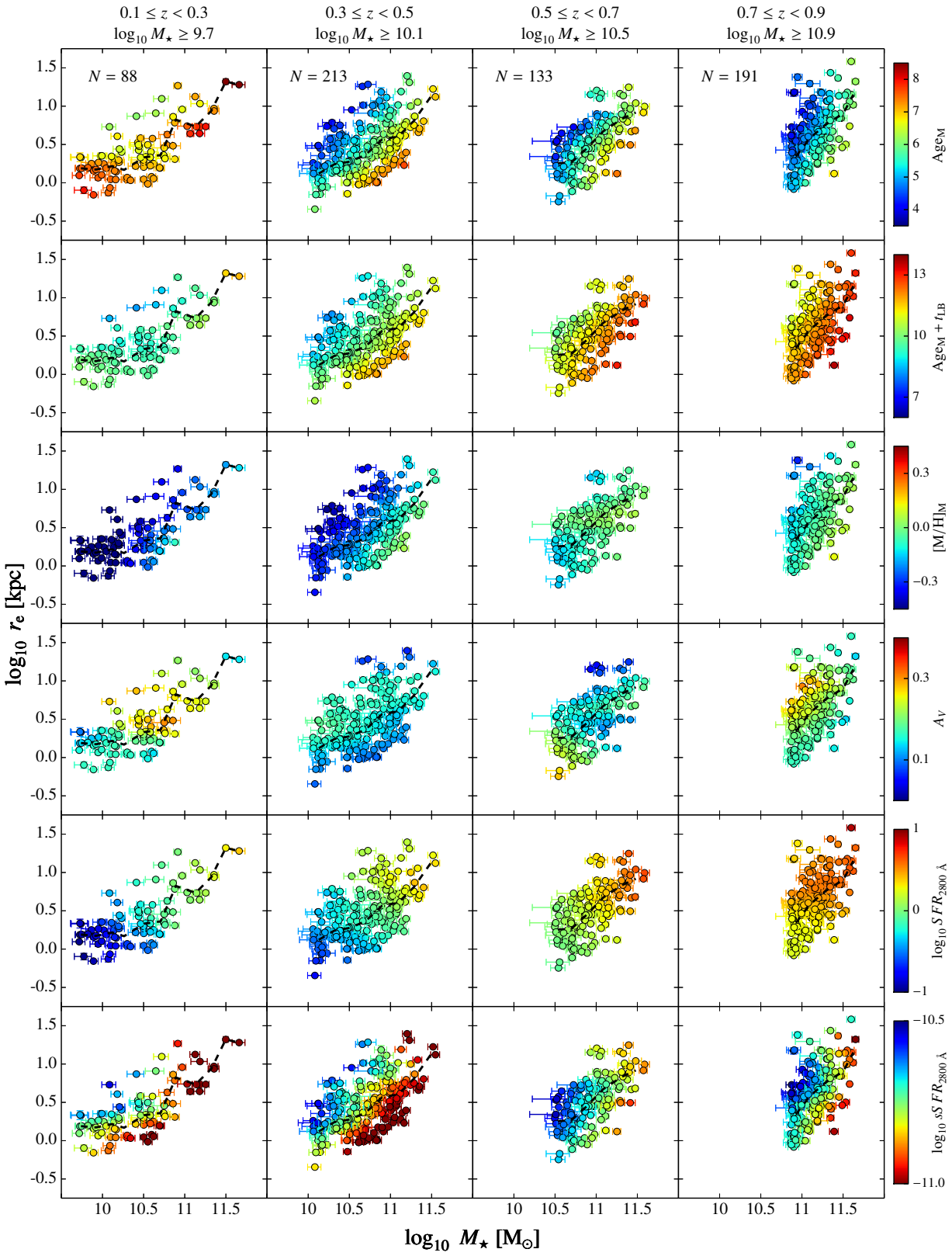

Figure 5.4: As Fig. 5.2, but using EMILES+Padova00 SSP models.

Table 5.2: Fitting parameters of Eq. 5.2 for the correlations between size and the stellar population parameters retrieved using BC03 SSP models.

BC03	$0.1 \leq z < 0.3$		$0.3 \leq z < 0.5$		$0.5 \leq z < 0.7$		$0.7 \leq z \leq 0.9$	
	$\bar{m}_s$	$\bar{n}_s$	$\bar{m}_s$	$\bar{n}_s$	$\bar{m}_s$	$\bar{n}_s$	$\bar{m}_s$	$\bar{n}_s$
$\mathrm{Age_M}$ [Gyr]								
$9.6 \leq \log_{10} M_\star < 10.0$	$-2.99^{+0.46}_{-0.47}$	$4.85^{+0.07}_{-0.07}$	–	–	–	–	–	–
$10.0 \leq \log_{10} M_\star < 10.4$	$-3.37^{+0.36}_{-0.37}$	$5.22^{+0.05}_{-0.05}$	$-1.50^{+0.11}_{-0.11}$	$3.77^{+0.02}_{-0.02}$	–	–	–	–
$10.4 \leq \log_{10} M_\star < 10.8$	$-1.95^{+0.28}_{-0.29}$	$5.49^{+0.06}_{-0.06}$	$-2.04^{+0.10}_{-0.10}$	$4.58^{+0.02}_{-0.02}$	$-1.37^{+0.12}_{-0.12}$	$3.92^{+0.03}_{-0.03}$	–	–
$10.8 \leq \log_{10} M_\star < 11.2$	$-1.71^{+0.78}_{-0.78}$	$6.18^{+0.16}_{-0.15}$	$-2.18^{+0.14}_{-0.14}$	$5.00^{+0.03}_{-0.03}$	$-2.21^{+0.18}_{-0.17}$	$4.27^{+0.04}_{-0.03}$	$-1.39^{+0.09}_{-0.08}$	$4.30^{+0.02}_{-0.02}$
$\log_{10} M_\star \geq 11.2$	$^{\dagger}4.80^{+16.59}_{-16.11}$	$6.87^{+0.42}_{-0.41}$	$-1.01^{+1.13}_{-1.08}$	$5.51^{+0.17}_{-0.17}$	$-0.96^{+0.47}_{-0.48}$	$4.56^{+0.09}_{-0.09}$	$-1.76^{+0.18}_{-0.17}$	$5.35^{+0.05}_{-0.05}$
$\mathrm{Age_M} + t_L$ [Gyr]								
$9.6 \leq \log_{10} M_\star < 10.0$	$-2.63^{+0.46}_{-0.46}$	$7.36^{+0.07}_{-0.07}$	–	–	–	–	–	–
$10.0 \leq \log_{10} M_\star < 10.4$	$-3.19^{+0.37}_{-0.38}$	$7.75^{+0.05}_{-0.05}$	$-2.01^{+0.12}_{-0.11}$	$7.95^{+0.02}_{-0.02}$	–	–	–	–
$10.4 \leq \log_{10} M_\star < 10.8$	$-2.03^{+0.29}_{-0.29}$	$8.04^{+0.06}_{-0.06}$	$-2.34^{+0.10}_{-0.10}$	$8.80^{+0.03}_{-0.03}$	$-1.54^{+0.13}_{-0.12}$	$9.71^{+0.03}_{-0.03}$	–	–
$10.8 \leq \log_{10} M_\star < 11.2$	$-1.51^{+0.80}_{-0.83}$	$8.76^{+0.15}_{-0.16}$	$-2.41^{+0.15}_{-0.15}$	$9.23^{+0.03}_{-0.04}$	$-2.16^{+0.18}_{-0.18}$	$10.07^{+0.04}_{-0.03}$	$-1.44^{+0.08}_{-0.08}$	$11.13^{+0.02}_{-0.02}$
$\log_{10} M_\star \geq 11.2$	$^{\dagger}5.68^{+16.63}_{-16.84}$	$9.61^{+0.42}_{-0.43}$	$-1.75^{+1.18}_{-1.09}$	$9.64^{+0.17}_{-0.17}$	$-0.91^{+0.46}_{-0.48}$	$10.39^{+0.09}_{-0.09}$	$-1.83^{+0.17}_{-0.17}$	$12.21^{+0.05}_{-0.05}$
$[\mathrm{M/H}]_\mathrm{M}$								
$9.6 \leq \log_{10} M_\star < 10.0$	$0.19^{+0.08}_{-0.07}$	$-0.26^{+0.01}_{-0.01}$	–	–	–	–	–	–
$10.0 \leq \log_{10} M_\star < 10.4$	$0.10^{+0.05}_{-0.05}$	$-0.07^{+0.01}_{-0.01}$	$-0.16^{+0.01}_{-0.01}$	$0.12^{+0.00}_{-0.00}$	–	–	–	–
$10.4 \leq \log_{10} M_\star < 10.8$	$-0.24^{+0.03}_{-0.03}$	$0.06^{+0.01}_{-0.01}$	$-0.12^{+0.01}_{-0.01}$	$0.13^{+0.00}_{-0.00}$	$0.19^{+0.01}_{-0.01}$	$0.25^{+0.00}_{-0.00}$	–	–
$10.8 \leq \log_{10} M_\star < 11.2$	$-0.39^{+0.06}_{-0.06}$	$0.09^{+0.01}_{-0.01}$	$-0.07^{+0.01}_{-0.01}$	$0.15^{+0.00}_{-0.00}$	$-0.04^{+0.02}_{-0.02}$	$0.27^{+0.00}_{-0.00}$	$0.08^{+0.01}_{-0.01}$	$0.17^{+0.00}_{-0.00}$
$\log_{10} M_\star \geq 11.2$	$^{\dagger} - 0.49^{+1.29}_{-1.30}$	$0.01^{+0.03}_{-0.03}$	$-0.12^{+0.08}_{-0.08}$	$0.19^{+0.01}_{-0.01}$	$-0.22^{+0.05}_{-0.05}$	$0.28^{+0.01}_{-0.01}$	$-0.02^{+0.02}_{-0.02}$	$0.19^{+0.00}_{-0.00}$
A_V								
$9.6 \leq \log_{10} M_\star < 10.0$	$0.02^{+0.04}_{-0.03}$	$0.13^{+0.00}_{-0.00}$	–	–	–	–	–	–
$10.0 \leq \log_{10} M_\star < 10.4$	$0.11^{+0.02}_{-0.03}$	$0.15^{+0.00}_{-0.00}$	$0.03^{+0.01}_{-0.01}$	$0.08^{+0.00}_{-0.00}$	–	–	–	–
$10.4 \leq \log_{10} M_\star < 10.8$	$0.11^{+0.02}_{-0.02}$	$0.19^{+0.00}_{-0.00}$	$-0.00^{+0.01}_{-0.01}$	$0.10^{+0.00}_{-0.00}$	$-0.05^{+0.01}_{-0.01}$	$0.17^{+0.00}_{-0.00}$	–	–
$10.8 \leq \log_{10} M_\star < 11.2$	$-0.03^{+0.05}_{-0.04}$	$0.23^{+0.01}_{-0.01}$	$-0.03^{+0.01}_{-0.01}$	$0.11^{+0.00}_{-0.00}$	$0.02^{+0.01}_{-0.01}$	$0.17^{+0.00}_{-0.00}$	$0.07^{+0.01}_{-0.01}$	$0.16^{+0.00}_{-0.00}$
$\log_{10} M_\star \geq 11.2$	$^{\dagger} - 0.13^{+0.91}_{-0.90}$	$0.24^{+0.02}_{-0.02}$	$0.05^{+0.05}_{-0.05}$	$0.12^{+0.01}_{-0.01}$	$-0.01^{+0.05}_{-0.05}$	$0.21^{+0.01}_{-0.01}$	$0.02^{+0.01}_{-0.01}$	$0.14^{+0.00}_{-0.00}$
$\log_{10} SFR_{2800\ \text{Å}}$								
$9.6 \leq \log_{10} M_\star < 10.0$	$0.65^{+0.04}_{-0.04}$	$-0.82^{+0.01}_{-0.01}$	–	–	–	–	–	–
$10.0 \leq \log_{10} M_\star < 10.4$	$0.63^{+0.04}_{-0.04}$	$-0.55^{+0.01}_{-0.01}$	$0.25^{+0.01}_{-0.01}$	$-0.46^{+0.00}_{-0.00}$	–	–	–	–
$10.4 \leq \log_{10} M_\star < 10.8$	$0.41^{+0.02}_{-0.02}$	$-0.27^{+0.01}_{-0.01}$	$0.34^{+0.01}_{-0.01}$	$-0.23^{+0.00}_{-0.00}$	$0.20^{+0.01}_{-0.01}$	$0.04^{+0.00}_{-0.00}$	–	–
$10.8 \leq \log_{10} M_\star < 11.2$	$0.21^{+0.05}_{-0.05}$	$0.02^{+0.01}_{-0.01}$	$0.28^{+0.01}_{-0.01}$	$0.02^{+0.00}_{-0.00}$	$0.37^{+0.01}_{-0.01}$	$0.25^{+0.00}_{-0.00}$	$0.25^{+0.00}_{-0.00}$	$0.28^{+0.00}_{-0.00}$
$\log_{10} M_\star \geq 11.2$	$^{\dagger}0.91^{+0.97}_{-0.98}$	$0.32^{+0.01}_{-0.02}$	$0.29^{+0.07}_{-0.08}$	$0.28^{+0.01}_{-0.01}$	$0.04^{+0.01}_{-0.01}$	$0.49^{+0.01}_{-0.01}$	$0.11^{+0.01}_{-0.01}$	$0.46^{+0.00}_{-0.00}$
$\log_{10} sSFR_{2800\ \text{Å}}$								
$9.6 \leq \log_{10} M_\star < 10.0$	$0.38^{+0.02}_{-0.02}$	$-10.65^{+0.00}_{-0.00}$	–	–	–	–	–	–
$10.0 \leq \log_{10} M_\star < 10.4$	$0.55^{+0.02}_{-0.02}$	$-10.76^{+0.00}_{-0.00}$	$0.22^{+0.01}_{-0.01}$	$-10.70^{+0.00}_{-0.00}$	–	–	–	–
$10.4 \leq \log_{10} M_\star < 10.8$	$0.08^{+0.01}_{-0.01}$	$-10.84^{+0.00}_{-0.00}$	$0.21^{+0.01}_{-0.01}$	$-10.79^{+0.00}_{-0.00}$	$-0.07^{+0.00}_{-0.00}$	$-10.62^{+0.00}_{-0.00}$	–	–
$10.8 \leq \log_{10} M_\star < 11.2$	$0.14^{+0.03}_{-0.03}$	$-10.89^{+0.01}_{-0.01}$	$0.16^{+0.01}_{-0.01}$	$-10.84^{+0.00}_{-0.00}$	$0.21^{+0.01}_{-0.01}$	$-10.65^{+0.00}_{-0.00}$	$0.16^{+0.01}_{-0.01}$	$-10.65^{+0.00}_{-0.00}$
$\log_{10} M_\star \geq 11.2$	$^{\dagger} - 1.09^{+0.48}_{-0.50}$	$-11.04^{+0.00}_{-0.00}$	$-0.11^{+0.06}_{-0.06}$	$-10.95^{+0.01}_{-0.01}$	$0.01^{+0.01}_{-0.01}$	$-10.71^{+0.00}_{-0.00}$	$0.07^{+0.01}_{-0.01}$	$-10.76^{+0.00}_{-0.00}$

Notes. The top and bottom numbers stablish the 1 σ confidence level of the parameters. All the bins are complete in stellar mass, $C = 0.95$, otherwise appear dashed. (†) The values $\bar{m}_s$ at $0.1 \leq z < 0.3$ and $\log_{10} M_\star \geq 11.2$ can be unreliable owing to the low number of galaxies.

Table 5.3: As Table 5.2, but using EMILES+BaSTI SSP models.

EMILES+BaSTI	$0.1 \leq z < 0.3$		$0.3 \leq z < 0.5$		$0.5 \leq z < 0.7$		$0.7 \leq z \leq 0.9$	
	$\bar{m}_s$	$\bar{n}_s$	$\bar{m}_s$	$\bar{n}_s$	$\bar{m}_s$	$\bar{n}_s$	$\bar{m}_s$	$\bar{n}_s$
$\mathrm{Age_M}$ [Gyr]								
$9.8 \leq \log_{10} M_\star < 10.1$	$-1.17^{+0.47}_{-0.48}$	$6.40^{+0.06}_{-0.06}$	–	–	–	–	–	–
$10.1 \leq \log_{10} M_\star < 10.5$	$-2.56^{+0.31}_{-0.32}$	$6.98^{+0.05}_{-0.05}$	$-1.95^{+0.13}_{-0.13}$	$5.33^{+0.03}_{-0.03}$	–	–	–	–
$10.5 \leq \log_{10} M_\star < 10.9$	$-2.01^{+0.28}_{-0.28}$	$7.57^{+0.07}_{-0.07}$	$-2.11^{+0.09}_{-0.09}$	$6.28^{+0.02}_{-0.02}$	$-1.85^{+0.14}_{-0.13}$	$5.50^{+0.03}_{-0.03}$	–	–
$10.9 \leq \log_{10} M_\star < 11.3$	$-3.32^{+0.58}_{-0.62}$	$8.02^{+0.10}_{-0.10}$	$-1.61^{+0.11}_{-0.11}$	$6.76^{+0.03}_{-0.03}$	$-2.41^{+0.16}_{-0.17}$	$6.03^{+0.03}_{-0.03}$	$-1.07^{+0.07}_{-0.07}$	$5.13^{+0.01}_{-0.01}$
$\log_{10} M_\star \geq 11.3$	$^{\dagger}22.72^{+15.89}_{-15.75}$	$8.43^{+0.49}_{-0.49}$	$-1.23^{+0.50}_{-0.52}$	$7.32^{+0.09}_{-0.09}$	$-2.18^{+0.25}_{-0.25}$	$6.43^{+0.05}_{-0.05}$	$-0.83^{+0.13}_{-0.13}$	$5.88^{+0.03}_{-0.03}$
$\mathrm{Age_M} + t_\mathrm{L}$ [Gyr]								
$9.8 \leq \log_{10} M_\star < 10.1$	$-1.01^{+0.47}_{-0.47}$	$8.91^{+0.06}_{-0.06}$	–	–	–	–	–	–
$10.1 \leq \log_{10} M_\star < 10.5$	$-2.38^{+0.31}_{-0.31}$	$9.52^{+0.05}_{-0.05}$	$-2.47^{+0.13}_{-0.13}$	$9.53^{+0.03}_{-0.03}$	–	–	–	–
$10.5 \leq \log_{10} M_\star < 10.9$	$-2.10^{+0.28}_{-0.28}$	$10.15^{+0.06}_{-0.06}$	$-2.43^{+0.09}_{-0.09}$	$10.57^{+0.03}_{-0.02}$	$-2.06^{+0.13}_{-0.13}$	$11.28^{+0.03}_{-0.03}$	–	–
$10.9 \leq \log_{10} M_\star < 11.3$	$-2.90^{+0.57}_{-0.59}$	$10.56^{+0.10}_{-0.10}$	$-1.79^{+0.11}_{-0.12}$	$11.05^{+0.03}_{-0.03}$	$-2.41^{+0.16}_{-0.16}$	$11.74^{+0.03}_{-0.03}$	$-1.11^{+0.07}_{-0.07}$	$11.95^{+0.01}_{-0.01}$
$\log_{10} M_\star \geq 11.3$	$^{\dagger}17.82^{+15.76}_{-15.44}$	$11.06^{+0.48}_{-0.48}$	$-1.59^{+0.47}_{-0.47}$	$11.57^{+0.09}_{-0.09}$	$-2.26^{+0.25}_{-0.25}$	$12.19^{+0.05}_{-0.05}$	$-0.91^{+0.14}_{-0.14}$	$12.71^{+0.03}_{-0.03}$
$[\mathrm{M/H}]_\mathrm{M}$								
$9.8 \leq \log_{10} M_\star < 10.1$	$0.07^{+0.06}_{-0.06}$	$-0.47^{+0.01}_{-0.01}$	–	–	–	–	–	–
$10.1 \leq \log_{10} M_\star < 10.5$	$-0.15^{+0.04}_{-0.04}$	$-0.28^{+0.01}_{-0.01}$	$-0.25^{+0.01}_{-0.01}$	$-0.05^{+0.00}_{-0.00}$	–	–	–	–
$10.5 \leq \log_{10} M_\star < 10.9$	$-0.25^{+0.03}_{-0.03}$	$-0.15^{+0.01}_{-0.01}$	$-0.15^{+0.01}_{-0.01}$	$-0.01^{+0.00}_{-0.00}$	$0.08^{+0.01}_{-0.01}$	$0.09^{+0.00}_{-0.00}$	–	–
$10.9 \leq \log_{10} M_\star < 11.3$	$-0.43^{+0.05}_{-0.05}$	$-0.09^{+0.01}_{-0.01}$	$-0.07^{+0.01}_{-0.01}$	$0.03^{+0.00}_{-0.00}$	$-0.02^{+0.02}_{-0.01}$	$0.12^{+0.00}_{-0.00}$	$-0.03^{+0.01}_{-0.01}$	$0.10^{+0.00}_{-0.00}$
$\log_{10} M_\star \geq 11.3$	$^{\dagger}0.04^{+1.17}_{-1.12}$	$-0.14^{+0.03}_{-0.03}$	$-0.10^{+0.05}_{-0.05}$	$0.10^{+0.01}_{-0.01}$	$-0.12^{+0.03}_{-0.03}$	$0.12^{+0.00}_{-0.00}$	$-0.07^{+0.02}_{-0.02}$	$0.14^{+0.00}_{-0.00}$
A_V								
$9.8 \leq \log_{10} M_\star < 10.1$	$0.02^{+0.05}_{-0.05}$	$0.16^{+0.00}_{-0.00}$	–	–	–	–	–	–
$10.1 \leq \log_{10} M_\star < 10.5$	$0.14^{+0.03}_{-0.03}$	$0.19^{+0.00}_{-0.00}$	$0.06^{+0.01}_{-0.01}$	$0.15^{+0.00}_{-0.00}$	–	–	–	–
$10.5 \leq \log_{10} M_\star < 10.9$	$0.17^{+0.02}_{-0.02}$	$0.23^{+0.00}_{-0.00}$	$0.04^{+0.01}_{-0.01}$	$0.15^{+0.00}_{-0.00}$	$-0.13^{+0.01}_{-0.01}$	$0.21^{+0.00}_{-0.00}$	–	–
$10.9 \leq \log_{10} M_\star < 11.3$	$-0.07^{+0.03}_{-0.03}$	$0.29^{+0.01}_{-0.01}$	$0.00^{+0.01}_{-0.01}$	$0.15^{+0.00}_{-0.00}$	$-0.04^{+0.01}_{-0.01}$	$0.16^{+0.00}_{-0.00}$	$0.12^{+0.01}_{-0.01}$	$0.23^{+0.00}_{-0.00}$
$\log_{10} M_\star \geq 11.3$	$^{\dagger} - 0.80^{+1.06}_{-1.08}$	$0.23^{+0.04}_{-0.04}$	$-0.02^{+0.03}_{-0.02}$	$0.16^{+0.00}_{-0.00}$	$-0.00^{+0.02}_{-0.02}$	$0.18^{+0.00}_{-0.00}$	$0.06^{+0.01}_{-0.01}$	$0.20^{+0.00}_{-0.00}$
$\log_{10} SFR_{2800\ \text{Å}}$								
$9.8 \leq \log_{10} M_\star < 10.1$	$0.30^{+0.04}_{-0.04}$	$-0.74^{+0.01}_{-0.01}$	–	–	–	–	–	–
$10.1 \leq \log_{10} M_\star < 10.5$	$0.27^{+0.03}_{-0.03}$	$-0.47^{+0.01}_{-0.01}$	$0.20^{+0.01}_{-0.01}$	$-0.38^{+0.00}_{-0.00}$	–	–	–	–
$10.5 \leq \log_{10} M_\star < 10.9$	$0.38^{+0.02}_{-0.02}$	$-0.23^{+0.00}_{-0.00}$	$0.28^{+0.01}_{-0.01}$	$-0.16^{+0.00}_{-0.00}$	$0.13^{+0.01}_{-0.01}$	$0.04^{+0.00}_{-0.00}$	–	–
$10.9 \leq \log_{10} M_\star < 11.3$	$0.11^{+0.05}_{-0.05}$	$0.16^{+0.01}_{-0.01}$	$0.37^{+0.01}_{-0.01}$	$0.14^{+0.00}_{-0.00}$	$0.33^{+0.02}_{-0.02}$	$0.31^{+0.00}_{-0.00}$	$0.22^{+0.00}_{-0.00}$	$0.36^{+0.00}_{-0.00}$
$\log_{10} M_\star \geq 11.3$	$^{\dagger}2.39^{+0.58}_{-0.58}$	$0.48^{+0.02}_{-0.02}$	$0.28^{+0.05}_{-0.05}$	$0.46^{+0.01}_{-0.01}$	$0.31^{+0.03}_{-0.03}$	$0.56^{+0.01}_{-0.01}$	$0.17^{+0.01}_{-0.01}$	$0.57^{+0.00}_{-0.00}$
$\log_{10} sSFR_{2800\ \text{Å}}$								
$9.8 \leq \log_{10} M_\star < 10.1$	$0.27^{+0.02}_{-0.02}$	$-10.72^{+0.00}_{-0.00}$	–	–	–	–	–	–
$10.1 \leq \log_{10} M_\star < 10.5$	$0.53^{+0.02}_{-0.02}$	$-10.83^{+0.00}_{-0.00}$	$0.15^{+0.01}_{-0.01}$	$-10.77^{+0.00}_{-0.00}$	–	–	–	–
$10.5 \leq \log_{10} M_\star < 10.9$	$0.15^{+0.01}_{-0.01}$	$-10.93^{+0.00}_{-0.00}$	$0.22^{+0.01}_{-0.01}$	$-10.88^{+0.00}_{-0.00}$	$-0.01^{+0.01}_{-0.01}$	$-10.72^{+0.00}_{-0.00}$	–	–
$10.9 \leq \log_{10} M_\star < 11.3$	$0.06^{+0.02}_{-0.02}$	$-10.93^{+0.00}_{-0.00}$	$0.24^{+0.01}_{-0.01}$	$-10.91^{+0.00}_{-0.00}$	$0.09^{+0.01}_{-0.01}$	$-10.79^{+0.00}_{-0.00}$	$0.14^{+0.01}_{-0.01}$	$-10.72^{+0.00}_{-0.00}$
$\log_{10} M_\star \geq 11.3$	$^{\dagger} - 2.35^{+0.25}_{-0.25}$	$-11.09^{+0.01}_{-0.01}$	$0.18^{+0.03}_{-0.03}$	$-10.93^{+0.01}_{-0.01}$	$0.18^{+0.01}_{-0.01}$	$-10.81^{+0.00}_{-0.00}$	$-0.04^{+0.01}_{-0.01}$	$-10.81^{+0.00}_{-0.00}$

Notes. The top and bottom numbers stablish the 1 σ confidence level of the parameters. All the bins are complete in stellar mass, $C = 0.95$, otherwise appear dashed. (†) The values $\bar{m}_s$ at $0.1 \leq z < 0.3$ and $\log_{10} M_\star \geq 11.3$ can be unreliable owing to the low number of galaxies

Table 5.4: As Table 5.2, but using EMILES+Padova00 SSP models.

EMILES+Padova00	$0.1 \leq z < 0.3$		$0.3 \leq z < 0.5$		$0.5 \leq z < 0.7$		$0.7 \leq z \leq 0.9$	
	$\bar{m}_s$	$\bar{n}_s$	$\bar{m}_s$	$\bar{n}_s$	$\bar{m}_s$	$\bar{n}_s$	$\bar{m}_s$	$\bar{n}_s$
$\mathrm{Age_M}$ [Gyr]								
$9.7 \leq \log_{10} M_\star < 10.1$	$-2.45^{+0.80}_{-0.78}$	$7.38^{+0.08}_{-0.09}$	–	–	–	–	–	–
$10.1 \leq \log_{10} M_\star < 10.5$	$-1.57^{+0.33}_{-0.33}$	$7.10^{+0.06}_{-0.06}$	$-2.35^{+0.13}_{-0.13}$	$5.36^{+0.03}_{-0.03}$	–	–	–	–
$10.5 \leq \log_{10} M_\star < 10.9$	$-0.63^{+0.34}_{-0.35}$	$6.95^{+0.07}_{-0.07}$	$-2.41^{+0.10}_{-0.10}$	$5.97^{+0.02}_{-0.02}$	$-1.51^{+0.16}_{-0.16}$	$5.31^{+0.03}_{-0.03}$	–	–
$10.9 \leq \log_{10} M_\star < 11.2$	$-1.03^{+0.55}_{-0.57}$	$7.42^{+0.11}_{-0.11}$	$-2.12^{+0.11}_{-0.11}$	$6.39^{+0.03}_{-0.03}$	$-1.82^{+0.13}_{-0.14}$	$5.82^{+0.03}_{-0.03}$	$-1.50^{+0.07}_{-0.07}$	$4.98^{+0.02}_{-0.02}$
$\log_{10} M_\star \geq 11.2$	$^{\dagger}5.87^{+4.82}_{-4.82}$	$8.28^{+0.41}_{-0.39}$	$-1.64^{+0.65}_{-0.63}$	$6.73^{+0.10}_{-0.10}$	$-1.75^{+0.27}_{-0.26}$	$6.42^{+0.06}_{-0.06}$	$-1.02^{+0.10}_{-0.10}$	$5.71^{+0.03}_{-0.03}$
$\mathrm{Age_M} + t_\mathrm{L}$ [Gyr]								
$9.7 \leq \log_{10} M_\star < 10.1$	$-1.85^{+0.75}_{-0.73}$	$9.77^{+0.09}_{-0.08}$	–	–	–	–	–	–
$10.1 \leq \log_{10} M_\star < 10.5$	$-1.45^{+0.33}_{-0.33}$	$9.52^{+0.06}_{-0.06}$	$-2.88^{+0.14}_{-0.14}$	$9.61^{+0.03}_{-0.03}$	–	–	–	–
$10.5 \leq \log_{10} M_\star < 10.9$	$-0.80^{+0.34}_{-0.33}$	$9.39^{+0.07}_{-0.07}$	$-2.74^{+0.10}_{-0.10}$	$10.28^{+0.02}_{-0.03}$	$-1.73^{+0.15}_{-0.16}$	$11.03^{+0.03}_{-0.03}$	–	–
$10.9 \leq \log_{10} M_\star < 11.2$	$-0.91^{+0.57}_{-0.55}$	$9.86^{+0.11}_{-0.12}$	$-2.32^{+0.11}_{-0.11}$	$10.70^{+0.03}_{-0.03}$	$-1.77^{+0.13}_{-0.13}$	$11.52^{+0.03}_{-0.03}$	$-1.50^{+0.07}_{-0.07}$	$11.73^{+0.02}_{-0.02}$
$\log_{10} M_\star \geq 11.2$	$^{\dagger}6.66^{+4.78}_{-4.72}$	$10.95^{+0.39}_{-0.39}$	$-2.07^{+0.63}_{-0.65}$	$10.98^{+0.10}_{-0.10}$	$-1.63^{+0.27}_{-0.26}$	$12.22^{+0.06}_{-0.06}$	$-1.06^{+0.10}_{-0.10}$	$12.50^{+0.03}_{-0.03}$
$[\mathrm{M/H}]_\mathrm{M}$								
$9.7 \leq \log_{10} M_\star < 10.1$	$0.09^{+0.09}_{-0.09}$	$-0.57^{+0.01}_{-0.01}$	–	–	–	–	–	–
$10.1 \leq \log_{10} M_\star < 10.5$	$-0.04^{+0.04}_{-0.04}$	$-0.42^{+0.01}_{-0.01}$	$-0.23^{+0.02}_{-0.02}$	$-0.27^{+0.00}_{-0.00}$	–	–	–	–
$10.5 \leq \log_{10} M_\star < 10.9$	$-0.20^{+0.04}_{-0.04}$	$-0.27^{+0.01}_{-0.01}$	$-0.24^{+0.01}_{-0.01}$	$-0.19^{+0.00}_{-0.00}$	$0.15^{+0.02}_{-0.02}$	$-0.08^{+0.00}_{-0.00}$	–	–
$10.9 \leq \log_{10} M_\star < 11.2$	$-0.15^{+0.06}_{-0.06}$	$-0.24^{+0.01}_{-0.01}$	$-0.27^{+0.01}_{-0.01}$	$-0.11^{+0.00}_{-0.00}$	$-0.01^{+0.02}_{-0.02}$	$-0.02^{+0.00}_{-0.00}$	$-0.13^{+0.01}_{-0.01}$	$-0.08^{+0.00}_{-0.00}$
$\log_{10} M_\star \geq 11.2$	$^{\dagger}0.31^{+0.42}_{-0.41}$	$-0.17^{+0.04}_{-0.03}$	$-0.27^{+0.08}_{-0.08}$	$-0.07^{+0.01}_{-0.01}$	$-0.11^{+0.03}_{-0.03}$	$-0.00^{+0.01}_{-0.01}$	$-0.12^{+0.02}_{-0.02}$	$-0.00^{+0.00}_{-0.00}$
A_V								
$9.7 \leq \log_{10} M_\star < 10.1$	$-0.10^{+0.06}_{-0.06}$	$0.15^{+0.01}_{-0.01}$	–	–	–	–	–	–
$10.1 \leq \log_{10} M_\star < 10.5$	$0.16^{+0.03}_{-0.03}$	$0.19^{+0.00}_{-0.00}$	$0.08^{+0.01}_{-0.01}$	$0.15^{+0.00}_{-0.00}$	–	–	–	–
$10.5 \leq \log_{10} M_\star < 10.9$	$0.14^{+0.02}_{-0.02}$	$0.23^{+0.00}_{-0.00}$	$0.06^{+0.01}_{-0.01}$	$0.14^{+0.00}_{-0.00}$	$-0.12^{+0.02}_{-0.02}$	$0.18^{+0.00}_{-0.00}$	–	–
$10.9 \leq \log_{10} M_\star < 11.2$	$-0.06^{+0.04}_{-0.04}$	$0.25^{+0.01}_{-0.01}$	$0.04^{+0.01}_{-0.01}$	$0.14^{+0.00}_{-0.00}$	$-0.05^{+0.01}_{-0.01}$	$0.14^{+0.00}_{-0.00}$	$0.12^{+0.01}_{-0.01}$	$0.21^{+0.00}_{-0.00}$
$\log_{10} M_\star \geq 11.2$	$^{\dagger} - 0.73^{+0.33}_{-0.31}$	$0.17^{+0.03}_{-0.03}$	$0.01^{+0.04}_{-0.04}$	$0.15^{+0.01}_{-0.01}$	$-0.05^{+0.02}_{-0.02}$	$0.15^{+0.01}_{-0.01}$	$0.07^{+0.01}_{-0.01}$	$0.20^{+0.00}_{-0.00}$
$\log_{10} SFR_{2800\ \text{Å}}$								
$9.7 \leq \log_{10} M_\star < 10.1$	$0.41^{+0.07}_{-0.07}$	$-0.83^{+0.01}_{-0.01}$	–	–	–	–	–	–
$10.1 \leq \log_{10} M_\star < 10.5$	$0.74^{+0.02}_{-0.03}$	$-0.56^{+0.01}_{-0.01}$	$0.45^{+0.01}_{-0.01}$	$-0.39^{+0.00}_{-0.00}$	–	–	–	–
$10.5 \leq \log_{10} M_\star < 10.9$	$0.49^{+0.02}_{-0.02}$	$-0.25^{+0.01}_{-0.01}$	$0.43^{+0.01}_{-0.01}$	$-0.18^{+0.00}_{-0.00}$	$0.21^{+0.01}_{-0.01}$	$0.09^{+0.00}_{-0.00}$	–	–
$10.9 \leq \log_{10} M_\star < 11.2$	$0.00^{+0.03}_{-0.03}$	$0.05^{+0.01}_{-0.01}$	$0.30^{+0.01}_{-0.01}$	$0.03^{+0.00}_{-0.00}$	$0.23^{+0.02}_{-0.02}$	$0.28^{+0.00}_{-0.00}$	$0.42^{+0.00}_{-0.00}$	$0.40^{+0.00}_{-0.00}$
$\log_{10} M_\star \geq 11.2$	$^{\dagger}1.66^{+0.17}_{-0.18}$	$0.33^{+0.01}_{-0.01}$	$-0.12^{+0.05}_{-0.05}$	$0.32^{+0.01}_{-0.01}$	$0.34^{+0.03}_{-0.03}$	$0.54^{+0.01}_{-0.01}$	$0.32^{+0.01}_{-0.01}$	$0.53^{+0.00}_{-0.00}$
$\log_{10} sSFR_{2800\ \text{Å}}$								
$9.7 \leq \log_{10} M_\star < 10.1$	$0.35^{+0.03}_{-0.03}$	$-10.75^{+0.00}_{-0.00}$	–	–	–	–	–	–
$10.1 \leq \log_{10} M_\star < 10.5$	$0.50^{+0.02}_{-0.02}$	$-10.81^{+0.00}_{-0.00}$	$0.27^{+0.01}_{-0.01}$	$-10.74^{+0.00}_{-0.00}$	–	–	–	–
$10.5 \leq \log_{10} M_\star < 10.9$	$0.33^{+0.02}_{-0.02}$	$-10.87^{+0.00}_{-0.00}$	$0.36^{+0.01}_{-0.01}$	$-10.87^{+0.00}_{-0.00}$	$0.14^{+0.01}_{-0.01}$	$-10.65^{+0.00}_{-0.00}$	–	–
$10.9 \leq \log_{10} M_\star < 11.2$	$0.07^{+0.02}_{-0.02}$	$-10.99^{+0.01}_{-0.01}$	$0.34^{+0.01}_{-0.01}$	$-10.93^{+0.00}_{-0.00}$	$0.04^{+0.01}_{-0.01}$	$-10.74^{+0.00}_{-0.00}$	$0.18^{+0.01}_{-0.01}$	$-10.70^{+0.00}_{-0.00}$
$\log_{10} M_\star \geq 11.2$	$^{\dagger} - 0.96^{+0.15}_{-0.15}$	$-11.21^{+0.01}_{-0.01}$	$0.03^{+0.05}_{-0.05}$	$-10.98^{+0.01}_{-0.01}$	$-0.01^{+0.02}_{-0.02}$	$-10.82^{+0.00}_{-0.00}$	$0.15^{+0.01}_{-0.01}$	$-10.82^{+0.00}_{-0.00}$

Notes. The top and bottom numbers stablish the 1 σ confidence level of the parameters. All the bins are complete in stellar mass, $C = 0.95$, otherwise appear dashed. (†) The values $\bar{m}_s$ at $0.1 \leq z < 0.3$ and $\log_{10} M_\star \geq 11.2$ can be unreliable owing to the low number of galaxies

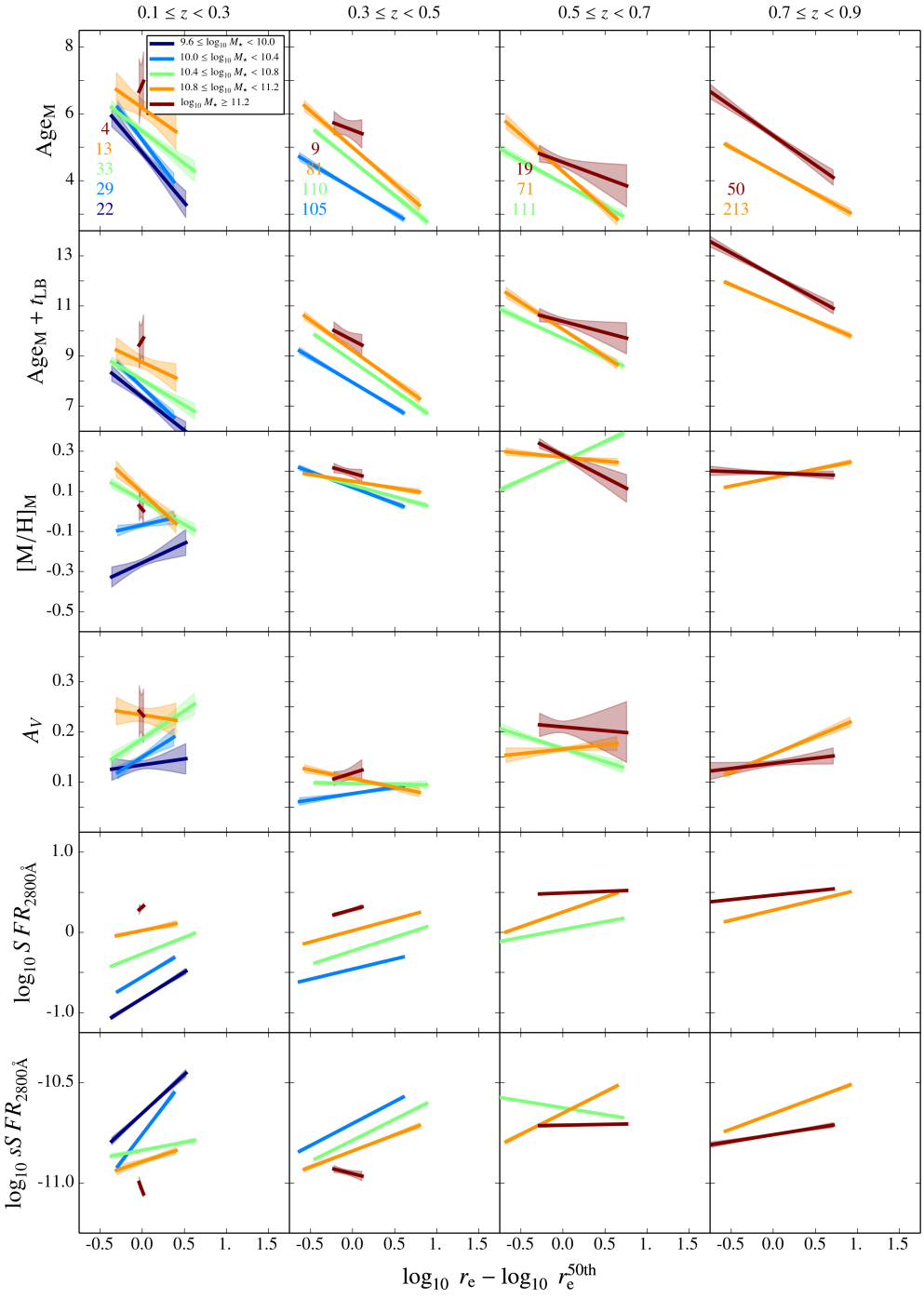

Figure 5.5: Correlations between stellar population parameters of quiescent galaxies (Y–axis) and their sizes (X–axis, deviations from the median circularized radii at different redshifts and stellar masses) since $z = 0.9$. *From top to bottom*, the mass-weighted age, formation epoch, metallicity, extinction, star formation rate (SFR), and specific star formation rate (sSFR) of quiescent galaxies using BC03 models. Shaded areas illustrate the 2 σ uncertainty level derived from the LOESS methodology. Different colours illustrate different stellar mass ranges (see inset). The number of galaxies in each panel is pointed out on the first row.

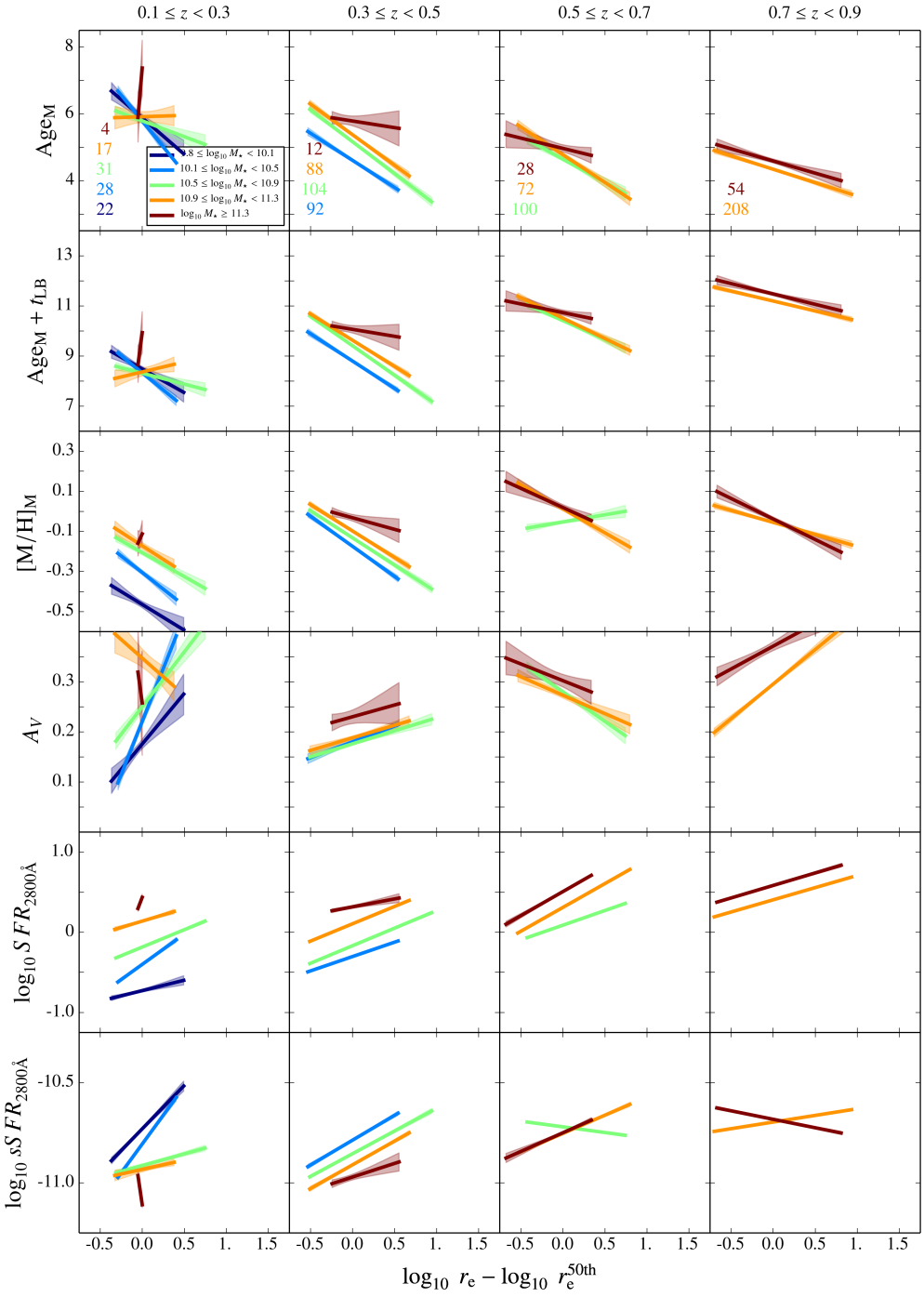

Figure 5.6: As Fig. 5.5, but using EMILES+BaSTI SSP models.

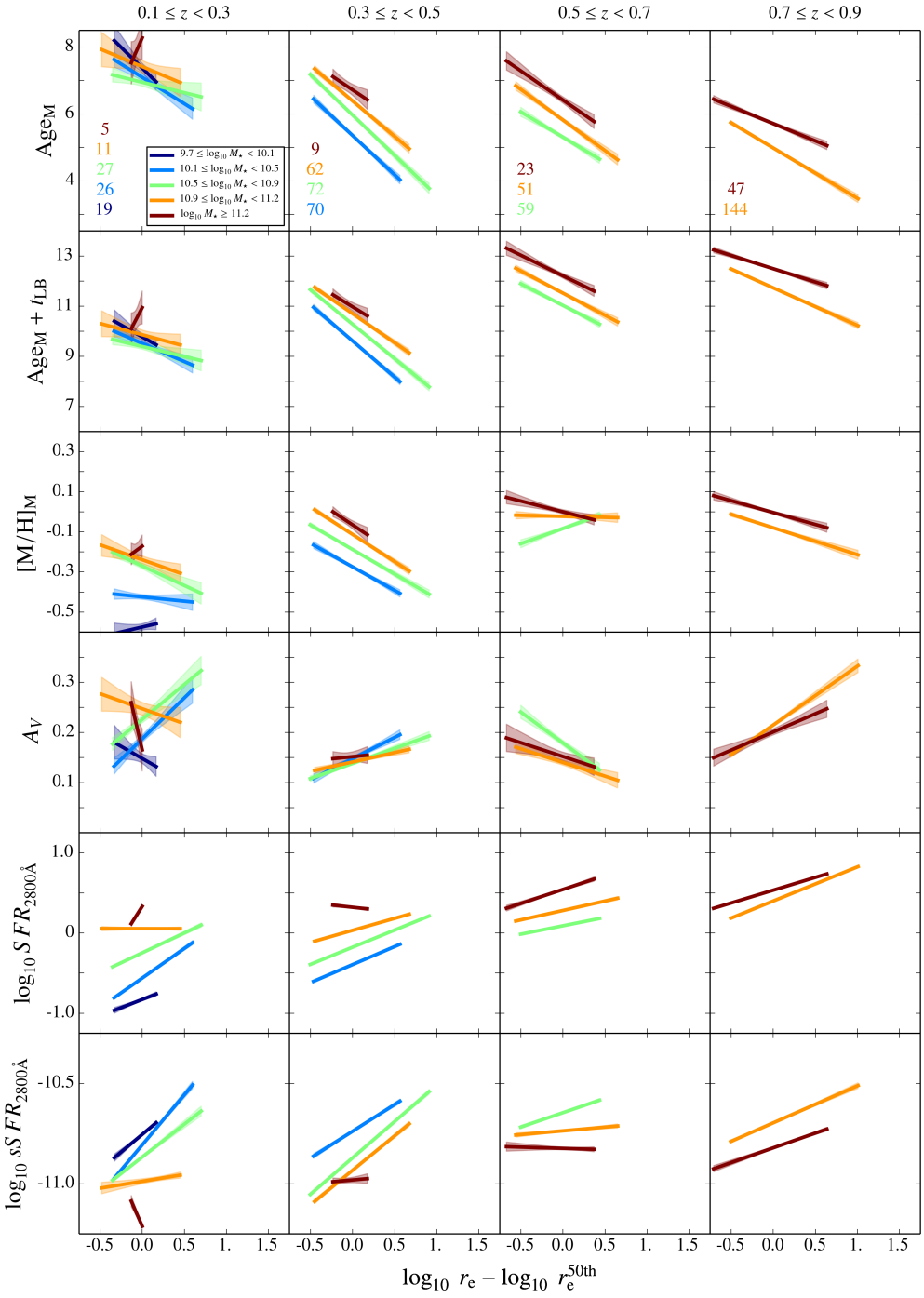

Figure 5.7: As Fig. 5.5, but using EMILES+Padova00 SSP models.

age difference between the most compact and most extended galaxies since $z = 0.9$ is $\sim$ 2–3 Gyr. Note that despite the stellar mass–size relation is less prominent for quiescent galaxies below $\log_{10} M_\star \lesssim$ 10–10.5 dex (e. g. Shen et al., 2003; Ferrarese et al., 2012; van der Wel et al., 2014; Guérou et al., 2015; Lange et al., 2015), the size-age correlation is also remarkable below this stellar mass limit.

Similar results are obtained for the mass-weighted formation epochs. The more compact the quiescent galaxy, the older its stellar population, that is, more compact quiescent galaxies were formed at earlier epochs than the extended ones at same stellar mass.

5.3.2 Metallicities in the stellar mass–size plane

From the stellar population predictions of both BC03 and EMILES, we also find out hints for a correlation between the size of a quiescent galaxy and its metal content (see Figs. 5.2–5.7 and Tables 5.2–5.4). The more compact the quiescent galaxy, the larger its metallicity. For EMILES SSP models (which presents a milder evolution of the metal content in quiescent galaxies, Sect. 3.8.2), the size-metallicity correlation is more clear than the BC03 ones (which show a maximum metallicity value or bump at $z \sim 0.6$ that is not reproduced by merger and "frosting" predictions, see Sect. 3.7.3 and Chapter 4). In addition, this correlation is observed at least since $z = 0.9$. Independently of the stellar mass range explored, more compact quiescent galaxies are also more metal rich than the extended ones of same stellar mass with a correlation of $\langle \bar{m}_{\mathrm{s},[\mathrm{M/H}]_\mathrm{M}} \rangle \sim -0.07$. Given the uncertainties and differences amongst the three SSP model predictions, and the limitation in the number of quiescent galaxies with reliable size measurements in ALHAMBRA, we cannot confirm that the correlation size-metallicity suffers either large variations in the redshift range explored or systematic differences amongst different stellar mass ranges at same redshift. Our results evidence that, on average, more compact quiescent galaxies at a fixed stellar mass are $\sim$ 0.2 dex more metal rich than their extended counterparts.

Quiescent galaxies with stellar masses of $\log_{10} M_\star \sim 10.7$ at $0.5 \leq z < 0.7$ present a different trend in the size-metallicity correlation, but this subsample is also the stellar mass range most affected by the lack of quiescent galaxies in ALHAMBRA (see also Sect. 3.6), and consequently this one may be affected by cosmic variance. We also notice a flattening or even a turnover in the slope for quiescent galaxies with $\log_{10} M_\star < 10.4$ at $z < 0.3$, which, if confirmed, could indicate hints for alternative evolutive paths as compared to the most massive galaxies.

5.3.3 Extinctions in the stellar mass–size plane

As highlighted in Sects. 3.7.4 and 3.8.3, there is no large discrepancies among the extinctions of quiescent galaxies (fairly constrained $A_V \lesssim 0.4$) and its evolution with redshift is strongly limited below $\Delta A_V < 0.1$, which a priori limits a remarkable correlation between size and extinction. Despite this, there could be a slight hint pointing out that more compact galaxies are compatible with lower levels of extinction in their stellar continuum than the extended quiescent galaxies ($\langle \bar{m}_{\mathrm{s},A_V} \rangle \sim 0.03$, see Figs. 5.2–5.7 and Tables 5.2–5.4). Owing to the narrow range of extinction values in these galaxies, the extinction differences between compact and extended quiescent galaxies are below 0.1. There are no evidences for a dependency of the size-extinction with either redshift or stellar mass.

5.3.4 SFRs in the stellar mass–size plane

The SFRs obtained from the luminosity at 2 800 Å (Sect. 3.4.1) show that quiescent galaxies with larger SFRs populate the upper part of the stellar mass-size plane. From Figs. 5.2–5.7 and Tables 5.2–5.4, we find that the more compact the quiescent galaxy is, the lower its SFR is at the same stellar mass. This result is remarkably supported by the SSP model sets of BC03 and EMILES. This size-SFR correlation is also obtained for all the quiescent galaxies in our sample since $z = 0.9$, and independently of the observed stellar mass range, $\langle \bar{m}_{\mathrm{s},\log_{10}\mathrm{SFR}} \rangle \sim 0.3$. In addition, this relation does not show any evolution with redshift, and it is

Table 5.5: Brief description of papers trying to constraint the stellar population parameters of compact galaxies.

References	Redshift	Stellar mass	Number	Parameters
Shankar & Bernardi (2009)†	$0.01 < z < 0.3$	$10^{9.7} < L_r^{\rm corr} < 10^{11.5}$	$\sim 48\,000$	Age
Trujillo et al. (2009)	$0.0 < z < 0.2$	$10^{10.9} < M_\star < 10^{11.1}$	328	Age, [M/H]
Belli et al. (2015)	$1.0 < z < 1.6$	$M_\star > 10^{10.6}$	62	Age
Guérou et al. (2015)	Virgo	$10^{8.0} < M_\star < 10^{10}$	8 + 39	Age, [M/H]
McDermid et al. (2015)	$z \lesssim 0.01$	$10^{9.8} < M_\star < 10^{12}$	260	Age, [M/H]
Fagioli et al. (2016)	$0.2 < z < 0.8$	$10^{10.5} < M_\star < 10^{11.5}$	1 519	Age
Gargiulo et al. (2016)	$0.5 < z < 1.0$	$M_\star > 10^{11}$	$> 2\,000$	Age
Williams et al. (2016)	$z \sim 1.2$	$M_\star > 10^{11}$	55	Age

Notes. From left to right, reference of the work, redshift bin, stellar mass range of the sample, number of galaxies, and stellar population parameters explored as a function of the galaxy size. All the stellar masses (luminosities) are in solar units [$M_\odot$] ([$L_\odot$]). All the work involve spectroscopic data. Belli et al. (2015) and Gargiulo et al. (2016) also include photometric SED-fitting for complementing spectroscopic predictions.
(†) In the work by Shankar & Bernardi (2009), luminosities are used as stellar mass proxy.

quite similar for different stellar mass ranges systematically, even for stellar masses $\log_{10} M_\star \lesssim 10.5$ where the stellar mass–size relation is less remarkable. Our results suggest that more compact quiescent galaxies have SFRs of the order ~ 0.5 dex lower than their compact counterparts.

In the same sense, sSFR also correlates with size. In Figs. 5.2–5.7 and Tables 5.2–5.4, we show that more compact quiescent galaxies also exhibit lower sSFR than the equal mass and extended ones, with differences < 0.5 dex. This result is obtained for all the stellar mass ranges since $z = 0.9$, which does not present significant variabilities amongst stellar mass ranges, $\langle \bar{m}_{\rm s,log_{10}\,sSFR} \rangle \sim 0.16$.

It is worth noting that, since the SFR tracer is based in the luminosity at 2 800 Å , the stellar continuum provides a non null SFR value even when there is not any star formation in the galaxy. Consequently, the intrinsic luminosity of the stellar content may drive, by itself, the correlation size-SFR/sSFR without the necessity of underlying star formation processes. This may be clearly degenerated with age effects. The study of the SFRs derived from the inclusion of dust emissions in the FIR would complement and confirm the size-SFR/sSFR correlations obtained in this research.

5.4 Comparison with previous work

Since the discovery of the stellar mass-size relation, there have been several previous work in the literature trying to constrain the stellar population parameters (mainly the age) of compact galaxies at different ranges of redshift and stellar mass (Shankar & Bernardi, 2009; Trujillo et al., 2009; Belli et al., 2015; Guérou et al., 2015; McDermid et al., 2015; Fagioli et al., 2016; Gargiulo et al., 2016; Williams et al., 2016). In this thesis we are able to present, for the first time, a comprehensive analysis of stellar populations up to $z \sim 1$ to explore the correlations between not only size and age, but also metallicity, extinction, and SFR. Despite this is so far a unique approach, we devote this section to comparing our results, obtained using photometric data, with the spectroscopic work in the literature. In each case, we describe the data, analysis techniques, and their main results within the context of this chapter. A brief description of these previous work is presented in Table 5.5.

- In **Shankar & Bernardi (2009)**, the authors explored the relation between half-light radii $R_{\rm e}$ and

the ages of 48 000 early-type galaxies from SDSS at $0.013 < z < 0.3$ and apparent magnitudes $14.5 \lesssim m_r \lesssim 17.5$. Size measurements were based on de Vaucouleur fit profiles of the surface brightness (axis ratios $b/a > 0.6$), where all the galaxies in the sample had ages older than 2 Gyr. To reduce the impact of unusual SFHs in the sample, all the brightest cluster galaxies (BCG) were also removed from the main sample. Ages were obtained from the catalogue of Gallazzi et al. (2005, a Bayesian statistical approach based on a multiple fit to age- and metallicity-sensitive absorption features and a library of Monte Carlo models), and where the corrected luminosity $L_r^{\rm corr}$ was used as proxy for stellar mass (Bernardi, 2009).

After dividing the sample in different bins of luminosity and age, authors revealed that early-type galaxies of ages larger than 9 Gyr systematically present lower effective radii of $\Delta \log_{10} R_{\rm e} \sim 0.1$ dex than the ones with ages lower than 6 Gyr at the same stellar mass (or $L_r^{\rm corr}$). This is in good agreement with our results, where the age difference between the more compact and extended quiescent galaxies is around 2–3 Gyr (in spite of our sample was not morphologically selected and our stellar masses were derived more consistently accounting for the mass-luminosity relation of the stellar populations). The authors found out that these differences in size were extended in the range of $L_r^{\rm corr}$ under study.

- The stellar populations of 29 superdense massive galaxies retrieved by **Trujillo et al. (2009)** from SDSS DR6 data also show systematic differences respect the ones obtained from a control sample composed of 299 galaxies with larger sizes. This sample was built from the New York University Value-Added Galaxy Catalog (Blanton et al., 2005b), which also provides effective radii $R_{\rm e}$ (Blanton et al., 2005a) and stellar masses (Blanton & Roweis, 2007) derived from a Chabrier (2003) IMF. These superdense or very compact galaxies were selected following several and strict constraints in order to build a reliable sample: (i) all the galaxies with stellar masses $M_\star > 8 \times 10^{10}$ and $R_{\rm e} < 1.5$ kpc were selected (at redshift $0.0 < z < 0.2$); (ii) according to the SDSS spectral classification, those sources classified as either stars or QSOs were also removed; (iii) after a visual inspection, all the galaxies close to bright stars, in close pairs, and edge-on disks were additionally removed from the sample. The final selection of superdense galaxies ends up with 29 candidates with a mean radius $R_{\rm e} \sim 1.3$ kpc, $z \sim 0.16$, $M_\star \sim 9.2 \times 10^{10}$, a mean velocity dispersion of $\langle\sigma\rangle\sim$ 196 km s^{-1}, and average Sérsic index $\langle n\rangle\sim$ 4.7. The control sample was selected following similar criteria, except for the effective radius selection that in this case was $4 < R_{\rm e} < 6$ kpc (typical size of galaxies in SDSS at the mass range of the superdense sample, see Shen et al., 2003), getting 299 candidates (stellar masses $0.8 < M_\star < 1.2 \times 10^{11}$, $\langle\sigma\rangle \sim 180$ km s^{-1}, and $\langle n\rangle\sim$ 3.8). The authors discarded that the presence of AGNs (which bias size estimations towards smaller sizes) affected their results (contamination around 7 % and 10 % for the compact and control sample respectively), using a BPT diagram or $\log_{10}$([O III]/Hβ) versus $\log_{10}$([N II]/Hα) diagram (Baldwin et al., 1981). The stellar population predictions of ages and metallicities were derived through the index-index diagram of the age sensitive Hβ_0 index (Cervantes & Vazdekis, 2009) and the metallicity one [Mg/Fe] (González, 1993) using an extension of the Vazdekis (1999a) models with the MILES library (Sánchez-Blázquez et al., 2006c; Cenarro et al., 2007).

  In this work, superdense massive galaxies present remarkable younger ages (2 Gyr) and higher metal contents ([Z/H]$\sim$ 0.2 dex) in comparison with the control sample, which were substantially older ($\sim$ 14 Gyr) and with slight sub-solar metallicities. Although the metallicity predictions pointed out to a common result with our predictions of stellar populations (the more compact quiescent galaxies present higher metallicity values), there is not agreement in the age trends. One likely explanation of these discrepancies is that, as the authors highlighted, there are limitations in the SDSS aperture size ($3''$ diameter) that biases the analysis to the inner 3 $R_{\rm e}$ of the superdense galaxies, whereas for the control sample is for 1 $R_{\rm e}$, which might drive the results to other direction.

  In addition, the authors explored that the analysis of the SFH in superdense galaxies, using the continuum and STARLIGHT code, reveals that the 64 % of the light coming from these galaxies is due to young populations created during the last 3 Gyr (which largely differs from the control sample

with a value of 7 %). This opens the possibility that these galaxies actually present very compact sizes owing to recent bursts of star formation in their inner regions that do not largely alters the stellar mass of the galaxy but that biased their sizes to lower values. In this sense, the authors looked for very compact sources, which actually are blue, whose result was the plausible selection of a channel to create compact galaxies that differs from the largely evolved quiescent galaxies or compact relics. Finally, an extra explanation for the disagreement with our results is that a separation of quiescent and star-forming galaxies was not performed in Trujillo et al. (2009), and consequently, this can also alter any stellar population prediction. In any case, discrepancies in the colours and stellar populations were found between galaxies of different sizes, which supports in any case that both subpopulations present discrepancies in their stellar populations.

- In the work by **Belli et al. (2015)**, they explored the stellar populations of a sample of 62 quiescent galaxies at the redshift range $1 < z < 1.6$ using Keck/LRIS spectra (that at this redshift matches with the optical rest-frame Balmer break), supplemented with photometric data. The sample was selected using the UVJ colour-colour diagram of Muzzin et al. (2013). Spitzer/MIPS 24μm fluxes were studied in order to confirm that these galaxies are red without the presence of large dust contents. SFRs were estimated by [O II] emissions and stellar population parameters determined through the `pyspecfit` code (Newman et al., 2014, Bayesian spectral fitting) using BC03 τ models with fixed solar metallicity $Z_\odot = 0.02 \pm 0.005$, Chabrier (2003) IMF, and Calzetti et al. (2000) extinction law in the range $0 < A_V < 4$.

  They retrieved that older quiescent galaxies populated the lower parts of the stellar mass–size diagram, and consequently, they are in average more compact. Although this study extended further than our upper redshift limit, it also confirms that older quiescent galaxies present more compact sizes. In addition, they obtained that extended quiescent galaxies arrived into the quiescent sample later than the compact ones, and therefore they were mainly formed in later formation epochs than the compact counterpart, as we obtain from our SED-fitting analysis in ALHAMBRA (Sect. 5.3.1).

- **Guérou et al. (2015)** studied the stellar populations of 8 low-mass and compact early-type galaxies from the Virgo cluster. These early-types were acquired with the 8.1 m Gemini North telescope and the Gemini Multi Object spectrograph (GMOS, Hook et al., 2004) IFU through a combination of one- and two-slit modes and field of view (FOV) $7'' \times 5''$. These galaxies present surface brightness in the range $17 \lesssim \mu_i \lesssim 20$ mag arcsec^{-2} and effective radii of $2.1'' \lesssim R_e \lesssim 9.1''$, which correspond to sizes of 165–740 pc. Ages and metallicities were derived through the stacked spectra of each galaxy using the code pPXF and MIUSCAT SSP models (unimodal IMF of slope 1.3 or Salpeter-like IMF) in the wavelength range $\lambda\lambda$ 4 200–5 400 Å, where Hβ and [O III] regions were masked out to avoid contaminations from emission lines. This methodology is similar to the performed by McDermid et al. (2015). Stellar masses were computed from the Sérsic-dependent virial theorem taking the velocity dispersion in one effective radius (representative of the enclosed dynamical mass, Cappellari et al., 2013b). In order to complete their sample in the stellar mass–size plane, Guérou et al. (2015) added 39 less compact and low-mass early-type galaxies from the Virgo cluster. These 39 early-type galaxies were obtained from the work by Toloba et al. (2014), using data from the Stellar content MAss and Kinematics of Cluster Early-type Dwarf galaxies (SMAKCED, Janz et al., 2014) spectroscopic and photometric survey. The stellar masses of the low-mass early-type galaxies from SMAKCED were derived in a similar way to Guérou et al. (2015) and comprise the range $10^8 < M_\star < 10^{10}$ and $-19 < M_r < -16$. Unlike Guérou et al. (2015), Toloba et al. (2014) used Lick indices in the LIS-5 Å system (in particular Hβ, HγA, Fe4668, and Mgb; Vazdekis et al., 2010) to determine ages and metallicities.

  After running the LOESS approach in the stellar mass–size plane for the stellar populations of the 8+39 low-mass early-type galaxies, Guérou et al. (2015) obtained that, for galaxies below $M_\star < 10^{10}$, more compact early-type galaxies are older and more metal-rich than the less compact galaxies at the

same stellar mass range. Again, despite the very local Universe (Virgo) is not accounted in this thesis, this agrees with our results at $0.1 < z < 0.3$ and $M_\star < 10^{10}$.

- From 260 early-type galaxies in the mass range $6 \times 10^9 < M_\star < 10^{12}$ at the nearby Universe, **McDermid et al. (2015)** studied the distribution of their stellar population parameters on the stellar mass–size plane. These early-type galaxies were obtained from the ATLAS^{3D} survey (Cappellari et al., 2011) using the SAURON spectrograph (Bacon et al., 2001) on the 4.2 m William Herschel Telescope (WHT). They determined ages, metallicities and [α/Fe] by a multiple fitting of the indices Hβ, Fe5015, and Mgb to a customized version of the Schiavon (2007) SSP models. Moreover, mass-weighted ages and metallicities were estimated for this sample of early-type galaxies fitting the spectrum using the penalized pixel fitting code (pPXF, Cappellari & Emsellem, 2004) and MIUSCAT SSP models (Vazdekis et al., 2012) with solar [α/Fe].

  After applying the LOESS algorithm with a regularization factor of $f = 0.6$, they obtained similar conclusions on the stellar mass–size plane for index based ages and metallicities, and the mass-weighted ones: more compact galaxies present both older ages and higher metallicities. This result agrees with our predictions of quiescent galaxies at $0.1 < z < 0.3$ and $\log_{10} M_\star > 10$. Notice that whilst our sample was built using the intrinsic colours of galaxies as spectral discriminator, the sample of McDermid et al. (2015) was morphologically selected and preserves the same correlations with size that we obtained, in part owing to early-type galaxies frequently present red colours.

- In the recent work by **Fagioli et al. (2016)**, the ages of compact and extended quiescent galaxies are also confronted. Making use of spectra from the 20k zCOSMOS-bright spectroscopic survey, authors selected quiescent galaxies at $0.2 \leq z \leq 0.8$ and stellar masses $\log_{10} M_\star \geq 10.5$ in order to discern the existence (or not) of a size-age correlation. The selection of the quiescent sample differs from the ones based on colour-colour or colour-magnitude diagrams, taking only those galaxies that do not present any emission in H_α, Hβ, and [O II]. In addition, the sample is biased to all the quiescent galaxies with redshift confidence Classes 3 and 4. Stellar masses were derived with the code ZEBRA+ (Oesch et al., 2010) using BC03 SSP models with declining SFRs, a broad range of stellar population parameters and Chabrier (2003) IMF. Sizes were defined from the semimajor axis, or half-light radius, provided by the extended version of Zurich estimator of structural types plus (ZEST+, Scarlata et al., 2007) in the HST/ACS $F814W$ images. All the spectra fulfilling the above criteria were stacked in bins of equal-sized redshift ($\Delta z = 0.2$, $0.2 \leq z \leq 0.8$) and stellar mass ($\Delta \log_{10} M_\star = 0.5$, $10.5 \leq \log_{10} M_\star \leq 11.5$) bins, and corrected of residual nebular emissions (Balmer lines, [O II], and [O III]) and galactic extinction through Schlegel et al. (1998) dust maps. The ages of each stacked spectrum were estimated by two methods: (i) via spectral fitting of the rest-frame range $\lambda\lambda$ 4 100–4 700 Å using pPXF and BC03 SSP models with fixed solar metallicity ([O II] and [O III] were masked out) and Salpeter (1955) IMF; (ii) making a multiple fitting of a redshift variable set of Lick indices (details of the indices used at each redshift in Fagioli et al., 2016) to the index predictions of Thomas et al. (2011, including variable α-abundances) SSP models, with Salpeter (1955) IMF and fixing metallicities to the averaged ones obtained by Gallazzi et al. (2005) for the global stellar mass-metallicity relation in the local Universe.

  The age predictions in this work agree in that more compact galaxies at $10.5 \leq \log_{10} M_\star \leq 11.0$ are older than their larger counterparts, in agreement with our results. However, for the stellar mass range $11.0 \leq \log_{10} M_\star \leq 11.5$, the authors did not find a clear correlation between the size and the age of quiescent galaxies, which is at odds with our outcomes in Sect. 5.3.1 and the ones by McDermid et al. (2015). This discrepancy with our results may come for various aspects: (i) the selection of quiescent galaxies is different than ours, as galaxies with little emission lines are rejected even if the star formation is not significant for the galaxy, which can bias the more extended sources that present younger ages; (ii) stellar masses are computed for a very broad range of models including various SFH and metallicities, which may diverge from the stellar masses derived from the stellar population

predictions of both SED-fitting and Lick indices, in fact, the IMF plays an important role in the determination of stellar mass (e. g. Ferré-Mateu et al., 2013) and this is different for age estimations; (iii) for full spectrum SED-fitting Fagioli et al. (2016) constrained metallicities to solar values, which modifies the age estimations as illustrated in Sects. E.1 and E.2; (iv) metallicity values were fixed to the metallicity values in the local Universe (Gallazzi et al., 2005) where any distinction between quiescent and star-forming galaxy was not done (and also affected by SDSS aperture effects), and at the same time, we detected systematic differences between the metallicity of more compact and most extended quiescent galaxies (also obtained in Trujillo et al., 2009; McDermid et al., 2015); v) the bias introduced for selecting only galaxies with confidence Classes 3 and 4 was not treated, which can partly removes oldest (compact) galaxies at a fixed stellar mass compromising the completeness of the sample. Consequently, the confirmation of the no presence of a size-age correlation in the mass range $11.0 \leq \log_{10} M_\star \leq 11.5$ may be the result of all these assumptions, as the age-metallicity degeneracy can modify the age estimations of these galaxies and their stellar masses. Indeed, the authors reported that without fixing metallicities the age and metallicity predictions are largely uncertainty. Despite these assumptions, for $10.5 \leq \log_{10} M_\star \leq 11.0$, their results agree with previous studies and ours.

- As part of the spectroscopic VIPERS redshift survey (resolving power $R = 220$, spectral range $\lambda\lambda$ 5 500–9 500 Å), **Gargiulo et al. (2016)** extracted a sample of more than 2 000 quiescent galaxies with stellar masses $\log_{10} M_\star > 11$ at $0.5 \leq z \leq 1.0$. Quiescent galaxies were extracted by the colour-colour diagram NUV$-r$ versus $r - K$, with a redshift quality flag in the range $2 \leq z_{\rm flag} \leq 9.5$. Stellar masses were derived from photometry and HYPERZ code using BC03 τ-models with sub-solar and solar metallicities and Chabrier (2003) IMF. Structural parameters (effective radius and Sérsic index) were estimated using GALFIT and the r (at $z > 0.8$) and i (at $z < 0.8$) bands of the CHFTLS-Wide ground-based images, to subsequently divide the sample in three size bins through the stellar mass density ($\Sigma = M_\star / 2\pi R_{\rm e}^2$; compact sources $\Sigma \geq 2\,000$ M$_\odot$ pc^{-2} and extended $\Sigma \leq 1\,000$ M$_\odot$ pc^{-2}). Four sources of incompleteness were taking into account (target sampling rate, success sampling rate, colour sampling rate, and reliable size rate) for retrieving ages and number densities. Stellar population ages of quiescent galaxies were estimated individually using both photometric SED-fitting and the $D_{\rm n}4000$ index.

  Gargiulo et al. (2016) obtained that compact quiescent galaxies are older and they evolve passively. On the other hand, extended quiescent galaxies are younger in comparison with their compact counterparts and their evolution since $z = 0.8$ up to $z = 0.5$ is not compatible with a passive evolution in agreement wit our results. In addition, Gargiulo et al. (2016) obtained that the number density of compact quiescent galaxies does not suffer a large evolution in number, unlike the extended ones that increase in number with cosmic time a factor ~ 4 from $z = 0.8$ to $z = 0.5$, which is substantially larger than ours.

- The recent work by **Williams et al. (2016)** presents spectroscopic ages derived from galaxies in the Cosmic Assembly Near-infrared Deep Extragalactic Legacy Survey (CANDELS, Koekemoer et al., 2011; Grogin et al., 2011). The sample was defined according to the selection performed by Cassata et al. (2011, quiescent galaxies with stellar masses $M_\star > 10^{11}$, $sSFR < 10^{-2}$ Gyr^{-1}, and at $z > 1$), where SFRs and stellar masses were determined via SED-fitting using SpeedyMC software (Acquaviva et al., 2011) and CANDELS multi-wavelength photometry. Circularized half-light radius were derived with GALFIT (Peng et al., 2002) and HST/WFC3 $F160W$ H-band imaging from CANDELS images (presented in van der Wel et al., 2012). Amongst these galaxies, there are 61 quiescent galaxies with publicly available spectra from Very Large Telescope (VLT) as part of the GOODS program (FORS2 and VIMOS spectrographs), that are used to derive stellar population ages. There are 22 compact quiescent galaxies (defined as those with stellar mass surface densities $\Sigma \gtrsim 3 \times 10^9$ M$_\odot$ kpc^{-2}) and 33 classified as normal size ($\Sigma < 3 \times 10^9$ M$_\odot$ kpc^{-2}) with average redshift 1.22 and 1.13 respectively. Differences between ages of compact and normal sizes were derived

comparing age-sensitive features $H\delta_A$ and D_n4000 of the stacked spectra of compact and normal sizes.

The results by Williams et al. (2016) show that both age estimators predict that compact quiescent galaxies are older than the less compact ones. For $H\delta A$ the age difference is $\sim$ 2.5 Gyr, whereas for D_n4000 is milder, $\sim$ 0.3 Gyr. This result supports ours, in which the difference in age between the more compact quiescent galaxies and the typical ones is 1–1.5 Gyr. An additional age diagnostic was performed using pPXF with the stacked spectra (in part for avoiding overestimations in $H\delta A$ due to CH and CN absorptions) in the range $\lambda\lambda$ 3 500–4 800 Å using Vazdekis et al. (2010) SSP models (Salpeter-like IMF), reaching the same conclusion: more compact quiescent galaxies are older than the more extended ones, which reinforces our conclusions.

In addition, authors examined [O II] emissions, confirming that the presence of these emissions are more frequent in extended quiescent galaxies, but they were not able to disentangle whether these emissions come from the presence of AGN or from remnants of star formation. The latter would support our results on the size-SFR correlation in which more extended galaxies present larger SFR values than their compact counterparts.

To conclude, there is a general good agreement in that more compact quiescent/spheroidal/red galaxies present differences in their stellar populations. Ages were more extensively studied, reaching a common conclusion: more extended quiescent galaxies contain younger stellar populations at the same stellar mass regime (Shankar & Bernardi, 2009; Belli et al., 2015; McDermid et al., 2015; Guérou et al., 2015; Williams et al., 2016; Fagioli et al., 2016; Gargiulo et al., 2016), and this correlation is well observed beyond the local Universe. In addition, some authors also observed that more compact galaxies are also more metal-rich (Trujillo et al., 2009; McDermid et al., 2015) all in agreement with our SED-fitting results, although their results are spectroscopically constrained to the local Universe and our photometric analysis largely extends this insight up to $z \sim 1$.

5.5 Summary and conclusions

After selecting all the quiescent galaxies from ALHAMBRA with reliable sizes (circularized effective radius) in HST fields, we obtain a subsample of more than 800 of galaxies with stellar population parameters. We use this subsample for discerning whether there are correlations between the stellar content of quiescent galaxies and their sizes at fixed stellar mass. We find out evidences for strong correlations between the size and the age, metallicity, and SFR/sSFR of quiescent galaxies, although there are also hints pointing out that there exists a slight correlation also with extinction. This outcome does not depend of the SSP model used, and it is obtained for three SSP model predictions: BC03, EMILES with BaSTI isochrones, and EMILES with Padova00 isochrones. Our results reveal remarkable insights:

- There is a tight correlation between the size of a quiescent galaxy and its age. A generalised trend in which more compact quiescent galaxies are older than their more extended counterparts. The difference in age is established around 2–3 Gyr for stellar masses $\log_{10} M_\star > 9.6$ and up to $z \sim 0.9$, where the average size-age correlation is $\langle \bar{m}_{s,\mathrm{Age_M}} \rangle \sim -1.9$ (see Eq. 5.2).
- Compact quiescent galaxies are systematically more metal rich than the less dense ones at the same stellar mass. The larger metallicity differences between compact and extended quiescent galaxies is 0.2 dex at least since $z = 0.9$, where the correlation size-metallicity is $\langle \bar{m}_{s,[\mathrm{M/H}]_\mathrm{M}} \rangle \sim -0.07$ in average.
- There are hints for extended quiescent galaxies presenting slight larger extinctions of < 0.1 independently of their stellar mass range and redshift, $\langle \bar{m}_{s,A_V} \rangle \sim 0.03$.
- The more compact the quiescent galaxy, the lower its SFR ($\langle \bar{m}_{s,\log_{10}\mathrm{SFR}} \rangle \sim 0.3$) and sSFR ($\langle \bar{m}_{s,\log_{10}\mathrm{sSFR}} \rangle \sim 0.16$), where the difference between the values of the compact and the extended ones is below 0.5 dex in both cases. This trend is observed for all the stellar masses present in our sample since $z = 0.9$.

Finally, we have compared our results with previous spectroscopic work that partially deal with this topic, mostly focused on probing potential age differences between compact and extended galaxies (Shankar & Bernardi, 2009; Trujillo et al., 2009; Belli et al., 2015; McDermid et al., 2015; Guérou et al., 2015; Williams et al., 2016; Fagioli et al., 2016; Gargiulo et al., 2016). Overall there is a very good agreement regarding such age effects. Interestingly, our results greatly extend some of the conclusions obtained in the nearby Universe: more compact quiescent galaxies are more metal-rich than their extended counterparts (Trujillo et al., 2009; McDermid et al., 2015), but this fact is also observed for the first time since $z \sim 1$ in this thesis thanks to the ALHAMBRA. In addition, correlations between size-extinction and -SFR/sSFR are explored, which constitute a complement for future studies.

In view of these results, the "puffing-up" scenario can be discarded as a responsible mechanism of the growth in size of galaxies (in good agreement with the pioneering work by Trujillo et al., 2011, which gave strong evidence against the "puffing-up" mechanism of gas expulsion), because this one would imply that compact galaxies were younger than their more extended counterparts. However, the "progenitor" bias agrees with the results obtained in this research, as well as mergers. Both the "progenitor" bias and mergers homogeneously acting along the stellar mass–size plane can explain the growth in size of quiescent galaxies since $z \sim 1$. In fact, a combination of both mechanisms is also likely after studying their effects on the massive sample (Chapter 4). Actually, there is a non-negligible contribution in number through mergers of less massive systems, which also increases the size of the host galaxies. A more extensive discussion of this topic is carried out in Chapter 7.

6

The merger history of massive spheroids since $z \sim 1$

> *Go to Heaven for the climate, Hell for the company.*
>
> Mark Twain

This chapter has been published as
Díaz-García et al. 2013, MNRAS, 433, 60D

Introducción al artículo

En este artículo pretendemos discernir si existen correlaciones entre los tamaños de las galaxias y la presencia o no de galaxias compañeras (también conocidas como galaxias satélite). Estos resultados son utilizados para investigar el papel de las fusiones de galaxias o "mergers" en el crecimiento en tamaño que experimentan las galaxias esferoidales o elípticas desde $z \sim 1$. En el caso en el que las galaxias más compactas presentasen una mayor presencia de galaxias compañero podría ser interpretado como un indicio de que el crecimiento en tamaño es conducido principalmente por mergers. Así, las galaxias más extensas ya habrían incrementado su tamaño mediante la acrección de las galaxias compañeros mostrando un deficit de galaxias compañero respecto a las galaxias compactas.

Para llevarlo a cabo, usamos una recopilación de 379 galaxias esferoidales masivas (masa estelar $M_\star \gtrsim 10^{11}$ M$_\odot$) procedentes del cartografiado infrarojo de Palomar/DEEP2, e investigamos si la presencia de compañeros o galaxias satélite depende del tamaño de la galaxia central. Este estudio se realiza desde desplazamiento al rojo $z \sim 1$ hasta el Universo local. Exploramos la presencia de compañeros para fracciones en masa hasta órdenes 1:10 y 1:100 respecto a la galaxia central y dentro de distancias proyectadas de 30, 50 y 100 kpc. Encontramos evidencias de que la presencia de compañeros entorno a esferoides masivos es independiente de si éstos son compactos o extensos. Esto sugiere que, al menos hasta $z \sim 1$, la tasa de fusiones de galaxias en estos objetos es bastante homogénea a lo largo de toda la población masiva, y su historia de fusiones no está correlacionada con el tamaño de la galaxia central. Este resultado podría indicar que, tanto los esferoides masivos compactos como los extensos, están afectados de igual manera por los mergers, y el crecimiento a través de este mecanismo afectaría por igual a las galaxias masivas, independientemente de su tamaño.

Además, este estudio da pie a que los mergers no pueden ser descartados por completo de los mecanismos propuestos para el crecimiento en tamaño de las galaxias de tipos tempranos. Hoy en día se está explorando otras alternativas como el "progenitor" bias para explicar dicho crecimiento (e. g. Valentinuzzi et al., 2010; Carollo et al., 2013; Belli et al., 2015), aunque ciertos autores han medido su contribución y es necesario más mecanismos para explicarlo por completo (Belli et al., 2015). Por otro lado, existen muchos estudios al respecto que apuntan a que existe una correlación entre el tamaño y el contenido estellar de las

galaxias rojas (mayormente estudios relacionados con la edad, e. g. Shankar & Bernardi, 2009; Trujillo et al., 2009; Belli et al., 2015; McDermid et al., 2015; Guérou et al., 2015; Williams et al., 2016; Fagioli et al., 2016; Gargiulo et al., 2016), siendo un indicativo de que el "progenitor" bias debe ser incluído entre los mecanismos responsables. Una combinación de ambos efectos sería crucial para explicar las correlaciones entre las poblaciones y el tamaño, ya que ambos efectos superpuestos serían más eficientes a la hora de explicar el aumento en el tamaño promedio de estas galaxias, manteniendo al mismo tiempo la coherencia con los resultados obtenidos en el Capítulo 5. En una línea paralela propuesta por otros autores (e. g. Gargiulo et al., 2016), la densidad numérica de los objetos compactos es otro parámetro a tener muy en cuenta para estudios futuros, ya que una densidad numérica constante de galaxias quiescentes compactas implicaría que estos objetos no han sufrido grandes modificaciones en tamaño y el "progenitor" bias tendría un mayor peso. Sin embargo, está muy lejos de estar clara esta situación, ya que existen numerosos estudios que defienden desde que la densidad de estos objetos decrece significativamente desde $z \sim 2$ (Valentinuzzi et al., 2010; Cassata et al., 2013; Poggianti et al., 2013; Quilis & Trujillo, 2013; Trujillo et al., 2014; van der Wel et al., 2014), hasta que prácticamente se mantiene constante (Saracco et al., 2010; Damjanov et al., 2014, 2015; Gargiulo et al., 2016).

Así mismo, este resultado será utilizado para extender el modelo fenomenológico desarrollado en el Capítulo 4 (ver también Sec. 9.4), tras descartar la hipótesis inicial de que las galaxias más compactas prodrían tener una mayor presencia de satélites o compañeros.

The merger history of massive spheroids since $z \sim 1$ is size independent

Díaz-García et al. 2013, MNRAS, 433, 60D

ABSTRACT: Using a compilation of 379 massive (stellar mass $M_\star \gtrsim 10^{11}\,M_\odot$) spheroid-like galaxies from the near-infrared Palomar/DEEP2 survey, we investigated, up to $z \sim 1$, whether the presence of companions depends on the size of the host galaxy. We explored the presence of companions for mass ratios with respect to the central massive galaxy down to 1:10 and 1:100, and within projected distances of 30, 50 and 100 kpc of these objects. We found evidence that these companions are equally distributed around both compact and extended massive spheroid-like galaxies. This suggests that, at least since $z \sim 1$, the merger activity in these objects is nearly homogeneous across the whole population and that the merger history is not affected by the size of the host galaxy. Our results could indicate that compact and extended massive spheroid-like galaxies are increasing in size at the same rate.

6.1 Introduction

For a given stellar mass, the size of low-redshift massive early-type galaxies (stellar mass $M \gtrsim 10^{11}\,M_\odot$) is found to be a factor of two larger than that of their counterparts at $z \sim 1$ (e. g., Trujillo et al., 2004; McIntosh et al., 2005; Trujillo et al., 2006b, 2007; Buitrago et al., 2008; Newman et al., 2012). In addition, the number density of such compact massive galaxies has decreased since that redshift (Cassata et al., 2011), with compact galaxies being extremely rare in the local Universe (Trujillo et al., 2009; Taylor et al., 2010) and having young ages ($1 - 2$ Gyr, Trujillo et al. 2009, 2012; Ferré-Mateu et al. 2012), meaning that they cannot be the relics of compact high-redshift galaxies. How have compact massive galaxies evolved in size to occupy the present-day distribution? Now that it has been shown that major merging cannot be the only mechanism responsible for making galaxies increase in size since that epoch (e. g. López-Sanjuan et al., 2012), two alternative ideas have been suggested: the puffing-up model (Fan et al., 2008, 2010; Damjanov et al., 2009) and the minor merging scenario (Naab et al., 2009; Hopkins et al., 2009b; Quilis & Trujillo, 2012).

In the puffing-up model, galaxies increase in size through the removal of enormous quantities of gas by means of active galactic nuclei (AGN) or supernova explosions during the early stages of the formation of spheroidal galaxies. Based on the analysis of stellar populations of local and high-redshift spheroidal galaxies, Trujillo et al. (2011) concluded that the evolution in size is independent of stellar age. This has been one of the main arguments against the puffing-up scenario. In the minor merging model, the size evolution observed in the massive spheroid-like galaxy population is caused mainly by the continuous bombardment of smaller pieces onto the main objects. Recent studies have tried to quantify the impact of the observed merger rates on the increase in size of massive galaxies (López-Sanjuan et al., 2012; Newman et al., 2012; Bluck et al., 2012). These studies focus on the evolution of the average size–mass relation. To progress these studies further, not only the average, but also the intrinsic dispersion of the size–mass relation should be examined with respect to the observed merger histories. Observations find a nearly constant, even decreasing, dispersion since $z \sim 1.5$ (Trujillo et al., 2007; Cassata et al., 2011; Newman et al., 2012), while cosmological simulations suggest that merging tends to increase the dispersion of the size–mass relation with cosmic time (e. g. Nipoti et al., 2012). A fundamental ingredient in such comparisons of models versus

observation is the variation of the merger rate with size at a given stellar mass; for example, if compact galaxies have higher merger activity, they will evolve faster across the size–mass relation. In this paper we explore whether merging occurs for all galaxies of a given stellar mass with the same probability, or whether it is more frequent for galaxies with smaller sizes, which are quite rare in the local Universe compared with compact ones at higher redshifts. Answering this question is crucial to understanding how the local stellar mass–size relation developed.

As a proxy for measuring the minor merging activity in massive spheroidal galaxies since $z \sim 1$ we study the frequency of companions around massive galaxies since that epoch. We assume that these companions will eventually be accreted onto the main galaxy. In particular, we study whether the companions are preferentially located around galaxies with a specific size in the size–mass relation or whether they are homogeneously distributed among the galaxy population independently of their stellar mass and size. We focused our analysis on redshifts up to $z \sim 1$. This is approximately the redshift at which our data, presented in Mármol-Queraltó et al. (2012, hereafter MQ12), allow us to explore with completeness the presence of companions around our sample of massive (stellar mass $M \gtrsim 10^{11}\mathrm{M}_{\odot}$) galaxies, for stellar mass ratios between the central massive galaxy (M_{central}) and its companion (M_{com}) down to $0.01 < M_{\mathrm{com}}/M_{\mathrm{central}} < 1$ (1:100).

This paper is organized as follows. In Section 6.2 we present the two samples used in this work: the sample of central massive spheroid-like galaxies, with a brief description of the Palomar/DEEP2 survey; and the sample of companions, from the Rainbow Database, around them. We explain the companion detection process in Section 6.3. We present the analysis of the data in Section 6.4, together with the contamination corrections arising from uncertainties in the photometric redshifts. Finally, in Section 6.5, we present the conclusions of our findings and a brief summary.

In this paper we adopt a standard ΛCDM cosmology, with $\Omega_{\mathrm{M}} = 0.3$, $\Omega_{\Lambda} = 0.7$, $H_0 = 100h$ km s^{-1} Mpc^{-1} and $h = 0.7$.

6.2 The data

To study whether the size of the massive spheroid-like galaxies is relevant for their merger history, we use a complete, mass-selected, large catalogue of massive galaxies. We explore which of these objects have companions that would be able to merge with the central massive galaxy. Thus, our analysis is based on two data sets: a catalogue with central massive spheroid-like galaxies and another sample containing their companion galaxies.

As the reference catalogue for the central massive spheroid-like galaxies we used the compilation of Trujillo et al. (2007, hereafter T07). The K_{s}-band imaging from the Palomar Observatory Wide-field Infrared (POWIR)/DEEP2 survey (Davis et al., 2003; Bundy et al., 2006; Conselice et al., 2007) was used to define a sample of 831 massive galaxies (stellar mass $M > 10^{11}\mathrm{M}_{\odot}$) up to $z = 2$ located over ∼710 arcmin^2 in the Extended Groth Strip (EGS). In addition, these objects were imaged with the Advanced Camera for Surveys (ACS) from the *Hubble* Space Telescope (HST) in the $F606W$ and $F814W$ bands, with the CFH12K camera from the Canada–France–Hawaii Telescope in the B, R and I bands, and with the Palomar 5-m telescope in the J and K_{s} bands. T07 present massive galaxies with spectroscopic redshifts that have been supplemented with photometric redshifts with an accuracy of $\Delta z/(1+z) \sim 0.07$. Stellar masses were estimated using a Chabrier (2003) initial mass function. T07 estimated the circularized half-light radius (r_{e}) and Sérsic indices n (Sersic, 1968) for all galaxies in the central sample. The criterion used to identify the massive spheroid-like objects is based on the Sérsic indices. The Sérsic index can be used to make a reliable morphological classification of galaxies, as it measures the shape of the surface brightness profile (Andredakis et al., 1995). In order to obtain a reliable sample of bulge-dominated galaxies and to exclude late-type galaxies with a bright nucleus, we selected the galaxies that have S érsic indices larger than 2.5 (see fig. 1 in Ravindranath et al. 2004).

To compile the sample of companion galaxies around our massive spheroid-like objects we used the

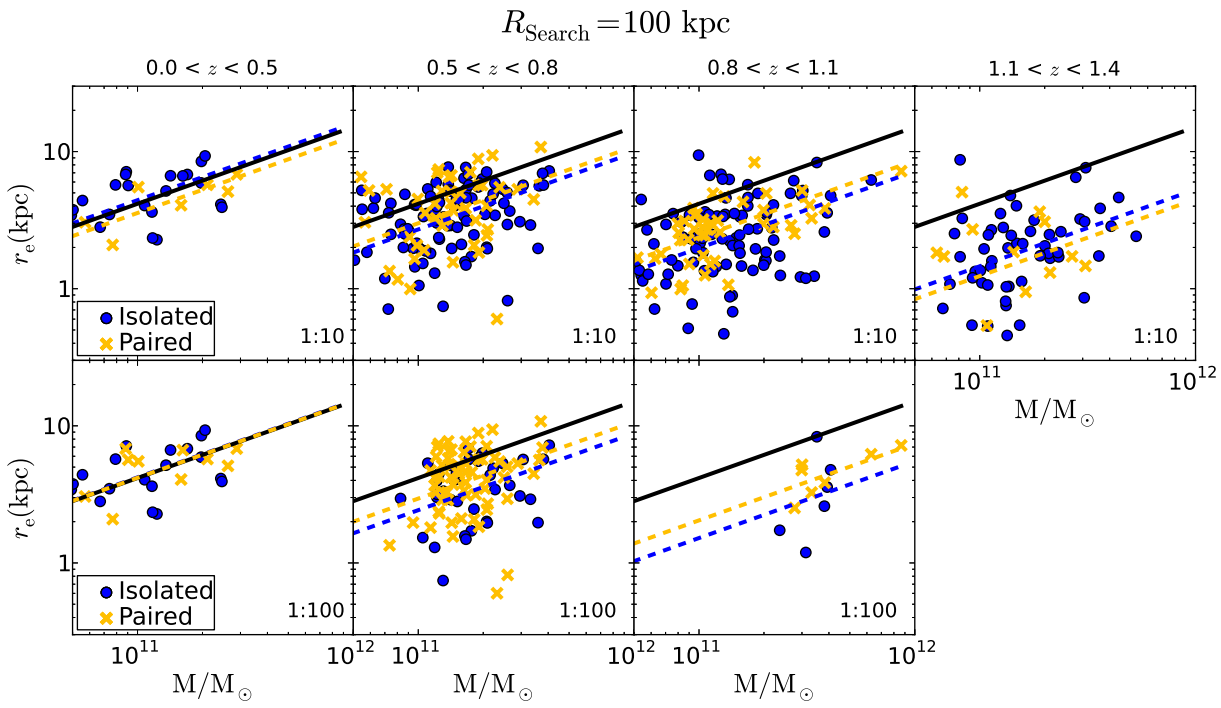

Figure 6.1: Size–mass relation of spheroid-like galaxies in various redshift bins. The different panels show the distribution of paired (yellow crosses) and isolated (blue dots) galaxies down to mass ratios of 1:10 (*upper panels*) and 1:100 (*lower panels*), in all cases within a projected distance of 100 kpc. The black line represents the local size–mass relation (Shen et al., 2003) for spheroid-like galaxies. For every redshift bin, the dashed yellow and blue lines show the best fits to the distribution of paired and isolated galaxies, respectively (see Section 6.4 for more details).

EGS IRAC-selected galaxy sample from the Rainbow Cosmological Database [1] published by Barro et al. (2011a, see also Pérez-González et al. 2008). This database provides spectral energy distributions (SEDs) ranging from the UV to the MIR, plus well-calibrated and reliable photometric redshifts and stellar masses (Barro et al., 2011b). In general, the companions sampled have photometric redshifts from the Rainbow Database. We refer to this resulting sample as the Rainbow catalogue.

In order to build a sample of central massive galaxies with the best estimates of redshifts and stellar masses we followed the same criterion as in MQ12: if a given central galaxy has a spectroscopic redshift in the Rainbow catalogue, both the redshift and the stellar mass are taken from this catalogue. Otherwise, spectroscopic redshifts and stellar masses are taken from T07. If the central galaxy has no spectroscopic redshift in either of the two above data sets, we take the Rainbow photometric redshift as long as it is in agreement with the photometric redshift of T07. More precisely, we impose that the condition that the difference between the photometric redshifts in the two catalogues has to be smaller than 0.070 at $0.0 < z < 0.5$, than 0.061 at $0.5 < z < 1.0$, and than 0.083 at $z > 1.0$. When a larger difference is found, the central galaxy is rejected for this study.

To ensure that the fraction of galaxies with companions along our explored redshift range is not biased by the stellar mass completeness limit of the Rainbow catalogue, we keep in the central sample only those galaxies that are at least 10 (100) times more massive than the stellar mass limit of the companion sample at each redshift. The stellar mass limit (75 % complete) of the Rainbow catalogueat each redshift is provided in Pérez-González et al. (2008) and ranges from $M \gtrsim 10^{8.5}$M$_\odot$ at $z \sim 0.2$ to $M \gtrsim 10^{10}$M$_\odot$ at $z \sim 1.2$ (see fig. 4 in Pérez-González et al. 2008). These stellar mass limits correspond to the stellar mass of a passively

[1] https://rainbowx.fis.ucm.es/Rainbow_Database/

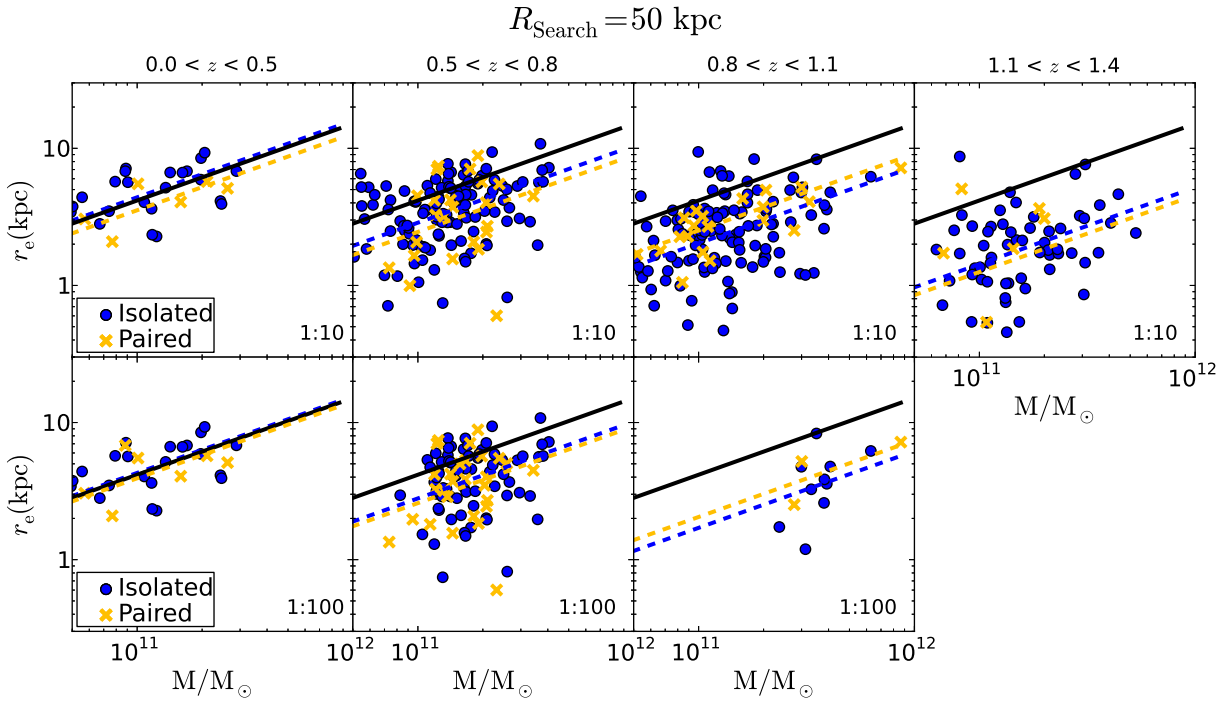

Figure 6.2: As Fig. 6.1, but using a search radius of 50 kpc for the companion detection process (see Section 6.3).

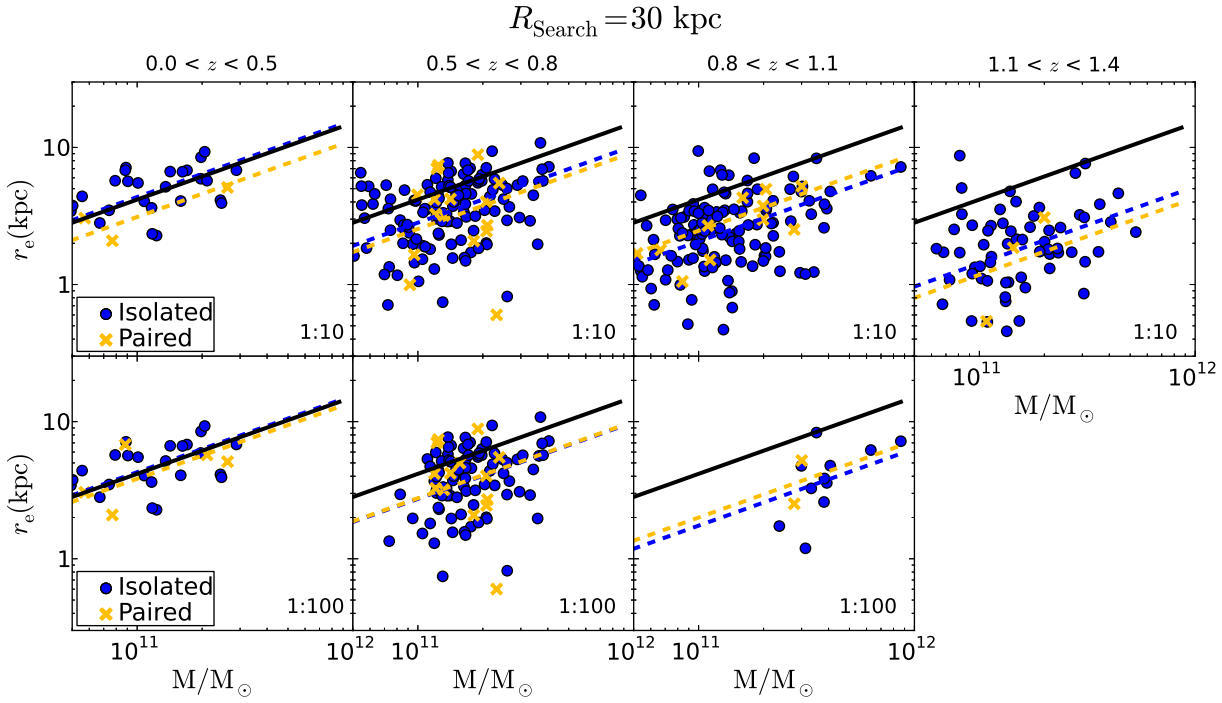

Figure 6.3: As Fig. 6.1, but using a search radius of 30 kpc for the companion detection process (see Section 6.3).

evolving galaxy formed in a single instantaneous burst of star formation that occurred at $z \sim \infty$ and having a 3.6-μm flux equal to the 75 % completeness level in the IRAC galaxy sample ([3.6]$\sim$ 24.75 $m_{\rm AB}$). In the redshift range $0 < z < 1.4$ we can probe companions with a mass fraction compared with their central objects (stellar mass $M \gtrsim 10^{11}{\rm M}_{\odot}$) down to 1 : 10. There are finally 379 massive spheroid-like galaxies that meet all the above criteria, out of which 239 have spectroscopic redshifts and 140 have photometric redshifts. In the redshift range $0 < z < 1.1$ we are able to explore the presence of companions down to a mass ratio of 1:100. The number of massive spheroid-like galaxies for which this study can be conducted is 145 (107 with spectroscopic redshifts and 38 with photometric redshifts).

6.3 Detection of companions

The process and criteria used to search for companions around massive spheroid-like galaxies is based on MQ12. A galaxy from the Rainbow catalogue is considered as a potential companion if the redshift difference between the object and the central host is less than the 1σ uncertainty, within a projected radial distance $R_{\rm search}$ around the central object. Usual values of $R_{\rm search}$ in the literature range from 30 to 150 kpc in our reference cosmology ($h = 0.7$, e. g. Patton et al., 2000; Bell et al., 2006; Mármol-Queraltó et al., 2012; Bluck et al., 2012). With these $R_{\rm search}$ values, the selected pairs will merge on a relatively short time-scale (t $\lesssim$ 2.5 Gyr, Lotz et al., 2010b). In the following we explore three search radii, namely $R_{\rm search} = 30$, 50 and 100 kpc. Larger search radii increase the background contamination, and the results become very uncertain. Finally, we consider only those companion objects within a mass range of $0.1 < M_{\rm com}/M_{\rm central} < 1$ if we explore our sample up to $z = 1.4$, and those within $0.01 < M_{\rm com}/M_{\rm central} < 1$ if the analysis is constrained to massive galaxies with $z < 1.1$. Hereafter, we refer to massive spheroid-like galaxies with companions as paired galaxies, and to massive spheroid-like galaxies without companions as isolated galaxies. These concepts are defined specifically for this work, so the definitions may differ from those of other publications.

It is clear that the main source of contamination in this sort of study comes from the uncertainties in the photometric redshifts. Owing to the background/foreground contamination, there exists a fraction of fake paired galaxies with this method of companion detection (see Section 6.4.1.1). In addition, there also exists a fraction of fake isolated galaxies, given that the redshift difference between the host galaxy and the potential candidate is set to be within a 1σ uncertainty (see Section 6.4.1.2). Note that these two effects can be constrained and corrected only by statistical methods. Because the study in this paper is performed over individual galaxies and it is not possible to state whether the companion of a particular massive central galaxy is real or a contaminant, we devote Section 6.4.1.3 to probing in detail the impact of these two effects on our results, as well as to accounting for them statistically by means of Monte Carlo simulations.

6.4 Analysis of the data

The main goal of the present work is to address whether the presence of companions, with mass ratios down to 1:10 and 1:100, depends on the size of massive spheroid-like galaxies. We split our sample in different redshift bins to analyse the cosmic time evolution of this dependence. In Figs. 6.1, 6.2, and 6.3 we show the size–mass relation of our sample of central massive spheroidal-like galaxies at different redshift bins and search radii $R_{\rm search} = 30, 50$, and 100 kpc; according to the criteria described in Section 6.3. A quick look to these plots suggests that the paired galaxies are distributed homogeneously through the size–mass relation at all redshifts, independently of whether we explore the existence of companions in the 1:10 or in the 1:100 mass ratio range. We will now quantify this in more detail.

Shen et al. (2003) parametrized the size–mass relation of spheroid-like galaxies in the local Universe from the Sloan Digital Sky Survey (SDSS, Stoughton et al., 2002) with a power-law function,

$$r_e\,({\rm kpc}) = b\left(\frac{M}{{\rm M}_{\odot}}\right)^{a}, \tag{6.1}$$

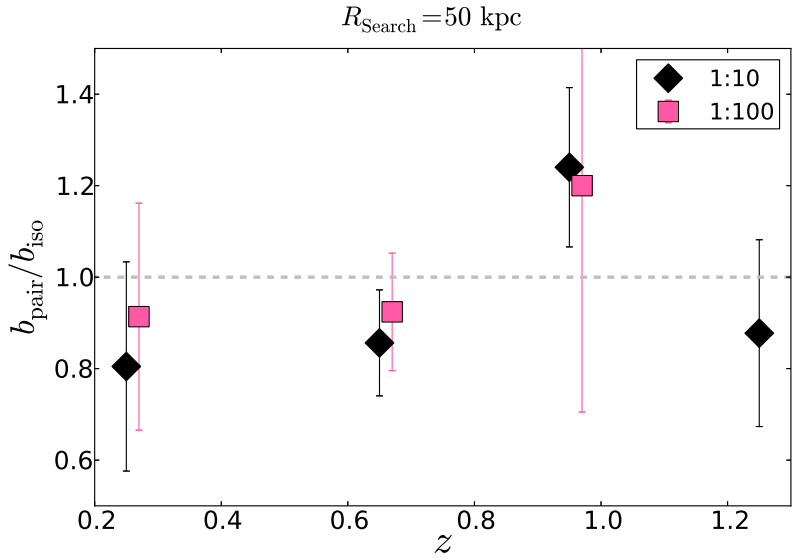

Figure 6.4: The ratio of the b-parameters of the size–mass relation (Eq. 6.1) for paired and isolated massive central galaxies in various redshift bins for two mass ratios (1:10, black diamonds; 1:100, pink squares). The figure shows the case of a search radius of 50 kpc. A ratio close to 1 implies that the average sizes of paired and isolated massive galaxies are the same.

finding $a = 0.56$ and $b = 2.88 \times 10^{-6}$ kpc. Interestingly, some recent studies (e. g. Damjanov et al., 2011; McLure et al., 2013) have found that the size–mass relation for spheroid-like galaxies with stellar masses $M \gtrsim 10^{10.5}\,\mathrm{M}_{\odot}$ does not change its slope, at least up to $z \sim 1.5$, and that this slope is compatible with that obtained by Shen et al. (2003) in the local Universe. For this reason, in what follows we will assume that a is independent of redshift. To quantify whether there exists a differences between the size distributions of paired and isolated galaxies in our sample, we fit the distributions in Figs. 6.1, 6.2, and 6.3 using Eq. (6.1). Error-weighted least-squares linear fittings were performed for the two galaxy samples in each redshift bin. We keep the power-law index a fixed to the value obtained by Shen et al. (2003) throughout the fitting process, while b is left as a free parameter. To determine the best fit, we assumed that the accuracy of the half-light radius is $\sigma_{r_{\rm e}}/r_{\rm e} \sim 0.2$ and constant for our galaxy sample (see Trujillo et al., 2007). In Figs. 6.1, 6.2, and 6.3 the yellow and blue dashed lines show the results of the fittings for the distributions of paired and isolated galaxies, respectively, and the black line is the local size–mass relation obtained by Shen et al. (2003) in the local Universe for early-type galaxies. In Table 6.1 we provide the best-fitting b-values together with their errors (confidence level of 68.3 %) for the distribution of paired ($b_{\rm pair}$) and isolated ($b_{\rm iso}$) galaxies. The ratio between the b-parameters of both populations is consistent with unity within the errors for every search radius and mass ratio, which implies that there is no significant shift between the two distributions.

To confirm the above result we performed Kolmogorov–Smirnov (KS) and t-Student (TS) tests for the distributions of paired and isolated galaxies in the size–mass plane. To do that, we performed the fitting of Eq. (6.1) to the whole central galaxy sample (see the global parameters in Table 6.1) for every redshift and mass range, and studied the distances to this relation for the paired and isolated galaxy populations. In Table 6.2 we show the Kolmogorov–Smirnov and t-Student estimators obtained for our sample of central massive galaxies, denoted $E_{\rm KS}$ and $E_{\rm TS}$ respectively, as well as their limiting values for confidence levels of 95 % of the two distributions, taking into account the degrees of freedom of each subsample. In all cases the estimators are smaller than the limiting values, and consequently we infer that the two distributions are statistically indistinguishable at the 95 % confidence level. This implies that the size–mass distributions of paired and isolated galaxies are not statistically different.

Table 6.1: The best-fitting parameter b (see Eq. 6.1) of the size–mass distribution for paired and isolated galaxies as a function of redshift, search radius and mass ratio.

	Parameter b [10^{-6}kpc]						
Mass ratio 1 : 10	$R_{\rm search}$ = 30 kpc		$R_{\rm search}$ = 50 kpc		$R_{\rm search}$ = 100 kpc		
Redshift	$b_{\rm pair}$	$b_{\rm iso}$	$b_{\rm pair}$	$b_{\rm iso}$	$b_{\rm pair}$	$b_{\rm iso}$	Global
$0.0 < z < 0.5$	2.15 ± 0.58	3.01 ± 0.28	2.45 ± 0.46	3.04 ± 0.29	2.47 ± 0.43	3.06 ± 0.30	2.90 ± 0.25
$0.5 < z < 0.8$	1.76 ± 0.20	1.96 ± 0.08	1.70 ± 0.16	1.98 ± 0.08	2.08 ± 0.14	1.87 ± 0.09	1.93 ± 0.07
$0.8 < z < 1.1$	1.71 ± 0.23	1.43 ± 0.06	1.74 ± 0.17	1.40 ± 0.06	1.64 ± 0.11	1.37 ± 0.06	1.45 ± 0.05
$1.1 < z < 1.4$	0.82 ± 0.22	0.99 ± 0.06	0.87 ± 0.15	0.99 ± 0.06	0.86 ± 0.11	1.01 ± 0.06	0.98 ± 0.05
Mass ratio 1 : 100	$R_{\rm search}$ = 30 kpc		$R_{\rm search}$ = 50 kpc		$R_{\rm search}$ = 100 kpc		
Redshift	$b_{\rm pair}$	$b_{\rm iso}$	$b_{\rm pair}$	$b_{\rm iso}$	$b_{\rm pair}$	$b_{\rm iso}$	Global
$0.0 < z < 0.5$	2.65 ± 0.55	2.96 ± 0.28	2.71 ± 0.47	2.97 ± 0.29	2.89 ± 0.42	2.91 ± 0.31	2.90 ± 0.25
$0.5 < z < 0.8$	1.91 ± 0.24	1.89 ± 0.09	1.79 ± 0.15	1.94 ± 0.10	2.04 ± 0.12	1.68 ± 0.12	1.90 ± 0.09
$0.8 < z < 1.1$	1.39 ± 0.46	1.21 ± 0.17	1.42 ± 0.38	1.18 ± 0.17	1.41 ± 0.25	1.05 ± 0.20	1.23 ± 0.16

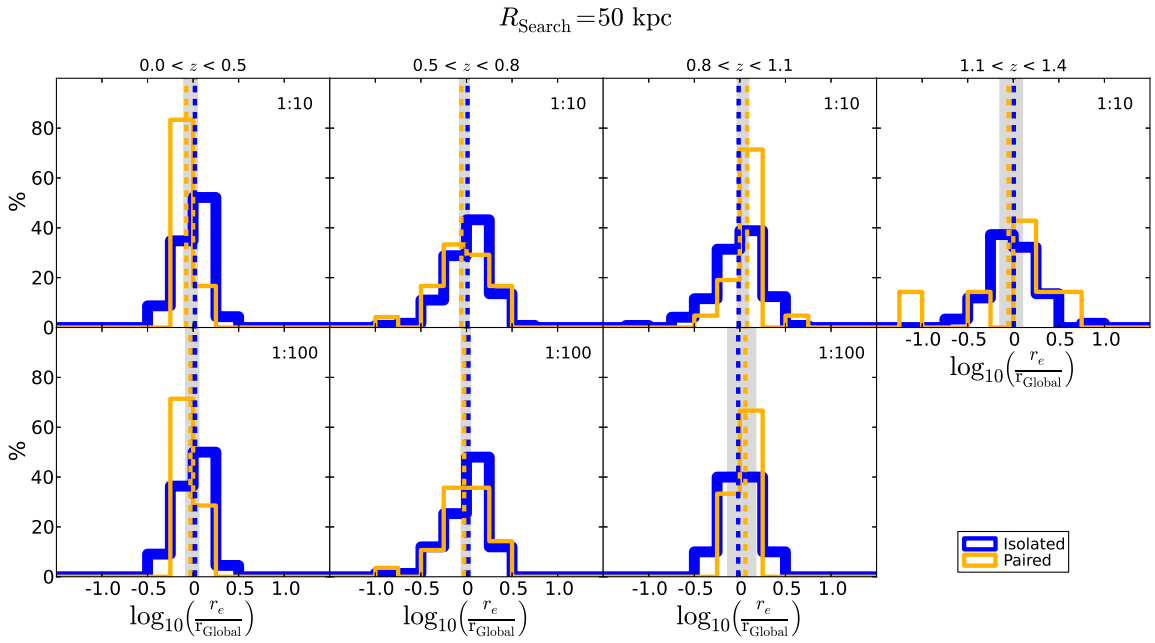

Figure 6.5: Histograms of the distances of paired (yellow) and isolated (blue) galaxies to the size–mass relation (Eq. 6.1) for the whole central galaxy sample, using a search radius of 50 kpc and mass ratios of 1:10 (*upper panels*) and 1:100 (*lower panels*). Dashed yellow and blue lines show the mean values of the paired and isolated distributions, respectively. The shadow area is the difference between the means of two distributions for a confidence level of 95 % per cent with the same degrees of freedom for a t-Student (TS) test. In all cases, the means of the two populations are statistically the same.

The most representative search radius for this study is 50 kpc, as both the background/foreground contamination and the detection contamination are fairly low ($\sim$ 10 % cent in both cases), and the number of paired galaxies ensures good statistics. For a search radius of 50 kpc, Fig. 6.4 illustrates that the ratio between the *b*-parameters of both populations (paired and isolated galaxies) is consistent with unity within the errors, implying that there is no significant shift between the two distributions. Figure 6.5 gives the histograms of the distances of paired (yellow) and isolated (blue) galaxies to the fitting of the size–mass relation (Eq. 6.1) of the whole central galaxy sample for a search radius of 50 kpc. Dashed yellow and blue lines show the mean values of the paired and isolated distributions, respectively. For a TS test, the shadow area is the difference between the mean values of the two distributions for a confidence level of 95 % with the same degrees of freedom. In all cases, the means of the two populations are statistically the same for a confidence level of 95 % in the TS test. Fig. 6.6 shows the cumulative distribution function (CDF) of the histograms in Fig. 6.5. The vertical red line is the largest difference between the CDFs of the paired and isolated galaxies. For a KS test, the shadow area is the difference between the CDFs of the two distributions for a confidence level of 95 % with the same degrees of freedom. In every panel, the red line is smaller than the shadow area, so the two distributions (paired and isolated) are statistically the same in the KS test. We obtained similar results for the search radii $R_{\rm search}$ = 30 and 100 kpc.

6.4.1 Systematic effect analysis

These results were obtained by comparing the distributions of paired and isolated galaxies, but neither the background/foreground contamination nor the fake isolated galaxy contamination were taken into account, as we cannot correct for these effects individually. The two effects are studied in Sections 6.4.1.1 and 6.4.1.2, respectively. Finally, Section 6.4.1.3 is devoted to checking the impact of these contamination sources on our results.

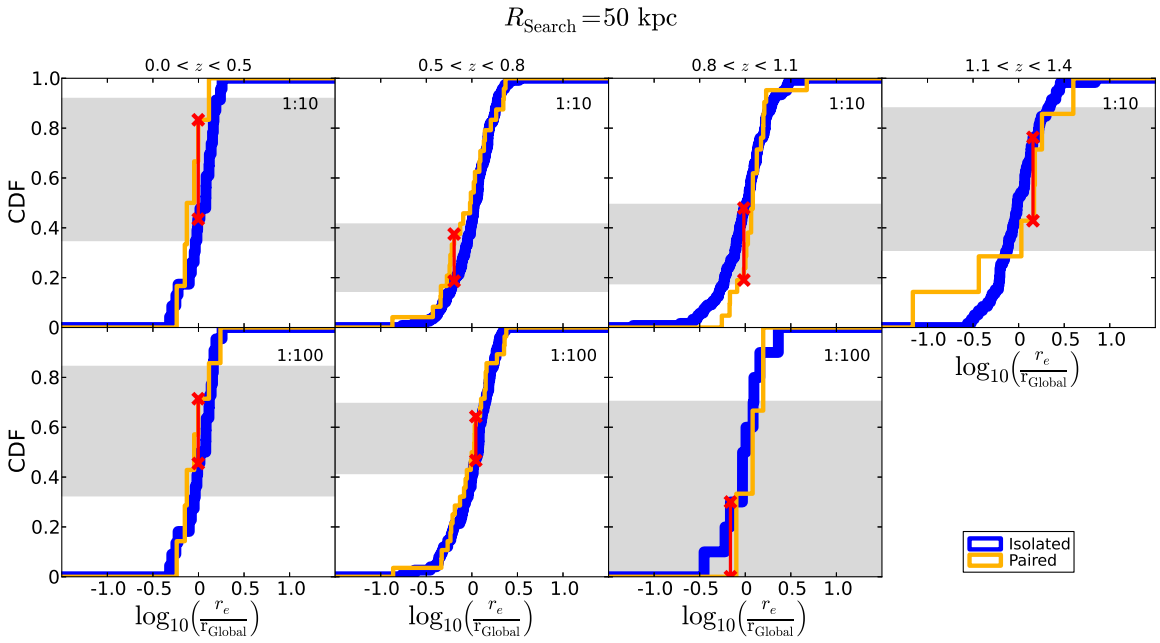

Figure 6.6: Cumulative distribution functions (CDFs) of the distances of paired (yellow) and isolated (blue) galaxies to the size–mass relation (Eq. 6.1) for the whole central galaxy sample, using a search radius of 50 kpc and mass ratios of 1:10 (*upper panels*) and 1:100 (*lower panels*). The red lines illustrate the largest distance between the CDFs of paired and isolated galaxies. The shadow area is the difference between the CDFs of two distributions for a confidence level of 95 % with the same degrees of freedom for a Kolmogorov–Smirnov (KS) test. In all cases, the shifts between the CDFs are statistically compatible.

Table 6.2: Test estimators obtained for the Kolmogorov–Smirnov (KS) and t-Student (TS) tests, denoted by $E_{\rm KS}$ and $E_{\rm TS}$ respectively. We present the values of the estimators for a confidence level of 95 %, denoted by $E_{\rm KS}(95\%)$ and $E_{\rm TS}(95\%)$, taking into account the degrees of freedom of each subsample.

	Test estimators							
	Mass ratio 1 : 10				**Mass ratio 1 : 100**			
	Kolmogorov-Smirnov		t-Student		Kolmogorov-Smirnov		t-Student	
Redshift	$E_{\rm KS}$	$E_{\rm KS}(95\%)$	$E_{\rm TS}$	$E_{\rm TS}(95\%)$	$E_{\rm KS}$	$E_{\rm KS}(95\%)$	$E_{\rm TS}$	$E_{\rm TS}(95\%)$
$R_{\rm search}$ = 30 kpc								
$0.0 < z < 0.5$	0.538	0.720	1.502	2.052	0.342	0.602	0.588	2.052
$0.5 < z < 0.8$	0.176	0.344	0.715	1.977	0.203	0.372	0.069	1.984
$0.8 < z < 1.1$	0.204	0.386	0.957	1.977	0.409	0.864	0.359	2.201
$1.1 < z < 1.4$	0.270	0.712	0.444	1.998				
$R_{\rm search}$ = 50 kpc								
$0.0 < z < 0.5$	0.408	0.569	1.284	2.052	0.298	0.538	0.550	2.052
$0.5 < z < 0.8$	0.189	0.293	1.261	1.977	0.176	0.291	0.649	1.984
$0.8 < z < 1.1$	0.289	0.308	1.467	1.977	0.300	0.749	0.563	2.201
$1.1 < z < 1.4$	0.334	0.505	0.458	1.998				
$R_{\rm search}$ = 100 kpc								
$0.0 < z < 0.5$	0.448	0.538	1.346	2.052	0.184	0.486	0.045	2.052
$0.5 < z < 0.8$	0.172	0.235	1.036	1.977	0.228	0.262	1.773	1.984
$0.8 < z < 1.1$	0.184	0.235	1.632	1.977	0.524	0.675	1.133	2.201
$1.1 < z < 1.4$	0.235	0.393	0.742	1.998				

6.4.1.1 Background/foreground contamination correction

For the method of companion detection described in Section 6.3, MQ12 showed that there exists an excess in the number of paired galaxies owing to the photometric redshift uncertainties (background/foreground contamination). Because we could be considering some galaxies to be companions when they are not really linked gravitationally to the host galaxy, leading to fake paired galaxies, such redshift uncertainties are the main source of contamination. Consequently, it is necessary to estimate statistically the background/foreground contamination and to check to what extent our results may be affected.

We followed the statistical process in MQ12 to estimate the background/foreground contamination. This method consists of placing mock massive galaxies randomly in the volume of the Rainbow catalogue. The number of mock galaxies in every redshift bin is the same as in our observed sample, and the mock galaxy parameters are the same as the massive spheroid-like galaxy parameters, for example for redshift and stellar mass. Once the mock galaxies are situated in the Rainbow catalogue volume, we apply the companion detection process explained above (including the 1σ uncertainty in the estimation of the redshifts) and compute the fraction of these mock galaxies having companions, $F_{\rm pair,mock}$, around them for search radii $R_{\rm search} = 30, 50$ and 100 kpc, for the mass ratios 1:10 and 1:100. To obtain a robust count of the paired mock galaxies, we repeat this process 100 000 times. We reasonably assume that the average fraction of paired mock galaxies, $\overline{F}_{\rm pair,mock}$, corresponds to the fraction of galaxies affected by the background/foreground contamination.

The observed fraction of paired galaxies, $F_{\rm pair,obs}$, is the sum of the real fraction of paired galaxies, $F_{\rm pair}$, plus the fraction of isolated galaxies affected by the background/foreground contamination, $(1 - F_{\rm pair}) \times \overline{F}_{\rm pair,mock}$. Thus, the true fraction of paired galaxies after statistical correction is

$$F_{\rm pair} = \frac{F_{\rm pair,obs} - \overline{F}_{\rm pair,mock}}{1 - \overline{F}_{\rm pair,mock}}. \tag{6.2}$$

The fraction of fake paired galaxies as a consequence of our companion detection process is

$$C_{\rm pair} = \frac{F_{\rm pair,obs} - F_{\rm pair}}{F_{\rm pair,obs}}. \tag{6.3}$$

The simulation results, shown in Table 6.3, indicate that up to ∼4, 9 and 24 % (∼6, 14 and 26 %) of the observed paired galaxies in the mass ratio 1:10 (1:100) actually have no companions within a search radius of 30, 50 and 100 kpc.

6.4.1.2 Fake isolated galaxies due to the 1σ uncertainty condition

In the companion detection process, the candidates were constrained to have a difference in redshift from the central massive galaxy that is lower than the 1σ uncertainty. Assuming that both the central galaxy and its companion have photometric redshifts, we expect to miss $F_\sigma \sim 30$ % of the companions in our search. MQ12 estimated that allowing for a difference of up to 2σ, instead of 1σ, in the search of companions, the background/foreground contamination effects increase by ∼50 %, whereas the fraction of paired galaxies changes by less than 30 %, as expected. Thus, the 1σ condition is the optimal one for merger fraction studies, as shown by MQ12.

Because in the present paper we study individual systems, we have taken into account the fraction of fake isolated galaxies due to the 1σ condition. We expect that the total fraction of massive spheroid-like galaxies with a companion, $F_{\rm pair,T}$, is

$$F_{\rm pair,T} = \frac{F_{\rm pair}}{1 - F_\sigma}. \tag{6.4}$$

If $N_{\rm central}$ is the number of massive galaxies, $(F_{\rm pair,T} - F_{\rm pair}) \times N_{\rm central}$ is the number of fake isolated galaxies attributable to the 1σ uncertainty condition. The fraction $C_{\rm iso}$ of observed isolated galaxies that

truly have a companion is

$$C_{\rm iso} = \frac{F_{\rm pair,T} - F_{\rm pair}}{1 - F_{\rm pair,obs}}. \quad (6.5)$$

Because $F_\sigma \sim 30$ %, we estimate that $C_{\rm iso}$ (see Table 6.3) is lower than 4, 7 and 14 % (7, 14 and 46 %) for search radii of 30, 50 and 100 kpc for the mass ratio 1:10 (1:100).

6.4.1.3 Reliability of results

Owing to the photometric redshift uncertainties, we must check whether the contamination in the companion detection can affect our results. Because we cannot correct for the contamination of central galaxies individually, we adopt a statistical Monte Carlo approach, as a sanity check, to ensure that the background/-foreground contamination and the 1σ assumption are not compromising our results. First, we randomly move central paired galaxies from the observed sample to the isolated sample, to reach the expected number of fake paired galaxies after the contamination correction according to Table 6.3. Second, we randomly move observed isolated galaxies to the set of paired galaxies, independently of their sizes or masses, until the expected numbers of fake isolated galaxies presented in Table 6.3 are recovered. Because the errors in the detection of companions are fully linked to the errors in the determination of the redshifts, we can reasonably assume that the fake paired and fake isolated galaxies will be randomly located around the size–mass relation, independently of the mass or size. We then apply KS and TS tests over the new samples of paired and isolated galaxies. We repeat this process one million times and determine the fraction of cases for which the two distributions are undistinguishable, according to the above statistical tests.

According to these tests, we obtain that for the vast majority of iterations ($\gtrsim$ 96 %) the size–mass distributions of paired and isolated massive central galaxies cannot be statistically distinguished. We therefore conclude that the potential contaminants described in this section do not compromise the findings of this work.

6.5 Summary and conclusions

Using a compilation of 379 massive (stellar mass $M \gtrsim 10^{11}$ $M_\odot$) spheroid-like galaxies from the near-infrared (NIR) Palomar/DEEP2 survey, we have demonstrated that, at least since $z \sim 1$, there are no significant differences between the distributions of massive spheroid-like galaxies with (paired) and without (isolated) companions over the size–mass plane. We found that the probability of finding companions around the host galaxy is independent of its size at a given mass, as the companions are not located preferentially around the more compact or extensive massive spheroid-like galaxies. Our finding is independent of the search radius, the redshift and the mass ratio between the spheroid-like massive central galaxy and its companion.

We explored the size–mass relation for the population of paired and isolated massive spheroid-like galaxies at various redshifts, keeping its slope constant and equal to that obtained by Shen et al. (2003) in the local Universe. We analysed the shift between the offsets of the size–mass relation of the paired and isolated populations, finding that they are compatible within errors in every case. We also performed two statistical tests, Kolmogorov-Smirnov and t-Student, over both populations to confirm that there are no significant differences between them. Given the methodology for identifying companions, the uncertainty in the redshift produces a contamination in the fraction of paired galaxies. This uncertainty is independent of the host galaxy position over the size–mass plane, and thus we can correct for this effect statistically but not individually. We checked that this contaminant factor does not affect our findings through a Monte Carlo approach.

Our results suggest that, at least since $z \sim 1$, the merger activity in massive spheroid-like galaxies is rather homogeneous across the whole population, and their merger history is not affected by the size of the host galaxy at a given stellar mass. This suggests that it is very likely that compact and extended spheroid-like massive galaxies are increasing in size at the same rate. Future studies confronting the observed merger

Table 6.3: Bias in the determination of paired and isolated galaxies attributable to the photometric redshift uncertainties. For each redshift range we present the number of massive galaxies $N_{\rm central}$, the observed fraction of paired massive galaxies $F_{\rm pair,obs}$, and the fraction of paired galaxies after the contamination correction $F_{\rm pair}$, with their errors. We show the overestimation in the number of paired galaxies attributable to the redshift uncertainties with this method of companion detection $C_{\rm pair}$. We also present the fraction of fake isolated galaxies, $C_{\rm iso}$, attributable to the assumption of a 1σ uncertainty criterion.

	Mass ratio 1 : 10					**Mass ratio 1 : 100**				
Redshift range	$N_{\rm central}$	$F_{\rm pair,obs}$	$F_{\rm pair}$	$C_{\rm pair}$	$C_{\rm iso}$	$N_{\rm central}$	$F_{\rm pair,obs}$	$F_{\rm pair}$	$C_{\rm pair}$	$C_{\rm iso}$
$R_{\rm search}$ = 30 kpc										
$0.0 < z < 0.5$	29	0.100	0.097 ± 0.010	0.03	0.05	29	0.200	0.192 ± 0.019	0.04	0.10
$0.5 < z < 0.8$	142	0.113	0.110 ± 0.005	0.03	0.05	103	0.136	0.127 ± 0.010	0.07	0.06
$0.8 < z < 1.1$	142	0.085	0.082 ± 0.004	0.04	0.04	13	0.154	0.147 ± 0.026	0.05	0.07
$1.1 < z < 1.4$	66	0.045	0.042 ± 0.006	0.07	0.02					
$R_{\rm search}$ = 50 kpc										
$0.2 < z < 0.5$	29	0.20	0.19 ± 0.02	0.06	0.10	29	0.27	0.23 ± 0.04	0.13	0.14
$0.5 < z < 0.8$	142	0.17	0.16 ± 0.01	0.09	0.08	103	0.27	0.23 ± 0.02	0.14	0.14
$0.8 < z < 1.1$	142	0.15	0.14 ± 0.01	0.08	0.07	13	0.23	0.20 ± 0.06	0.14	0.11
$1.1 < z < 1.4$	66	0.11	0.09 ± 0.01	0.12	0.04					
$R_{\rm search}$ = 100 kpc										
$0.0 < z < 0.5$	29	0.23	0.18 ± 0.05	0.24	0.10	29	0.37	0.20 ± 0.08	0.45	0.14
$0.5 < z < 0.8$	142	0.32	0.25 ± 0.03	0.23	0.15	103	0.62	0.50 ± 0.04	0.20	0.56
$0.8 < z < 1.1$	142	0.32	0.26 ± 0.02	0.19	0.16	13	0.54	0.41 ± 0.12	0.24	0.38
$1.1 < z < 1.4$	66	0.20	0.12 ± 0.03	0.38	0.17					

history of massive galaxies with the evolution of the size–mass relation, regarding both its median and intrinsic dispersion, will benefit from the observational constraints presented in this work.

Acknowledgements

The authors acknowledge the referee's comments, which led to improvements in this work. They also thank Carlos Hernández-Monteagudo for his very useful advice. LADG acknowledges support from the "Caja Rural de Teruel" to develop this research. AJC is a Ramón y Cajal Fellow of the Spanish Ministry of Economy and Competitiveness. This work was supported by the "Programa Nacional de Astronomía y Astrofísica" of the Spanish Ministry of Economy and Competitiveness under grants AYA2012-30789, AYA2010-21322-C03-02, AYA2009-10368 and AYA2009-07723-E. This work made use of the Rainbow Cosmological Surveys Database, which is operated by the Universidad Complutense de Madrid (UCM).

7 Discussion

Venceréis, porque tenéis sobrada fuerza bruta. Pero no convenceréis, porque para convencer hay que persuadir.

Miguel de Unamuno

This thesis aims at improving our understanding of the evolution of quiescent galaxies since $z \sim 1$, with the ultimate goal of providing a general picture for the formation and evolution of these objects along the history of the Universe. Making use of data from the ALHAMBRA survey and the SED-fitting code MUFFIT, developed as part of this work, this thesis is novel at facing for the first time an extensive, observational study that comprises the time evolution of the number density of quiescent galaxies, as well as their masses, stellar populations (ages, metallicities and extinctions) and sizes, to ultimately build up a phenomenological evolutionary model based on the merger, "frosting" and "progenitor bias" scenarios that tries to reconcile the observed trends in the above parameters. This chapter is devoted to present a global interpretation of the evidences found so far in this thesis within the context of galaxy evolution.

Before starting, it is worth noting that the stellar population results presented in this work are unavoidably affected by systematics in the analysis techniques and the model ingredients, as it is the case of any work in this topic, irrespective of whether it is spectroscopic or photometric. This is in fact the reason why, in this thesis, different input SSP models for feeding MUFFIT and several assumptions related with the SFHs involved in the SED-fitting process (see Sects. 3.8 and 3.9) have been considered. At this point, the systematics introduced by the above constrains translate into stellar populations differences that are larger than the random uncertainties in the determination of the stellar population parameters of the quiescent galaxy sample. This, in turn, highlights the statistical power of using large galaxy samples in combination with the MLE method for deconvolving uncertainty effects and determining the stellar population properties of galaxies via SED-fitting. Despite of the above systematics, there is a reasonable qualitative agreement in several results, e. g. the non passive evolution of the quiescent galaxy sample and the slight decrease of the median metallicity of these galaxies since $z \sim 1$.

In addition, the phenomenological model of evolution detailed in Chapter 4 can also be understood as an independent criterion to assess on the reliability of the retrieved stellar populations. Despite the phenomenological model itself may be a first order approach to reality, hence introducing some level of systematics in the final predictions, it is clear that the evolution with redshift of parameters such as the age, metallicity, stellar mass and the number density of quiescent galaxies should in principle be self-consistent and reconciled at first order under the merging, "frosting" and progenitor bias scenarios, provided that some of them are in turn constrained by previous work. In this sense, a major success of this work is the ability to constrain, for the first time, the role of the above mechanisms altogether into a common evolutive pathway for quiescent galaxies, in the light of their age and metallicity PDFs, stellar masses and number densities since $z \sim 1$. In particular, the use of the MUFFIT SED-fitting methodology with the EMILES SSP models

on the ALHAMBRA data show quite satisfactory agreements. Overall, and irrespective of the SSP models employed, there are striking hints to favour that mergers have a remarkable impact on the evolution of the quiescent galaxy population since $z \sim 1$, and that some level of "frosting" is necessary for reproducing the observations.

7.1 A global view on the evolution of quiescent galaxies since $z \sim 1$

The PDFs of mass-weighted ages, metallicities and extinctions of quiescent galaxies since $z \sim 1$ constrain in an unprecedented way the evolution of these objects during the last 8 Gyr. Thanks to the statistical deconvolution of uncertainty effects (MLE method, details in Appendix D) and to the large and complete in mass set of quiescent galaxies involved in this thesis (8 547 objects), it has been possible to explore the evolution of quiescent galaxies as a whole. In particular, the intrinsic dispersions of the PDFs constitute new observables for constraining how these galaxies have evolved during the last 8 Gyr. In addition, the stellar population results are complemented with structural parameters of quiescent galaxies, like their effective radii, to shed light on the mechanisms involved in the increase of the galaxy sizes with time, and hence on the formation and evolutive pathways of these objects.

This section is devoted to discuss the main results of this thesis within the framework of galaxy formation and evolution.

7.1.1 New insights for the green valley

Dust corrections play an important role in understanding how quiescent galaxies are distributed inside the UVJ diagram as a function of their parameters: stellar mass, age, metallicity, and extinction. One of the most important results regarding the study of this diagram is that the green valley is largely populated by dusty star-forming galaxies ($\sim$ 65 %), and that when the effects of reddening are corrected for in an intrinsic UVJ diagram, the population of galaxies in the "real" green valley is much lower than observed. This implies that the transition of galaxies from the blue cloud to the red sequence, and hence the related mechanisms for quenching, seems to be much more efficient and faster than previously considered.

In spite of it is out of the scope of this thesis shedding light on the responsible mechanism for quenching, any successful mechanisms proposed for shutting down the star formation should account for a less populated green valley and a shorter transition timescale. For instance, the common presence of AGNs in galaxies with intermediate host-galaxy colours (in the green valley) at $z \lesssim 1$ (Nandra et al., 2007; Bundy et al., 2008; Georgakakis et al., 2008; Silverman et al., 2008; Hickox et al., 2009; Schawinski et al., 2009) was interpreted as an evidence for AGNs heating up the gas in the host-galaxy (Silk & Rees, 1998; Di Matteo et al., 2008) and shutting down the star formation rapidly (Bower et al., 2006; Croton et al., 2006; Faber et al., 2007; Schawinski et al., 2007). In the light of the results in this thesis, AGN feedback should be more efficient than previously expected as quenching mechanism.

In fact, previous studies (Bell et al., 2005; Cowie & Barger, 2008; Brammer et al., 2009; Cardamone et al., 2010) also supported that the population of galaxies in the green valley has bluer intrinsic colours and is largely dominated by galaxies reddened by dust. Based on the results by Cardamone et al. (2010), $\sim$ 75 % of galaxies in the green valley have intrinsic blue colours in good agreement with this thesis ($\sim$ 65 %). In the same work, after a dust correction of the $U - V$ colour, most of the galaxies hosting an AGN belong to the red sequence, $(U - V)_{\rm int} \gtrsim 1.5$, or the blue cloud, $(U - V)_{\rm int} \lesssim 0.8$, with a poor presence of AGNs at intermediate colours, favouring again the idea of either a faster or less frequent quenching mechanism due to AGNs.

7.1.2 On the ages of quiescent galaxies

Quiescent galaxies exhibit the older ages at any cosmic time. On average, the more massive the quiescent galaxy, the older their stellar populations. Therefore, this suggests that the most massive quiescent galaxies

were the first galaxies in the Universe that built-up their stellar content. Depending on the SSP models used in this thesis, the formation epochs of the most massive and earliest quiescent galaxies ($\log_{10} M_\star \geq 11.2$; $z \sim 1$) vary in the range $z_f \sim 4.5$–6, i.e., when the Universe was 1–1.5 Gyr old. Quiescent galaxies with lower stellar masses ($\log_{10} M_\star < 10.5$) exhibit more recent formation epochs, down to $z_f \lesssim 1.5$. This result is in agreement with the "downsizing" scenario.

An interesting aspect, core of the goal of this thesis, is to understand how these galaxies evolved since $z \sim 1$. For a strictly passive evolution, the galaxy age evolution should follow the natural ageing of their stellar populations, hence the redshift at which the stellar mass was assembled, or the formation epoch, should not present any variation with time (z_f constant). This thesis, however, finds evidences pointing out that the age evolution of quiescent galaxies departs from passiveness, showing on average a milder ageing. This conclusion is obtained even assuming different constraints on the SFHs during the MUFFIT analysis (Sect. 3.9).

To reconcile the observation, three different scenarios or mechanisms are proposed:

i) Mergers. Mergers are an efficient mechanism to include new (ex-situ) stars from less massive systems. Less massive systems are expected to contain younger stellar populations due to the age-mass relation, and in qualitative agreement with the "downsizing" scenario, hence being potential contributors to slowing down the ageing of quiescent galaxies. For this case, the number of mergers involving the quiescent galaxy population is key to discern whether this mechanism can match the observed non-passive evolution.

ii) Remnants of star formation, or "frosting". The inclusion of new (in-situ) stars may also explain why these galaxies do not evolve passively. Remnants of gas inside the galaxy or the fall of new gas from the cosmic web can originate new, younger stellar populations producing a delay in the ageing of each individual galaxy. Since the non-passive evolution of quiescent galaxies is observed at all the stellar mass ranges under study in this work, "frosting" is needed to affect the whole quiescent population to reveal as a reliable mechanism.

iii) The "progenitor" bias. Motivated by the generalized increase in number of quiescent galaxies since $z \sim 1$ (more prominent at decreasing stellar masses), the arrival of recently quenched galaxies with younger stellar populations is another alternative mechanism.

Moreover, the three above scenarios contribute to modify the width of the mass-weighted age PDF of quiescent galaxies, which in this thesis is observed to increase with cosmic time and represents an additional hint for the variation of their stellar content.

7.1.3 On the metallicities of quiescent galaxies

In this work, quiescent galaxies are generally found to be metal rich, with metallicities around solar and super-solar values, except for the local and less massive quiescent galaxies that exhibit sub-solar metallicities. Both the results derived from BC03 and EMILES SSP models support the galaxy mass-metallicity relation (at increasing stellar mass, quiescent galaxies present larger metallicities), that seems to be present since early times (at least since $z \sim 1$), with hints of being steeper at lower redshifts. In addition, this work reveals evidences for a slight decrease of the median of the metallicity PDF (0.1–0.2 dex) of quiescent galaxies since $z \sim 0.6$–1.1 (BC03 and EMILES respectively), which is obtained under most SFHs assumed in this work and constitutes one of the most striking results of this thesis. Both a steeper MZR at larger cosmic times and the continuous decrease of the median metallicity with time support that quiescent galaxies are continuously modifying their stellar contents, and asses on the potential evolutive pathways that these galaxies should undergo to reconcile the observed trends. In particular, regarding the three scenarios proposed above:

i) Mergers with less massive systems can contribute to the observed variation of the global metallicity, as less massive systems host stellar populations less metal rich than the principal galaxy in the pair

(more massive) owing to the stellar mass-metallicity relation. Again, the number of mergers will determine whether this mechanism can alter the median of the mass-weighted metallicity PDF of quiescent galaxies since $z \sim 1$.

ii) A priori, "frosting" would not explain a decrease of the global metallicity in a monolithic collapse, as the continuous enrichment of metals by evolution will shed subsequent more rich in metals populations of stars, or at least with similar metallicities. However, in the chemo-evolutionary population synthesis model by Vazdekis et al. (1996, no interchange of any matter with the neighbourhood, or closed-box model), when star formation processes are very efficient (specially at high IMF slopes), at certain time the global metallicity of the galaxy starts to decrease. Owing to the efficient star formation, the available gas decreases very rapidly and the enrichment of metals is also rapid reaching a maximum. Then, all the available gas comes mostly from the oldest and numerous low-metallicity stars, which is less processed, producing new stellar populations that can reduce the metallicity 0.2 dex at $\sim$ 10 Gyr after the initial star formation for a Salpeter-like IMF (for bottom heavy IMFs, the effect is even more significant).

iii) The increasing number of quiescent galaxies since $z \sim 1$ is more remarkable at lower stellar masses, and therefore, the "progenitor" bias can play an important role in the decrease of the median metallicity specially at lower stellar masses, where the median metallicity shows more prominent changes. The determination of the stellar populations of the galaxies quenching their star formation (new quiescent galaxies) is a challenge, although as we determine in Chapter 4, it can be constrained.

Moreover, the widths of the mass-weighted metallicity PDFs will suffer modifications as a result of mergers, "frosting", and the "progenitor" bias. For quiescent galaxies more massive than $\log_{10} M_\star = 10.8$ and EMILES SSP models, the width of the mass-weighted metallicity PDF increases with cosmic time, whereas for the rest of cases the width decreases (EMILES at $\log_{10} M_\star < 10.8$, and BC03 SSP models for all the stellar mass ranges).

7.1.4 Extinctions of quiescent galaxies

The extinction values of quiescent galaxies derived in this thesis are typically low $A_V < 0.6$, with median values in the range $A_V = 0.15$–0.3. However, they do not present large variations with cosmic time. For BC03 SSP models, there is a slight dependency with stellar mass and redshift, in the sense that the most massive quiescent galaxies also present the largest extinctions, and these ones increase at lower redshifts. However, such extinction dependencies are almost negligible using EMILES models, which drive to roughly constant values ($A_V \sim 0.2$).

Mergers between quiescent and star-forming galaxies (the latter with larger extinctions, specially in the most recent star forming regions) will increase the overall extinction of the resulting galaxy. The orbits in the merger, as well as the distribution of dust regions in the progenitor galaxies would drive how the global extinction of the final galaxy is affected.

Since star-forming galaxies are typically more reddened by dust than quiescent ones, the "progenitor" bias may contribute to change the median of the extinction PDF. Although the mechanism responsible for shutting down the star formation is unknown, the typical extinction values of galaxies quenching their star formation are also unknown, as this is a very tricky process involving many parameters such as stellar feedbacks. In fact, the evolution of extinction inside star forming galaxies is unclear, and the quenching mechanism can also be tightly related with extinction (e. g. sudden removal of gas, "strangulation", heating of galaxy's gas by AGN, Silk & Rees, 1998; Balogh et al., 2000; Dekel & Birnboim, 2006; Hopkins et al., 2006; Nandra et al., 2007; Bundy et al., 2008; Di Matteo et al., 2008; Diamond-Stanic et al., 2012; Peng et al., 2015).

Concerning "frosting", we do not expect that low levels of in-situ star formation can alter typical extinction values in quiescent galaxies, which are expected to have low reserves of available gas and where current star formation processes are not significant yet.

7.1.5 Mechanisms involved in the built-up of quiescent galaxies

The phenomenological model proposed in this thesis (Chapter 4) represents a valuable tool for predicting how the different mechanisms of mergers, "frosting", and the "progenitor" bias alter the mass-weighted age and metallicity PDFs, so as to determining how quiescent galaxies evolve.

After estimating the impact of mergers, "frosting", and the "progenitor" bias, these three mechanisms are proposed to get involved in the evolution of quiescent galaxies, playing a role in different scales depending on the cosmic epoch and the stellar mass range. In the light of this thesis, the three mechanisms are necessary to explain at first order the observed evolution in age, metallicity, mass and number density, and their effects act in parallel (see Fig. 7.1). That is, a unique mechanism does not seem to be enough to explain the evolution of the quiescent population. The three mechanisms together are able to reduce the medians of both mass-weighted age and metallicity PDFs, with the impact of each mechanism varying with cosmic time (see Fig. 7.1). However, the changes in the widths of the mass-weighted age PDFs are mainly restricted to mergers, while mergers and "frosting" are the mechanisms able to modify (increase) the width of the mass-weighted metallicity PDF (see right column in Fig. 7.1).

7.1.5.1 The role of mergers in the built-up of quiescent galaxies

As it is unveiled in Chapter 4, mergers are one of the three mechanisms that is able to substantially alter the quiescent galaxy population: (i) they alter the stellar content of quiescent galaxies by adding the stellar populations from less massive systems, including star-forming galaxies with younger stellar populations. (ii) After merging, galaxies in the pair built a more massive galaxy, which can be included in the sample under study, including the stellar content of the progenitors (which differs owing to the stellar mass–age and –metallicity relation) and modifying the number density of the quiescent population. (iii) Mergers can reduce the number of quiescent galaxies (mergers between two quiescent galaxies), which highlights the stellar populations of the new galaxies included in the quiescent sample. (iv) There is a sufficient number of mergers as to modify both the median and width of the stellar population PDFs, and their strong effects should be considered in future studies. (v) Major mergers (mass ratio $1/4 \leq \mu_{\rm MM} \leq 1$) are more efficient than minor mergers (mass ratio $1/10 \leq \mu_{\rm mm} \leq 1/4$) to modify the PDFs of quiescent galaxies since $z \sim 1$. (vi) Mergers delay the ageing of quiescent galaxies by 0.5–1 Gyr since $z \sim 1$ with respect to a passive evolution, and diminish the median of the mass-weighted metallicity PDF by 0.1 dex. (vii) Mergers are able to increase the width of the age and metallicity PDFs, except for BC03 and metallicity PDF that remains almost constant.

It is also important to note the fact that the importance of mergers change with cosmic time, specially for major mergers, whereas for minor mergers it is roughly constant since $z \sim 1$. This remarks that the role of mergers in the evolution of the quiescent population is more important at higher redshifts rather than at larger cosmic times, although the latter is not negligible either. In addition, mergers of star-forming galaxies are less frequent than for quiescent ones (see Eqs. 4.6–4.9). Therefore, the impact of mergers also depends on the spectral type.

7.1.5.2 The role of "frosting" in the built-up of quiescent galaxies

In the light of the results of this thesis, "frosting" is an indispensable mechanism for the evolution of quiescent galaxies. Mergers and the "progenitor" bias are not able to account for the rejuvenation of the quiescent population as compared to a complete passive evolution, and the inclusion of "frosting" in the evolutive pathway is unavoidable (consistent concluded for both BC03 and EMILES SSP model predictions). Furthermore, although the incorporation of new young stars is expected to be moderate, some level of "frosting" should be present in all quiescent galaxies, as in fact this helps to increase the number density of these galaxies above $\log_{10} M_\star = 11.2$. The rate of "frosting" can be observationally constrained by the increase in number density of quiescent galaxies, using either the variation of the number density of quiescent galaxies (power-law function, see Sect. 3.6) or stellar mass functions (Appendix F) for setting an upper limit (the

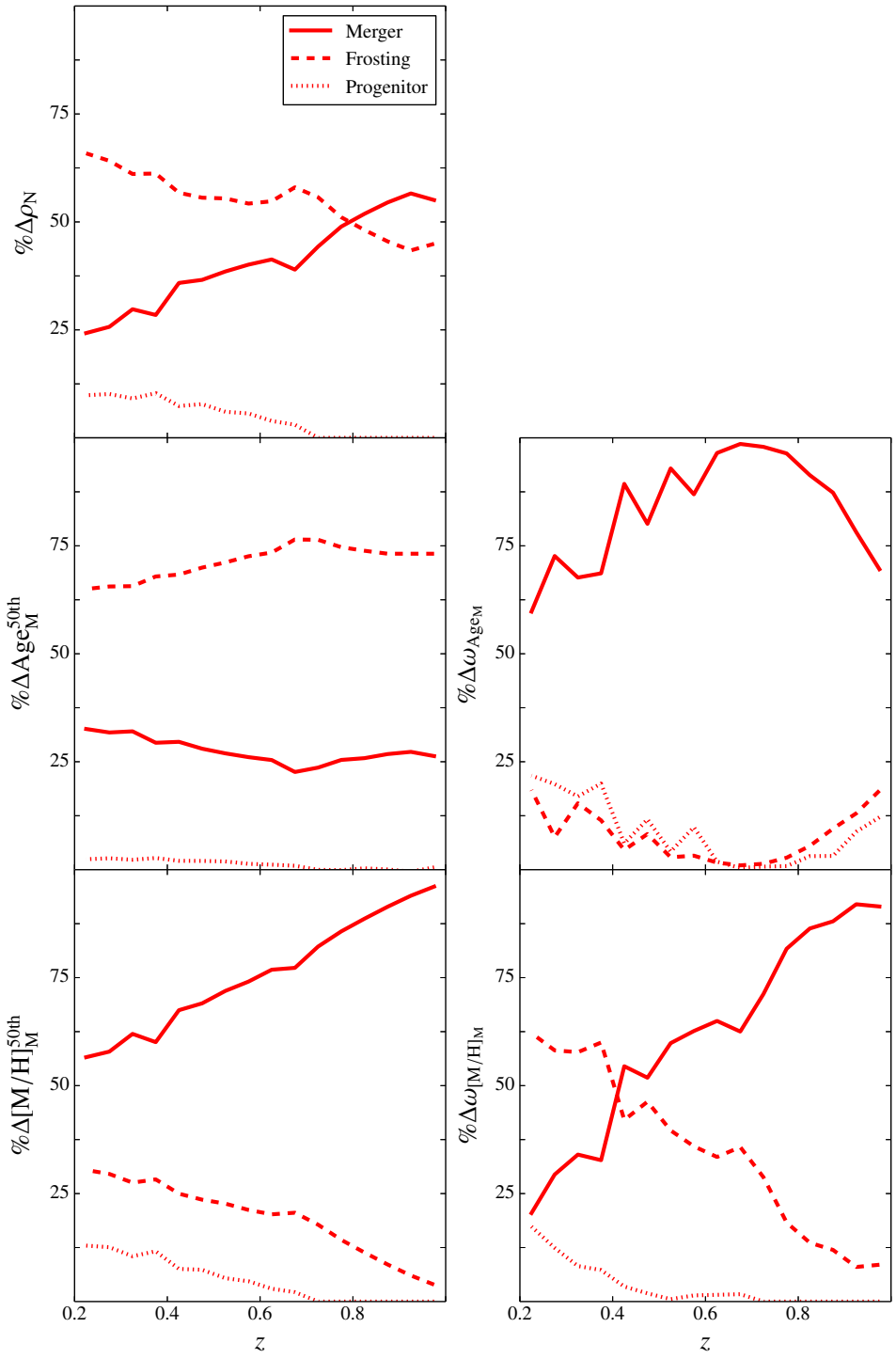

Figure 7.1: Relative contributions of mergers (solid line), "frosting" (dashed line), and the "progenitor" bias (dotted line) on the estimated variations of the number density (*top panel*), the median and width of the mass-weighted age PDF (*middle panels*), and the median and width of the mass-weighted metallicity PDF (*bottom panels*) of massive quiescent galaxies between $z = 1$ and $z = 0.2$ using EMILES+Padova00 SSP models.

inclusion of mergers and the "progenitor" bias can actually decrease this upper limit).

If the "frosting" rate is too large, the SFR of the galaxy would enter the levels of star-forming galaxies, so "frosting" rates must be below ~ 6 % (as obtained by the phenomenological model, except for a slight larger value of 8 % in the case of BC03, see also Sect. 3.4). Whilst it is assumed that the residuals of star formation inside quiescent galaxies do not alter significantly the metallicity of the host galaxies, a certain level of "frosting" integrated over time increases the stellar mass of the affected quiescent galaxies, hence being able to modify their number density as well as to include younger stellar populations and lower metallicities coming from the less massive galaxies that increased in mass via "frosting". In fact, this assumption sets a lower-limit for the impact of "frosting" since, as we mentioned above, a chemo-evolutionary population synthesis model as the one proposed by Vazdekis et al. (1996) predicts that galaxies with very efficient SFRs reach a maximum in metallicity and then they experiment a decrease in metallicity (more remarkable for bottom heavy IMFs, where there is a larger presence of low mass stars). Notice that this decrease in the metallicity by "frosting" would be restricted only to the most massive galaxies, which present the shortest formation timescales (e. g. Thomas et al., 2005; McDermid et al., 2015) and bottom heavy IMFs (e. g. Cenarro et al., 2003; van Dokkum & Conroy, 2010; Spiniello et al., 2012; Ferreras et al., 2013), although this is not included in our phenomenological model.

Alternatively, the accretion of gas poorer in metals from the cosmic web is also able to produce new populations with lower metallicities, but we do not account for this accretion. Overall, "frosting" presents negligible effects on the widths of the stellar population parameter PDFs, its main effect is to maintain constant the width of the PDFs.

7.1.5.3 The role of the "progenitor" bias in the built-up of quiescent galaxies

The star-forming galaxies that shut down their star formation becoming part of the quiescent sample, or the "progenitor" bias, is also an efficient mechanism for altering the overall properties of the quiescent population, strongly constrained by the number density of galaxies that experiment a quenching event. The stellar populations of these new quenched galaxies will contribute with younger stars and slightly lower metallicities, as star-forming galaxies present typically lower metallicities than quiescent ones (see Gallazzi et al., 2005, 2014; Peng et al., 2015). The "progenitor" bias also enlarges the width of the mass-weighted age PDF, whereas the width of the mass-weighted metallicity PDF is not affected by it.

As the mechanism for quenching is rather unknown, three approaches for the "progenitor" bias are considered, presenting similar effects. The "progenitor" bias based on the variability of the number density of massive star-forming galaxies must be treated as a lower limit, as the number of new massive star-forming galaxies are not taken into account (for the phenomenological model, stellar masses above $\log_{10} M_\star \geq 11.2$). Massive galaxies at $z \lesssim 1$ are predominantly quiescent galaxies, and therefore, the impact of the "progenitor" bias is not so significant for the most massive quiescent galaxies, unlike for less massive ones.

7.1.6 The growth in size of quiescent galaxies

In addition to the evolution of ages, metallicities, masses and number densities, very interesting conclusions on the assembly of quiescent galaxies can be retrieved from the distribution of their stellar population parameters in the stellar mass–size plane. The analysis conducted in this work reveals that more compact quiescent galaxies are older, more metal rich, less reddened by dust and present lower sSFR values than their more extended counterparts at fixed stellar mass. These results allow to shed light on the different mechanism acting in the growth in size of these galaxies since $z \sim 1$. The correlation between size and age for quiescent galaxies is an additional prove to discard the "puffing-up" scenario as the responsible mechanism of the growth in size of galaxies, as this one would imply that compact galaxies were younger than their more extended counterparts. The pioneering work by Trujillo et al. (2011) also discard the "puffing-up" mechanism of gas expulsion as the responsible of the growth in size of galaxies using spectroscopic data, in good agreement with our results.

Mergers and the "progenitor" bias agree with the results obtained in this topic. From the results obtained in the phenomenological model and the evolution of the stellar populations of quiescent galaxies, it is inferred that mergers and the "progenitor" bias must be present playing an important role along with "frosting". Both mergers and the "progenitor" bias have been extensively studied for explaining the growth in size of quiescent galaxies (Hopkins et al., 2009b; Naab et al., 2009; Valentinuzzi et al., 2010; Trujillo et al., 2011; Carollo et al., 2013; Belli et al., 2015). The latter because late-types or star-forming galaxies are typically more extended than early-types or quiescent galaxies, hence lying on the upper parts of the quiescent stellar mass–size relation after shutting down their star formation. Regarding "frosting", despite there may be a generalized presence of low levels of star formation, it is not clear how this may affect the derived sizes. If the remnants of star formation lie on the inner parts of the galaxy, "frosting" will tend to reduce the apparent size of the galaxy. On the contrary, new stars created in the surroundings of the inner parts (as a disk or shell around the bulge or galactic nucleus) would probably produce an apparent growth in size for the host galaxy. Therefore "frosting" can also be considered as another mechanism to produce the increase in size of galaxies. Overall, the growth in size of quiescent galaxies may not be driven by a unique mechanism.

As revealed by Díaz-García et al. (2013, or Chapter 6), the merger history of galaxies does not depend on the galaxy size and the growth in size via mergers seems to affect similarly to the whole quiescent population. In addition, under this scenario, the number of compact quiescent galaxies (below a fixed size) must decrease with cosmic time. Unfortunately, there exists not a clear consensus about the evolution of the number density of compact quiescent galaxies, as some previous studies support that this number is roughly constant(Saracco et al., 2010; Damjanov et al., 2014, 2015; Gargiulo et al., 2016), whereas other work state that it exhibits a significant or mild decrement (Valentinuzzi et al., 2010; Cassata et al., 2013; Poggianti et al., 2013; Quilis & Trujillo, 2013; Trujillo et al., 2014; van der Wel et al., 2014). If the number density of compact quiescent galaxies would remain constant with cosmic time, the "progenitor" bias would be the main mechanism responsible for the growth in size of the quiescent population, whereas if the number of compact galaxies were lower at larger cosmic times, then mergers rise as the most important mechanism. The sample of quiescent galaxies with reliable size measurements presented in this thesis is not large enough as to carry out a reliable, direct study about the evolution in number density of compact quiescent galaxies, although from the results obtained in Chapters 4 and 6, the number density of compact quiescent galaxies is expected to show a decrease in number.

From the results obtained in Chapters Chapter 3–6, it is possible to draw the following general picture on the growth in size of the quiescent population:

- Instead of a unique mechanism to explain the growth in size of quiescent galaxies, there seems to be a combination of various mechanisms that act in parallel to produce the increase in size observed in quiescent galaxies: mergers, the "progenitor" bias and, maybe, "frosting". In a "downsizing" scenario, the first galaxies that quenched their star formation were the galaxies that experimented the most efficient star formation episodes, with very short formation timescales, being in turn the most massive galaxies. The formation and evolution of the stellar populations of quiescent galaxies also relate to the size of the galaxy, i. e. with the stellar mass density of the galaxy, where the most compact ones at fixed stellar mass would be formed earlier and more efficiently. After shutting down their star formation, they were incorporated to the quiescent population, and under this hypothesis, all the galaxies that were formed later will present more extended sizes and younger stellar populations, which produces the size–age, –metallicity, –extinction, and –SFR/sSFR correlations. Once these galaxies belong to the quiescent sample, they continue growing in size via mergers and (maybe) "frosting". The continuous arrival of new quiescent galaxies, with larger sizes, also contributes to modify the stellar mass–size relation (e. g. in Belli et al., 2015, the authors constrained that the "progenitor" bias can be only responsible for about half of the growth in size at $1 < z < 1.6$).

- Although the growth in size is likely produced by a combination of various mechanisms, their role depend on the cosmic time. For instance, massive quiescent galaxies ($\log_{10} M_\star \geq 11.2$) suffer a rapid

increase in number at $1 < z < 3$ (e. g. Arnouts et al., 2007; Domínguez Sánchez et al., 2011; Ilbert et al., 2010, 2013), which implies a more striking contribution of the "progenitor" bias than at $z < 1$, provided that the majority of massive galaxies are already red at this redshift range (e. g. Davidzon et al., 2013; Ilbert et al., 2013; Moustakas et al., 2013; Tomczak et al., 2014). In addition, at higher redshifts major mergers were more frequent (e. g. Lin et al., 2008; de Ravel et al., 2009; López-Sanjuan et al., 2012; Xu et al., 2012; López-Sanjuan et al., 2013) and the rate of "frosting" could be also higher, provided the larger reserves of gas (Bell, 2003; Kannappan, 2004; Erb et al., 2006; Reddy et al., 2006; Dalcanton, 2007). This also would explain that the increase in size of quiescent galaxies were more efficient at $1 < z < 2$ rather than at $0 < z < 1$ (e. g. Trujillo et al., 2007; van Dokkum et al., 2008; Newman et al., 2012; van der Wel et al., 2014).

- At fixed redshift, the role of the different mechanisms to produce the growth in size of quiescent galaxies varies with stellar mass. As discussed above, at $z < 1$ there is a generalized increase in the number density of quiescent galaxies, that at decreasing stellar mass is systematically more prominent and explained by a larger "progenitor" bias. This implies that the contribution to the continuous assembly of the stellar mass–size relation also changes with stellar mass.

7.2 A general picture on the formation and evolution of galaxies: the "primordial density" scenario

In the light of the results in this thesis, it is possible to draw a general picture on the formation and evolution of quiescent galaxies, hereafter the "primordial density" scenario. The first and most massive galaxies were formed at epochs very close to the origin of the Universe ($z_f \gtrsim 6$), where the stellar mass density of the galaxy also plays a role. The material out of which the first galaxies formed had also high density, hence favouring the rapid star formation and creation of their stellar populations. Such star formation processes would be very efficient, being carried out in very short time scales as to produce a very fast an efficient enrichment of metals. Under this hypothesis, galaxies building up their stellar content from less dense primordial gas clouds would be assembled in later epochs, larger timescales and with a less efficient metal enrichment. Once galaxies shut down their star formation (e. g. "strangulation", outflows, or by other mechanisms), they belong to the quiescent population at a given epoch.

The first galaxies that quenched their star formation were the densest (most massive) ones, as they suffered the most efficient evolution as for consuming their reserves of gas. This would explain an earlier increase in number of massive quiescent galaxies (like the observed at $1 < z < 3$) and the size–age, –metallicity, –extinction, and SFR/sSFR correlations obtained in Chapter 5, whereas the increase in number of the less massive ones would be important at later epochs ($z < 1$). At $z \sim 1$, most massive galaxies $\log_{10} M_\star \gtrsim 10.8$ belong to the quiescent population. Only the most extended galaxies at fixed stellar masses are still hosting some degree of star formation (star-forming galaxies) before quenching their star formation. Still, quiescent galaxies at $z \lesssim 1$ contain small amounts of gas as to support a residual star formation that can explain "frosting". The star formation is not a dominant process in these galaxies, and the on-going assembly of the quiescent population at $z \lesssim 1$ is mainly driven by mergers at high-mass regimes.

As a result of the shutting down of star formation, the role of mergers (hierarchical scenario) becomes one of the most important mechanisms modifying the number and stellar populations of massive quiescent galaxies, through the accretion of less massive systems with available gas and younger stellar populations that produce both a delay in the ageing with respect to a passive evolution and a decrease in the median metallicity of the population. In addition, mergers act producing an increment in galaxy size. At decreasing stellar masses, the evolutive process is similar to massive galaxies although more extended in cosmic time and happening at later epochs. This supports the correlations between size and stellar population parameters, and that the increase in number of quiescent systems is more prominent at decreasing stellar masses and at $z < 1$. Note that the "primordial density" scenario also comprises the "downsizing" scenario and the MZR.

The proposed "primordial density" scenario for the evolution and formation of galaxies allows for making predictions on additional observables that have not been explored in this thesis:

- At fixed stellar mass, more compact quiescent galaxies should contain stellar populations with larger abundances of α-elements in comparison with the less compact ones. Since the most compact galaxies are more efficient in forming stars, their formation timescales shall be shorter. It is though that the enrichment of the ISM must be carried out by supernovae (SN) type II (massive stars) instead of the SN type Ia when formation timescales are shorter, and the stars of these compact galaxies will therefore exhibit larger [α/Fe] values (see also Thomas et al., 1999; Pipino & Matteucci, 2004; Thomas et al., 2005; de La Rosa et al., 2011). This fact was already observed by McDermid et al. (2015), where more compact galaxies systematically show larger [α/Fe] values than the extended ones at the same stellar mass, supporting the "primordial density" scenario.

- The median of the [α/Fe] PDF of quiescent galaxies must decrease since $z \sim 1$. As above, the densest galaxies were the galaxies with the shortest formation timescales and the first in shutting down their star formation. Galaxies formed later (the "progenitor" bias) experimented larger formation timescales with lower [α/Fe] values. Mergers with less massive galaxies may also contribute to reduce the global [α/Fe] of quiescent galaxies. In addition, "frosting" supports this scenario, because the ISM will be largely enriched by SN type Ia instead of SN type II, moving [α/Fe] towards lower values.

- As the density of the galaxy at fixed stellar mass show a tight correlation with its stellar content, and based on the IMF radial profiles and the correlation between metallicity and the IMF slope found by (Martín-Navarro et al., 2015a,b), there might be a correlation between the size of a galaxy and its IMF at fixed stellar mass. If this is the case, the median IMF slope of quiescent galaxies would also exhibit variations with cosmic time due to mergers and the "progenitor" bias, and maybe "frosting".

In summary, we find evidences that would support that the formation and evolution of the stellar populations of quiescent galaxies relate to the total barionic mass, but also with the stellar mass density of the galaxy. Further studies and cosmological simulations are necessary to confirm and explore the proposed "primordial density" scenario.

8

Conclusions

> *The discipline you learn and character you build from setting and achieving a goal can be more valuable than the achievement of the goal itself.*
>
> Bo Bennett

A significant part of the work in this thesis was devoted to the design and development of MUFFIT. We demonstrate that MUFFIT is a reliable stellar population code for multi-filter galaxy data, which is suited to and optimized for analysing the stellar content of galaxies in ALHAMBRA-like surveys. In particular:

- MUFFIT is able to increase the accuracy of photo-z determinations by $\sim$ 15–20 % when the results provided by external photo-z codes (e. g. BPZ and EAZY) are used as input ingredient. MUFFIT reaches great photo-z accuracies of $\sigma_{\mathrm{NMAD}} \lesssim 0.006$ for quiescent galaxies in ALHAMBRA-like surveys with a really low number of outliers, $\eta_1 = 0.5$ % and $\eta_2 = 6.5$ %, in comparison with spectroscopic redshifts of real galaxies.

- Despite being optimized for analysing quiescent galaxies, we demonstrated that MUFFIT can be used for determining the EW of strong emission lines, after comparing with local spectroscopic surveys such as SDSS. Using ALHAMBRA and MUFFIT, we successfully confirm previous results of stellar masses from COSMOS, and spectroscopic stellar populations of galaxies from SDSS such as the age–metallicity maps of early-type galaxies at $z < 0.22$, and the individual ages, metallicities, stellar masses, and redshifts for a subset of galaxies in common between ALHAMBRA and SDSS.

- Overall, we demonstrate that is possible to determine reliable stellar population parameters of red galaxies (age, metallicity, extinction, and stellar mass) using MUFFIT or SED-fitting methods like MUFFIT. This confirms that, when the stellar continuum of galaxies is not affected by colour systematics, as it typically happens for spectroscopic data, multifilter photometric data provides meaningful information to determine reliable stellar population parameters via SED-fitting, at least at the spectral resolution and the wavelength coverage of ALHAMBRA.

Making use of a subsample of 8 547 quiescent galaxies from the ALHAMBRA survey, of high quality and complete in stellar mass, we conducted a detailed and unprecedented study of stellar populations since $z \sim 1$, including ages, metallicities and extinctions. The main results from this study are:

- A pure and clean definition of the sample of quiescent galaxies is key to perform this kind of studies. Apart from a significant fraction of cool stars in ALHAMBRA (24 % at $22.5 \leq m_{F814W} \leq 23$) with typical red colours that mimic those of quiescent galaxies, the inclusion of the extinctions of galaxies

retrieved by MUFFIT in ALHAMBRA improves previous selection criteria proposed in the literature, reducing the sample contamination due to dusty-star forming galaxies significantly. In particular, after accounting for extinction corrections, we set new color limits of $(m_{F365} - m_{F551})_{\rm int} > 1.5$ for the colour-colour locus of true quiescent galaxies. From this analysis, we conclude that the contamination of dusty star-forming galaxies ($\sim$ 20 %) is less severe for massive galaxies ($\log_{10} M_\star \geq 11$, 2–8 % from $z \sim 0.1$ to $z \sim 1.1$) than for the least massive ones (40 %, for $9.2 \leq \log_{10} M_\star \leq 9.6$ at $0.1 \leq z \leq 0.3$) when classical UVJ diagrams are used for this purpose. In addition, star-forming galaxies reddened by dust that contaminate the quiescent galaxy populations tend to concentrate close to the colour limits of the quiescent region at the UVJ diagrams. This result is additionally supported by two SFR tracers based on the dust emission at 24 μm and the luminosity at 2 800 Å.

- From the extinction corrections performed in this work, we conclude that 65 % of the galaxies that reside in the green valley are actually obscured star-forming galaxies. Consequently, the green valley is less populated than expected, imposing new constraints in mechanisms for quenching star formation in galaxies as AGN feedbacks.

- The distribution of ALHAMBRA galaxies in the SFR and sSFR vs the stellar mass planes reveals a bimodality, where the main sequence of galaxies (star-forming galaxies) populate the upper SFR and sSFR regions. The most massive quiescent galaxies exhibit larger SFRs than their lower mass counterparts. The most efficient processes of star formation in the quiescent population reside in the lowest mass systems, as the most massive ones present the lowest sSFR values.

- We present, for the first time, a comprehensive analysis of the distributions of quiescent galaxies in a dust-corrected UVJ-diagram as a function of their ages, metallicities, extinctions, and stellar masses since $z \sim 1$.

  At any redshift, the most massive quiescent galaxies lie on the reddest parts of the UVJ-diagram. Quiescent galaxies with the bluest intrinsic colours, $(m_{F365} - m_{F551})_{\rm int} \lesssim 1.7$ and $(m_{F551} - J)_{\rm int} \lesssim 1.2$, are also the galaxies with the largest extinction values ($A_V \gtrsim 0.4$). When dust corrections are not taken into account, quiescent galaxies with large dust contents are in the upper parts of the UVJ-diagram in agreement with extinction law predictions.

  The ages of quiescent galaxies show correlations with the intrinsic colours $(m_{F365} - m_{F551})_{\rm int}$ and $(m_{F551} - J)_{\rm int}$. The oldest ages populate the upper parts of the UVJ-diagram at $(m_{F365} - m_{F551})_{\rm int} > 1.8$; whereas the youngest quiescent galaxies present the bluest colours of the diagram. Metallicities correlate strongly to the colour $(m_{F551} - J)_{\rm int}$ and weakly to $(m_{F365} - m_{F551})_{\rm int}$. The most metal rich quiescent galaxies, $[{\rm M/H}]_{\rm M} > 0.1$ dex, also present the reddest colours $(m_{F551} - J)_{\rm int} > 1.1$. When reddening effects are not considered, the above correlations are generally weaker or more degenerated.

- There is an increasing number of quiescent galaxies since $z \sim 1$. The increase in number density for less massive galaxies ($10 \leq \log_{10} M_\star < 10.4$) is more striking than for the most massive ones ($\log_{10} M_\star \geq 11.2$), with variations in number of $\sim$ 50 % and 5 % every $\Delta z = 0.2$ respectively.

To explore the evolution of quiescent galaxies since $z \sim 1$ through the study of their stellar content, we developed, for the first time, a novel methodology for removing the impact of uncertainty effects and retrieving redshift-dependent PDFs of mass-weighted ages, metallicities and extinctions. The derived PDFs allowed us to determine that:

- Since $z = 1.1$, quiescent galaxies predominantly contain both old stellar populations with solar and super-solar metallicities, except for the local and less massive quiescent galaxies that reveal sub-solar metallicities. The stellar content of quiescent galaxies present a relation with the stellar mass. The more massive the quiescent galaxy is, the older and more metal rich it is since $z \sim 1$ (in agreement with the "downsizing" scenario and the MZR). Furthermore, the galaxy mass-metallicity relation seems to be present since earlier times, with hints of being steeper at lower redshifts.

- Quiescent galaxies are older at larger cosmic times, but their age evolution since $z \sim 1$ is not compatible with a pure passive evolution. The widths of the mass-weighted age PDFs (intrinsic dispersions) present values of $\omega_{\mathrm{Age_M}} \sim$ 1–2 Gyr and a slight correlation with the stellar mass and redshift.

- There are evidences for a decrease of the median of the metallicity PDF of quiescent galaxies since $z \sim$ 0.6–1.1. This decrement amounts to 0.1–0.2 dex. The width of the mass-weighted metallicity PDF is broader at larger redshifts, where the most massive galaxies present the narrowest PDFs.

- All the quiescent galaxies present low extinction values of $A_V < 0.6$, with median values in the range $A_V = 0.15$–0.3. The width of the extinction PDF becomes larger at higher redshifts, specially in the more massive ones.

- As expected, there is a quantitative dependency of the stellar population results on the use of different input SSP models feeding MUFFIT, as well as on any assumption related with the SFHs involved in the SED-fitting process. In fact, the use of different SSP models and SFH constraints introduce systematics in the final results that dominate the random uncertainties intrinsic to the determination of the stellar population parameters. Despite this, there is a reasonable qualitative agreement in the results derived from the different input SSP models and SFHs assumed in this thesis.

For the first time, we created and developed a phenomenological model aimed at shedding light on the mechanisms involved in the evolution of galaxies, quantifying the relative contributions of mergers, "frosting", and the "progenitor" bias required to reconcile both the number density and the stellar population evolution of massive quiescent galaxies reported in this thesis. In this sense, the main results of our phenomenological model are:

- Mergers play a remarkable role in the evolution of massive quiescent galaxies since $z = 1$. Estimations from merger rates involving massive quiescent galaxies points out that around a third of this population suffers at least one major merger (mass ratio $1 \geq \mu_{\mathrm{MM}} \geq 1/4$) and one minor merger (mass ratio $1/4 \geq \mu_{\mathrm{mm}} \geq 1/10$) between $z = 1$ and $z = 0.2$.

- Mergers increase the number density of massive quiescent galaxies around $\Delta \log_{10} \rho_{\mathrm{N}} \sim$ 0.1–0.25 dex (0.07–0.21 dex is due to major mergers, whereas for the minor ones is 0.03–0.06 dex).

- Mergers are the responsible for part of the evolution in the median age of massive quiescent galaxies, accounting for 0.5–1 Gyr since $z \sim 1$. They can explain the increase in the width of the mass-weighted age PDF observed since $z = 1$, whose impact is $\Delta\omega_{\mathrm{Age_M}} =$ 1–2 Gyr. Regarding metallicity, mergers induce a slight decrease of $\lesssim 0.1$ dex in the median metallicity of the massive quiescent population, whereas the width of the metallicity PDF increases less than 0.1 dex.

- "Frosting" reveals to be a necessary mechanism to explain the evolution of the age PDFs of massive quiescent galaxies. Despite we assume that the enrichment of metals in the host galaxy is negligible via "frosting", this mechanism is able to explain up to 0.05 dex of the evolution of the mean of the mass-weighted metallicity PDF. "Frosting" is also an efficient mechanism that strongly affects the number density of massive quiescent galaxies, which in turn constitutes an additional constraint to the frosting efficiency, τ_{f}, when the evolution in number is taken into account.

- The "progenitor" bias tends to reduce the median age of the massive quiescent population since $z \sim 1$ in a less efficient way than mergers do. In addition, we find that this mechanism does not alter the width of the age PDF significantly. Regarding metallicity, the evolution of the mass-weighted metallicity PDFs of massive quiescent galaxies is not very much affected by the "progenitor" bias, which helps to decrease the median metallicity by less than 0.03 dex since $z \sim 1$, without increasing substantially its width.

- For the first time, the evolution of the ages and metallicities of massive quiescent galaxies, along with their evolution in number, are reasonably explained by the conjunction of mergers, "frosting", and the "progenitor" bias. Under this scenario, we constrained the contribution of "frosting" at τ_f = 0.02–0.08 Gyr^{-1}. The combination of EMILES SSP models and Padova00 isochrones show the best agreement between the evolution of massive quiescent galaxies derived from ALHAMBRA data and the predictions retrieved using MUFFIT and our phenomenological model.

Regarding the role that the galaxy size plays in the evolution of quiescent galaxies, using a subsample of several hundred ALHAMBRA galaxies in common with HST/ACS data we find out evidences for strong correlations between the galaxy sizes and their ages, metallicities, and SFRs/sSFRs, as well as hints for a slight correlation with the extinction. Our results reveal remarkable insights:

- More compact quiescent galaxies are older than their more extended counterparts at fixed stellar mass. The difference in age is established around 2–3 Gyr for stellar masses of $\log_{10} M_\star > 9.6$ and up to $z \sim 0.9$, with an average size-age correlation of $\langle \bar{m}_{s,\mathrm{Age_M}} \rangle \sim -1.9$.

- Compact quiescent galaxies are systematically more metal rich than the less dense ones at the same stellar mass. The larger metallicity differences between compact and extended quiescent galaxies are ~ 0.2 dex at least since $z = 0.9$, with an average size-metallicity correlation of $\langle \bar{m}_{s,[\mathrm{M/H}]_\mathrm{M}} \rangle \sim -0.07$.

- There are hints for extended quiescent galaxies presenting slightly larger extinctions of < 0.1 independently on their stellar mass ranges and redshifts, with $\langle \bar{m}_{s,A_V} \rangle \sim 0.03$.

- The more compact the quiescent galaxy, the lower its SFR ($\langle \bar{m}_{s,\log_{10}\mathrm{SFR}} \rangle \sim 0.3$) and sSFR ($\langle \bar{m}_{s,\log_{10}\mathrm{sSFR}} \rangle \sim 0.16$), with the differences between compact and extended ones being below 0.5 dex in both cases. This trend is observed for all the stellar masses present in our sample since $z = 0.9$.

The above relations between galaxy sizes and stellar population parameters are complemented with the study of the role of mergers in the growth of quiescent galaxies. We conclude that early-type galaxies are homogeneously affected by mergers independently of their size. Consequently, we cannot discard that the "progenitor" bias is the only mechanism to produce the growth in size of quiescent galaxies since $z \sim 1$, but a combination of mergers the "progenitor" bias and, maybe, "frosting", may be the real driver of this growth. Combining the results of the stellar populations and the phenomenological model, the relevance of each mechanism in the growth in size depends on redshift and stellar mass.

In the view of these results, we are in a privileged position to propose a scenario of galaxy formation and evolution: the "primordial density" scenario. Under this scenario, the most compact and massive galaxies were firstly formed at epochs very close to the origin of the Universe ($z_f \gtrsim 6$). The remaining galaxies were originated in subsequent epochs building up their stellar content from less dense gas clouds. Simultaneously, galaxies experiment mergers that also contribute to the assembly and formation of galaxies, being a source of new gas and stars with different metal composition than the host galaxy and producing an increase in size. Once galaxies quench their star formation, these are involved in a dominant hierarchical merging, which contributes to the formation and evolution of galaxies becoming one of the most relevant mechanisms that continue the assembly of galaxies.

9 Future work

“Learn from yesterday, live for today, hope for tomorrow. The important thing is not to stop questioning.”

Albert Einstein

We briefly present current and future projects for extending or complementing the results obtained in this Ph. D. thesis. Part of them comprise improvements of the code MUFFIT, in order to adapt it to new tasks or methodologies, because MUFFIT is subject to continuous improvements and updates owing to its easy adaptability. Although, we also include some future applications of the retrieved results and techniques or a fine-tuned revision of them (see details in each section).

9.1 Additional stellar population parameters in the SED-fitting analysis

In addition to age, metallicity, and extinction, there are other stellar population parameters that can alter the SED of a galaxy, and consequently, that can modify their colours affecting the retrieval of all them. In future, we will treat the universality of the IMF (Sect. 9.1.1), and the influence of different [α/Fe] abundances (Sect. 9.1.2). Finally, more complex SFHs are also suitable to produce different galaxy SEDs, and its inclusion along the SED-fitting process may provide quite interesting results (Sect. 9.1.3).

9.1.1 Introducing different IMF slopes

The state-of-the-art studies about stellar populations show that there are evidences as for the non-universality of the IMF (e. g. Cenarro et al., 2003; van Dokkum & Conroy, 2010; Spiniello et al., 2012; Ferreras et al., 2013; Weidner et al., 2013). Early-type galaxies with larger velocity dispersions tend to present steeper IMFs (e. g. Ferreras et al., 2013), i. e. an excess or larger proportion of low mass stars than the expected for a Salpeter-like IMF. This would have an impact on their stellar population predictions based on models that not include this "new" parameter (Ferré-Mateu et al., 2013). A larger contribution of low mass stars (bottom heavy or steeper IMF slopes) would imply redder SED colours (Vazdekis et al., 2012), which a priori may introduce systematics on the SED-fitting predictions.

With the new generation of SSP models, the implementation of the IMF as another parameter in the SED-fitting analysis is straightforward. In particular, the SSP model set of EMILES includes various both observational and analytic parametrizations for the IMF (see also Vazdekis et al., 1996, 2012). The additional benefit of these models is the wide spectral range covered for them $\lambda\lambda$1680 Å–5 μm (further details in Sect. 3.2.1 and Vazdekis et al., 2016), as they also include the SED in the NIR range where the flux coming from low mass stars is more prominent. In fact, the most extended IMF-sensitive indices are based on

features in the red part of the spectrum (Cenarro et al., 2003; Ferreras et al., 2013; La Barbera et al., 2013, 2017, e. g. CaT, TiO_1, TiO_2, Na8190, Na I λ8190 Å, Na I λ1.14 μm, and Na I λ2.21 μm). These models are adequate for our purposes, as they cover the full spectral range of ALHAMBRA in a wide redshift range ($z \lesssim 1.1$). However, there are many stellar population parameters involved in the SED-fitting that produce additional degeneracies in the retrieved solutions. At lower redshifts, this effect is even more prominent (see Sect. 2.4.2 and Fig. 3.18), as the extinction is worse constrained when only photometry in the optical range is available. In fact, the introduction of a non-universal IMF also introduces an extra factor of degeneracy that should be explored. Consequently, a detailed analysis and study of the reliability for retrieving IMF slopes by SED-fitting techniques, such as MUFFIT, has to be done. There exists the possibility that only with photometry in the optical range, in ALHAMBRA at lower redshifts, the IMF slope may not be constrained easily. In addition, at larger redshifts a larger part of the UV is imaged and galaxies are also younger, that is, the IMF effects can be more remarkable and the subtle alterations in the flux by different IMF slopes may be differentiated and measured. This would restrict the study of the non-universality of the IMF to a certain redshift range in ALHAMBRA, although this is still under development and study.

Regarding this issue, we carried out a first and preliminary attempt for determining the IMF slopes of the quiescent galaxies in ALHAMBRA. For this case, we select the galaxies classified as quiescent in Chapter 3 using EMILES SSP models, and we reran MUFFIT including different IMF slopes. In particular, we selected the bimodal parametrization for the IMF (BI, Vazdekis et al., 1996), which is based in observational results (Scalo, 1986; Kroupa et al., 1993), with slopes equal to 1.0, 1.3, 1.8, and 2.3 (BI1.0, BI1.3, BI1.8, and BI2.3 respectively), where the equivalent Salpeter-like IMF slope is 1.3. As in Chapter 3, the retrieved distributions of age, metallicity, extinction, and IMF slope are deconvolved of uncertainties through the MLE method detailed in Appendix D. For illustrating, we plot the results obtained for BaSTI isochrones in Figs. 9.1 and 9.2. Concisely, the quiescent population does not evolve passively at least since $z \sim 1$ and the decrement in the median of the metallicity PDF is still obtained whilst the non-universality of the IMF is assumed. Furthermore, the stellar mass-metallicity relation is also present, although the stellar mass-age correlation is much milder in comparison with the results obtained in Sect. 3.8. The extinction and metallicity PDFs do not present remarkable modifications after adding the IMF as another free parameter. Regarding the IMF slopes, we retrieved in this preliminary test that at increasing stellar mass, the IMF slope is larger. We also appreciate a variation of the median of the IMF slope PDF with redshift, but the intrinsic dispersion, specially at lower redshifts, is almost as long as the IMF slope range (1–2.3) of the models. This might confirm our suspects and the IMF slope would not be properly determined completely, although a further study is necessary. It is noteworthy that the most massive bin at $z \sim 1$ present very high IMF slopes (larger than 2) and the intrinsic dispersion of the IMF is lower (lower than 0.5).

9.1.2 The [α/Fe] abundances

In spite of our intention is also to explore the [α/Fe] abundances of ALHAMBRA quiescent galaxies and that MUFFIT is already ready for including [α/Fe] as another stellar population parameter during the SED-fitting process, we cannot carry out this study yet. The main impediment is the lack of SSP models in a regular grid of stellar population parameters and that also cover a wide spectral range. We considered the novel evolutionary stellar population synthesis models by Vazdekis et al. (2015) with MILES, which includes α-enhanced models (BaSTI isochrones Pietrinferni et al., 2006) with values [α/Fe] = +0.00 and +0.40, but the spectral range of these SSP models is not enough ($\lambda\,\lambda$ 3540–7410 Å) for our aims. Nevertheless, we would need a set of SSP models that covers the full ALHAMBRA spectral range up to $z \sim 1$, i. e. $\lambda\lambda \sim$ 1700 Å–2.5 μm.

As there is no SSP models fulfilling all the conditions yet, we will explore other alternatives:

i) Determination of the systematics and/or degeneracies in the results of quiescent galaxies (age, metallicity, extinction, and stellar mass) introduced by the assumption of constant [α/Fe] values in the models.

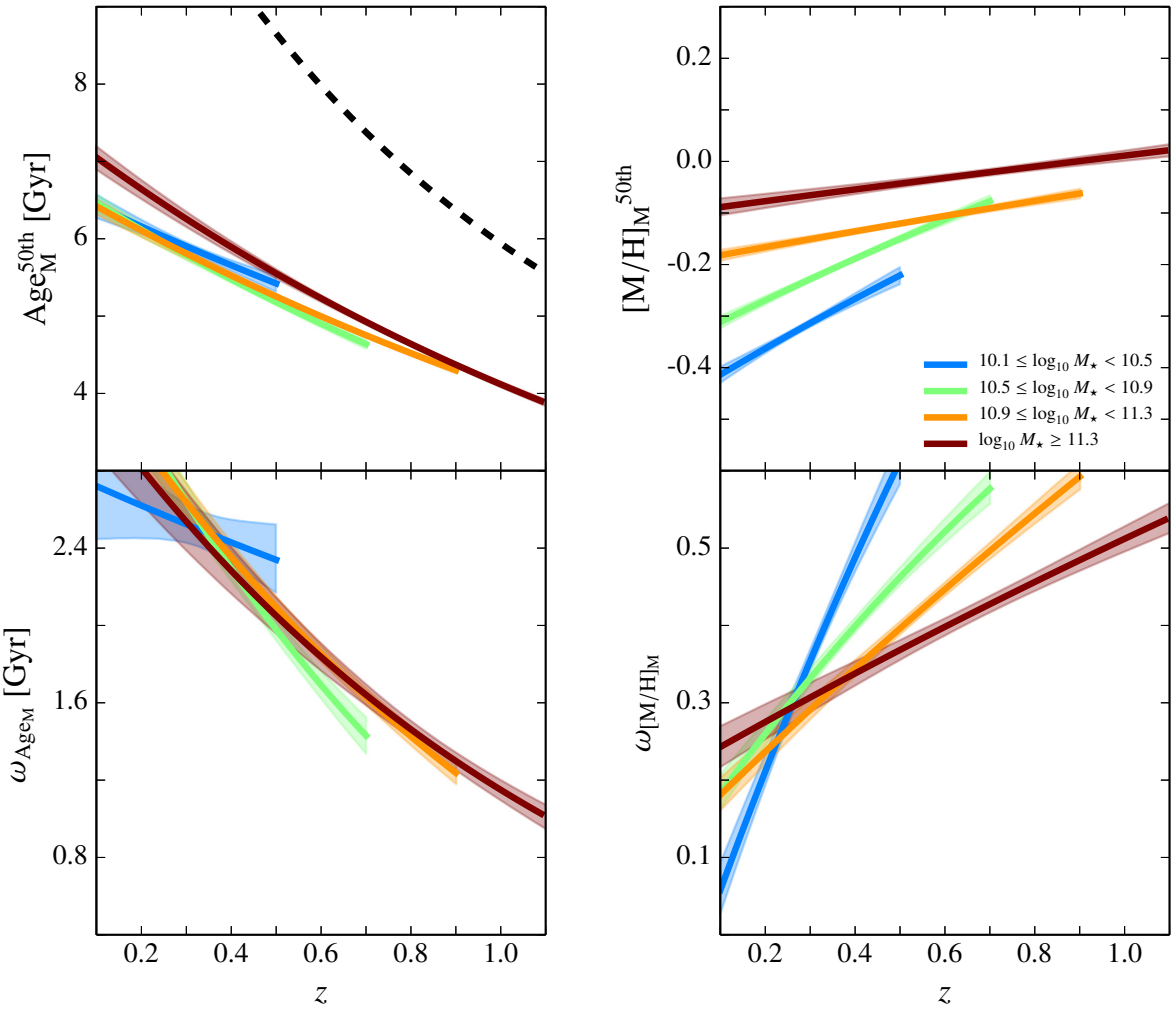

Figure 9.1: The distribution median (*top panels*) and width (ω, *bottom panels*) evolution of the mass weighted age (*left-hand side*) and metallicity (*right-hand side*) using EMILES with BaSTI isochrones and various IMF slopes for the quiescent population at different redshifts and stellar mass bins. The shaded regions delimit the 1 σ uncertainties of both parameters. Dashed black line illustrates the age of the Universe at different redshifts.

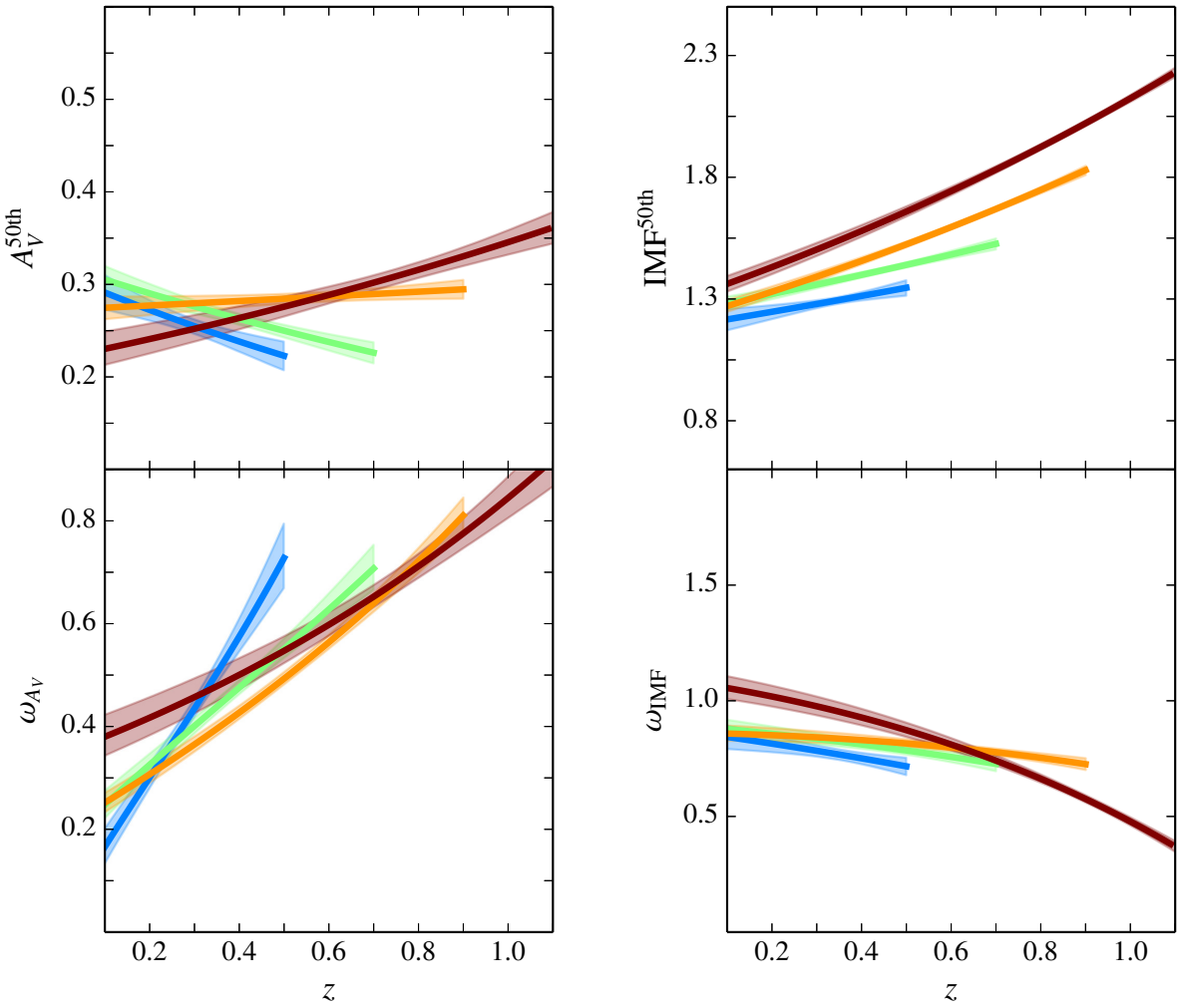

Figure 9.2: The distribution median (*top panels*) and width (ω, *bottom panels*) evolution of the extinction (*left-hand side*) and IMF slope (*right-hand side*) using EMILES with BaSTI isochrones for the quiescent population at different redshifts and stellar mass bins. The shaded regions delimit the 1 σ uncertainties of both parameters.

ii) Making use of the models by Vazdekis et al. (2015), we will explore whether we can discern [α/Fe], or its accuracy, only using the optical range $\lambda\,\lambda$ 3540–7410 Å via SED-fitting (e. g., by Monte Carlo simulations as in Sect. 2.4.2).

9.1.3 Determination of SFHs

The next step in the development of MUFFIT is the inclusion of models with more complex SFHs rather than the only use of combinations of two SSPs (or two instantaneous bursts). We plan to construct composite stellar populations from SSP models using different analytical functions for the SFR or SFHs, such as the most extended ones: exponentially declining (the most extended ones and usually referred as τ-models), single bursts of a τ duration, linearly declining, or delayed exponentially declining SFHs. The inclusion of composite stellar populations will open the possibility for exploring other interesting topics, as the formation time-scales (duration of the main star formation episodes that built the bulk of stars), which can be also related with the presence of different α-abundances in early-type galaxies (e. g. Thomas et al., 2005; McDermid et al., 2015); as well as correlations between formation time-scales and stellar masses or with other stellar population parameters. In addition, this implementation can support a more reliable SED-fitting for star-forming galaxies, as these galaxies are still suffering strong processes of star formation.

9.2 Stellar population parameters as a funcion of rest-frame UVJ colours

Motivated by the results obtained in Sect. 3.5, rest-frame colours of quiescent galaxies can be used for constraining stellar population parameters, such as age, metallicity, and extinction. From the results obtained with ALHAMBRA, we can parametrise the dependence or correlation of the age, metallicity, and extinction with the rest-frame UVJ colours through functions of the form: $f(U-V, V-J, M_\star, z)$. These relations would be very useful to determine in an alternative and fast approach the stellar population of quiescent galaxies by their rest-frame colours, redshift, and stellar mass. These relations will be specially useful for large photometric surveys with a low number of bands, such as SDSS-like surveys, as long as the photometric system of the survey contains the bands U, V, and J (at least close to their spectral range). Although these functions are not providing the proper stellar population parameters of the candidates, we can set statistical limits on their stellar population parameters. In fact, for very large samples the distribution of stellar population parameters retrieved by this approach should be quite similar to the real one, as the UVJ colours are observationally linked to the distribution of stellar population parameters.

9.3 Multidimensional PDFs of stellar population parameters

In Chapter 3, we retrieve the mass-weighted age, metallicity, and extinction PDFs. These PDFs correspond to the most simple case, in which the stellar population parameter PDFs are unidimensional for each of these three parameters. In a general case, there are correlations amongst the parameters, that is, some values of age and metallicity are not present simultaneously and for certain ages some metallicities are more frequent than others at fixed stellar mass. In fact, there exist correlations amongst stellar population parameters (see also Gallazzi et al., 2005). These correlations are clearer on the stellar mass–size plane in which more compact galaxies are older and more metallic, whereas the young ones (or the extended ones) present lower metallicities. For solve this, we are extending the MLE method presented in Appendix D for constructing multidimensional PDFs (deconvolving uncertainty effects as well), which would include age, metallicity, and extinction. This way, we would obtain for any stellar mass and redshift the probability or density number of quiescent galaxies with certain age, metallicity and extinction simultaneously. Multidimensional PDFs will also contribute to provide better predictions of the merger, "frosting", and the "progenitor" bias effects treated in Chapter 4, which are based on a Monte Carlo approach of the unidimensional PDFs of age and metallicity (for this case we would need the bidimensional PDF of age and metallicity).

9.4 Expansion of the phenomenological model

Although the effects of mergers, "frosting", and the "progenitor" bias obtained from the phenomenological model (Chapter 4) are very clear and in good agreement with the observations of the evolution of the quiescent galaxy sample, we pretend to include some features:

i) Effects of mergers, "frosting", and the "progenitor" bias on the distribution of extinction values of quiescent galaxies. The effects of these three mechanisms fairly explain the age and metallicity evolution of the quiescent population since $z \sim 1$ (mainly for EMILES SSP models), but the effects on the extinction PDF are not explored yet.

ii) Stellar population parameters of star-forming galaxies obtained by MUFFIT or via SED-fitting. Once the reliability of the retrieved stellar population parameters of star-forming galaxies is confirmed (also including predictions from τ models, see Sect. 9.1.3), we will include their PDFs in the phenomenological model. This will check the self-consistency of the predictions, reinforcing the reliability of the star-forming PDFs of stellar population parameters (as we do with the quiescent sample).

iii) The inclusion of multidimensional PDFs for stellar population parameters. As we explain in Sect. 9.3, the construction of multidimensional PDFs of stellar population parameters is justified by the presence of correlations amongst them. Notice that this may increase the effects of mergers or the "progenitor" bias. In addition, we will study their effects on extra PDF parameters, rather than the PDF median and width.

iv) Effects of uncertainties. Those parameters that were observationally constrained (as the involved in Eqs. 4.3 and 4.6–4.9) contain uncertainties that can alter the results obtained in the phenomenological model. The inclusion of these uncertainties can strongly reinforce any prediction obtained by this model.

v) Alternative assumptions for "frosting". The assumption of a fixed and constant mass fraction in "frosting" may be unrealistic. Variations in the prescriptions adopted for "frosting", e. g. including correlations with redshift and/or stellar mass, can shed light on the reliability and real impact that can introduce this mechanism, as well as understanding the systematics of this naive assumption.

vi) Expansion of the phenomenological model to determine the role of mergers, "frosting", and the "progenitor" bias in the growth in size of quiescent galaxies since $z \sim 1$. It is clear from Chapter 4, that these three mechanisms have prominent effect on the stellar populations of quiescent galaxies. Therefore, the three mechanisms can alter the size of the quiescent population in a different level, as well as to modify the spatial distribution of the stellar populations of a galaxy (i. e. the building-up of the stellar population gradients). By this expansion of the phenomenological model, we will discern the role of each of the three mechanisms in the growth in size and assembly of the quiescent population.

Actually, the results retrieved in Chapter 6 are required for the expansion of the phenomenological model. A priori if mergers are the main mechanism for producing the increase in size, we need to know whether they predominantly act on the most compact galaxies or not (from Chapter 6, the merger history is independent of the galaxy size).

9.5 Spatially-resolved stellar populations

Multi-filter surveys provide spatially resolved photo-spectra, similar to an IFU of low spectral resolution, allowing us to perform 2D stellar population studies of galaxies with apparent sizes larger than the system PSF. The imminent arrival of the new large-scale multi-filter surveys J-PLUS and J-PAS motivates the development of a novel technique for this aim, as there will be a huge number of spatially-resolved galaxies.

The large area planned for these surveys (more than 8 000 deg^2) will provide an unprecedented sample of spatially-resolved galaxies, for which we should be able to retrieve the spatial distribution of their stellar populations only using their multi-filter photometric data.

To take advantage of the opportunity that J-PLUS and J-PAS offer, we are performing a new methodology to retrieve the 2D distributions of the stellar content of their spatially-resolved galaxies ($z \lesssim 0.1$ for effective radius in the range 2.5–3 $R_{\rm eff}$). Although the lack of high spectral resolution might be an obstacle, the large number of galaxies imaged in these surveys will reinforce any result statistically. In fact, this kind of studies will provide the largest sample of spatially-resolved stellar populations with tens of thousands of galaxies with high photometric quality up to various effective radii, 2.5–3 $R_{\rm eff}$, whereas state-of-the-art spectroscopic IFU studies only comprise hundreds of galaxies actually (e. g. CALIFA and MaNGA; Sánchez et al., 2012; Bundy et al., 2015, respectively) or down to 1.5 $R_{\rm eff}$. The basis for exploiting these datasets in this topic is at an advanced state of development (fully detailed in San Roman et al., submitted to A&A). In brief, we distinguish four main steps in the methodology:

i) PSF homogenization of the images. Each single image in a survey is the result of multiple exposures, each of them with different PSFs. Furthermore, the PSF varies amongst the filters of the photometric system. Consequently, a homogenization of the PSF is necessary to obtain a reliable photometry of the same area or region in a galaxy. Otherwise, the light coming for each of the regions will be redistributed in a different way depending of the band. This would imply that the photometry of each region was not equivalent amongst filters, introducing colour terms or systematics that alters the SED of each region.

ii) Spatially binning of the regions of a galaxy. Once the PSF homogenization is done (each of the regions in a galaxy are photometrically equivalent for all the bands), the regions of each spatially-resolved galaxy are defined through a centroidal Voronoi tessellation (CVT) method, as detailed by Cappellari & Copin (2003). The CVT is carried out for constructing regions with similar signal-to-noise ratio. This implies that regions in the inner parts are also the smaller ones, whereas the outermost are the largest ones. For defining the regions or binning, the bluest band is selected (e. g. $F365W$ in ALHAMBRA), because it is usually the band with a lower signal-to-noise ratio.

iii) Determination of the stellar population parameters of each region. For each region in the spatially resolved galaxies, we retrieve the photometry in each band or image integrating the flux in each spatial bin, obtaining the SED of the different regions and uncertainties. Using MUFFIT and the SED obtained for each region, we retrieve the stellar population parameters via SED-fitting.

iv) Spatial distribution of the stellar population parameters: age, metallicity, and extinction. Once the stellar population parameters are determined, the study of their distribution across the galaxy can be done by the central pixel of each region or the distance from the central region of the galaxy. For instance, radial profiles of age, metallicity, and extinction can be derived from the results, although more complex 2D structures in galaxies can be explored as well. In fact, the effects of environment or asymmetries on the distributions of the stellar populations are able to be faced too.

It is worth mentioning that previously to the implementation in J-PLUS and J-PAS, all these techniques have been put to the test using 30 massive early-type galaxies from the ALHAMBRA survey as test bench (San Roman et al., in prep.) at $z < 0.3$ and out to 2–3.5 $R_{\rm eff}$. From the 2D results of ALHAMBRA, we highlight that the age gradients of early-type galaxies are on average flat ($\Delta \log_{10} {\rm Age_L} = 0.01 \pm 0.03$ dex $R_{\rm eff}^{-1}$), the metallicity ones are negative ($\Delta[{\rm M/H}]_{\rm L} = -0.10 \pm 0.09$ dex $R_{\rm eff}^{-1}$), and the extinction ones are also flat ($\Delta A_V = -0.04 \pm 0.09$ mag $R_{\rm eff}^{-1}$). All these results in good agreement with spectroscopic IFU results from CALIFA and MaNGA (González Delgado et al., 2014b, 2015; Goddard et al., 2017).

For illustrating, the 2D maps of stellar populations of NGC5485 and NGC3994 (see stamps in Fig. 9.3) obtained only using J-PLUS photometric data are shown in Figs. 9.4 and 9.5. It is worth mentioning that

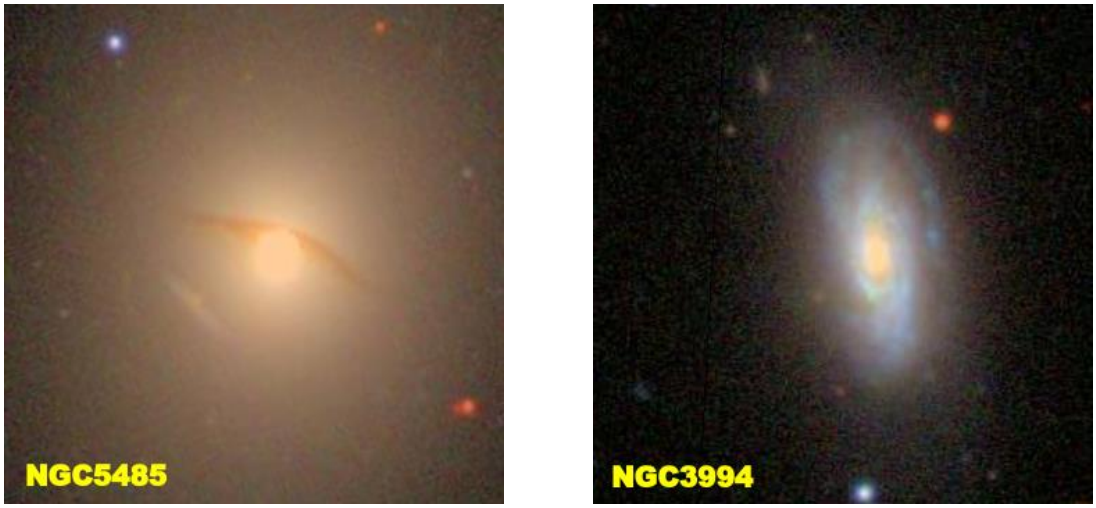

Figure 9.3: Stamps of the spatially-resolved galaxies NGC5485 (*left panel*) and NGC3994 (*right panel*). The stamps were obtained from the SDSS database (Eisenstein et al., 2011).

in the case of the early-type galaxy NGC5485, the presence of a dust lane is clear from the stamp visually. This dust lane is close to the bulge of the galaxy and it corresponds to a darker region of the galaxy (see Fig. 9.3). After applying all the steps detailed above, the regions of the dust lane successfully match with regions of high extinction after the analysis of their stellar populations using MUFFIT (see Fig. 9.4). This fact again reinforces the reliability of our results, and it allows us to properly retrieve the stellar populations below dust. In addition, the 2D distributions of age and metallicity do not present remarkable differences in the dust lane regions respect the surrounding ones, which support that the extinction is well constrained in these regions. Regarding the distributions of age and metallicity, NGC5485 presents flat and shallow age and metallicity gradients (see Fig. 9.4). The gradient of extinction is slightly negative (large extinction in the galactic nucleus). For the late-type galaxy NGC3994, a region close to the galactic center were masked owing to the presence of a low-ionization nuclear emission-line region (LINER). This LINER compromises the SED-fitting process, because AGN templates are not included in MUFFIT affecting various bands and the continuum. Moreover, the removal of those bands affected by emission lines would reduce the number of photometric bands drastically (30–40 %, J-PLUS is composed of 12 filters), where the contribution of the LINER in the continuum is also unknown. Consequently for now, this region is masked and it will be treated more carefully in the future. After masking the LINER, the metallicity and extinction gradients are negative (larger metallicities and extinctions at decreasing effective radii), whereas the age one is flat (see Fig. 9.5).

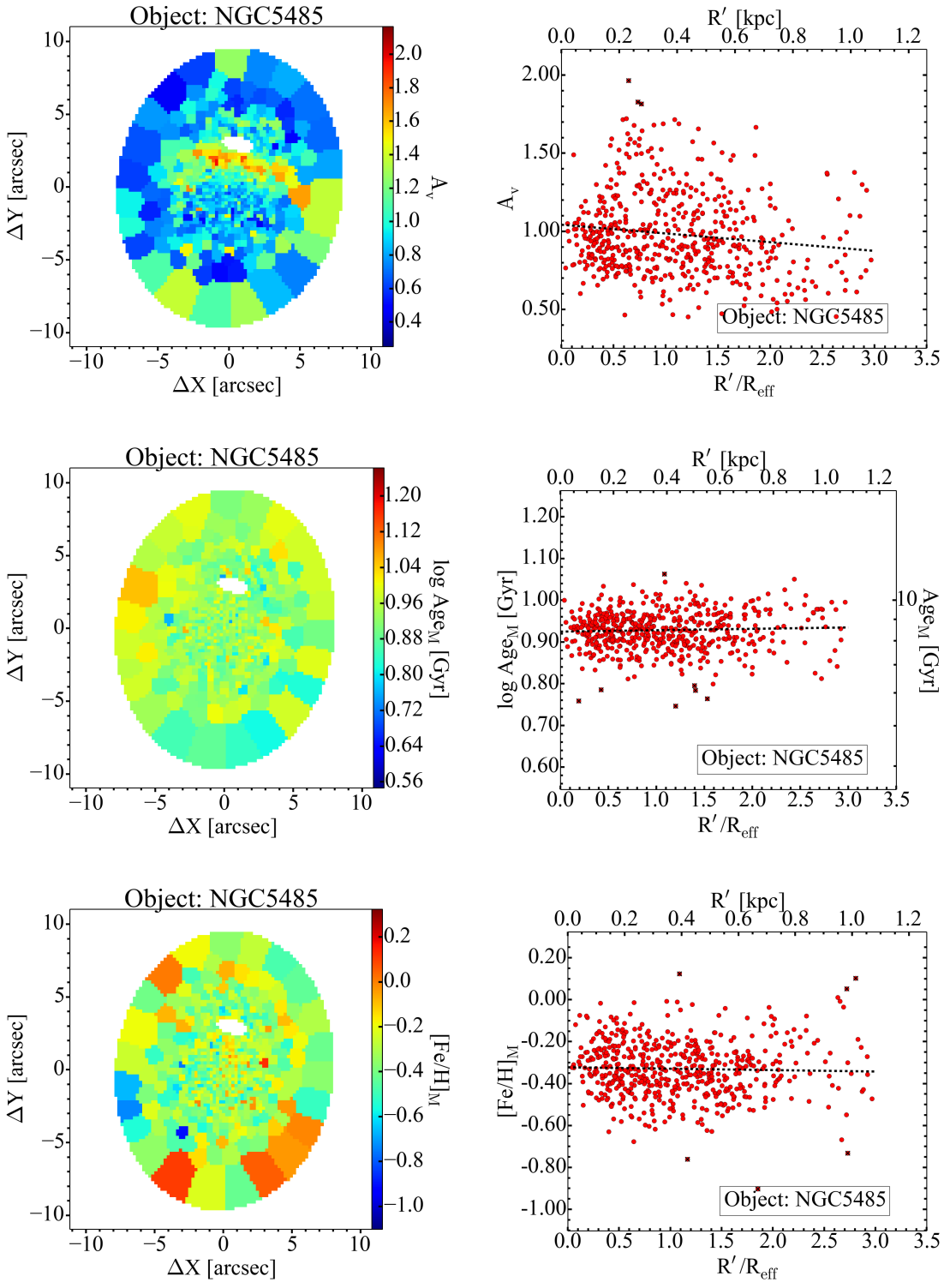

Figure 9.4: 2D distributions of extinction (*top panels*), mass-weighted age (*middle panels*) and metallicity (*bottom panels*) of the galaxy NGC5485 using EMILES+Padova00 SSP models. The 2D maps are plotted on the left-hand side (parameters colour coded depending of the stellar population parameter value, see colour bars), whereas the radial distributions or gradients are on the right-hand side (as a function of the circularized galactocentric distance R′). Each red dot illustrates a bin in the 2D map. Dashed black lines illustrate the error-weighted linear fittings of the red dots. Black crosses are the regions that were removed from the error-weighted linear fitting (sigma-clipping), in order to remove outliers.

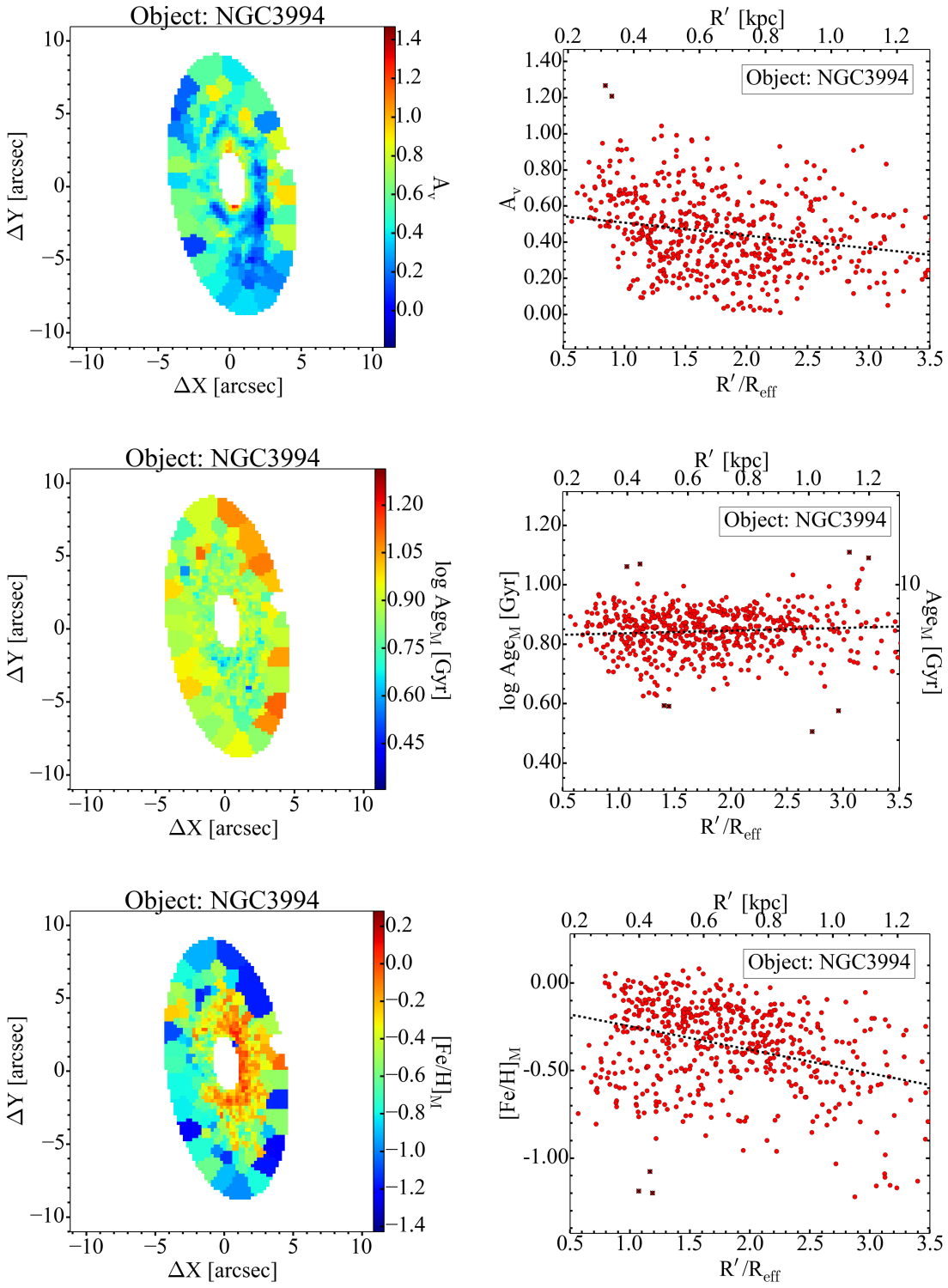

Figure 9.5: 2D distributions of extinction (*top panels*), mass-weighted age (*middle panels*) and metallicity (*bottom panels*) of the galaxy NGC3994 using EMILES+Padova00 SSP models. The 2D maps are plotted on the left-hand side (parameters colour coded depending of the stellar population parameter value, see colour bars), whereas the radial distributions or gradients are on the right-hand side (as a function of the circularized galactocentric distance R′). Each red dot illustrates a bin in the 2D map. Dashed black lines illustrate the error-weighted linear fittings of the red dots. Black crosses are the regions that were removed from the error-weighted linear fitting (sigma-clipping), in order to remove outliers.

Appendices

A

Detection and removal of faint stars in the quiescent sample

The performance of the MUFFIT module devoted to analysing stars is basically the same than for the galaxy version, excepting that instead of using mixture of SSP models it takes templates of stars to provide stellar parameters (effective temperature, metallicity, surface gravity, chemical composition, and extinction).

We ran the stellar version of MUFFIT with all the sources in the ALHAMBRA catalogue that present an apparent magnitude in the range $22.5 \leq m_{F814W} < 23$, using as input models the stellar library of Coelho et al. (2005) with the main grid of parameters: effective temperatures in steps of 250 K, $3500 \leq T_{\rm eff} \leq 7000$ K; surfaces gravities with steps of 0.5, $0.0 \leq \log_{10} \leq 5.0$; metallicities in the range [Fe/H] = −2.5 to +0.5; and chemical compositions $[\alpha/{\rm Fe}] = 0.0$ and 0.4. In addition, we added extinction values ranging $A_V = 0.0$–3.1 to the star models taking $R_V = 3.1$ and assuming a Fitzpatrick (1999) extinction law.

After the SED-fitting analysis and thanks to the Monte Carlo process performed by MUFFIT, we obtained two sets of χ^2 values for each source, one from the SED-fitting treating the source as a galaxy and another one as a star. Therefore, the χ^2 distribution with the lower values (the most likely set of templates, galaxy or star) will discern whether the source is a galaxy or not. Although this method takes advantage of the photometry in all the bands, all the sources show apparent magnitudes in the range $22.5 \leq m_{F814W} < 23$, with a reasonable low signal-to-noise ratio that makes the distinction between distributions more difficult in several cases. To solve this drawback, we carried out a KS test, that allowed us to discern whether both χ^2 distributions are different or not and what is the probability. We assume that a source in the range $22.5 \leq m_{F814W} < 23$ is a star if satisfies that: the median of χ^2 values (from the χ^2 distribution) is lower using star templates than SSP templates, and that the KS-test additionally shows that both distributions of χ^2 values (star and galaxy) are not equivalent at a significance level of 1 σ. Under these constraints, we got that in the redshift range $0.1 \leq z \leq 1.1$, there are 439 star candidates in the quiescent sample with $22.5 \leq m_{F814W} < 23$. Taking into account that there are 2 284 quiescent galaxies in our sample at the same magnitude and redshift bin before the faint star/galaxy classification, we have removed the $\sim$ 19 % of the sample at $22.5 \leq m_{F814W} < 23$. After removing all the faint star candidates in this magnitude range, our sample is composed of 13 796 quiescent galaxies.

To check whether the method developed for ALHAMBRA for removing stars in the range $22.5 \leq m_{F814W} < 23$ is reliable or not, we cross matched the ALHAMBRA and COSMOS photometric catalogues (Capak et al., 2007) to built a subset of shared sources in both surveys. Making the most of the ACS camera in COSMOS, we compared the stars or point sources detected in COSMOS and the ones by our method to estimate the degree of accuracy. There are 230 sources in common with our sample of quiescent candidates with apparent magnitudes $22.5 \leq m_{F814W} < 23$, in which we found out 50 star candidates with apparent magnitudes $22.5 \leq m_{F814W} < 23$ using the ALHAMBRA photometry and MUFFIT. From the star/galaxy classification of COSMOS (Leauthaud et al., 2007) in this subsample of 230 sources, we checked that 47 (94 %) of them are classified as point sources in COSMOS. Nevertheless, there are 9 stars that were not detected in the common subset with $22.5 \leq m_{F814W} < 23$ following the COSMOS classification, which

points out that there are about a 24 % of faint stars that should be removed. This means that in the case in which we can extrapolate these percentages from the subsample in common with COSMOS to our sample of quiescent galaxies in ALHAMBRA, we have removed 84 % of faint stars in ALHAMBRA, and that there are a contamination around 4 % of stars in our sample of quiescent galaxies at $22.5 \leq m_{F814W} < 23$; as long as the star/galaxy classification of COSMOS was assumed as the optimal star/galaxy classification.

Figures A.1 and A.2 illustrate two cases in the process of detection and removal of faint stars from the quiescent sample. In Fig. A.1, we exhibit an ALHAMBRA source at $m_{F814W} = 22.8$ that was classified as star with the methodology explained above and in agreement with the stellar classification of COSMOS. From its stamp in COSMOS (top left panel) is easy to see that this source is a point-like candidate, unfortunately in ALHAMBRA (top right), the size of the PSF masks this feature. The middle panel of Fig. A.1 presents a good perspective of the MUFFIT efficiency for removing red and faint stellar sources from the quiescent sample. The statistical support of the Monte Carlo approach, using the proper signal-to-noise ratio of each band, allows us to discern that this source is actually a star with a significance level of $\sim 2.5\,\sigma$ (98 %). Regarding the best-fitting stellar model (bottom panel of Fig. A.1), we observe that the optical range is well fitted by both Coelho et al. (2005, red markers) and BC03 (blue markers), but at the bluer and redder parts of the SED (black markers) a stellar model slightly fits better than a mixture of two SSPs. Note that for this case, there are no measurements in the m_{F365W}, m_{F396W}, and H bands owing to they are under their limit magnitudes. In Fig. A.2, we illustrate a red galaxy with $m_{F814W} = 22.7$ that was confirmed as galaxy by MUFFIT. Whilst in the COSMOS stamp this galaxy shows a remarkable and larger projected size, the ALHAMBRA PSF blurs the sources enough as to present a similar projected sizes than the stellar case (see top right panels in Figs. A.1 and A.2). Middle panel in Fig. A.2 shows a dominant set of lower χ^2 values, or best-fitting, of the mixture of two BC03 SSPs respect the stellar ones, which is clearly stated after comparing the galaxy SED with both best-fitting model predictions (bottom panel). Notice that two BC03 SSP models rather fit the whole spectral range of ALHAMBRA, fitting simultaneously UV, optical, and NIR; unlike Coelho et al. (2005) models.

The election of a $1\,\sigma$ significance level is a compromise between the percentage of stars that remain in the sample, or contaminants, and the galaxies that were removed mistakenly. Indeed, the significance level for the KS-test can be used as an estimator to remove stars from the sample. In this sense, if we relaxed the significance level toward lower values, we would be able to detect more faint stars, but we also would remove more fake stars that really are galaxies. Even though this drawback, notice that our SED-fitting analysis at a $1\,\sigma$ significance level made a substantial improvement in the faint end of the quiescent sample, where the contamination of faint stars were initially 24 % and now this is reduced up to 4 %, for which we have removed less than 1 % of galaxies in $22.5 \leq m_{F814W} < 23$ and much less in the total sample.

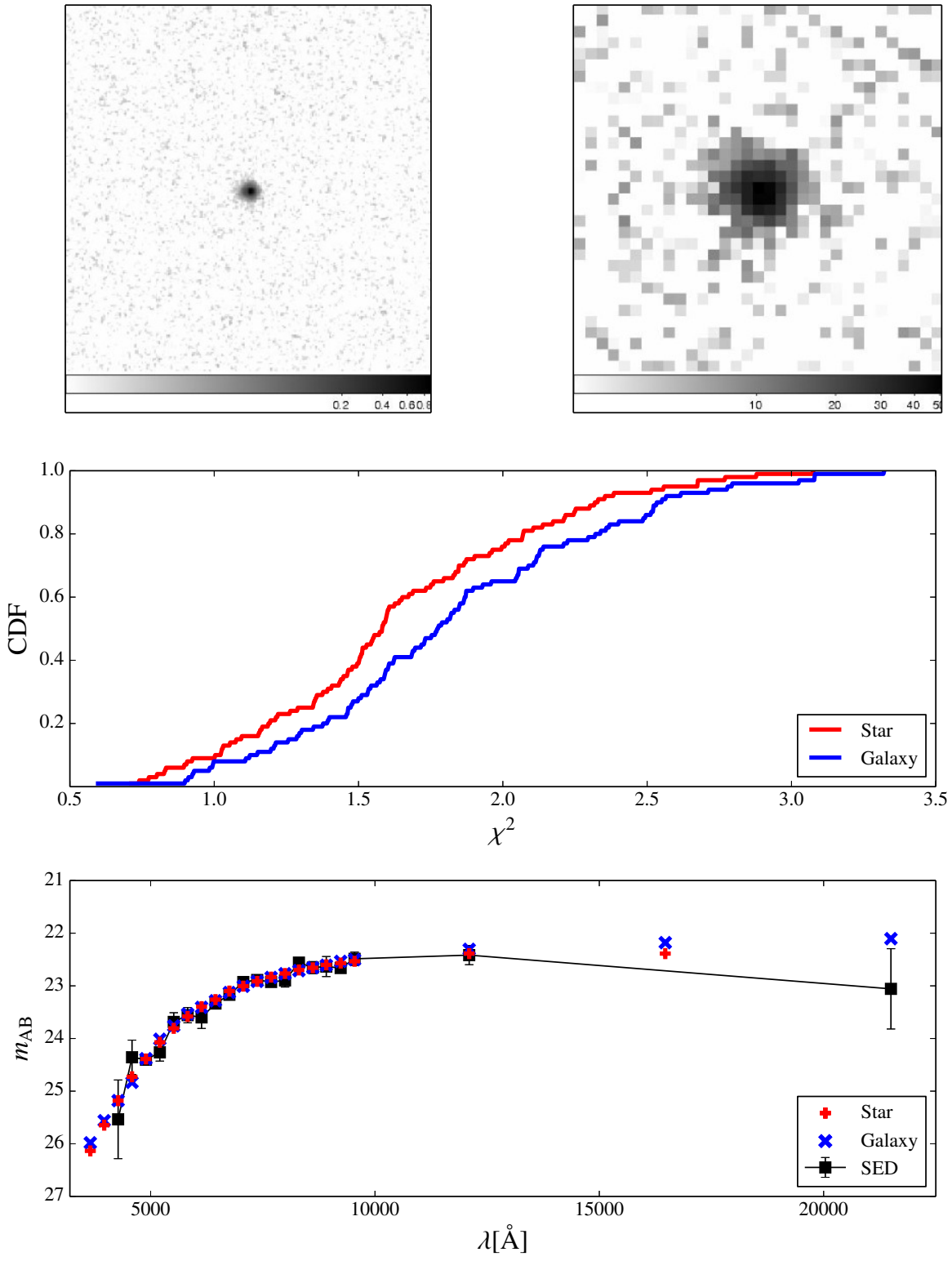

Figure A.1: Red source identified as faint star and removed from the ALHAMBRA quiescent sample. *Top left* and *top right panels*, stamps of the faint star candidate in COSMOS (ACS camera, pixel scale $0.03''$ pixel^{-1}) and ALHAMBRA (LAICA camera, resolution $0.22''$ pixel^{-1}) respectively, both stamps correspond to an aperture of $7'' \times 7''$. *Middle panel*, cumulative distribution function (CDF) of the χ^2 distributions obtained during the Monte Carlo process treating the source as an star (red) and as a galaxy (blue). *Bottom panel*, best-fitting Coelho et al. (2005) model (red) and mixture of two BC03 SSPs (blue) to the source photometry (black).

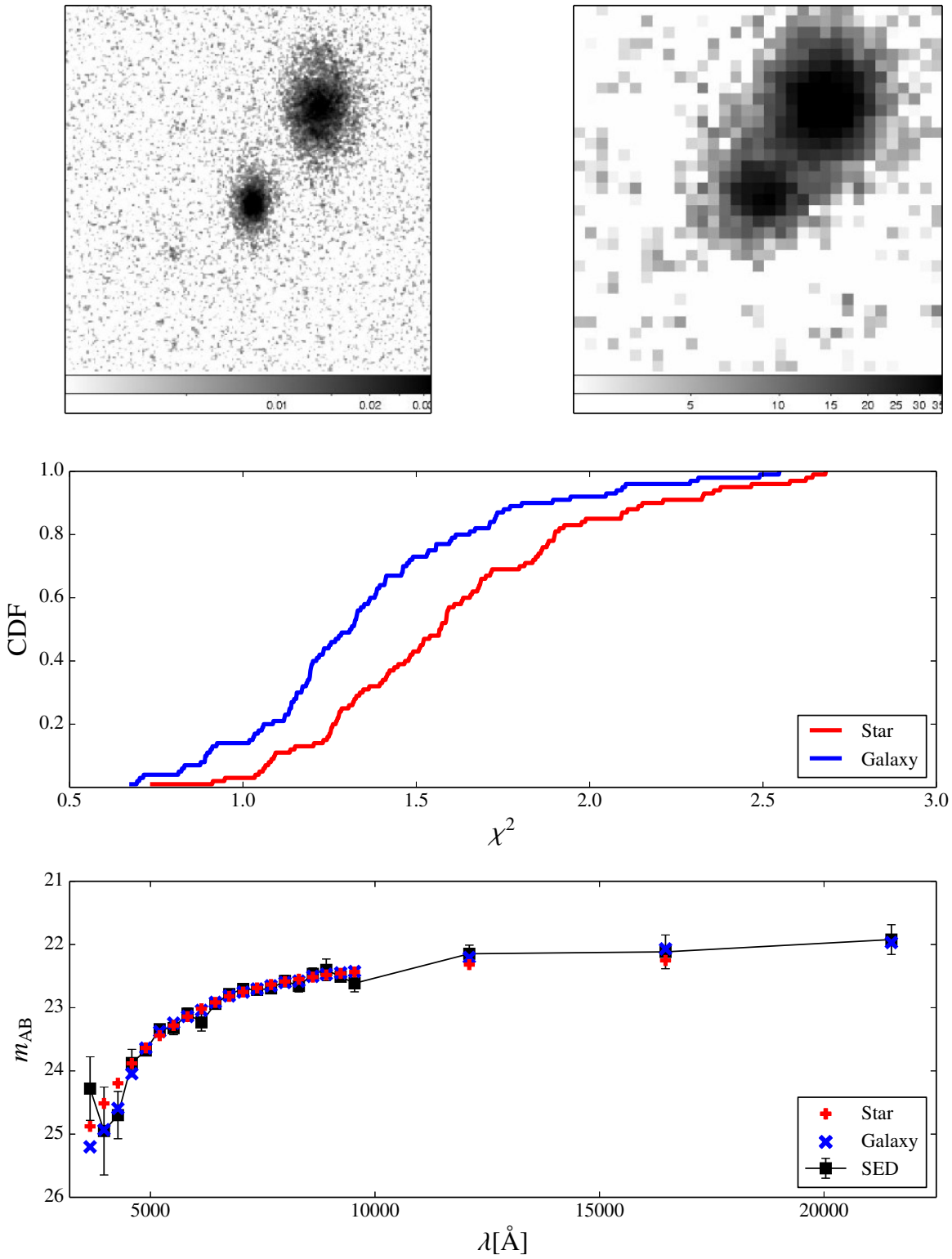

Figure A.2: As Fig. A.1, but for this case the source was not classified as red star, i. e. identified as galaxy, in the range $22.5 \leq m_{F814W} \leq 23.0$.

B

Stellar mass completeness determination

Our aim is to develop a method for parametrizing the stellar mass completeness of the ALHAMBRA galaxies, which must be applicable to the sample of quiescent galaxies in this work, and where this parametrization must be easily recomputed for any completeness level, C. Firstly, we explore the possibility of using a Fermi-Dirac like distribution function in order to model the stellar mass completeness in Appendix B.1, since this analytical function was already taken in previous works with satisfactory results (e. g. Sandage et al., 1979, although for magnitude completeness); along with a first approach to estimate the sets of mass completeness levels. Posteriorly in Appendix B.2, we detail the definitive method taken for this research to determine the stellar mass completeness of the quiescent sample.

B.1 Parametrization of the stellar mass completeness

The most natural way to estimate the stellar mass completeness of quiescent galaxies in this work (from the ALHAMBRA Gold catalogue) would be made the most of the full ALHAMBRA catalogue because of it is complete up to $m_{F814W} \sim 24.5$ (Molino et al., 2014), unlike the Gold catalogue that only comprises its bright part ($m_{F814W} \leq 23$). We also analysed all the galaxies in this deeper range with MUFFIT, seeking to estimate their stellar masses and rest-frame colours, the latter with the only purpose of extracting all the quiescent galaxies in the luminosity range $23 < m_{F814W} \leq 24$ (i. e. one magnitude deeper than our main sample for this research) following the selection criteria in Sect. 3.3. At this point, we likely estimated the percentage of galaxies we were missing after comparing the number of quiescent galaxies brighter than $m_{F814W} = 23$ with the total sample of quiescent galaxies down to $m_{F814W} = 24$ at different stellar mass and redshift bins. By this method, we estimated the bias introduced by the apparent magnitude selection ($m_{F814W} \leq 23$) over our quiescent galaxy sample.

Furthermore, our interest resides on parametrising the decay observed through any kind of function, and we tested a Fermi-Dirac distribution function for this goal. A Fermi-Dirac distribution function is formally expressed as

$$f_{\mathrm{FD}}(z, M_\star) = \frac{1}{\exp\left[(M_{\mathrm{F}}(z) - \log_{10} M_\star)/\Delta_{\mathrm{F}}(z)\right] + 1} \,, \tag{B.1}$$

where $M_{\mathrm{F}}(z)$ is the stellar mass value (in dex) for which the completeness reaches 50 % ($C = 0.5$) and $\Delta_{\mathrm{F}}(z)$ is related with the decrease rate on the number of galaxies. Note that both $M_{\mathrm{F}}(z)$ and $\Delta_{\mathrm{F}}(z)$ are redshift dependent. To check that the stellar mass completeness introduced by the apparent magnitude selection ($m_{F814W} \leq 23$) can be reproduced by this analytical function, we fitted the bias introduced by the apparent magnitude selection through a χ^2-test of Eq. B.1 and parameters $5 \leq M_{\mathrm{F}}(z) \leq 14$ and $0.02 \leq \Delta_{\mathrm{F}}(z) < 2$. In Fig. B.1 and for the redshift bin $0.4 \leq z < 0.5$, we show the stellar mass completeness ($m_{F814W} \leq 23$, solid blue line) and the Fermi-Dirac function that best fits it (dashed red line). We therefore confirm that this function fits properly the stellar mass completeness of our sample. The stellar mass value limit for a given

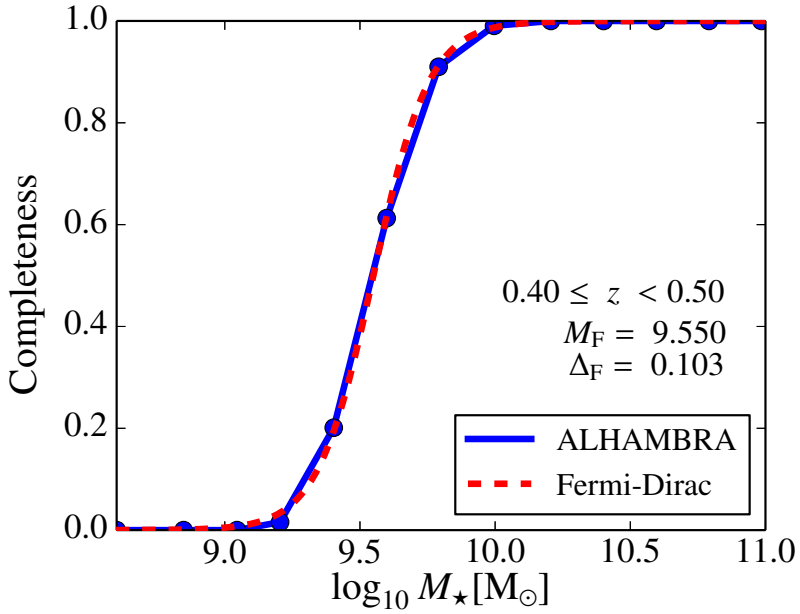

Figure B.1: Stellar mass completeness of the ALHAMBRA sample of quiescent galaxies complete in flux down to $m_{F814W} \leq 23$. In blue, we illustrate the values recovered by the method explained in Appendix B.1 at the redshift bin $0.4 \leq z < 0.5$. The red dashed line illustrates the Fermi-Dirac like function that best fits our results at this redshift range, along with the parameters ($M_{\rm F}$ and $\Delta_{\rm F}$) of the function.

completeness level and redshift, $M_C(z)$, can be easily derived from Eq. B.1 as

$$\log_{10} M_C(z) = \Delta_{\rm F}(z) \ln\left[(1 - C) - 1\right] + M_{\rm F}(z) \,. \tag{B.2}$$

Indeed, these results are a good estimation of the stellar mass completeness itself. Although it also presents a disadvantage or uncertainty, we do not know how much complete in stellar mass is the sample of galaxies at $23 < m_{F814W} \leq 24$, since we can only confirm that it is complete in apparent magnitude but not in stellar mass. This method may be a good approach for magnitudes around $m_{F814W} \sim 23$ and for large stellar mass completeness ($C \gtrsim 0.7$). For magnitudes closer to $m_{F814W} = 24$, the ALHAMBRA sample may also affected by incompleteness and the reliability of the predictions may be compromised. In Appendix B.2, we present an alternative and more general method, which is indeed the method used for this work.

B.2 Likelihood-maximisation method

We perform a more generic method that suppress the disadvantages noted above taking advantage of stellar mass functions, $\Phi(M)$, from deeper surveys. In particular, we took the stellar mass functions from the COSMOS survey for quiescent galaxies (Ilbert et al., 2010). We aim measuring how the low-mass end of the ALHAMBRA sample differs from much deeper surveys, where these differences are leaded by the mass incompleteness. In this second method, we followed a process similar to the work of Sandage et al. (1979, STY), that lies in a likelihood maximisation in which we include the completeness term. This likelihood $\mathcal{L}$ encompasses the probability of observing a galaxy accounting for both the selection and observational effects. Formally,

$$\ln \mathcal{L} = \sum_{i=1}^{N_{\rm g}} \frac{\Phi(M_i) f(M_i)}{\int_{M_{i,\rm min}}^{M_{i,\rm max}} \Phi(M') f(M') \, {\rm d}M'} \,, \tag{B.3}$$

where N_g is the number of galaxies in the sub-sample, $f(M_i)$ is the stellar mass completeness (Eq. B.1) for a galaxy with stellar mass M_i at certain redshift, $M_{i,\min}$ and $M_{i,\max}$ are respectively the minimum and maximum stellar mass at the redshift in which the galaxy ith resides, and $\Phi(M)$ is the stellar mass function characterised by the functional form of a Schechter-like function (Schechter, 1976) through three parameters (α, $\mathcal{M}_*$, and the normalisation Φ^*; see Fontana et al., 2004; Pérez-González et al., 2008; Vergani et al., 2008; Ilbert et al., 2010, 2013) expressed as:

$$\Phi(M)\,\mathrm{d}M = \Phi^* \left(\frac{M}{\mathcal{M}_*}\right)^{\alpha} \exp\left(-\frac{M}{\mathcal{M}_*}\right) \mathrm{d}\left(\frac{M}{\mathcal{M}_*}\right). \tag{B.4}$$

Notice that this likelihood must be re-maximised at each redshift bin of interest, but it is not necessary to define stellar mass bins. After fixing both α and $\mathcal{M}_*$ to the values obtained in Ilbert et al. (2010, the term Φ^* is not relevant because it is cancelled in Eq. B.3), the maximisation of Eq. B.3 provides us M_F and Δ_F.

Finally, we compare the values M_F and Δ_F obtained in Appendix B.1 with the values from the maximization of Eq. B.3 reaching a good agreement between both predictions. M_F and Δ_F present negligible discrepancies (< 0.1 dex and < 0.05 dex respectively) after comparing both techniques, where the reference values for the present work those obtained by the likelihood method. In Table 3.2, the values M_F and Δ_F are presented, as well as the stellar mass limits for different completeness levels for the quiescent galaxies in ALHAMBRA down to $m_{F814W} = 23$.

C

Distribution of stellar population parameters on the UVJ-diagram

Althought the LOESS methodology (bidimensional and locally weighted regression method to model the trends of our quiescent sample) is a non-novel and reliable statistical procedure to diminish the impact of uncertainties on the results. It is possible that this method might emulate a transition or tendency that is not real, because it builds a non-parametric model, by a surface in the present case, through subtle transitions using the average values in contiguous cells or bins. Even when the number of sources is very low and their uncertainties are large, the errors in the LOESS determination might drive unreliable predictions. As a sanity check, we studied the distribution of the stellar population parameters along the rest-frame colour map $m_{F365} - m_{F551}$ and $m_{F551} - J$ for both rest-frame colours and the intrinsic ones (corrected of dust effects, further details in Sect. 3.5), see Figs. C.1 and C.2. A preliminary visual inspection on these figures already reveals a clear tendency in the same sense that the obtained after running the LOESS methodology. Thereby, the LOESS methodology not only confirms this tendency after taking the uncertainties into account, it also constructs a subtle model that provides us the stellar population parameters for any couple of rest-frame colours $m_{F365} - m_{F551}$ and $m_{F551} - J$.

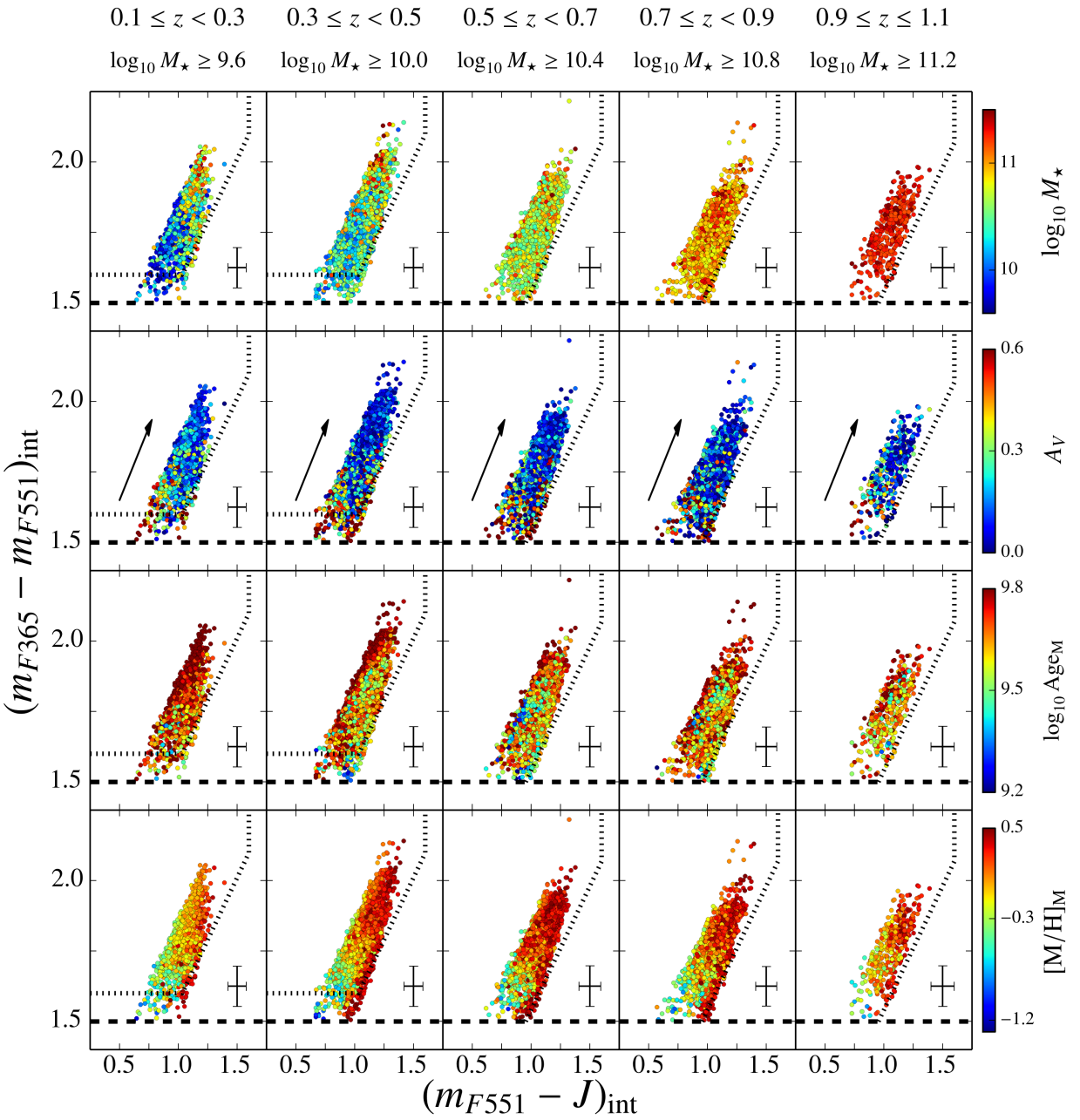

Figure C.1: The stellar-population parameters in the rest-frame UVJ-diagram. At different redshift bins, we present the intrinsic colours $(m_{F551} - J)_{\rm int}$ (X-axis) and $(m_{F365} - m_{F551})_{\rm int}$ (Y-axis) after correcting for extinction for the mass complete sample of quiescent galaxies (see stellar mass completeness on the top). The different stellar-population parameters are colour coded in function of their values, see the inset colour bars in each panel. *From top to bottom*, stellar mass, extinction, and both mass-weighted age and metallicity. Black crosses illustrate the median uncertainties in both $(m_{F551} - J)_{\rm int}$ and $(m_{F365} - m_{F551})_{\rm int}$ intrinsic colours. Dashed black line encloses the rest-frame colour ranges assumed for selecting quiescent galaxies in Moresco et al. (2013, see Eq. 3.1), while dotted line illustrates our colour limit for selecting quiescent galaxies $(m_{F365} - m_{F551})_{\rm int} > 1.5$. We illustrate the colour variations owing to a reddening of $A_V = 0.5$ (black arrow), assuming the extinction law of Fitzpatrick (1999).

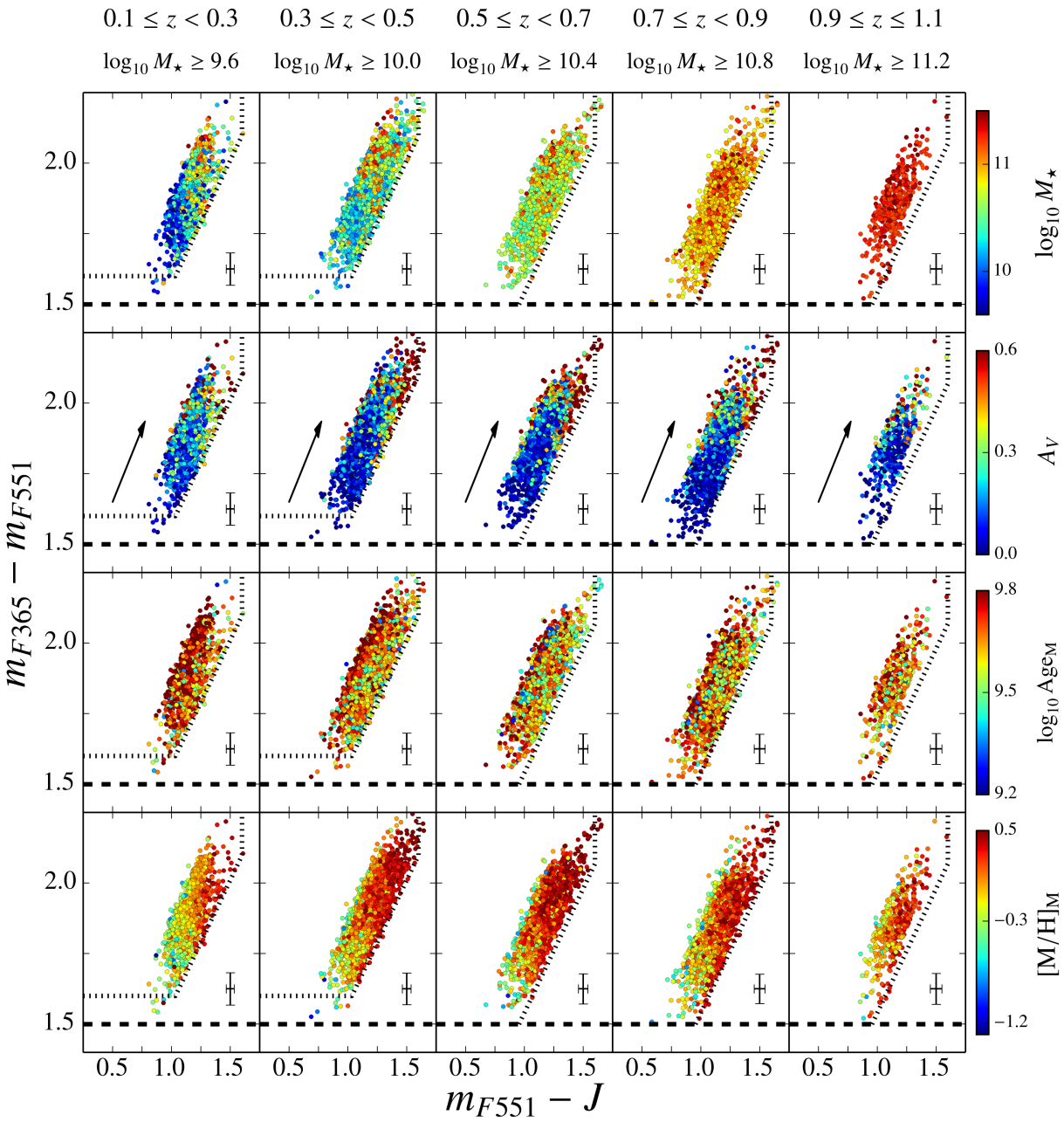

Figure C.2: As Fig. C.1, but we plot the rest-frame colours $m_{F551} - J$ (X-axis) and $m_{F365} - m_{F551}$ (Y-axis) instead.

D

Probability distribution functions of age, metallicity, and extinction: the MLE method

The MLE has been successfully used for different purposes in astronomy (e. g. Naylor & Jeffries, 2006; Makarov et al., 2006; Arzner et al., 2007; López-Sanjuan et al., 2008, 2015a) with statistically meaningful uncertainties to accounting for. In particular, we departed from the MLE methodology developed by López-Sanjuan et al. (2014, originally performed for removing cosmic variance effects) in order to adapt it to our requirements: deconvolution of uncertainty effects in the distributions of ages, metallicities, and extinctions of the quiescent population.

In the present MLE, we assumed that the distribution of stellar-population parameters of quiescent galaxies (age, metallicity, and extinction in this work) are correctly expressed by Gaussian-like probability distributions in the log-space (i. e. a log-normal distribution in the real space), and therefore the distribution shape is mainly parametrised by the mean, μ, and the standard deviation, $\sigma^{\rm int}$, of the distribution. Furthermore, these distributions are perturbed by observational errors, where the observed values differ from the real ones also following a Gaussian distribution. As our main goal is to describe how the quiescent galaxy population evolves since $z \leq 1.1$ (i. e. the evolution of the stellar-population distributions), we introduced in Eq. A.5 of López-Sanjuan et al. (2014) that μ and $\sigma^{\rm int}$ are redshift dependent: $\mu = \mu(z)$ and $\sigma^{\rm int} = \sigma^{\rm int}(z)$. In a general case $\mu(z)$ and $\sigma^{\rm int}(z)$ can adopt any functional form, although for simplicity we can assume linear or quadratic dependencies of the form: $\mu(z) = \mu_2 \times z^2 + \mu_1 \times z + \mu_0$ and $\sigma^{\rm int}(z) = \sigma_2 \times z^2 + \sigma_1 \times z + \sigma_0$. Thereby, instead of searching the two parameters μ and $\sigma^{\rm int}$ that maximizes the probability at different redshift bins, we derive the coefficients of the functional forms of $\mu(z)$ and $\sigma^{\rm int}(z)$ (for the above example μ_2, μ_1, μ_0, σ_2, σ_1, and σ_0) that maximize the likelihood for this work:

$$\mathcal{L}(p_j \,|\, \mu_p, \sigma_p^{\rm int}, p_{{\rm e},j}) = -\frac{1}{2} \sum_j \left[\ln\left({p_{{\rm e},j}}^2 + \sigma_p^{\rm int}(z)^2 \right) + \frac{\left(\mu_p(z) - p_j\right)^2}{{p_{{\rm e},j}}^2 + \sigma_p^{\rm int}(z)^2} \right] , \tag{D.1}$$

where p_j is the stellar-population parameter (age, metallicity, or extinction) of the jth galaxy in the sample, $p_{{\rm e},j}$ its uncertainty, z_j its photo redshift, $\mu_p(z)$ and $\sigma_p^{\rm int}(z)$ the mean and the standard deviation of the stellar-population parameter distribution without observational error effects.

The assumption of the redshift dependency favours the determination of μ_p and $\sigma_p^{\rm int}$ in those bins with a reduced number of galaxies, such as the most local and massive quiescent galaxies in this research, $0.1 \leq z < 0.3$ and $\log_{10} M_\star \geq 11.2$ dex, for which the number of galaxies is quite limited owing to the little volume sampled in the ALHAMBRA survey (see Table 3.3). Notice that the insertion of a redshift dependence also introduces a correlation with the rest of observational parameters p, since we are using photo z with an accuracy of $\sigma_z/(1+z) \leq 0.0053$ (see Sect. 3.3.5). Owing to the photo z is treated as another free parameter by MUFFIT in the bin provided by BPZ in the Gold catalogue, the parameters derived by MUFFIT includes the photo-z uncertainties naturally. In addition, Díaz-García et al. (2015) checked that the ALHAMBRA

photo-z accuracy presented negligible effects on the stellar population determination (age, metallicity and extinction uncertainties below 0.18 Gyr, 0.04 dex and 0.03 respectively for $\sigma_z/(1+z) \leq 0.009$), and we therefore neglect any correlation with redshift, which preserves Eq. D.1 analytical as well. Furthermore, the dynamical range of redshift for this work ($0.1 \leq z \leq 1.1$) is much larger than the photo-z uncertainties, i. e. $\sigma_z << z_{\rm max} - z_{\rm min}$.

The process of maximization of Eq. D.1 was carried out by the `Python` implementation EMCEE[1] (Foreman-Mackey et al., 2013), an affine invariant sampling algorithm for a Markov chain Monte Carlo method (MCMC), which also provides uncertainties and correlations for the parameters that maximize such equation. Consequently, the MLE for this research is equivalent to deconvolve the observational errors from our desired stellar-population distributions, or at least to minimize their effects. Figure D.1 illustrates a MLE deconvolution for the subsample of 1480 quiescent galaxies at $0.7 \leq z < 0.9$ and $10.8 \leq \log_{10} M_\star < 11.2$ dex (BC03 SSP models), in which we assume that there is no a redshift dependency of $\mu(z)$ and $\sigma^{\rm int}(z)$ (i. e. $\mu_2 = \mu_1 = \sigma_2 = \sigma_1 = 0$; μ_0 and σ_0 provide the average values in the bin). The histograms of the observed stellar-population parameters (thin line; age, metallicity, and extinction) are fitted by a log-normal distribution correctly (dashed line, before removing observational errors), supporting our initial assumption. After running the MLE, we rebuild the probability function of ages, metallicities and extinctions (solid line), in which we reduced or deconvolved the noise effects of the observed distributions (thin line). As expected, the main effect of observational errors is the increment of the width of the distributions, but also there exist slight shifts in the medians of the distributions. The parameters μ and $\sigma^{\rm int}$ of Fig. D.1 also present negligible correlations, which were derived from EMCEE, as shown by Fig. D.2.

Finally, we normalised the log-normal distributions of all stellar-population parameters to the fitted number densities of Sect. 3.6 (see Table 3.5). This allow us to provide PDFs of age, metallicity, and extinctions for the quiescent galaxy population for the first time, that can be easily recomputed for any redshift. Due to the nature of the parameters, the analytical form of the PDF of age, metallicity, and extinction are formally expressed as

$$\mathrm{PDF}(\mathrm{Age}, z, M_\star) = \frac{\rho_{\rm N}(z, M_\star)}{\sqrt{2\pi}\ \mathrm{Age}\ \sigma^{\rm int}_{\rm Age}(z, M_\star)} \times \exp\left[-\frac{\left(\ln \mathrm{Age} - \mu_{\rm Age}(z, M_\star)\right)^2}{2\sigma^{\rm int}_{\rm Age}(z, M_\star)^2}\right], \tag{D.2}$$

$$\mathrm{PDF}([\mathrm{M/H}], z, M_\star) = \frac{\rho_{\rm N}(z, M_\star)}{\sqrt{2\pi}\ (1 - [\mathrm{M/H}])\ \sigma^{\rm int}_{[\mathrm{M/H}]}(z, M_\star)} \times \\ \times \exp\left[-\frac{(\ln\{1 - [\mathrm{M/H}]\} - \mu_{[\mathrm{M/H}]}(z, M_\star))^2}{2\sigma^{\rm int}_{[\mathrm{M/H}]}(z, M_\star)^2}\right], \tag{D.3}$$

$$\mathrm{PDF}(A_V, z, M_\star) = \frac{\rho_{\rm N}(z, M_\star)}{\sqrt{2\pi}\ A_V\ \sigma^{\rm int}_{A_V}(z, M_\star)} \times \exp\left[-\frac{(\ln A_V - \mu_{A_V}(z, M_\star))^2}{2\sigma^{\rm int}_{A_V}(z, M_\star)^2}\right]. \tag{D.4}$$

From these definitions, the medians and widths, ω, of age, metallicity, and extinction are expressed as:

$$\mathrm{Age}^{\rm 50th}(z, M_\star) = \exp\left\{\mu_{\rm Age}(z, M_\star)\right\}, \tag{D.5}$$

$$A_V^{\rm 50th}(z, M_\star) = \exp\left\{\mu_{A_V}(z, M_\star)\right\}, \tag{D.6}$$

$$[\mathrm{M/H}]^{\rm 50th}(z, M_\star) = 1 - \exp\left\{\mu_{[\mathrm{M/H}]}(z, M_\star)\right\}, \tag{D.7}$$

$$\omega_p(z, M_\star) = \exp\left\{\mu_p(z, M_\star) + \sigma^{\rm int}_p(z, M_\star)\right\} - \exp\left\{\mu_p(z, M_\star) - \sigma^{\rm int}_p(z, M_\star)\right\}, \tag{D.8}$$

where the superscript 50th denotes median and p refers to age, metallicity, and extinction.

[1] http://dan.iel.fm/emcee

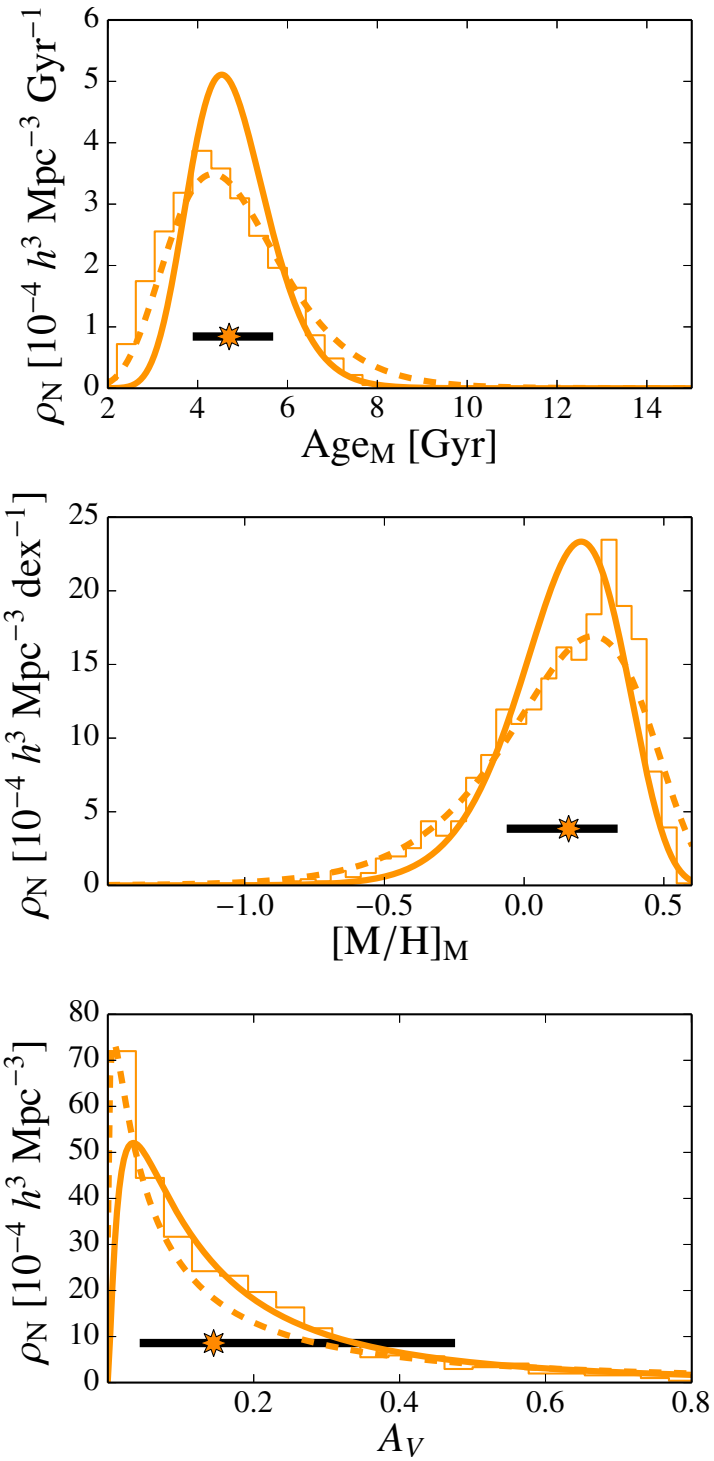

Figure D.1: Histograms of stellar-population parameters (thin line, derived using BC03 SSP models) of the 1480 quiescent galaxies with stellar mass $10.8 \leq \log_{10} M_\star < 11.2$ dex and at redshift $0.7 \leq z < 0.9$. *From top to bottom*, mass-weighted age, mass-weighted metallicity, and extinction. The dashed line is the distribution fit, whereas the orange solid line is the parameter distributions after applying the MLE method for diminishing individual uncertainty effects (further details in the text). The star-shape marker and the solid black line illustrate the median and the 1 σ width of the distributions respectively. All the curves were normalised to the fitted number density (see Sect. 3.6 and Table 3.5).

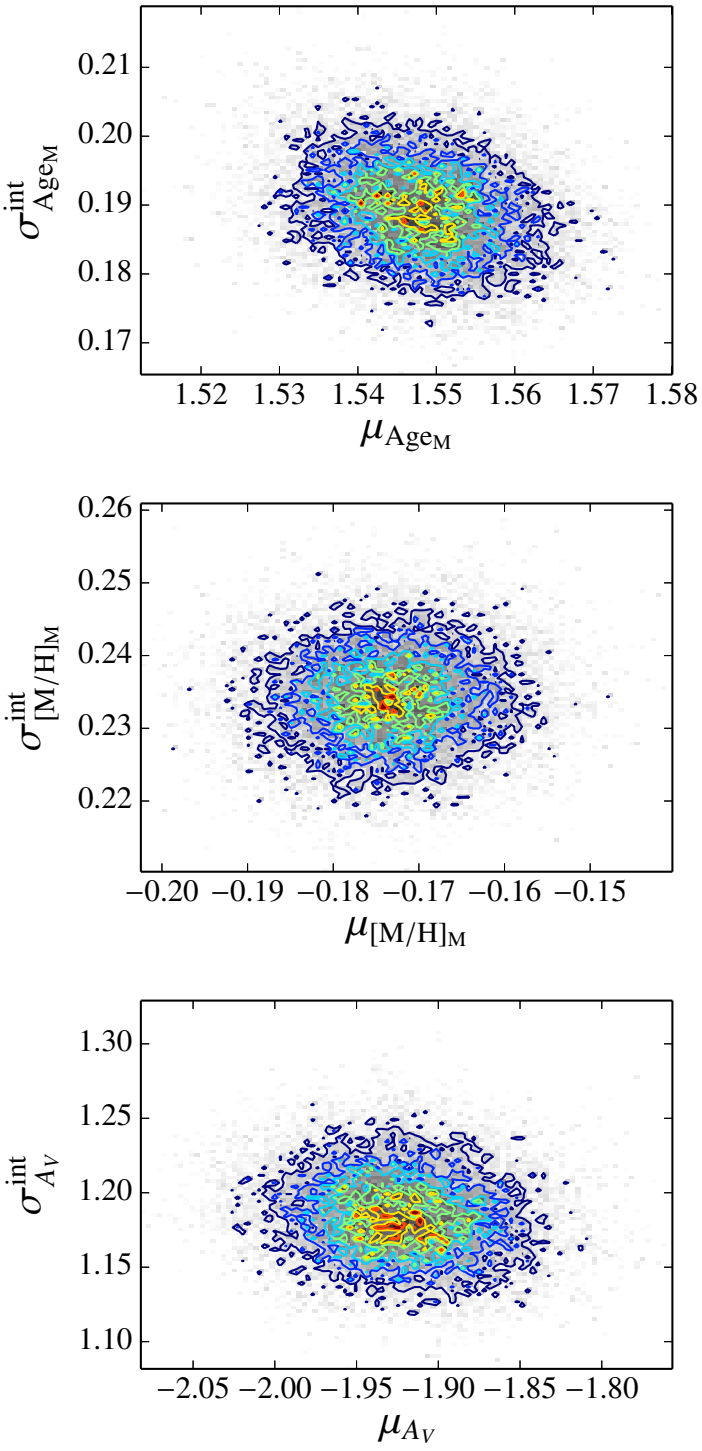

Figure D.2: *From top to bottom*, correlations between μ and $\sigma^{\rm int}$ for age, metallicity, and extinction of the 1480 quiescent galaxies with stellar mass $10.8 \leq \log_{10} M_\star < 11.2$ dex and at redshift $0.7 \leq z < 0.9$ (see also Fig. D.1). Redder colours are related to higher densities, whereas bluer ones to lower densities.

As previously commented in Sect. 3.8, we simultaneously analyse the distribution of stellar population parameters of quiescent galaxies using three sets of SSP models: BC03, and the two isochrone sets of EMILES (BaSTI and Padova00, details in Sect. 3.2.1). As these SSP sets can provide different diagnostics of stellar-population distributions, we provide their error deconvolution by the MLE methodology described in this appendix or stellar population PDFs. Below, the formation epoch, age, metallicity and extinction PDFs for the ALHAMBRA quiescent galaxies are presented in Appendix D.1, Appendix D.2, and Appendix D.3 for BC03, EMILES+BaSTI isochrones, and EMILES+Padova00 isochrones SSP models respectively.

D.1 Stellar-population PDFs of the ALHAMBRA quiescent galaxies: BC03 SSP models

For BC03 SSP models, we adopted a linear dependency for ages and extinctions (i. e. $\mu_2 = \sigma_2 = 0$) and a quadratic one for metallicity. Notice that the dependence with stellar mass was treated running the MLE at different stellar mass ranges in which our sample is complete. Only for the mass range $10.0 \leq \log_{10} M_\star < 10.4$ and the metallicity case, we impose $\sigma_2 = 0$ because a linear dependency of $\sigma^{\rm int}(z)$ is enough for this case, and it helps to limit the degrees of freedom in the maximization of Eq. D.1. In order to check the feasibility of these assumptions, we compare the $\mu(z)$ and $\sigma^{\rm int}(z)$ curves obtained after carrying out the MLE method, in the redshift range in which the sample is complete, with those values obtained after setting $\mu_2 = \mu_1 = \sigma_2 = \sigma_1 = 0$ in narrower redshift bins of $\Delta z = 0.2$ (i. e. the average $\mu(z)$ and $\sigma^{\rm int}(z)$ in narrow enough redshift bins). As a result, we observe that the linear and quadratic assumptions are fairly suitable in each case (see Fig D.3). All the parameters and uncertainties obtained after the maximization of Eq. D.1, and that are necessary to build the stellar population PDFs (Eqs. D.2–D.4) retrieved using BC03 SSP models, are provided in Tables D.1–D.3. The parameters to compute the number densities for the PDF normalization at any redshift are in Table 3.5 (details in Sect. 3.6). It is worth mentioning that for higher redshifts than the limits of our sample ($0.1 \leq z \leq 1.1$, see Table 3.2 and Fig. 3.2, or Sect. 3.3.4 for further details), these parameters are extrapolations of our quiescent sample and its reliability may be questionable. Indeed, we cannot confirm whether a linear or quadratic functional form of $\mu(z)$ and $\sigma^{\rm int}(z)$ is still reliable further than the limits of the present sample.

Owing to the low number of galaxies in the stellar mass range $9.6 \leq \log_{10} M_\star < 10.0$, the reliability of the results provided by the MLE method detailed above is compromised, and therefore, we do not provide their redshift-dependent PDF parameters. Although we set reference values of their average medians and widths in the redshift bin $0.1 \leq z < 0.3$ running the MLE method with $\mu_2 = \mu_1 = \sigma_2 = \sigma_1 = 0$ (see values in Tables 3.7–3.9). In addition, below $0.1 \leq z < 0.2$ and $\log_{10} M_\star \geq 11.2$, the assumption of linearity for $\sigma^{\rm int}(z)$ in the extinction case is mathematically motivated, but physically it is too strict since it rapidly converges to $\sigma^{\rm int}(z = 0.1) \sim 0.0$. Actually our sample $\sigma^{\rm int}(z)$ and $\mu(z)$ extinction converge to a constant value further than $z < 0.2$. Consequently, only for quiescent galaxies at $0.1 \leq z < 0.2$ and $\log_{10} M_\star \geq 11.2$, we impose $\sigma^{\rm int}(0.1 \leq z < 0.2) = \sigma^{\rm int}(z = 0.2) = 0.14 \pm 0.03$ and $\mu(0.1 \leq z < 0.2) = \mu(z = 0.2) = -1.29 \pm 0.09$. Finally, notice that for the lowest extinction values in Eq. D.4 ($A_V \sim 0$), the probability might be underestimated because the log-normal function falls to zero at this regime of values.

The analysis of these stellar populations is faced in Sect.3.7.

D.2 Stellar-population PDFs of the ALHAMBRA quiescent galaxies: EMILES and BaSTI isochrones

For EMILES SSP models and BaSTI theoretical isochrones, we also carried out the MLE methodology with the distributions of age, formation epoch, metallicity and extinction retrieved for the complete in mass sample of quiescent galaxies in ALHAMBRA. Although the trends are qualitatively similar to the obtained in Appendix D.1, there are quantitative discrepancies between both sets of SSP models. For age, formation

epoch and extinction distributions, a linear dependency with redshift is assumed for $\mu(z)$ and $\sigma^{\rm int}(z)$, i. e. $\mu_2 = \sigma_2 = 0$. As in Appendix D.1 and from Fig. D.4, the assumption of linearity for $\mu(z)$ and $\sigma^{\rm int}(z)$ is supported after comparing with the MLE solutions retrieved when $\mu 2 = \mu 1 = \sigma_2 = \sigma_1 = 0$ (see square markers in Fig. D.4) at redshift bins of $\Delta z = 0.2$ in the range $0.1 \leq z \leq 1.1$, that is, in narrow redshift bins in order to split the redshift dependency of $\mu(z)$ and $\sigma^{\rm int}(z)$. Nevertheless, it is remarkable that for BaSTI isochrones we appreciate a decrement of the median of the metallicity PDF too, although the assumption of a quadratic form for $\mu(z)$ and $\sigma^{\rm int}(z)$ is not further necessary for the metallicity PDF case. From Fig. D.4, the metallicity PDFs are fairly parametrised with a linear dependency with redshift for $\mu(z)$ and $\sigma^{\rm int}(z)$ at $0.1 \leq z \leq 1.1$. The parameters and uncertainties obtained after deconvolving the stellar population parameters, provided by MUFFIT using EMILES+BaSTI isochrones, that are necessary to build the stellar population PDFs (Eqs. D.2–D.4) of quiescent galaxies in ALHAMBRA, are provided in Tables D.4–D.6. Again, the normalization of these PDFs must matches with the quiescent number densities provided in Sect. 3.6.

As in the section above, the low number of galaxies with stellar mass $9.6 \leq \log_{10} M_\star < 10.0$ at $0.1 \leq z \leq 0.3$ made that we removed this bin from the redshift MLE analysis. Instead, we ran it forcing $\mu 2 = \mu 1 = \sigma_2 = \sigma_1 = 0$ in order to obtain reference and average values for this stellar mass range. For the complete analysis of the stellar-population distributions and implications, we refer readers to Sect. 3.8.

D.3 Stellar-population PDFs of the ALHAMBRA quiescent galaxies: EMILES and Padova00 isochrones

For Padova00 isochrones, we only appreciate mild quantitative variations respect the BaSTI ones. As above in Appendix D.2, we repeated the same process and assumed a linear dependency for $\mu(z)$ and $\sigma^{\rm int}(z)$ for all the stellar-population parameters in the MLE process, see Fig. D.5. The parameters of the stellar-population PDF (see Eqs. D.2–D.4) for quiescent galaxies are presented in Tables D.7–D.9, along with their uncertainties, in the redshift range $0.1 \leq z \leq 1.1$. As mentioned above, further than these redshift limits any result is an extrapolation of the results and the linear assumption may be compromised.

For those quiescent galaxies with stellar mass $9.6 \leq \log_{10} M_\star < 10.0$ (restricted by completeness reasons at $0.1 \leq z \leq 0.3$), we provide reference values for its stellar population PDF assuming $\mu 2 = \mu 1 = \sigma_2 = \sigma_1 = 0$ (see Sect. 3.8). A more detailed study of the stellar populations retrieved using EMILES and Padova00 isochrones is performed in Sect. 3.8.

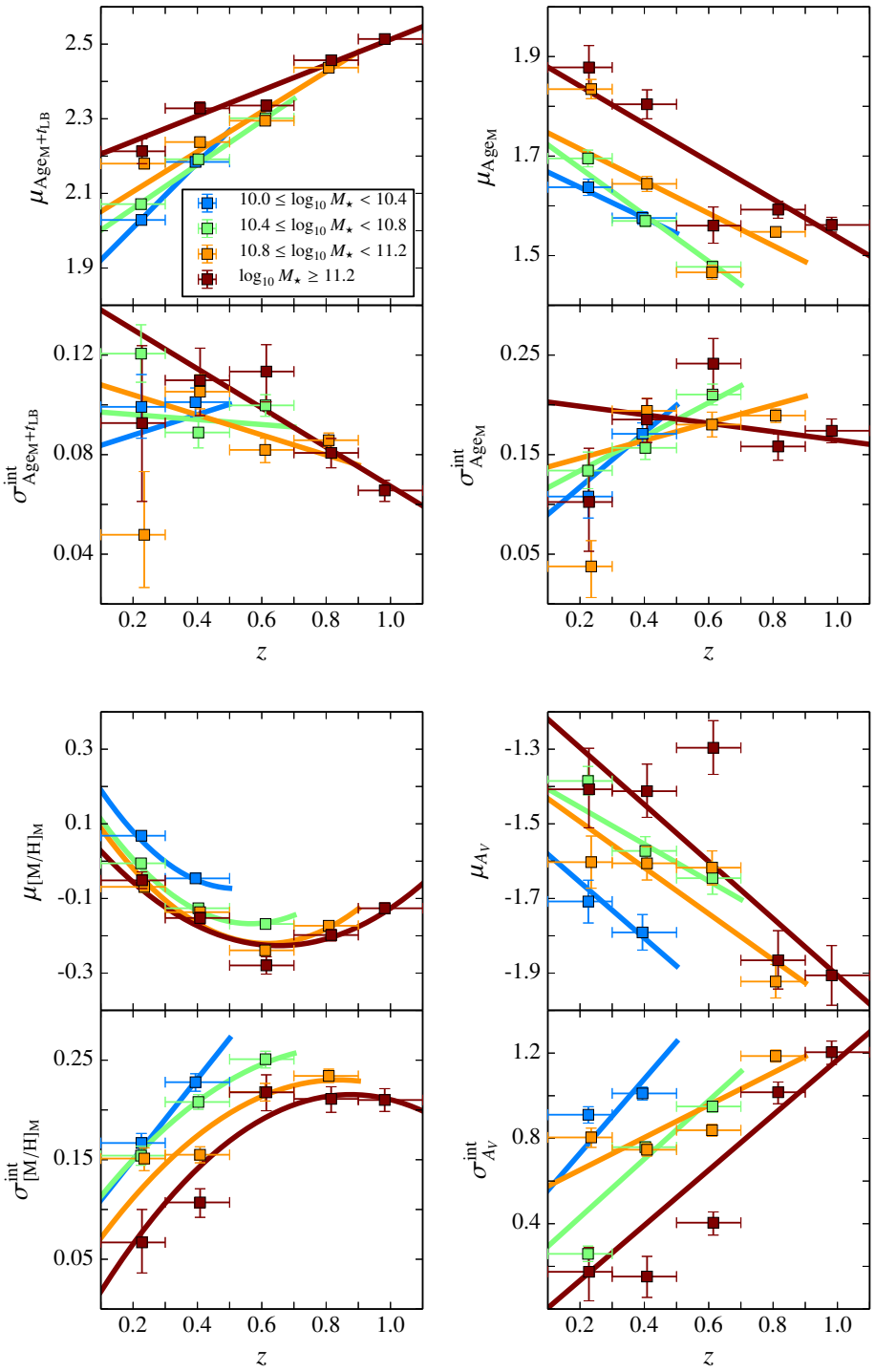

Figure D.3: The formation epoch (*top left*), age (*top right*), metallicity (*bottom left*), and extinction (*bottom right*) PDF parameters μ and σ^{int} of the quiescent galaxy population at different redshifts using BC03 SSP models. Solid lines correspond to the assumption of linear (formation epoch, age, and extinction) and quadratic functions (metallicity) for $\mu(z)$ and $\sigma^{\mathrm{int}}(z)$ at different stellar mass ranges; whereas square-shape markers are the average values for these parameters assuming a non-redshift dependency (i. e. $\mu_2 = \mu_1 = \sigma_2 = \sigma_1 = 0$) in redshift bins of $\Delta z = 0.2$. Horizontal bars delimit the redshift range in which the averaged values were computed, while vertical bars enclose the 1 σ confidence level.

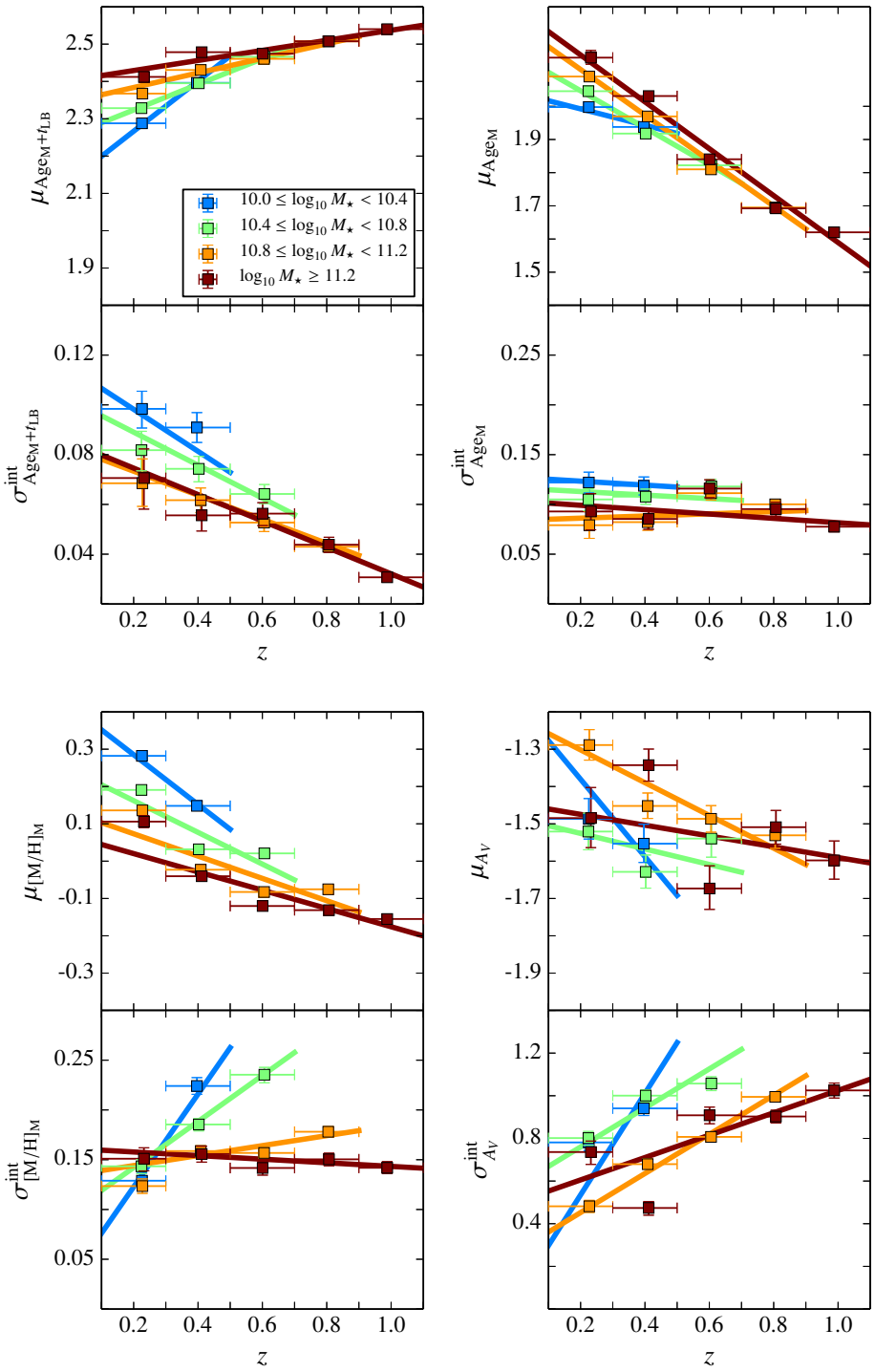

Figure D.4: The formation epoch (*top left*), age (*top right*), metallicity (*bottom left*), and extinction (*bottom right*) PDF parameters μ and σ^{int} of the quiescent galaxy population at different redshifts using EMILES SSP models and BaSTI isochrones. Solid lines correspond to the assumption of linear (formation epoch, age, and extinction) and quadratic functions (metallicity) for $\mu(z)$ and $\sigma^{\mathrm{int}}(z)$ at different stellar mass ranges; whereas square-shape markers are the average values for these parameters assuming a non-redshift dependency (i. e. $\mu_2 = \mu_1 = \sigma_2 = \sigma_1 = 0$) in redshift bins of $\Delta z = 0.2$. Horizontal bars delimit the redshift range in which the averaged values were computed, while vertical bars enclose the 1 σ confidence level.

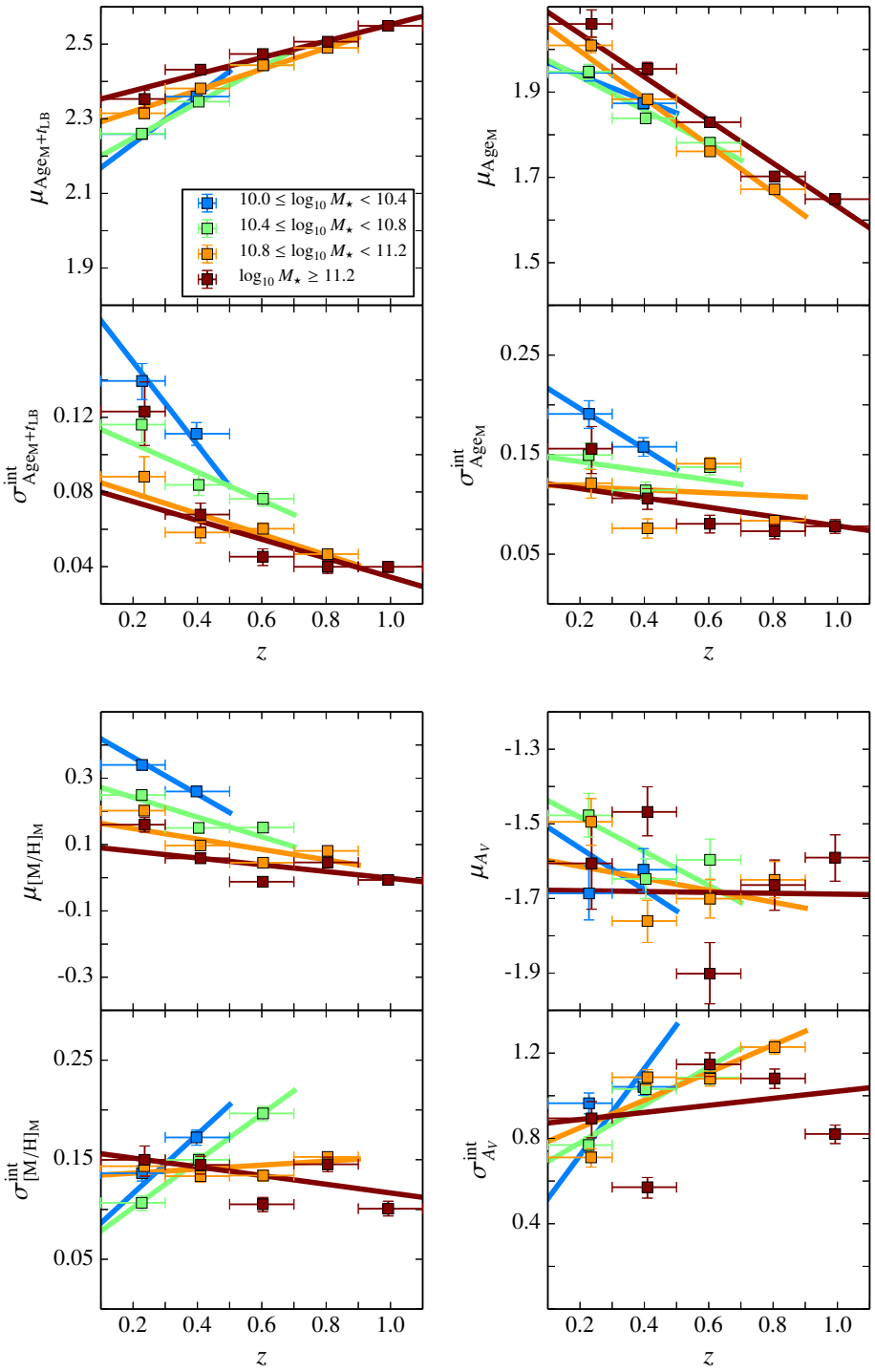

Figure D.5: The formation epoch (*top left*), age (*top right*), metallicity (*bottom left*), and extinction (*bottom right*) PDF parameters μ and σ^{int} of the quiescent galaxy population at different redshifts using EMILES SSP models and Padova00 isochrones. Solid lines correspond to the assumption of linear (formation epoch, age, and extinction) and quadratic functions (metallicity) for $\mu(z)$ and $\sigma^{\mathrm{int}}(z)$ at different stellar mass ranges; whereas square-shape markers are the average values for these parameters assuming a non-redshift dependency (i. e. $\mu_2 = \mu_1 = \sigma_2 = \sigma_1 = 0$) in redshift bins of $\Delta z = 0.2$. Horizontal bars delimit the redshift range in which the averaged values were computed, while vertical bars enclose the 1 σ confidence level.

Table D.1: Parameters $\mu(z, M_\star)$ and $\sigma^{\rm int}(z, M_\star)$ of the probability distribution functions of luminosity and mass-weighted ages and formation epochs (see Eq. D.2), which were derived using BC03 SSP models.

$\mathrm{Age_L}$ [Gyr]	$N_{\rm gal}$	$\mu_{\mathrm{Age_L}}$		$\sigma^{\rm int}_{\mathrm{Age_L}}$	
		μ_1	μ_0	σ_1	σ_0
$10.0 \leq \log_{10} M_\star < 10.4$	1429	$-0.64^{+0.09}_{-0.09}$	$1.57^{+0.03}_{-0.03}$	$0.33^{+0.10}_{-0.09}$	$0.08^{+0.03}_{-0.03}$
$10.4 \leq \log_{10} M_\star < 10.8$	2526	$-0.64^{+0.04}_{-0.04}$	$1.59^{+0.02}_{-0.02}$	$0.32^{+0.05}_{-0.04}$	$0.05^{+0.02}_{-0.02}$
$10.8 \leq \log_{10} M_\star < 11.2$	3181	$-0.37^{+0.03}_{-0.03}$	$1.54^{+0.02}_{-0.02}$	$0.17^{+0.03}_{-0.03}$	$0.11^{+0.02}_{-0.02}$
$\log_{10} M_\star \geq 11.2$	1122	$-0.34^{+0.04}_{-0.05}$	$1.62^{+0.04}_{-0.04}$	$0.02^{+0.04}_{-0.04}$	$0.20^{+0.03}_{-0.03}$
$\mathrm{Age_M}$ [Gyr]	$N_{\rm gal}$	$\mu_{\mathrm{Age_M}}$		$\sigma^{\rm int}_{\mathrm{Age_M}}$	
		μ_1	μ_0	σ_1	σ_0
$10.0 \leq \log_{10} M_\star < 10.4$	1429	$-0.31^{+0.10}_{-0.09}$	$1.70^{+0.03}_{-0.03}$	$0.27^{+0.11}_{-0.10}$	$0.06^{+0.04}_{-0.04}$
$10.4 \leq \log_{10} M_\star < 10.8$	2526	$-0.47^{+0.04}_{-0.05}$	$1.77^{+0.02}_{-0.02}$	$0.17^{+0.04}_{-0.04}$	$0.10^{+0.02}_{-0.02}$
$10.8 \leq \log_{10} M_\star < 11.2$	3181	$-0.33^{+0.03}_{-0.03}$	$1.78^{+0.02}_{-0.02}$	$0.09^{+0.03}_{-0.03}$	$0.13^{+0.02}_{-0.02}$
$\log_{10} M_\star \geq 11.2$	1122	$-0.38^{+0.04}_{-0.04}$	$1.92^{+0.04}_{-0.04}$	$-0.04^{+0.04}_{-0.03}$	$0.21^{+0.03}_{-0.03}$
$\mathrm{Age_L} + t_{\rm LB}$ [Gyr]	$N_{\rm gal}$	$\mu_{\mathrm{Age_L}+t_{\rm LB}}$		$\sigma^{\rm int}_{\mathrm{Age_L}+t_{\rm LB}}$	
		μ_1	μ_0	σ_1	σ_0
$10.0 \leq \log_{10} M_\star < 10.4$	1429	$0.88^{+0.05}_{-0.05}$	$1.70^{+0.02}_{-0.02}$	$-0.01^{+0.05}_{-0.05}$	$0.10^{+0.02}_{-0.02}$
$10.4 \leq \log_{10} M_\star < 10.8$	2526	$0.68^{+0.02}_{-0.02}$	$1.78^{+0.01}_{-0.01}$	$0.04^{+0.02}_{-0.02}$	$0.07^{+0.01}_{-0.01}$
$10.8 \leq \log_{10} M_\star < 11.2$	3181	$0.62^{+0.01}_{-0.01}$	$1.83^{+0.01}_{-0.01}$	$-0.01^{+0.01}_{-0.01}$	$0.09^{+0.01}_{-0.01}$
$\log_{10} M_\star \geq 11.2$	1122	$0.45^{+0.02}_{-0.02}$	$1.98^{+0.02}_{-0.02}$	$-0.05^{+0.02}_{-0.02}$	$0.13^{+0.02}_{-0.01}$
$\mathrm{Age_M} + t_{\rm LB}$ [Gyr]	$N_{\rm gal}$	$\mu_{\mathrm{Age_M}+t_{\rm LB}}$		$\sigma^{\rm int}_{\mathrm{Age_M}+t_{\rm LB}}$	
		μ_1	μ_0	σ_1	σ_0
$10.0 \leq \log_{10} M_\star < 10.4$	1429	$0.87^{+0.06}_{-0.06}$	$1.83^{+0.02}_{-0.02}$	$0.04^{+0.06}_{-0.06}$	$0.08^{+0.02}_{-0.02}$
$10.4 \leq \log_{10} M_\star < 10.8$	2526	$0.58^{+0.03}_{-0.03}$	$1.94^{+0.01}_{-0.01}$	$-0.01^{+0.02}_{-0.02}$	$0.10^{+0.01}_{-0.01}$
$10.8 \leq \log_{10} M_\star < 11.2$	3181	$0.54^{+0.02}_{-0.02}$	$2.00^{+0.01}_{-0.01}$	$-0.04^{+0.01}_{-0.01}$	$0.11^{+0.01}_{-0.01}$
$\log_{10} M_\star \geq 11.2$	1122	$0.34^{+0.02}_{-0.02}$	$2.17^{+0.02}_{-0.02}$	$-0.08^{+0.02}_{-0.02}$	$0.15^{+0.02}_{-0.02}$

Notes. The top and bottom numbers stablish the 1 σ confidence level of the parameters.

Table D.2: Parameters $\mu(z, M_\star)$ and $\sigma^{\rm int}(z, M_\star)$ of the probability distribution functions of luminosity and mass-weighted metallicities (see Eq. D.3), which were derived using BC03 SSP models.

$[\mathrm{M/H}]_\mathrm{L}$	$N_{\rm gal}$	$\mu_{[\mathrm{M/H}]_\mathrm{L}}$			$\sigma^{\rm int}_{[\mathrm{M/H}]_\mathrm{L}}$		
		μ_2	μ_1	μ_0	σ_2	σ_1	σ_0
$10.0 \leq \log_{10} M_\star < 10.4$	1429	$1.73^{+0.61}_{-0.58}$	$-1.38^{+0.35}_{-0.36}$	$0.29^{+0.05}_{-0.05}$	$^{*}0.00^{+0.00}_{-0.00}$	$0.59^{+0.07}_{-0.06}$	$0.01^{+0.02}_{-0.02}$
$10.4 \leq \log_{10} M_\star < 10.8$	2526	$1.38^{+0.21}_{-0.20}$	$-1.22^{+0.17}_{-0.18}$	$0.22^{+0.03}_{-0.03}$	$-0.49^{+0.20}_{-0.19}$	$0.71^{+0.16}_{-0.17}$	$0.02^{+0.03}_{-0.03}$
$10.8 \leq \log_{10} M_\star < 11.2$	3181	$1.49^{+0.11}_{-0.10}$	$-1.34^{+0.12}_{-0.12}$	$0.21^{+0.03}_{-0.03}$	$-0.83^{+0.10}_{-0.10}$	$0.98^{+0.11}_{-0.11}$	$-0.04^{+0.03}_{-0.03}$
$\log_{10} M_\star \geq 11.2$	1122	$0.77^{+0.12}_{-0.12}$	$-0.60^{+0.16}_{-0.15}$	$0.00^{+0.04}_{-0.05}$	$-0.49^{+0.09}_{-0.08}$	$0.73^{+0.10}_{-0.12}$	$-0.05^{+0.04}_{-0.02}$
$[\mathrm{M/H}]_\mathrm{M}$	$N_{\rm gal}$	$\mu_{[\mathrm{M/H}]_\mathrm{M}}$			$\sigma^{\rm int}_{[\mathrm{M/H}]_\mathrm{M}}$		
		μ_2	μ_1	μ_0	σ_2	σ_1	σ_0
$10.0 \leq \log_{10} M_\star < 10.4$	1429	$1.49^{+0.66}_{-0.64}$	$-1.55^{+0.38}_{-0.41}$	$0.33^{+0.06}_{-0.06}$	$^{*}0.00^{+0.00}_{-0.00}$	$0.40^{+0.07}_{-0.07}$	$0.07^{+0.02}_{-0.02}$
$10.4 \leq \log_{10} M_\star < 10.8$	2526	$1.29^{+0.22}_{-0.22}$	$-1.46^{+0.19}_{-0.19}$	$0.25^{+0.04}_{-0.04}$	$-0.26^{+0.20}_{-0.20}$	$0.45^{+0.18}_{-0.18}$	$0.07^{+0.03}_{-0.04}$
$10.8 \leq \log_{10} M_\star < 11.2$	3181	$1.16^{+0.11}_{-0.12}$	$-1.43^{+0.14}_{-0.13}$	$0.22^{+0.03}_{-0.03}$	$-0.29^{+0.11}_{-0.11}$	$0.49^{+0.12}_{-0.12}$	$0.03^{+0.03}_{-0.03}$
$\log_{10} M_\star \geq 11.2$	1122	$0.83^{+0.12}_{-0.12}$	$-1.09^{+0.16}_{-0.15}$	$0.13^{+0.04}_{-0.04}$	$-0.32^{+0.09}_{-0.08}$	$0.57^{+0.10}_{-0.12}$	$-0.04^{+0.04}_{-0.02}$

Notes. $^{(*)}$ For $10.0 \leq \log_{10} M_\star < 10.4$, a linear redshift-dependency of $\sigma^{\rm int}_{[\mathrm{M/H}]}$ was assumed.
The top and bottom numbers stablish the 1 σ confidence level of the parameters.

Table D.3: Parameters $\mu(z, M_\star)$ and $\sigma^{\rm int}(z, M_\star)$ of the extinction probability distribution functions (see Eq. D.4), which were derived using BC03 SSP models.

A_V	$N_{\rm gal}$	μ_{A_V}		$\sigma^{\rm int}_{A_V}$	
		μ_1	μ_0	σ_1	σ_0
$10.0 \leq \log_{10} M_\star < 10.4$	1429	$-0.78^{+0.38}_{-0.35}$	$-1.50^{+0.11}_{-0.12}$	$1.71^{+0.30}_{-0.29}$	$0.39^{+0.10}_{-0.10}$
$10.4 \leq \log_{10} M_\star < 10.8$	2526	$-0.50^{+0.15}_{-0.14}$	$-1.36^{+0.06}_{-0.06}$	$1.36^{+0.13}_{-0.12}$	$0.16^{+0.06}_{-0.06}$
$10.8 \leq \log_{10} M_\star < 11.2$	3181	$-0.61^{+0.11}_{-0.11}$	$-1.37^{+0.07}_{-0.07}$	$0.76^{+0.07}_{-0.07}$	$0.50^{+0.04}_{-0.04}$
$^{*}\log_{10} M_\star \geq 11.2$	1122	$-0.76^{+0.14}_{-0.13}$	$-1.14^{+0.09}_{-0.09}$	$1.29^{+0.05}_{-0.05}$	$-0.12^{+0.03}_{-0.02}$

Notes. $^{(*)}$ For quiescent galaxies at $0.1 \leq z < 0.2$ and $\log_{10} M_\star \geq 11.2$, the assumption of linear $\sigma^{\rm int}(z)$ and $\mu(z)$ is too strict, and we impose $\sigma^{\rm int}(0.1 \leq z < 0.2) = \sigma^{\rm int}(z = 0.2) = 0.14 \pm 0.03$ and $\mu(0.1 \leq z < 0.2) = \mu(z = 0.2) = -1.29 \pm 0.09$ (details in text).
The top and bottom numbers stablish the 1 σ confidence level of the parameters.

Table D.4: Parameters $\mu(z, M_\star)$ and $\sigma^{\rm int}(z, M_\star)$ of the probability distribution functions of luminosity and mass-weighted ages and formation epochs (see Eq. D.2), which were derived using EMILES SSP models with BaSTI isochrones.

$\mathrm{Age_L}$ [Gyr]	$N_{\rm gal}$	$\mu_{\mathrm{Age_L}}$		$\sigma^{\rm int}_{\mathrm{Age_L}}$	
		μ_1	μ_0	σ_1	σ_0
$10.0 \leq \log_{10} M_\star < 10.4$	1074	$-0.72^{+0.10}_{-0.10}$	$1.97^{+0.03}_{-0.03}$	$0.09^{+0.08}_{-0.08}$	$0.17^{+0.03}_{-0.03}$
$10.4 \leq \log_{10} M_\star < 10.8$	2216	$-0.77^{+0.04}_{-0.04}$	$2.00^{+0.02}_{-0.02}$	$0.02^{+0.03}_{-0.03}$	$0.17^{+0.02}_{-0.02}$
$10.8 \leq \log_{10} M_\star < 11.2$	3787	$-0.83^{+0.02}_{-0.02}$	$2.07^{+0.01}_{-0.01}$	$-0.01^{+0.02}_{-0.02}$	$0.14^{+0.01}_{-0.01}$
$\log_{10} M_\star \geq 11.2$	2391	$-0.79^{+0.02}_{-0.02}$	$2.11^{+0.02}_{-0.02}$	$-0.04^{+0.02}_{-0.02}$	$0.17^{+0.01}_{-0.01}$
$\mathrm{Age_M}$ [Gyr]	$N_{\rm gal}$	$\mu_{\mathrm{Age_M}}$		$\sigma^{\rm int}_{\mathrm{Age_M}}$	
		μ_1	μ_0	σ_1	σ_0
$10.0 \leq \log_{10} M_\star < 10.4$	1074	$-0.25^{+0.08}_{-0.08}$	$2.04^{+0.03}_{-0.03}$	$-0.02^{+0.07}_{-0.07}$	$0.13^{+0.02}_{-0.02}$
$10.4 \leq \log_{10} M_\star < 10.8$	2216	$-0.56^{+0.04}_{-0.04}$	$2.16^{+0.02}_{-0.02}$	$-0.02^{+0.03}_{-0.03}$	$0.12^{+0.02}_{-0.02}$
$10.8 \leq \log_{10} M_\star < 11.2$	3787	$-0.69^{+0.02}_{-0.02}$	$2.25^{+0.01}_{-0.01}$	$0.01^{+0.02}_{-0.02}$	$0.08^{+0.01}_{-0.01}$
$\log_{10} M_\star \geq 11.2$	2391	$-0.71^{+0.02}_{-0.02}$	$2.30^{+0.02}_{-0.02}$	$-0.02^{+0.02}_{-0.02}$	$0.10^{+0.01}_{-0.01}$
$\mathrm{Age_L} + t_{\rm LB}$ [Gyr]	$N_{\rm gal}$	$\mu_{\mathrm{Age_L}+t_{\rm LB}}$		$\sigma^{\rm int}_{\mathrm{Age_L}+t_{\rm LB}}$	
		μ_1	μ_0	σ_1	σ_0
$10.0 \leq \log_{10} M_\star < 10.4$	1074	$0.55^{+0.06}_{-0.06}$	$2.02^{+0.02}_{-0.02}$	$-0.12^{+0.05}_{-0.05}$	$0.17^{+0.02}_{-0.02}$
$10.4 \leq \log_{10} M_\star < 10.8$	2216	$0.38^{+0.02}_{-0.02}$	$2.10^{+0.01}_{-0.01}$	$-0.10^{+0.02}_{-0.02}$	$0.15^{+0.01}_{-0.01}$
$10.8 \leq \log_{10} M_\star < 11.2$	3787	$0.26^{+0.01}_{-0.01}$	$2.18^{+0.01}_{-0.01}$	$-0.09^{+0.01}_{-0.01}$	$0.12^{+0.01}_{-0.01}$
$\log_{10} M_\star \geq 11.2$	2391	$0.20^{+0.01}_{-0.01}$	$2.25^{+0.01}_{-0.01}$	$-0.08^{+0.01}_{-0.01}$	$0.12^{+0.01}_{-0.01}$
$\mathrm{Age_M} + t_{\rm LB}$ [Gyr]	$N_{\rm gal}$	$\mu_{\mathrm{Age_M}+t_{\rm LB}}$		$\sigma^{\rm int}_{\mathrm{Age_M}+t_{\rm LB}}$	
		μ_1	μ_0	σ_1	σ_0
$10.0 \leq \log_{10} M_\star < 10.4$	1074	$0.67^{+0.05}_{-0.06}$	$2.13^{+0.02}_{-0.02}$	$-0.08^{+0.05}_{-0.05}$	$0.12^{+0.02}_{-0.02}$
$10.4 \leq \log_{10} M_\star < 10.8$	2216	$0.34^{+0.02}_{-0.02}$	$2.25^{+0.01}_{-0.01}$	$-0.07^{+0.02}_{-0.02}$	$0.10^{+0.01}_{-0.01}$
$10.8 \leq \log_{10} M_\star < 11.2$	3787	$0.20^{+0.01}_{-0.01}$	$2.34^{+0.01}_{-0.01}$	$-0.05^{+0.01}_{-0.01}$	$0.08^{+0.01}_{-0.01}$
$\log_{10} M_\star \geq 11.2$	2391	$0.13^{+0.01}_{-0.01}$	$2.40^{+0.01}_{-0.01}$	$-0.05^{+0.01}_{-0.01}$	$0.09^{+0.01}_{-0.01}$

Notes. The top and bottom numbers stablish the 1 σ confidence level of the parameters.

Table D.5: Parameters $\mu(z, M_\star)$ and $\sigma^{\rm int}(z, M_\star)$ of the probability distribution functions of luminosity and mass-weighted metallicities (see Eq. D.3), which were derived using EMILES SSP models with BaSTI isochrones.

		$\mu_{[\rm M/H]_L}$		$\sigma^{\rm int}_{[\rm M/H]_L}$	
$[\rm M/H]_L$	$N_{\rm gal}$	μ_1	μ_0	σ_1	σ_0
$10.0 \leq \log_{10} M_\star < 10.4$	1074	$-0.46^{+0.06}_{-0.06}$	$0.42^{+0.02}_{-0.02}$	$0.45^{+0.05}_{-0.04}$	$0.01^{+0.01}_{-0.01}$
$10.4 \leq \log_{10} M_\star < 10.8$	2216	$-0.23^{+0.03}_{-0.03}$	$0.30^{+0.01}_{-0.01}$	$0.23^{+0.02}_{-0.02}$	$0.07^{+0.01}_{-0.01}$
$10.8 \leq \log_{10} M_\star < 11.2$	3787	$-0.01^{+0.02}_{-0.02}$	$0.19^{+0.01}_{-0.01}$	$0.09^{+0.01}_{-0.01}$	$0.10^{+0.01}_{-0.01}$
$\log_{10} M_\star \geq 11.2$	2391	$0.06^{+0.02}_{-0.02}$	$0.12^{+0.01}_{-0.01}$	$0.02^{+0.02}_{-0.02}$	$0.13^{+0.01}_{-0.01}$
		$\mu_{[\rm M/H]_M}$		$\sigma^{\rm int}_{[\rm M/H]_M}$	
$[\rm M/H]_M$	$N_{\rm gal}$	μ_1	μ_0	σ_1	σ_0
$10.0 \leq \log_{10} M_\star < 10.4$	1074	$-0.67^{+0.07}_{-0.07}$	$0.42^{+0.02}_{-0.02}$	$0.47^{+0.06}_{-0.06}$	$0.03^{+0.02}_{-0.02}$
$10.4 \leq \log_{10} M_\star < 10.8$	2216	$-0.43^{+0.03}_{-0.03}$	$0.25^{+0.01}_{-0.01}$	$0.23^{+0.03}_{-0.03}$	$0.10^{+0.01}_{-0.01}$
$10.8 \leq \log_{10} M_\star < 11.2$	3787	$-0.30^{+0.02}_{-0.02}$	$0.13^{+0.01}_{-0.01}$	$0.05^{+0.01}_{-0.01}$	$0.13^{+0.01}_{-0.01}$
$\log_{10} M_\star \geq 11.2$	2391	$-0.25^{+0.02}_{-0.02}$	$0.07^{+0.01}_{-0.01}$	$-0.02^{+0.01}_{-0.01}$	$0.16^{+0.01}_{-0.01}$

Notes. The top and bottom numbers stablish the 1 σ confidence level of the parameters.

Table D.6: Parameters $\mu(z, M_\star)$ and $\sigma^{\rm int}(z, M_\star)$ of the probability distribution functions of extinctions (see Eq. D.4), which were derived using EMILES SSP models with BaSTI isochrones.

		μ_{A_V}		$\sigma^{\rm int}_{A_V}$	
A_V	$N_{\rm gal}$	μ_1	μ_0	σ_1	σ_0
$10.0 \leq \log_{10} M_\star < 10.4$	1074	$-1.04^{+0.32}_{-0.32}$	$-1.17^{+0.09}_{-0.09}$	$2.38^{+0.25}_{-0.25}$	$0.06^{+0.08}_{-0.08}$
$10.4 \leq \log_{10} M_\star < 10.8$	2216	$-0.21^{+0.17}_{-0.17}$	$-1.48^{+0.07}_{-0.07}$	$0.91^{+0.13}_{-0.13}$	$0.58^{+0.05}_{-0.06}$
$10.8 \leq \log_{10} M_\star < 11.2$	3787	$-0.44^{+0.08}_{-0.08}$	$-1.21^{+0.04}_{-0.05}$	$0.92^{+0.06}_{-0.06}$	$0.27^{+0.04}_{-0.03}$
$\log_{10} M_\star \geq 11.2$	2391	$-0.14^{+0.09}_{-0.09}$	$-1.45^{+0.07}_{-0.06}$	$0.52^{+0.06}_{-0.06}$	$0.50^{+0.05}_{-0.05}$

Notes. The top and bottom numbers stablish the 1 σ confidence level of the parameters.

Table D.7: Parameters $\mu(z, M_\star)$ and $\sigma^{\rm int}(z, M_\star)$ of the probability distribution functions of luminosity and mass-weighted ages (see Eq. D.2), which were derived using EMILES SSP models with Padova00 isochrones.

$\mathrm{Age_L}$ [Gyr]	$N_{\rm gal}$	$\mu_{\mathrm{Age_L}}$		$\sigma^{\rm int}_{\mathrm{Age_L}}$	
		μ_1	μ_0	σ_1	σ_0
$10.0 \leq \log_{10} M_\star < 10.4$	889	$-0.70^{+0.13}_{-0.13}$	$1.86^{+0.04}_{-0.05}$	$0.01^{+0.10}_{-0.10}$	$0.27^{+0.04}_{-0.03}$
$10.4 \leq \log_{10} M_\star < 10.8$	1702	$-0.55^{+0.05}_{-0.06}$	$1.81^{+0.03}_{-0.03}$	$-0.01^{+0.04}_{-0.04}$	$0.23^{+0.02}_{-0.02}$
$10.8 \leq \log_{10} M_\star < 11.2$	2627	$-0.72^{+0.03}_{-0.03}$	$1.93^{+0.02}_{-0.02}$	$0.03^{+0.02}_{-0.02}$	$0.15^{+0.01}_{-0.01}$
$\log_{10} M_\star \geq 11.2$	1453	$-0.66^{+0.03}_{-0.03}$	$1.99^{+0.02}_{-0.02}$	$-0.02^{+0.02}_{-0.02}$	$0.17^{+0.02}_{-0.01}$
$\mathrm{Age_M}$ [Gyr]	$N_{\rm gal}$	$\mu_{\mathrm{Age_M}}$		$\sigma^{\rm int}_{\mathrm{Age_M}}$	
		μ_1	μ_0	σ_1	σ_0
$10.0 \leq \log_{10} M_\star < 10.4$	889	$-0.29^{+0.11}_{-0.11}$	$2.00^{+0.04}_{-0.04}$	$-0.20^{+0.09}_{-0.09}$	$0.24^{+0.03}_{-0.03}$
$10.4 \leq \log_{10} M_\star < 10.8$	1702	$-0.39^{+0.04}_{-0.05}$	$2.01^{+0.02}_{-0.02}$	$-0.05^{+0.03}_{-0.03}$	$0.15^{+0.02}_{-0.02}$
$10.8 \leq \log_{10} M_\star < 11.2$	2627	$-0.55^{+0.02}_{-0.02}$	$2.11^{+0.02}_{-0.02}$	$-0.01^{+0.02}_{-0.02}$	$0.12^{+0.01}_{-0.01}$
$\log_{10} M_\star \geq 11.2$	1453	$-0.51^{+0.03}_{-0.02}$	$2.14^{+0.02}_{-0.02}$	$-0.05^{+0.01}_{-0.01}$	$0.13^{+0.01}_{-0.01}$
$\mathrm{Age_L} + t_{\rm LB}$ [Gyr]	$N_{\rm gal}$	$\mu_{\mathrm{Age_L}+t_{\rm LB}}$		$\sigma^{\rm int}_{\mathrm{Age_L}+t_{\rm LB}}$	
		μ_1	μ_0	σ_1	σ_0
$10.0 \leq \log_{10} M_\star < 10.4$	889	$0.61^{+0.07}_{-0.07}$	$1.96^{+0.03}_{-0.03}$	$-0.21^{+0.06}_{-0.06}$	$0.24^{+0.02}_{-0.02}$
$10.4 \leq \log_{10} M_\star < 10.8$	1702	$0.54^{+0.03}_{-0.03}$	$1.98^{+0.01}_{-0.01}$	$-0.12^{+0.02}_{-0.02}$	$0.18^{+0.01}_{-0.01}$
$10.8 \leq \log_{10} M_\star < 11.2$	2627	$0.34^{+0.01}_{-0.01}$	$2.10^{+0.01}_{-0.01}$	$-0.06^{+0.01}_{-0.01}$	$0.12^{+0.01}_{-0.01}$
$\log_{10} M_\star \geq 11.2$	1453	$0.26^{+0.01}_{-0.01}$	$2.19^{+0.01}_{-0.01}$	$-0.07^{+0.01}_{-0.01}$	$0.12^{+0.01}_{-0.01}$
$\mathrm{Age_M} + t_{\rm LB}$ [Gyr]	$N_{\rm gal}$	$\mu_{\mathrm{Age_M}+t_{\rm LB}}$		$\sigma^{\rm int}_{\mathrm{Age_M}+t_{\rm LB}}$	
		μ_1	μ_0	σ_1	σ_0
$10.0 \leq \log_{10} M_\star < 10.4$	889	$0.65^{+0.07}_{-0.07}$	$2.10^{+0.03}_{-0.03}$	$-0.22^{+0.06}_{-0.06}$	$0.19^{+0.02}_{-0.02}$
$10.4 \leq \log_{10} M_\star < 10.8$	1702	$0.47^{+0.03}_{-0.03}$	$2.15^{+0.01}_{-0.01}$	$-0.08^{+0.02}_{-0.02}$	$0.12^{+0.01}_{-0.01}$
$10.8 \leq \log_{10} M_\star < 11.2$	2627	$0.28^{+0.01}_{-0.01}$	$2.26^{+0.01}_{-0.01}$	$-0.06^{+0.01}_{-0.01}$	$0.09^{+0.01}_{-0.01}$
$\log_{10} M_\star \geq 11.2$	1453	$0.22^{+0.01}_{-0.01}$	$2.33^{+0.01}_{-0.01}$	$-0.05^{+0.01}_{-0.01}$	$0.08^{+0.01}_{-0.01}$

Notes. The top and bottom numbers stablish the 1 σ confidence level of the parameters.

Table D.8: Parameters $\mu(z, M_\star)$ and $\sigma^{\rm int}(z, M_\star)$ of the probability distribution functions of luminosity and mass-weighted metallicities (see Eq. D.3), which were derived using EMILES SSP models with Padova00 isochrones.

$[\mathrm{M/H}]_\mathrm{L}$	$N_{\rm gal}$	$\mu_{[\mathrm{M/H}]_\mathrm{L}}$		$\sigma^{\rm int}_{[\mathrm{M/H}]_\mathrm{L}}$	
		μ_1	μ_0	σ_1	σ_0
$10.0 \leq \log_{10} M_\star < 10.4$	889	$-0.33^{+0.06}_{-0.06}$	$0.41^{+0.02}_{-0.02}$	$0.30^{+0.05}_{-0.05}$	$0.05^{+0.01}_{-0.01}$
$10.4 \leq \log_{10} M_\star < 10.8$	1702	$-0.05^{+0.03}_{-0.03}$	$0.27^{+0.01}_{-0.01}$	$0.24^{+0.02}_{-0.02}$	$0.04^{+0.01}_{-0.01}$
$10.8 \leq \log_{10} M_\star < 11.2$	2627	$0.07^{+0.02}_{-0.02}$	$0.19^{+0.01}_{-0.01}$	$0.05^{+0.01}_{-0.01}$	$0.11^{+0.01}_{-0.01}$
$\log_{10} M_\star \geq 11.2$	1453	$0.13^{+0.02}_{-0.02}$	$0.12^{+0.01}_{-0.01}$	$-0.03^{+0.02}_{-0.02}$	$0.15^{+0.01}_{-0.01}$
$[\mathrm{M/H}]_\mathrm{M}$	$N_{\rm gal}$	$\mu_{[\mathrm{M/H}]_\mathrm{M}}$		$\sigma^{\rm int}_{[\mathrm{M/H}]_\mathrm{M}}$	
		μ_1	μ_0	σ_1	σ_0
$10.0 \leq \log_{10} M_\star < 10.4$	889	$-0.56^{+0.07}_{-0.07}$	$0.47^{+0.02}_{-0.02}$	$0.30^{+0.06}_{-0.06}$	$0.06^{+0.02}_{-0.02}$
$10.4 \leq \log_{10} M_\star < 10.8$	1702	$-0.30^{+0.03}_{-0.03}$	$0.30^{+0.01}_{-0.01}$	$0.24^{+0.03}_{-0.03}$	$0.05^{+0.01}_{-0.01}$
$10.8 \leq \log_{10} M_\star < 11.2$	2627	$-0.16^{+0.02}_{-0.02}$	$0.18^{+0.01}_{-0.01}$	$0.02^{+0.01}_{-0.01}$	$0.13^{+0.01}_{-0.01}$
$\log_{10} M_\star \geq 11.2$	1453	$-0.10^{+0.02}_{-0.02}$	$0.10^{+0.02}_{-0.02}$	$-0.04^{+0.02}_{-0.02}$	$0.16^{+0.01}_{-0.01}$

Notes. The top and bottom numbers stablish the 1 σ confidence level of the parameters.

Table D.9: Parameters $\mu(z, M_\star)$ and $\sigma^{\rm int}(z, M_\star)$ of the probability distribution functions of extinctions (see Eq. D.4), which were derived using EMILES SSP models with Padova00 isochrones.

A_V	$N_{\rm gal}$	μ_{A_V}		$\sigma^{\rm int}_{A_V}$	
		μ_1	μ_0	σ_1	σ_0
$10.0 \leq \log_{10} M_\star < 10.4$	889	$-0.56^{+0.44}_{-0.42}$	$-1.45^{+0.13}_{-0.14}$	$2.04^{+0.33}_{-0.33}$	$0.31^{+0.11}_{-0.10}$
$10.4 \leq \log_{10} M_\star < 10.8$	1702	$-0.45^{+0.20}_{-0.19}$	$-1.39^{+0.08}_{-0.09}$	$0.89^{+0.14}_{-0.15}$	$0.60^{+0.06}_{-0.06}$
$10.8 \leq \log_{10} M_\star < 11.2$	2627	$-0.16^{+0.13}_{-0.13}$	$-1.58^{+0.08}_{-0.08}$	$0.65^{+0.09}_{-0.09}$	$0.72^{+0.06}_{-0.06}$
$\log_{10} M_\star \geq 11.2$	1453	$-0.01^{+0.14}_{-0.14}$	$-1.68^{+0.10}_{-0.10}$	$0.17^{+0.11}_{-0.11}$	$0.86^{+0.08}_{-0.08}$

Notes. The top and bottom numbers stablish the 1 σ confidence level of the parameters.

E

Effects of the constraints on the SFH for different SSP models

As we introduce in Sect. 3.9, alternative SFH assumptions produce different stellar-population predictions at the redshift range $0.1 \leq z \leq 1.1$ for the quiescent galaxies in ALHAMBRA. All the effects on the stellar population parameters owing to the constraints on the SFH are detailed when using BC03 (Sect. E.1) and EMILES SSP models (Sect. E.2). In order to illustrate and facilitate the reading of this section, we gather all the figures in Sect. E.3, where Figs. E.1–E.16 correspond to the effects of SFH constraints when using BC03 SSP models, Figs. E.17–E.28 to the EMILES+BaSTI ones, and Figs. E.29–E.38 to the EMILES+Padova00 ones.

E.1 Influence of SFH priors on stellar population results and BC03 SSP models

The effects of constraining some parameters to fixed values (Sects. E.1.1 and E.1.2), as well as the effects of imposing some constraints in the mixture of SSPs (Sects. E.1.3–E.1.6) are treated using the same set of SSP models than in Sect. 3.7.2, i. e. BC03 SSP models and Chabrier IMF.

E.1.1 Constant values of extinction

Our interest is focused on how changes our results when the extinction is equal to a constant value. A unique value of $A_V = 0.2$ is applied on the BC03 SSP models using again the Fitzpatrick (1999) extinction law, which corresponds to an average and arbitrary value of extinction for quiescent galaxies (see Sect. 3.7.4). We reran MUFFIT with the same sample of ALHAMBRA galaxies classified as quiescent in Sect. 3.3, and the new PDFs are recomputed using the MLE method (detailed in Appendix D) under the same assumptions.

The first consequence of fixing extinction is that the median age retrieved from MUFFIT is slightly older (see solid lines in Fig. E.1 top panels) than in the case in which the extinction is a free parameter (see dashed lines in top panels of Fig. E.1). Moreover, the ages of quiescent galaxies present a flatter relation with redshift, and therefore, quiescent galaxies would suffer larger variations in their stellar content (non-passive evolution) since $z \sim 1$ respect the results in Sect. 3.7.4. Although, the differences respect the ages without constraining extinction are very subtle and they remain below $\lesssim 1$ Gyr. In general, the age distributions retrieved from the analysis with $A_V = 0.2$ are narrower (bottom panels in Fig. E.1).

Regarding the mass-weighted metallicity, the effects of a constant extinction in the analysis are almost negligible with variations on the median of the metallicity PDF of $\Delta[\mathrm{M/H}]^{50\mathrm{th}} \lesssim 0.05$ dex. In average, the median metallicities are lower than in a general case without constant extinction. In fact, the solutions are compatible in a 1 σ uncertainty level (see Fig. E.2). On the contrary, the PDFs of metallicity are wider for

an analysis fixing $A_V = 0.2$. This is not surprising, because colour degeneracies are driving the new results: the larger (lower) the extinction is, the more metal poor (rich) the SSP model is to provide the same SED colour.

Consequently, the qualitative trends retrieved in Sect. 3.7 also remain when the extinction of quiescent galaxies is fixed. The results again agree with a non-passive evolution of the quiescent population, where the global ageing of these galaxies is slowed down respect a complete quenched scenario. Even though the extinction is fixed, the median metallicity also shows a mild drop towards lower redshifts.

E.1.2 Constant values of metallicity

It is broadly accepted that quiescent galaxies are mainly rich in metals, but also metallicity is usually a parameter of harder determination (e. g. Gallazzi et al., 2005, with spectroscopic indices in the optical range). This makes some authors to assume that massive quiescent galaxies ($\log_{10} M_\star \gtrsim 10.7$ dex) have metallicities around solar values, [M/H] ~ 0.0 dex, in their analysis of stellar populations (e. g. Whitaker et al., 2013; Belli et al., 2015; Fumagalli et al., 2016). We explore the consequences of this assumption in our results.

As Fig. E.3 shows, this constraint has a strong impact on the retrieved ages. The ages are older at lower redshifts, up to $\Delta\text{Age}^{50\text{th}} \sim 2$ Gyr for $\log_{10} M_\star \geq 10.8$ dex, when setting the metallicity to solar values. At high redshifts, $z \gtrsim 0.7$, the effect is the opposite and the new ages are younger, $\Delta\text{Age}^{50\text{th}} \sim 1$ Gyr at $z > 0.9$, than the case with free metallicity. Figure E.3 highlights that under this constraint, quiescent galaxies are closer to a passive evolution. In a completely passive scenario, the medians of the formation epoch PDFs would be constant with cosmic time, and we observe a delay of ~ 1 Gyr for the most massive case $\log_{10} M_\star \geq 11.2$ since $z = 1.1$. The rest of the stellar mass bins shows a stronger evolution with redshift. When metallicity is set to solar values, the deviation from passiveness is larger as the stellar mass decreases. The trends of the widths of the mass-weighted formation epoch and age PDFs are similar to the ones obtained in Sect. 3.7, although in this case the PDFs are wider.

The extinction retrieved with [M/H] = 0.0 dex also suffers great changes. We find out that the SED of quiescent galaxies fits better with larger values of extinction (see Fig. E.4) when metallicity is fixed to solar values. While in Sect. 3.7.4 the results suggest median values of extinction of $A_V \lesssim 0.3$, after fixing [M/H] = 0.0 dex the range of extinction values in quiescent galaxies increases up to $A_V \sim 0.5$. We do not observe a clear dependence of extinction with stellar mass (all values compatible for a significance level of 1 σ), that is, this constraint makes that the extinction in quiescent galaxies is the same for all the stellar mass ranges under study. In addition, at decreasing redshift the extinction is also lower, unlike in Sect. 3.7.4 where the extinction increases mildly at lower redshifts. In concordance with the results without metallicity constraints, the widths of the extinction PDFs decrease at local redshifts, but these present larger values.

Although the metallicity is constrained to solar values, the passiveness of quiescent galaxies is not compatible with our results, which suggests an evolution of the stellar content in these galaxies whatever was the responsible mechanism. On the other hand, the extinction is a parameter more susceptible to constraints in metallicity. Their values suffer more dramatic increments and the correlation with redshift can also change to the opposite sense.

E.1.3 Closed-box enrichment of metals

During the analysis carried out by MUFFIT with the photometric data of ALHAMBRA, we did not force any metallicity constraint during the mixture of the two SSP models. In this way, no constraints in metallicity can account for more complex assembly scenarios, such as cool gas falls or the accretion of ex-situ stellar populations via mergers. For instance, the young component in the SSP mixture is allowed to be more metal-poor than the older one. However, this degree of freedom in metallicity is not necessarily compatible with a monolithic collapse, in which the stellar evolution of the galaxy is expected to enrich the ISM and hence the subsequent population of stars. To test this scenario, we repeated the whole SED-fitting process with all

the galaxies in the ALHAMBRA survey (Sect. 3.3) forcing that the metallicity of the younger component, $[M/H]_{young}$, is larger or equal to the older one, $[M/H]_{old}$.

The consequences of the assumption of a strict closed-box star formation process for the quiescent sample are presented in Figs. E.5 and E.6. We do not appreciate qualitative changes in the retrieved median of the mass-weighted formation epoch and age distributions, but a general and systematic shift in their median values of $\Delta Age^{50th} \sim 1$ Gyr towards younger values. However, quiescent galaxies with $\log_{10} M_\star \leq 10.8$ change their correlation with redshift, obtaining that current age PDFs are narrower at lower redshifts. For the massive bins $\log_{10} M_\star \geq 10.8$, the width of the distribution of age values varies poorly and they are compatible with the results of Sect. 3.7.2.

As expected, the more affected parameter under the assumption $[M/H]_{young} \geq [M/H]_{old}$ is the proper metallicity, where its values are systematically lower than in Sect. 3.7.3. The most significant differences appear at larger redshifts $\Delta[M/H]^{50th} < 0.2$ dex, whereas at lower redshifts metallicities are very similar to the obtained in Sect. 3.7.3, $\Delta[M/H]^{50th} < 0.05$ dex. The redshift dependence of the median of the metallicity PDF is still present under this closed-box assumption, with a maximum at $z \sim 0.5$, i. e. in a slight earlier epoch as compared to the prediction in Sect. 3.7.3. The width of the metallicity PDF also shows larger discrepancies at larger redshifts, although preserving the correlation with both stellar mass and reshift.

The extinction PDFs do not present large discrepancies under the closed-box assumption. We only appreciate slightly larger extinction values in comparison with Sect. 3.7.4.

In addition, we repeated the analysis forcing $[M/H]_{young} \geq [M/H]_{old}$ and adding extra conditions on the BC03 SSP models: $[M/H] \geq -0.64$ dex (see Figs. E.7 and E.8) and $[M/H] \geq -0.33$ dex (see Figs. E.9 and E.10). The above additional constraints do not alter significantly the formation epoch and age PDFs. The MZR is slightly diluted and all the quiescent galaxies present similar metallicity values at any stellar mass range, although preserving the maximum of median metallicity at $z \sim 0.55$. Regarding extinction, the last condition $[M/H] \geq -0.33$ dex forces that median extinction decreases at decreasing redshifts.

E.1.4 Soft enrichment of metals

We re-explored the SFH case $[M/H]_{young} \geq [M/H]_{old}$, but also assuming that the metallicity of the young component is not much more rich in metals than the old component or $[M/H]_{young} \gtrsim [M/H]_{old}$. In this case, a closed-box enrichment of metals is also present, but without allowing mixtures of extreme metallicity values (e. g. a SSP mixture of $[M/H]_{young} = 0.55$ dex and $[M/H]_{old} = -1.65$ dex models is not allowed), which would imply an extreme enrichment of metals in the more recent star formation regions. Concretely, only contiguous and equal metallicity values are allow in the mixture of SSPs, where the most metal-rich component can be only the young component. After running MUFFIT with the new model data set and selecting quiescent galaxies as in Sect. 3.3, we obtained the results summarised in Figs. E.11 and E.12.

As in Sect. E.1.3, the $[M/H]_{young} \gtrsim [M/H]_{old}$ assumption produces a systematic decrease on the retrieved medians of mass-weighted age PDFs, although this is milder $\Delta Age^{50th} \lesssim 0.5$ Gyr (see Fig. E.11). The age–stellar mass relation, or "downsizing" scenario, is still clear and at increasing stellar mass, quiescent galaxies are older at any redshift. For those quiescent galaxies with $\log_{10} M_\star < 11.2$, their PDFs of mass-weighted age become narrower than in Sect. 3.7.2. However for $\log_{10} M_\star \geq 11.2$, we detect no change on the width of the age PDF with a statistical significance respect the results without SFH assumptions.

The metallicity increases for all the stellar masses and redshifts (see Fig. E.12), specially for the lower stellar mass bins. At any redshift the quiescent population have super-solar metallicities with a peak at $z \sim 0.55$. Under the constraint $[M/H]_{young} \gtrsim [M/H]_{old}$, there is no a clear metallicity–stellar mass relation and all the quiescent galaxies have the same metallicity, which disagrees with previous studies in which the MZR is always present (e. g. Trager et al., 2000; Tremonti et al., 2004; Gallazzi et al., 2005; Panter et al., 2008; González Delgado et al., 2014a). Nevertheless, the maximum of metallicity persists and also the qualitative trend in metallicity with redshift retrieved in Sect. 3.7.3. The width of the mass-weighted metallicity PDFs present stronger evolution with redshift than in Sect. 3.7.3. This width is also correlated with the stellar mass, in the sense that, the mass-weighted metallicity PDFs of lower stellar masses are also

the wider distributions of metallicity values.

The median extinction exhibits prominent changes. This tends to reduce towards lower redshifts and it is larger than in the case without any metallicity restriction. The width of the distribution is correlated with the stellar mass. Thus, at decreasing stellar mass the width of the extinction PDF increases. The dependence with redshift does not change remarkably, and at lower redshifts the extinction PDFs are narrower.

E.1.5 Constant metal content during the galaxy assembly

Another plausible hypothesis is to assume a constant metal content during the assembly of the galaxy, i. e. $[M/H]_{young} = [M/H]_{old}$. In fact, this is the typical assumption in many studies in which authors use τ-models to determine stellar population parameters. Figures E.13 and E.14 illustrate the results of forcing $[M/H]_{young} = [M/H]_{old}$. The outcomes are quite similar to the obtained in Sect. E.1.4.

The conclusion for age PDFs is basically the same than in Sect. E.1.4. The constraint $[M/H]_{young} = [M/H]_{old}$ favours younger stellar populations and the "downsizing" is present at least up to $z \sim 1$. In general, the width of the age distributions are narrower than in the results without metallicity constraints.

The MZR is not satisfied under $[M/H]_{young} = [M/H]_{old}$, and any correlation between stellar mass and metallicity does not exist yet. The median metallicities are also larger reaching values of $[M/H]^{50th} > 0.2$ dex at $z \sim 0.5$–0.6 for any stellar mass bin. Since $z \sim 0.6$, the median of the mass-weighted metallicity PDF decreases until solar values at $z \sim 0.1$. The width of the metallicity PDF is wider at larger redshifts.

As in Sect. E.1.4, extinction decreases at decreasing redshift (unlike when the metallicity constraint is not imposed) and the more massive, the more reddened-by-dust and narrower the PDF is.

E.1.6 Fall of metal-poor cold gas from the cosmic web

The scenario in which massive galaxies experiment a fall of metal-poor cold gas from the cosmic web is also explored. Under this hypothesis, the new gas would be poorer in metals owing to the absence of an active star formation, and therefore, the new populations of stars would be poorer in metals as well. This assumption would imply that $[M/H]_{young} \leq [M/H]_{old}$, which is actually contrary to a closed-boxed enrichment of metals (treated in Sect. E.1.3).

After running MUFFIT again, but imposing this constraint in metallicity, the new results are summarised in Figs. E.15 and E.16. For both mass-weighted formation epoch and age distributions, the evolution with redshift of the median of the PDF does not present remarkable modifications in comparison with the results without any constraint (see solid and dashed lines in Fig. E.15). Systematically, we find that the quiescent population shows subtle older stellar populations of $\Delta Age^{50th} < 0.2$ Gyr when $[M/H]_{young} \leq [M/H]_{old}$. Therefore, under this constraint, the conclusions about the evolution of the median of the age and formation epoch PDF remain unaltered respect the obtained in the general analysis (Sect. 3.7): there are no hints for passive evolution. Concerning the intrinsic widths of these distributions, there is a minor increment, although this is not prominent and it is close to be compatible given the uncertainties of the MLE method.

As expected, after forcing $[M/H]_{young} \leq [M/H]_{old}$ the metallicity PDF predictions retrieved from MUFFIT for the quiescent populations suffer modifications. All the quiescent galaxies with stellar masses above $\log_{10} M_\star = 10.4$ show compatible medians of metallicity PDFs, independently of the redshift in which they are observed up to $z \sim 1.1$, although the less massive systems present a wider range of values (mainly at $z > 0.4$, see Fig. E.16). Consequently, the constraint $[M/H]_{young} \leq [M/H]_{old}$ vanishes the MZR in the most massive bins keeping the maximum of the median of the metallicity PDF at $z \sim 0.65$. In addition, the median of the metallicity PDF increases around $\Delta[M/H]^{50th} = 0.1$–0.2 dex with respect the ones obtained without constraints (see dashed lines in Fig. E.16). In general, the metallicity PDFs are slightly narrower with respect to the ones obtained without any assumption, $\Delta\omega_{[M/H]_M} < 0.1$ dex, almost compatible at 1 σ significance level.

Under $[M/H]_{young} \leq [M/H]_{old}$, the extinction PDFs do no present significant changes. Both the median and width of the extinction PDF present similar values and trends with redshift than the obtained without any

constraint (see Fig. E.16). This is the less altered stellar population parameter by $[M/H]_{young} \leq [M/H]_{old}$.

E.2 Influence of SFH priors on stellar population results with EMILES SSP models

As in Sect. E.1, we explored how the stellar population predictions retrieved from the SED-fitting analysis change after assuming certain SFH priors using EMILES SSP models. As the effects of the SFH constraints are similar independently of the EMILES isochrone, we treat the analysis of the results without referring the isochrone.

E.2.1 SFH metallicity constraints

The metallicity constraints explored in Sects. E.1.3–E.1.6 for BC03 models showed that these ones are able to modify the stellar population predictions quantitatively. In fact, for some of them, the MZR was compromised using BC03 SSP models. Thereby, the constraints on the metallicities of the SSP mixture is revisited for EMILES SSP models, in order to quantify their effects for this model set. We repeat the analysis forcing $[M/H]_{young} \geq [M/H]_{old}$ (Figs. E.17 and E.18 for BaSTI, Figs. E.29 and E.30 for Padova00), $[M/H]_{young} \gtrsim [M/H]_{old}$ (Figs. E.19 and E.20 for BaSTI, Figs. E.31 and E.32 for Padova00), $[M/H]_{young} = [M/H]_{old}$ (Figs. E.21 and E.22 for BaSTI, Figs. E.33 and E.34 for Padova00), and $[M/H]_{young} \leq [M/H]_{old}$ (Figs. E.23 and E.24 for BaSTI, Figs. E.35 and E.36 for Padova00), to subsequently detail their effects.

In general, these SFH assumptions drive PDF trends similar to the obtained for BC03 (Sects. E.1.3–E.1.6). The mass-weighted age PDF shows the greatest agreement with the BC03 ones after imposing the four metallicity constraints. In brief, when an enrichment or non-variability of the metal content is assumed during the assembly of the quiescent population ($[M/H]_{young} \geq [M/H]_{old}$, $[M/H]_{young} \gtrsim [M/H]_{old}$, and $[M/H]_{young} = [M/H]_{old}$) the medians of the mass-weighted age PDFs suffer a systematic decrease, alike the BC03 case. However, in an scenario with a fall of new gas ($[M/H]_{young} \leq [M/H]_{old}$), there is an ageing of the median PDF in comparison with the case without any SFH constraint. In addition, the age–mass relation is also present in all the cases and the evolution of the median of the age PDF agrees with a non-passive evolution since $z \sim 1$. Concerning the widths of the mass-weighted age PDF, these present a general increment of their values for all the constraints in metallicity (i. e. these are wider when $[M/H]_{young} \geq [M/H]_{old}$, $[M/H]_{young} \gtrsim [M/H]_{old}$, $[M/H]_{young} = [M/H]_{old}$, and $[M/H]_{young} \leq [M/H]_{old}$), although their dependencies with redshift do not present significant alterations (in some cases the correlation between width and redshift is slightly more prominent).

The most striking results respect the ones obtained for BC03 models concerns the mass-weighted metallicity PDF. When we use EMILES SSP models, independently of the metallicity constraint imposed, the MZR is always present at any redshift (unlike BC03, where for the cases $[M/H]_{young} \gtrsim [M/H]_{old}$, $[M/H]_{young} = [M/H]_{old}$, and $[M/H]_{young} \leq [M/H]_{old}$ the MZR was compromised). Under the fall of new gas assumption ($[M/H]_{young} \leq [M/H]_{old}$), the medians of the mass-weighted metallicity PDFs exhibit an increment of their values for all stellar masses, whereas for the rest of metallicity priors we find a generalised decrement of the median of the PDF. Noteworthy, for the massive case ($\log_{10} M_\star \geq 11.2$) and Padova00 isochrones, the constraints $[M/H]_{young} \geq [M/H]_{old}$ and $[M/H]_{young} = [M/H]_{old}$ are the only cases in which the median of the mass-weighted metallicity PDF increases at decreasing redshift. The widths of the metallicity PDFs show trends similar to the BC03 case.

The extinction PDFs are the stellar population distributions less affected by these metallicity constraints in the composition of our mixture of models. For EMILES SSP models, all the quiescent galaxies present similar median extinctions in the range $A_V \sim 0.2$–0.25 independently of their stellar masses and redshift, with subtle changes in their PDFs owing to the different assumptions, but compatible within a $1\,\sigma$ confidence level (see figures in Appendix E). The widths of the extinction PDFs are still correlated with redshift after imposing $[M/H]_{young} \geq [M/H]_{old}$, $[M/H]_{young} \gtrsim [M/H]_{old}$, $[M/H]_{young} = [M/H]_{old}$, and $[M/H]_{young} \leq$

$[M/H]_{old}$.

In addition, we explore a case with two constraints at the same time: $[M/H]_{young} \geq [M/H]_{old}$ and $A_V = 0$ (see also Figs. E.25 and E.26, for BaSTI results; and Figs. E.37 and E.38, for Padova00 results). As in the case with only $[M/H]_{young} \geq [M/H]_{old}$, the median of the age PDF decreases under both assumptions and the age-stellar mass relation is still satisfied, but closer to a passive evolution. The width of the age PDF also increases respect the values obtained without constraints (see Sect. 3.8). However, the median metallicity increases (unlike with only $[M/H]_{young} \geq [M/H]_{old}$), and consequently, the effect of including $A_V = 0$ affects more intensively to metallicity values, although the MZR also remains. The width of the metallicity PDF slightly increases ant the correlations with redshift do not show great modifications, as with the only constraint of $[M/H]_{young} \geq [M/H]_{old}$.

E.2.2 Stellar population predictions assuming a constant and local MZR

The goal of this subsection is to determine how the stellar population parameters change when the MZR is assumed to be constant with redshift and equal to the local MZR presented in Peng et al. (2015). This analysis is performed with the BaSTI isochrones only as they present more suitable metallicity bins. Therefore, we repeat the analysis forcing that metallicity (both components in the mixture) is equal to [M/H] = −0.25, 0.06, and 0.15 for stellar masses $10.0 \leq \log_{10} M_\star < 10.4$, $10.4 \leq \log_{10} M_\star < 10.8$, and $\log_{10} M_\star \geq 10.8$ respectively (these reference stellar masses are the determined ones without constraints in Sect. 3.8). The stellar population distributions are also deconvolved of uncertainty effects through the MLE method to retrieve the PDFs of stellar population parameters.

The impact of forcing the metallicity to the local values is strong on the distributions of mass-weighted ages (see Fig. E.27). Even though the age–stellar mass relation is still obtained, the median of the age PDF experiments a remarkable decrease of 3 Gyr, where for decreasing stellar mass this shift is more prominent. In addition, the dependency of the median age with redshift advocates a rather non-passive evolution of the stellar content of quiescent galaxies, which would imply a larger inclusion of new or younger stars to the quiescent population. The widths of the mass-weighted age PDFs also show an increment of their values for any stellar mass bin respect the values obtained in Sect. 3.8. There are negligible differences amongst the widths of the age PDFs of different stellar mass bins ($\omega_{\mathrm{Age_M}} \sim 2$ Gyr). As in Sect. 3.8, the width of the age PDF does not show a significant dependency with redshift.

Regarding the median of the extinction PDF (Fig. E.28 in Appendix E), the extinction is no longer constant under the local metallicity constraint, and it decreases with cosmic time. There are no evidences of a dependency of extinction with stellar mass either, and the new range of median extinctions spans $A_V = 0.1$–0.5. The width of the extinction PDF also increases, and it is wider for the less massive quiescent galaxies. Finally, the correlation between the width of the extinction PDF and redshift is also present and it is more prominent than in the case without metallicity constraints (see dashed lines in Fig. E.28).

E.3 Figures of the constraints on the SFH for both BC03 and EMILES SSP models

All the figures from Sects. E.1 (Figs. E.1–E.16) and E.2 (Figs. E.17–E.28 and Figs. E.29–E.38, for BaSTI and Padova00 isochrones respectively) are shown below. See details in captions.

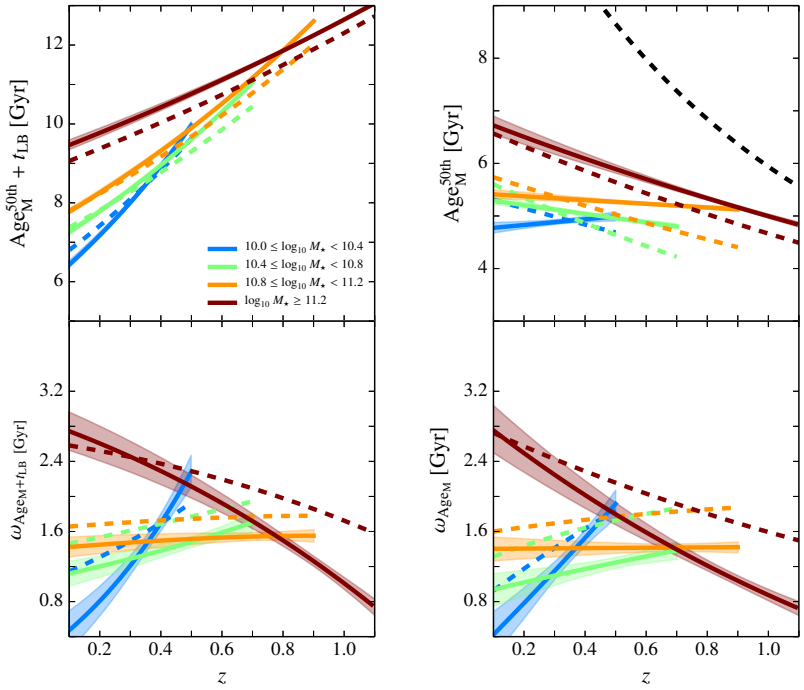

Figure E.1: Evolution of the median (*top panels*) and width (ω, *bottom panels*) of the mass-weighted formation epoch (*left column*) and age (*right column*) distributions of the quiescent population at $0.1 \leq z \leq 1.1$ for different stellar mass bins when extinction is fixed to $A_V = 0.2$ (BC03 models). The shaded regions delimit the 1 σ uncertainties of both parameters. Dashed coloured lines are the same parameters obtained without fixing extinction to a constant value (see Sect. 3.7). Dashed black line illustrates the age of the Universe at different redshifts.

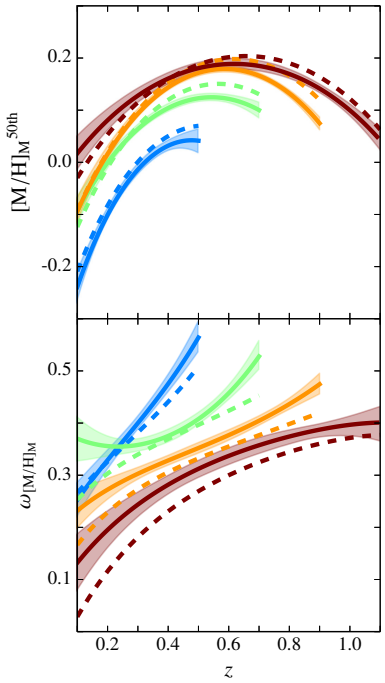

Figure E.2: As Fig. E.1, but for mass-weighted metallicity.

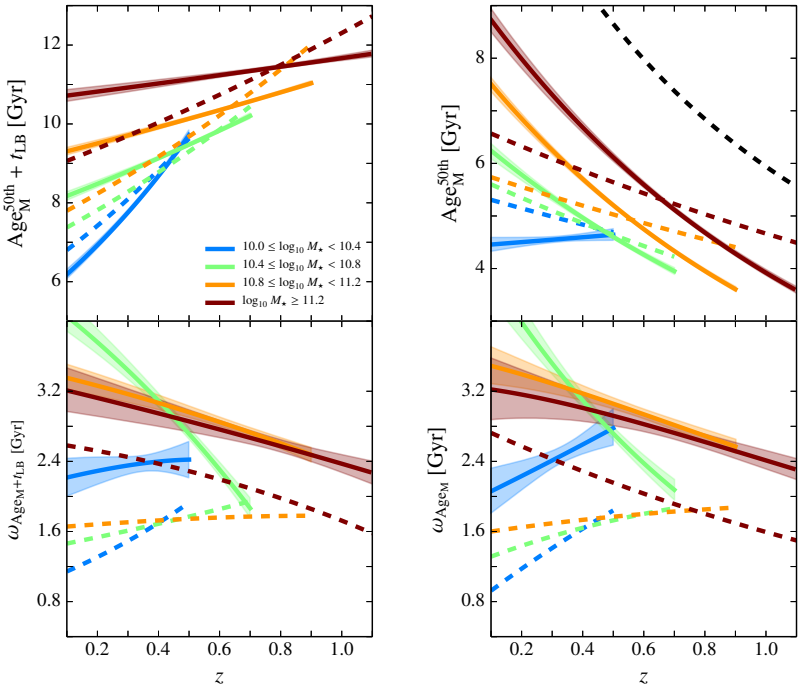

Figure E.3: Evolution of the median (*top panels*) and width (ω, *bottom panels*) of the mass-weighted formation epoch (*left column*) and age (*right column*) distributions of the quiescent population at $0.1 \leq z \leq 1.1$ for different stellar mass bins when metal content is fixed to solar metallicity [M/H] = 0.0 dex (BC03 models). The shaded regions delimit the 1 σ uncertainties of both parameters. Dashed coloured lines are the same parameters obtained without fixing metallicity (see Sect. 3.7). Dashed black line illustrates the age of the Universe at different redshifts.

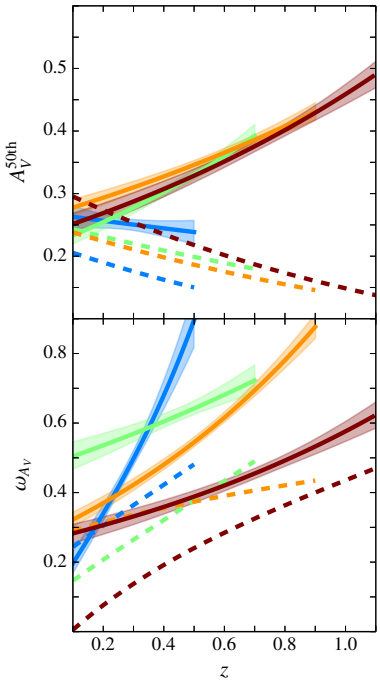

Figure E.4: As Fig. E.3, but for extinction distribution values.

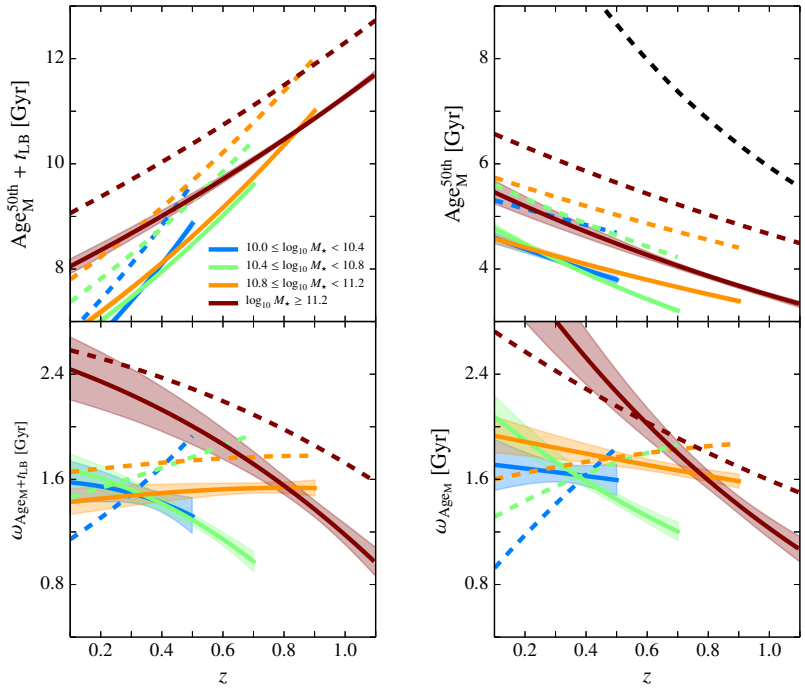

Figure E.5: Evolution of the median (*top panels*) and width (ω, *bottom panels*) of the mass-weighted formation epoch (*left column*) and age (*right column*) distributions of the quiescent population at $0.1 \leq z \leq 1.1$ for different stellar mass bins after imposing that the components in the SSP mixture $[\mathrm{M/H}]_{\mathrm{young}} \geq [\mathrm{M/H}]_{\mathrm{old}}$ (BC03 models). The shaded regions delimit the 1 σ uncertainties of both parameters. Dashed coloured lines are the same parameters obtained without metallicity constraints (see Sect. 3.7). Dashed black line illustrates the age of the Universe at different redshifts.

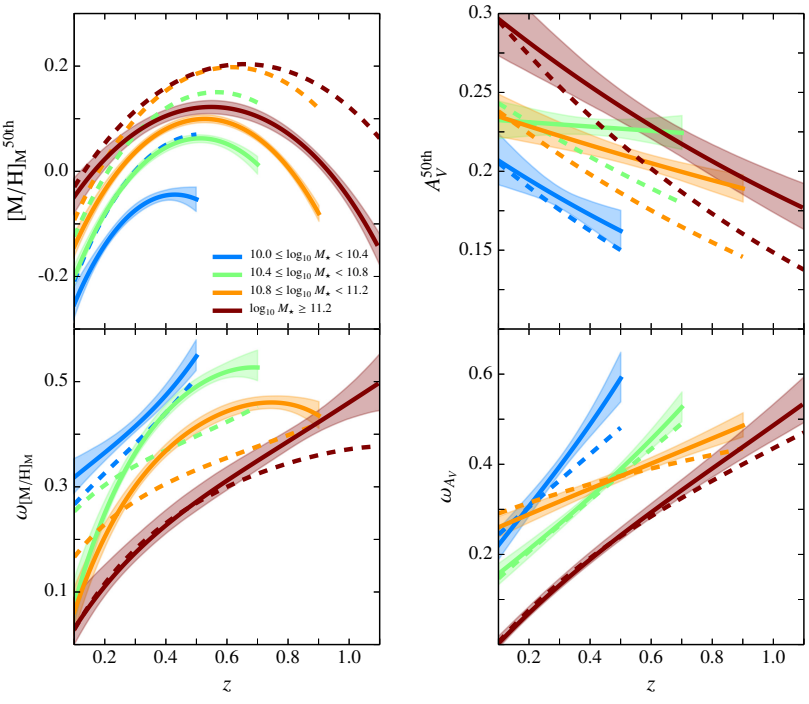

Figure E.6: As Fig. E.5, but for mass-weighted metallicity and extinction.

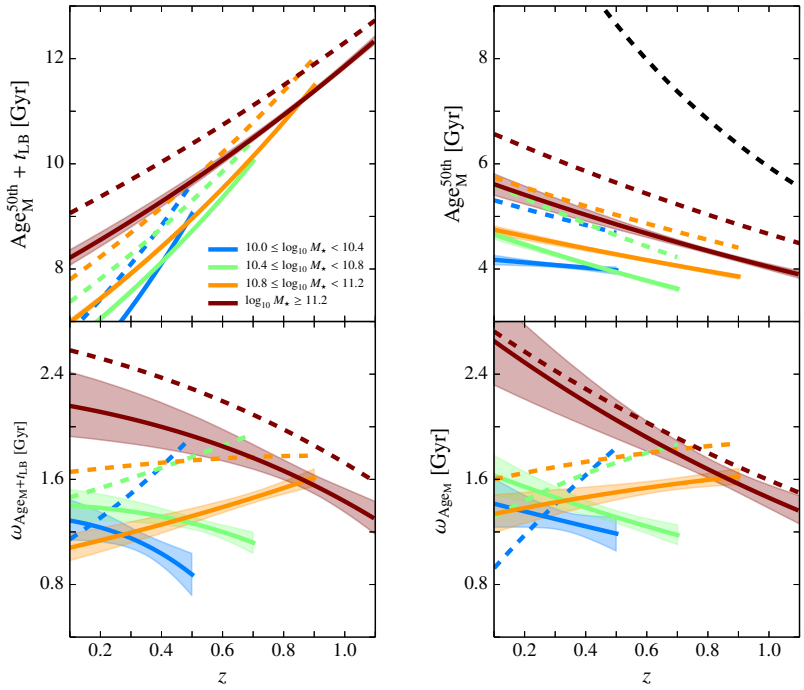

Figure E.7: Evolution of the median (*top panels*) and width (ω, *bottom panels*) of the mass-weighted formation epoch (*left column*) and age (*right column*) distributions of the quiescent population at $0.1 \leq z \leq 1.1$ for different stellar mass bins after imposing that the components in the SSP mixture $[\mathrm{M/H}]_{\mathrm{young}} \geq [\mathrm{M/H}]_{\mathrm{old}}$ and $[\mathrm{M/H}] \geq -0.64$ dex (BC03 models). The shaded regions delimit the 1 σ uncertainties of both parameters. Dashed coloured lines are the same parameters obtained without metallicity constraints (see Sect. 3.7). Dashed black line illustrates the age of the Universe at different redshifts.

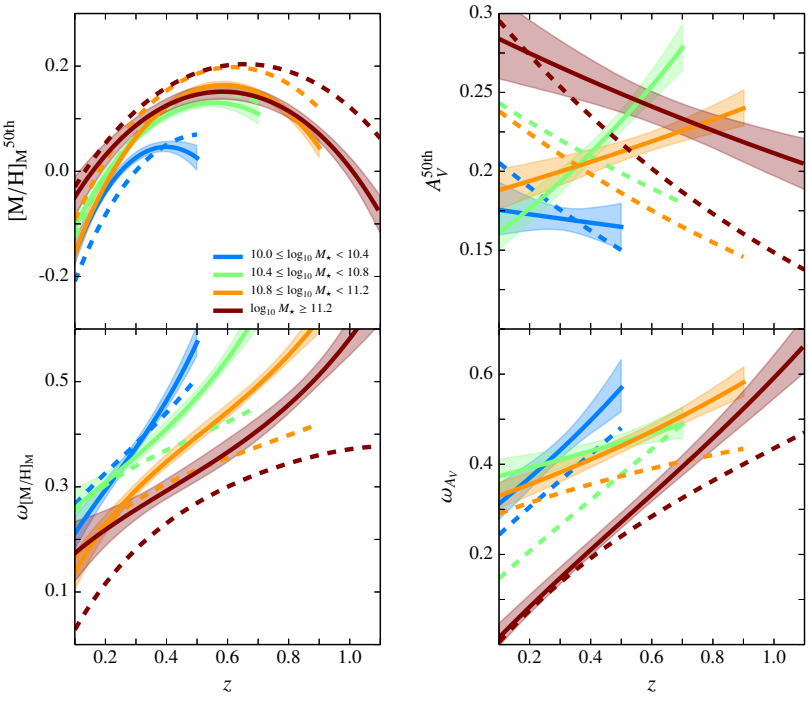

Figure E.8: As Fig. E.7, but for mass-weighted metallicity and extinction.

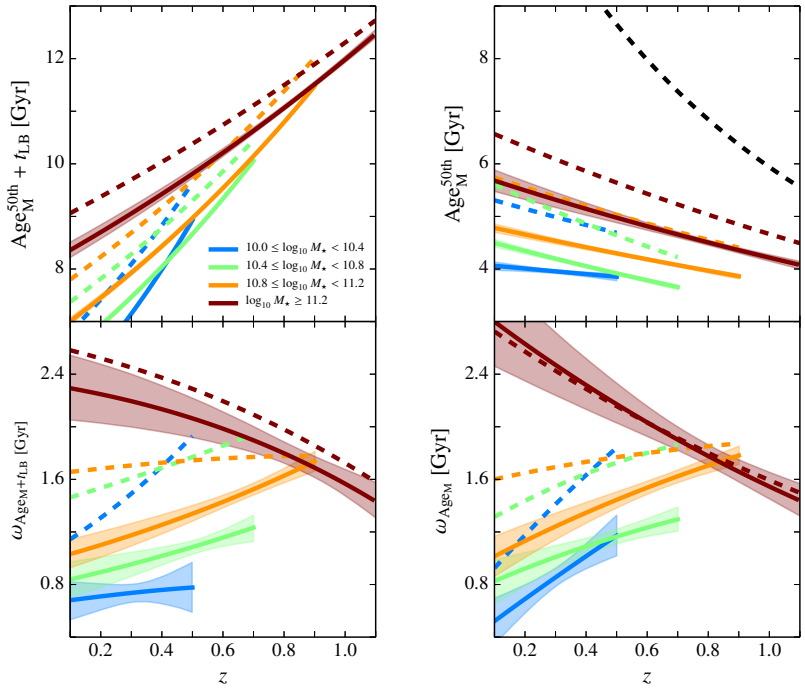

Figure E.9: Evolution of the median (*top panels*) and width (ω, *bottom panels*) of the mass-weighted formation epoch (*left column*) and age (*right column*) distributions of the quiescent population at $0.1 \leq z \leq 1.1$ for different stellar mass bins after imposing that the components in the SSP mixture $[\mathrm{M/H}]_{\mathrm{young}} \geq [\mathrm{M/H}]_{\mathrm{old}}$ and $[\mathrm{M/H}] \geq -0.33$ dex (BC03 models). The shaded regions delimit the 1 σ uncertainties of both parameters. Dashed coloured lines are the same parameters obtained without metallicity constraints (see Sect. 3.7). Dashed black line illustrates the age of the Universe at different redshifts.

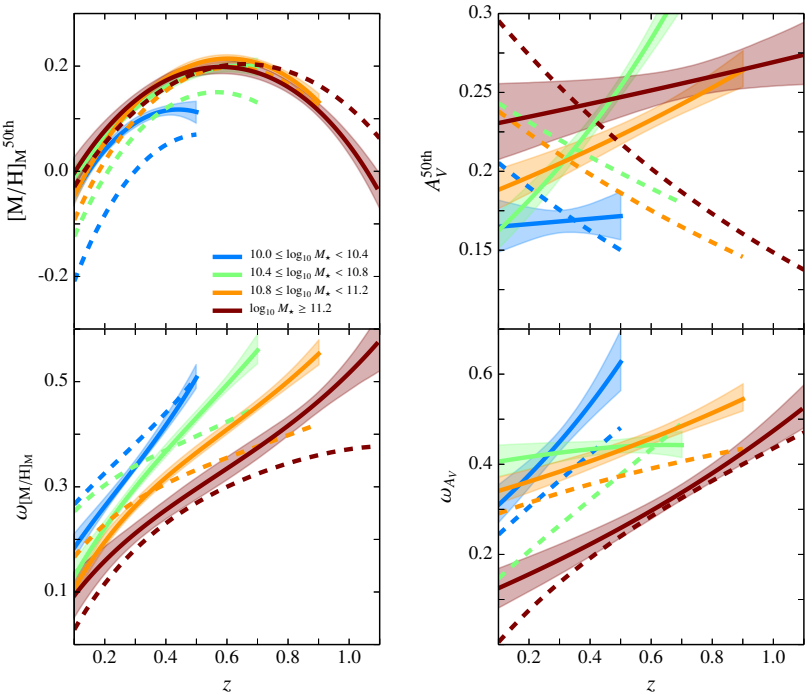

Figure E.10: As Fig. E.9, but for mass-weighted metallicity and extinction.

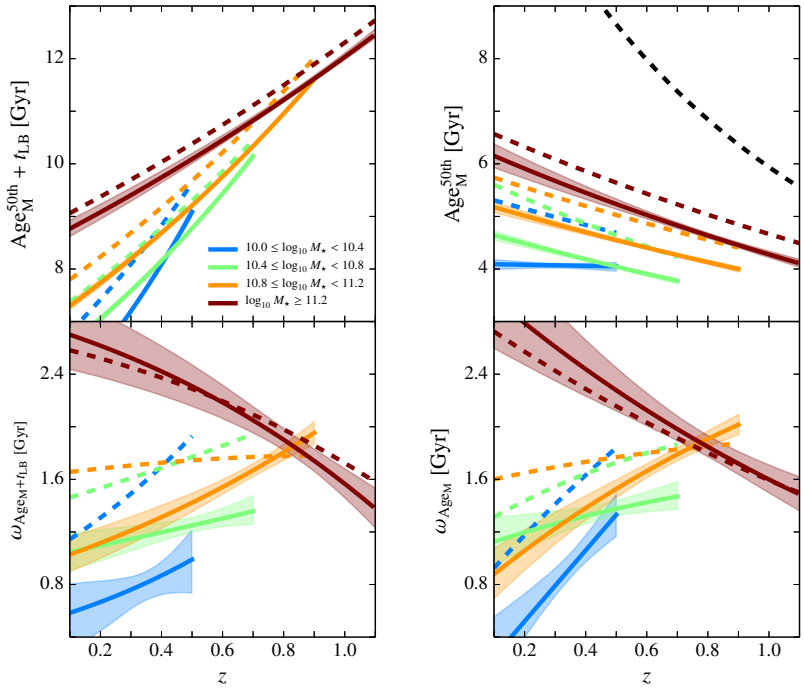

Figure E.11: Evolution of the median (*top panels*) and width (ω, *bottom panels*) of the mass-weighted formation epoch (*left column*) and age (*right column*) distributions of the quiescent population at $0.1 \leq z \leq 1.1$ for different stellar mass bins after imposing that the components in the SSP mixture $[\mathrm{M/H}]_{\mathrm{young}} \gtrsim [\mathrm{M/H}]_{\mathrm{old}}$ (BC03 models). The shaded regions delimit the 1 σ uncertainties of both parameters. Dashed coloured lines are the same parameters obtained without metallicity constraints (see Sect. 3.7). Dashed black line illustrates the age of the Universe at different redshifts.

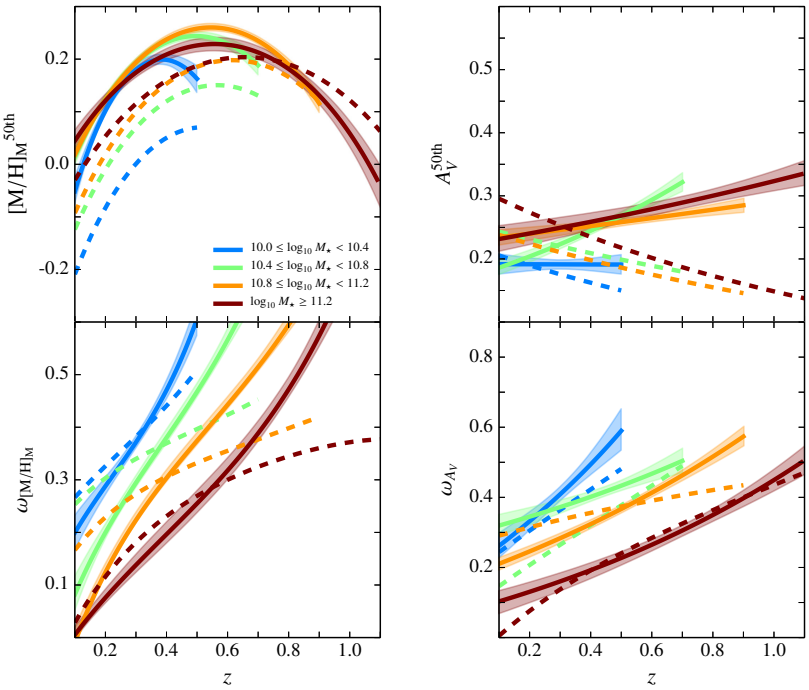

Figure E.12: As Fig. E.11, but for mass-weighted metallicity and extinction.

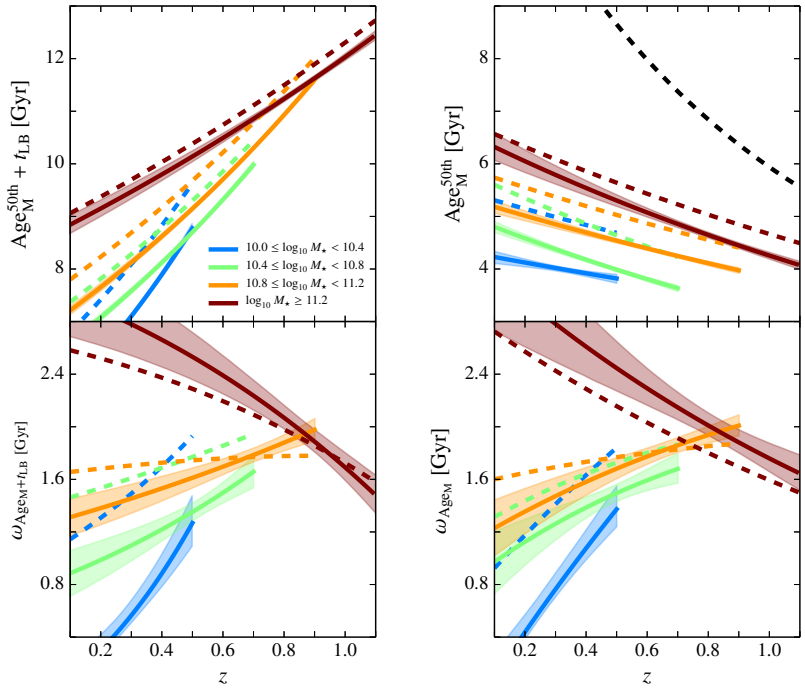

Figure E.13: Evolution of the median (*top panels*) and width (ω, *bottom panels*) of the mass-weighted formation epoch (*left column*) and age (*right column*) distributions of the quiescent population at $0.1 \leq z \leq 1.1$ for different stellar mass bins after imposing that the components in the SSP mixture $[\mathrm{M/H}]_{\mathrm{young}} = [\mathrm{M/H}]_{\mathrm{old}}$ (BC03 models). The shaded regions delimit the 1 σ uncertainties of both parameters. Dashed coloured lines are the same parameters obtained without metallicity constraints (see Sect. 3.7). Dashed black line illustrates the age of the Universe at different redshifts.

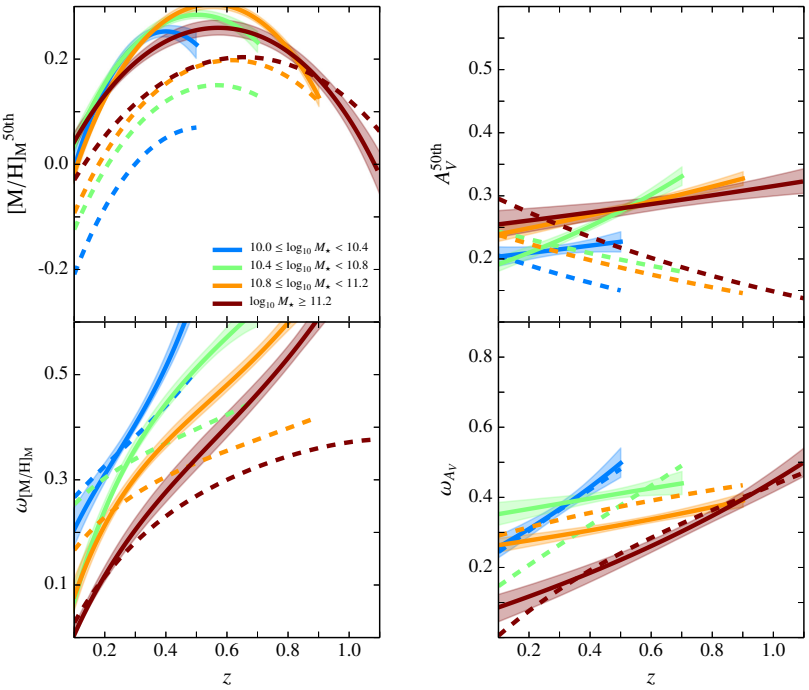

Figure E.14: As Fig. E.13, but for mass-weighted metallicity and extinction.

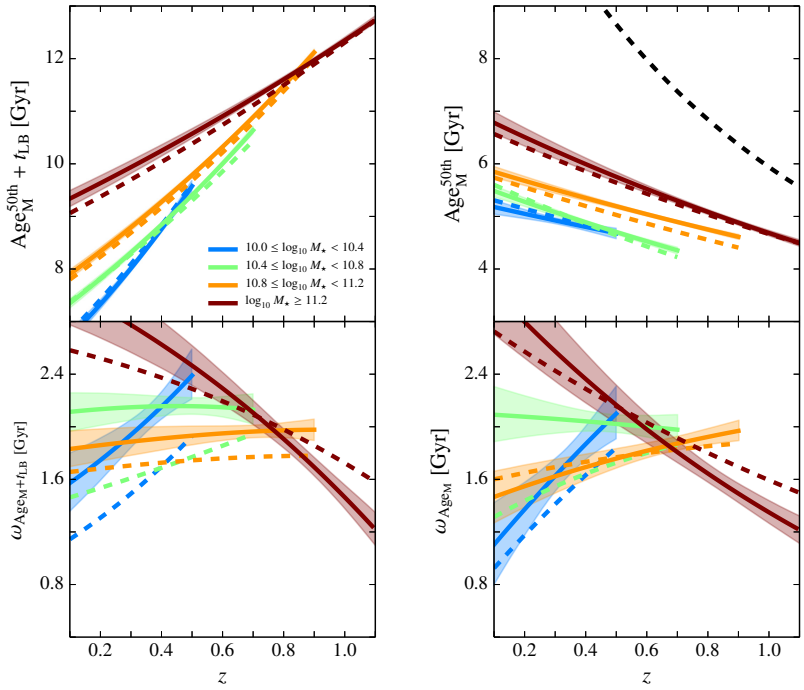

Figure E.15: Evolution of the median (*top panels*) and width (ω, *bottom panels*) of the mass-weighted formation epoch (*left column*) and age (*right column*) distributions of the quiescent population at $0.1 \leq z \leq 1.1$ for different stellar mass bins after imposing that the components in the SSP mixture $[\mathrm{M/H}]_{\mathrm{young}} \leq [\mathrm{M/H}]_{\mathrm{old}}$ (BC03 models). The shaded regions delimit the 1 σ uncertainties of both parameters. Dashed coloured lines are the same parameters obtained without metallicity constraints (see Sect. 3.7). Dashed black line illustrates the age of the Universe at different redshifts.

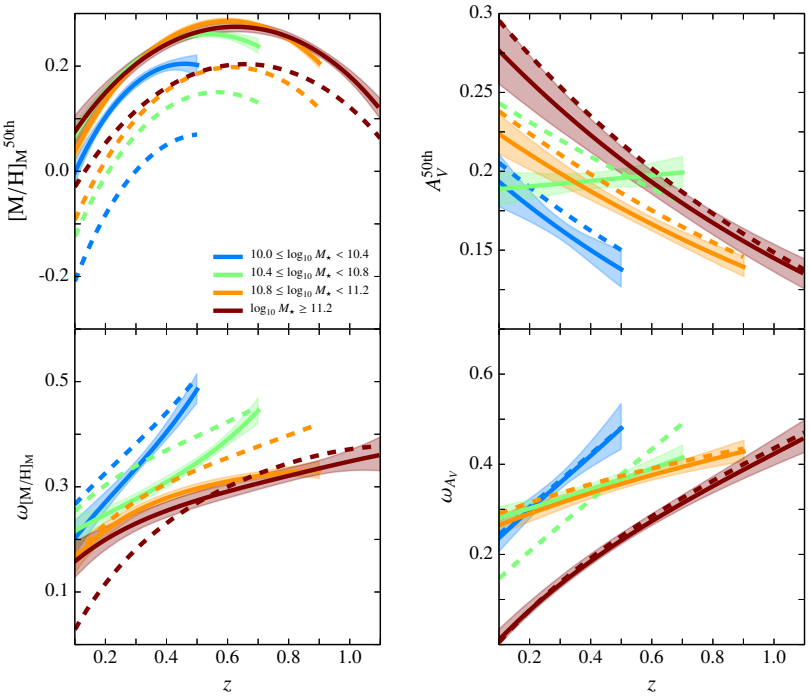

Figure E.16: As Fig. E.15, but for mass-weighted metallicity and extinction.

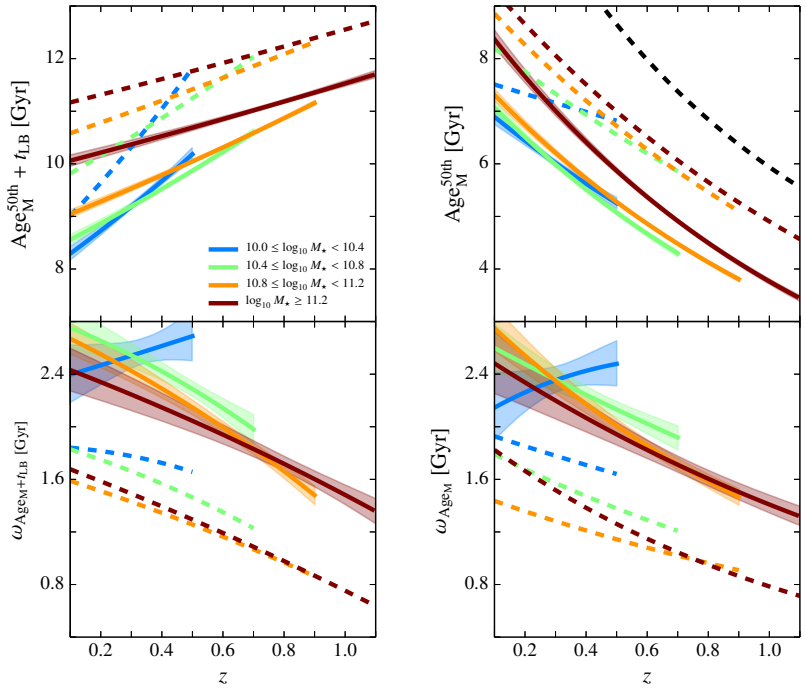

Figure E.17: Evolution of the median (*top panels*) and width (ω, *bottom panels*) of the mass-weighted formation epoch (*left column*) and age (*right column*) distributions of the quiescent population at $0.1 \leq z \leq 1.1$ for different stellar mass bins after imposing that the metallicities in the SSP mixture $[\mathrm{M/H}]_{\mathrm{young}} \geq [\mathrm{M/H}]_{\mathrm{old}}$ (EMILES+BaSTI). The shaded regions delimit the 1 σ uncertainties of both parameters. Dashed coloured lines are the same parameters obtained without constraints (see Sect. 3.8). Dashed black line illustrates the age of the Universe at different redshifts.

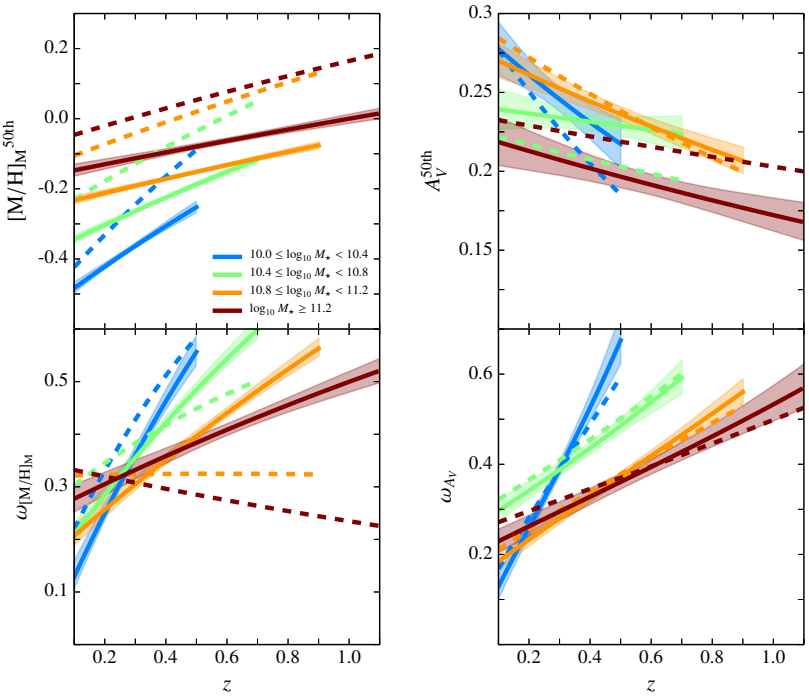

Figure E.18: As Fig. E.17, but for mass-weighted metallicity and extinction.

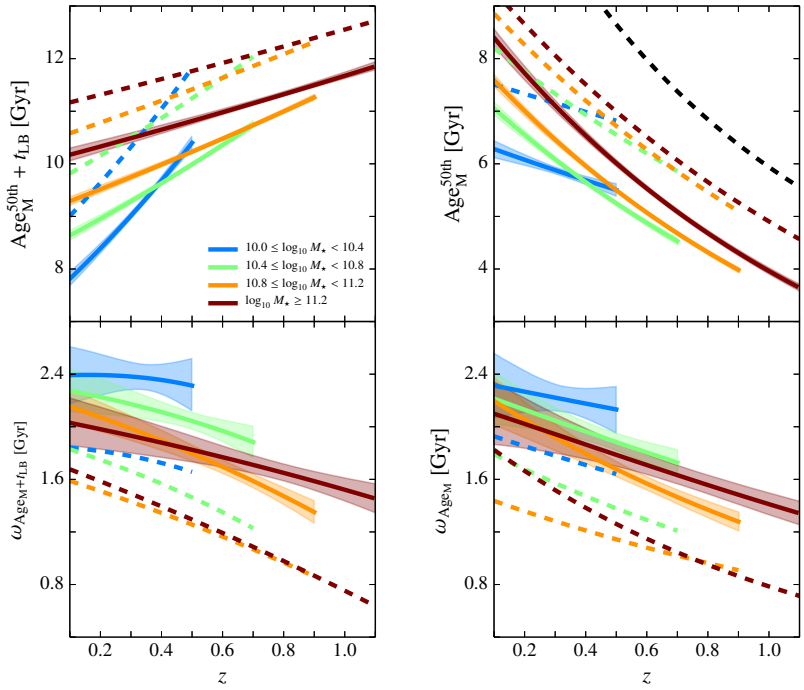

Figure E.19: Evolution of the median (*top panels*) and width (ω, *bottom panels*) of the mass-weighted formation epoch (*left column*) and age (*right column*) distributions of the quiescent population at $0.1 \leq z \leq 1.1$ for different stellar mass bins after imposing that the metallicities in the SSP mixture $[\mathrm{M/H}]_{\mathrm{young}} \gtrsim [\mathrm{M/H}]_{\mathrm{old}}$ (EMILES+BaSTI). The shaded regions delimit the 1 σ uncertainties of both parameters. Dashed coloured lines are the same parameters obtained without constraints (see Sect. 3.8). Dashed black line illustrates the age of the Universe at different redshifts.

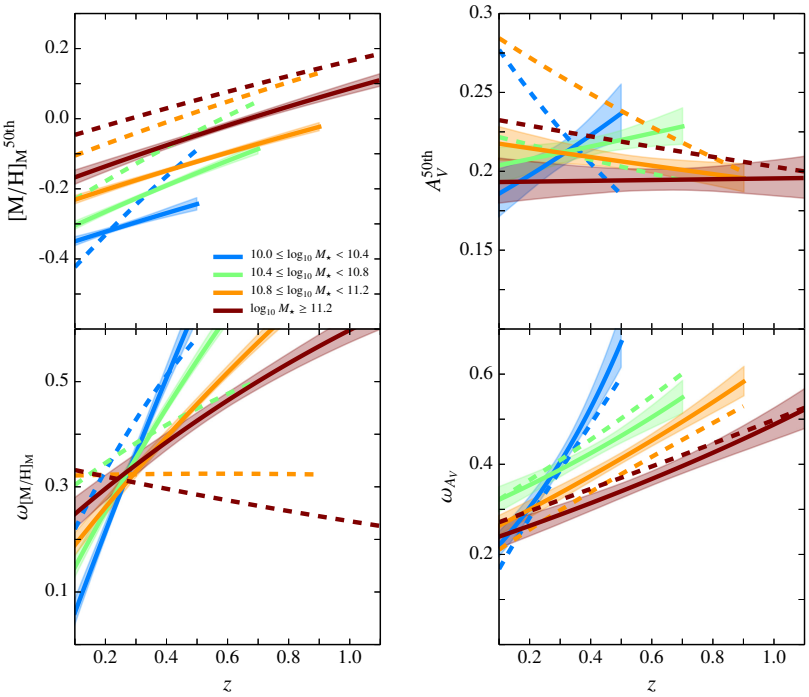

Figure E.20: As Fig. E.19, but for mass-weighted metallicity and extinction.

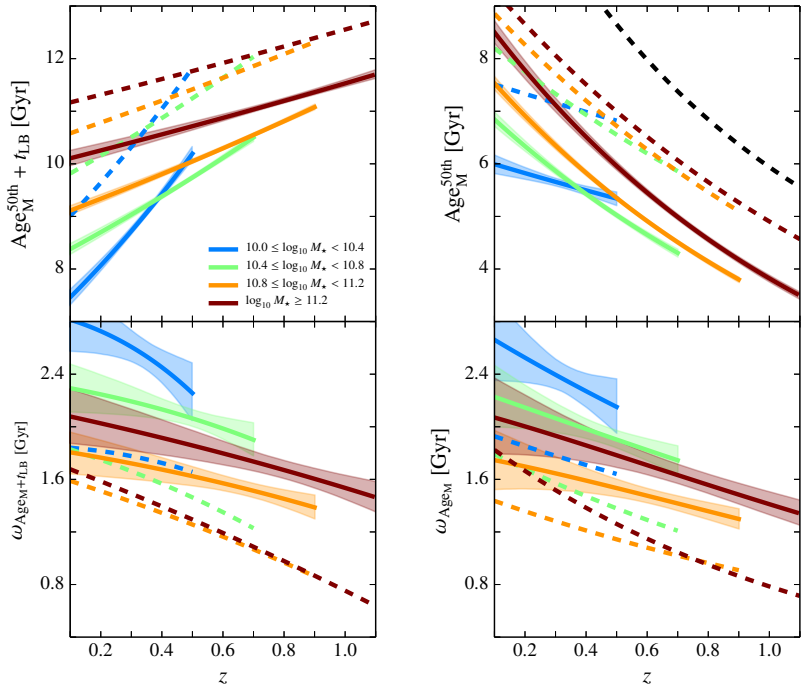

Figure E.21: Evolution of the median (*top panels*) and width (ω, *bottom panels*) of the mass-weighted formation epoch (*left column*) and age (*right column*) distributions of the quiescent population at $0.1 \leq z \leq 1.1$ for different stellar mass bins after imposing that the metallicities in the SSP mixture $[\mathrm{M/H}]_{\mathrm{young}} = [\mathrm{M/H}]_{\mathrm{old}}$ (EMILES+BaSTI). The shaded regions delimit the 1 σ uncertainties of both parameters. Dashed coloured lines are the same parameters obtained without constraints (see Sect. 3.8). Dashed black line illustrates the age of the Universe at different redshifts.

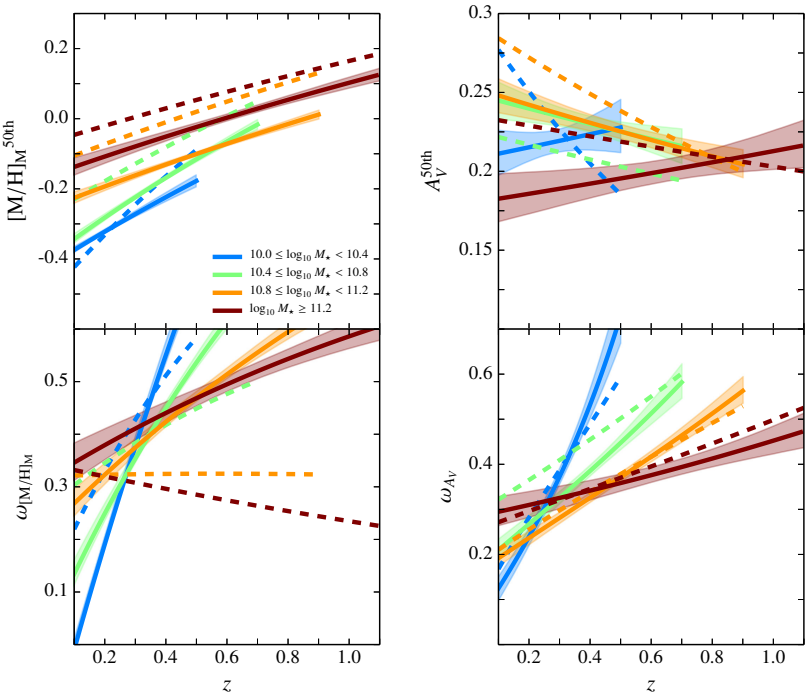

Figure E.22: As Fig. E.21, but for mass-weighted metallicity and extinction.

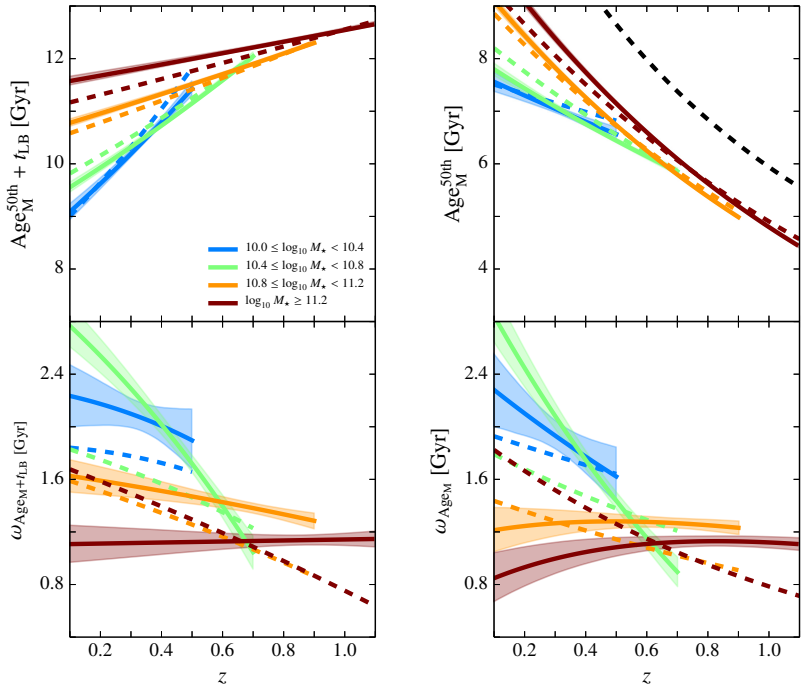

Figure E.23: Evolution of the median (*top panels*) and width (ω, *bottom panels*) of the mass-weighted formation epoch (*left column*) and age (*right column*) distributions of the quiescent population at $0.1 \leq z \leq 1.1$ for different stellar mass bins after imposing that the metallicities in the SSP mixture $[\mathrm{M/H}]_{\mathrm{young}} \leq [\mathrm{M/H}]_{\mathrm{old}}$ (EMILES+BaSTI). The shaded regions delimit the 1 σ uncertainties of both parameters. Dashed coloured lines are the same parameters obtained without constraints (see Sect. 3.8). Dashed black line illustrates the age of the Universe at different redshifts.

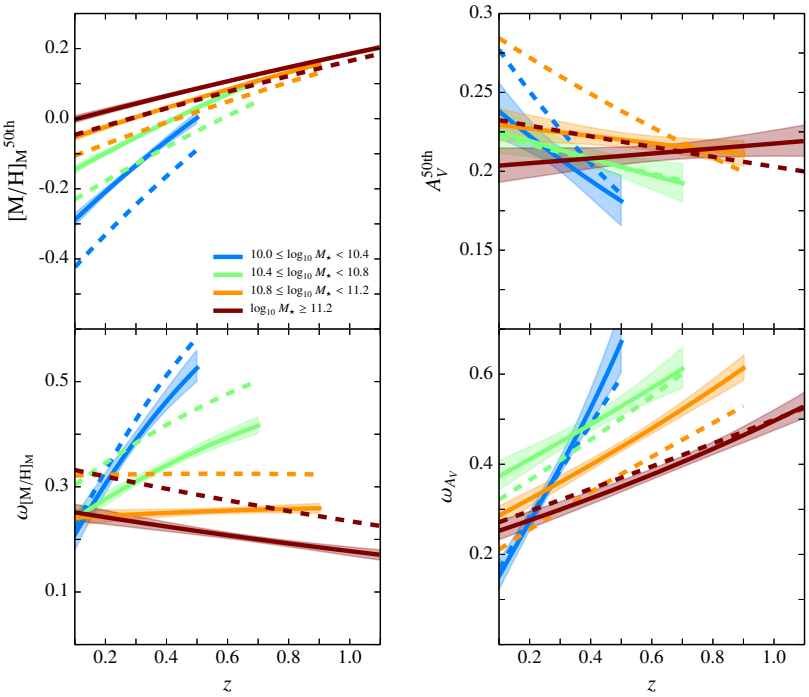

Figure E.24: As Fig. E.23, but for mass-weighted metallicity and extinction.

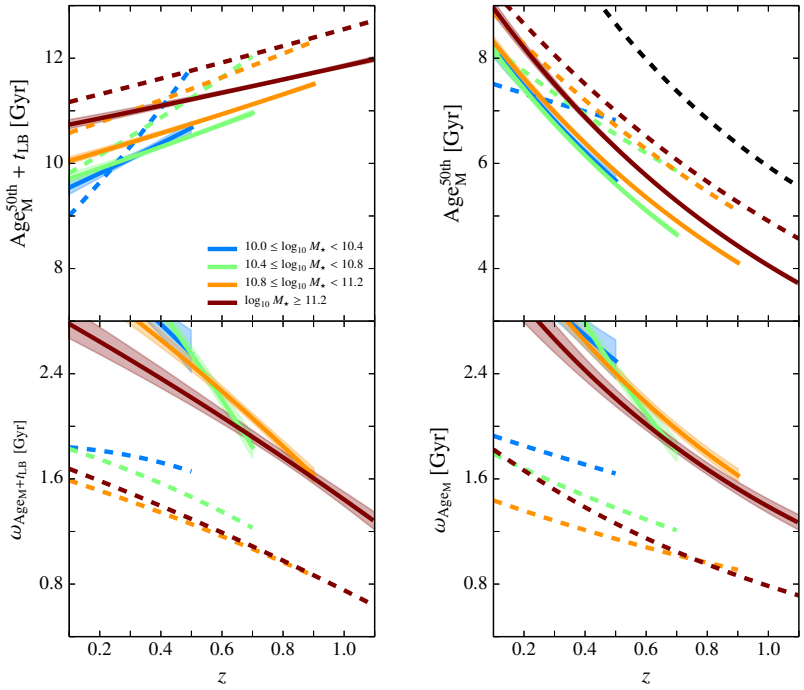

Figure E.25: Evolution of the median (*top panels*) and width (ω, *bottom panels*) of the mass-weighted formation epoch (*left column*) and age (*right column*) distributions of the quiescent population at $0.1 \leq z \leq 1.1$ for different stellar mass bins after imposing that the components in the SSP mixture $[\mathrm{M/H}]_{\mathrm{young}} \geq [\mathrm{M/H}]_{\mathrm{old}}$ and $A_V = 0.0$ (EMILES+BaSTI). The shaded regions delimit the 1 σ uncertainties of both parameters. Dashed coloured lines are the same parameters obtained without constraints (see Sect. 3.8). Dashed black line illustrates the age of the Universe at different redshifts.

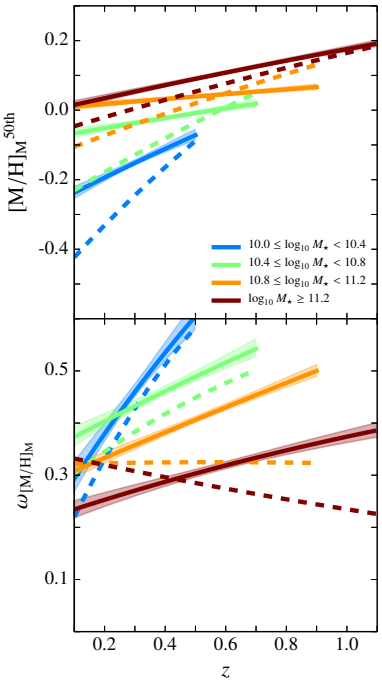

Figure E.26: As Fig. E.25, but for mass-weighted metallicity.

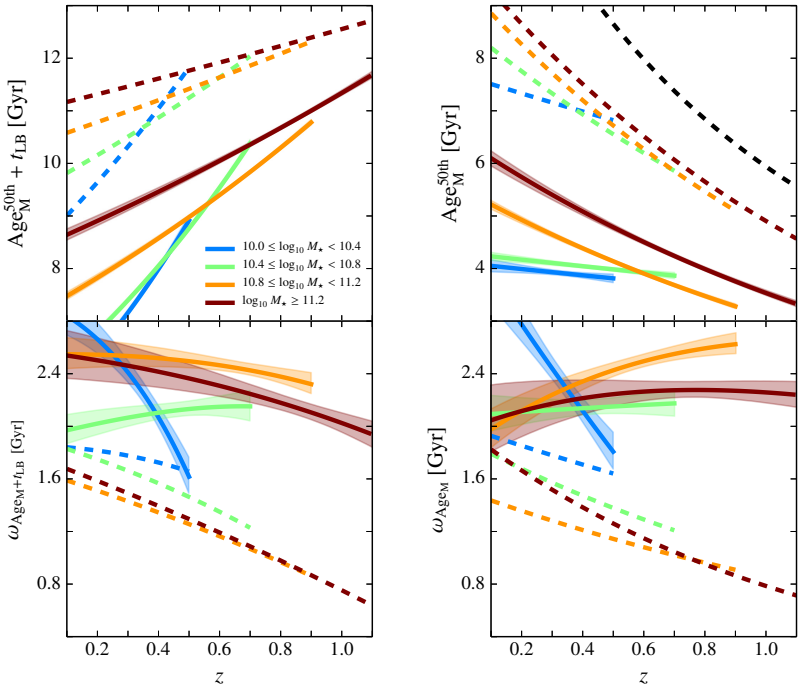

Figure E.27: Evolution of the median (*top panels*) and width (ω, *bottom panels*) of the mass-weighted formation epoch (*left column*) and age (*right column*) distributions of the quiescent population at $0.1 \leq z \leq 1.1$ for different stellar mass bins after imposing that the metallicities in the SSP mixture are the local ones observed for each stellar mass bin (EMILES+BaSTI). The shaded regions delimit the 1 σ uncertainties of both parameters. Dashed coloured lines are the same parameters obtained without constraints (see Sect. 3.8). Dashed black line illustrates the age of the Universe at different redshifts.

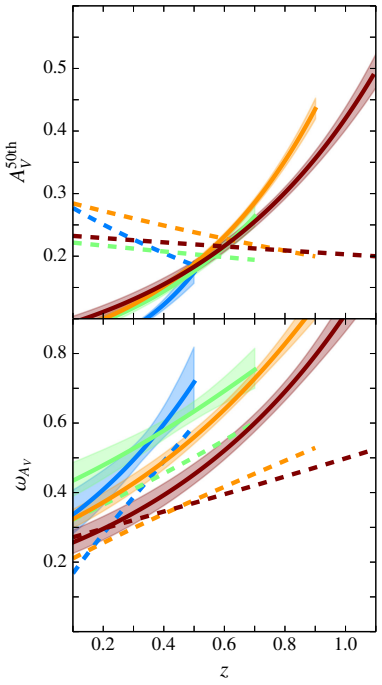

Figure E.28: As Fig. E.27, but for extinction.

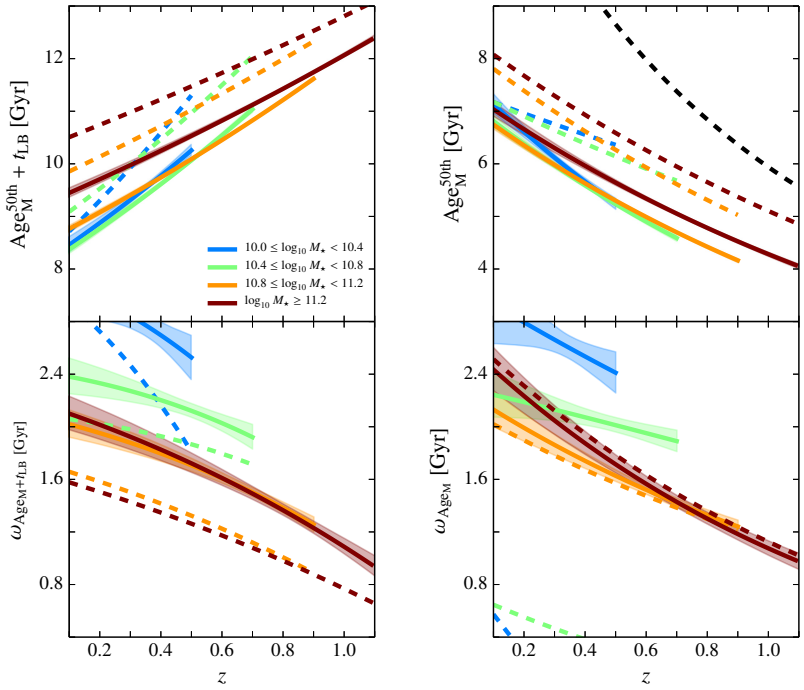

Figure E.29: Evolution of the median (*top panels*) and width (ω, *bottom panels*) of the mass-weighted formation epoch (*left column*) and age (*right column*) distributions of the quiescent population at $0.1 \leq z \leq 1.1$ for different stellar mass bins after imposing that the metallicities in the SSP mixture $[\mathrm{M/H}]_{\mathrm{young}} \geq [\mathrm{M/H}]_{\mathrm{old}}$ (EMILES+Padova00). The shaded regions delimit the 1 σ uncertainties of both parameters. Dashed coloured lines are the same parameters obtained without constraints (see Sect. 3.8). Dashed black line illustrates the age of the Universe at different redshifts.

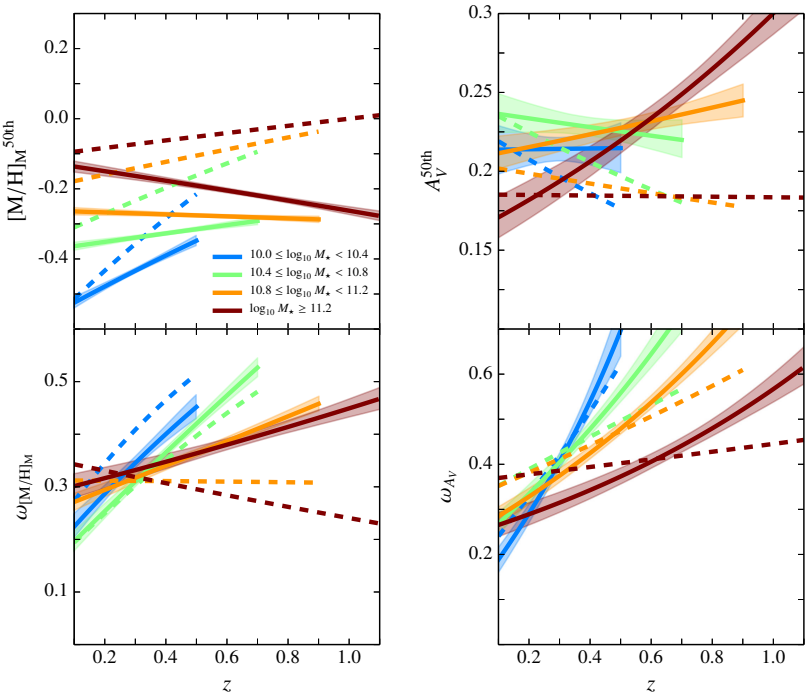

Figure E.30: As Fig. E.29, but for mass-weighted metallicity and extinction.

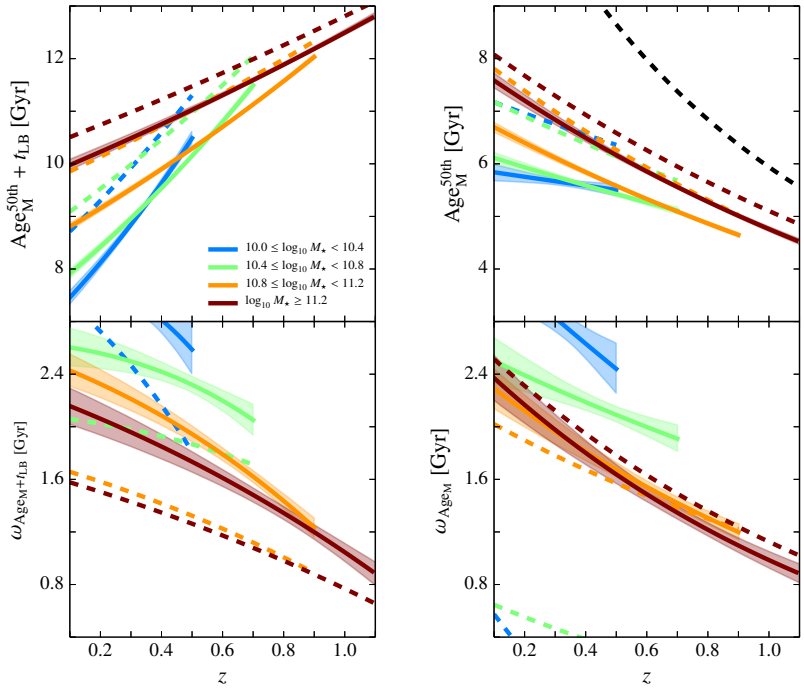

Figure E.31: Evolution of the median (*top panels*) and width (ω, *bottom panels*) of the mass-weighted formation epoch (*left column*) and age (*right column*) distributions of the quiescent population at $0.1 \leq z \leq 1.1$ for different stellar mass bins after imposing that the metallicities in the SSP mixture $[\mathrm{M/H}]_{\mathrm{young}} \gtrsim [\mathrm{M/H}]_{\mathrm{old}}$ (EMILES+Padova00). The shaded regions delimit the 1 σ uncertainties of both parameters. Dashed coloured lines are the same parameters obtained without constraints (see Sect. 3.8). Dashed black line illustrates the age of the Universe at different redshifts.

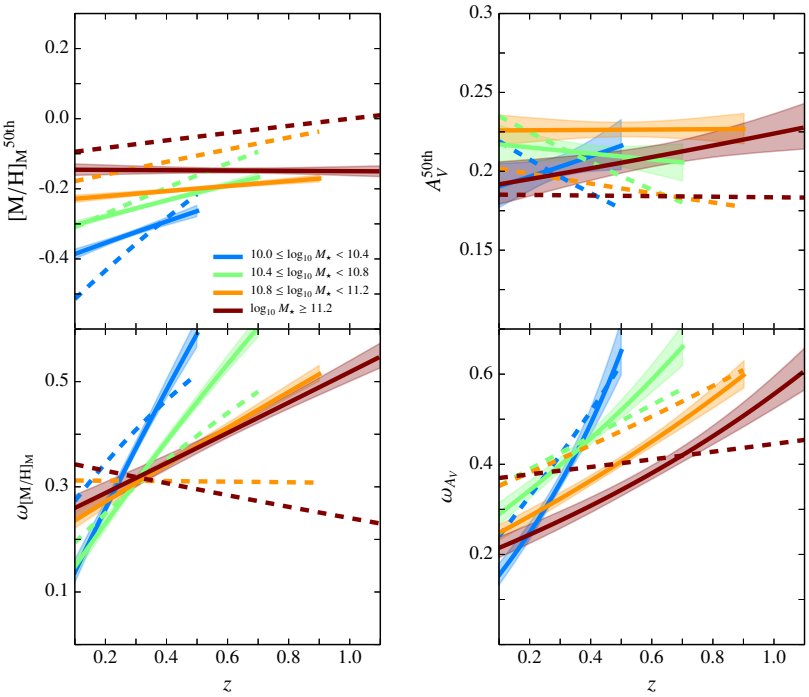

Figure E.32: As Fig. E.31, but for mass-weighted metallicity and extinction.

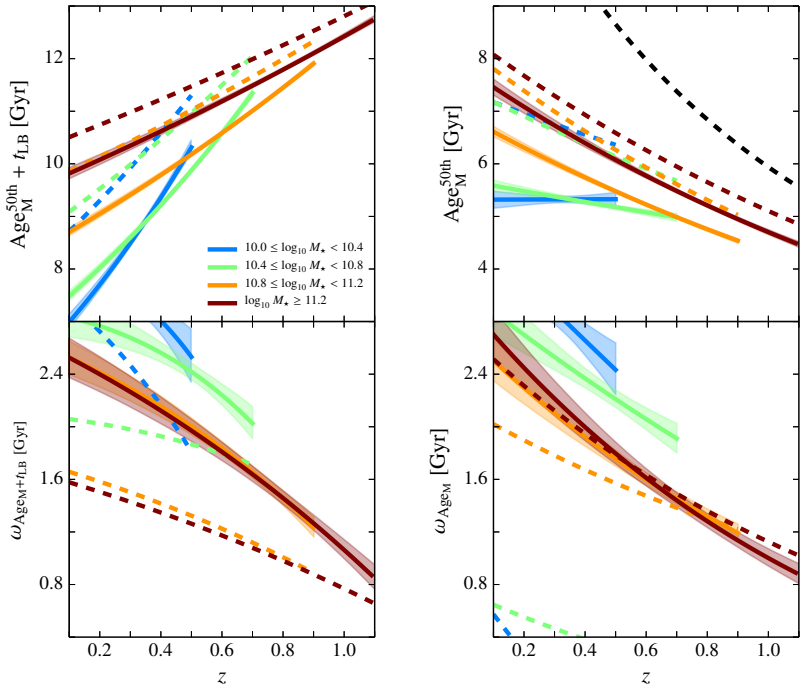

Figure E.33: Evolution of the median (*top panels*) and width (ω, *bottom panels*) of the mass-weighted formation epoch (*left column*) and age (*right column*) distributions of the quiescent population at $0.1 \leq z \leq 1.1$ for different stellar mass bins after imposing that the metallicities in the SSP mixture $[\mathrm{M/H}]_{\mathrm{young}} = [\mathrm{M/H}]_{\mathrm{old}}$ (EMILES+Padova00). The shaded regions delimit the 1 σ uncertainties of both parameters. Dashed coloured lines are the same parameters obtained without constraints (see Sect. 3.8). Dashed black line illustrates the age of the Universe at different redshifts.

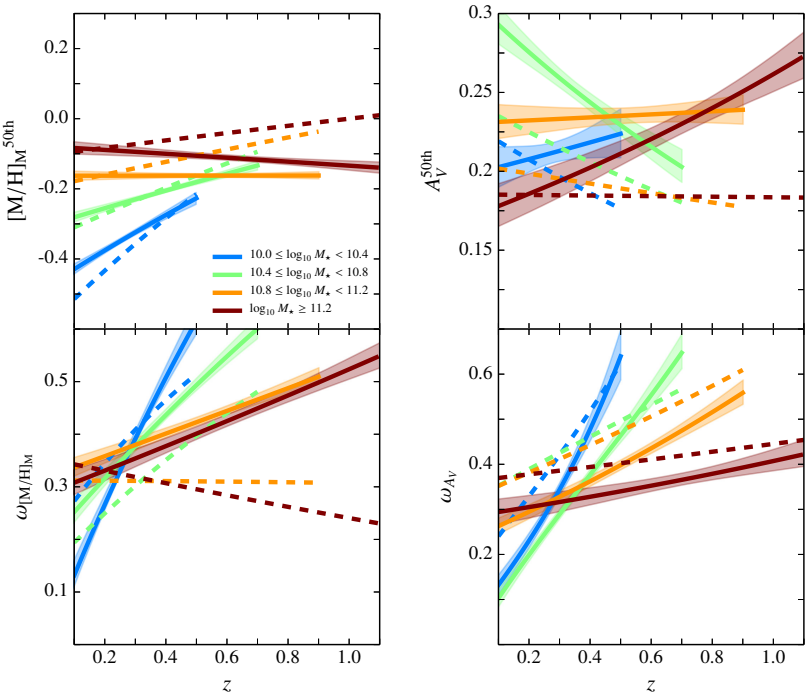

Figure E.34: As Fig. E.33, but for mass-weighted metallicity and extinction.

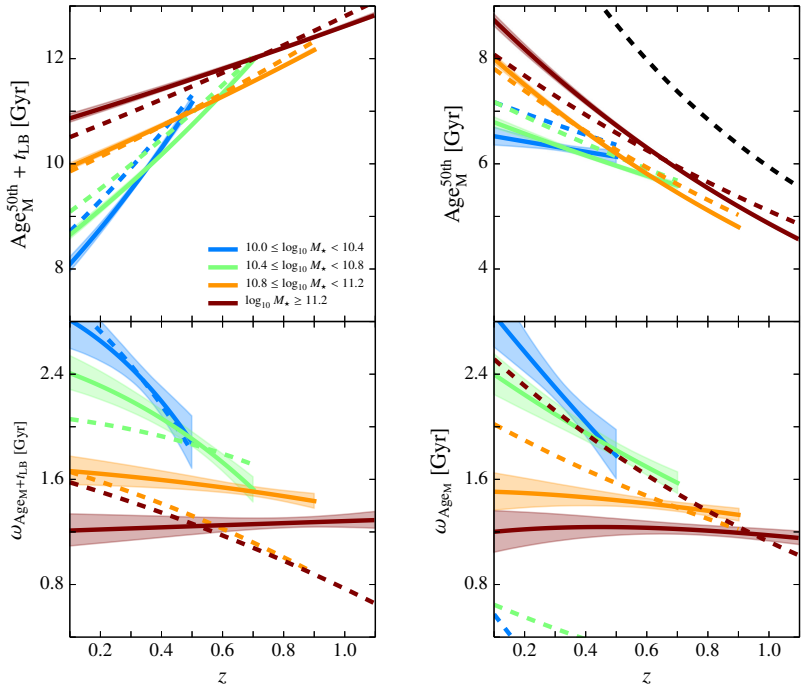

Figure E.35: Evolution of the median (*top panels*) and width (ω, *bottom panels*) of the mass-weighted formation epoch (*left column*) and age (*right column*) distributions of the quiescent population at $0.1 \leq z \leq 1.1$ for different stellar mass bins after imposing that the metallicities in the SSP mixture $[\mathrm{M/H}]_{\mathrm{young}} \leq [\mathrm{M/H}]_{\mathrm{old}}$ (EMILES+Padova00). The shaded regions delimit the 1 σ uncertainties of both parameters. Dashed coloured lines are the same parameters obtained without constraints (see Sect. 3.8). Dashed black line illustrates the age of the Universe at different redshifts.

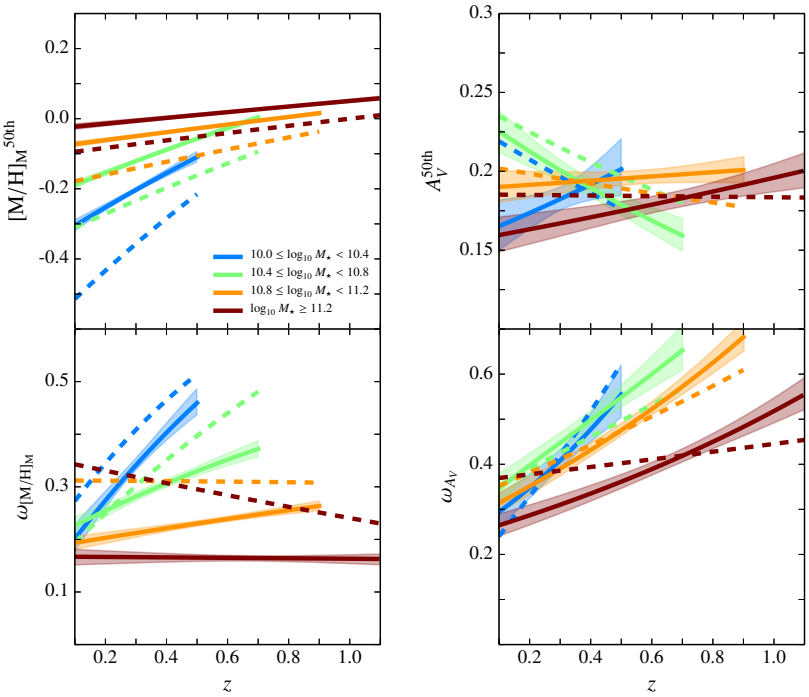

Figure E.36: As Fig. E.35, but for mass-weighted metallicity and extinction.

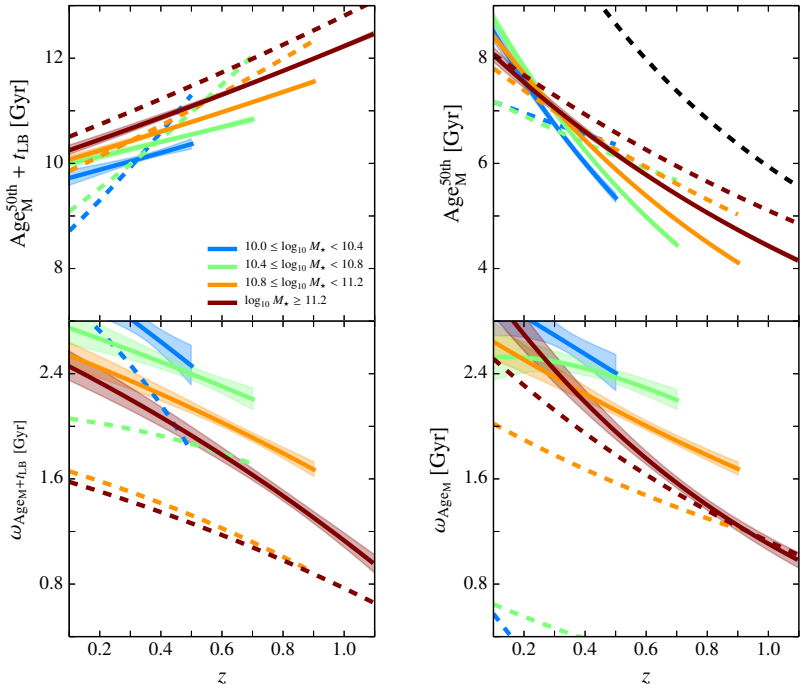

Figure E.37: Evolution of the median (*top panels*) and width (ω, *bottom panels*) of the mass-weighted formation epoch (*left column*) and age (*right column*) distributions of the quiescent population at $0.1 \leq z \leq 1.1$ for different stellar mass bins after imposing that the components in the SSP mixture $[\mathrm{M/H}]_{\mathrm{young}} \geq [\mathrm{M/H}]_{\mathrm{old}}$ and $A_V = 0.0$ (EMILES+Padova00). The shaded regions delimit the 1 σ uncertainties of both parameters. Dashed coloured lines are the same parameters obtained without constraints (see Sect. 3.8). Dashed black line illustrates the age of the Universe at different redshifts.

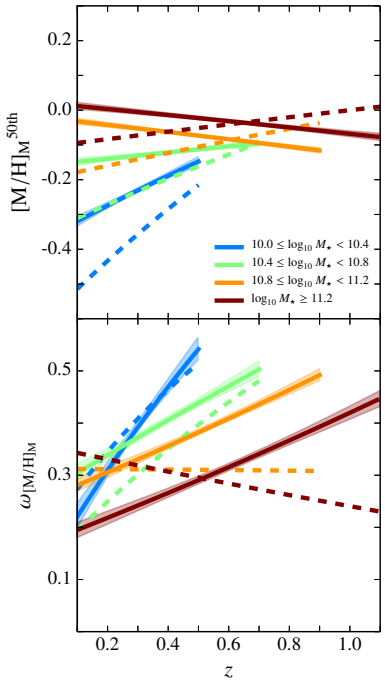

Figure E.38: As Fig. E.37, but for mass-weighted metallicity.

F

Stellar mass functions in the ALHAMBRA survey

The determination of the number of quiescent and star-forming galaxies at any redshift and stellar mass is key for estimating the number of mergers involving the different merger channels and mass ratios, but also for the determination of the contributions in number of "frosting" and "progenitor" bias (see Sects. 4.2–4.4). As both quiescent and star-forming galaxies are involved, the derivation of an analytic and redshift dependent stellar mass function (MF) of both spectral types would be enough to accurately estimate the number of galaxies involved at any cosmic time, spectral-type, and stellar mass. We performed a novel methodology for computing analytic MFs at any redshift. In order to avoid the classical limitations related to redshift bin definitions for the determination of a MF, the redshift of each galaxy is accounted for the MF at which the galaxy is observed. This implies that MF main parameters also present an intrinsic redshift dependency, where dramatic and great changes in the shape of a MF are not expected during the elapsed cosmic time of this work ($z \leq 1.1$). Although the determination of MFs have been extensively treated during the last decade (Pérez-González et al., 2008; Drory et al., 2009; Ilbert et al., 2010; Pozzetti et al., 2010; Davidzon et al., 2013; Ilbert et al., 2013; Moustakas et al., 2013; Tomczak et al., 2014; Moutard et al., 2016), we do not pretend to perform a detailed study of the MF either studying its evolution with redshift at this stage. We rather determine MF for estimating the number of galaxies involved in our phenomenological model (Chapter 4), which must be self-consistent with our stellar population predictions.

For the derivation of the MF, we included a set of assumptions in the analytical functions involved:

i) A single Schechter-like function (Schechter, 1976) is assumed for the analytic form of the MF for both spectral-types, quiescent and star-forming galaxies, formally expressed as

$$\Phi(M_\star, z)\, \mathrm{d}M_\star = \Phi^*(z) \left(\frac{M_\star}{\mathcal{M}_*(z)}\right)^{\alpha(z)} \exp\left(-\frac{M_\star}{\mathcal{M}_*(z)}\right) \mathrm{d}\left(\frac{M_\star}{\mathcal{M}_*(z)}\right) ; \tag{F.1}$$

or in the stellar mass log-space as

$$\Phi(M_\star, z)\, \mathrm{d}M_\star = \Phi^*(z)\, \ln(10)\, \exp\left[-10^{(M_\star - \mathcal{M}_*(z))}\right] 10^{(\alpha(z)+1)(M_\star - \mathcal{M}_*(z))}\, \mathrm{d}M_\star , \tag{F.2}$$

where $\mathcal{M}_*(z)$ and $\alpha(z)$ are the Schechter parameters that determine the shape of the MF, and $\Phi^*(z)$ its normalization. These three parameters are determined for each spectral type, and we assume that they are redshift dependent (similar assumption were used in López-Sanjuan et al., 2016, although for the $B-$band luminosity function).

ii) The redshift dependency of $\mathcal{M}_*(z)$ and $\alpha(z)$ is assumed as

$$\alpha(z) = \alpha_1 \times z + \alpha_0 \tag{F.3}$$

$$\log_{10} \mathcal{M}_*(z) = \mathcal{M}_1 \times z + \mathcal{M}_0 . \tag{F.4}$$

In addition, the normalization of the MF, $\Phi^*(z)$, depends of redshift. As in Ilbert et al. (2005), $\Phi^*(z)$ is directly related with the number density of galaxies at any redshift by $\int_{M^{\rm l}_{\rm min}}^{M^{\rm l}_{\rm max}} \Phi(M_\star, z) f_{\rm FD}(z, M_\star)\, {\rm d}M_\star = \int_{M^{\rm l}_{\rm min}}^{M^{\rm l}_{\rm max}} \rho_{\rm N}(M_\star, z)\, {\rm d}M_\star$, where $\rho_{\rm N}(M_\star, z)$ is the density number of galaxies observed, and $f_{\rm FD}(z, M_\star)$ is the stellar mass completeness. Assuming a number density of the same form that Eq. 3.11 and using a range in stellar mass in which the sample is also complete, $f_{\rm FD}(z, M_\star) = 1$, $\Phi^*(z)$ is expressed as,

$$\Phi^*(z) = \frac{\rho_0 (1+z)^\gamma}{\Gamma\left(\alpha(z)+1, \frac{M^{\rm l}_{\rm max}}{\mathcal{M}_*(z)}\right) - \Gamma\left(\alpha(z)+1, \frac{M^{\rm l}_{\rm min}}{\mathcal{M}_*(z)}\right)}\,, \tag{F.5}$$

where Γ is the incomplete Euler gamma function and $\Phi^*(z)$ depends of $\alpha(z)$ and $\mathcal{M}_*(z)$.

iii) Throughout the derivation of the MF, a Fermi-Dirac like function is assumed for the stellar mass completeness (see Eq. B.1), which adds two additional parameters: $M_{\rm F}$ and $\Delta_{\rm F}$ (see Appendix B for further details).

For deriving all the parameters involved in the MF, our starting point is the methodology developed by Sandage et al. (1979), the so-called STY method, that is based in a maximum likelihood estimator. From the above assumptions, the likelihood for estimating the MF parameters in this work is

$$\ln \mathcal{L} = \sum_{i=1}^{\rm N_g} \ln\left(\frac{\Phi(z_i, M_{\star,i}) f_{\rm FD}(z_i, M_{\star,i})}{\int_0^\infty \Phi(z_i, M_\star) f_{\rm FD}(z_i, M_\star)\, {\rm d}M_\star}\right), \tag{F.6}$$

where $\rm N_g$ is the number of galaxies of the whole sample (including galaxies below the completeness level), z_i is the redshift of each galaxy, and $M_{\star,i}$ its stellar mass. For the maximization of Eq. F.6, we used the code EMCEE (Foreman-Mackey et al., 2013, an affine invariant sampling algorithm for a Markov chain Monte Carlo method), which also provides the correlations for the parameters involved in the MF. Although in a general case, the parameters $M_{\rm F}$ and $\Delta_{\rm F}$ can be also derived by the maximization of Eq. F.6, they were previously fixed by the method presented in Appendix B and a spline interpolation at different redshifts. From the maximization of Eq. F.6, we derive α_1, α_0, $\mathcal{M}_1$, and $\mathcal{M}_0$ (i. e. $\alpha(z)$ and $\mathcal{M}_*(z)$, see Eqs. F.3 and F.4).

For the estimation of $\Phi^*(z)$, we fitted the number density of galaxies with stellar masses in the range $10^{10.76} \leq M_\star \leq 10^{11.15}$ ($M^{\rm l}_{\rm min}$ and $M^{\rm l}_{\rm max}$ respectively) in the redshift range in which the sample is complete in stellar mass (as in Sect. 3.6, i. e. by a $\rm V_{max}$ method). This stellar mass range was established as a compromise in order to cover a large range in redshift with a large number of galaxies. The redshift range $0.5 \leq z \leq 0.7$ was excluded from the fit of ρ_0 and γ, to avoid the lack of galaxies observed at this range (see Sect. 3.6).

It is worth mentioning that with this methodology, the impact of cosmic variance observed at $z \sim 0.6$ (see Sect. 3.6) is diluted. In addition, this method is able to extend the MF further the stellar mass completeness of the sample (until the stellar mass completeness is close to zero), as we know the percentage of galaxies that are not observed due to incompleteness by $f_{\rm FD}(z, M_\star)$. This method also increases the reliability of the MF predictions in the most local sample, because this one is more limit in number (lower volume covered), but it is supported by the evolution of all the galaxies in previous epochs and same stellar mass, as we do not expect very dramatic evolution in number of galaxies in short cosmic time periods ($\Delta z \sim 0.2$).

After running our methodology for estimating MFs with the results from BC03 SSP models (redshifts, stellar masses and the stellar mass completeness parameters), we obtain that for quiescent galaxies the parameters involved are

$$\Phi_{\rm Q}^{\rm BC03}(z, M_\star) \begin{cases} \log_{10}(\mathcal{M}_*(z)/{\rm M}_\odot) &= 10.84 - 0.005 \times z\,, \\ \alpha(z) &= -0.91 + 0.24 \times z\,, \\ \log_{10}\rho_0 &= -3.21\,, \\ \gamma &= -0.80\,, \end{cases} \tag{F.7}$$

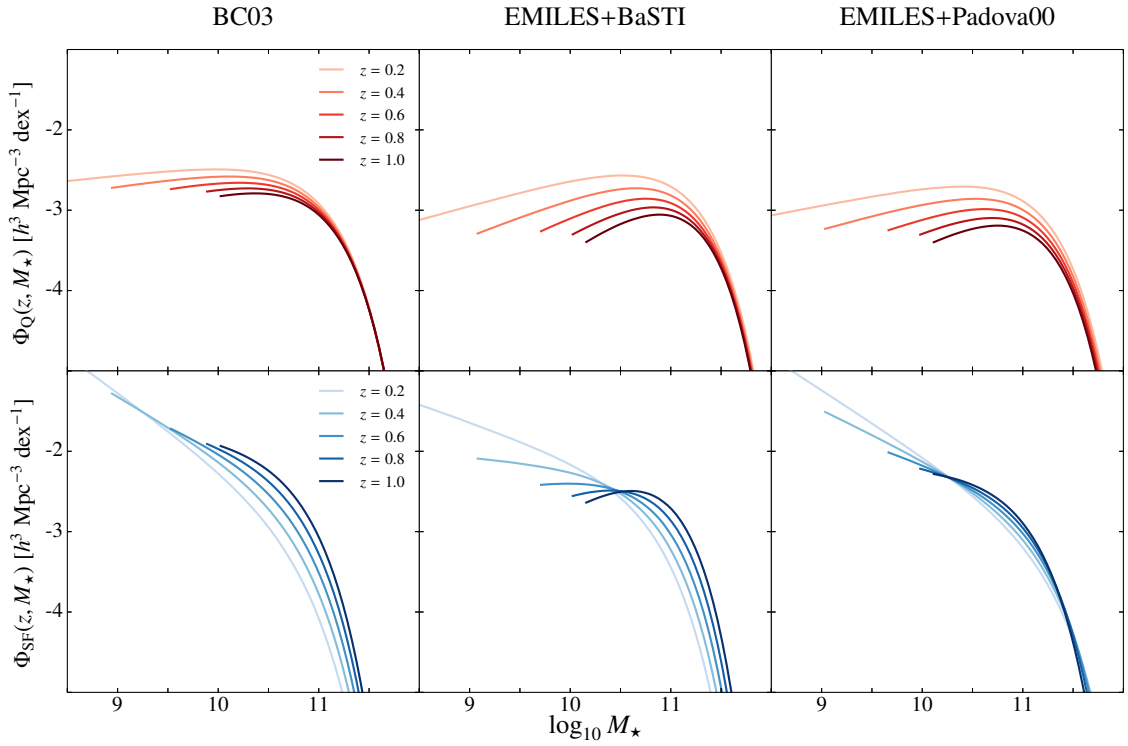

Figure F.1: Evolution of the stellar mass functions (MF) of quiescent (*top panels*) and star-forming (*bottom panels*) galaxies at different redshifts using BC03 (*left panels*), EMILES+BaSTI (*middle panels*), and EMILES+Padova00 (*right panels*) SSP models. All the values were obtained assuming $h = 0.71$.

whereas for the star forming ones, these values are the following

$$\Phi_{\rm SF}^{\rm BC03}(z, M_\star) \begin{cases} \log_{10}(\mathcal{M}_*(z)/\mathrm{M}_\odot) &= 10.24 - 0.05 \times z\,, \\ \alpha(z) &= -2.10 + 0.93 \times z\,, \\ \log_{10}\rho_0 &= -4.60\,, \\ \gamma &= 4.27\,. \end{cases} \tag{F.8}$$

For consistency, the Schechter parameters of the MF for EMILES predictions were also derived. As we show in Sect. 3.8, the age and metallicities retrieved with this model set differs from the ones obtained by BC03, and therefore, the stellar mass predictions can be also altered. After comparing the EMILES+BaSTI stellar masses with the ones obtained using BC03 SSP models, we found out that there is a systematic shift between both predictions of 0.15 dex (EMILES+BaSTI more massive than BC03). Consequently, for the stellar completeness parameter $M_{\rm F}$ we add this shift getting a nice MF fitting. For BaSTI isochrones these parameters are

$$\Phi_{\rm Q}^{\rm BaSTI}(z, M_\star) \begin{cases} \log_{10}(\mathcal{M}_*(z)/\mathrm{M}_\odot) &= 10.99 - 0.05 \times z\,, \\ \alpha(z) &= -0.78 + 0.68 \times z\,, \\ \log_{10}\rho_0 &= -2.95\,, \\ \gamma &= -1.75\,, \end{cases} \tag{F.9}$$

$$\Phi_{\rm SF}^{\rm BaSTI}(z, M_\star) \begin{cases} \log_{10}(\mathcal{M}_*(z)/\mathrm{M}_\odot) &= 10.67 - 0.04 \times z\,, \\ \alpha(z) &= -1.76 + 1.63 \times z\,, \\ \log_{10}\rho_0 &= -3.91\,, \\ \gamma &= 2.76\,, \end{cases} \tag{F.10}$$

For the Padova00 ones, the systematic shift in stellar mass respect the BC03 one is 0.11 dex (EMILES+Padova00 more massive as well). As a result, we respectively obtained for quiescent and star-forming galaxies that

$$\Phi_{\rm Q}^{\rm Padova00}(z, M_\star) \begin{cases} \log_{10}(\mathcal{M}_*(z)/{\rm M}_\odot) &= 11.00 - 0.08 \times z\,, \\ \alpha(z) &= -0.86 + 0.53 \times z\,, \\ \log_{10}\rho_0 &= -3.13\,, \\ \gamma &= -1.72\,, \end{cases} \tag{F.11}$$

$$\Phi_{\rm SF}^{\rm Padova00}(z, M_\star) \begin{cases} \log_{10}(\mathcal{M}_*(z)/{\rm M}_\odot) &= 11.18 - 0.38 \times z\,, \\ \alpha(z) &= -2.01 + 0.98 \times z\,, \\ \log_{10}\rho_0 &= -3.62\,, \\ \gamma &= 1.22\,. \end{cases} \tag{F.12}$$

The MF of quiescent galaxies present a generalised increment of quiescent galaxies since $z = 1.0$ at any stellar mass, top panels in Fig. F.1, as expected from the evolution in number density of quiescent galaxies (Sect. 3.6). In addition, it is interesting that the evolution in number of massive star-forming galaxies (bottom panels in Fig. F.1) exhibits a continuous decrement in number, which is an additional support for the inclusion of the "progenitor" bias in our phenomenological model. A detailed study of the evolution of MFs, as well as their parameter (specially $\alpha(z)$ and $\mathcal{M}_*(z)$) is out of the scope of this research. The main goal of this section is only to determine the evolution of the densities of quiescent and star-forming galaxies to be applied in our phenomenological model, which agree greatly with the number densities observed in ALHAMBRA in the stellar mass range 95 % complete. In addition, we illustrate in Fig. F.2 the kind of correlations and degeneracies affecting the MF parameters in our methodology for retrieving MFs. Notice that there are degeneracies amongst α_1, α_0, $\mathcal{M}_1$, and $\mathcal{M}_0$, which drives the well known α-$\mathcal{M}_*$ degeneracy. In addition, there are degeneracies between γ and $\log_{10}\rho_0$, which affects the normalisation factor $\Phi^*(z)$. As expected from Eq. F.5, degeneracies in α-$\mathcal{M}_*$ drives a degeneracy between $\Phi^*(z)$ and $\alpha(z)$,$\mathcal{M}_*(z)$, and also with $\log_{10}\rho_0$,γ.

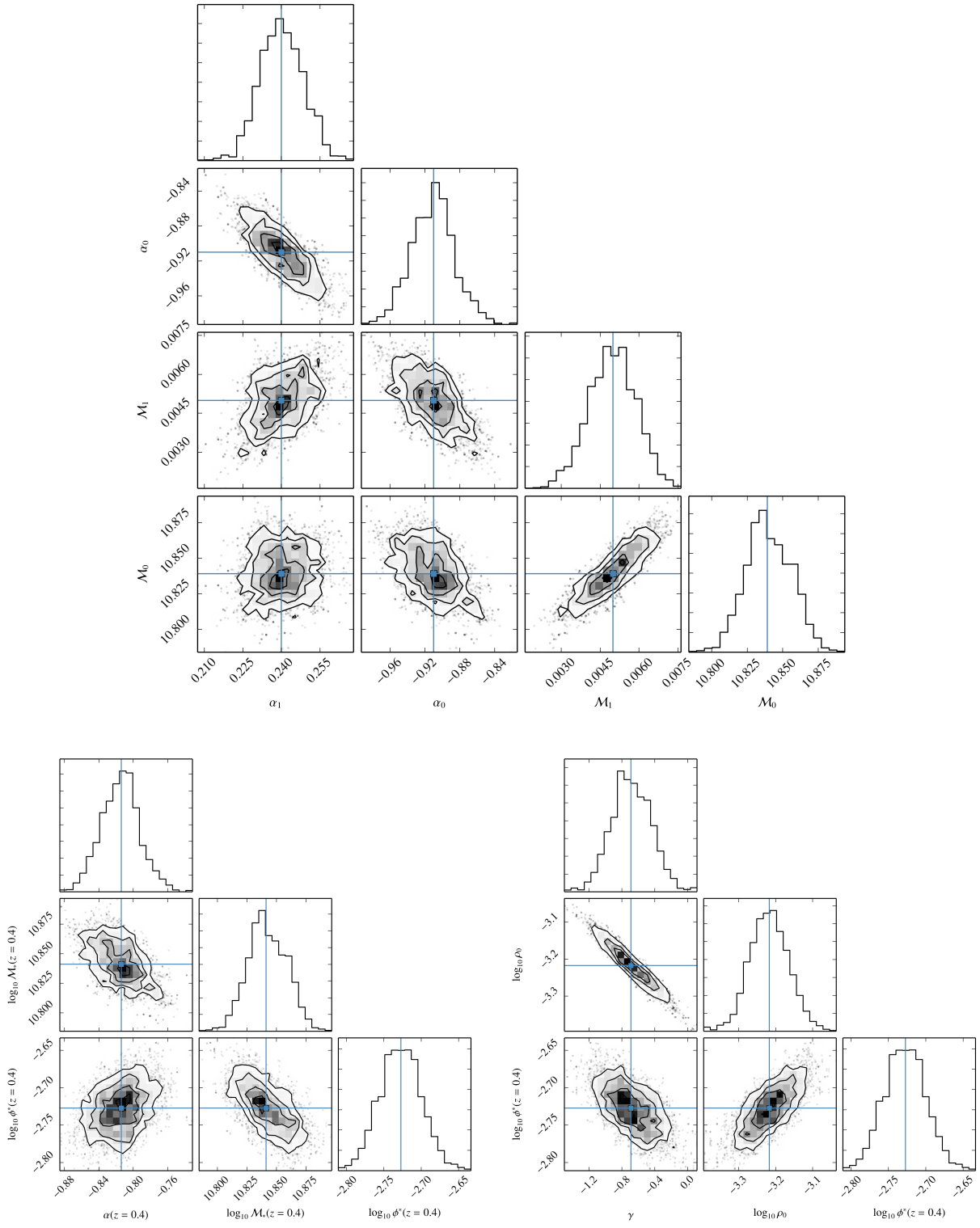

Figure F.2: Correlations and degeneracies of the redshift-dependent Schechter parameters involved in our methodology for deriving stellar mass functions (MF). All the panels correspond to the MF parameters of quiescent galaxies using BC03 SSP models. To illustrate possible degeneracies, the parameters $\alpha(z)$, $\mathcal{M}_*(z)$, and $\log_{10}\Phi^*$ were estimated at $z = 0.4$ (*bottom-left panel*). Darker colours indicate regions of the parameter values with higher densities, obtained from the EMCEE code (a Markov chain Monte Carlo method). Blue crosses illustrate the median value for each parameter. The histograms of the Markov chains for each of the parameters are shown on the right-hand side of each row.

Bibliography

“Memory... is the diary that we all carry about with us.”

Oscar Wilde

AARSETH, S. J. & BINNEY, J. 1978, Monthly Notices of the Royal Astronomical Society, **MNRAS**, **185, 227**. *On the relaxation of galaxies and clusters from aspherical initial conditions*

ABADI, M. G., MOORE, B., & BOWER, R. G. 1999, Monthly Notices of the Royal Astronomical Society, **MNRAS**, **308, 947**. *Ram pressure stripping of spiral galaxies in clusters*

ABAZAJIAN, K. N., ADELMAN-MCCARTHY, J. K., AGÜEROS, M. A., et al. 2009, Astrophysical Journal Supplements, **ApJS**, **182, 543**. *The Seventh Data Release of the Sloan Digital Sky Survey*

ABRAHAM, R. G., TANVIR, N. R., SANTIAGO, B. X., et al. 1996, Monthly Notices of the Royal Astronomical Society, **MNRAS**, **279, L47**. *Galaxy morphology to I=25 mag in the Hubble Deep Field*

ACQUAVIVA, V., GAWISER, E., & GUAITA, L. 2011, Astrophysical Journal, **ApJ**, **737, 47**. *Spectral Energy Distribution Fitting with Markov Chain Monte Carlo: Methodology and Application to $z = 3.1$ Lyα-emitting Galaxies*

ADELMAN-MCCARTHY, J. K., AGÜEROS, M. A., ALLAM, S. S., et al. 2006, Astrophysical Journal Supplements, **ApJS**, **162, 38**. *The Fourth Data Release of the Sloan Digital Sky Survey*

ALONGI, M., BERTELLI, G., BRESSAN, A., et al. 1993, Astronomy and Astrophysics Suplement, **A&AS**, **97, 851**. *Evolutionary sequences of stellar models with semiconvection and convective overshoot. I - Z = 0.008*

ANDREDAKIS, Y. C., PELETIER, R. F., & BALCELLS, M. 1995, Monthly Notices of the Royal Astronomical Society, **MNRAS**, **275, 874**. *The Shape of the Luminosity Profiles of Bulges of Spiral Galaxies*

APARICIO VILLEGAS, T., ALFARO, E. J., CABRERA-CAÑO, J., et al. 2010, Astronomical Journal, **AJ**, **139, 1242**. *The ALHAMBRA Photometric System*

ARAGON, A., GORGAS, J., & REGO, M. 1987, Astronomy and Astrophysics, **A&A**, **185, 97**. *An interpretation of the line-strength indices in old stellar populations using an evolutionary synthesis approach*

ARIMOTO, N. & YOSHII, Y. 1986, Astronomy and Astrophysics, **A&A**, **164, 260**. *Photometric and chemical evolution of galaxies based on an evolutionary method of population synthesis*

ARIMOTO, N. & YOSHII, Y. 1987, Astronomy and Astrophysics, **A&A**, **173, 23**. *Chemical and photometric properties of a galactic wind model for elliptical galaxies*

ARNOUTS, S., LE FLOC'H, E., CHEVALLARD, J., et al. 2013, Astronomy and Astrophysics, **A&A**, **558, A67**. *Encoding of the infrared excess in the NUVrK color diagram for star-forming galaxies*

ARNOUTS, S., MOSCARDINI, L., VANZELLA, E., et al. 2002, Monthly Notices of the Royal Astronomical Society, **MNRAS**, **329, 355**. *Measuring the redshift evolution of clustering: the Hubble Deep Field South*

ARNOUTS, S., WALCHER, C. J., LE FÈVRE, O., et al. 2007, Astronomy and Astrophysics, **A&A**, **476, 137**. *The SWIRE-VVDS-CFHTLS surveys: stellar mass assembly over the last 10 Gyr. Evidence for a major build up of the red sequence between $z = 2$ and $z = 1$*

ARZNER, K., GÜDEL, M., BRIGGS, K., et al. 2007, Astronomy and Astrophysics, **A&A**, **468, 501**. *Unbinned maximum-likelihood estimators for low-count data. Applications to faint X-ray spectra in the Taurus molecular cloud*

BACON, R., COPIN, Y., MONNET, G., et al. 2001, Monthly Notices of the Royal Astronomical Society, **MNRAS**, **326, 23**. *The SAURON project - I. The panoramic integral-field spectrograph*

BALDRY, I. K., BALOGH, M. L., BOWER, R. G., et al. 2006, Monthly Notices of the Royal Astronomical Society, **MNRAS**, **373, 469**. *Galaxy bimodality versus stellar mass and environment*

BALDRY, I. K., GLAZEBROOK, K., BRINKMANN, J., et al. 2004, Astrophysical Journal, **ApJ**, **600, 681**. *Quantifying the Bimodal Color-Magnitude Distribution of Galaxies*

BALDWIN, J. A., PHILLIPS, M. M., & TERLEVICH, R. 1981, Publications of the ASP, **PASP**, **93, 5**. *Classification parameters for the emission-line spectra of extragalactic objects*

BALOGH, M. L., MORRIS, S. L., YEE, H. K. C., CARLBERG, R. G., & ELLINGSON, E. 1999, Astrophysical Journal, **ApJ**, **527, 54**. *Differential Galaxy Evolution in Cluster and Field Galaxies at $z \sim 0.3$*

BALOGH, M. L., NAVARRO, J. F., & MORRIS, S. L. 2000, Astrophysical Journal, **ApJ**, **540, 113**. *The Origin of Star Formation Gradients in Rich Galaxy Clusters*

BARNES, J. E. & HERNQUIST, L. 1996, Astrophysical Journal, **ApJ**, **471, 115**. *Transformations of Galaxies. II. Gasdynamics in Merging Disk Galaxies*

BARRO, G., PÉREZ-GONZÁLEZ, P. G., GALLEGO, J., et al. 2011a, Astrophysical Journal Supplements, **ApJS**, **193, 13**. *UV-to-FIR Analysis of Spitzer/IRAC Sources in the Extended Groth Strip. I. Multi-wavelength Photometry and Spectral Energy Distributions*

BARRO, G., PÉREZ-GONZÁLEZ, P. G., GALLEGO, J., et al. 2011b, Astrophysical Journal Supplements, **ApJS**, **193, 30**. *UV-to-FIR Analysis of Spitzer/IRAC Sources in the Extended Groth Strip. II. Photometric Redshifts, Stellar Masses, and Star Formation Rates*

BAUM, W. A. 1959, Publications of the ASP, **PASP**, **71, 106**. *Population Inferences from Star Counts, Surface Brightness and Colors*

BELL, E. F. 2003, Astrophysical Journal, **ApJ**, **586, 794**. *Estimating Star Formation Rates from Infrared and Radio Luminosities: The Origin of the Radio-Infrared Correlation*

BELL, E. F., PAPOVICH, C., WOLF, C., et al. 2005, Astrophysical Journal, **ApJ**, **625, 23**. *Toward an Understanding of the Rapid Decline of the Cosmic Star Formation Rate*

BELL, E. F., PHLEPS, S., SOMERVILLE, R. S., et al. 2006, Astrophysical Journal, **ApJ**, **652, 270**. *The Merger Rate of Massive Galaxies*

BELL, E. F., WOLF, C., MEISENHEIMER, K., et al. 2004, Astrophysical Journal, **ApJ**, **608, 752**. *Nearly 5000 Distant Early-Type Galaxies in COMBO-17: A Red Sequence and Its Evolution since $z \sim 1$*

BELL, E. F., ZHENG, X. Z., PAPOVICH, C., et al. 2007, Astrophysical Journal, **ApJ**, **663, 834**. *Star Formation and the Growth of Stellar Mass*

BELLI, S., NEWMAN, A. B., & ELLIS, R. S. 2015, Astrophysical Journal, **ApJ**, **799, 206**. *Stellar Populations from Spectroscopy of a Large Sample of Quiescent Galaxies at $z > 1$: Measuring the Contribution of Progenitor Bias to Early Size Growth*

BENÍTEZ, N. 2000, Astrophysical Journal, **ApJ**, **536, 571**. *Bayesian Photometric Redshift Estimation*

BENÍTEZ, N., DUPKE, R., MOLES, M., et al. 2014, **ArXiv e-prints, 1403.5237**. *J-PAS: The Javalambre-Physics of the Accelerated Universe Astrophysical Survey*

BENÍTEZ, N., MOLES, M., AGUERRI, J. A. L., et al. 2009, Astrophysical Journal, **ApJ**, **692, L5**. *Optimal Filter Systems for Photometric Redshift Estimation*

BENSON, A. J., BOWER, R. G., FRENK, C. S., et al. 2003, Astrophysical Journal, **ApJ**, **599, 38**. *What Shapes the Luminosity Function of Galaxies?*

BERNARDI, M. 2009, Monthly Notices of the Royal Astronomical Society, **MNRAS**, **395, 1491**. *Evolution in the structural properties of early-type brightest cluster galaxies at small lookback time and dependence on the environment*

BERNARDI, M., NICHOL, R. C., SHETH, R. K., MILLER, C. J., & BRINKMANN, J. 2006, Astronomical Journal, **AJ**, **131, 1288**. *Evolution and Environment of Early-Type Galaxies*

BERTELLI, G., BRESSAN, A., CHIOSI, C., FAGOTTO, F., & NASI, E. 1994, Astronomy and Astrophysics Suplement, **A&AS**, **106**. *Theoretical isochrones from models with new radiative opacities*

BESSELL, M. S. 2005, Annual Review of Astronomy and Astrophysics, **ARA&A**, **43, 293**. *Standard Photometric Systems*

BEZANSON, R., VAN DOKKUM, P., & FRANX, M. 2012, Astrophysical Journal, **ApJ**, **760, 62**. *Evolution of Quiescent and Star-forming Galaxies since $z \tilde{} 1.5$ as a Function of their Velocity Dispersions*

BEZANSON, R., VAN DOKKUM, P. G., TAL, T., et al. 2009, Astrophysical Journal, **ApJ**, **697, 1290**. *The Relation Between Compact, Quiescent High-redshift Galaxies and Massive Nearby Elliptical Galaxies: Evidence for Hierarchical, Inside-Out Growth*

BLANTON, M. R., EISENSTEIN, D., HOGG, D. W., SCHLEGEL, D. J., & BRINKMANN, J. 2005a, Astrophysical Journal, **ApJ**, **629, 143**. *Relationship between Environment and the Broadband Optical Properties of Galaxies in the Sloan Digital Sky Survey*

BLANTON, M. R. & ROWEIS, S. 2007, Astronomical Journal, **AJ**, **133, 734**. *K-Corrections and Filter Transformations in the Ultraviolet, Optical, and Near-Infrared*

BLANTON, M. R., SCHLEGEL, D. J., STRAUSS, M. A., et al. 2005b, Astronomical Journal, **AJ**, **129, 2562**. *New York University Value-Added Galaxy Catalog: A Galaxy Catalog Based on New Public Surveys*

BLUCK, A. F. L., CONSELICE, C. J., BOUWENS, R. J., et al. 2009, Monthly Notices of the Royal Astronomical Society, **MNRAS**, **394, L51**. *A surprisingly high pair fraction for extremely massive galaxies at z ˜ 3 in the GOODS NICMOS survey*

BLUCK, A. F. L., CONSELICE, C. J., BUITRAGO, F., et al. 2012, Astrophysical Journal, **ApJ**, **747, 34**. *The Structures and Total (Minor + Major) Merger Histories of Massive Galaxies up to $z \sim 3$ in the HST GOODS NICMOS Survey: A Possible Solution to the Size Evolution Problem*

BOLZONELLA, M., MIRALLES, J.-M., & PELLÓ, R. 2000, Astronomy and Astrophysics, **A&A**, **363, 476**. *Photometric redshifts based on standard SED fitting procedures*

BOWER, R. G., BENSON, A. J., MALBON, R., et al. 2006, Monthly Notices of the Royal Astronomical Society, **MNRAS**, **370, 645**. *Breaking the hierarchy of galaxy formation*

BOWER, R. G., LUCEY, J. R., & ELLIS, R. S. 1992, Monthly Notices of the Royal Astronomical Society, **MNRAS**, **254, 601**. *Precision Photometry of Early Type Galaxies in the Coma and Virgo Clusters - a Test of the Universality of the Colour / Magnitude Relation - Part Two - Analysis*

BRAMMER, G. B., VAN DOKKUM, P. G., & COPPI, P. 2008, Astrophysical Journal, **ApJ**, **686, 1503**. *EAZY: A Fast, Public Photometric Redshift Code*

BRAMMER, G. B., WHITAKER, K. E., VAN DOKKUM, P. G., et al. 2009, Astrophysical Journal, **ApJ**, **706, L173**. *The Dead Sequence: A Clear Bimodality in Galaxy Colors from $z = 0$ to $z = 2.5$*

BRESSAN, A., CHIOSI, C., & FAGOTTO, F. 1994, Astrophysical Journal Supplements, **ApJS**, **94, 63**. *Spectrophotometric evolution of elliptical galaxies. 1: Ultraviolet excess and color-magnitude-redshift relations*

BRESSAN, A., FAGOTTO, F., BERTELLI, G., & CHIOSI, C. 1993, Astronomy and Astrophysics Suplement, **A&AS**, **100, 647**. *Evolutionary sequences of stellar models with new radiative opacities. II - Z = 0.02*

BRINCHMANN, J., CHARLOT, S., WHITE, S. D. M., et al. 2004, Monthly Notices of the Royal Astronomical Society, **MNRAS**, **351, 1151**. *The physical properties of star-forming galaxies in the low-redshift Universe*

BROWN, M. J. I., DEY, A., JANNUZI, B. T., et al. 2007, Astrophysical Journal, **ApJ**, **654, 858**. *The Evolving Luminosity Function of Red Galaxies*

BRUZUAL, G. & CHARLOT, S. 2003, Monthly Notices of the Royal Astronomical Society, **MNRAS**, **344, 1000**. *Stellar population synthesis at the resolution of 2003*

BRUZUAL A., G. 1983, Astrophysical Journal, **ApJ**, **273, 105**. *Spectral evolution of galaxies. I - Early-type systems*

BUITRAGO, F., TRUJILLO, I., CONSELICE, C. J., et al. 2008, Astrophysical Journal, **ApJ**, **687, L61**. *Size Evolution of the Most Massive Galaxies at $1.7 < z < 3$ from GOODS NICMOS Survey Imaging*

BUITRAGO, F., TRUJILLO, I., CONSELICE, C. J., & HÄUSSLER, B. 2013, Monthly Notices of the Royal Astronomical Society, **MNRAS**, **428, 1460**. *Early-type galaxies have been the predominant morphological class for massive galaxies since only $z \sim 1$*

BUNDY, K., BERSHADY, M. A., LAW, D. R., et al. 2015, Astrophysical Journal, **ApJ**, **798, 7**. *Overview of the SDSS-IV MaNGA Survey: Mapping nearby Galaxies at Apache Point Observatory*

BUNDY, K., ELLIS, R. S., CONSELICE, C. J., et al. 2006, Astrophysical Journal, **ApJ**, **651, 120**. *The Mass Assembly History of Field Galaxies: Detection of an Evolving Mass Limit for Star-Forming Galaxies*

BUNDY, K., FUKUGITA, M., ELLIS, R. S., et al. 2009, Astrophysical Journal, **ApJ**, **697, 1369**. *The Greater Impact of Mergers on the Growth of Massive Galaxies: Implications for Mass Assembly and Evolution since $z \simeq 1$*

BUNDY, K., GEORGAKAKIS, A., NANDRA, K., et al. 2008, Astrophysical Journal, **ApJ**, **681, 931**. *AEGIS: New Evidence Linking Active Galactic Nuclei to the Quenching of Star Formation*

BUNDY, K., TREU, T., & ELLIS, R. S. 2007, Astrophysical Journal, **ApJ**, **665, L5**. *The Mass Assembly History of Spheroidal Galaxies: Did Newly Formed Systems Arise via Major Mergers?*

BURSTEIN, D., FABER, S. M., GASKELL, C. M., & KRUMM, N. 1984, Astrophysical Journal, **ApJ**, **287, 586**. *Old stellar populations. I - A spectroscopic comparison of galactic globular clusters, M31 globular clusters, and elliptical galaxies*

CALZETTI, D. 1997, in American Institute of Physics Conference Series, **AIPC**, Vol. 408, American Institute of Physics Conference Series, ed. W. H. Waller, **403–412**. *UV opacity in nearby galaxies and application to distant galaxies*

CALZETTI, D., ARMUS, L., BOHLIN, R. C., et al. 2000, Astrophysical Journal, **ApJ**, **533, 682**. *The Dust Content and Opacity of Actively Star-forming Galaxies*

CALZETTI, D., KENNICUTT, R. C., ENGELBRACHT, C. W., et al. 2007, Astrophysical Journal, **ApJ**, **666, 870**. *The Calibration of Mid-Infrared Star Formation Rate Indicators*

CAPAK, P., AUSSEL, H., AJIKI, M., et al. 2007, Astrophysical Journal Supplements, **ApJS**, **172, 99**. *The First Release COSMOS Optical and Near-IR Data and Catalog*

CAPPELLARI, M. & COPIN, Y. 2003, Monthly Notices of the Royal Astronomical Society, **MNRAS**, **342, 345**. *Adaptive spatial binning of integral-field spectroscopic data using Voronoi tessellations*

CAPPELLARI, M. & EMSELLEM, E. 2004, Publications of the ASP, **PASP**, **116, 138**. *Parametric Recovery of Line-of-Sight Velocity Distributions from Absorption-Line Spectra of Galaxies via Penalized Likelihood*

CAPPELLARI, M., EMSELLEM, E., KRAJNOVIĆ, D., et al. 2011, Monthly Notices of the Royal Astronomical Society, **MNRAS**, **413, 813**. *The ATLAS^{3D} project - I. A volume-limited sample of 260 nearby early-type galaxies: science goals and selection criteria*

CAPPELLARI, M., MCDERMID, R. M., ALATALO, K., et al. 2013a, Monthly Notices of the Royal Astronomical Society, **MNRAS**, **432, 1862**. *The ATLAS^{3D} project - XX. Mass-size and mass-σ distributions of early-type galaxies: bulge fraction drives kinematics, mass-to-light ratio, molecular gas fraction and stellar initial mass function*

CAPPELLARI, M., SCOTT, N., ALATALO, K., et al. 2013b, Monthly Notices of the Royal Astronomical Society, **MNRAS**, **432, 1709**. *The ATLAS^{3D} project - XV. Benchmark for early-type galaxies scaling relations from 260 dynamical models: mass-to-light ratio, dark matter, Fundamental Plane and Mass Plane*

CARDAMONE, C. N., URRY, C. M., SCHAWINSKI, K., et al. 2010, Astrophysical Journal, **ApJ**, **721, L38**. *Dust-corrected Colors Reveal Bimodality in the Host-galaxy Colors of Active Galactic Nuclei at $z \sim 1$*

CARDELLI, J. A., CLAYTON, G. C., & MATHIS, J. S. 1989, Astrophysical Journal, **ApJ**, **345, 245**. *The relationship between infrared, optical, and ultraviolet extinction*

CARLBERG, R. G. 1984a, Astrophysical Journal, **ApJ**, **286, 403**. *Dissipative formation of an elliptical galaxy*

CARLBERG, R. G. 1984b, Astrophysical Journal, **ApJ**, **286, 416**. *Dissipative models for the sequence of elliptical galaxies*

CAROLLO, C. M., BSCHORR, T. J., RENZINI, A., et al. 2013, Astrophysical Journal, **ApJ**, **773, 112**. *Newly Quenched Galaxies as the Cause for the Apparent Evolution in Average Size of the Population*

CASSATA, P., GIAVALISCO, M., GUO, Y., et al. 2011, Astrophysical Journal, **ApJ**, **743, 96**. *The Relative Abundance of Compact and Normal Massive Early-type Galaxies and Its Evolution from Redshift $z \sim 2$ to the Present*

CASSATA, P., GIAVALISCO, M., WILLIAMS, C. C., et al. 2013, Astrophysical Journal, **ApJ**, **775, 106**. *Constraining the Assembly of Normal and Compact Passively Evolving Galaxies from Redshift $z = 3$ to the Present with CANDELS*

CASSATA, P., GUZZO, L., FRANCESCHINI, A., et al. 2007, Astrophysical Journal Supplements, **ApJS**, **172, 270**. *The Cosmic Evolution Survey (COSMOS): The Morphological Content and Environmental Dependence of the Galaxy Color-Magnitude Relation at $z \sim 0.7$*

CASUSO, E. *1991*. **Thesis (Ph. D.)**, Univ. de la Laguna, Spain, (1991)

CAVA, A., PÉREZ-GONZÁLEZ, P. G., ELICHE-MORAL, M. C., et al. 2015, Astrophysical Journal, **ApJ**, **812, 155**. *SHARDS: A Global View of the Star Formation Activity at z ˜ 0.84 and z ˜ 1.23*

CENARRO, A. J., CARDIEL, N., GORGAS, J., et al. 2001a, Monthly Notices of the Royal Astronomical Society, **MNRAS**, **326, 959**. *Empirical calibration of the near-infrared* Ca II *triplet - I. The stellar library and index definition*

CENARRO, A. J., GORGAS, J., CARDIEL, N., et al. 2001b, Monthly Notices of the Royal Astronomical Society, **MNRAS**, **326, 981**. *Empirical calibration of the near-infrared* Ca II *triplet - II. The stellar atmospheric parameters*

CENARRO, A. J., GORGAS, J., CARDIEL, N., VAZDEKIS, A., & PELETIER, R. F. 2002, Monthly Notices of the Royal Astronomical Society, **MNRAS**, **329, 863**. *Empirical calibration of the near-infrared Ca II triplet - III. Fitting functions*

CENARRO, A. J., GORGAS, J., VAZDEKIS, A., CARDIEL, N., & PELETIER, R. F. 2003, Monthly Notices of the Royal Astronomical Society, **MNRAS**, **339, L12**. *Near-infrared line-strengths in elliptical galaxies: evidence for initial mass function variations?*

CENARRO, A. J., PELETIER, R. F., SÁNCHEZ-BLÁZQUEZ, P., et al. 2007, Monthly Notices of the Royal Astronomical Society, **MNRAS**, **374, 664**. *Medium-resolution Isaac Newton Telescope library of empirical spectra - II. The stellar atmospheric parameters*

CENARRO, A. J. & TRUJILLO, I. 2009, Astrophysical Journal, **ApJ**, **696, L43**. *Mild Velocity Dispersion Evolution of Spheroid-Like Massive Galaxies Since z ˜ 2*

CERVANTES, J. L. & VAZDEKIS, A. 2009, Monthly Notices of the Royal Astronomical Society, **MNRAS**, **392, 691**. *An optimized Hβ index for disentangling stellar population ages*

CHABRIER, G. 2003, Publications of the ASP, **PASP**, **115, 763**. *Galactic Stellar and Substellar Initial Mass Function*

CHARLOT, S. & FALL, S. M. 2000, Astrophysical Journal, **ApJ**, **539, 718**. *A Simple Model for the Absorption of Starlight by Dust in Galaxies*

CHEN, Y.-M., KAUFFMANN, G., TREMONTI, C. A., et al. 2012, Monthly Notices of the Royal Astronomical Society, **MNRAS**, **421, 314**. *Evolution of the most massive galaxies to z= 0.6 - I. A new method for physical parameter estimation*

CHIOSI, C. & CARRARO, G. 2002, Monthly Notices of the Royal Astronomical Society, **MNRAS**, **335, 335**. *Formation and evolution of elliptical galaxies*

CHOI, J., CONROY, C., MOUSTAKAS, J., et al. 2014, Astrophysical Journal, **ApJ**, **792, 95**. *The Assembly Histories of Quiescent Galaxies since* $z = 0.7$ *from Absorption Line Spectroscopy*

CICONE, C., MAIOLINO, R., STURM, E., et al. 2014, Astronomy and Astrophysics, **A&A**, **562, A21**. *Massive molecular outflows and evidence for AGN feedback from CO observations*

CID FERNANDES, R., MATEUS, A., SODRÉ, L., STASIŃSKA, G., & GOMES, J. M. 2005, Monthly Notices of the Royal Astronomical Society, **MNRAS**, **358, 363**. *Semi-empirical analysis of Sloan Digital Sky Survey galaxies - I. Spectral synthesis method*

CITRO, A., POZZETTI, L., MORESCO, M., & CIMATTI, A. 2016, Astronomy and Astrophysics, **A&A**, **592, A19**. *Inferring the star-formation histories of the most massive and passive early-type galaxies at* $z < 0.3$

CLEVELAND, W. & DEVLIN, S. 1979, Journal of the American Statistical Association, **JASA**, **83, 596**. *Locally weighted regression: an approach to regression analysis by local fitting*

CLEVELAND, W. S. 1988, Journal of the American Statistical Association, **JASA**, **74, 829**. *Robust locally weighted regression and smoothing scatterplots*

COELHO, P., BARBUY, B., MELÉNDEZ, J., SCHIAVON, R. P., & CASTILHO, B. V. 2005, Astronomy and Astrophysics, **A&A**, **443, 735**. *A library of high resolution synthetic stellar spectra from 300 nm to 1.8 μm with solar and α-enhanced composition*

COELHO, P., BRUZUAL, G., CHARLOT, S., et al. 2007, Monthly Notices of the Royal Astronomical Society, **MNRAS**, **382, 498**. *Spectral models for solar-scaled and α-enhanced stellar populations*

COELHO, P., MENDES DE OLIVEIRA, C., & CID FERNANDES, R. 2009, Monthly Notices of the Royal Astronomical Society, **MNRAS**, **396, 624**. *An analysis of the composite stellar population in M32*

COLE, S., LACEY, C. G., BAUGH, C. M., & FRENK, C. S. 2000, Monthly Notices of the Royal Astronomical Society, **MNRAS**, **319, 168**. *Hierarchical galaxy formation*

CONROY, C. 2013, Annual Review of Astronomy and Astrophysics, **ARA&A**, **51, 393**. *Modeling the Panchromatic Spectral Energy Distributions of Galaxies*

CONROY, C. & GUNN, J. E. 2010, Astrophysical Journal, **ApJ**, **712, 833**. *The Propagation of Uncertainties in Stellar Population Synthesis Modeling. III. Model Calibration, Comparison, and Evaluation*

CONROY, C. & VAN DOKKUM, P. 2012, Astrophysical Journal, **ApJ**, **747, 69**. *Counting Low-mass Stars in Integrated Light*

CONSELICE, C. J. 2006, Astrophysical Journal, **ApJ**, **638, 686**. *Early and Rapid Merging as a Formation Mechanism of Massive Galaxies: Empirical Constraints*

CONSELICE, C. J., BLUCK, A. F. L., BUITRAGO, F., et al. 2011, Monthly Notices of the Royal Astronomical Society, **MNRAS**, **413, 80**. *The Hubble Space Telescope GOODS NICMOS Survey: overview and the evolution of massive galaxies at* $1.5 < z < 3$

CONSELICE, C. J., BUNDY, K., TRUJILLO, I., et al. 2007, Monthly Notices of the Royal Astronomical Society, **MNRAS**, **381, 962**. *The properties and evolution of a K-band selected sample of massive galaxies at* $z \sim 0.4$*-2 in the Palomar/DEEP2 survey*

COOPER, M. C., AIRD, J. A., COIL, A. L., et al. 2011, Astrophysical Journal Supplements, **ApJS**, **193, 14**. *The DEEP3 Galaxy Redshift Survey: Keck/DEIMOS Spectroscopy in the GOODS-N Field*

COWIE, L. L. & BARGER, A. J. 2008, Astrophysical Journal, **ApJ**, **686, 72**. *An Integrated Picture of Star Formation, Metallicity Evolution, and Galactic Stellar Mass Assembly*

COWIE, L. L., SONGAILA, A., HU, E. M., & COHEN, J. G. 1996, Astronomical Journal, **AJ**, **112, 839**. *New Insight on Galaxy Formation and Evolution From Keck Spectroscopy of the Hawaii Deep Fields*

CRISTÓBAL-HORNILLOS, D., AGUERRI, J. A. L., MOLES, M., et al. 2009, Astrophysical Journal, **ApJ**, **696, 1554**. *Near-Infrared Galaxy Counts and Evolution from the Wide-Field ALHAMBRA Survey*

CROTON, D. J., SPRINGEL, V., WHITE, S. D. M., et al. 2006, Monthly Notices of the Royal Astronomical Society, **MNRAS**, **365, 11**. *The many lives of active galactic nuclei: cooling flows, black holes and the luminosities and colours of galaxies*

DADDI, E., CIMATTI, A., RENZINI, A., et al. 2004, Astrophysical Journal, **ApJ**, **617, 746**. *A New Photometric Technique for the Joint Selection of Star-forming and Passive Galaxies at* $1.4 < z < 2.5$

DADDI, E., DICKINSON, M., MORRISON, G., et al. 2007, Astrophysical Journal, **ApJ**, **670, 156**. *Multiwavelength Study of Massive Galaxies at* $z \sim 2$*. I. Star Formation and Galaxy Growth*

DADDI, E., RENZINI, A., PIRZKAL, N., et al. 2005, Astrophysical Journal, **ApJ**, **626, 680**. *Passively Evolving Early-Type Galaxies at* $1.4 < z < 2.5$ *in the Hubble Ultra Deep Field*

DALCANTON, J. J. 2007, Astrophysical Journal, **ApJ**, **658, 941**. *The Metallicity of Galaxy Disks: Infall versus Outflow*

DALE, D. A. & HELOU, G. 2002, Astrophysical Journal, **ApJ**, **576, 159**. *The Infrared Spectral Energy Distribution of Normal Star-forming Galaxies: Calibration at Far-Infrared and Submillimeter Wavelengths*

DAMEN, M., LABBÉ, I., FRANX, M., et al. 2009, Astrophysical Journal, **ApJ**, **690, 937**. *The Evolution of the Specific Star Formation Rate of Massive Galaxies to* $z \sim 1.8$ *in the Extended Chandra Deep Field South*

DAMJANOV, I., ABRAHAM, R. G., GLAZEBROOK, K., et al. 2011, Astrophysical Journal, **ApJ**, **739, L44**. *Red Nuggets at High Redshift: Structural Evolution of Quiescent Galaxies Over 10 Gyr of Cosmic History*

DAMJANOV, I., GELLER, M. J., ZAHID, H. J., & HWANG, H. S. 2015, Astrophysical Journal, **ApJ**, **806, 158**. *Quiescent Compact Galaxies at Intermediate Redshift in the COSMOS Field. The Number Density*

DAMJANOV, I., HWANG, H. S., GELLER, M. J., & CHILINGARIAN, I. 2014, Astrophysical Journal, **ApJ**, **793, 39**. *The Number Density of Quiescent Compact Galaxies at Intermediate Redshift*

DAMJANOV, I., MCCARTHY, P. J., ABRAHAM, R. G., et al. 2009, Astrophysical Journal, **ApJ**, **695, 101**. *Red Nuggets at* $z \sim 1.5$*: Compact Passive Galaxies and the Formation of the Kormendy Relation*

DAVIDZON, I., BOLZONELLA, M., COUPON, J., et al. 2013, Astronomy and Astrophysics, **A&A**, **558, A23**. *The VIMOS Public Extragalactic Redshift Survey (VIPERS). A precise measurement of the galaxy stellar mass function and the abundance of massive galaxies at redshifts* $0.5 < z < 1.3$

DAVIS, M., EFSTATHIOU, G., FRENK, C. S., & WHITE, S. D. M. 1985, Astrophysical Journal, **ApJ**, **292, 371**. *The evolution of large-scale structure in a universe dominated by cold dark matter*

DAVIS, M., FABER, S. M., NEWMAN, J., et al. 2003, in Proceedings of the **SPIE**, Vol. 4834, Discoveries and Research Prospects from 6- to 10-Meter-Class Telescopes II, ed. P. Guhathakurta, **161–172**. *Science Objectives and Early Results of the DEEP2 Redshift Survey*

DAVIS, M., GUHATHAKURTA, P., KONIDARIS, N. P., et al. 2007, Astrophysical Journal, **ApJ**, **660, L1**. *The All-Wavelength Extended Groth Strip International Survey (AEGIS) Data Sets*

DE LA ROSA, I. G., LA BARBERA, F., FERRERAS, I., & DE CARVALHO, R. R. 2011, Monthly Notices of the Royal Astronomical Society, **MNRAS**, **418, L74**. *The link between the star formation history and [α/Fe]*

DE LA ROSA, I. G., LA BARBERA, F., FERRERAS, I., et al. 2016, Monthly Notices of the Royal Astronomical Society, **MNRAS**, **457, 1916**. *The fate of high-redshift massive compact galaxies*

DE LUCIA, G., SPRINGEL, V., WHITE, S. D. M., CROTON, D., & KAUFFMANN, G. 2006, Monthly Notices of the Royal Astronomical Society, **MNRAS**, **366, 499**. *The formation history of elliptical galaxies*

DE RAVEL, L., LE FÈVRE, O., TRESSE, L., et al. 2009, Astronomy and Astrophysics, **A&A**, **498, 379**. *The VIMOS VLT Deep Survey. Evolution of the major merger rate since* $z \sim 1$ *from spectroscopically confirmed galaxy pairs*

DEBATTISTA, V. P., MAYER, L., CAROLLO, C. M., et al. 2006, Astrophysical Journal, **ApJ**, **645, 209**. *The Secular Evolution of Disk Structural Parameters*

DEKEL, A. & BIRNBOIM, Y. 2006, Monthly Notices of the Royal Astronomical Society, **MNRAS**, **368, 2**. *Galaxy bimodality due to cold flows and shock heating*

DEKEL, A., SARI, R., & CEVERINO, D. 2009, Astrophysical Journal, **ApJ**, **703, 785**. *Formation of Massive Galaxies at High Redshift: Cold Streams, Clumpy Disks, and Compact Spheroids*

DI MATTEO, T., COLBERG, J., SPRINGEL, V., HERNQUIST, L., & SIJACKI, D. 2008, Astrophysical Journal, **ApJ**, **676, 33**. *Direct Cosmological Simulations of the Growth of Black Holes and Galaxies*

DIAMOND-STANIC, A. M., MOUSTAKAS, J., TREMONTI, C. A., et al. 2012, Astrophysical Journal, **ApJ**, **755, L26**. *High-velocity Outflows without AGN Feedback: Eddington-limited Star Formation in Compact Massive Galaxies*

DÍAZ-GARCÍA, L. A., CENARRO, A. J., LÓPEZ-SANJUAN, C., et al. 2015, Astronomy and Astrophysics, **A&A**, **582, A14**. *Stellar populations of galaxies in the ALHAMBRA survey up to* $z \sim 1$*. I. MUFFIT: A multi-filter fitting code for stellar population diagnostics*

DÍAZ-GARCÍA, L. A., MÁRMOL-QUERALTÓ, E., TRUJILLO, I., et al. 2013, Monthly Notices of the Royal Astronomical Society, **MNRAS**, **433, 60**. *The merger history of massive spheroids since* $z \sim 1$ *is size-independent*

DICKINSON, M., GIAVALISCO, M., & GOODS TEAM. 2003, in The Mass of Galaxies at Low and High Redshift, ed. R. Bender & A. Renzini, **324**. *The Great Observatories Origins Deep Survey*

DOMÍNGUEZ SÁNCHEZ, H., PÉREZ-GONZÁLEZ, P. G., ESQUEJ, P., et al. 2016, Monthly Notices of the Royal Astronomical Society, **MNRAS**, **457, 3743**. *Pathways to quiescence: SHARDS view on the star formation histories of massive quiescent galaxies at* $1.0 < z < 1.5$

DOMÍNGUEZ SÁNCHEZ, H., POZZI, F., GRUPPIONI, C., et al. 2011, Monthly Notices of the Royal Astronomical Society, **MNRAS**, **417, 900**. *The evolution of quiescent galaxies at high redshifts (*$z \geq 1.4$*)*

DRAINE, B. T. 2003a, Astrophysical Journal, **ApJ**, **598, 1017**. *Scattering by Interstellar Dust Grains. I. Optical and Ultraviolet*

DRAINE, B. T. 2003b, Astrophysical Journal, **ApJ**, **598, 1026**. *Scattering by Interstellar Dust Grains. II. X-Rays*

DRORY, N., BUNDY, K., LEAUTHAUD, A., et al. 2009, Astrophysical Journal, **ApJ**, **707, 1595**. *The Bimodal Galaxy Stellar Mass Function in the COSMOS Survey to* $z \sim 1$*: A Steep Faint End and a New Galaxy Dichotomy*

EDVARDSSON, B., ANDERSEN, J., GUSTAFSSON, B., et al. 1993, Astronomy and Astrophysics, **A&A**, **275, 101**. *The Chemical Evolution of the Galactic Disk - Part One - Analysis and Results*

EIGENTHALER, P. & ZEILINGER, W. W. 2013, Astronomy and Astrophysics, **A&A**, **553, A99**. *Age and metallicity gradients in fossil ellipticals*

EISENSTEIN, D. J., HOGG, D. W., FUKUGITA, M., et al. 2003, Astrophysical Journal, **ApJ**, **585, 694**. *Average Spectra of Massive Galaxies in the Sloan Digital Sky Survey*

EISENSTEIN, D. J., WEINBERG, D. H., AGOL, E., et al. 2011, Astronomical Journal, **AJ**, **142, 72**. *SDSS-III: Massive Spectroscopic Surveys of the Distant Universe, the Milky Way, and Extra-Solar Planetary Systems*

ELBAZ, D., DADDI, E., LE BORGNE, D., et al. 2007, Astronomy and Astrophysics, **A&A**, **468, 33**. *The reversal of the star formation-density relation in the distant universe*

ERB, D. K., SHAPLEY, A. E., PETTINI, M., et al. 2006, Astrophysical Journal, **ApJ**, **644, 813**. *The Mass-Metallicity Relation at* $z \gtrsim 2$

FABER, S. M. 1972, Astronomy and Astrophysics, **A&A**, **20, 361**. *Quadratic programming applied to the problem of galaxy population synthesis.*

FABER, S. M. 1973, Astrophysical Journal, **ApJ**, **179, 731**. *Variations in Spectral-Energy Distributions and Absorption-Line Strengths among Elliptical Galaxies*

FABER, S. M., FRIEL, E. D., BURSTEIN, D., & GASKELL, C. M. 1985, Astrophysical Journal Supplements, **ApJS**, **57, 711**. *Old stellar populations. II - an analysis of K-giant spectra*

FABER, S. M., PHILLIPS, A. C., KIBRICK, R. I., et al. 2003, in Proceedings of the **SPIE**, Vol. 4841, Instrument Design and Performance for Optical/Infrared Ground-based Telescopes, ed. M. Iye & A. F. M. Moorwood, **1657–1669**. *The DEIMOS spectrograph for the Keck II Telescope: integration and testing*

FABER, S. M., WILLMER, C. N. A., WOLF, C., et al. 2007, Astrophysical Journal, **ApJ**, **665, 265**. *Galaxy Luminosity Functions to* $z \sim 1$ *from DEEP2 and COMBO-17: Implications for Red Galaxy Formation*

FAGIOLI, M., CAROLLO, C. M., RENZINI, A., et al. 2016, Astrophysical Journal, **ApJ**, **831, 173**. *Minor Mergers or Progenitor Bias? The Stellar Ages of Small and Large Quenched Galaxies*

FAGOTTO, F., BRESSAN, A., BERTELLI, G., & CHIOSI, C. 1994a, Astronomy and Astrophysics Suplement, **A&AS**, **104, 365**. *Evolutionary sequences of stellar models with new radiative opacities. III. Z=0.0004 and Z=0.05*

FAGOTTO, F., BRESSAN, A., BERTELLI, G., & CHIOSI, C. 1994b, Astronomy and Astrophysics Suplement, **A&AS**, **105, 29**. *Evolutionary sequences of stellar models with new radiative opacities. IV. Z=0.004 and Z=0.008*

FAGOTTO, F., BRESSAN, A., BERTELLI, G., & CHIOSI, C. 1994c, Astronomy and Astrophysics Suplement, **A&AS**, **105, 39**. *Evolutionary sequences of stellar models with very high metallicity. V. Z=0.1*

FALCÓN-BARROSO, J., SÁNCHEZ-BLÁZQUEZ, P., VAZDEKIS, A., et al. 2011, Astronomy and Astrophysics, **A&A**, **532, A95**. *An updated MILES stellar library and stellar population models*

FAN, L., LAPI, A., BRESSAN, A., et al. 2010, Astrophysical Journal, **ApJ**, **718, 1460**. *Cosmic Evolution of Size and Velocity Dispersion for Early-type Galaxies*

FAN, L., LAPI, A., DE ZOTTI, G., & DANESE, L. 2008, Astrophysical Journal, **ApJ**, **689, L101**. *The Dramatic Size Evolution of Elliptical Galaxies and the Quasar Feedback*

FASANO, G., POGGIANTI, B. M., COUCH, W. J., et al. 2000, Astrophysical Journal, **ApJ**, **542, 673**. *The Evolution of the Galactic Morphological Types in Clusters*

FERRARESE, L., CÔTÉ, P., CUILLANDRE, J.-C., et al. 2012, Astrophysical Journal Supplements, **ApJS**, **200, 4**. *The Next Generation Virgo Cluster Survey (NGVS). I. Introduction to the Survey*

FERRÉ-MATEU, A., VAZDEKIS, A., & DE LA ROSA, I. G. 2013, Monthly Notices of the Royal Astronomical Society, **MNRAS**, **431, 440**. *The impact of a non-universal Initial Mass Function on the star formation histories of early-type galaxies*

FERRÉ-MATEU, A., VAZDEKIS, A., TRUJILLO, I., et al. 2012, Monthly Notices of the Royal Astronomical Society, **MNRAS**, **423, 632**. *Young ages and other intriguing properties of massive compact galaxies in the local Universe*

FERRERAS, I., LA BARBERA, F., DE LA ROSA, I. G., et al. 2013, Monthly Notices of the Royal Astronomical Society, **MNRAS**, **429, L15**. *Systematic variation of the stellar initial mass function with velocity dispersion in early-type galaxies*

FERRERAS, I., LISKER, T., CAROLLO, C. M., LILLY, S. J., & MOBASHER, B. 2005, Astrophysical Journal, **ApJ**, **635, 243**. *Evolution of Field Early-Type Galaxies: The View from GOODS CDFS*

FERRERAS, I., LISKER, T., PASQUALI, A., & KAVIRAJ, S. 2009, Monthly Notices of the Royal Astronomical Society, **MNRAS**, **395, 554**. *Exploring the formation of spheroidal galaxies out to z ˜ 1.5 in GOODS*

FERRERAS, I. & SILK, J. 2000, Astrophysical Journal, **ApJ**, **541, L37**. *How Young are Early-type Cluster Galaxies? Quantifying the Young Stellar Component in a Rich Cluster at z=0.41*

FERRERAS, I., TRUJILLO, I., MÁRMOL-QUERALTÓ, E., et al. 2014, Monthly Notices of the Royal Astronomical Society, **MNRAS**, **444, 906**. *Constraints on the merging channel of massive galaxies since* $z \sim 1$

FITZPATRICK, E. L. 1999, Publications of the ASP, **PASP**, **111, 63**. *Correcting for the Effects of Interstellar Extinction*

FONTANA, A., POZZETTI, L., DONNARUMMA, I., et al. 2004, Astronomy and Astrophysics, **A&A**, **424, 23**. *The K20 survey. VI. The distribution of the stellar masses in galaxies up to* $z \sim 2$

FONTANA, A., SALIMBENI, S., GRAZIAN, A., et al. 2006, Astronomy and Astrophysics, **A&A**, **459, 745**. *The Galaxy mass function up to* $z = 4$ *in the GOODS-MUSIC sample: into the epoch of formation of massive galaxies*

FOREMAN-MACKEY, D., HOGG, D. W., LANG, D., & GOODMAN, J. 2013, Publications of the ASP, **PASP**, **125, 306**. *emcee: The MCMC Hammer*

FRITZ, A., SCODEGGIO, M., ILBERT, O., et al. 2014, Astronomy and Astrophysics, **A&A**, **563, A92**. *The VIMOS Public Extragalactic Redshift Survey (VIPERS):. A quiescent formation of massive red-sequence galaxies over the past 9 Gyr*

FUMAGALLI, M., FRANX, M., VAN DOKKUM, P., et al. 2016, Astrophysical Journal, **ApJ**, **822, 1**. *Ages of Massive Galaxies at* $0.5 < z < 2.0$ *from 3D-HST Rest-frame Optical Spectroscopy*

GABOR, J. M. & DAVÉ, R. 2012, Monthly Notices of the Royal Astronomical Society, **MNRAS**, **427, 1816**. *The growth of red sequence galaxies in a cosmological hydrodynamic simulation*

GALLAZZI, A., BELL, E. F., ZIBETTI, S., BRINCHMANN, J., & KELSON, D. D. 2014, Astrophysical Journal, **ApJ**, **788, 72**. *Charting the Evolution of the Ages and Metallicities of Massive Galaxies since* $z = 0.7$

GALLAZZI, A., CHARLOT, S., BRINCHMANN, J., & WHITE, S. D. M. 2006, Monthly Notices of the Royal Astronomical Society, **MNRAS**, **370, 1106**. *Ages and metallicities of early-type galaxies in the Sloan Digital Sky Survey: new insight into the physical origin of the colour-magnitude and the* Mg_2-σ_V *relations*

GALLAZZI, A., CHARLOT, S., BRINCHMANN, J., WHITE, S. D. M., & TREMONTI, C. A. 2005, Monthly Notices of the Royal Astronomical Society, **MNRAS**, **362, 41**. *The ages and metallicities of galaxies in the local universe*

GARGIULO, A., BOLZONELLA, M., SCODEGGIO, M., et al. 2016, **ArXiv e-prints, 1611.07047**. *VIMOS Public Extragalactic Redshift Survey (VIPERS). The distinct build-up of dense and normal massive passive galaxies*

GAWISER, E., VAN DOKKUM, P. G., HERRERA, D., et al. 2006, Astrophysical Journal Supplements, **ApJS**, **162, 1**. *The Multiwavelength Survey by Yale-Chile (MUSYC): Survey Design and Deep Public UBVRIz' Images and Catalogs of the Extended Hubble Deep Field-South*

GEORGAKAKIS, A., NANDRA, K., YAN, R., et al. 2008, Monthly Notices of the Royal Astronomical Society, **MNRAS**, **385, 2049**. *The role of AGN in the colour transformation of galaxies at redshifts* $z \sim 1$

GIAVALISCO, M., FERGUSON, H. C., KOEKEMOER, A. M., et al. 2004, Astrophysical Journal, **ApJ**, **600, L93**. *The Great Observatories Origins Deep Survey: Initial Results from Optical and Near-Infrared Imaging*

GIRARDI, L., BRESSAN, A., BERTELLI, G., & CHIOSI, C. 2000, Astronomy and Astrophysics Suplement, **A&AS**, **141, 371**. *Evolutionary tracks and isochrones for low- and intermediate-mass stars: From 0.15 to 7* M_{sun}, *and from Z=0.0004 to 0.03*

GIRARDI, L., BRESSAN, A., CHIOSI, C., BERTELLI, G., & NASI, E. 1996, Astronomy and Astrophysics Suplement, **A&AS**, **117, 113**. *Evolutionary sequences of stellar models with new radiative opacities. VI. Z=0.0001.*

GLAZEBROOK, K., ELLIS, R., SANTIAGO, B., & GRIFFITHS, R. 1995, Monthly Notices of the Royal Astronomical Society, **MNRAS**, **275, L19**. *The morphological identification of the rapidly evolving population of faint galaxies*

GODDARD, D., THOMAS, D., MARASTON, C., et al. 2017, Monthly Notices of the Royal Astronomical Society, **MNRAS**, **465, 688**. *SDSS-IV MaNGA: stellar population gradients as a function of galaxy environment*

GONZÁLEZ, J. J. 1993. *Line strength gradients and kinematic profiles in elliptical galaxies*. **Thesis (Ph. D.)**, University of California, Santa Cruz, 1993. Source: Dissertation Abstracts International, Volume: **54-05**, Section: B, page: **2551**.

GONZÁLEZ DELGADO, R. M., CERVIÑO, M., MARTINS, L. P., LEITHERER, C., & HAUSCHILDT, P. H. 2005, Monthly Notices of the Royal Astronomical Society, **MNRAS**, **357, 945**. *Evolutionary stellar population synthesis at high spectral resolution: optical wavelengths*

GONZÁLEZ DELGADO, R. M., CID FERNANDES, R., GARCÍA-BENITO, R., et al. 2014a, Astrophysical Journal, **ApJ**, **791, L16**. *Insights on the Stellar Mass-Metallicity Relation from the CALIFA Survey*

GONZÁLEZ DELGADO, R. M., GARCÍA-BENITO, R., PÉREZ, E., et al. 2015, Astronomy and Astrophysics, **A&A**, **581, A103**. *The CALIFA survey across the Hubble sequence. Spatially resolved stellar population properties in galaxies*

GONZÁLEZ DELGADO, R. M., PÉREZ, E., CID FERNANDES, R., et al. 2014b, Astronomy and Astrophysics, **A&A**, **562, A47**. *The star formation history of CALIFA galaxies: Radial structures*

GORGAS, J., FABER, S. M., BURSTEIN, D., et al. 1993, Astrophysical Journal Supplements, **ApJS**, **86, 153**. *Old stellar populations. IV - Empirical functions for features in the spectra of G and K stars*

GORGAS, J., JABLONKA, P., & GOUDFROOIJ, P. 2007, Astronomy and Astrophysics, **A&A**, **474, 1081**. *Stellar population gradients in bulges along the Hubble sequence. I. The data*

GOTT, III, J. R. 1975, Astrophysical Journal, **ApJ**, **201, 296**. *On the Formation of Elliptical Galaxies*

GOTT, III, R. J. 1973, Astrophysical Journal, **ApJ**, **186, 481**. *Dynamics of Rotating Stellar Systems: Collapse and Violent Relaxation*

GRIFFITH, R. L., COOPER, M. C., NEWMAN, J. A., et al. 2012, Astrophysical Journal Supplements, **ApJS**, **200, 9**. *The Advanced Camera for Surveys General Catalog: Structural Parameters for Approximately Half a Million Galaxies*

GROGIN, N. A., KOCEVSKI, D. D., FABER, S. M., et al. 2011, Astrophysical Journal Supplements, **ApJS**, **197, 35**. *CANDELS: The Cosmic Assembly Near-infrared Deep Extragalactic Legacy Survey*

GUÉROU, A., EMSELLEM, E., MCDERMID, R. M., et al. 2015, Astrophysical Journal, **ApJ**, **804, 70**. *The Next Generation Virgo Cluster Survey. XII. Stellar Populations and Kinematics of Compact, Low-mass Early-type Galaxies from Gemini GMOS-IFU Spectroscopy*

GUIDERDONI, B. & ROCCA-VOLMERANGE, B. 1987, Astronomy and Astrophysics, **A&A**, **186, 1**. *A model of spectrophotometric evolution for high-redshift galaxies*

GUNN, J. E. & GOTT, III, J. R. 1972, Astrophysical Journal, **ApJ**, **176, 1**. *On the Infall of Matter Into Clusters of Galaxies and Some Effects on Their Evolution*

GUNN, J. E., STRYKER, L. L., & TINSLEY, B. M. 1981, Astrophysical Journal, **ApJ**, **249, 48**. *Evolutionary synthesis of the stellar population in elliptical galaxies. III - Detailed optical spectra*

GUZZO, L., SCODEGGIO, M., GARILLI, B., et al. 2014, Astronomy and Astrophysics, **A&A**, **566, A108**. *The VIMOS Public Extragalactic Redshift Survey (VIPERS). An unprecedented view of galaxies and large-scale structure at* $0.5 < z < 1.2$

HARKER, J. J., SCHIAVON, R. P., WEINER, B. J., & FABER, S. M. 2006, Astrophysical Journal, **ApJ**, **647, L103**. *Population Synthesis Models for Late Buildup of the Red Sequence*

HATTON, S., DEVRIENDT, J. E. G., NININ, S., et al. 2003, Monthly Notices of the Royal Astronomical Society, **MNRAS**, **343, 75**. *GALICS- I. A hybrid N-body/semi-analytic model of hierarchical galaxy formation*

HÄUSSLER, B., BARDEN, M., BAMFORD, S. P., & ROJAS, A. 2011, in Astronomical Society of the Pacific Conference Series, Vol. 442, Astronomical Data Analysis Software and Systems XX, ed. I. N. Evans, A. Accomazzi, D. J. Mink, & A. H. Rots, **155**. *Galapagos: A Semi-Automated Tool for Galaxy Profile Fitting*

HEAP, S. R. & LINDLER, D. J. 2007, in Astronomical Society of the Pacific Conference Series, Vol. 374, From Stars to Galaxies: Building the Pieces to Build Up the Universe, ed. A. Vallenari, R. Tantalo, L. Portinari, & A. Moretti, **409**. *Hubble's Next Generation Spectral Library (NGSL)*

HEAVENS, A., PANTER, B., JIMENEZ, R., & DUNLOP, J. 2004, **Nature**, **428, 625**. *The star-formation history of the Universe from the stellar populations of nearby galaxies*

HERNÁN-CABALLERO, A., ALONSO-HERRERO, A., PÉREZ-GONZÁLEZ, P. G., et al. 2013, Monthly Notices of the Royal Astronomical Society, **MNRAS**, **434, 2136**. *SHARDS: stellar populations and star formation histories of a mass-selected sample of* $0.65 < z < 1.1$ *galaxies*

HICKOX, R. C., JONES, C., FORMAN, W. R., et al. 2009, Astrophysical Journal, **ApJ**, **696, 891**. *Host Galaxies, Clustering, Eddington Ratios, and Evolution of Radio, X-Ray, and Infrared-Selected AGNs*

HICKSON, P., GIBSON, B. K., & CALLAGHAN, K. A. S. 1994, Monthly Notices of the Royal Astronomical Society, **MNRAS**, **267, 911**. *Multi-narrowband Imaging - a New Technique for Multi-Object Spectrophotometry*

HIRSCHMANN, M., NAAB, T., OSTRIKER, J. P., et al. 2015, Monthly Notices of the Royal Astronomical Society, **MNRAS**, **449, 528**. *The stellar accretion origin of stellar population gradients in massive galaxies at large radii*

HOGG, D. W. 1999, **ArXiv e-prints, 9905116**. *Distance measures in cosmology*

HOOK, I. M., JØRGENSEN, I., ALLINGTON-SMITH, J. R., et al. 2004, Publications of the ASP, **PASP**, **116, 425**. *The Gemini-North Multi-Object Spectrograph: Performance in Imaging, Long-Slit, and Multi-Object Spectroscopic Modes*

HOPKINS, P. F., COX, T. J., & HERNQUIST, L. 2008a, Astrophysical Journal, **ApJ**, **689, 17**. *Dissipation and the Fundamental Plane: Observational Tests*

HOPKINS, P. F., COX, T. J., KEREŠ, D., & HERNQUIST, L. 2008b, Astrophysical Journal Supplements, **ApJS**, **175, 390**. *A Cosmological Framework for the Co-Evolution of Quasars, Supermassive Black Holes, and Elliptical Galaxies. II. Formation of Red Ellipticals*

HOPKINS, P. F., COX, T. J., YOUNGER, J. D., & HERNQUIST, L. 2009a, Astrophysical Journal, **ApJ**, **691, 1168**. *How do Disks Survive Mergers?*

HOPKINS, P. F., HERNQUIST, L., COX, T. J., et al. 2006, Astrophysical Journal Supplements, **ApJS**, **163, 1**. *A Unified, Merger-driven Model of the Origin of Starbursts, Quasars, the Cosmic X-Ray Background, Supermassive Black Holes, and Galaxy Spheroids*

HOPKINS, P. F., HERNQUIST, L., COX, T. J., KERES, D., & WUYTS, S. 2009b, Astrophysical Journal, **ApJ**, **691, 1424**. *Dissipation and Extra Light in Galactic Nuclei. IV. Evolution in the Scaling Relations of Spheroids*

HOPKINS, P. F., SOMERVILLE, R. S., COX, T. J., et al. 2009c, Monthly Notices of the Royal Astronomical Society, **MNRAS**, **397, 802**. *The effects of gas on morphological transformation in mergers: implications for bulge and disc demographics*

HUBBLE, E. P. 1926, Astrophysical Journal, **ApJ**, **64, 321**. *Extragalactic nebulae.*

HUBBLE, E. P. 1936. *Realm of the Nebulae*

HUERTAS-COMPANY, M., ROUAN, D., TASCA, L., SOUCAIL, G., & LE FÈVRE, O. 2008, Astronomy and Astrophysics, **A&A**, **478, 971**. *A robust morphological classification of high-redshift galaxies using support vector machines on seeing limited images. I. Method description*

HUNTER, J. D. 2007, Computing In Science & Engineering, **CISE**, **9, 90**. *Matplotlib: A 2D graphics environment*

ILBERT, O., ARNOUTS, S., MCCRACKEN, H. J., et al. 2006, Astronomy and Astrophysics, **A&A**, **457, 841**. *Accurate photometric redshifts for the CFHT legacy survey calibrated using the VIMOS VLT deep survey*

ILBERT, O., CAPAK, P., SALVATO, M., et al. 2009, Astrophysical Journal, **ApJ**, **690, 1236**. *Cosmos Photometric Redshifts with 30-Bands for 2-deg^2*

ILBERT, O., MCCRACKEN, H. J., LE FÈVRE, O., et al. 2013, Astronomy and Astrophysics, **A&A**, **556, A55**. *Mass assembly in quiescent and star-forming galaxies since $z \sim 4$ from UltraVISTA*

ILBERT, O., SALVATO, M., LE FLOC'H, E., et al. 2010, Astrophysical Journal, **ApJ**, **709, 644**. *Galaxy Stellar Mass Assembly Between $0.2 < z < 2$ from the S-COSMOS Survey*

ILBERT, O., TRESSE, L., ZUCCA, E., et al. 2005, Astronomy and Astrophysics, **A&A**, **439, 863**. *The VIMOS-VLT deep survey. Evolution of the galaxy luminosity function up to $z = 2$ in first epoch data*

JANZ, J., LAURIKAINEN, E., LISKER, T., et al. 2014, Astrophysical Journal, **ApJ**, **786, 105**. *A Near-infrared Census of the Multicomponent Stellar Structure of Early-type Dwarf Galaxies in the Virgo Cluster*

JIMENEZ, R., BERNARDI, M., HAIMAN, Z., PANTER, B., & HEAVENS, A. F. 2007, Astrophysical Journal, **ApJ**, **669, 947**. *The Ages, Metallicities, and Star Formation Histories of Early-Type Galaxies in the SDSS*

JOHNSON, H. L. & MORGAN, W. W. 1953, Astrophysical Journal, **ApJ**, **117, 313**. *Fundamental stellar photometry for standards of spectral type on the revised system of the Yerkes spectral atlas*

JØRGENSEN, I. 1999, Monthly Notices of the Royal Astronomical Society, **MNRAS**, **306, 607**. *E and S0 galaxies in the central part of the Coma cluster: ages, metal abundances and dark matter*

KANNAPPAN, S. J. 2004, Astrophysical Journal, **ApJ**, **611, L89**. *Linking Gas Fractions to Bimodalities in Galaxy Properties*

KAUFFMANN, G., HECKMAN, T. M., WHITE, S. D. M., et al. 2003, Monthly Notices of the Royal Astronomical Society, **MNRAS**, **341, 54**. *The dependence of star formation history and internal structure on stellar mass for 10^5 low-redshift galaxies*

KAUFFMANN, G., WHITE, S. D. M., & GUIDERDONI, B. 1993, Monthly Notices of the Royal Astronomical Society, **MNRAS**, **264, 201**. *The Formation and Evolution of Galaxies Within Merging Dark Matter Haloes*

KAVIRAJ, S., DEVRIENDT, J. E. G., FERRERAS, I., & YI, S. K. 2005, Monthly Notices of the Royal Astronomical Society, **MNRAS**, **360, 60**. *The elliptical galaxy colour-magnitude relation as a discriminant between the monolithic and merger paradigms*

KAVIRAJ, S., SCHAWINSKI, K., DEVRIENDT, J. E. G., et al. 2007, Astrophysical Journal Supplements, **ApJS**, **173, 619**. *UV-Optical Colors As Probes of Early-Type Galaxy Evolution*

KEREŠ, D., KATZ, N., WEINBERG, D. H., & DAVÉ, R. 2005, Monthly Notices of the Royal Astronomical Society, **MNRAS**, **363, 2**. *How do galaxies get their gas?*

KHOCHFAR, S. & BURKERT, A. 2003, Astrophysical Journal, **ApJ**, **597, L117**. *The Importance of Spheroidal and Mixed Mergers for Early-Type Galaxy Formation*

KHOCHFAR, S. & BURKERT, A. 2006a, Astronomy and Astrophysics, **A&A**, **445, 403**. *Orbital parameters of merging dark matter halos*

KHOCHFAR, S. & SILK, J. 2006b, Astrophysical Journal, **ApJ**, **648, L21**. *A Simple Model for the Size Evolution of Elliptical Galaxies*

KITZBICHLER, M. G. & WHITE, S. D. M. 2008, Monthly Notices of the Royal Astronomical Society, **MNRAS**, **391, 1489**. *A calibration of the relation between the abundance of close galaxy pairs and the rate of galaxy mergers*

KOBAYASHI, C. 2004, Monthly Notices of the Royal Astronomical Society, **MNRAS**, **347, 740**. *GRAPE-SPH chemodynamical simulation of elliptical galaxies - I. Evolution of metallicity gradients*

KOCHANEK, C. S., EISENSTEIN, D. J., COOL, R. J., et al. 2012, Astrophysical Journal Supplements, **ApJS**, **200, 8**. *AGES: The AGN and Galaxy Evolution Survey*

KODAMA, T. & ARIMOTO, N. 1997, Astronomy and Astrophysics, **A&A**, **320, 41**. *Origin of the colour-magnitude relation of elliptical galaxies.*

KOEKEMOER, A. M., FABER, S. M., FERGUSON, H. C., et al. 2011, Astrophysical Journal Supplements, **ApJS**, **197, 36**. *CANDELS: The Cosmic Assembly Near-infrared Deep Extragalactic Legacy Survey-The Hubble Space Telescope Observations, Imaging Data Products, and Mosaics*

KOLEVA, M., PRUGNIEL, P., BOUCHARD, A., & WU, Y. 2009, Astronomy and Astrophysics, **A&A**, **501, 1269**. *ULySS: a full spectrum fitting package*

KOLEVA, M., PRUGNIEL, P., OCVIRK, P., LE BORGNE, D., & SOUBIRAN, C. 2008, Monthly Notices of the Royal Astronomical Society, **MNRAS**, **385, 1998**. *Spectroscopic ages and metallicities of stellar populations: validation of full spectrum fitting*

KRIEK, M., VAN DOKKUM, P. G., LABBÉ, I., et al. 2009, Astrophysical Journal, **ApJ**, **700, 221**. *An Ultra-Deep Near-Infrared Spectrum of a Compact Quiescent Galaxy at $z = 2.2$*

KROUPA, P. 2001, Monthly Notices of the Royal Astronomical Society, **MNRAS**, **322, 231**. *On the variation of the initial mass function*

KROUPA, P., TOUT, C. A., & GILMORE, G. 1993, Monthly Notices of the Royal Astronomical Society, **MNRAS**, **262, 545**. *The distribution of low-mass stars in the Galactic disc*

KUNTSCHNER, H., LUCEY, J. R., SMITH, R. J., HUDSON, M. J., & DAVIES, R. L. 2001, Monthly Notices of the Royal Astronomical Society, **MNRAS**, **323, 615**. *On the dependence of spectroscopic indices of early-type galaxies on age, metallicity and velocity dispersion*

LA BARBERA, F., FERRERAS, I., DE CARVALHO, R. R., et al. 2012, Monthly Notices of the Royal Astronomical Society, **MNRAS**, **426, 2300**. *SPIDER - VII. Revealing the stellar population content of massive early-type galaxies out to $8R_e$*

LA BARBERA, F., FERRERAS, I., DE CARVALHO, R. R., et al. 2011, Astrophysical Journal, **ApJ**, **740, L41**. *On the Radial Stellar Content of Early-type Galaxies as a Function of Mass and Environment*

LA BARBERA, F., FERRERAS, I., VAZDEKIS, A., et al. 2013, Monthly Notices of the Royal Astronomical Society, **MNRAS**, **433, 3017**. *SPIDER VIII - constraints on the stellar initial mass function of early-type galaxies from a variety of spectral features*

LA BARBERA, F., PASQUALI, A., FERRERAS, I., et al. 2014, Monthly Notices of the Royal Astronomical Society, **MNRAS**, **445, 1977**. *SPIDER - X. Environmental effects in central and satellite early-type galaxies through the stellar fossil record*

LA BARBERA, F., VAZDEKIS, A., FERRERAS, I., et al. 2017, Monthly Notices of the Royal Astronomical Society, **MNRAS**, **464, 3597**. *IMF and [Na/Fe] abundance ratios from optical and NIR spectral features in early-type galaxies*

LANGE, R., DRIVER, S. P., ROBOTHAM, A. S. G., et al. 2015, Monthly Notices of the Royal Astronomical Society, **MNRAS**, **447, 2603**. *Galaxy And Mass Assembly (GAMA): mass-size relations of $z < 0.1$ galaxies subdivided by Sérsic index, colour and morphology*

LARSON, R. B. 1969, Monthly Notices of the Royal Astronomical Society, **MNRAS**, **145, 405**. *A model for the formation of a spherical galaxy*

LARSON, R. B. 1974a, Monthly Notices of the Royal Astronomical Society, **MNRAS**, **166, 585**. *Dynamical models for the formation and evolution of spherical galaxies*

LARSON, R. B. 1974b, Monthly Notices of the Royal Astronomical Society, **MNRAS**, **169, 229**. *Effects of supernovae on the early evolution of galaxies*

LARSON, R. B. 1975, Monthly Notices of the Royal Astronomical Society, **MNRAS**, **173, 671**. *Models for the formation of elliptical galaxies*

LARSON, R. B., TINSLEY, B. M., & CALDWELL, C. N. 1980, Astrophysical Journal, **ApJ**, **237, 692**. *The evolution of disk galaxies and the origin of S0 galaxies*

LE BORGNE, J.-F., BRUZUAL, G., PELLÓ, R., et al. 2003, Astronomy and Astrophysics, **A&A**, **402, 433**. *STELIB: A library of stellar spectra at $R \sim 2000$*

LE FÈVRE, O., SAISSE, M., MANCINI, D., et al. 2003, in Proceedings of the **SPIE**, Vol. 4841, Instrument Design and Performance for Optical/Infrared Ground-based Telescopes, ed. M. Iye & A. F. M. Moorwood, **1670–1681**. *Commissioning and performances of the VLT-VIMOS instrument*

LE FLOC'H, E., AUSSEL, H., ILBERT, O., et al. 2009, Astrophysical Journal, **ApJ**, **703, 222**. *Deep Spitzer 24 μm COSMOS Imaging. I. The Evolution of Luminous Dusty Galaxies–Confronting the Models*

LEAUTHAUD, A., MASSEY, R., KNEIB, J.-P., et al. 2007, Astrophysical Journal Supplements, **ApJS**, **172, 219**. *Weak Gravitational Lensing with COSMOS: Galaxy Selection and Shape Measurements*

LEJEUNE, T., CUISINIER, F., & BUSER, R. 1998, Astronomy and Astrophysics Suplement, **A&AS**, **130, 65**. *A standard stellar library for evolutionary synthesis. II. The M dwarf extension*

LEJEUNE, T. & SCHAERER, D. 2001, Astronomy and Astrophysics, **A&A**, **366, 538**. *Database of Geneva stellar evolution tracks and isochrones for $(UBV)_J(RI)_C$ JHKLL'M, HST-WFPC2, Geneva and Washington photometric systems*

LILLY, S. J., LE BRUN, V., MAIER, C., et al. 2009, Astrophysical Journal Supplements, **ApJS**, **184, 218**. *The zCOSMOS 10k-Bright Spectroscopic Sample*

LILLY, S. J., LE FÈVRE, O., RENZINI, A., et al. 2007, Astrophysical Journal Supplements, **ApJS**, **172, 70**. *zCOSMOS: A Large VLT/VIMOS Redshift Survey Covering $0 < z < 3$ in the COSMOS Field*

LIN, L., PATTON, D. R., KOO, D. C., et al. 2008, Astrophysical Journal, **ApJ**, **681, 232**. *The Redshift Evolution of Wet, Dry, and Mixed Galaxy Mergers from Close Galaxy Pairs in the DEEP2 Galaxy Redshift Survey*

LIU, G.-C., LU, Y.-J., CHEN, X.-L., DU, W., & ZHAO, Y.-H. 2013, Research in Astronomy and Astrophysics, **RAA**, **13, 1025**. *On fitting the full spectrum of luminous red galaxies by using ULySS and STARLIGHT*

LONOCE, I., LONGHETTI, M., SARACCO, P., GARGIULO, A., & TAMBURRI, S. 2014, Monthly Notices of the Royal Astronomical Society, **MNRAS**, **444, 2048**. *Spectral detection of multiple stellar populations in $z \sim 1$ early-type galaxies*

LÓPEZ-COMAZZI, A. 2015. *Tasa de formación estelar en ALHAMBRA*. **Thesis (Master)**

LÓPEZ-SANJUAN, C., BALCELLS, M., GARCÍA-DABÓ, C. E., et al. 2009, Astrophysical Journal, **ApJ**, **694, 643**. *Robust Determination of the Major Merger Fraction at $z = 0.6$ in the Groth Strip*

LÓPEZ-SANJUAN, C., BALCELLS, M., PÉREZ-GONZÁLEZ, P. G., et al. 2010, Astrophysical Journal, **ApJ**, **710, 1170**. *The Minor Role of Gas-Rich Major Mergers in the Rise of Intermediate-Mass Early Types at $z \leq 1$*

LÓPEZ-SANJUAN, C., CENARRO, A. J., HERNÁNDEZ-MONTEAGUDO, C., et al. 2015a, Astronomy and Astrophysics, **A&A**, **582, A16**. *The ALHAMBRA survey: Estimation of the clustering signal encoded in the cosmic variance*

LÓPEZ-SANJUAN, C., CENARRO, A. J., HERNÁNDEZ-MONTEAGUDO, C., et al. 2014, Astronomy and Astrophysics, **A&A**, **564, A127**. *The ALHAMBRA survey: An empirical estimation of the cosmic variance for merger fraction studies based on close pairs*

LÓPEZ-SANJUAN, C., CENARRO, A. J., VARELA, J., et al. 2015b, Astronomy and Astrophysics, **A&A**, **576, A53**. *The ALHAMBRA survey: accurate merger fractions derived by PDF analysis of photometrically close pairs*

LÓPEZ-SANJUAN, C., GARCÍA-DABÓ, C. E., & BALCELLS, M. 2008, Publications of the ASP, **PASP**, **120, 571**. *A Maximum Likelihood Method for Bidimensional Experimental Distributions and Its Application to the Galaxy Merger Fraction*

LÓPEZ-SANJUAN, C., LE FÈVRE, O., DE RAVEL, L., et al. 2011, Astronomy and Astrophysics, **A&A**, **530, A20**. *The VIMOS VLT Deep Survey. The contribution of minor mergers to the growth of $L_B \gtrsim L_B^*$ galaxies since $z \sim 1$ from spectroscopically identified pairs*

LÓPEZ-SANJUAN, C., LE FÈVRE, O., ILBERT, O., et al. 2012, Astronomy and Astrophysics, **A&A**, **548, A7**. *The dominant role of mergers in the size evolution of massive early-type galaxies since $z \sim 1$*

LÓPEZ-SANJUAN, C., LE FÈVRE, O., TASCA, L. A. M., et al. 2013, Astronomy and Astrophysics, **A&A**, **553, A78**. *MASSIV: Mass Assembly Survey with SINFONI in VVDS. V. The major merger rate of star-forming galaxies at $0.9 < z < 1.8$ from IFS-based close pairs*

LÓPEZ-SANJUAN, C., TEMPEL, E., BENÍTEZ, N., et al. 2016, **ArXiv e-prints, 1611.09231**. *The ALHAMBRA survey : B−band luminosity function of quiescent and star-forming galaxies at $0.2 \leq z < 1$ by PDF analysis*

LOTZ, J. M., JONSSON, P., COX, T. J., & PRIMACK, J. R. 2010a, Monthly Notices of the Royal Astronomical Society, **MNRAS**, **404, 590**. *The effect of gas fraction on the morphology and time-scales of disc galaxy mergers*

LOTZ, J. M., JONSSON, P., COX, T. J., & PRIMACK, J. R. 2010b, Monthly Notices of the Royal Astronomical Society, **MNRAS**, **404, 575**. *The effect of mass ratio on the morphology and time-scales of disc galaxy mergers*

MADAU, P., POZZETTI, L., & DICKINSON, M. 1998, Astrophysical Journal, **ApJ**, **498, 106**. *The Star Formation History of Field Galaxies*

MAGRIS C., G., MATEU P., J., MATEU, C., et al. 2015, Publications of the ASP, **PASP**, **127, 16**. *On the Recovery of Galaxy Properties from SED Fitting Solutions*

MAIOLINO, R., GALLERANI, S., NERI, R., et al. 2012, Monthly Notices of the Royal Astronomical Society, **MNRAS**, **425, L66**. *Evidence of strong quasar feedback in the early Universe*

MAKAROV, D., MAKAROVA, L., RIZZI, L., et al. 2006, Astronomical Journal, **AJ**, **132, 2729**. *Tip of the Red Giant Branch Distances. I. Optimization of a Maximum Likelihood Algorithm*

MARASTON, C. & STRÖMBÄCK, G. 2011, Monthly Notices of the Royal Astronomical Society, **MNRAS**, **418, 2785**. *Stellar population models at high spectral resolution*

MARASTON, C., STRÖMBÄCK, G., THOMAS, D., WAKE, D. A., & NICHOL, R. C. 2009, Monthly Notices of the Royal Astronomical Society, **MNRAS**, **394, L107**. *Modelling the colour evolution of luminous red galaxies - improvements with empirical stellar spectra*

MARCHESINI, D., MUZZIN, A., STEFANON, M., et al. 2014, Astrophysical Journal, **ApJ**, **794, 65**. *The Progenitors of Local Ultra-massive Galaxies Across Cosmic Time: From Dusty Star-bursting to Quiescent Stellar Populations*

MARIGO, P., GIRARDI, L., BRESSAN, A., et al. 2008, Astronomy and Astrophysics, **A&A**, **482, 883**. *Evolution of asymptotic giant branch stars. II. Optical to far-infrared isochrones with improved TP-AGB models*

MÁRMOL-QUERALTÓ, E., CARDIEL, N., CENARRO, A. J., et al. 2008, Astronomy and Astrophysics, **A&A**, **489, 885**. *A new stellar library in the region of the CO index at 2.3 μm. New index definition and empirical fitting functions*

MÁRMOL-QUERALTÓ, E., TRUJILLO, I., PÉREZ-GONZÁLEZ, P. G., VARELA, J., & BARRO, G. 2012, Monthly Notices of the Royal Astronomical Society, **MNRAS**, **422, 2187**. *Satellites around massive galaxies since* $z \sim 2$

MARSHALL, H. L. 1985, Astrophysical Journal, **ApJ**, **299, 109**. *The evolution of optically selected quasars with Z less than 2.2 and B less than 20*

MARTIN, D. C., SMALL, T., SCHIMINOVICH, D., et al. 2007, Astrophysical Journal Supplements, **ApJS**, **173, 415**. *The Star Formation and Extinction Coevolution of UV-Selected Galaxies over* $0.05 < z < 1.2$

MARTÍN-NAVARRO, I., BARBERA, F. L., VAZDEKIS, A., FALCÓN-BARROSO, J., & FERRERAS, I. 2015a, Monthly Notices of the Royal Astronomical Society, **MNRAS**, **447, 1033**. *Radial variations in the stellar initial mass function of early-type galaxies*

MARTÍN-NAVARRO, I., VAZDEKIS, A., LA BARBERA, F., et al. 2015b, Astrophysical Journal, **ApJ**, **806, L31**. *IMF–Metallicity: A Tight Local Relation Revealed by the CALIFA Survey*

MARTINEZ-VALPUESTA, I., SHLOSMAN, I., & HELLER, C. 2006, Astrophysical Journal, **ApJ**, **637, 214**. *Evolution of Stellar Bars in Live Axisymmetric Halos: Recurrent Buckling and Secular Growth*

MARTINS, L. P., GONZÁLEZ DELGADO, R. M., LEITHERER, C., CERVIÑO, M., & HAUSCHILDT, P. 2005, Monthly Notices of the Royal Astronomical Society, **MNRAS**, **358, 49**. *A high-resolution stellar library for evolutionary population synthesis*

MASSA, D. 1987, Astronomical Journal, **AJ**, **94, 1675**. *The variability of UV extinction-curve shapes and its impact upon dereddened UV energy distributions*

MATHIS, H., CHARLOT, S., & BRINCHMANN, J. 2006, Monthly Notices of the Royal Astronomical Society, **MNRAS**, **365, 385**. *Extracting star formation histories from medium-resolution galaxy spectra*

MATHIS, J. S. 1990, Annual Review of Astronomy and Astrophysics, **ARA&A**, **28, 37**. *Interstellar dust and extinction*

MATTEUCCI, F. & TORNAMBE, A. 1987, Astronomy and Astrophysics, **A&A**, **185, 51**. *Chemical evolution of elliptical galaxies*

MCCLURE, R. D. & VAN DEN BERGH, S. 1968, Astronomical Journal, **AJ**, **73, 313**. *Five-color intermediate-band photometry of stars, clusters, and galaxies.*

MCDERMID, R. M., ALATALO, K., BLITZ, L., et al. 2015, Monthly Notices of the Royal Astronomical Society, **MNRAS**, **448, 3484**. *The ATLAS^{3D} Project - XXX. Star formation histories and stellar population scaling relations of early-type galaxies*

MCGLYNN, T. A. 1984, Astrophysical Journal, **ApJ**, **281, 13**. *Dissipationless collapse of galaxies and initial conditions*

MCINTOSH, D. H., BELL, E. F., RIX, H.-W., et al. 2005, Astrophysical Journal, **ApJ**, **632, 191**. *The Evolution of Early-Type Red Galaxies with the GEMS Survey: Luminosity-Size and Stellar Mass-Size Relations Since z=1*

MCLURE, R. J., PEARCE, H. J., DUNLOP, J. S., et al. 2013, Monthly Notices of the Royal Astronomical Society, **MNRAS**, **428, 1088**. *The sizes, masses and specific star formation rates of massive galaxies at* $1.3 < z < 1.5$*: strong evidence in favour of evolution via minor mergers*

MOLES, M., BENÍTEZ, N., AGUERRI, J. A. L., et al. 2008, Astronomical Journal, **AJ**, **136, 1325**. *The Alhambra Survey: a Large Area Multimedium-Band Optical and Near-Infrared Photometric Survey*

MOLINO, A., BENÍTEZ, N., MOLES, M., et al. 2014, Monthly Notices of the Royal Astronomical Society, **MNRAS**, **441, 2891**. *The ALHAMBRA Survey: Bayesian photometric redshifts with 23 bands for 3 deg*

MONACHESI, A., TRAGER, S. C., LAUER, T. R., et al. 2012, Astrophysical Journal, **ApJ**, **745, 97**. *The Star Formation History of M32*

MORESCO, M., POZZETTI, L., CIMATTI, A., et al. 2013, Astronomy and Astrophysics, **A&A**, **558, A61**. *Spot the difference. Impact of different selection criteria on observed properties of passive galaxies in zCOSMOS-20k sample*

MOSTER, B. P., SOMERVILLE, R. S., NEWMAN, J. A., & RIX, H.-W. 2011, Astrophysical Journal, **ApJ**, **731, 113**. *A Cosmic Variance Cookbook*

MOUSTAKAS, J., COIL, A. L., AIRD, J., et al. 2013, Astrophysical Journal, **ApJ**, **767, 50**. *PRIMUS: Constraints on Star Formation Quenching and Galaxy Merging, and the Evolution of the Stellar Mass Function from z = 0-1*

MOUTARD, T., ARNOUTS, S., ILBERT, O., et al. 2016, Astronomy and Astrophysics, **A&A**, **590, A103**. *The VIPERS Multi-Lambda Survey. II. Diving with massive galaxies in 22 square degrees since z = 1.5*

MUZZIN, A., MARCHESINI, D., STEFANON, M., et al. 2013, Astrophysical Journal, **ApJ**, **777, 18**. *The Evolution of the Stellar Mass Functions of Star-forming and Quiescent Galaxies to z = 4 from the COSMOS/UltraVISTA Survey*

NAAB, T., JOHANSSON, P. H., & OSTRIKER, J. P. 2009, Astrophysical Journal, **ApJ**, **699, L178**. *Minor Mergers and the Size Evolution of Elliptical Galaxies*

NANDRA, K., GEORGAKAKIS, A., WILLMER, C. N. A., et al. 2007, Astrophysical Journal, **ApJ**, **660, L11**. *AEGIS: The Color-Magnitude Relation for X-Ray-selected Active Galactic Nuclei*

NAYLOR, T. & JEFFRIES, R. D. 2006, Monthly Notices of the Royal Astronomical Society, **MNRAS**, **373, 1251**. *A maximum-likelihood method for fitting colour-magnitude diagrams*

NEWMAN, A. B., ELLIS, R. S., ANDREON, S., et al. 2014, Astrophysical Journal, **ApJ**, **788, 51**. *Spectroscopic Confirmation of the Rich z = 1.80 Galaxy Cluster JKCS 041 using the WFC3 Grism: Environmental Trends in the Ages and Structure of Quiescent Galaxies*

NEWMAN, A. B., ELLIS, R. S., BUNDY, K., & TREU, T. 2012, Astrophysical Journal, **ApJ**, **746, 162**. *Can Minor Merging Account for the Size Growth of Quiescent Galaxies? New Results from the CANDELS Survey*

NIPOTI, C., TREU, T., LEAUTHAUD, A., et al. 2012, Monthly Notices of the Royal Astronomical Society, **MNRAS**, **422, 1714**. *Size and velocity-dispersion evolution of early-type galaxies in a Λ cold dark matter universe*

NOESKE, K. G., WEINER, B. J., FABER, S. M., et al. 2007, Astrophysical Journal, **ApJ**, **660, L43**. *Star Formation in AEGIS Field Galaxies since z=1.1: The Dominance of Gradually Declining Star Formation, and the Main Sequence of Star-forming Galaxies*

O'CONNELL, R. W. 1976, Astrophysical Journal, **ApJ**, **206, 370**. *Galaxy spectral synthesis. I - Stellar populations in the nuclei of giant ellipticals*

O'CONNELL, R. W. 1980, Astrophysical Journal, **ApJ**, **236, 430**. *Galaxy spectral synthesis. II - M32 and the ages of galaxies*

OCVIRK, P., PICHON, C., LANÇON, A., & THIÉBAUT, E. 2006, Monthly Notices of the Royal Astronomical Society, **MNRAS**, **365, 74**. *STECKMAP: STEllar Content and Kinematics from high resolution galactic spectra via Maximum A Posteriori*

O'DONNELL, J. E. 1994, Astrophysical Journal, **ApJ**, **422, 158**. *R_V-dependent optical and near-ultraviolet extinction*

OESCH, P. A., CAROLLO, C. M., FELDMANN, R., et al. 2010, Astrophysical Journal, **ApJ**, **714, L47**. *The Buildup of the Hubble Sequence in the Cosmos Field*

OKE, J. B. & GUNN, J. E. 1983, Astrophysical Journal, **ApJ**, **266, 713**. *Secondary standard stars for absolute spectrophotometry*

OTEO, I., BONGIOVANNI, Á., CEPA, J., et al. 2013, Monthly Notices of the Royal Astronomical Society, **MNRAS**, **433, 2706**. *Lyman break and ultraviolet-selected galaxies at z ∼ 1 - I. Stellar populations from the ALHAMBRA survey*

PANTER, B., JIMENEZ, R., HEAVENS, A. F., & CHARLOT, S. 2008, Monthly Notices of the Royal Astronomical Society, **MNRAS**, **391, 1117**. *The cosmic evolution of metallicity from the SDSS fossil record*

PAPOVICH, C., MOUSTAKAS, L. A., DICKINSON, M., et al. 2006, Astrophysical Journal, **ApJ**, **640, 92**. *Spitzer Observations of Massive, Red Galaxies at High Redshift*

PATTON, D. R., CARLBERG, R. G., MARZKE, R. O., et al. 2000, Astrophysical Journal, **ApJ**, **536, 153**. *New Techniques for Relating Dynamically Close Galaxy Pairs to Merger and Accretion Rates: Application to the Second Southern Sky Redshift Survey*

PELETIER, R. F. 2013. *XXIII Canary islands winter school of astrophysics. Stellar Populations, ed. J. Falcón-Barroso & J. H. Knapen*

PELETIER, R. F. & VALENTIJN, E. A. 1989, Astrophysics and Space Science, **Ap&SS**, **156, 127**. *Stellar populations as a function of radius in giant elliptical galaxies*

PENG, C. Y., HO, L. C., IMPEY, C. D., & RIX, H.-W. 2002, Astronomical Journal, **AJ**, **124, 266**. *Detailed Structural Decomposition of Galaxy Images*

PENG, Y., MAIOLINO, R., & COCHRANE, R. 2015, **Nature**, **521, 192**. *Strangulation as the primary mechanism for shutting down star formation in galaxies*

PENG, Y.-J., LILLY, S. J., KOVAČ, K., et al. 2010, Astrophysical Journal, **ApJ**, **721, 193**. *Mass and Environment as Drivers of Galaxy Evolution in SDSS and zCOSMOS and the Origin of the Schechter Function*

PÉREZ-GONZÁLEZ, P. G., CAVA, A., BARRO, G., et al. 2013, Astrophysical Journal, **ApJ**, **762, 46**. *SHARDS: An Optical Spectro-photometric Survey of Distant Galaxies*

PÉREZ-GONZÁLEZ, P. G., RIEKE, G. H., VILLAR, V., et al. 2008, Astrophysical Journal, **ApJ**, **675, 234**. *The Stellar Mass Assembly of Galaxies from $z = 0$ to $z = 4$: Analysis of a Sample Selected in the Rest-Frame Near-Infrared with Spitzer*

PICKLES, A. & DEPAGNE, É. 2010, Publications of the ASP, **PASP**, **122, 1437**. *All-Sky Spectrally Matched UBVRI-ZY and u'g'r'i'z' Magnitudes for Stars in the Tycho2 Catalog*

PICKLES, A. J. 1985, Astrophysical Journal, **ApJ**, **296, 340**. *Differential population synthesis of early-type galaxies. III - Synthesis results*

PICKLES, A. J. 1998, Publications of the ASP, **PASP**, **110, 863**. *A Stellar Spectral Flux Library: 1150-25000 Å*

PIETRINFERNI, A., CASSISI, S., SALARIS, M., & CASTELLI, F. 2004, Astrophysical Journal, **ApJ**, **612, 168**. *A Large Stellar Evolution Database for Population Synthesis Studies. I. Scaled Solar Models and Isochrones*

PIETRINFERNI, A., CASSISI, S., SALARIS, M., & CASTELLI, F. 2006, Astrophysical Journal, **ApJ**, **642, 797**. *A Large Stellar Evolution Database for Population Synthesis Studies. II. Stellar Models and Isochrones for an α-enhanced Metal Distribution*

PIPINO, A. & MATTEUCCI, F. 2004, Monthly Notices of the Royal Astronomical Society, **MNRAS**, **347, 968**. *Photochemical evolution of elliptical galaxies - I. The high-redshift formation scenario*

POGGIANTI, B. M., BRIDGES, T. J., CARTER, D., et al. 2001, Astrophysical Journal, **ApJ**, **563, 118**. *Ages of S0 and Elliptical Galaxies in the Coma Cluster*

POGGIANTI, B. M., CALVI, R., BINDONI, D., et al. 2013, Astrophysical Journal, **ApJ**, **762, 77**. *Superdense Galaxies and the Mass-Size Relation at Low Redshift*

POGGIANTI, B. M., SMAIL, I., DRESSLER, A., et al. 1999, Astrophysical Journal, **ApJ**, **518, 576**. *The Star Formation Histories of Galaxies in Distant Clusters*

POSTMAN, M., COE, D., BENÍTEZ, N., et al. 2012, Astrophysical Journal Supplements, **ApJS**, **199, 25**. *The Cluster Lensing and Supernova Survey with Hubble: An Overview*

POVIĆ, M., HUERTAS-COMPANY, M., AGUERRI, J. A. L., et al. 2013, Monthly Notices of the Royal Astronomical Society, **MNRAS**, **435, 3444**. *The ALHAMBRA survey: reliable morphological catalogue of 22 051 early- and late-type galaxies*

POZZETTI, L., BOLZONELLA, M., LAMAREILLE, F., et al. 2007, Astronomy and Astrophysics, **A&A**, **474, 443**. *The VIMOS VLT Deep Survey. The assembly history of the stellar mass in galaxies: from the young to the old universe*

POZZETTI, L., BOLZONELLA, M., ZUCCA, E., et al. 2010, Astronomy and Astrophysics, **A&A**, **523, A13**. *zCOSMOS - 10k-bright spectroscopic sample. The bimodality in the galaxy stellar mass function: exploring its evolution with redshift*

PREVOT, M. L., LEQUEUX, J., PREVOT, L., MAURICE, E., & ROCCA-VOLMERANGE, B. 1984, Astronomy and Astrophysics, **A&A**, **132, 389**. *The typical interstellar extinction in the Small Magellanic Cloud*

PRITCHET, C. 1977, Astrophysical Journal Supplements, **ApJS**, **35, 397**. *Stellar population synthesis of galactic nuclei*

PROCTOR, R. N., FORBES, D. A., & BEASLEY, M. A. 2004, Monthly Notices of the Royal Astronomical Society, **MNRAS**, **355, 1327**. *A robust method for the analysis of integrated spectra from globular clusters using Lick indices*

PRUGNIEL, P. & SOUBIRAN, C. 2001, Astronomy and Astrophysics, **A&A**, **369, 1048**. *A database of high and medium-resolution stellar spectra*

QUILIS, V., MOORE, B., & BOWER, R. 2000, Science, **288, 1617**. *Gone with the Wind: The Origin of S0 Galaxies in Clusters*

QUILIS, V. & TRUJILLO, I. 2012, Astrophysical Journal, **ApJ**, **752, L19**. *Satellites around Massive Galaxies Since $z \sim 2$: Confronting the Millennium Simulation with Observations*

QUILIS, V. & TRUJILLO, I. 2013, Astrophysical Journal, **ApJ**, **773, L8**. *Expected Number of Massive Galaxy Relics in the Present Day Universe*

RAVINDRANATH, S., FERGUSON, H. C., CONSELICE, C., et al. 2004, Astrophysical Journal, **ApJ**, **604, L9**. *The Evolution of Disk Galaxies in the GOODS-South Field: Number Densities and Size Distribution*

REDDY, N. A., STEIDEL, C. C., FADDA, D., et al. 2006, Astrophysical Journal, **ApJ**, **644, 792**. *Star Formation and Extinction in Redshift $z \sim 2$ Galaxies: Inferences from Spitzer MIPS Observations*

RICCIARDELLI, E., VAZDEKIS, A., CENARRO, A. J., & FALCÓN-BARROSO, J. 2012, Monthly Notices of the Royal Astronomical Society, **MNRAS**, **424, 172**. *MIUSCAT: extended MILES spectral coverage - II. Constraints from optical photometry*

RÖCK, B., VAZDEKIS, A., PELETIER, R. F., KNAPEN, J. H., & FALCÓN-BARROSO, J. 2015, Monthly Notices of the Royal Astronomical Society, **MNRAS**, **449, 2853**. *Stellar population synthesis models between 2.5 and 5 μm based on the empirical IRTF stellar library*

RODRIGUES, M., PUECH, M., HAMMER, F., ROTHBERG, B., & FLORES, H. 2012, Monthly Notices of the Royal Astronomical Society, **MNRAS**, **421, 2888**. *A decrease of the gas exchanges between galaxies and the intergalactic medium, from 12 to 6 billion years ago*

ROGERS, B., FERRERAS, I., PELETIER, R., & SILK, J. 2010, Monthly Notices of the Royal Astronomical Society, **MNRAS**, **402, 447**. *Exploring the star formation history of elliptical galaxies: beyond simple stellar populations with a new line strength estimator*

ROMANO, D., SILVA, L., MATTEUCCI, F., & DANESE, L. 2002, Monthly Notices of the Royal Astronomical Society, **MNRAS**, **334, 444**. *Chemical evolution in a model for the joint formation of quasars and spheroids*

RUHLAND, C., BELL, E. F., HÄUSSLER, B., et al. 2009, Astrophysical Journal, **ApJ**, **695, 1058**. *The Evolution of the Scatter of the Cosmic Average Color-Magnitude Relation: Demonstrating Consistency with the Ongoing Formation of Elliptical Galaxies*

RUIZ-LARA, T., PÉREZ, I., GALLART, C., et al. 2015, Astronomy and Astrophysics, **A&A**, **583, A60**. *Recovering star formation histories: Integrated-light analyses vs. stellar colour-magnitude diagrams*

SALPETER, E. E. 1955, Astrophysical Journal, **ApJ**, **121, 161**. *The Luminosity Function and Stellar Evolution.*

SÁNCHEZ, S. F., KENNICUTT, R. C., GIL DE PAZ, A., et al. 2012, Astronomy and Astrophysics, **A&A**, **538, A8**. *CALIFA, the Calar Alto Legacy Integral Field Area survey. I. Survey presentation*

SÁNCHEZ-BLÁZQUEZ, P., FORBES, D. A., STRADER, J., BRODIE, J., & PROCTOR, R. 2007, Monthly Notices of the Royal Astronomical Society, **MNRAS**, **377, 759**. *Spatially resolved spectroscopy of early-type galaxies over a range in mass*

SÁNCHEZ-BLÁZQUEZ, P., GORGAS, J., CARDIEL, N., CENARRO, J., & GONZÁLEZ, J. J. 2003, Astrophysical Journal, **ApJ**, **590, L91**. *Differences in Carbon and Nitrogen Abundances between Field and Cluster Early-Type Galaxies*

SÁNCHEZ-BLÁZQUEZ, P., GORGAS, J., CARDIEL, N., & GONZÁLEZ, J. J. 2006a, Astronomy and Astrophysics, **A&A**, **457, 787**. *Stellar populations of early-type galaxies in different environments. I. Line-strength indices. Relations of line-strengths with σ*

SÁNCHEZ-BLÁZQUEZ, P., GORGAS, J., CARDIEL, N., & GONZÁLEZ, J. J. 2006b, Astronomy and Astrophysics, **A&A**, **457, 809**. *Stellar populations of early-type galaxies in different environments. II. Ages and metallicities*

SÁNCHEZ-BLÁZQUEZ, P., JABLONKA, P., NOLL, S., et al. 2009, Astronomy and Astrophysics, **A&A**, **499, 47**. *Evolution of red-sequence cluster galaxies from redshift 0.8 to 0.4: ages, metallicities, and morphologies*

SÁNCHEZ-BLÁZQUEZ, P., PELETIER, R. F., JIMÉNEZ-VICENTE, J., et al. 2006c, Monthly Notices of the Royal Astronomical Society, **MNRAS**, **371, 703**. *Medium-resolution Isaac Newton Telescope library of empirical spectra*

SANDAGE, A., TAMMANN, G. A., & YAHIL, A. 1979, Astrophysical Journal, **ApJ**, **232, 352**. *The velocity field of bright nearby galaxies. I - The variation of mean absolute magnitude with redshift for galaxies in a magnitude-limited sample*

SANDERS, D. B., SALVATO, M., AUSSEL, H., et al. 2007, Astrophysical Journal Supplements, **ApJS**, **172, 86**. *S-COSMOS: The Spitzer Legacy Survey of the Hubble Space Telescope ACS 2 deg^2 COSMOS Field I: Survey Strategy and First Analysis*

SANTOS, F. C. JR., J., ALLOIN, D., BICA, E., & BONATTO, C. J. 2002, in IAU Symposium, Vol. 207, Extragalactic Star Clusters, ed. D. P. Geisler, E. K. Grebel, & D. Minniti, **727**. *Template Integrated Spectra of Star Clusters*

SARACCO, P., LONGHETTI, M., & GARGIULO, A. 2010, Monthly Notices of the Royal Astronomical Society, **MNRAS**, **408, L21**. *The number density of superdense early-type galaxies at $1 < z < 2$ and the local cluster galaxies*

SAWICKI, M. 2012, Publications of the ASP, **PASP**, **124, 1208**. *SEDfit: Software for Spectral Energy Distribution Fitting of Photometric Data*

SCALO, J. M. 1986, Fundamental Cosmic Physics, **FCPh**, **11, 1**. *The stellar initial mass function*

SCARLATA, C., CAROLLO, C. M., LILLY, S., et al. 2007, Astrophysical Journal Supplements, **ApJS**, **172, 406**. *COSMOS Morphological Classification with the Zurich Estimator of Structural Types (ZEST) and the Evolution Since $z = 1$ of the Luminosity Function of Early, Disk, and Irregular Galaxies*

SCHAWINSKI, K., THOMAS, D., SARZI, M., et al. 2007, Monthly Notices of the Royal Astronomical Society, **MNRAS**, **382, 1415**. *Observational evidence for AGN feedback in early-type galaxies*

SCHAWINSKI, K., VIRANI, S., SIMMONS, B., et al. 2009, Astrophysical Journal, **ApJ**, **692, L19**. *Do Moderate-Luminosity Active Galactic Nuclei Suppress Star Formation?*

SCHECHTER, P. 1976, Astrophysical Journal, **ApJ**, **203, 297**. *An analytic expression for the luminosity function for galaxies.*

SCHIAVON, R. P. 2007, Astrophysical Journal Supplements, **ApJS**, **171, 146**. *Population Synthesis in the Blue. IV. Accurate Model Predictions for Lick Indices and UBV Colors in Single Stellar Populations*

SCHIAVON, R. P., CALDWELL, N., & ROSE, J. A. 2004, Astronomical Journal, **AJ**, **127, 1513**. *The Integrated Spectrum of M67 and the Spectroscopic Age of M32*

SCHIAVON, R. P., FABER, S. M., KONIDARIS, N., et al. 2006, Astrophysical Journal, **ApJ**, **651, L93**. *The DEEP2 Galaxy Redshift Survey: Mean Ages and Metallicities of Red Field Galaxies at $z \sim 0.9$ from Stacked Keck DEIMOS Spectra*

SCHIMINOVICH, D., WYDER, T. K., MARTIN, D. C., et al. 2007, Astrophysical Journal Supplements, **ApJS**, **173, 315**. *The UV-Optical Color Magnitude Diagram. II. Physical Properties and Morphological Evolution On and Off of a Star-forming Sequence*

SCHLAFLY, E. F. & FINKBEINER, D. P. 2011, Astrophysical Journal, **ApJ**, **737, 103**. *Measuring Reddening with Sloan Digital Sky Survey Stellar Spectra and Recalibrating SFD*

SCHLEGEL, D. J., FINKBEINER, D. P., & DAVIS, M. 1998, Astrophysical Journal, **ApJ**, **500, 525**. *Maps of Dust Infrared Emission for Use in Estimation of Reddening and Cosmic Microwave Background Radiation Foregrounds*

SCHMIDT, M. 1968, Astrophysical Journal, **ApJ**, **151, 393**. *Space Distribution and Luminosity Functions of Quasi-Stellar Radio Sources*

SCHWEIZER, F. & SEITZER, P. 1992, Astronomical Journal, **AJ**, **104, 1039**. *Correlations between UBV colors and fine structure in E and S0 galaxies - A first attempt at dating ancient merger events*

SCOVILLE, N., ARNOUTS, S., AUSSEL, H., et al. 2013, Astrophysical Journal Supplements, **ApJS**, **206, 3**. *Evolution of Galaxies and Their Environments at z = 0.1-3 in COSMOS*

SCOVILLE, N., AUSSEL, H., BRUSA, M., et al. 2007, Astrophysical Journal Supplements, **ApJS**, **172, 1**. *The Cosmic Evolution Survey (COSMOS): Overview*

SEARLE, L., SARGENT, W. L. W., & BAGNUOLO, W. G. 1973, Astrophysical Journal, **ApJ**, **179, 427**. *The History of Star Formation and the Colors of Late-Type Galaxies*

SERRA, P. & TRAGER, S. C. 2007, Monthly Notices of the Royal Astronomical Society, **MNRAS**, **374, 769**. *On the interpretation of the age and chemical composition of composite stellar populations determined with line-strength indices*

SERSIC, J. L. 1968. *Atlas de galaxias australes*

SHANKAR, F. & BERNARDI, M. 2009, Monthly Notices of the Royal Astronomical Society, **MNRAS**, **396, L76**. *The age dependence of the size-stellar mass relation and some implications*

SHEN, S., MO, H. J., WHITE, S. D. M., et al. 2003, Monthly Notices of the Royal Astronomical Society, **MNRAS**, **343, 978**. *The size distribution of galaxies in the Sloan Digital Sky Survey*

SHETH, K., VOGEL, S. N., REGAN, M. W., THORNLEY, M. D., & TEUBEN, P. J. 2005, Astrophysical Journal, **ApJ**, **632, 217**. *Secular Evolution via Bar-driven Gas Inflow: Results from BIMA SONG*

SILK, J. & REES, M. J. 1998, Astronomy and Astrophysics, **A&A**, **331, L1**. *Quasars and galaxy formation*

SILVERMAN, J. D., MAINIERI, V., LEHMER, B. D., et al. 2008, Astrophysical Journal, **ApJ**, **675, 1025**. *The Evolution of AGN Host Galaxies: From Blue to Red and the Influence of Large-Scale Structures*

SIUDEK, M., MAŁEK, K., SCODEGGIO, M., et al. 2016, **ArXiv e-prints, 1605.05503**. *The VIMOS Public Extragalactic Redshift Survey (VIPERS). Star formation history of passive galaxies*

SKELTON, R. E., BELL, E. F., & SOMERVILLE, R. S. 2012, Astrophysical Journal, **ApJ**, **753, 44**. *Modeling the Red Sequence: Hierarchical Growth yet Slow Luminosity Evolution*

SOMERVILLE, R. S., HOPKINS, P. F., COX, T. J., ROBERTSON, B. E., & HERNQUIST, L. 2008, Monthly Notices of the Royal Astronomical Society, **MNRAS**, **391, 481**. *A semi-analytic model for the co-evolution of galaxies, black holes and active galactic nuclei*

SOMERVILLE, R. S. & PRIMACK, J. R. 1999, Monthly Notices of the Royal Astronomical Society, **MNRAS**, **310, 1087**. *Semi-analytic modelling of galaxy formation: the local Universe*

SPINIELLO, C., TRAGER, S. C., KOOPMANS, L. V. E., & CHEN, Y. P. 2012, Astrophysical Journal, **ApJ**, **753, L32**. *Evidence for a Mild Steepening and Bottom-heavy Initial Mass Function in Massive Galaxies from Sodium and Titanium-oxide Indicators*

SPINRAD, H. & TAYLOR, B. J. 1971, Astrophysical Journal Supplements, **ApJS**, **22, 445**. *The Stellar Content of the Nuclei of Nearby Galaxies. I. M31, M32, and M81*

SPRINGEL, V., WHITE, S. D. M., JENKINS, A., et al. 2005, **Nature**, **435, 629**. *Simulations of the formation, evolution and clustering of galaxies and quasars*

STONE, R. P. S. 1996, Astrophysical Journal Supplements, **ApJS**, **107, 423**. *Spectrophotometry of Flux Calibration Stars for Hubble Space Telescope*

STOUGHTON, C., LUPTON, R. H., BERNARDI, M., et al. 2002, Astronomical Journal, **AJ**, **123, 485**. *Sloan Digital Sky Survey: Early Data Release*

STRATEVA, I., IVEZIĆ, Ž., KNAPP, G. R., et al. 2001, Astronomical Journal, **AJ**, **122, 1861**. *Color Separation of Galaxy Types in the Sloan Digital Sky Survey Imaging Data*

TAYLOR, E. N., FRANX, M., GLAZEBROOK, K., et al. 2010, Astrophysical Journal, **ApJ**, **720, 723**. *On the Dearth of Compact, Massive, Red Sequence Galaxies in the Local Universe*

THEIS, C., BURKERT, A., & HENSLER, G. 1992, Astronomy and Astrophysics, **A&A**, **265, 465**. *Chemo-dynamical evolution of massive spherical galaxies*

THOMAS, D., GREGGIO, L., & BENDER, R. 1999, Monthly Notices of the Royal Astronomical Society, **MNRAS**, **302, 537**. *Constraints on galaxy formation from α-enhancement in luminous elliptical galaxies*

THOMAS, D., MARASTON, C., & BENDER, R. 2003, Monthly Notices of the Royal Astronomical Society, **MNRAS**, **339, 897**. *Stellar population models of Lick indices with variable element abundance ratios*

THOMAS, D., MARASTON, C., BENDER, R., & MENDES DE OLIVEIRA, C. 2005, Astrophysical Journal, **ApJ**, **621, 673**. *The Epochs of Early-Type Galaxy Formation as a Function of Environment*

THOMAS, D., MARASTON, C., & JOHANSSON, J. 2011, Monthly Notices of the Royal Astronomical Society, **MNRAS**, **412, 2183**. *Flux-calibrated stellar population models of Lick absorption-line indices with variable element abundance ratios*

THOMAS, D., MARASTON, C., SCHAWINSKI, K., SARZI, M., & SILK, J. 2010, Monthly Notices of the Royal Astronomical Society, **MNRAS**, **404, 1775**. *Environment and self-regulation in galaxy formation*

TIFFT, W. G. 1963, Astronomical Journal, **AJ**, **68, 302**. *Multicolor photoelectric photometry of bright galaxies*

TINSLEY, B. M. 1968, Astrophysical Journal, **ApJ**, **151, 547**. *Evolution of the Stars and Gas in Galaxies*

TINSLEY, B. M. 1972, Astronomy and Astrophysics, **A&A**, **20, 383**. *Galactic Evolution*

TINSLEY, B. M. 1978, Astrophysical Journal, **ApJ**, **222, 14**. *Evolutionary synthesis of the stellar population in elliptical galaxies. II - Late M giants and composition effects*

TINSLEY, B. M. & GUNN, J. E. 1976, Astrophysical Journal, **ApJ**, **203, 52**. *Evolutionary synthesis of the stellar population in elliptical galaxies. I - Ingredients, broad-band colors, and infrared features*

TOFT, S., VAN DOKKUM, P., FRANX, M., et al. 2007, Astrophysical Journal, **ApJ**, **671, 285**. *Hubble Space Telescope and Spitzer Imaging of Red and Blue Galaxies at $z \sim 2.5$: A Correlation between Size and Star Formation Activity from Compact Quiescent Galaxies to Extended Star-forming Galaxies*

TOJEIRO, R., HEAVENS, A. F., JIMENEZ, R., & PANTER, B. 2007, Monthly Notices of the Royal Astronomical Society, **MNRAS**, **381, 1252**. *Recovering galaxy star formation and metallicity histories from spectra using VESPA*

TOLOBA, E., GUHATHAKURTA, P., PELETIER, R. F., et al. 2014, Astrophysical Journal Supplements, **ApJS**, **215, 17**. *Stellar Kinematics and Structural Properties of Virgo Cluster Dwarf Early-type Galaxies from the SMAKCED Project. II. The Survey and a Systematic Analysis of Kinematic Anomalies and Asymmetries*

TOLSTOY, E., HILL, V., & TOSI, M. 2009, Annual Review of Astronomy and Astrophysics, **ARA&A**, **47, 371**. *Star-Formation Histories, Abundances, and Kinematics of Dwarf Galaxies in the Local Group*

TOMCZAK, A. R., QUADRI, R. F., TRAN, K.-V. H., et al. 2014, Astrophysical Journal, **ApJ**, **783, 85**. *Galaxy Stellar Mass Functions from ZFOURGE/CANDELS: An Excess of Low-mass Galaxies since $z = 2$ and the Rapid Buildup of Quiescent Galaxies*

TOOMRE, A. 1977, in Evolution of Galaxies and Stellar Populations, ed. B. M. Tinsley & R. B. G. Larson, D. Campbell, **401**. *Mergers and Some Consequences*

TOSI, M. 1988, Astronomy and Astrophysics, **A&A**, **197, 33**. *Models of galactic chemical evolution - The problem of uniqueness*

TRAGER, S. C., FABER, S. M., & DRESSLER, A. 2008, Monthly Notices of the Royal Astronomical Society, **MNRAS**, **386, 715**. *The stellar population histories of early-type galaxies - III. The Coma cluster*

TRAGER, S. C., FABER, S. M., WORTHEY, G., & GONZÁLEZ, J. J. 2000, Astronomical Journal, **AJ**, **120, 165**. *The Stellar Population Histories of Early-Type Galaxies. II. Controlling Parameters of the Stellar Populations*

TRAGER, S. C., WORTHEY, G., FABER, S. M., BURSTEIN, D., & GONZÁLEZ, J. J. 1998, Astrophysical Journal Supplements, **ApJS**, **116, 1**. *Old Stellar Populations. VI. Absorption-Line Spectra of Galaxy Nuclei and Globular Clusters*

TREMONTI, C. A., HECKMAN, T. M., KAUFFMANN, G., et al. 2004, Astrophysical Journal, **ApJ**, **613, 898**. *The Origin of the Mass-Metallicity Relation: Insights from 53,000 Star-forming Galaxies in the Sloan Digital Sky Survey*

TRUJILLO, I., CARRASCO, E. R., & FERRÉ-MATEU, A. 2012, Astrophysical Journal, **ApJ**, **751, 45**. *Ultra-deep Sub-kiloparsec View of nearby Massive Compact Galaxies*

TRUJILLO, I., CENARRO, A. J., DE LORENZO-CÁCERES, A., et al. 2009, Astrophysical Journal, **ApJ**, **692, L118**. *Superdense Massive Galaxies in the Nearby Universe*

TRUJILLO, I., CONSELICE, C. J., BUNDY, K., et al. 2007, Monthly Notices of the Royal Astronomical Society, **MNRAS**, **382, 109**. *Strong size evolution of the most massive galaxies since $z \sim 2$*

TRUJILLO, I., FERRÉ-MATEU, A., BALCELLS, M., VAZDEKIS, A., & SÁNCHEZ-BLÁZQUEZ, P. 2014, Astrophysical Journal, **ApJ**, **780, L20**. *NGC 1277: A Massive Compact Relic Galaxy in the Nearby Universe*

TRUJILLO, I., FERRERAS, I., & DE LA ROSA, I. G. 2011, Monthly Notices of the Royal Astronomical Society, **MNRAS**, **415, 3903**. *Dissecting the size evolution of elliptical galaxies since $z \sim 1$: puffing-up versus minor-merging scenarios*

TRUJILLO, I., FEULNER, G., GORANOVA, Y., et al. 2006a, Monthly Notices of the Royal Astronomical Society, **MNRAS**, **373, L36**. *Extremely compact massive galaxies at $z \sim 1.4$*

TRUJILLO, I., FÖRSTER SCHREIBER, N. M., RUDNICK, G., et al. 2006b, Astrophysical Journal, **ApJ**, **650, 18**. *The Size Evolution of Galaxies since $z \sim 3$: Combining SDSS, GEMS, and FIRES*

TRUJILLO, I., RUDNICK, G., RIX, H.-W., et al. 2004, Astrophysical Journal, **ApJ**, **604, 521**. *The Luminosity-Size and Mass-Size Relations of Galaxies out to $z \sim 3$*

VALDES, F., GUPTA, R., ROSE, J. A., SINGH, H. P., & BELL, D. J. 2004, Astrophysical Journal Supplements, **ApJS**, **152, 251**. *The Indo-US Library of Coudé Feed Stellar Spectra*

VALENTINUZZI, T., POGGIANTI, B. M., SAGLIA, R. P., et al. 2010, Astrophysical Journal, **ApJ**, **721, L19**. *Superdense Massive Galaxies in the ESO Distant Cluster Survey (EDisCS)*

VAN DER WEL, A., BELL, E. F., HÄUSSLER, B., et al. 2012, Astrophysical Journal Supplements, **ApJS**, **203, 24**. *Structural Parameters of Galaxies in CANDELS*

VAN DER WEL, A., FRANX, M., VAN DOKKUM, P. G., et al. 2014, Astrophysical Journal, **ApJ**, **788, 28**. *3D-HST+CANDELS: The Evolution of the Galaxy Size-Mass Distribution since $z = 3$*

VAN DER WEL, A., RIX, H.-W., HOLDEN, B. P., BELL, E. F., & ROBAINA, A. R. 2009, Astrophysical Journal, **ApJ**, **706, L120**. *Major Merging: The Way to Make a Massive, Passive Galaxy*

VAN DOKKUM, P. G. & CONROY, C. 2010, **Nature**, **468, 940**. *A substantial population of low-mass stars in luminous elliptical galaxies*

VAN DOKKUM, P. G. & FRANX, M. 2001, Astrophysical Journal, **ApJ**, **553, 90**. *Morphological Evolution and the Ages of Early-Type Galaxies in Clusters*

VAN DOKKUM, P. G., FRANX, M., KRIEK, M., et al. 2008, Astrophysical Journal, **ApJ**, **677, L5**. *Confirmation of the Remarkable Compactness of Massive Quiescent Galaxies at $z \sim 2.3$: Early-Type Galaxies Did not Form in a Simple Monolithic Collapse*

VAZDEKIS, A. 1999a, Astrophysical Journal, **ApJ**, **513, 224**. *Evolutionary Stellar Population Synthesis at 2 Å Spectral Resolution*

VAZDEKIS, A. & ARIMOTO, N. 1999b, Astrophysical Journal, **ApJ**, **525, 144**. *A Robust Age Indicator for Old Stellar Populations*

VAZDEKIS, A., CASUSO, E., PELETIER, R. F., & BECKMAN, J. E. 1996, Astrophysical Journal Supplements, **ApJS**, **106, 307**. *A New Chemo-evolutionary Population Synthesis Model for Early-Type Galaxies. I. Theoretical Basis*

VAZDEKIS, A., CENARRO, A. J., GORGAS, J., CARDIEL, N., & PELETIER, R. F. 2003, Monthly Notices of the Royal Astronomical Society, **MNRAS**, **340, 1317**. *Empirical calibration of the near-infrared CaII triplet - IV. The stellar population synthesis models*

VAZDEKIS, A., COELHO, P., CASSISI, S., et al. 2015, Monthly Notices of the Royal Astronomical Society, **MNRAS**, **449, 1177**. *Evolutionary stellar population synthesis with MILES - II. Scaled-solar and α-enhanced models*

VAZDEKIS, A., KOLEVA, M., RICCIARDELLI, E., RÖCK, B., & FALCÓN-BARROSO, J. 2016, Monthly Notices of the Royal Astronomical Society, **MNRAS**, **463, 3409**. *UV-extended E-MILES stellar population models: young components in massive early-type galaxies*

VAZDEKIS, A., RICCIARDELLI, E., CENARRO, A. J., et al. 2012, Monthly Notices of the Royal Astronomical Society, **MNRAS**, **424, 157**. *MIUSCAT: extended MILES spectral coverage - I. Stellar population synthesis models*

VAZDEKIS, A., SÁNCHEZ-BLÁZQUEZ, P., FALCÓN-BARROSO, J., et al. 2010, Monthly Notices of the Royal Astronomical Society, **MNRAS**, **404, 1639**. *Evolutionary stellar population synthesis with MILES - I. The base models and a new line index system*

VERGANI, D., SCODEGGIO, M., POZZETTI, L., et al. 2008, Astronomy and Astrophysics, **A&A**, **487, 89**. *The VIMOS VLT Deep Survey. Tracing the galaxy stellar mass assembly history over the last 8 Gyr*

VIIRONEN, K., MARÍN-FRANCH, A., LÓPEZ-SANJUAN, C., et al. 2015, Astronomy and Astrophysics, **A&A**, **576, A25**. *High redshift galaxies in the ALHAMBRA survey . I. Selection method and number counts based on redshift PDFs*

WAKE, D. A., SHETH, R. K., NICHOL, R. C., et al. 2008, Monthly Notices of the Royal Astronomical Society, **MNRAS**, **387, 1045**. *The 2dF-SDSS LRG and QSO Survey: evolution of the clustering of luminous red galaxies since $z = 0.6$*

WALCHER, J., GROVES, B., BUDAVÁRI, T., & DALE, D. 2011, Astrophysics and Space Science, **Ap&SS**, **331, 1**. *Fitting the integrated spectral energy distributions of galaxies*

WEIDNER, C., FERRERAS, I., VAZDEKIS, A., & LA BARBERA, F. 2013, Monthly Notices of the Royal Astronomical Society, **MNRAS**, **435, 2274**. *The (galaxy-wide) IMF in giant elliptical galaxies: from top to bottom*

WESTERA, P., LEJEUNE, T., BUSER, R., CUISINIER, F., & BRUZUAL, G. 2002, Astronomy and Astrophysics, **A&A**, **381, 524**. *A standard stellar library for evolutionary synthesis. III. Metallicity calibration*

WHITAKER, K. E., LABBÉ, I., VAN DOKKUM, P. G., et al. 2011, Astrophysical Journal, **ApJ**, **735, 86**. *The NEWFIRM Medium-band Survey: Photometric Catalogs, Redshifts, and the Bimodal Color Distribution of Galaxies out to $z \sim 3$*

WHITAKER, K. E., VAN DOKKUM, P. G., BRAMMER, G., et al. 2010, Astrophysical Journal, **ApJ**, **719, 1715**. *The Age Spread of Quiescent Galaxies with the NEWFIRM Medium-band Survey: Identification of the Oldest Galaxies Out to $z \sim 2$*

WHITAKER, K. E., VAN DOKKUM, P. G., BRAMMER, G., et al. 2013, Astrophysical Journal, **ApJ**, **770, L39**. *Quiescent Galaxies in the 3D-HST Survey: Spectroscopic Confirmation of a Large Number of Galaxies with Relatively Old Stellar Populations at $z \sim 2$*

WHITE, M., ZHENG, Z., BROWN, M. J. I., DEY, A., & JANNUZI, B. T. 2007, Astrophysical Journal, **ApJ**, **655, L69**. *Evidence for Merging or Disruption of Red Galaxies from the Evolution of Their Clustering*

WHITE, S. D. M., FRENK, C. S., DAVIS, M., & EFSTATHIOU, G. 1987, Astrophysical Journal, **ApJ**, **313, 505**. *Clusters, filaments, and voids in a universe dominated by cold dark matter*

WHITFORD, A. E. 1978, Astrophysical Journal, **ApJ**, **226, 777**. *Spectral scans of the nuclear bulge of the Galaxy - Comparison with other galaxies*

WILKINSON, D. M., MARASTON, C., THOMAS, D., et al. 2015, Monthly Notices of the Royal Astronomical Society, **MNRAS**, **449, 328**. *P-MaNGA: full spectral fitting and stellar population maps from prototype observations*

WILLIAMS, C. C., GIAVALISCO, M., BEZANSON, R., et al. 2016, **ArXiv e-prints, 1607.06089**. *Morphology Dependence Of Stellar Age in Quenched Galaxies at Redshift ~ 1.2: Massive Compact Galaxies Are Older Than More Extended Ones*

WILLIAMS, R. J., QUADRI, R. F., FRANX, M., VAN DOKKUM, P., & LABBÉ, I. 2009, Astrophysical Journal, **ApJ**, **691, 1879**. *Detection of Quiescent Galaxies in a Bicolor Sequence from $z = 0$–2*

WILLMER, C. N. A., FABER, S. M., KOO, D. C., et al. 2006, Astrophysical Journal, **ApJ**, **647, 853**. *The Deep Evolutionary Exploratory Probe 2 Galaxy Redshift Survey: The Galaxy Luminosity Function to $z \sim 1$*

WOLF, C., MEISENHEIMER, K., KLEINHEINRICH, M., et al. 2004, Astronomy and Astrophysics, **A&A**, **421, 913**. *A catalogue of the Chandra Deep Field South with multi-colour classification and photometric redshifts from COMBO-17*

WOLF, C., MEISENHEIMER, K., RIX, H.-W., et al. 2003, Astronomy and Astrophysics, **A&A**, **401, 73**. *The COMBO-17 survey: Evolution of the galaxy luminosity function from 25 000 galaxies with $0.2 < z < 1.2$*

WOOD, D. B. 1966, Astrophysical Journal, **ApJ**, **145, 36**. *Multicolor Photoelectric Photometry of Galaxies*

WORTHEY, G. 1994a, Astrophysical Journal Supplements, **ApJS**, **95, 107**. *Comprehensive stellar population models and the disentanglement of age and metallicity effects*

WORTHEY, G., FABER, S. M., GONZALEZ, J. J., & BURSTEIN, D. 1994b, Astrophysical Journal Supplements, **ApJS**, **94, 687**. *Old stellar populations. 5: Absorption feature indices for the complete LICK/IDS sample of stars*

WORTHEY, G. & OTTAVIANI, D. L. 1997, Astrophysical Journal Supplements, **ApJS**, **111, 377**. *$H\gamma$ and $H\delta$ Absorption Features in Stars and Stellar Populations*

WU, H., SHAO, Z., MO, H. J., XIA, X., & DENG, Z. 2005, Astrophysical Journal, **ApJ**, **622, 244**. *Optical and Near-Infrared Color Profiles in Nearby Early-Type Galaxies and the Implied Age and Metallicity Gradients*

WYDER, T. K., MARTIN, D. C., SCHIMINOVICH, D., et al. 2007, Astrophysical Journal Supplements, **ApJS**, **173, 293**. *The UV-Optical Galaxy Color-Magnitude Diagram. I. Basic Properties*

XU, C. K., ZHAO, Y., SCOVILLE, N., et al. 2012, Astrophysical Journal, **ApJ**, **747, 85**. *Major-merger Galaxy Pairs in the COSMOS Field–Mass-dependent Merger Rate Evolution since $z = 1$*

YI, S. K., KIM, Y.-C., & DEMARQUE, P. 2003, Astrophysical Journal Supplements, **ApJS**, **144, 259**. *The Y^2 Stellar Evolutionary Tracks*

ZHENG, X. Z., BELL, E. F., PAPOVICH, C., et al. 2007, Astrophysical Journal, **ApJ**, **661, L41**. *The Dependence of Star Formation on Galaxy Stellar Mass*

ZHENG, Z., WANG, H., GE, J., et al. 2016, **ArXiv e-prints, 1612.01523**. *SDSS-IV MaNGA: environmental dependence of stellar age and metallicity gradients in nearby galaxies*

ZIRM, A. W., VAN DER WEL, A., FRANX, M., et al. 2007, Astrophysical Journal, **ApJ**, **656, 66**. *NICMOS Imaging of DRGs in the HDF-S: A Relation between Star Formation and Size at $z \sim 2.5$*

Acronym list

2D . . . . . Two-dimensional

ACS . . . . . Advanced Camera for Surveys

AEGIS . . . . . The All-Wavlength Extended Groth Strip International Survey

AGB . . . . . The Asymptotic Giant Branch

AGN . . . . . Active Galactic Nuclei

ALHAMBRA . Advanced Large Homogeneous Area Medium Band Redshift Astronomical Survey

BaSTI . . . . . Stellar isochrones by Pietrinferni et al. (2004) included in EMILES

BC03 . . . . . Bruzual & Charlot (2003)

BCG . . . . . Brightest Cluster Galaxy

BI . . . . . Bimodal initial mass function

BI1.0 . . . . . Bimodal initial mass function with slope 1.0. Others values can be found.

BPZ . . . . . Bayesian Photometric Redshift code

CAHA . . . . . Calar Alto Observatory

CALIFA . . . . . The Calar Alto Legacy Integral Field Area

CANDELS . . . . Cosmic Assembly Near-infrared Deep Extragalactic Legacy Survey

CCD . . . . . Charge-coupled Devices

CDF . . . . . Cumulative Distribution Function

CEFCA . . . . . Centro de Estudios de Física del Cosmos de Aragón

CFHT . . . . . Canada-Hawai-France Telescope

CLASH . . . . . Cluster Lensing and Supernova Survey with Hubble

CMD . . . . . Colour–magnitude Diagram

COMBO-17 ... Classifying Objects by Medium-Band Observations

COSMOS ..... Cosmological Evolution Survey

CVT..... Centroidal Voronoi Tessellation

DEEP2 ..... Deep Extragalactic Evolutionary Probe 2

DEIMOS ..... Deep Imaging Multi-Object Spectrograph

DSF..... Dusty Star Forming galaxies

E-CDFS ..... Extended Chandra Deep Field South

EAZY ..... Easy and Accurate z-phot from Yale

EGS..... Extended Groth Strip

ESO..... European Southern Observatory

EW..... Equivalent Width

FAST..... Fitting and Assessment of Synthetic Templates

FOV..... Field of View

FWHM ..... Full Width at Half Maximum

G05 ..... Gallazzi et al. (2005)

GMOS ..... Gemini Multi Object Spectrograph

GOODS-N .... The Great Observatories Origins Deep Survey North

HR ..... Hertzsprung–Russell diagrams

HST..... *Hubble* Space Telescope

IFU ..... Integral Field Unit

IMF..... Initial Mass Function

IR ..... Infrared

IRAC..... The Infrared Array Camera

ISM ..... Interstellar Medium

J-PAS ..... Javalambre Physics of the Accelerating Universe

J-PLUS..... Javalambre Photometric Local Universe Survey

JHU ..... Johns Hopkins University

KS ..... Kolmogorov–Smirnov test

LAICA..... Large Area Imager For Calar Alto

ΛCDM ..... Lambda-Cold Dark Matter

LE PHARE .... Photometric Analysis for redshift estimations code

LINER ..... Low-Ionization Nuclear Emission-line Region

LOESS ..... Locally Weighted regression

LRIS ..... The Low Resolution Imaging Spectrometer

M32 ..... Messier 32 galaxy

MaNGA ..... Mapping Nearby Galaxies at Apache Point Observatory

MASSIV ..... Mass Assembly Survey with SINFONI in VVDS

MCMC ..... Markov chain Monte Carlo method

MF ..... Stellar Mass Function

MILES ..... Medium-resolution Isaac Newton Telescope of Empirical Spectra

MIR ..... Mid-infrared

MLE ..... Maximum Likelihood Estimator method

MPA ..... Max Planck Institute for Astrophysics

MQ12 ..... Mármol-Queraltó et al. (2012)

MSSL ..... Mullar Space Sciencie Laboratory

MUFFIT ..... MUlti-Filter FITting code for stellar population diagnostics

MUSYC ..... Multiwavelength Survey by Yale-Chile

MW ..... Milky Way

MZR ..... Stellar-mass Metallicity Relation

NGSL ..... Next Generation Spectral Library

NIR ..... Near-infrared

Padova00 ..... Stellar isochrones by Girardi et al. (2000) included in EMILES

PDF ..... Probability Distribution Function

POWIR ..... Palomar Observatory Wide-field Infrared

PSF ..... Point Spread Function

QSO ..... Quasi-stellar Object or quasar

RAS ..... Royal Astronomical Society

RMS ..... Root Mean Square

RS ..... Red Sequence

SAURON ..... Spectroscopic Areal Unit for Research on Optical Nebulae

SDSS ..... Sloan Digital Sky Survey

SED ..... Spectral Energy Distribution

SFD . . . . . Schlegel et al. (1998) dust maps

SFH . . . . . Star Formation History

SFR . . . . . Star Formation Rate

SHARDS . . . . . Survey for High-z Absorption Red and Dead Sources

SMAKCED . . . . Stellar content MAss and Kinematics of Cluster Early-type Dwarf galaxies

SN . . . . . Supernovae

SPH . . . . . Smoothed Particle Hydrodynamics

SQL . . . . . Structured Query Language

SSAG . . . . . Synthetic Spectral Atlas of Galaxies

sSFR . . . . . Specific Star Formation Rate

SSP . . . . . Single Stellar Population

STECKMAP . . Stellar Content and Kinematics from high resolution galactic spectra via Maximum A Posteriori

STY . . . . . Sandage et al. (1979) method for deriving stellar mass functions

T07 . . . . . Trujillo et al. (2007)

TS . . . . . t-Student test

ULySS . . . . . University of Lyon Spectroscopic Analysis Software

UV . . . . . Ultraviolet

VESPA . . . . . Versatile Spectral Analysis

VIMOS . . . . . VIsible Multi-Object Spectrograph

VIPERS . . . . . VIMOS Public Extragalactic Survey

VLT . . . . . Very Large Telescope

WFC3 . . . . . The low-resolution Wide Field Camera

WHT . . . . . William Herschel Telescope

ZAMS . . . . . Zero Age Main Sequence

ZEST+ . . . . . Zurich estimator of structural types plus